Trends in C-H bond dehydrogenation energetics for small molecule conversion

by

Karthik Akkiraju

B.Tech (Hons.), M.Tech,

Metallurgical and Materials Engineering,
Indian Institute of Technology Madras, 2015

Submitted to the Department of Materials Science and Engineering
in Partial Fulfillment of the Requirements for the Degree of

DOCTOR OF PHILOSOPHY
IN MATERIALS SCIENCE AND ENGINEERING

at the

Massachusetts Institute of Technology

February 2022

Signature of Author: _____

Department of Materials Science and Engineering,
December 20, 2021

Certified by: _____

Yang Shao-Horn
JR East Professor of Energy
Thesis Supervisor

Accepted by: _____

Frances Ross
Ellen Swallow Richards Professor in Materials Science and Engineer
Chair, Department Committee on Graduate Studies

Trends in C-H bond dehydrogenation energetics for small molecule conversion

by

Karthik Akkiraju

Submitted to the Department of Materials Science and Engineering on December 20th, 2021, in partial fulfillment of the requirements for the degree of Doctor of Philosophy

Abstract

Low-temperature activation of C-H bonds and the conversion of C-H bond containing small molecules has remained a holy grail of chemical reactions over the past few decades. The design of materials to maximize product selectivity for wide–ranging energy and environmental applications is typically carried out by a creating of small library of materials. Optimal catalysts are identified by a series of measurements, and in most cases the underlying reaction mechanism is not well understood leading to difficulty in designing future catalysts. Systematic studies have to be carried out in order to investigate the catalyst surface under reaction conditions to probe the nature of reaction intermediates as well as the products of the reaction.

In this thesis, we studied the interaction of small molecules such as formaldehyde, methanol, methane, and propane with oxide surfaces to reveal trends in adsorption energies, product selectivity, and reaction rates. We achieve this by developing suitable design descriptors by studying the reaction mechanism *in situ*. We first generated a library of manganese oxide catalysts to probe the reaction mechanism for formaldehyde oxidation to CO_2 at room temperature. We identified γ-MnO_x to have one of the highest reaction rates for formaldehyde oxidation and show that catalytic activity can further be improved by the addition of water. We then show that room temperature selective methanol oxidation towards methyl formate and methane oxidation to CO_2 can be realized by increasing the surface oxygen activity of iridium oxide-based catalysts. We further developed a rational design approach for perovskite oxides by tuning the surface O $2p$-band center to selectively oxidize methanol to formaldehyde. Finally, we extended this descriptor-based approach for oxidative dehydrogenation of propane to propene. Thus, using a combination of kinetic measurements, surface sensitive *in situ* techniques, and theoretical calculations, we show how catalyst surface can be designed to optimize product selectivity.

Thesis Supervisor: Prof. Yang Shao-Horn
Title: JR East Professor of Energy

Dedicated to Red Bull, potatoes, and hot pot.
Life without you is meaningless.

Acknowledgements

The work described in this thesis spanning over the years was a fun-filled roller coaster ride with many amazing folks who I was lucky enough to share this adventure with.

None of this work or any of my skills would have existed without Yang's commitment towards mentoring and training me. The sheer numbers of meetings, chats, dinners, and emails have not only shaped this thesis but also the way I think and approach life. Her methodology of questioning underlying assumptions, rigor for consistency, and care for ensuring that I always had veggie options have been constant motivators through the years.

Next, I would like to thank my committee members, Prof. Grossman and Prof. Jaramillo, for their insightful comments during the committee meetings. Their remarks have not only opened up new avenues of research but also a unique perspective to look at the work described here.

I am thankful to Jonathan, Reshma, Yirui, Jackie, John, and Ding-Yuan for sharing shift duties and taking walks up and down the Berkeley hill with me. I am quite grateful to all my collaborators for sharing a similar vision to understand the nitty-gritty details described in the work here. I would like to convey my sincere appreciation to David and Wolfgang from BASF for patiently sitting through my slides. Also to Jinhu, Gregor, and Annette from FHI, Ding-Yuan, John, and Jin from Cornell, Dane and Ryan from UW-Madison for being kind enough to share their research expertise with me. I would like to thank Ethan and Hendrik from ALS for all their help in planning experiments and the invaluable advice as we spent hours troubleshooting.

The warm and collegiate atmosphere at EEL is the biggest reason for me having spent more time in the lab than in my apartment. It definitely started with Joe who was both my mentor and office mate. His professional yet friendly methods are something that I aspire to possess and would wish the best for his future endeavors. Reshma and Jonathan have been my longest serving office mates, mentors, partners-in-crime, buddies, road-trippers, and beyond. I cannot imagine what directions my life would have taken without their friendship and support. I also happy to have had the privilege of fighting temperature wars with Graham and then settling scores by going to lunch right after. I would also like to thank Jackie for sharing high impact gossip on demand. And just when I thought I had spent enough time in the lab, Daniele made the final leg of grad school even better with his quality parties. I am also grateful to Manuel for introducing me to DFT as well as to Livia for the numerous lunches to ponder over what trends meant.

Life is lab would have been as fun if it not were for the innumerable lunches and outings with Nenian, Kiarash, Jiayu, Sarah, Yirui, Yang, Pinar, Shuting, Yunguang, Thaneer, Jiayu, Botao, Nicolo, Daniel, Jeff, Shuai, Bin, Yu, Juan, Marcel, Dongwook, Chris, Patrick, Luke, Kakuya, Baba, Pierre, Nir, Seiha, Alex, Michal, Kwabi, and Wesley. I have also had a chance to work with Dan and Jim from EHS, Angelita from DMSE, Brian from facilities and am thankful to them for helping me to set up instruments in the lab safely.

My interest for research would not have lasted for so long if not for the encouragement I got as I got started. I would like to thank Prof. Murty and Prof. Bichler as well as amazing friends at

IITM including Koundinya, Niraj, Ajeet, Ameey as well as Karen, Audrey, Juan, and Vishank at UBC.

Outside of lab, I have been extremely fortunate to have wonderful roommates over the years, including Ethan, Peter, Robin, Stephen, Peter, Diego, Tristan who were kind enough to be okay with my absurd timings. Also, I am quite thankful to the wonderful people at GSC (Michael, Somu, Xueying, Sarah), GMC, MIT Cricket Club, and Improv Boston for being a source of constant entertainment and drama outside of lab. I am also quite happy to have spent time in Cambridge during the same time that establishments such as Flour, Saloniki, Clover, Cava, Happy Lamb, Toscanini, and Dakzen existed.

I can with confidence conclude that taking an 8000-mile flight was totally worth it because of the people who made the rookie mistake of getting one coffee with me and being stuck with me. Irene tops the list for all the laughs, cookouts, and miles being driven around. A big special thanks again to Reshma, Jonathan, Nenian, and Daniele for being there when it mattered. Finally, I would like to thank my parents, my sister, and my grandparents for having the confidence in me that I never could have never dreamt of.

Had it been not for all of you, I would have probably finished a year earlier.
So long and thanks for all the fish.

List of Abbreviations

A	pre-exponential factor or attempt frequency
A_S	surface area per mass
BEP	Brønsted (or Bell)-Evans-Polanyi scaling
BET	Brunauer–Emmett–Teller theory of the adsorption of gases
CUS	coordinatively unsaturated sites
DFT	density functional theory
pDOS	partial density of states
DRIFTS	diffuse reflectance infrared Fourier transform spectroscopy
ΔG	Gibbs energy of reaction
$\Delta G^{\ddagger}$	activation barrier for a transition state
E_A	activation energy of a reaction
E_{vac}	oxygen ion vacancy formation energy
EXAFS	extended X-ray absorption fine structure
GGA	generalized gradient approximation
K	equilibrium constant
k	photoelectron wavevector
k_B	Boltzmann constant
k_n	rate constant of reaction n
μ	chemical potential
n	reaction order
ODH	oxidative dehydrogenation
PAW	projector augmented wave pseudopotential

PBE	Perdew–Burke–Ernzerhof exchange model
r	rate of reaction
TEM	transmission electron microscopy
TGA	thermogravimetric analysis
TOF	turnover frequency
θ	surface coverage
U	Hubbard on-site Coulombic interaction
XAFS	X-ray absorption fine structure
XANES	X-ray absorption near edge spectroscopy
XAS	X-ray absorption spectroscopy
XPS	X-ray photoelectron spectroscopy
AP-XPS	ambient pressure x-ray photoelectron spectroscopy
XRD	X-ray diffraction
HCHO	formaldehyde
CH_3OH	methanol
$HCOOCH_3$	methyl Formate
C_3H_8	propane
C_3H_6	propene

Table of Contents

Chapter 6 – Regulating oxygen activity of perovskites to promote activity and selectivity for propane oxidative dehydrogenation

Chapter 7– Summary and perspectives

Appendix A

Chapter 1 – Introduction

1.1 Environmental and energy relevance of heterogeneous catalysis

Heterogeneous catalyst is 'a functional material that continually creates active sites with its reactants under reaction conditions'. These sites change the rates of chemical reactions of the reactants localized on them without changing the thermodynamic equilibrium between the materials.[1] Specifically, industrial heterogeneous (thermal and electro) catalysis accounts for 35-40% of the global gross domestic product (GDP) and is involved in 95% of the total volume of products of the chemical industry.[2] Historically, catalysts have played a major role in altering the course of human civilization, for example, increased ammonia generation using the Haber-Bosch process[4] increased the number of humans supported on an arable land from 1.9 to 4.3 with an increase of 30-50% crop yield. Looking ahead into the future, a civilization-altering change is envisaged to tackle the effects of climate change and meeting industrial demands towards a sustainable future as shown in Figure 1.1.

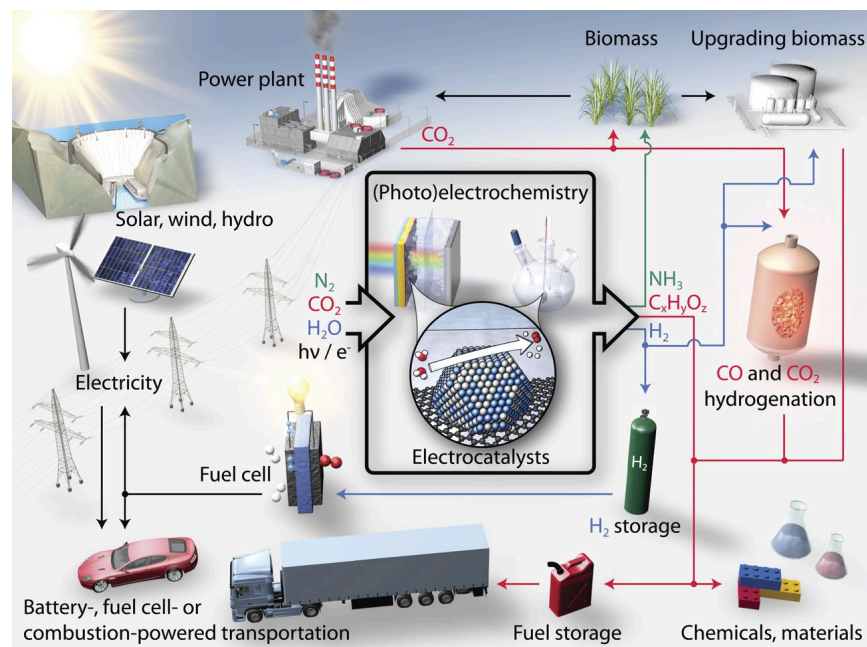***Figure 1.1****: **Schematic of a sustainable energy landscape centered on heterogeneous catalysis**. Figure taken from ref[2] with permission, Copyright 2017 American Association for the Advancement of Science.*

In this thesis, we identify the three key areas of industrial chemical production, air quality, and energy storage-conversion (Figure 1.2) where heterogeneous catalysis focused on C-H bonds

would play a major role in providing alternate yet sustainable solutions. Firstly, in the area of industrial chemical production, sustainable sources in the form of natural gas and renewables are needed to replace crude oil sources.[3,4] However, during natural gas extraction small molecules such as methane (CH_4), ethane (C_2H_6), and propane (C_3H_8) which form a large fraction (75 – 90%) of natural gas are routinely flared to produce carbon dioxide (CO_2), which is a less potent greenhouse gas.[5–7] Alternatively, such alkanes can be converted directly into value-added fuels using (electro-) chemical catalytic methods.[8] Addressing selective alkane oxidation to value added fuels would provide a twofold solution to tackle the needs of an ever-growing chemical industry as well as improve air quality by reducing greenhouse gas emissions. Current strategies include using oxidative coupling of methane to form C2 compounds, [11] benzene methane dehydroaromatization (MDA),[12] conversion of methane to methanol[11] and formaldehyde.[12] Similarly, oxidative dehydrogenation (ODH) of propane (C_3H_8) to propene (C_3H_6) is the starting step for the chemical industry to produce acetone.[13] However, a tradeoff exists between product selectivity (%) and total conversion (%) due to the inert nature of the C-H bond and the ease of activation of reaction intermediates formed after the initial C-H activation.[11]

Selectivity-conversion limitations are well known for direct conversion of methane (CH_4) to methanol (CH_3OH),[14] methanol (CH_3OH) to formaldehyde (HCHO), C_3H_8 conversion to C_3H_6.[15] Despite numerous proposed strategies to overcome selectivity-conversion limitations such as the use of aqueous reaction conditions, tuning reaction conditions, usage of methanol collectors,[11] and bio-inspired catalyst designs,[16] the development of new materials with higher yields remains a holy grail in chemistry. The challenge of selective oxidation is not only limited to alkane oxidation reactions but is a common theme encountered in heterogeneous catalytic reactions such as production of value added fuels during CO_2 reduction,[17] hydrogen peroxide production,[18] and selective oxidation of alcohols and aldehydes.[19] While efficient catalysts for selective oxidation remain to be researched, the importance of improving activity and stability of catalysts for reactions such as oxygen evolution reaction[20], oxygen reduction reaction,[21] hydrogen evolution reaction,[22] and nitrogen reduction[23] in the context of meeting energy needs cannot be understated.[2]
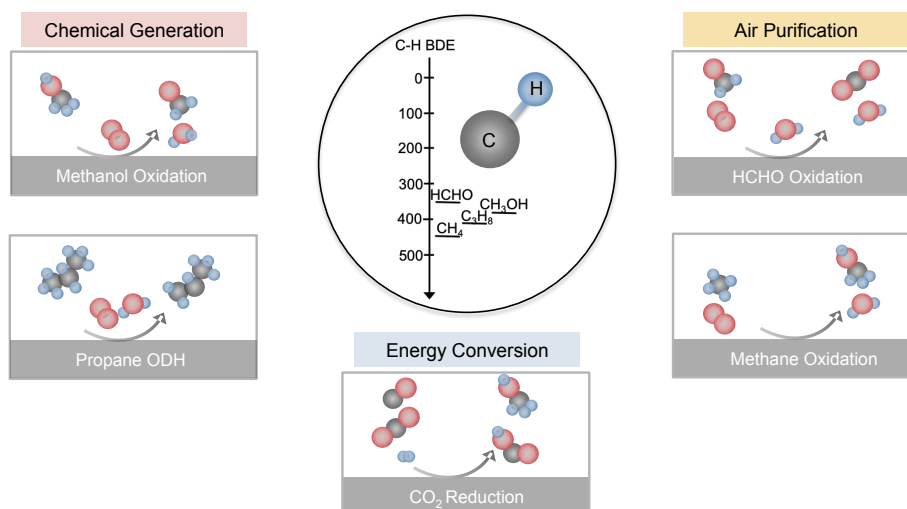
Figure 1.2: C-H bond for energy and environmental applications*. Small molecule conversion with different C-H bond dissociation energies[24] for applications in energy conversion for CO_2 reduction to value added fuels,[25] chemical production for propane oxidative dehydrogenation (ODH) to propene,[12] methanol to formaldehyde conversion,[26] and air purification for HCHO oxidation to CO_2[27] and methane conversion to methanol.[8]*

Secondly, there is need to control and reduce existing atmospheric emissions of CH_4, CO_2, and other volatile organic compounds (VOCs). Decades of industrial growth has led to declining air quality across the globe, especially in India and China where both indoor and outdoor air pollution are known to cause millions of pre-mature deaths every year.[28] Specifically, indoor air pollutants involve small molecules such as carbon monoxide (CO), VOCs such as formaldehyde, acetaldehyde, and acetone arising from construction practices and incomplete combustion.[29] Such molecules are potentially carcinogenic and a way to eliminate these toxic pollutants is the conversion to relatively harmless CO_2 via multiple dehydrogenation steps. Furthermore, environmental factors such as relative humidity and surface poisoning need to be accounted to ensure practical operability of the catalysts.[30] Moreover, the cost effectiveness of these catalysts also needs to be addressed as currently noble metal based-catalysts supported on oxide supports are used for air purification applications.[30]

Finally, in the area of energy storage and conversion, atmosphere CO_2 capture and direct conversion to value-added fuels as mitigation of CO_2 emissions has become one of the grand scientific challenge of the 21st century.[31] Herein, several hydrogenation steps are needed for the

conversion of CO_2 to generate CH_4, CH_3OH, H_2, and other higher order products. Also, factors such as pH, cation effects, anion effects, and electrochemical conditions affect product selectivity.[25] Hence, the role of several intertwined parameters need to be studied for CO_2 hydrogenation energetics in the context of CO_2 reduction.

A common underlying theme for all the sustainable energy and environmental applications discussed above is the ubiquitous presence of small molecules with C-H bonds with varied bond dissociation energy (Figure 1.2). This thesis will focus on tuning the (de)-hydrogenation energetics of such C-H bonds using rational design approach of materials for efficiently creating new bonds or the scission of existing bonds.

1.2 Descriptor-based approaches in heterogeneous catalysis

The search of new materials can be achieved through fundamental insights of the material system at hand by understanding trends across material and environmental spaces. Typically, this is achieved by means of descriptors which are a set of physically meaningful parameters that describe the actuating mechanisms of a certain property.[32] Descriptors, features, or fingerprints are proved or hypothesized to have a causal relationship with the target property and can be used for the prediction of target properties without calculating or measuring them directly.[33] In principle, descriptors can correspond to a single characteristic of the system or be a composite built out of several such characteristics. Typical material descriptors are ACS type-atomic identities, composition, and structure that can be mapped onto a certain functionality.[33] The descriptor itself should be easier to determine than the property itself, for both experimental and computational methods. Also, the dimensions of the descriptors have to be as low as possible, should be able to uniquely characterize a material if possible, and materials that are very different (similar) should be characterized by very different (similar) descriptor values.[34] Once identified descriptors could just be heuristic features for which causal relationship does not exist or they can be based on physical models (formula based) to show how property depends on a particular descriptor. For example, the public happiness in cities in China was seen to be correlated to the air quality in those cities[35] (Figure 1.3a) or the activation barrier for CH_4, C_2H_6, and CH_3OH adsorption on surfaces is correlated to the hydrogen adsorption energy[36] (Figure 1.3b) which is a relatively easier-to-compute metric than the

activation barrier. Both these simplified correlations provide an excellent starting point for future predictions of better happiness, which in turn can be related to the quality of air. Quality of air can further be correlated to catalytic removal of CH_4 from the atmosphere. However, it is important to note that several underlying assumptions about the reaction mechanisms have to be made in order to develop a descriptor based-approach.
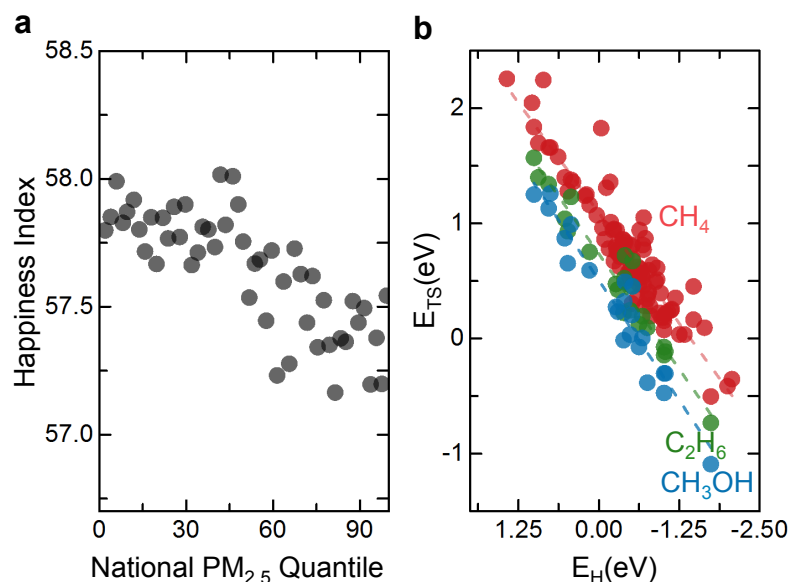
Figure 1.3: Trends in public happiness index and small molecule activation. Correlation between (a) expressed happiness on social media and measured particulate matter in the atmoshhere in chinese cities, reproduced with permission from ref.[35], Copyright Springer Nature 2016. (b) hydrogen adsorption energy and energy of the transistion state energy for the activation of CH_4, C_2H_6, and C_3H_6 on relevant catalytic surfaces. Reproduced with permission from ref.[36], Copyright Springer Nature 2016.

In the case of heterogeneous catalysis, the first step towards a descriptor-based approach is the development of a micro-kinetic modeling for predicting reaction rates. To develop a micro-kinetic reaction model, elementary reaction reactions making up the catalytic cycle are proposed using a combination of density functional theory (DFT), spectroscopy, and kinetic measurements. For example, consider a simple reaction, $A_2 + 2B \leftrightarrow 2AB$, centered on the surface site (*) with the elementary reaction steps shown below,[37]

$$A_2 + 2^* \leftrightarrow 2A^*$$

$$B + * \leftrightarrow B^*$$

$$A^* + B^* \leftrightarrow AB^* + *$$

$$AB^* \leftrightarrow AB + *$$
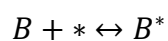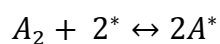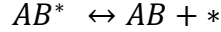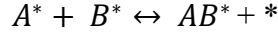
Once the elementary steps are known, we assume that the rate constants for the forward and backward reactions for each of the reaction steps and write down the reaction rates for each of the steps,[37]

$$R_1 = r_1 - r_{-1} = k_1 \theta_*^2 p_{A_2} - k_{-1} \theta_A$$

$$R_2 = r_2 - r_{-2} = k_2 \theta_*^1 p_B - k_{-2} \theta_B$$

$$R_3 = r_3 - r_{-3} = k_3 \theta_A \theta_B - k_{-3} \theta_{AB}$$

$$R_4 = r_4 - r_{-4} = k_4 \theta_{AB} - k_{-3} \theta_* p_{AB}$$

To understand the change in each of the surface species, we evaluate the rate of change in the coverage of reaction intermediates,[37]

$$\frac{\partial \theta_A}{\partial t} = 2R_1 - R_3 = 2\left(k_1 \theta_*^2 p_{A_2} - k_{-1} \theta_A\right) - \left(k_3 \theta_A \theta_B - k_{-3} \theta_{AB}\right)$$

$$\frac{\partial \theta_B}{\partial t} = R_2 - R_3 = \left(k_2 \theta_*^1 p_B - k_{-2} \theta_B\right) - \left(k_3 \theta_A \theta_B - k_{-3} \theta_{AB}\right)$$

$$\frac{\partial \theta_{AB}}{\partial t} = R_3 - R_4 = \left(k_3 \theta_A \theta_B - k_{-3} \theta_{AB}\right) - \left(k_4 \theta_{AB} - k_{-3} \theta_* p_{AB}\right)$$

$$\sum_i \theta_i = 0$$

Finding complete solutions for all the rate equations is not feasible due to the large number of variables involved. Hence, approximates such as the steady state approximation (SSA) where there is no accumulation of intermediate, $\frac{\partial \theta_i}{\partial t} = 0$; and quasi-equilibrium approximation (QSSA) where the fast steps are assumed to be in equilibrium are made to simplify the equations mathematically by reducing the number of variables. With such simplifications, we are able to generate expressions for the reaction rates with terms containing pressure of the reaction and product gases and the equilibrium constant containing the activation energy term.

Further, transition state theory (TST) is used to generate the potential energy diagram. The potential energy diagram is divided into two parts, the reactants and products region, with the region in-between called the transition state (TS). For a multistep reaction, plotting the energies of the initial, transition, and the final states can generate an entire diagram with different rate constants for each step. Computing the reaction energies for the transition state is a painstakingly expensive process and typically the transition state energy (E_{a_i}) is assumed to be related to the driving force (ΔE_i) of the reaction via the Bronstead-Evans-Polyani (BEP) relation,[38]

$$E_{a_i} = \alpha_i \Delta E_i + \beta_i, \text{Where } \alpha_1 > 0 \text{ and } \alpha_2 > 0$$

The BEP relation can be justified by assuming that the transition state usually resembles the bonding behavior of the adsorbed molecule albeit slightly different geometry. Incorporating the BEP relation in the micro kinetic model leads to the important conclusion that the relevant ΔE of the slowest step (rds) can be used to predict the catalytic rates. Therefore, the simplification of micro kinetic models led to the first descriptor model in heterogeneous catalysis proposed by Paul Sabatier. The Sabatier principle states that the optimal heterogeneous catalyst should bind the substrate neither too weakly nor too strongly (Figure 1.4).[39] Building on this principle, Ruetschi[40] and Trassati[41] have shown the correlations between M-O bond energies, oxide formation energy for over-potential for oxygen evolution reaction (OER). It is to be noted that these correlations remained heuristic in spirit and did not involve rigorous investigation of the reaction mechanism or the nature of the reaction intermediates. A major breakthrough was achieved by Nørskov and co-workers through a mechanistic understanding of the reaction at hand to develop 'rational' descriptors and provide the much-needed predictive capability for catalyst design.[42,43] A schematic of this procedure employed for ammonia synthesis where N_2 dissociation was predicted to be rate determining using DFT and a CoMo alloy was predicted to have the highest rate for the ammonia formation.[44] Moreover, experimentally, such an alloy was shown to reside at the top of the volcano for ammonia TOF.[44]

Further, using density functional theory (DFT), Nørskov and co-workers have shown that the adsorption energy of AH_x molecule is linearly correlated to the adsorption energy of the atom A[45] and used this result to develop selectivity maps for CO hydrogenation during methane steam reforming.[46] Moreover, the adsorption energetics for several metals has been correlated to the *d-*

band center of the transition metals for several adsorbates such as CO, N_2, H_2, O_2, and OH.[43] More recently, geometric structure defined by the generalized coordination numbers[47] and surface distortion %[48] have been used to correlate the ORR activity of Pt-based nanoparticle catalysts. This description of active site using weighted geometric factors to complex surface geometries and compositions has only been limited to Pt-based catalysts.

Historically, noble metal-based catalysts have been used in the field of heterogeneous catalysis ranging from single atoms to nanoparticles.[49] Noble metal catalysts provide immense flexibility in tuning the catalytic activity by means of changing the size/shape of the catalyst particles,[50] type of the oxide support used and the interaction of metal with the support,[51] oxidation state of the metal,[52] substitution leading to bi-metallic[53] and more recently higher entropic materials.[54] Further, noble-metal based catalysts have also been used for hydrogenation and dehydrogenation reaction such as methane to syngas,[55] benzene to phenol,[56] propane to propene,[57] epoxidation of propene,[58] selective oxidation of styrene,[59] and HCHO oxidation to CO_2.[60] Unsurprisingly, the majority of computational work based on the descriptor approach has focused on metal catalysts.[37] However, the scarcity and the high price of these noble metal catalysts combined with the expected increase in the CO_2 emissions in the chemical industry during chemical production demand an immediate solution.[61] Hence, there is a need to replace traditionally used noble metal catalyst with more earth abundant materials that are cheaper, environmentally acceptable mining practices, and having a robust supply chain framework. With the development of new materials also comes the challenge of developing newer descriptors as previously developed insights for metallic catalysts may or may not be fully applicable to a newer class of materials.
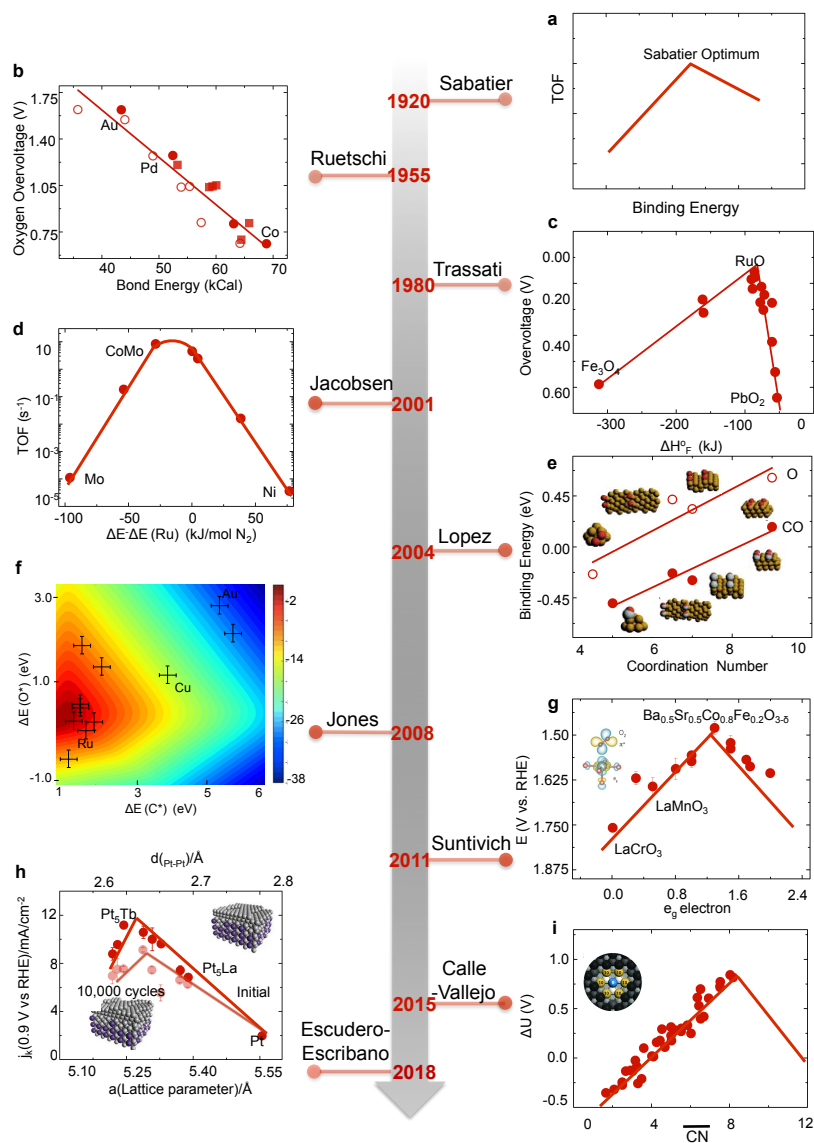
Figure 1.4: Timeline of descriptor-based approach for heterogeneous catalysis. *In catalysis, the Sabatier principle indicates the maximum activity is achieved with neither too strong nor too weak binding of intermediates to the surface. Early studies found that some physicochemical properties are catalytic descriptors. For instance, the enthalpy of formation of metal hydroxides from metals was linearly correlated with the catalytic of metals for oxygen evolution reaction (OER).[62] Similarly, the hydrogen evolution reaction (HER) activity of metals was found to follow a volcano-shaped relation with the enthalpy of formation of metal hydrides.[63] Following the advances in surface science and DFT, energetic and electronic structure descriptors have been established. Nitrogen binding energy was found to have a volcano dependence on the turn over frequency (TOF) of metal catalysts for ammonia synthesis,[64] oxygen and CO adsorption was seen to be correlated with Au coordination number.[65] Likewise, the OER activity of perovskite oxides was shown to have a volcano-style relation with the occupancy of e_g orbital.[66] Structural parameters such as surface coordination number[65] and geometric parameters such as surface strain[67] have also been proposed as surface binding and catalytic descriptors. Panel **b** is*

23

*reprinted with permission from ref.[62], AIP Publishing. Panels **e, c,** and **f** are reprinted with permission from refs.[63,65]. Copyright Elsevier. Panels **d** is reprinted with permission from ref.[64]. Copyright ACS. Panels **g, h,** and **i** are reprinted with permission from refs.[66,62,67] Copyright AAAS. Figure has been modified from an existing version in ref.[68].*

1.3 Oxides for heterogeneous catalysis

Oxide catalysts provide an excellent opportunity to be investigated for dehydrogenation and hydrogenation reactions due to their cost-effectiveness, while also being earth abundant and easy to synthesis.[69,70] Transition metal-oxide based catalysts such as perovskites[71] and manganese oxides[72] have rich chemical and physical properties which provide opportunities to rationally design materials for the applications discussed above while being competitive to noble metal catalysts. For example, manganese oxide catalysts (CARULITE$^{®}$) are already being used for commercial air purification applications while perovskites catalysts have been shown to have comparable performance to commercial Pt-based catalysts for NO oxidation.[73] The physical origin of the exceptional performance of oxide catalysts can be explained in terms of the acidic-basic as well as the redox properties of oxides.[74] Basic oxides typically consistent of lower valent metals such as alkali or alkaline earth metals. The reactivity of basic oxide depends on the ionicity of the metal-oxygen bond and the more basic/reactive oxides are more susceptible to hydroxide and carbonate formation on the surface.[74] On the other hand, acidic properties are typically characteristic of higher valent metals such as V^{5+}, Nb^{5+}, or Cr^{5+}. The higher valent oxides with d^0 configuration can lead to increased covalent-nature of the bond due to the Jahn-Teller effect.[74] In contrast, redox properties of a catalyst are typically described by the interplay between two oxidation states. In the higher oxidation state, the catalyst acts as a source of oxygen and is reduced upon initial reaction. The catalyst is then re-oxidized during the subsequent steps to complete the catalytic cycle.[74] Both acidic/basic and redox properties are relevant for selective oxidation reactions and need to be characterized to understand the nature of the active reaction site.[75,76] Descriptors such as surface oxygen content, [77] basicity,[78,79] acidity (electron-pair acceptor),[80] e_g occupancy,[81] and oxygen vacancies[82] which have been used to describe reactivity on oxides are expected as basic (oxygen), acid (metal), and mixed acid-base catalyst sites can have different strengths of reaction intermediates and can yield different products.[75,76]

Typically, acidic properties measurements are estimated experimentally using NH_3 adsorption [83,84] while basic properties are estimated using CO_2 adsorption.[85,86] However, such experimental probes are limited to detecting the oxygen or metal sites separately and multiple techniques are required to fully characterize the catalyst surface sites.[87] While, descriptors such as number of transition metal valence electrons,[88] transition-metal oxidation state,[88] e_g occupancy[81] have been correlated with catalytic activity for smaller datasets of oxides, this approach does not capture metal-oxygen covalency especially for the late transition metal oxidation.[89] Moreover, C-H bond (de-) hydrogenation reactions involve different types of adsorbents with C and O binding on metal and oxygen sites. Hence, there is a need to unify various acid-base and redox descriptors reported previously that correlate with catalytic properties. Furthermore, tuning product selectivity during heterogeneous catalysis is a multi-dimensional phenomenon with macroscopic parameters such as temperature, pressure, composition, heat and mass flow factors becoming part of the parameter space in the search for the ideal material. Typically, all these factors are not included in the descriptor approach. Hence, there is a need to identify robust descriptors that can consider various reaction sites on the surface along with the environmental conditions.

1.4 Universality of O 2*p*-band center descriptor for oxide catalysis

The O 2*p*-band center can influence the energetics of redox processes for oxide bulk and surfaces such as oxygen vacancy formation and re-filling, and adsorption energies on oxide surfaces. The effectiveness of the O 2*p*-band center descriptor on the energetics can be qualitatively understood in terms of a rigid band model,[90] which has been successfully used to describe late transition metal perovskites.[91] In this model, oxidation of oxides, for example, through filling of oxygen vacancy, involves moving electrons from E_{Fermi} to O 2*p*-band, resulting in an upshift of O 2*p*-band center toward E_{Fermi}. This upshift in O 2*p*-band center is both the result of E_{Fermi} moving down due to electron depletion from E_{Fermi} to the newly added oxygen, and an increase in the total oxygen DOS relative to the transition metal DOS. Thus, the energetics for O_{vac} filling becomes less negative (i.e. less favorable) with shallower O 2*p*-band center. Similarly, adsorption of O and OH on oxide surfaces can also oxidize the system, where adsorption energetics should become less favorable with shallower O 2*p*-band center. Similarly, the opposite trends occur with reduction of the system, for example, by creation of O_{vac} on metal oxide surfaces, where electrons are transferred from O 2*p*-band to E_{Fermi}, resulting in a downshift

of O 2p-band center away from E_{Fermi}. This downshift of O 2p-band center is the result of adding electrons to E_{Fermi} and reduction in the oxygen DOS relative to the transition metal DOS. Therefore, reduction of oxides involving O_{vac} formation becomes easier with shallower O 2p-band center.

The bulk O 2p-band center of oxides can be straightforwardly obtained from density functional theory (DFT) calculations.[92,93] For trends in O 2p-band center for a set of materials to be viable, the O 2p-band center needs to be calculated using the same DFT methodology for all the materials under study. Moreover, thousands of oxygen 2p band values are already available from several large-scale computational studies carried out for solid oxide fuel cells[94] and OER applications.[95] These existing databases can further be leveraged for other catalytic reactions as well. Further, the O 2p-band center can be experimentally obtained by valence band X-ray photoemission (XPS) and X-ray emission (XES) spectroscopy.[96–98] More specifically, XES spectra aligned with valence-band XPS measurements yield O 2p-band spectra relative to the oxide Fermi level.[99] The computed bulk O 2p-band center value can then be validated against experimental values.

Moreover, it has been shown that the O 2p-band center correlates well with the charge transfer energy, defined as the difference between the O 2p non-bonding peak and the lowest occupied TM 3d state[100] for both perovskite[101] and spinel oxides.[102] While the charge-transfer energy was shown to be a more powerful descriptor for perovskites during electro-catalysis,[100] both the computation and the experimental derivation of the charge transfer energy involves the additional step of accounting for the transition metal d orbital. We also note that the simpler descriptors such as the electron count, oxidation potential are relevant and easier to obtain do not capture the entire reactivity of oxide catalysts across the periodic table. [89] Hence, we propose that the charge transfer and (to a slightly lesser extent) the O 2p-band can be the general descriptors to explain oxide reactivity. Also, with the bulk and surface O 2p-band centers correlating[103] is important from the standpoint of using the easier to obtain bulk O 2p-band center to correlate to surface-specific properties, as will be discussed more later. The bulk O 2p-band center descriptor has been used extensively to infer correlations with catalytically relevant properties and functions, including oxygen ion migration,[104,105] oxygen evolution catalytic activity in basic

solution,[106] oxide work function,[107] oxidative dehydrogenation of carbonate solvents at positive electrodes in Li-ion batteries.[108,109]

The first oxide property shown to correlate with the O 2p-band center[103] was the O_{vac} formation energy, which decreases with shallower O 2p-band center, as shown for bulk[104] and surface[110] of perovskite oxides (Figure 1.5a). Increasing number of d electrons for metal cations and increasing oxidation state (e.g. from V^{x+} to Ni^{x+} and from M^{3+} to M^{4+})[108] is associated with shifting E_{Fermi} closer to the centroid of oxygen DOS, making the O 2p center shallower, which coincides with reduced oxygen vacancy formation energy. This trend derives from the charge compensation for the formation of oxygen vacancy, which largely takes place through the reduction of two M ions for reducible oxides.[111] In addition, the energy penalty for the formation of bulk and surface oxygen vacancies shows similar slopes with respect to the surface O 2p-band center, close to -2 expected for two electrons transferred per oxygen vacancy.[109]

Besides oxygen vacancies, the O 2p-band center of oxides has been shown to correlate with the binding energy of adsorbates on the oxide surface. For example, the binding energy of electronegative adsorbates such as OH and O adsorbed on the metal sites of the (100) surface of perovskites have a positive slope with the O 2p-band center (Figure 1.5b),[103] indicative of the oxide being oxidized. Similarly, adsorption of hydrogen (H-O_{oxide})[110] or C-containing species (O_2C-O_{oxide} and H_3C-O_{oxide})[110] on surface oxygen sites of (001) perovskites, shows a strong dependency on the O 2p-band center (Figure 1.5c). Adsorption of a hydrogen atom on the surface oxygen site of perovskites is accompanied by transfer of one electron and the reduction of a transition metal cation, which is similar to that upon adsorption of C-containing species with formation of C-O_{oxide} bonds.[108–110]

Making the O 2p-band center shallower using late transition metal cations and increasing cation oxidation state, associated with greater metal-oxygen covalency, can facilitate adsorption of species such as CH_3OH, CO_2[112] and NO[73] on surface oxygen sites instead of surface metal sites. For example, the adsorption of NO and NO_2 on oxygen sites of (001) $La_{1-x}Sr_xCoO_3$, forming NO-O_{oxide}[73] and NO_2-O_{oxide}, is energetically more favorable than that adsorption on metal sites, and shows a negative slope with the surface O 2p-band center, indicative of surface oxide reduction. This trend is consistent with increased signal associated with NO_x species measured by X-ray photoemission spectroscopy (XPS) when increasing Sr in $La_{1-x}Sr_xCoO_3$.[73] Similarly,

the energetics of CO_2-O_{oxide} (surface carbonate) formation becomes more favorable with shallower O 2p-band center, indicative of more reactive oxygens on oxide surfaces, which agrees with the observation of more (bi-) carbonate species using XPS.[112]
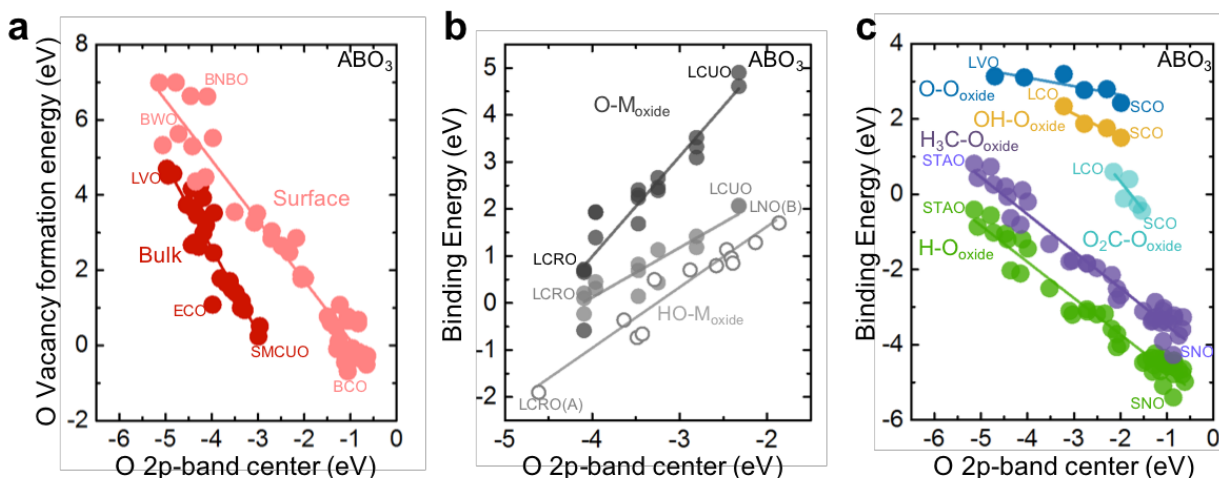

Figure 1.5: Bulk and surface properties as a function of O 2p-band center for perovskite oxides. *(a) Bulk and (001) surface O_{vac} formation energies as a function of bulk and surface O 2p-band centers respectively computed with PBE+U for ABO$_3$ perovskites). Data are adapted from refs.[104,110], (b) OH and O binding energy on transition metal site of ABO$_3$(001) perovskites as a function of the surface O 2p-band center computed with PBE (filled circle) and PBE+U (empty circles. Data are adapted from ref.[98], (c) H,[110] CH$_3$,[110] CO$_2$, O,[113] and OH[113] binding energies on oxygen site of ABO$_3$(001) perovskites as a function of bulk (O-O$_{oxide}$ and HO-O$_{oxide}$) and surface (H-O$_{oxide}$, H$_3$C-O$_{oxide}$ and O$_2$C-O$_{oxide}$) O 2p-band centers computed with PBE[98] (O-O$_{oxide}$ and HO-O$_{oxide}$) and PBE+U (H-O$_{oxide}$, H$_3$C-O$_{oxide}$ and O$_2$C-O$_{oxide}$). Data are adapted from refs.[110,113]. Abbreviations: BTO: BaTiO$_3$, STO: SrTiO$_3$, PTO: PrTiO$_3$, BCO: BaCoO$_3$, BWO: BaWO$_3$, BNBO: BaNbO$_3$, LCUO: LaCuO$_3$, LCRO: LaCrO$_3$, LNO: LaNiO$_3$, LVO: LaVO$_3$, SCO: SrCoO$_3$, LCO: LaCoO$_3$, STAO: SrTaO$_3$, SNO: SrNiO$_3$.*

The O 2p-band-dependent energetics discussed for perovskites hold true for other oxide crystal families and ligands. For example, the O 2p-band center of Ruddlesden-Popper ((La_xSr_{1-x})$_2$$MO_4$, with M = Co, Ni, Cu) correlates with the formation energies of interstitial oxygen in the structure (Figure 1.6a).[114] In addition, the energetics for hydrogen adsorption on surface oxygen sites of Li_xMO_2 (M = V, Cr, Mn, Fe, Co and Ni; x = 0, 0.5, and 1) as well as surface O_{vac} formation have negative slopes with the O 2p-band center (Figure 1.6b), indicative of greater driving force for oxide reduction with shallower O 2p-band center, in agreement with trends found for perovskites (Figure 1.5a). Hydrogen adsorption on surface oxygen sites becomes increasingly energetically favorable with shallower O 2p-band center compared to hydrogen adsorption on surface metal

sites. Like perovskites, the more active surface oxygen sites come from highly covalent oxides with late transition metals (i.e. Ni), and transition metals in high oxidation states (x = 0.5 (M^{3+}/M^{4+}) or x = 0.0 (M^{4+}), Figure 1.6b). Moreover, similar correlations are observed between the energetics of surface O_{vac} formation and H-O_{oxide} and O 2p-band center for a larger library of oxides with different crystal structures including layered oxides, rocksalts, and rutiles (Figure 1.6c). Notably, these trends hold even when different ligands (S^{2-}, F^-, PO_4^{3-}, AsO_4^{3}) are considered, where the ligand vacancy formation energy and hydrogen adsorption correlate with the ligand p-band center suggesting that a more general "anion p-band center" quantity may describe the energetics of oxidation/reduction, metal-anion bond strength, and resulting catalytic activity trends for systems beyond oxides, e.g., sulfides, fluorides,[109] and possibly more. A multivariable statistical analysis has indicated that developing multivariate models including O 2p-band center, band gap and metal-ligand distance can greatly increase the predictive power of the more general ligand p-band correlation.[109]

This concept has been further extended beyond the band center of oxide bulk and surface to the O 2p-band center of surface adsorbates themselves. For example, oxygen adsorption energy, is correlated with the O 2p-band center of adsorbed O on the surface of oxides (rutiles and perovskites) and metals (Figure 1.6d).[115] Similarly, differently-coordinated surface oxygens of RuO_2 crystal orientations have different O 2p-band centers due to different coordination, local environment, and bond angles, resulting in modified O binding energies on surface Ru site.[116] This concept of local O 2p-band can be combined with the idea of a general anion p-band center to open the possibility of a generalized form of this electronic structure descriptor to predict adsorbate energetics on different materials, beyond oxides and O-containing adsorbates.
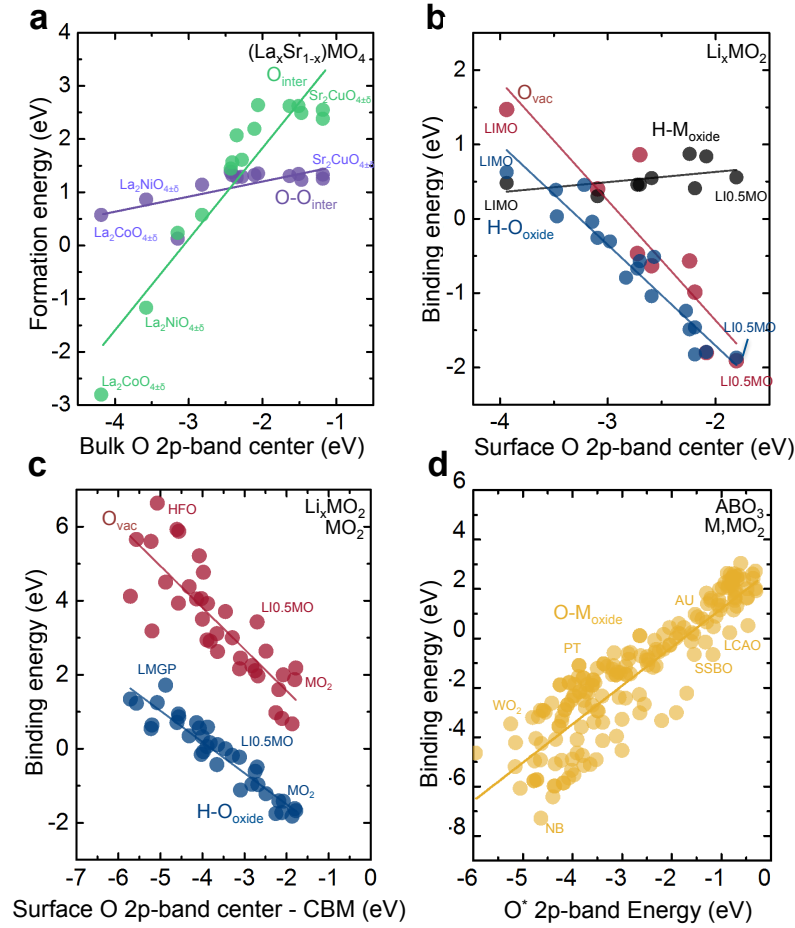
Figure 1.6: Bulk and surface properties as a function of O 2p-band center across different material families. *(a) Defect formation energies as a function of O 2p-band center for Ruddlesden-Popper phases $((La_xSr_{1-x})_2MO_{3+0.0625})$ with M = Co, Ni, Cu),[114] Data are adapted from ref.[114], (b) Hydrogen binding energy at metal (H-M_{oxide}) and oxygen (H-O_{oxide}) site, and O_{vac} formation energy on the $Li_xMO_2(10\bar{1}4)$ surface of layered compounds (M = V, Cr, Mn, Fe, Co, and Ni) as a function of the surface O 2p-band center computed with RPBE, where H-M_{oxide} while H-O_{oxide} and O_{vac} have negative. Data are adapted from ref.[117], (c) Hydrogen binding energy at oxygen site (H-O_{oxide}), and O_{vac} formation energy on the surface of different oxide crystal families, including layer compounds, rocksalt, rutile oxides, as a function of the surface O 2p-band center with respect to the conduction band minimum (CBM) computed with PBE Data are adapted from ref.[109], (d) Energy required to create adsorbed O as a function of O 2p-band center of adsorbed O computed for rutile, perovskite oxides, and metal surfaces.[115] Data are adapted from ref.[115]. Abbreviations: LIMO: $LiMnO_3$, LI0.5IMO: $Li_{0.5}MnO_2$, MO_2: MnO_2, HFO: HfO_2, LMGP: LiMGP, NB: Nb, PT: Pt, AU: Au, LCAO: $LaCaO_3$, SSBO:$SrSbO_3$.*

The O 2p-band center has been proposed as a descriptor for the (electro-) catalytic activity of oxides. The role of the O 2p-band center in oxygen electro-catalysis has been studied extensively.[103,98,100,118] The surface oxygen exchange kinetics, which measures the rate of oxygen incorporation/release into/from oxides ($O_2 + 4e^- \Leftrightarrow 2O^{2-}$)[103], central to the efficiency of solid oxide fuel cells, increases over many orders of magnitude with shallower/deeper O 2p-band center (Figure 1.7a).[103] The enhanced rate can be attributed to reduced energy for O_{vac} formation in oxides with shallow O 2p-band center, where oxygen vacancies serve as active sites for adsorption and dissociation of molecular oxygen. On the other hand, the surface exchange kinetics of Ruddlesden-Popper (($La_xSr_{1-x})_2MO_4$, with M = Co, Ni, Cu)[105] decreases with higher O 2p-band center, which can be attributed to increasing formation energy of oxide and peroxide interstitials.[114] The observed opposite slopes of surface exchange rates between perovskites and Ruddlesden-Popper oxides is a direct consequence of different active sites and catalytic mechanisms which involve vacancy- and interstitial-mediated processes for perovskites and Ruddlesden-Poppers, respectively. In addition, having higher O 2p-band center (e.g. $Hf_{0.5}Ba_{0.5}CoO_3$ and $Pr_{0.5}Ba_{0.5}CoO_3$) correlates with greater catalytic activity of oxygen evolution reaction (OER) for perovskites in basic solution (Figure 1.7b).[106]
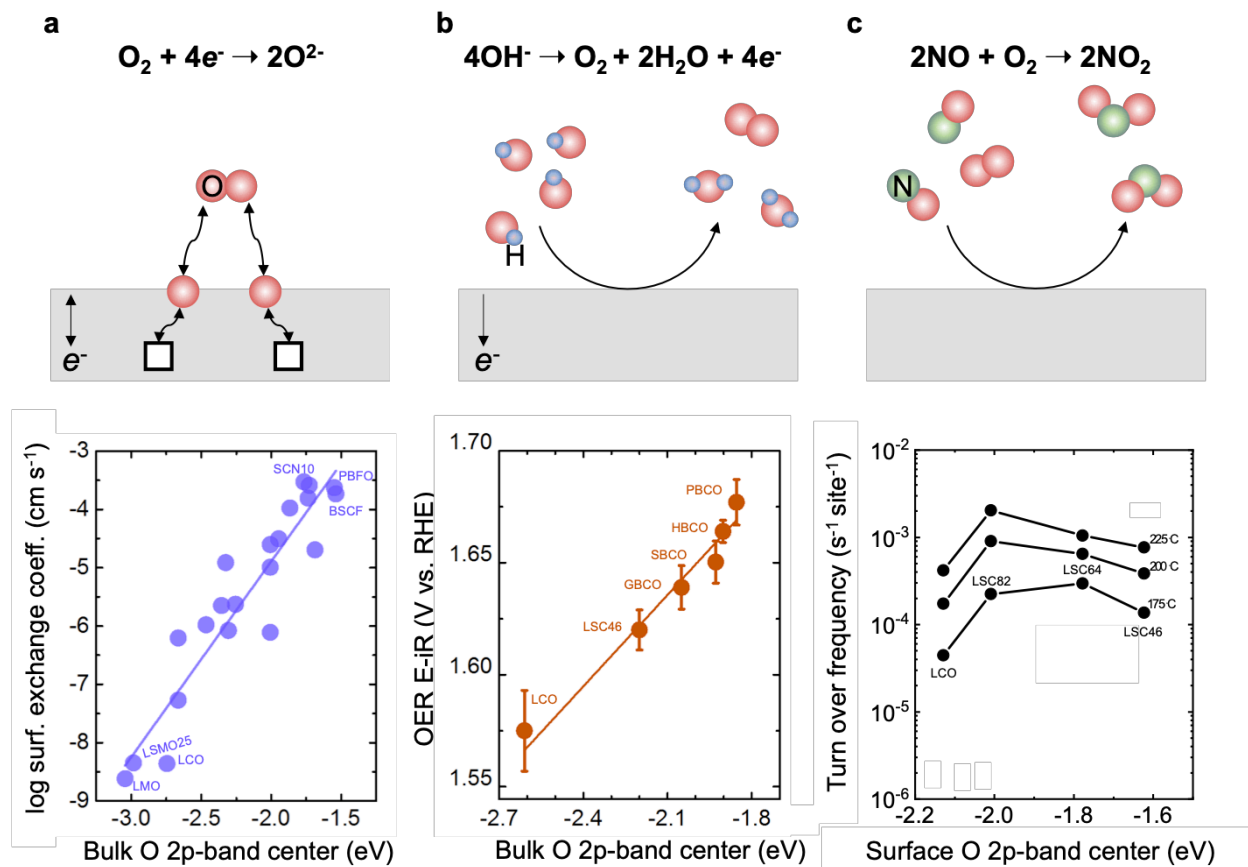
a $O_2 + 4e^- \rightarrow 2O^{2-}$

b $4OH^- \rightarrow O_2 + 2H_2O + 4e^-$

c $2NO + O_2 \rightarrow 2NO_2$

Figure 1.7: Surface catalytic properties as a function of O 2p-band center for perovskite oxides. *(a) Oxygen surface exchange coefficient as a function of the bulk O 2p-band center relative to E_{Fermi} computed with PBE+U for ABO_3 perovskite oxides.[103] Data are adapted from ref.[103]. (b) OER activities measured at 0.5 mA/cm^2_{ox} as a function of the bulk O 2p-band center relative to E_{Fermi} computed with PBE+U for ABO_3 perovskites.[106,100] Data are adapted from refs.[106,100]. (c) NO oxidation turnover frequency for $La_xSr_{1-x}CoO_3$ perovskites as a function of the surface O 2p-band center relative to E_{Fermi} computed with PBE +U.[73] Data are adapted from ref.[73]. Abbreviations: LMO: $LaMnO_3$, LCO: $LaCoO_3$, LSMO25: $La_{0.75}Sr_{0.25}MnO_3$, BSCF: $Ba_{0.5}Sr_{0.5}Co_{0.75}Fe_{0.25}O_3$, SCN10: $SrCo_{0.9}Nb_{0.1}O_{3\delta-}$, PBFO: $Pr_{0.5}Ba_{0.5}FeO_6$, LSC82: $La_{0.8}Sr_{0.2}CoO_3$, LSC64: $La_{0.6}Sr_{0.4}CoO_3$, LSC46: $La_{0.4}Sr_{0.6}CoO_3$, GBCO: $Gd_{0.5}Ba_{0.5}CoO_3$, SBCO: $Sr_{0.5}Ba_{0.5}CoO_3$, HBCO: $Hf_{0.5}Ba_{0.5}CoO_3$, PBCO: $Pr_{0.5}Ba_{0.5}CoO_3$*

The O 2p-band center also serves as an effective descriptor for other electro catalytic reactions and heterogeneous catalysis on oxide surfaces. The O 2p-band descriptor is correlated with the hydrogen evolution reaction (HER) activity of A-site modified Co-based perovskites,[119] and Co-based double perovskites, where a volcano-type relationship was observed for the HER activity with respect to the O 2p-band center.[120] NO oxidation kinetics exhibit a volcano trend with the O 2p-band center of $La_{1-x}Sr_xCoO_3$, where the most active composition is found for x = 0.2.[73] This

volcano trend with O $2p$-band center can be understood by considering that NO oxidation is limited by NO adsorption on oxygen sites to form NO-O$_{oxide}$ for the left-hand side of the volcano (LaCoO$_3$), and by NO$_2$ removal or O$_{vac}$ re-filling for the right-hand side of the volcano (La$_{1-x}$Sr$_x$CoO$_3$ with x > 0.2),[73] in agreement with lower O$_{vac}$ formation energy (i.e. more difficult oxygen vacancy filling) for high O $2p$-band center (Figure 1.5a). Similarly, the kinetics for propane[121] and methane oxidation[122] show a volcano trend with the surface O $2p$-band center for perovskites.

1.5 Understanding reaction mechanisms in situ/in operando

An important aspect of investigating reaction mechanism is to track the catalyst under reaction conditions to identify the key reaction species that coverage can be tuned to increase the activity and selectivity of the reaction. Synchrotron-based techniques such as x-ray absorption spectroscopy (XAS) and ambient pressure x-ray photoelectron spectroscopy (AP-XPS) are increasing being used to characterize catalytic reactions in situ with the ability to track reaction intermediates, state of the catalysts, as well as measure the products. Using synchrotron techniques, a wide variety of reactant gases (CH$_4$, CH$_3$OH, C$_3$H$_8$, and O$_2$) can be introduced in the chamber and the solid-gas interface can be studied under relatively high pressures (~1 Torr).[123,124] In addition to synchrotron-based techniques, lab-based diffuse reflectance infrared Fourier transform spectroscopy (DRIFTS) provides another opportunity to probe reaction intermediates in-situ as a function of time, temperature, and gas composition.[125]

1.6 Thermodynamic calculations using density functional theory (DFT)

DFT is a complementary tool to in-situ spectroscopy and kinetic measurements to identify reaction intermediates both by computing potential energy pathway for competing catalytic pathways as well as to compute the infrared (IR) spectra. DFT provides an excellent opportunity to simplified picture of the catalyst surface by means of developing slab models of catalyst surfaces and investigating different configurations of molecule interaction with surface sites.[37]Although, realistic catalyst surfaces are known to have heterogeneous reaction sites and undergo surface re-construction under catalytic conditions, DFT has proved to identify trends in experimental activity for OER,[101] ORR,[126] and NH$_3$[127] generation reactions.

1.7 Scope of the Thesis

In the conclusion, the electronic structure of oxides catalyst has been used to tune the activity of environmentally relevant catalytic processes. We have shown that activity metrics of reactions such as TOF, over potential as well as binding energy of key reaction intermediates such as oxygen, hydrogen, hydroxyl, CO_2, and oxygen vacancies can be correlated to the oxygen $2p$-band descriptor. While there have been several studies correlating activity metrics to descriptors, understanding product selectivity has remained an elusive target.

In this thesis, we use a combined experimental and theoretical approach using AP-XPS, DRIFTS, DFT, and plug-flow reactor measurements to understand C-H bond dissociation kinetics as well as product selectivity during small molecule oxidation. **Chapter 2** demonstrates the role of water in altering reaction kinetics for HCHO oxidation on a commercial manganese oxide catalyst by investigating the reaction mechanism using DFT, DRIFTS, and plug-flow reactor studies. **Chapter 3** expands on the reaction mechanism developed for commercial manganese oxide to a library of manganese oxide with different crystal structures to identify descriptors to enhance reaction rates for HCHO oxidation. With insights from Chapter 2 and Chapter 3, in **Chapter 4** we employ AP-XPS, DFT, and plug-flow studies to understand the nature of the active species and product selectivity for C-H bond containing molecules, CH_3OH and CH_4, using IrO_x-type catalysts. Further, in **Chapter 5** we use perovskite oxides to develop a descriptor-based approach for selective conversion of CH_3OH to HCHO by correlating surface reactivity to surface electronic structure. Next, in **Chapter 6**, we expand the descriptor based for perovskites by developing a library of perovskites using DFT to predict reaction rates and active catalysts for propane ODH. Lastly, in **Chapter 7** we propose future directions for the field of selective heterogeneous catalysis and offer perspectives on the role of heterogeneous catalysis in a sustainable society**.**

1.8 References

(1)   Schlögl, R. Heterogeneous Catalysis. *Angew. Chemie Int. Ed.* **2015**, *54* (11), 3465–3520. https://doi.org/10.1002/anie.201410738.

(2)   Seh, Z. W.; Kibsgaard, J.; Dickens, C. F.; Chorkendorff, I.; Nørskov, J. K.; Jaramillo, T. F. Combining

Theory and Experiment in Electrocatalysis: Insights into Materials Design. *Science* **2017**, *355* (6321), eaad4998. https://doi.org/10.1126/science.aad4998.

(3)   Statistical Review of World Energy | Energy economics | BP https://www.bp.com/en/global/corporate/energy-economics/statistical-review-of-world-energy.html (accessed Nov 30, 2018).

(4)   *Future of The Natural Gas: An InterdIscIplinary MIT Study*.

(5)   Grant, J. T.; Venegas, J. M.; McDermott, W. P.; Hermans, I. Aerobic Oxidations of Light Alkanes over Solid Metal Oxide Catalysts. *Chem. Rev.* **2018**, *118* (5), 2769–2815. https://doi.org/10.1021/acs.chemrev.7b00236.

(6)   Tollefson, J. "Flaring" Wastes 3.5% of World's Natural Gas. *Nature* **2016**. https://doi.org/10.1038/nature.2016.19141.

(7)   Schlgl, R. Concepts in Selective Oxidation of Small Alkane Molecules. In *Modern Heterogeneous Oxidation Catalysis*; Wiley-VCH Verlag GmbH & Co. KGaA: Weinheim, Germany; pp 1–42. https://doi.org/10.1002/9783527627547.ch1.

(8)   Yuan, S.; Li, Y.; Peng, J.; Questell-Santiago, Y. M.; Akkiraju, K.; Giordano, L.; Zheng, D. J.; Bagi, S.; Román-Leshkov, Y.; Shao-Horn, Y. Conversion of Methane into Liquid Fuels—Bridging Thermal Catalysis with Electrocatalysis. *Advanced Energy Materials*. Wiley-VCH Verlag October 1, 2020, p 2002154. https://doi.org/10.1002/aenm.202002154.

(9)   Olah, G. A. Beyond Oil and Gas: The Methanol Economy. *Angew. Chemie Int. Ed.* **2005**, *44* (18), 2636–2639. https://doi.org/10.1002/anie.200462121.

(10)   Liu, W.-C.; Baek, J.; Somorjai, G. A. The Methanol Economy: Methane and Carbon Dioxide Conversion. *Top. Catal.* **2018**, *61* (7–8), 530–541. https://doi.org/10.1007/s11244-018-0907-4.

(11)   Latimer, A. A.; Kakekhani, A.; Kulkarni, A. R.; Nørskov, J. K. Direct Methane to Methanol: The Selectivity−Conversion Limit and Design Strategies. **2018**. https://doi.org/10.1021/acscatal.8b00220.

(12)   Carrero, C. A.; Schloegl, R.; Wachs, I. E.; Schomaecker, R. Critical Literature Review of the Kinetics for the Oxidative Dehydrogenation of Propane over Well-Defined Supported Vanadium Oxide Catalysts. *ACS Catal.* **2014**, *4* (10), 3357–3380. https://doi.org/10.1021/cs5003417.

(13)   Schwach, P.; Pan, X.; Bao, X. Direct Conversion of Methane to Value-Added Chemicals over Heterogeneous Catalysts: Challenges and Prospects. *Chem. Rev.* **2017**, *117* (13), 8497–8520. https://doi.org/10.1021/acs.chemrev.6b00715.

(14)   Ravi, M.; Ranocchiari, M.; van Bokhoven, J. A. The Direct Catalytic Oxidation of Methane to Methanol-A Critical Assessment. *Angew. Chemie Int. Ed.* **2017**, *56* (52), 16464–16483. https://doi.org/10.1002/anie.201702550.

(15)   Cavani, F.; Trifirò, F. The Oxidative Dehydrogenation of Ethane and Propane as an Alternative Way for the Production of Light Olefins. *Catal. Today* **1995**, *24* (3), 307–313. https://doi.org/10.1016/0920-5861(95)00051-G.

(16)   Labinger, J. A.; Bercaw, J. E. Understanding and Exploiting C–H Bond Activation. *Nature* **2002**, *417* (6888), 507–514. https://doi.org/10.1038/417507a.

(17)   Zhu, D. D.; Liu, J. L.; Qiao, S. Z. Recent Advances in Inorganic Heterogeneous Electrocatalysts for Reduction of Carbon Dioxide. *Adv. Mater.* **2016**, *28* (18), 3423–3452. https://doi.org/10.1002/adma.201504766.

(18)   Yang, S.; Verdaguer-Casadevall, A.; Arnarson, L.; Silvioli, L.; Čolić, V.; Frydendal, R.; Rossmeisl, J.;

Chorkendorff, I.; Stephens, I. E. L. Toward the Decentralized Electrochemical Production of H_2O_2: A Focus on the Catalysis. *ACS Catal.* **2018**, *8* (5), 4064–4081. https://doi.org/10.1021/acscatal.8b00217.

(19) Putin, E.; Asadulaev, A.; Ivanenkov, Y.; Aladinskiy, V.; Sanchez-Lengeling, B.; Aspuru-Guzik, A.; Zhavoronkov, A. Reinforced Adversarial Neural Computer for *de Novo* Molecular Design. *J. Chem. Inf. Model.* **2018**, *58* (6), 1194–1204. https://doi.org/10.1021/acs.jcim.7b00690.

(20) Suen, N.-T.; Hung, S.-F.; Quan, Q.; Zhang, N.; Xu, Y.-J.; Chen, H. M. Electrocatalysis for the Oxygen Evolution Reaction: Recent Development and Future Perspectives. *Chem. Soc. Rev.* **2017**, *46* (2), 337–365. https://doi.org/10.1039/C6CS00328A.

(21) Shao, M.; Chang, Q.; Dodelet, J.-P.; Chenitz, R. Recent Advances in Electrocatalysts for Oxygen Reduction Reaction. *Chem. Rev.* **2016**, *116* (6), 3594–3657. https://doi.org/10.1021/acs.chemrev.5b00462.

(22) Zeng, M.; Li, Y. Recent Advances in Heterogeneous Electrocatalysts for the Hydrogen Evolution Reaction. *J. Mater. Chem. A* **2015**, *3* (29), 14942–14962. https://doi.org/10.1039/C5TA02974K.

(23) Medford, A. J.; Hatzell, M. C. Photon-Driven Nitrogen Fixation: Current Progress, Thermodynamic Considerations, and Future Outlook. *ACS Catal.* **2017**, *7* (4), 2624–2643. https://doi.org/10.1021/acscatal.7b00439.

(24) Deshlahra, P.; Iglesia, E. Reactivity and Selectivity Descriptors for the Activation of C–H Bonds in Hydrocarbons and Oxygenates on Metal Oxides. *J. Phys. Chem. C* **2016**, *120* (30), 16741–16760. https://doi.org/10.1021/ACS.JPCC.6B04604.

(25) Nitopi, S.; Bertheussen, E.; Scott, S. B.; Liu, X.; Engstfeld, A. K.; Horch, S.; Seger, B.; Stephens, I. E. L.; Chan, K.; Hahn, C.; Nørskov, J. K.; Jaramillo, T. F.; Chorkendorff, I. Progress and Perspectives of Electrochemical CO2 Reduction on Copper in Aqueous Electrolyte. *Chem. Rev.* **2019**, *119* (12), 7610–7672. https://doi.org/10.1021/ACS.CHEMREV.8B00705.

(26) Millar, G. J.; Collins, M. Industrial Production of Formaldehyde Using Polycrystalline Silver Catalyst. *Industrial and Engineering Chemistry Research*. American Chemical Society August 23, 2017, pp 9247–9265. https://doi.org/10.1021/acs.iecr.7b02388.

(27) Yusuf, A.; Snape, C.; He, J.; Xu, H.; Liu, C.; Zhao, M.; Chen, G. Z.; Tang, B.; Wang, C.; Wang, J.; Behera, S. N. Advances on Transition Metal Oxides Catalysts for Formaldehyde Oxidation: A Review. *Catal. Rev.* **2017**, *59* (3), 189–233. https://doi.org/10.1080/01614940.2017.1342476.

(28) Lelieveld, J.; Pozzer, A.; Pöschl, U.; Fnais, M.; Haines, A.; Münzel, T. Loss of Life Expectancy from Air Pollution Compared to Other Risk Factors: A Worldwide Perspective. *Cardiovasc. Res.* **2020**, *116* (11), 1910–1917. https://doi.org/10.1093/CVR/CVAA025.

(29) Vardoulakis, S.; Giagloglou, E.; Steinle, S.; Davis, A.; Sleeuwenhoek, A.; Galea, K. S.; Dixon, K.; Crawford, J. O. Indoor Exposure to Selected Air Pollutants in the Home Environment: A Systematic Review. *Int. J. Environ. Res. Public Heal. 2020, Vol. 17, Page 8972* **2020**, *17* (23), 8972. https://doi.org/10.3390/IJERPH17238972.

(30) Song, S.; Zhang, S.; Zhang, X.; Verma, P.; Wen, M. Advances in Catalytic Oxidation of Volatile Organic Compounds over Pd-Supported Catalysts: Recent Trends and Challenges. *Front. Mater.* **2020**, *7*, 342. https://doi.org/10.3389/FMATS.2020.595667/BIBTEX.

(31) Lewis, N. S.; Nocera, D. G. Powering the Planet: Chemical Challenges in Solar Energy Utilization. *Proceedings of the National Academy of Sciences of the United States of America*. National Academy of Sciences October 24, 2006, pp 15729–15735. https://doi.org/10.1073/pnas.0603395103.

(32) Wagner, N.; Rondinelli, J. M. Theory-Guided Machine Learning in Materials Science. *Front. Mater.* **2016**, *3*, 28. https://doi.org/10.3389/fmats.2016.00028.

(33) Zunger, A. Inverse Design in Search of Materials with Target Functionalities. *Nat. Rev. Chem.* **2018**, *2* (4), 0121. https://doi.org/10.1038/s41570-018-0121.

(34) Ghiringhelli, L. M.; Vybiral, J.; Levchenko, S. V.; Draxl, C.; Scheffler, M. Big Data of Materials Science: Critical Role of the Descriptor. *Phys. Rev. Lett.* **2015**, *114* (10), 105503. https://doi.org/10.1103/PhysRevLett.114.105503.

(35) Zheng, S.; Wang, J.; Sun, C.; Zhang, X.; Kahn, M. E. Air Pollution Lowers Chinese Urbanites' Expressed Happiness on Social Media. *Nature Human Behaviour*. Nature Publishing Group March 1, 2019, pp 237–243. https://doi.org/10.1038/s41562-018-0521-2.

(36) Latimer, A. A.; Kulkarni, A. R.; Aljama, H.; Montoya, J. H.; Yoo, J. S.; Tsai, C.; Abild-Pedersen, F.; Studt, F.; Nørskov, J. K. Understanding Trends in C–H Bond Activation in Heterogeneous Catalysis. *Nat. Mater.* **2017**, *16* (2), 225–229. https://doi.org/10.1038/nmat4760.

(37) Nørskov, J. K.; Studt, F.; Abild-Pedersen, F.; Bligaard, T. Fundamental Concepts in Heterogeneous Catalysis. *Fundam. Concepts Heterog. Catal.* **2014**, *9781118888957*, 1–196. https://doi.org/10.1002/9781118892114.

(38) and, J. C.; Hu*, P.; Peter Ellis, †; Sam French, †; Gordon Kelly, ‡ and; Lok‡, C. M. Brønsted−Evans−Polanyi Relation of Multistep Reactions and Volcano Curve in Heterogeneous Catalysis. *J. Phys. Chem. C* **2008**, *112* (5), 1308–1311. https://doi.org/10.1021/JP711191J.

(39) Medford, A. J.; Vojvodic, A.; Hummelshøj, J. S.; Voss, J.; Abild-Pedersen, F.; Studt, F.; Bligaard, T.; Nilsson, A.; Nørskov, J. K. From the Sabatier Principle to a Predictive Theory of Transition-Metal Heterogeneous Catalysis. *J. Catal.* **2015**, *328*, 36–42. https://doi.org/10.1016/J.JCAT.2014.12.033.

(40) Rüetschi, P.; Delahay, P. Influence of Electrode Material on Oxygen Overvoltage: A Theoretical Analysis. *J. Chem. Phys.* **1955**, *23* (3), 556–560. https://doi.org/10.1063/1.1742029.

(41) Trasatti, S. Electrocatalysis by Oxides - Attempt at a Unifying Approach. *J. Electroanal. Chem.* **1980**, *111* (1), 125–131. https://doi.org/10.1016/S0022-0728(80)80084-2.

(42) Nørskov, J. K.; Bligaard, T.; Rossmeisl, J.; Christensen, C. H. Towards the Computational Design of Solid Catalysts. *Nat. Chem.* **2009**, *1* (1), 37–46. https://doi.org/10.1038/nchem.121.

(43) Nørskov, J. K.; Studt, F.; Abild-Pedersen, F.; Bligaard, T. *Fundamental Concepts in Heterogeneous Catalysis*.

(44) Jacobsen, C. J. H.; Dahl, S.; Clausen, B. S.; Bahn, S.; Ashildur, L. A.; Nørskov, J. K. Catalyst Design by Interpolation in the Periodic Table: Bimetallic Ammonia Synthesis Catalysts. **2001**. https://doi.org/10.1021/JA010963D.

(45) Abild-Pedersen, F.; Greeley, J.; Studt, F.; Rossmeisl, J.; Munter, T. R.; Moses, P. G.; Skúlason, E.; Bligaard, T.; Nørskov, J. K. Scaling Properties of Adsorption Energies for Hydrogen-Containing Molecules on Transition-Metal Surfaces. *Phys. Rev. Lett.* **2007**, *99* (1), 016105. https://doi.org/10.1103/PHYSREVLETT.99.016105/FIGURES/3/MEDIUM.

(46) Jones, G.; Jakobsen, J. G.; Shim, S. S.; Kleis, J.; Andersson, M. P.; Rossmeisl, J.; Abild-Pedersen, F.; Bligaard, T.; Helveg, S.; Hinnemann, B.; Rostrup-Nielsen, J. R.; Chorkendorff, I.; Sehested, J.; Nørskov, J. K. First Principles Calculations and Experimental Insight into Methane Steam Reforming over Transition Metal Catalysts. *J. Catal.* **2008**, *259* (1), 147–160. https://doi.org/10.1016/J.JCAT.2008.08.003.

(47) Calle-Vallejo, F.; Tymoczko, J.; Colic, V.; Vu, Q. H.; Pohl, M. D.; Morgenstern, K.; Loffreda, D.; Sautet, P.; Schuhmann, W.; Bandarenka, A. S. Finding Optimal Surface Sites on Heterogeneous Catalysts by Counting Nearest Neighbors. *Science (80-.).* **2015**, *350* (6257), 185–189. https://doi.org/10.1126/science.aab3501.

(48)   Chattot, R.; Le Bacq, O.; Beermann, V.; Kühl, S.; Herranz, J.; Henning, S.; Kühn, L.; Asset, T.; Guétaz, L.; Renou, G.; Drnec, J.; Bordet, P.; Pasturel, A.; Eychmüller, A.; Schmidt, T. J.; Strasser, P.; Dubau, L.; Maillard, F. Surface Distortion as a Unifying Concept and Descriptor in Oxygen Reduction Reaction Electrocatalysis. *Nat. Mater.* **2018**, *17* (9), 827–833. https://doi.org/10.1038/s41563-018-0133-2.

(49)   Liu, L.; Corma, A. Metal Catalysts for Heterogeneous Catalysis: From Single Atoms to Nanoclusters and Nanoparticles. *Chem. Rev.* **2018**, *118* (10), 4981–5079. https://doi.org/10.1021/ACS.CHEMREV.7B00776.

(50)   Gong, X. Q.; Selloni, A.; Dulub, O.; Jacobson, P.; Diebold, U. Small Au and Pt Clusters at the Anatase TiO2(101) Surface: Behavior at Terraces, Steps, and Surface Oxygen Vacancies. *J. Am. Chem. Soc.* **2007**, *130* (1), 370–381. https://doi.org/10.1021/JA0773148.

(51)   Tauster, S. J. Strong Metal-Support Interactions. *Acc. Chem. Res.* **2002**, *20* (11), 389–394. https://doi.org/10.1021/AR00143A001.

(52)   Moseler, M.; Walter, M.; Yoon, B.; Landman, U.; Habibpour, V.; Harding, C.; Kunz, S.; Heiz, U. Oxidation State and Symmetry of Magnesia-Supported Pd 13O x Nanocatalysts Influence Activation Barriers of CO Oxidation. *J. Am. Chem. Soc.* **2012**, *134* (18), 7690–7699. https://doi.org/10.1021/JA211121M/SUPPL_FILE/JA211121M_SI_001.PDF.

(53)   Zhang, H.; Watanabe, T.; Okumura, M.; Haruta, M.; Toshima, N. Catalytically Highly Active Top Gold Atom on Palladium Nanocluster. *Nat. Mater. 2011 111* **2011**, *11* (1), 49–52. https://doi.org/10.1038/nmat3143.

(54)   Sun, Y.; Dai, S. High-Entropy Materials for Catalysis: A New Frontier. *Sci. Adv.* **2021**, *7* (20). https://doi.org/10.1126/SCIADV.ABG1600/ASSET/0B8BA449-7251-4A98-A8C7-157A2A1571C6/ASSETS/GRAPHIC/ABG1600-F6.JPEG.

(55)   Stötzel, J.; Frahm, R.; Kimmerle, B.; Nachtegaal, M.; Grunwaldt, J. D. Oscillatory Behavior during the Catalytic Partial Oxidation of Methane: Following Dynamic Structural Changes of Palladium Using the QEXAFS Technique. *J. Phys. Chem. C* **2012**, *116* (1), 599–609. https://doi.org/10.1021/JP2052294/SUPPL_FILE/JP2052294_SI_001.PDF.

(56)   Bal, R.; Tada, M.; Sasaki, T.; Iwasawa, Y. Direct Phenol Synthesis by Selective Oxidation of Benzene with Molecular Oxygen on an Interstitial-N/Re Cluster/Zeolite Catalyst. *Angew. Chemie Int. Ed.* **2006**, *45* (3), 448–452. https://doi.org/10.1002/ANIE.200502940.

(57)   Hayashi, T.; Tanaka, K.; Haruta, M. Selective Vapor-Phase Epoxidation of Propylene over Au/TiO2Catalysts in the Presence of Oxygen and Hydrogen. *J. Catal.* **1998**, *178* (2), 566–575. https://doi.org/10.1006/JCAT.1998.2157.

(58)   Lee, S.; Molina, L. M.; López, M. J.; Alonso, J. A.; Hammer, B.; Lee, B.; Seifert, S.; Winans, R. E.; Elam, J. W.; Pellin, M. J.; Vajda, S. Selective Propene Epoxidation on Immobilized Au6–10 Clusters: The Effect of Hydrogen and Water on Activity and Selectivity. *Angew. Chemie Int. Ed.* **2009**, *48* (8), 1467–1471. https://doi.org/10.1002/ANIE.200804154.

(59)   Zhu, Y.; Qian, H.; Zhu, M.; Jin, R. Thiolate-Protected Aun Nanoclusters as Catalysts for Selective Oxidation and Hydrogenation Processes. *Adv. Mater.* **2010**, *22* (17), 1915–1920. https://doi.org/10.1002/ADMA.200903934.

(60)   Guo, J.; Lin, C.; Jiang, C.; Zhang, P. Review on Noble Metal-Based Catalysts for Formaldehyde Oxidation at Room Temperature. *Appl. Surf. Sci.* **2019**, *475*, 237–255. https://doi.org/10.1016/J.APSUSC.2018.12.238.

(61)   Aresta, M.; Ed; Deublein, D. Managing CO2 Emissions in the Chemical Industry. *Manag. CO* **2010**. https://doi.org/10.1002/9783527633623.

(62)   Rüetschi, P.; Delahay, P. Influence of Electrode Material on Oxygen Overvoltage: A Theoretical Analysis. *J. Chem. Phys.* **1955**, *23* (3), 556–560. https://doi.org/10.1063/1.1742029.

(63)   Trasatti, S. Work Function, Electronegativity, and Electrochemical Behaviour of Metals. III. Electrolytic Hydrogen Evolution in Acid Solutions. *J. Electroanal. Chem.* **1972**, *39* (1), 163–184. https://doi.org/10.1016/S0022-0728(72)80485-6.

(64)   Claus J. H. Jacobsen, *,†; Søren Dahl, †; Bjerne S. Clausen, †; Sune Bahn, ‡; Ashildur Logadottir, ‡ and; Nørskov‡, J. K. Catalyst Design by Interpolation in the Periodic Table: Bimetallic Ammonia Synthesis Catalysts. **2001**. https://doi.org/10.1021/JA010963D.

(65)   Lopez, N.; Janssens, T. V. W.; Clausen, B. S.; Xu, Y.; Mavrikakis, M.; Bligaard, T.; Nørskov, J. K. On the Origin of the Catalytic Activity of Gold Nanoparticles for Low-Temperature CO Oxidation. *J. Catal.* **2004**, *223* (1), 232–235. https://doi.org/https://doi.org/10.1016/j.jcat.2004.01.001.

(66)   Suntivich, J.; May, K. J.; Gasteiger, H. A.; Goodenough, J. B.; Shao-Horn, Y. A Perovskite Oxide Optimized for Molecular Orbital Principles. *Science (80-.).* **2011**, *334* (6061), 1383–1385. https://doi.org/10.1126/science.1212858.

(67)   Escudero-Escribano, M.; Malacrida, P.; Hansen, M. H.; Vej-Hansen, U. G.; Velázquez-Palenzuela, A.; Tripkovic, V.; Schiøtz, J.; Rossmeisl, J.; Stephens, I. E. L.; Chorkendorff, I. Tuning the Activity of Pt Alloy Electrocatalysts by Means of the Lanthanide Contraction. *Science* **2016**, *352* (6281), 73–76. https://doi.org/10.1126/science.aad8892.

(68)   J. Peng, D. S. Koda, K. Akkiraju,.., J. C. Grossman, K. Reuter, R. Gomez-Bombarelli, and Y, S.-H. Human- and Machine-Centered Design of Molecules and Materials for Chemical Transformations and Energy Storage,. *Under Rev.* **2021**.

(69)   Royer, S.; Duprez, D.; Can, F.; Courtois, X.; Batiot-Dupeyrat, C.; Laassiri, S.; Alamdari, H. Perovskites as Substitutes of Noble Metals for Heterogeneous Catalysis: Dream or Reality. *Chem. Rev.* **2014**, *114* (20), 10292–10368. https://doi.org/10.1021/CR500032A.

(70)   Peña, M. A.; Fierro, J. L. G. Chemical Structures and Performance of Perovskite Oxides. *Chem. Rev.* **2001**, *101* (7), 1981–2017. https://doi.org/10.1021/CR980129F.

(71)   Hwang, J.; Rao, R. R.; Giordano, L.; Katayama, Y.; Yu, Y.; Shao-Horn, Y. Perovskites in Catalysis and Electrocatalysis. *Science* **2017**, *358* (6364), 751–756. https://doi.org/10.1126/science.aam7092.

(72)   Post, J. E. Manganese Oxide Minerals: Crystal Structures and Economic and Environmental Significance. *Proc. Natl. Acad. Sci.* **1999**, *96* (7), 3447–3454. https://doi.org/10.1073/PNAS.96.7.3447.

(73)   Hwang, J.; Rao, R. R.; Giordano, L.; Akkiraju, K.; Wang, X. R.; Crumlin, E. J.; Bluhm, H.; Shao-Horn, Y. Regulating Oxygen Activity of Perovskites to Promote NOx Oxidation and Reduction Kinetics. *Nat. Catal. 2021* **2021**, 1–11. https://doi.org/10.1038/s41929-021-00656-4.

(74)   Busca, G. Heterogeneous Catalytic Materials: Solid State Chemistry, Surface Chemistry and Catalytic Behaviour. *Heterog. Catal. Mater. Solid State Chem. Surf. Chem. Catal. Behav.* **2014**, 1–463. https://doi.org/10.1016/C2012-0-00113-5.

(75)   Badlani, M.; Wachs, I. E. Methanol: A "Smart" Chemical Probe Molecule. *Catal. Letters* **2001**, *75* (3–4), 137–149. https://doi.org/10.1023/A:1016715520904.

(76)   Tatibouët, J. M. Methanol Oxidation as a Catalytic Surface Probe. *Applied Catalysis A: General*. Elsevier January 2, 1997, pp 213–252. https://doi.org/10.1016/S0926-860X(96)00236-0.

(77)   Levasseur, B.; Kaliaguine, S. Methanol Oxidation on LaBO3 (B=Co, Mn, Fe) Perovskite-Type Catalysts Prepared by Reactive Grinding. *Appl. Catal. A Gen.* **2008**, *343* (1–2), 29–38. https://doi.org/10.1016/j.apcata.2008.03.016.

(78)   Tesquet, G.; Faye, J.; Hosoglu, F.; Mamede, A.-S.; Dumeignil, F.; Capron, M. Ethanol Reactivity over La1+x FeO3+δ Perovskites. *Appl. Catal. A Gen.* **2016**, *511*, 141–148.

https://doi.org/10.1016/j.apcata.2015.12.005.

(79) Polo-Garzon, F.; Fung, V.; Liu, X.; Hood, Z. D.; Bickel, E. E.; Bai, L.; Tian, H.; Foo, G. S.; Chi, M.; Jiang, D.; Wu, Z. Understanding the Impact of Surface Reconstruction of Perovskite Catalysts on CH 4 Activation and Combustion. *ACS Catal.* **2018**, *8* (11), 10306–10315. https://doi.org/10.1021/acscatal.8b02307.

(80) Polo-Garzon, F.; Yang, S.-Z.; Fung, V.; Foo, G. S.; Bickel, E. E.; Chisholm, M. F.; Jiang, D.; Wu, Z. Controlling Reaction Selectivity through the Surface Termination of Perovskite Catalysts. *Angew. Chemie* **2017**, *129* (33), 9952–9956. https://doi.org/10.1002/ANGE.201704656.

(81) Tan, S.; Sayed, F.; Yang, S.; Li, Z.; Wu, J.; Ajayan, P. M. Strong Effect of B-Site Substitution on the Reactivity of Layered Perovskite Oxides Probed via Isopropanol Conversion. *ACS Mater. Lett.* **2019**, *1* (2), 230–236. https://doi.org/10.1021/acsmaterialslett.9b00095.

(82) Zhang, Y.; Mullins, D. R.; Savara, A. Surface Reactions and Catalytic Activities for Small Alcohols over LaMnO 3 (100) and La 0.7 Sr 0.3 MnO 3 (100): Dehydrogenation, Dehydration, and Oxidation . *J. Phys. Chem. C* **2020**, *124* (6), 3650–3663. https://doi.org/10.1021/acs.jpcc.9b10797.

(83) Kubokawa, Y. DETERMINATION OF ACIDITY OF SOLID CATALYSTS BY AMMONIA CHEMISORPTION. *J. Phys. Chem.* **2002**, *67* (4), 769–771. https://doi.org/10.1021/J100798A011.

(84) Kester, P. M.; Miller, J. T.; Gounder, R. Ammonia Titration Methods To Quantify Brønsted Acid Sites in Zeolites Substituted with Aluminum and Boron Heteroatoms. *Ind. Eng. Chem. Res.* **2018**, *57* (19), 6673–6683. https://doi.org/10.1021/ACS.IECR.8B00933.

(85) Hattori, H. Solid Base Catalysts: Generation, Characterization, and Catalytic Behavior of Basic Sites. *J. Japan Pet. Inst.* **2004**, *47* (2), 67–81. https://doi.org/10.1627/JPI.47.67.

(86) A. Aziz, M. A.; A. Jalil, A.; S. Wongsakulphasatch; N. Vo, D.-V. Understanding the Role of Surface Basic Sites of Catalysts in CO 2 Activation in Dry Reforming of Methane: A Short Review. *Catal. Sci. Technol.* **2020**, *10* (1), 35–45. https://doi.org/10.1039/C9CY01519A.

(87) Polo-Garzon, F.; Wu, Z. Acid–Base Catalysis over Perovskites: A Review. *J. Mater. Chem. A* **2018**, *6* (7), 2877–2894. https://doi.org/10.1039/C7TA10591F.

(88) Calle-Vallejo, F.; Inoglu, N. G.; Su, H. Y.; Martínez, J. I.; Man, I. C.; Koper, M. T. M.; Kitchin, J. R.; Rossmeisl, J. Number of Outer Electrons as Descriptor for Adsorption Processes on Transition Metals and Their Oxides. *Chem. Sci.* **2013**, *4* (3), 1245–1249. https://doi.org/10.1039/C2SC21601A.

(89) Hong, W. T.; Welsch, R. E.; Shao-Horn, Y. Descriptors of Oxygen-Evolution Activity for Oxides: A Statistical Evaluation. *J. Phys. Chem. C* **2016**, *120* (1), 78–86. https://doi.org/10.1021/acs.jpcc.5b10071.

(90) Sellmyer, D. J. Electronic Structure of Metallic Compounds and Alloys: Experimental Aspects. *Solid State Phys. - Adv. Res. Appl.* **1978**, *33* (C), 83–248. https://doi.org/10.1016/S0081-1947(08)60469-5.

(91) Lankhorst, M. H. R.; Bouwmeester, H. J. M.; Verweij, H. Use of the Rigid Band Formalism to Interpret the Relationship between O Chemical Potential and Electron Concentration in <span Class. *Phys. Rev. Lett.* **1996**, *77* (14), 2989. https://doi.org/10.1103/PhysRevLett.77.2989.

(92) Lee, Y.-L.; Morgan, D.; Kleis, J.; Rossmeisl, J. Ab Initio Defect Energetics in LaBO3 Perovskite Solid Oxide Fuel Cell Materials. *ECS Trans.* **2009**, *25* (2), 2761. https://doi.org/10.1149/1.3205837.

(93) Lee, Y.-L.; Kleis, J.; Rossmeisl, J.; Morgan, D. Ab Initio Energetics of LaBO3(001) (B=Mn,Fe,CO, and Ni) for Solid Oxide Fuel Cell Cathodes. *Phys. Rev. B* **2009**, *80* (22), 224101. https://doi.org/10.1103/PhysRevB.80.224101.

(94) Jacobs, R.; Mayeshiba, T.; Booske, J.; Morgan, D. Material Discovery and Design Principles for Stable, High Activity Perovskite Cathodes for Solid Oxide Fuel Cells. *Adv. Energy Mater.* **2018**, *8* (11), 1702708.

https://doi.org/10.1002/aenm.201702708.

(95) Montoya, J. H.; Doyle, A. D.; Nørskov, J. K.; Vojvodic, A. Trends in Adsorption of Electrocatalytic Water Splitting Intermediates on Cubic ABO $_3$ Oxides. *Phys. Chem. Chem. Phys.* **2018**, *20* (5), 3813–3818. https://doi.org/10.1039/C7CP06539F.

(96) Hong, W. T.; Stoerzinger, K. A.; Moritz, B.; Devereaux, T. P.; Yang, W.; Shao-Horn, Y. Probing LaMO3 Metal and Oxygen Partial Density of States Using X-Ray Emission, Absorption, and Photoelectron Spectroscopy. *J. Phys. Chem. C* **2015**, *119* (4), 2063–2072. https://doi.org/10.1021/JP511931Y.

(97) Hong, W. T.; Stoerzinger, K. A.; Lee, Y.-L.; Giordano, L.; Grimaud, A.; Johnson, A. M.; Hwang, J.; Crumlin, E. J.; Yang, W.; Shao-Horn, Y. Charge-Transfer-Energy-Dependent Oxygen Evolution Reaction Mechanisms for Perovskite Oxides. *Energy Environ. Sci.* **2017**, *10* (10), 2190–2200. https://doi.org/10.1039/C7EE02052J.

(98) Jacobs, R.; Hwang, J.; Shao-Horn, Y.; Morgan, D. Assessing Correlations of Perovskite Catalytic Performance with Electronic Structure Descriptors. *Chem. Mater.* **2019**, *31* (3), 785–797. https://doi.org/10.1021/acs.chemmater.8b03840.

(99) Hong, W. T.; Stoerzinger, K. A.; Moritz, B.; Devereaux, T. P.; Yang, W.; Shao-Horn, Y. Probing LaMO3 Metal and Oxygen Partial Density of States Using X-Ray Emission, Absorption, and Photoelectron Spectroscopy. *J. Phys. Chem. C* **2015**, *119* (4), 2063–2072. https://doi.org/10.1021/jp511931y.

(100) Hong, W. T.; Stoerzinger, K. A.; Lee, Y.-L.; Giordano, L.; Grimaud, A.; Johnson, A. M.; Hwang, J.; Crumlin, E. J.; Yang, W.; Shao-Horn, Y. Charge-Transfer-Energy-Dependent Oxygen Evolution Reaction Mechanisms for Perovskite Oxides. *Energy Environ. Sci.* **2017**, *10* (10), 2190–2200. https://doi.org/10.1039/C7EE02052J.

(101) Grimaud, A.; Diaz-Morales, O.; Han, B.; Hong, W. T.; Lee, Y.-L.; Giordano, L.; Stoerzinger, K. A.; Koper, M. T. M.; Shao-Horn, Y. Activating Lattice Oxygen Redox Reactions in Metal Oxides to Catalyse Oxygen Evolution. *Nat. Chem.* **2017**, *9* (5), 457–465. https://doi.org/10.1038/nchem.2695.

(102) Sun, Y.; Liao, H.; Wang, J.; Chen, B.; Sun, S.; Ong, S. J. H.; Xi, S.; Diao, C.; Du, Y.; Wang, J.-O.; Breese, M. B. H.; Li, S.; Zhang, H.; Xu, Z. J. Covalency Competition Dominates the Water Oxidation Structure– Activity Relationship on Spinel Oxides. *Nat. Catal. 2020 37* **2020**, *3* (7), 554–563. https://doi.org/10.1038/s41929-020-0465-6.

(103) Lee, Y.-L.; Kleis, J.; Rossmeisl, J.; Shao-Horn, Y.; Morgan, D. Prediction of Solid Oxide Fuel Cell Cathode Activity with First-Principles Descriptors. *Energy Environ. Sci.* **2011**, *4* (10), 3966–3970. https://doi.org/10.1039/C1EE02032C.

(104) Mayeshiba, T. T.; Morgan, D. D. Factors Controlling Oxygen Migration Barriers in Perovskites. *Solid State Ionics* **2016**, *296*, 71–77. https://doi.org/10.1016/j.ssi.2016.09.007.

(105) Lee, Y. L.; Lee, D.; Wang, X. R.; Lee, H. N.; Morgan, D.; Shao-Horn, Y. Kinetics of Oxygen Surface Exchange on Epitaxial Ruddlesden-Popper Phases and Correlations to First-Principles Descriptors. *J. Phys. Chem. Lett.* **2016**, *7* (2), 244–249. https://doi.org/10.1021/acs.jpclett.5b02423.

(106) Grimaud, A.; May, K. J.; Carlton, C. E.; Lee, Y.-L.; Risch, M.; Hong, W. T.; Zhou, J.; Shao-Horn, Y. Double Perovskites as a Family of Highly Active Catalysts for Oxygen Evolution in Alkaline Solution. *Nat. Commun.* **2013**, *4*, 2439. https://doi.org/10.1038/ncomms3439.

(107) Ma, T.; Jacobs, R.; Booske, J.; Morgan, D. Understanding the Interplay of Surface Structure and Work Function in Oxides: A Case Study on SrTiO3. *APL Mater.* **2020**, *8* (7), 71110. https://doi.org/10.1063/1.5143325.

(108) Giordano, L.; Karayaylali, P.; Yu, Y.; Katayama, Y.; Maglia, F.; Lux, S.; Shao-Horn, Y. Chemical Reactivity Descriptor for the Oxide-Electrolyte Interface in Li-Ion Batteries. *J. Phys. Chem. Lett.* **2017**, *8*

(16), 3881–3887. https://doi.org/10.1021/acs.jpclett.7b01655.

(109)   Giordano, L.; Østergaard, T. M.; Muy, S.; Yu, Y.; Charles, N.; Kim, S.; Zhang, Y.; Maglia, F.; Jung, R.; Lund, I.; Rossmeisl, J.; Shao-Horn, Y. Ligand-Dependent Energetics for Dehydrogenation: Implications in Li-Ion Battery Electrolyte Stability and Selective Oxidation Catalysis of Hydrogen-Containing Molecules. *Chem. Mater.* **2019**, *31* (15), 5464–5474. https://doi.org/10.1021/acs.chemmater.9b00767.

(110)   Li, Y.; Cheng, W.; Sui, Z. J.; Zhou, X. G.; Chen, D.; Yuan, W. K.; Zhu, Y. A. Origin of Chemisorption Energy Scaling Relations over Perovskite Surfaces. *J. Phys. Chem. C* **2019**, *123* (46), 28275–28283. https://doi.org/10.1021/acs.jpcc.9b08741.

(111)   Di Valentin, C.; Pacchioni, G.; Selloni, A. Electronic Structure of Defect States in Hydroxylated and Reduced Rutile TiO2(110) Surfaces. *Phys. Rev. Lett.* **2006**, *97* (16), 166803. https://doi.org/10.1103/PhysRevLett.97.166803.

(112)   Hwang, J.; Rao, R. R.; Katayama, Y.; Lee, D.; Wang, X. R.; Crumlin, E.; Venkatesan, T.; Lee, H. N.; Shao-Horn, Y. CO $_2$ Reactivity on Cobalt-Based Perovskites. *J. Phys. Chem. C* **2018**, acs.jpcc.8b06104. https://doi.org/10.1021/acs.jpcc.8b06104.

(113)   Yoo, J. S.; Rong, X.; Liu, Y.; Kolpak, A. M. Role of Lattice Oxygen Participation in Understanding Trends in the Oxygen Evolution Reaction on Perovskites. *ACS Catal.* **2018**, *8* (5), 4628–4636. https://doi.org/10.1021/acscatal.8b00612.

(114)   Xie, W.; Lee, Y. L.; Shao-Horn, Y.; Morgan, D. Oxygen Point Defect Chemistry in Ruddlesden-Popper Oxides (La1-XSrx)2MO4±? (M = Co, Ni, Cu). *J. Phys. Chem. Lett.* **2016**, *7* (10), 1939–1944. https://doi.org/10.1021/acs.jpclett.6b00739.

(115)   Dickens, C. F.; Montoya, J. H.; Kulkarni, A. R.; Bajdich, M.; Nørskov, J. K. An Electronic Structure Descriptor for Oxygen Reactivity at Metal and Metal-Oxide Surfaces. *Surf. Sci.* **2019**, *681*, 122–129. https://doi.org/10.1016/j.susc.2018.11.019.

(116)   Rao, R. R.; Kolb, M. J.; Giordano, L.; Pedersen, A. F.; Katayama, Y.; Hwang, J.; Mehta, A.; You, H.; Lunger, J. R.; Zhou, H.; Halck, N. B.; Vegge, T.; Chorkendorff, I.; Stephens, I. E. L.; Shao-Horn, Y. Operando Identification of Site-Dependent Water Oxidation Activity on Ruthenium Dioxide Single-Crystal Surfaces. *Nat. Catal.* **2020**, *3* (6), 516–525. https://doi.org/10.1038/s41929-020-0457-6.

(117)   Østergaard, T. M.; Giordano, L.; Castelli, I. E.; Maglia, F.; Antonopoulos, B. K.; Shao-Horn, Y.; Rossmeisl, J. Oxidation of Ethylene Carbonate on Li Metal Oxide Surfaces. *J. Phys. Chem. C* **2018**, *122* (19), 10442–10449. https://doi.org/10.1021/acs.jpcc.8b01713.

(118)   Grimaud, A.; May, K. J.; Carlton, C. E.; Lee, Y. L.; Risch, M.; Hong, W. T.; Zhou, J.; Shao-Horn, Y. Double Perovskites as a Family of Highly Active Catalysts for Oxygen Evolution in Alkaline Solution. *Nat. Commun.* **2013**, *4* (1), 1–7. https://doi.org/10.1038/ncomms3439.

(119)   Guan, D.; Zhou, J.; Huang, Y.-C.; Dong, C.-L.; Wang, J.-Q.; Zhou, W.; Shao, Z. Screening Highly Active Perovskites for Hydrogen-Evolving Reaction via Unifying Ionic Electronegativity Descriptor. *Nat. Commun. 2019 101* **2019**, *10* (1), 1–8. https://doi.org/10.1038/s41467-019-11847-w.

(120)   Dou, Y.; Xie, Y.; Hao, X.; Xia, T.; Li, Q.; Wang, J.; Huo, L.; Zhao, H. Addressing Electrocatalytic Activity and Stability of LnBaCo2O5+δ Perovskites for Hydrogen Evolution Reaction by Structural and Electronic Features. *Appl. Catal. B Environ.* **2021**, *297*, 120403. https://doi.org/10.1016/J.APCATB.2021.120403.

(121)   Nitadori, T.; Ichiki, T.; Misono, M. Catalytic Properties of Perovskite-Type Mixed Oxides (ABO $_3$) Consisting of Rare Earth and 3d Transition Metals. The Roles of the A- and B-Site Ions . *Bull. Chem. Soc. Jpn.* **1988**, *61* (3), 621–626. https://doi.org/10.1246/bcsj.61.621.

(122)   Chen, Z. B.; Ling, T. R.; Lee, M. D. Kinetic Study of Methane Oxidation over Perovskite Oxides La1-XSrxCoO3. *React. Kinet. Catal. Lett.* **1997**, *62* (1), 185–190. https://doi.org/10.1007/BF02475731.

(123)   Salmeron, M. From Surfaces to Interfaces: Ambient Pressure XPS and Beyond. *Top. Catal. 2018 6120* **2018**, *61* (20), 2044–2051. https://doi.org/10.1007/S11244-018-1069-0.

(124)   Stoerzinger, K. A.; Hong, W. T.; Crumlin, E. J.; Bluhm, H.; Shao-Horn, Y. Insights into Electrochemical Reactions from Ambient Pressure Photoelectron Spectroscopy. *Acc. Chem. Res.* **2015**, *48* (11), 2976–2983. https://doi.org/10.1021/acs.accounts.5b00275.

(125)   Meunier, F. C. Pitfalls and Benefits of in Situ and Operando Diffuse Reflectance FT-IR Spectroscopy (DRIFTS) Applied to Catalytic Reactions. *React. Chem. Eng.* **2016**, *1* (2), 134–141. https://doi.org/10.1039/C5RE00018A.

(126)   Kulkarni, A.; Siahrostami, S.; Patel, A.; Nørskov, J. K. Understanding Catalytic Activity Trends in the Oxygen Reduction Reaction. *Chem. Rev.* **2018**, *118* (5), 2302–2312. https://doi.org/10.1021/ACS.CHEMREV.7B00488.

(127)   Honkala, K.; Hellman, A.; Remediakis, I. N.; Logadottir, A.; Carlsson, A.; Dahl, S.; Christensen, C. H.; Nørskov, J. K. Ammonia Synthesis from First-Principles Calculations. *Science (80-.).* **2005**, *307* (5709), 555–558. https://doi.org/10.1126/SCIENCE.1106435.

Chapter 2. Towards room temperature formaldehyde oxidation on manganese oxide

2.1 Introduction

Formaldehyde (HCHO), a volatile organic compound (VOC), is a component of indoor air which is a potential carcinogen and respiratory irritant.[1,2] A number of various adsorbent,[3,4] photocatalytic,[5] and catalytic strategies[6,7] have been devised to eliminate formaldehyde at room temperature. Noble metal-based catalysts supported on inexpensive oxide support such as Au/CeO$_2$,[8] Ag/HZSM,[9] Pt/TiO$_2$[10] can effectively oxidize formaldehyde (HCHO) to carbon dioxide (CO$_2$) at room temperature but the high cost of noble metal based catalysts limits their widespread usage. Alternatively, transition metal oxides of manganese,[11,12,13] cobalt,[14,15] and composites based on these oxides such as MnO$_x$-CeO$_2$,[1] CuO/MnO$_2$,[16] Co$_3$O$_4$- CeO$_2$[17] have been explored for HCHO oxidation despite their lower activity. Specifically, manganese oxides have been studied extensively because of their formaldehyde oxidation activity[18] and the ability to tune the activity by modifying the tunnel structure,[19] morphology,[20] and alkali metal additives.[21] Along with the catalyst surface tuning, introduction of water vapor into the reaction gas stream of HCHO and O$_2$ is also known to improve the rate of CO$_2$ generation at room temperature for manganese oxide catalysts.[22,23,24] However, surface poisoning of monoclinic[1], spinel[13], and δ-MnO$_2$[16,19,21] manganese oxide phases limits the usage for formaldehyde oxidation due to accumulation of bidentate formate[9,8,13] and carbonate[26,25] reaction intermediates as observed by Diffuse Reflectance Infrared Transmission Spectroscopy (DRIFTS). While the reaction kinetics of oxidation of reactions intermediates to CO$_2$ on these different crystal structures can be different owing to the differences in water content,[22] surface defects,[27] and manganese oxidation state,[28] the build-up of formate and carbonate intermediates observed in situ with DRIFTS over time indicates the generality of the poisoning phenomenon and the need to understand dehydrogenation kinetics.

Unfortunately, the deactivation of catalysts under steady state conditions still presents a practical challenge [17,29] and the reaction mechanism of formaldehyde oxidation in the presence of water at room temperature is not well understood.[30] Different reaction pathways have been proposed for the conversion of HCHO to CO$_2$ via the formation of dioxymethylene (DOM, HCHOO$_{oxide}$) and formate (HCOO$_{oxide}$) reaction intermediates as shown in Figure A.1.1A[11] as well as formate

(HCOO$_{oxide}$) and carbonate (CO$_2$O$_{oxide}$) reaction intermediates without the formation of DOM (HCHOO$_{oxide}$) in Figure A.1.1B[22,13] for birnessite MnO$_x$. Not all the reaction intermediates (DOM, formate, carbonate) have been consistently observed during HCHO oxidation as the role of surface-species such as adsorbed water, hydroxyl, or oxygen is different amongst the investigated manganese oxides.[31] Although the presence of surface-species such as adsorbed water, hydroxyl[26,32] or oxygen[8,17] has shown to increase the HCHO oxidation activity, the specific role of each of these species in the reaction mechanism has not been explored comprehensively. For example, water is known to affect the reaction mechanism for oxidation of HCHO via competitive adsorption, solvation effect, renewal of surface hydroxyls, mediating H-transfer, or forming active -OOH type species.[33,34]

As the precise role of water involved in aiding formaldehyde oxidation and the reaction intermediates involved in the mechanism is unclear, there is a compelling need to understand the reaction kinetics and to probe reaction intermediates under HCHO concentrations relevant for indoor air pollution. Typical international guideline values and recommendations for formaldehyde indoor air concentration lie in the range of 0.002-0.3 ppm$_{HCHO}$,[Table.5,2], Unfortunately, previous studies in literature have been limited to inlet formaldehyde concentration in the range of few tens to hundreds of parts per million (ppm) under wide-ranging relative humidity of 0-50%.[29,35,36]

In this study, formaldehyde oxidation kinetics were examined for a series of formaldehyde concentrations (0.5-20 ppm$_{HCHO}$) to understand the role of water, oxygen, and catalyst loading for commercial birnessite manganese oxide under continuous flow and transient reaction conditions. Using in situ DRIFTS and density functional theory (DFT) calculations on a model β-MnO$_2$ (110) surface, the nature of reaction intermediates and their interaction with water is discussed. It is demonstrated that surface poisoning by carbonaceous species can be overcome on a commercial birnessite manganese oxide at room temperature by tuning the surface coverage of various reaction intermediates. A generalized framework for the elimination of bidentate formate and carbonate reaction intermediates is then suggested via understanding the role of surface oxygen, hydroxyl, and adsorbed water species.

2.2 Experimental and computational methods

2.2.1 Experimental details

Material

MnO_x catalyst sample was directly procured from BASF Corporation with a BET surface area of 180 m^2g. X-Ray diffraction pattern shown in Figure A.1.2A of the manganese oxide used in the study can be described by a layered birnessite phase with edge sharing MnO_6 octahedra[22] and potassium additives as seen in the K $2p$ region of the XPS (Figure A.1.2B). Surface hydroxyls, surface adsorbed oxygen, and structural water[22] were also observed in the thermo-gravimetric (TG) mass loss curve (Figure A.1.2C).

Plug flow reactor measurements

25/100 mg catalyst was mixed with oven-dried sand (2.5 g) and loaded into a quartz tube (3.81 mm id). A total flow rate of 200 ml min^{-1} was used for all the plug flow reactor experiments and the flow rate of individual gases, HCHO, CO, CO_2, O_2, and N_2 was controlled using dedicated mass flow controllers. A water bubbler at room temperature connected to the N_2 gas line was used to introduce water vapor into the gas stream. The gas composition was analyzed using a PIKE FTIR gas cell attached to a Bruker Vertex 70 FT-IR spectrophotometer after measuring for HCHO and CO_2 gas sensitivity as shown in Figure A.1.3A and Figure A.1.3B respectively. 32 scans were collected at a resolution of 4 cm^{-1} every 12.5 min. prior to flowing the reaction gas mixture, the catalyst was purged with $100\%_{N2}$ at room temperature for 2 hrs to remove any weakly adsorbed water and background spectrum was collected in $100\%_{N2}$. To evaluate the role of water and oxygen in HCHO oxidation, the catalyst was exposed to 0.5-20 ppm_{HCHO} in four different gas mixtures, $10\%_{O2}/Balance_{N2}$, $100\%_{N2}$, $0.7\%_{H2O}/Balance_{N2}$, and $0.7\%_{H2O}/10\%_{O2}/Balance_{N2}$ at room temperature and also $10\%_{O2}/Balance_{N2}$, $100\%_{N2}$, $0.7\%_{H2O}/Balance_{N2}$, and $0.7\%_{H2O}/10\%_{O2}/Balance_{N2}$ without HCHO in the gas steam (referred to as transient conditions) to understand reaction kinetics at room temperature.

The % conversion of HCHO to CO_2 is calculated using the formula, CO_2 conversion (%) = 100*(ppm$_{CO2}$/ppm$_{HCHO}$), where ppm$_{HCHO}$ is the inlet concentration of formaldehyde gas that the catalyst was exposed to and ppm$_{CO2}$ is the CO_2 generated. The percentage of HCHO adsorbed (%) (and not oxidized) was calculated using the formula, 100*(ppm$_{HCHOout}$/ppm$_{HCHOin}$), where ppm$_{HCHOin}$ was the inlet concentration of formaldehyde gas that the catalyst was exposed to and ppm$_{HCHOout}$ was the HCHO measured after exposure to the catalyst. Surface coverage of carbonaceous species was calculated by subtracting the total amount of CO_2 converted from the amount of HCHO that the catalyst adsorbed to the breakthrough point using the equation,

$\theta(ML) = \frac{10^{-9} * N_A * F * (\int(C^O_{HCHO} - C_{HCHO})dt - \int C_{CO_2} dt)}{N_s * V_M}$, N_A is the Avogadro's number, V_m is the molar

volume (mol l^{-1}), F is the flow rate (ml min^{-1}), C^O_{HCHO} is the inlet HCHO concentration in ppm$_m$, C_{HCHO} is the outlet HCHO gas concentration in ppm$_m$, C_{CO_2} is the outlet gas concentration in ppm$_m$, N_s is the total available surface sites ($1.5*10^{19}$ sites) calculated using a surface site density of 10 sites/nm^2 [37] assuming that 1/3 of the sites are available for HCHO adsorption. Breakthrough time was defined as the time when less than 90% of the inlet HCHO concentration is adsorbed.

In situ DRIFTS

In situ Diffuse Reflectance Infrared Fourier Transmission Spectroscopy (DRIFTS) measurements were carried out using the Praying Mantis setup (Harrick) in an environmental chamber with KBr windows. Manganese oxide (25 mg) and KBr powder (25 mg) were mixed and loaded into the reaction chamber. Similar to the plug flow experiments, prior to flowing the reaction gas mixture; the catalyst was purged with 100%$_{N2}$ at room temperature for 2 hrs to remove any weakly adsorbed water. Background spectrum shown in Figure A.1.4 was collected under a flow of 10%$_{O2}$/Balance$_{N2}$ at room temperature while relevant spectra were collected by averaging 128 scans at a resolution of 2 cm^{-1} every 3 min after background subtraction. Inlet reaction gas mixtures 0.5 ppm$_{HCHO}$-20 ppm$_{HCHO}$ with balance mixtures of 100%$_{N2}$, 10%$_{O2}$/Balance$_{N2}$, 0.7%$_{H2O}$/Balance$_{N2}$, 0.7%$_{H2O}$/10%$_{O2}$/Balance$_{N2}$, and 1.9%$_{H2O}$/Balance$_{N2}$ were studied. To identify reaction intermediates, different combinations of catalyst loading, HCHO concentration, and flow rates were used to access different surface coverage of reaction intermediates as shown in Table A.1.1. Peaks at 1567, 1384, and 1354 cm^{-1} in Figure A.1.5A and

2882 cm^{-1} in Figure A.1.5B were assigned to the $\nu_{as}(OCO)$, $\delta(CH)$, $\nu_{as}(OCO)$, $\upsilon(CH)$ stretching modes of bidentate formate species (HCOO$_{Oxide}$)[38,39,26] while the peak at 1728 cm^{-1} was assigned to $\upsilon(CO)$ stretching mode of molecularly adsorbed HCHO.[40] Peaks at 969, 1054, 1420 cm^{-1} in Figure A.1.5A and 2944 cm^{-1} in Figure A.1.5B were assigned to $\upsilon(CO)$, $\rho(CH_2)$, $\delta(CH_2)$, and $\upsilon(CH_2)$ stretching modes of dioxymethylene (DOM, HCHOO$_{oxide}$) species.[40,41] The decrease in intensity at 3590 cm^{-1} in Figure A.1.5B was assigned to the terminal/CUS surface hydroxyl (OH$_{CUS}$) associated with K$^+$ ions.[26] and the increase in intensity at 3280 cm^{-1} was assigned to lattice/bridge hydroxyl species, OH$_{BRI}$. To evaluate the nature of the peaks at 1512 and 1324 cm^{-1}, the catalyst was exposed to CO_2 using the gas mixture of 100%$_{CO2}$ which revealed peaks 1512 cm^{-1} and 1324 cm^{-1} (Figure A.1.6A) suggesting the peaks correspond to $\nu_{as}(OCO)$ and $\upsilon_s(OCO)$ stretching modes of bidentate carbonate-type species (COO$_{2oxide}$).[42,43] Water adsorption was carried out using 1.9%$_{H2O}$/Balance$_{N2}$ to identify water-related vibration modes. The peak at 1648 cm^{-1} and 1350 cm^{-1} peaks were assigned to the water bending (H$_2$O$_{water}$) and water-alkali metal mode of interactions in Figure A.1.6A respectively and the broad peak between 2800-3700 cm^{-1} in Figure A.1.6B was assigned to the OH$_{water}$ stretching of water overlapping with the OH$_{BRI}$ peak. The peak assignments are in agreement with previous experimental studies and are further supported by computed peaks of DOM, bidentate formate, and carbonate reaction intermediates from DFT which are also comparable to previously computed wavenumbers as shown in Table A.1.2.

2.2.2 Theoretical calculations

Density Functional Theory

β-MnO$_2$ (rutile) crystal structure was chosen as a model system as it is the thermodynamically most stable crystal structure of manganese oxide,[44] is known to be active in a variety of catalytic [45,46] and battery applications[47,48] and has been extensively used to model manganese oxide catalysts for NO oxidation [49–51] and battery applications.[52,53] Furthermore, the local structure of birnessite manganese oxide is poorly crystalline and difficult to characterize due to the presence of water and alkali atoms in the structure.[54]

The (110) facet of β-MnO$_2$ was chosen to compute adsorption energies as it has the lowest surface energy amongst the commonly encountered facets such as (001), (100), (111), (101), and (100), as shown in Table A.1.3. The (110) surface comprises of 2c bridge (BRI) oxygen atoms and 5c coordinately unsaturated (CUS) manganese atom sites (Mn$_{CUS}$) that are amenable to adsorption at room temperature (Figure A.1.7A). The (100) surface of the birnessite phase and the stoichiometric rutile (110) with the bridge oxygen (O$_{BRI}$) and the row of 5c Mn metal atom sites amenable to adsorption are shown in Figure A.1.7A and Figure A.1.7B respectively.

The surface phase diagram of the (110) MnO$_2$ surface was developed as a function of oxygen and water chemical potential (Figure A.1.8) with reference to the stoichiometric surface. To model the dry reaction conditions, relevant oxygen pressure range from 0 to10%, at 25 °C were considered where the surface structure was predicted to be stoichiometric with the bridge sites completely filled with oxygen while the O$_{CUS}$ sites being vacant as shown in Figure A.1.8, which is in agreement with the weak oxygen adsorption of +1.07 eV on the Mn$_{CUS}$ sites and strong adsorption of -0.55 eV for the bridge sites consistent with the +0.99 eV for the Mn$_{CUS}$ and -0.63 eV for the bridge site reported previously for MnO$_2$ (110).[49] Next, as the oxide surface contained terminal/CUS hydroxyl species as evidence from TGA (Figure A.1.2C) and DRIFTS (Figure A.1.5B), OH on Mn$_{CUS}$ (OH$_{CUS}$) was considered to understand the role of surface hydroxyl for HCHO oxidation. Also, the presence of K$^+$ ions favors the dissociation of water by -0.2 eV relative to the surface without K$^+$ addition in Figure A.1.9C and compared in Table A.1.4. Next, we also considered surface adsorbed oxygen (O$_{CUS}$) on the Mn$_{CUS}$ site to model the adsorbed oxygen that have been reported to be the active species during HCHO oxidation for birnessite manganese oxides using during low temperature O$_2$-TPR.[55] Such O$_{CUS}$ are also formed more favorably by -0.44 eV in the presence of K$^+$ atoms when compared to the stoichiometric surface without K$^+$ atoms as seen in Figure A.1.9A, Figure A.1.9B, and Table A.1.4. Finally, we also considered surface with both OH$_{CUS}$ and O$_{CUS}$ to model the synergistic effect of both species in aiding HCHO oxidation.[56] Finally, to understand the role of water in aiding HCHO oxidation and the interaction of water with reaction intermediates, we considered addition of molecular water to the oxide surface with formate and carbonate reaction intermediates.

VASP package [57–59] was used to perform the DFT calculations with the PBE functional[60] and PAW projectors.[61,62] Hubbard correction of U = 2.8 eV and J = 1.2 [63] (U$_{eff}$ = 1.6 eV) was used for Mn 3d.

The cut off energy was chosen as 550 eV while the Monkhorst–Pack [64] The calculated super cell was a 1 × 2 repeated unit, with 4 Mn–O layers (2 free to relax and 2 fixed) was used for the generation of the surface phase diagram while a larger unit 1x3 was used for the reaction pathway evaluation. 8x8x1 k-point sampling for the super cell was used for the 1x2 unit cell while 5x8x1 was used for the 1x3 unit cell. The Gibbs free energies were calculated by correcting the DFT energies (E) by Zero Point Energy (ZPE) and vibrational entropy using the formula, $\Delta G = E + ZPE - T\Delta S$.[65] For the surface, the contributions of all atoms beyond the fully reduced surface were considered for the ZPE and vibrational entropy terms.[66,67] The adsorbed species were referenced to the table value of gas-phase values. Gas phase O_2 reference was calculated using the formula,

$$G_{O2} = G_{H2O} - G_{H2} - \Delta G_{exp}$$

Two different methodologies were used to calculate the energy of the dissociated hydrogen to form a bridge hydroxyl to model coverage at high and low coverage. In the first method, the binding energy of the configuration was calculated using a surface containing carbonaceous reaction intermediate and the bridge hydroxyls co-adsorbed on a single simulation cell of 3 x 1 Å, modelling high hydroxyl coverage (θ_{high}) while in the second case, two different simulation cells of 3 x 1 Å were used for the bridge hydroxyls and the carbonaceous intermediate to model the low hydroxyl coverage (θ_{low}).

2.3 Catalyst deactivation with increasing HCHO concentration

Complete removal of formaldehyde was observed by exposing the manganese dioxide to formaldehyde at low concentrations at room temperature (Figure 1A). Total conversion of HCHO to CO_2 of ~16 % was noted for the reaction condition of 0.5 ppm_{HCHO}/Balance$_{N2}$ for 1500 min, while the addition of water vapor resulted in nearly complete HCHO conversion to CO_2 for the reaction conditions of 0.5 ppm_{HCHO}/0.7%$_{H2O}$/Balance$_{N2}$ and 0.5 ppm_{HCHO}/0.7%$_{H2O}$/10%$_{O2}$/Balance$_{N2}$.

Unfortunately, the catalyst became deactivated after 5000 minutes in presence of water vapor, as seen by the decrease in CO_2 conversion in the inset of Figure 1A. Moreover, DRIFTS spectra after flowing 0.5 ppm_{HCHO}/Balance$_{N2}$ for 1500 minutes revealed the presence of bidentate formate (HCOO$_{oxide}$: 1565, 1373, 1350 and 1320 cm^{-1}[38,39,26] and carbonate (CO_2O_{oxide}: 1512 and

1340 cm^{-1} in Figure 1B)[42,43] reaction intermediates (Figure 1B). Interestingly, dioxymethylene reaction intermediate (DOM, $HCHOO_{oxide}$: 1432, 1154 and 996 cm^{-1})[40,41] reported previously[11] was not observed. On the other hand, DRIFTS measurements after exposure for 1500 minutes in presence of water vapor, for the reaction conditions of 0.5 ppm_{HCHO}/0.7%$_{H2O}$/ $Balance_{N2}$ and 0.5 ppm_{HCHO}/0.7%$_{H2O}$/10%$_{O2}$/$Balance_{N2}$, showed molecular water (H-O-H bending at 1648 cm^{-1}, Figure 1B) and OH stretching in water (2680-3550 cm^{-1} in Figure 1C). The peak intensities from potential reaction intermediates from HCHO oxidation were not observed with experimental certainty. We subsequently purged the DRIFTS reaction chamber with 100%$_{N2}$ to reduce the signals from water, which revealed much lower intensities of $HCOO_{oxide}$ and CO_2O_{oxide} reaction intermediates in comparison to the reaction condition of 0.5 ppm_{HCHO}/$Balance_{N2}$ (Figure 1B). Therefore, the complete conversion of HCHO to CO_2 with the addition of water vapor can be attributed to the reduced built up of reaction intermediates such as $HCOO_{oxide}$ and CO_2O_{oxide} on the catalyst surface facilitated by water. Furthermore, the corresponding hydroxyl region after 100%$_{N2}$ purging in both the cases where 0.7%$_{H2O}$ was present in the gas stream revealed the loss of intensity at 3590 cm^{-1} assigned to OH_{CUS} (Figure 1C) and the increase in intensity in the 2700 cm^{-1} and 3600 cm^{-1} region attributed to formation of the bridge hydroxyl (OH_{BRI}). Therefore, the complete conversion of HCHO to CO_2 (Figure 1A), along with the lower intensity of the carbonaceous reaction intermediates (Figure 1B) and the decrease in OH_{CUS} intensity peak intensity and the formation of the OH_{BRI} and suggests that the deactivation of the catalyst in the presence of water vapor is not due to buildup of carbonaceous reaction intermediates but due to the decrease in the intensity of OH_{CUS} and the buildup of OH_{BRI}. Next, we studied the role of increasing HCHO concentration in the gas stream to understand the nature of the reaction intermediates.
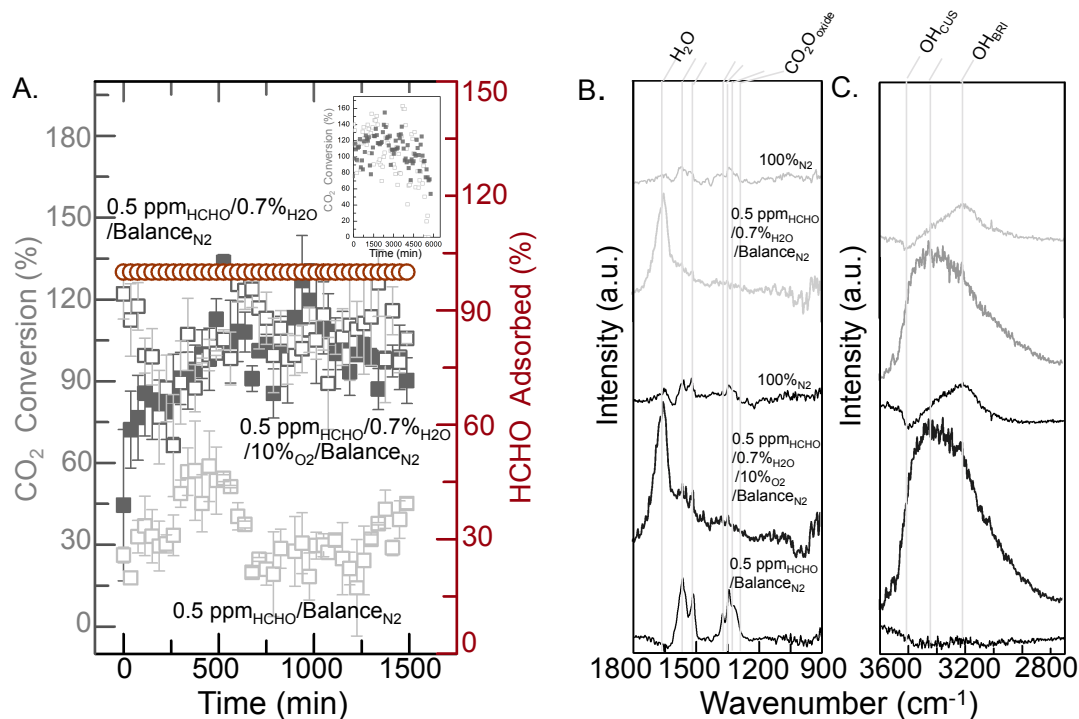
Figure 1: Complete HCHO oxidation at low concentration. A) Reactor data for 0.5 $ppm_{HCHO}/Balance_{N2}$ (light grey), $0.5ppm_{HCHO}/0.7\%_{H2O}/10\%_{O2}/Balance_{N2}$ (dark grey), and $0.5ppm_{HCHO}/0.7\%_{H2O}/10\%_{O2}/Balance_{N2}$ (medium grey) inlet gas compositions showing CO_2 converted (%) and HCHO adsorbed (%) for 1500 min and inset showing decrease in CO_2 converted for the $0.5ppm_{HCHO}/0.7\%_{H2O}/10\%_{O2}/Balance_{N2}$ (dark grey), and $0.5ppm_{HCHO}/0.7\%_{H2O}/10\%_{O2}/Balance_{N2}$ (medium grey) at ~5000 min. HCHO adsorbed is not shown in this case due to detection limitation. DRIFTS spectra collected B) in the 900-1800 cm^{-1} region showing the formation formate ($HCOO_{oxide}$), and carbonate (COO_{2oxide}) reaction intermediates in the dry conditions (light grey), after flowing 0.5 $ppm_{HCHO}/Balance_{N2}$ for 1500 min whereas only water-related peak at 1647 cm^{-1} is observed case when water vapor was also present in the gas stream (medium and light grey). Purging with $100\%_{N2}$ for 400 min removed the water related peak at 1647 cm^{-1} to reveal smaller intensity of the carbonate and formate reaction intermediates, C) in the 2700-3700 cm^{-1} region showing water related O-H stretching peak in the presence of water in the gas stream for the $0.5ppm_{HCHO}/0.7\%_{H2O}/10\%_{O2}/Balance_{N2}$ and $0.5ppm_{HCHO}/0.7\%_{H2O}/10\%_{O2}/Balance_{N2}$ and purging with $100\%_{N2}$ revealed a loss of intensity of the OH_{CUS} at 3590 cm^{-1} and a gain in intensity of OH_{BRI} between 2700 and 3600 cm^{-1}. Catalyst loading was 25 mg MnO_x and total gas flow rate was 200 ml min^{-1} and error bars are obtained from three separate measurements. The % conversion of HCHO to CO_2 was calculated using the formula, $\%conversion = 100*(ppm_{CO2}/ppm_{HCHO})$, where ppm_{HCHO} was the inlet concentration of formaldehyde gas that the catalyst was exposed to and ppm_{CO2} was the CO_2 generated. The % HCHO adsorbed was calculated using the formula, $\%conversion = 100*(ppm_{HCHOout}/ppm_{HCHOin})$, where ppm_{HCHOin} was the inlet concentration of formaldehyde gas that the catalyst was exposed to and $ppm_{HCHOout}$ was the HCHO measured after exposure to the catalyst. 25 mg MnO_x catalyst was mixed with 25 mg KBr for the DRIFTS measurements and total flow rate was 200 ml min^{-1} was used for all the measurements.

With increasing HCHO concentrations from 0.5 ppm to 20 ppm, the time for complete HCHO removal as well as the HCHO conversion (%) was reduced considerably. Increasing HCHO concentration from 0.5 ppm_{HCHO} to 20 ppm_{HCHO} with 0.7%$_{H2O}$/Balance$_{N2}$ decreased the time for complete HCHO removal from 4500 min to 50 min, as shown in Figure 2A. Interestingly, the CO_2 conversion (%) for HCHO concentrations of 1 ppm and greater was found to first increase and then decrease with time, where the peak of CO_2 conversion (%) was associated with the onset of HCHO release as seen in Figure 2A. The correlation of the onset of HCHO release and the decrease in CO_2 conversion (%) can be attributed to the lack of surface adsorption sites for HCHO due to gradual buildup of reaction intermediates from HCHO adsorption with time. This hypothesis is in agreement with shortened time for complete HCHO removal with greater coverage of HCHO adsorbed on the catalyst surface (estimated from CO_2 conversion and HCHO adsorbed in Figures 2A), giving rise to increased HCHO surface coverage from ~0 to 1.12 ML from 0.5 to 20 ppm HCHO concentration as seen in Figure 2B, which will be further discussed in the context of DRIFTS measurements in later sections. Further support came from the observation that increasing catalyst loading or surface area in the measurements from 25 mg to 100 mg lengthened the time of complete HCHO removal as shown in Figure 2C. Interestingly, the percentage of conversion to CO_2 was not enhanced by having greater total catalyst surface area (Figure 2C), where similar turnover frequency (TOF) was found for a greater catalyst loading. (Table A.1.5). This observation suggests that the adsorption of HCHO on the catalyst area is not rate limiting for the conversion kinetics of HCHO to CO_2, and further mechanistic details will be discussed in the later section. In addition, the presence of water vapor in the measurements or the adsorption of water on the catalyst surface can reduce the availability of surface sites for HCHO adsorption and shorten the time of complete HCHO removal. The time of complete HCHO removal was ~175 minutes under 20 ppm_{HCHO}/Balance$_{N2}$ and 20 ppm_{HCHO}/10%$_{O2}$/Balance$_{N2}$ which was much longer than those (~50 minutes) obtained from 0.7%$_{H2O}$/10%$_{O2}$/Balance$_{N2}$ and 20 ppm_{HCHO}/0.7%$_{H2O}$/Balance$_{N2}$, as shown in Figure 2DD. Moreover, the addition of water vapor was found to greatly enhance the percentage of conversion from HCHO to CO_2, as shown by much greater percentage of CO_2 conversion (~40%) for 20 ppm_{HCHO} with 0.7%$_{H2O}$/10%$_{O2}$/Balance$_{N2}$ and 0.7%$_{H2O}$/Balance$_{N2}$ than those of with 10%$_{O2}$/Balance$_{N2}$ and Balance$_{N2}$ (~7%, Fig. 2D). To confirm the role of water in decreasing

the time of complete HCHO removal, we first exposed the catalyst to 20 ppm$_{HCHO}$/0.7%$_{H2O}$/Balance$_{N2}$ for ~50 minutes to the onset of HCHO release and then switched 20 ppm$_{HCHO}$/Balance$_{N2}$, which yielded additional ~100 min for complete HCHO removal (Figure A.1.10). Next, we studied the role of water and HCHO concentration in affecting the nature of reaction intermediates using DRIFTS.
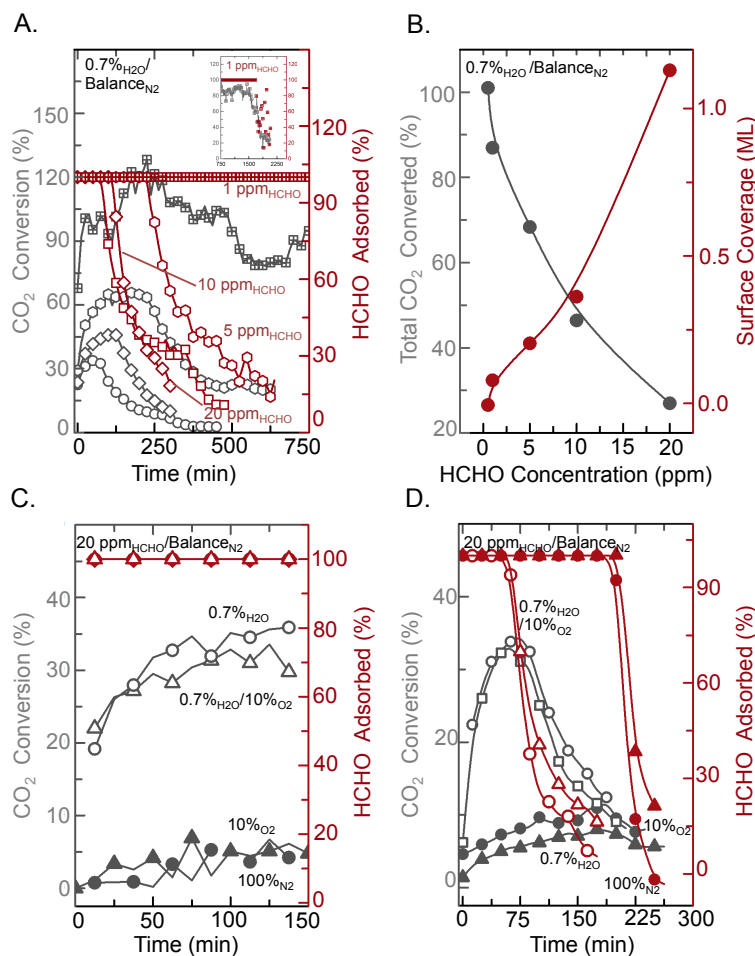
Figure. 2: Effect of water and HCHO concentration in HCHO conversion to CO₂. *Reactor data showing A) CO₂ conversion (%) and HCHO adsorption (%) with time showing an increase in CO₂ conversion with time until HCHO adsorption breakthrough for HCHO concentrations of 1-20 ppm with 0.7%$_{H2O}$/Balance$_{N2}$, B) Total CO₂ converted (%) and surface coverage of carbonaceous reaction intermediates till HCHO breakthrough as a function of HCHO concentration showing an increase in CO₂ conversion from 30% and surface coverage of 1.05 ML to ~0 ML at 20 ppm$_{HCHO}$/0.7%$_{H2O}$/Balance$_{N2}$ HCHO to ~100% at 0.5 ppm $_{HCHO}$ /0.7%$_{H2O}$/Balance$_{N2}$ with decreasing the low concentration, C) CO₂ conversion (%) and HCHO adsorption (%) with time for the 20 ppm$_{HCHO}$/0.7%$_{H2O}$/Balance$_{N2}$ with 25 mg and 100 mg MnO$_x$ catalyst loading, D) CO₂ conversion (%) and HCHO adsorption (%)with time for 20 ppm$_{HCHO}$/0.7%$_{H2O}$/Balance$_{N2}$, 20 ppm$_{HCHO}$/10%$_{O2}$/0.7%$_{H2O}$ /Balabce$_{N2}$, 20 ppm$_{HCHO}$/Balance$_{N2}$*

*and 20 ppm$_{HCHO}$/10%$_{O2}$/Balance$_{N2}$ reaction conditions. Total gas flow rate was 200 ml min^{-1} for all the reactor experiments. Total CO$_2$ conversion (%) and surface coverage of carbonaceous species was calculated by subtracting the total amount of CO$_2$ converted from the amount of HCHO adsorbed up to the breakthrough point using the equation, $\theta(ML) = \frac{10^{-9}*N_A*F*\left(\int(C_{HCHO}^O - C_{HCHO})dt - \int C_{CO_2}dt\right)}{N_s*V_M}$, N$_A$ is the Avogadro's number, V$_m$ is the molar volume (mol l^{-1}), F is the flow rate (ml min^{-1}), C_{HCHO}^O is the inlet HCHO concentration in ppm$_m$, C_{HCHO} is the outlet HCHO gas concentration in ppm$_m$, C_{CO_2} is the outlet gas concentration in ppm$_m$, N$_s$ is the total available surface sites (1.5*10^{19} sites) calculated using a surface site density of 10 sites/nm^2 [37] assuming that 1/3 of the sites are available for HCHO adsorption. Breakthrough time was defined as the time when less than 90% of the inlet HCHO concentration is adsorbed.*

2.4 In situ DRIFTS measurements with increasing HCHO concentration

In situ DRIFTS measurements were performed to understand the role of HCHO concentration and water on the nature and amount of reaction intermediates on the catalyst surface, which could influence the time of complete HCHO removal and the percentage of HCHO to CO$_2$ conversion. DRIFTS spectra were dominated by molecular water (H-O-H bending at 1648 cm^{-1} and O-H stretching between 2800-3600 cm^{-1} in Figure A.1.6) at low HCHO concentrations of 0.5 and 1 ppm with 0.7%$_{H2O}$/Balance$_{N2}$ in Figure 3A, bidentate formate (HCOO$_{oxide}$: 1567, 1384, 1354, 1320 cm^{-1}) [38,39,26] and carbonate (COO2$_{oxide}$: 1512 and 1340 cm^{-1})[43] became dominant with increasing HCHO concentrations from 5 to 20 ppm, which was accompanied with significant reduction in the intensity of H-O-H bending at 1648 cm^{-1} as seen in Figure 3A. In addition, the peaks of DOM (HCHOO$_{oxide}$: 1432, 1154 and 996 cm^{-1}) were not discerned up to 120 minutes within experimental uncertainty for all the HCHO concentrations examined in presence of water vapour (0.7%$_{H2O}$/Balance$_{N2}$ in Figure 3A and **A.1.**11A specifically for HCHOO$_{oxide}$ and HCOO$_{oxide}$ regions). Moreover, the spectra obtained under 20 ppm$_{HCHO}$/0.7%$_{H2O}$/10%$_{O2}$/Balance$_{N2}$ were found to be similar to those obtained without oxygen in the gas stream (20 ppm$_{HCHO}$/0.7%$_{H2O}$/10%$_{O2}$/Balance$_{N2}$) as shown in Figure **A.1.**12A-D, indicating minimum influence of oxygen on the coverage of steady-state reaction intermediates on the catalyst surface.

Further, the peak intensities of H-O-H bending (at 1648 cm^{-1}), bidentate formate (HCOO$_{oxide}$: 1567, 1384, 1354, 1320 cm^{-1}) [38,39,26] increased with time for all the inlet concentrations of HCHO

(Figures S13A-E). The relative intensities of surface intermediates of $HCOO_{oxide}$ at 1567 cm^{-1} and $-H_2O_{water}$ at 1648 cm^{-1} under 20 $ppm_{HCHO}/0.7\%_{H2O}/Balance_{N2}$ were found to increase with time (up to 120 minutes) while that of CO_2O_{oxide} at 1512 cm^{-1} was found to peak at ~50 minutes, which was accompanied with the onset of HCHO release and peak percentage of conversion to CO_2 at ~50 minutes, as shown in Figure 3B, and relevant DRIFTS full spectra are shown in Figure A.1.12A and A.1.12C and specifically the carbonate region in Figure A.1.14A. Therefore, the onset of HCHO release at high HCHO concentrations in presence of water vapour can be accompanied with complete blocking of surface sites for HCHO adsorption due to the built-up of formate on the catalyst surface while the more active conversion kinetics from HCHO to CO_2 in the presence of water can be correlated with surface coverage of carbonate (greater coverage of carbonate rendering high conversion percentage). On the other hand, DOM peak intensities became pronounced at increasing HCHO concentration without water vapour (Figure 3C and Figure A.1.11B specifically for the $HCOO_{oxide}$ and $HCHOO_{oxide}$ regions) which suggests that the dehydrogenation kinetics of $HCHOO_{oxide}$ on the catalyst surface to other reaction intermediates such as HCOOoxide could be slower in the absence of water. Furthermore, spectra obtained under 20 $ppm_{HCHO}/10\%_{O2}/Balance_{N2}$ are similar to those without oxygen as shown in Figure A.1.15A-D indicating minimum influence of oxygen on the surface coverage of reaction intermediates. The relative intensities of both $HCOO_{oxide}$ at 1567 cm^{-1} and $HCHOO_{oxide}$ between 900-1110 cm^{-1} under 20 ppm $HCHO/Balance_{N2}$ were found to increase with time (up to 180 minutes) while that of CO_2O_{oxide} at 1512 cm^{-1} was largely unchanged after initial increase, as shown in Figure 3D and the corresponding DRIFTS spectra in Figure A.1.15A and A.1.15B with the carbonate region specifically in Figure A.1.14B. Therefore, the onset of HCHO release at high HCHO concentrations without water vapour can be accompanied with complete blocking of surface sites for HCHO adsorption due to the build-up of $HCOO_{oxide}$, COO_{2oxide} as well as $HCHOO_{oxide}$ on the surface, where the kinetics of dehydrogenation of $HCHOO_{oxide}$ to $HCOO_{oxide}$ is slower than that in presence of water vapour (as indicated by minimum $HCHOO_{oxide}$ detected with water vapour), allowing longer time for complete HCHO removal in Figure 3D. Unfortunately, the conversion from HCHO to CO_2 at high concentrations without water vapour was lower than in the case where water vapour was present along with the trend of CO_2 evolution decreasing at the HCHO release, which was accompanied by no decrease in the surface coverage of COO_{2oxide} (Figure 3D), in agreement with the two hypotheses that the amount of

CO_2 evolution scales with surface coverage of carbonate on the catalyst surface as well as a direct pathway discussed earlier. Furthermore, in the case where water vapour was in the gas stream, the presence of a large water peak, OH_{water} in the 2900-3500 cm^{-1} ranges in Figure A.1.12A and A.1.12B makes it difficult to infer the hydroxyl peak region. In case where no water vapour was present, decrease in the OH_{CUS} peak at ~3590 cm^{-1} was observed in Figure A.1.15C and A.1.15D suggesting that OH_{CUS} species are involved during the formation of $HCHOO_{oxide}$, $HCOO_{oxide}$, and CO_2O_{oxide} reaction intermediates. (For example, $HCHOO_{oxide}+OH_{CUS} \rightarrow HCOO_{oxide}+H_2O$). Next, we used both reactor studies and DRIFTS to understand how to avoid surface poisoning by the removal of $HCHOO_{oxide}$, $HCOO_{oxide}$, and CO_2O_{oxide} reaction intermediates
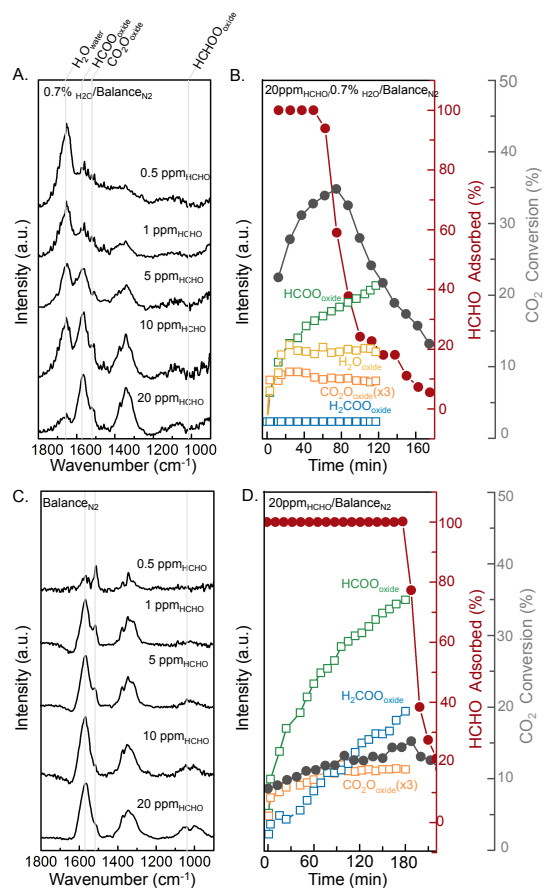
Figure. 3: Effect of HCHO and H₂O concentrations on nature of reaction intermediates. *A) DRIFTS spectrum in the 900-1800 cm^{-1} region for 0.5-20ppm$_{HCHO}$/0.7%$_{H2O}$/Balance$_{N2}$ at 120 min showing water (H₂O, yellow), bidentate formate (HCOO$_{oxide}$, green), and carbonate (COO$_{2oxide}$, orange) related peaks and no DOM (HCHOO$_{oxide}$, blue) peaks in any of the spectra. B) Integrated intensities of the HCOO$_{oxide}$, COO$_{2oxide}$, and H₂O species for the 20*

$ppm_{HCHO}/0.7\%_{H2O}/Balance_{N2}$ cases showing that increased $HCOO_{oxide}$ intensity with time while $COO2_{oxide}$ intensity increased initially for 40 min and then decreased with time. Reactor data showed CO_2 conversion % (gray) increasing with time until HCHO adsorption breakthrough (red) after which CO_2 conversion (%) starts decreasing. C) DRIFTS spectrum in the 900-1800 cm^{-1} region for $0.5-20ppm_{HCHO}/Balance_{N2}$ at 120 min showing that $HCHOO_{oxide}$, $HCOO_{oxide}$, and $COO2_{oxide}$ reaction intermediates with the major reaction intermediates changing from $COO2_{oxide}$ to $HCOO_{oxide}$ and $HCHOO_{oxide}$ with increasing HCHO concentration, D) Integrated intensities of the $HCOO_{oxide}$, $COO2_{oxide}$, and $HCHOO_{oxide}$ reaction intermediates for the 20 $ppm_{HCHO}/Balance_{N2}$ where $HCHOO_{oxide}$, $HCOO_{oxide}$, and $COO2_{oxide}$ increased with time Reactor data also showed CO_2 conversion (%, gray) increasing with time and decreasing at the HCHO adsorption breakthrough (red). Catalyst loading was 25 mg MnO_x while and total gas flow rate was 200 ml min^{-1}. 25 mg MnO_x catalyst was mixed with 25 mg KBr for the DRIFTS measurements and total gas flow rate was 200 ml min^{-1}. Integrated intensities are calculated using the H_2O at 1647 cm^{-1}, $HCOO_{oxide}$ peak at 1567 cm^{-1}, $COO2_{oxide}$ peak at 1512 cm^{-1} and the $HCHOO_{oxide}$ region between 900-1100 cm^{-1} and the specific regions are shown in Figure A.1.11A, B and the corresponding hydroxyl regions are shown in Figure A.1.12B and Figure A.1.15B respectively.

Transient experiments of gas detection at the reactor outlet and DRIFTS experiments were conducted by flowing gas free of HCHO after exposure to 20 ppm HCHO concentrations with and without water vapour. After exposing the catalyst under 20 $ppm_{HCHO}/Balance_{N2}$ for 200 minutes to achieve breakthrough, (Figure A.1.16) $100\%_{N2}$ was flown subsequently for 160 minutes at room temperature, during which HCHO and CO_2 concentrations at the reactor outlet were measured and DRIFTS experiments were conducted to monitor changes in the reaction intermediates. Considerable HCHO was detected, which suggested that weakly bound HCHO could desorb using N_2 gas purging. In addition, desorption of HCHO, decreased from ~25 to ~1 ppm with time (Figure 4A), which was accompanied with considerable reduction in the relative intensity of $HCHOO_{oxide}$ (Figure A.1.17A), and notable growth in the $HCOO_{oxide}$ intensity was seen before reaching plateaus after ~80 minutes while the $COO2_{oxide}$ intensity did not change considerably. These observations can be explained by assuming the presence of a weakly adsorbed intermediate such as $HCHOO_{oxide}$, which could both desorb as HCHO and dehydrogenate to $HCOO_{oxide}$. Also, no new $COO2_{oxide}$ formation under transient reaction conditions suggested that the observed $HCHOO_{oxide}$ does not convert to $COO2_{oxide}$ and a second pathway for the carbonate formation is possible, aided by both surface hydroxyl and oxygen species (e.g. $HCHO + OH_{CUS} + 2O_{oxide} \rightarrow COO2_{oxide} + O_{oxide} + H_2O$). On the other hand, minute CO_2 was detected, which may suggest that further dehydrogenation of $HCOO_{oxide}$, (e.g. $HCOO_{oxide} + O_{oxide} \rightarrow CO_2 + O_{oxide}H$), and removal of $COO2_{oxide}$ (e.g. $COO2_{oxide} \rightarrow CO_2 + O_{oxide}$),

on the surface are rate-limiting for the evolution of CO_2 rendering the catalyst surface blocked or poisoned by formate and carbonate reaction intermediates. Finally, the lack of CO_2 conversion in the absence of HCHO and the lack of any changes in the corresponding hydroxyl region (Figure A.1.17C) also support the hypothesis that a direct pathway of HCHO conversion to CO_2 is responsible for the CO_2 conversion under dry conditions prior to breakthrough.

In contrast, flowing $0.7\%_{H2O}$/$Balance_{N2}$ after exposure to 20 ppm_{HCHO}/$0.7\%_{H2O}$/$Balance_{N2}$ for 200 min revealed that some HCHO desorption and considerable CO_2 generation was accompanied with reduction in the relative intensity of $HCOO_{oxide}$, and $COO2_{oxide}$, reaction intermediates with time (Figure 4B and Figure A.1.17C). This observation suggests that CO_2 may formation may result from dehydrogenation of $HCOO_{oxide}$ and conversion of $COO2_{oxide}$, which is catalysed by the presence of water vapour, leading to the formation of OH_{BRI}, (2800-3600 cm^{-1} in Figure A.1.14D) and for e.g. $HCOO_{oxide}+O_{oxide}+ H_2O \rightarrow CO_2 + OH_{BRI} + H_2O$ and $COO2_{oxide}+ H_2O \rightarrow CO_2 + O_{oxide} + H_2O$) unlike the reactions without water (Figure A.1.14B) where no significant CO_2 was generated and no formation of OH_{BRI} was observed. The presence of the large water peaks in the corresponding hydroxyl region in Figure A.1.17D makes it difficult to infer changes in the hydroxyl region in this case.

To further support that water can facilitate the conversion of bidentate formate and carbonate to CO_2, the following experiment was conducted, where $1.9\%_{H2O}$/$Balance_{N2}$ (at a higher flow rate of 250 ml min^{-1}) was introduced after the catalyst was poisoned with reaction intermediates by introducing 20 ppm_{HCHO}/$Balance_{N2}$ in Figure 4C to catalyse the conversion of $HCHOO_{oxide}$, $HCOO_{oxide}$, and $COO2_{oxide}$ to CO_2. This hypothesis is supported by DRIFTS measurements. In particular, the introduction of $1.9\%_{H2O}$/$Balance_{N2}$ following 20 ppm_{HCHO}/$Balance_{N2}$ for 180 minutes removed $HCHOO_{oxide}$ peaks and considerably reduced the intensities of $HCOO_{oxide}$ and $COO2_{oxide}$ reaction intermediates as revealed after flowing 100% N_2 to remove H_2O species, and complete removal of $HCOO_{oxide}$, and $COO2_{oxide}$ was possible after 300 min (Figure 4C). In addition, $COO2_{oxide}$ peak disappeared prior to the removal of $HCOO_{oxide}$ in Figure 4C. Furthermore, the introduction of $1.9\%_{H2O}$/$Balance_{N2}$ was accompanied with a redshift in the peak at 1384 cm^{-1} and 1350 cm^{-1} as shown in Figure A.1.18A corresponding to the $\delta(CH)$ and $\nu_{as}(OCO)$ vibrating modes of bidentate $HCOO_{oxide}$. This redshift can be attributed to water non-

covalent interactions with formate adsorbed on the surface, which is supported by DFT results (Figures S19A-D) and in agreement with previous work on water interactions between chemical species and hydrogen bond formation.[68,69] 20 ppm_{HCHO}/$Balance_{N2}$ was re-adsorbed after complete removal of reaction intermediates after flowing using 1.9%$_{H2O}$/$Balance_{N2for}$ for 300 min, and the DRIFTS spectra showed the formation of $HCOO_{oxide}$, and COO_{2oxide} reaction intermediates (Figure 4C) although with reduced intensity suggesting that some of the reaction sites leading to $HCOO_{oxide}$, and COO_{2oxide} formation are not completely replenished after purging the catalyst surface with water following the initial surface poisoning. We also observed a decrease in the intensity of OH_{CUS} peak at 3590 cm^{-1} and a slight increase in the OH_{BRI} peak in the 2800-3300 cm^{-1} regions during the initial 20 ppm_{HCHO}/$Balance_{N2}$ adsorption (Figure A.1.18B). Interestingly, during the conversion of $HCOO_{oxide}$ and COO_{2oxide} to CO_2 after H_2O adsorption, only an increase in OH_{BRI} peak intensity was observed but OH_{CUS} peak intensity did not decrease. These results suggested that the adsorption of HCHO as DOM ($HCHOO_{oxide}$), dehydrogenation of $HCHOO_{oxide}$ to $HCOO_{oxide}$ is aided by OH_{CUS}, (e.g. $HCHOO_{oxide}$ + OH_{CUS} → $HCOO_{oxide}$ + H_2O) and the conversion of $HCOO_{oxide}$ to CO_2 is accompanied by OH_{BRI} formation ($HCOO_{oxide}$+ O_{BRI}→ COO_{oxide} + OH_{BRI}). This hypothesis is further supported by DRIFTS spectra obtained upon re-adsorption of 20 ppm_{HCHO}/$Balance_{N2}$ where $HCHOO_{oxide}$, $HCOO_{oxide}$, and COO_{2oxide} reaction intermediates are observed in Figure 4A along with a further decrease in the OH_{CUS} peak intensity in Figure A.1.18B.

Reactor experiments upon flowing 1.9%$_{H2O}$/$Balance_{N2}$ after achieving breakthrough with 20 ppm_{HCHO}/$Balance_{N2}$ are shown in Figure 4D and of significance to note is that minimal HCHO desorption was found but considerable CO_2 was generated over time. This result further supports that the presence of water is key to catalyse the conversion of surface reaction intermediates such as $HCOO_{oxide}$, COO_{2oxide} and $HCHOO_{oxide}$ to CO_2 as discussed in the DRIFTS results in Figure 4C.   After flowing 1.9%$_{H2O}$/$Balance_{N2}$ for 500 minutes, 20 ppm_{HCHO}/$Balance_{N2}$ was re-introduced, where the time for complete removal of HCHO to 120 min from 180 min upon the first exposure of 20 ppm_{HCHO}/$Balance_{N2}$ (Figure A.1.20A). Subsequent reflowing of 1.9%$_{H2O}$/$Balance_{N2}$ and re-introduction of 20 ppm_{HCHO}/$Balance_{N2}$ further reduced the time of complete HCHO removal to 110 min with a decrease in the CO_2 generated (Figure A.1.20A). Similar results were found with flowing 1.9%$_{H2O}$/10%$_{O2}$/$Balance_{N2}$ to those of

1.9%$_{H_2O}$/Balance$_{N2}$ (Figure A.1.20B). These results further support that water vapour can generate reaction intermediates on the catalyst surface such as bridge hydroxyl, which can block the re-adsorption of HCHO on the surface, leading to shortened time of complete HCHO, in agreement with the decreased intensity of reaction intermediates after HCHO re-adsorption in Figure 4C.

Moreover, after exposing the catalyst to 20 ppm$_{HCHO}$/Balance$_{N2}$ for 12 min to obtain equal peak intensities of HCOO$_{oxide}$, and COO2$_{oxide}$ reaction intermediates (Figure A.1.19A), and flowing 0.7%$_{H_2O}$/Balance$_{N2}$ reduced the intensities of HCOO$_{oxide}$, and COO2$_{oxide}$. However, the peak intensity ratio of formate and carbonate reaction intermediates remained constant in Figure A.1.21C, suggesting that kinetics from carbonate to CO_2 are too rapid to observe any changes in the relative intensities of HCOO$_{oxide}$, and COO2$_{oxide}$ reaction intermediates or the bidentate HCOO$_{oxide}$ does not convert to carbonate. This result is consistent with the no increase in COO2$_{oxide}$ intensity under transient reaction conditions in Figure 4A and the presence of a second reaction pathway for carbonate formation. The corresponding hydroxyl region showed only a slight decrease in the intensity of the OH$_{CUS}$ peak at 3590 cm^{-1} and the OH$_{BRI}$ peak between 2900-3300 cm^{-1} during the adsorption of 20 ppm$_{HCHO}$/Balance$_{N2}$ as shown in Figure A.1.20B. Addition of water and the removal of formate and carbonate reaction intermediates using 0.7%$_{H_2O}$/Balance$_{N2}$ led to an increase in the intensity of the OH$_{BRI}$ peak consistent with the observations in Figure A.1.15B, where OH$_{CUS}$ consumption was hypothesized to aid DOM, formate, and carbonate formation while the OH$_{BRI}$ formation was responsible in facilitation of CO_2 formation via dehydrogenation of HCOO$_{oxide}$. Hence, it was concluded that formate and carbonate intermediates formed on different reaction sites and the diffusion of intermediates across different surface sites does not occur at room temperature. To understand HCHO oxidation via different reaction pathways, we next computed HCHO oxidation energetics on MnO_2(110) surface termination with various surface adsorbed oxygen and hydroxyl species.
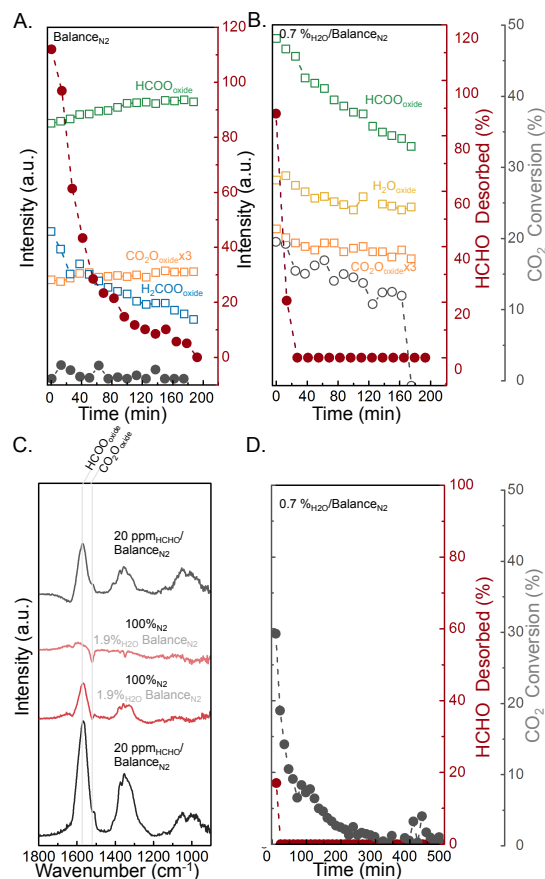
Figure 4: Effect of transient reaction conditions without HCHO in the gas stream on the nature of reaction intermediates. *A) Integrated intensities of the bidentate formate (HCOO$_{oxide}$, green) carbonate (COO$_{2oxide}$, orange,), and DOM (HCHOO$_{oxide}$, blue) reaction intermediates during purging under nitrogen where HCHOO$_{oxide}$ intensity decreased monotonically with time while HCOO$_{oxide}$ intensity increased with time and COO$_{2oxide}$ intensity did not change considerably along with HCHO desorption and no significant CO$_2$ conversion (%), B) Integrated intensities of the adsorbed H$_2$O, HCOO$_{oxide}$, COO$_{2oxide}$, and HCHOO$_{oxide}$ reaction intermediates for transient reaction conditions with purging under 0.7%$_{H2O}$/Balance case where HCOO$_{oxide}$, and COO$_{2oxide}$ intensities decreased with time with higher CO$_2$ conversion (%) and lower HCHO desorption (%, red). C) DRIFTS spectrum in the 900-1800 cm^{-1} region showing the formation of HCOO$_{oxide}$, COO$_{2oxide}$, and HCHOO$_{oxide}$ reaction intermediates after flowing 20 ppm$_{HCHO}$/Balance$_{N2}$for 180 min followed by flowing 1.9%$_{H2O}$/Balance$_{N2}$ for 180 and 300 min at 250 ml min^{-1} and purging with 100%$_{N2}$, and re-adsorption of 20 ppm$_{HCHO}$/Balance$_{N2}$ for 180 min. D) Reactor data showing CO$_2$ conversion (%) and HCHO desorbed under 1.9%$_{H2O}$/Balance$_{N2}$ at 250 ml min^{-1} after flowing 20 ppm$_{HCHO}$/Balance$_{N2}$ for 180 min. Catalyst loading was 25 mg MnO$_x$ while and total gas flow rate was 200 ml min^{-1}unless specified otherwise. 25 mg MnO$_x$ catalyst was mixed with 25 mg KBr for the DRIFTS measurements and total gas flow rate was 200 ml min^{-1} unless specified otherwise. Integrated intensities are calculated using the H$_2$O peak at 1647 cm^{-1}, HCOO$_{oxide}$ peak at 1567 cm^{-1}, COO$_{2oxide}$ peak at 1512 cm^{-1} and the HCHOO$_{oxide}$ region between 900-1100 cm^{-1}.*

2.5 Computed energetics for formaldehyde oxidation on rutile MnO_2 (110)

We next considered MnO_2 (110) with adsorbed oxygen (O_{CUS}), hydroxyl (OH_{CUS}), and H_2O (H_2O_{CUS}) to understand the reaction mechanism for HCHO oxidation to CO_2. Oxygen-TPD revealed low temperature adsorbed oxygen on the birnessite catalyst previously[55] and DRIFTS spectra in Figures A.1.15C,D, A.1.17B and TGA measurements in the presence of surface hydroxyls species. Therefore, the role of surface adsorbed oxygen and hydroxyls was investigated under reaction conditions of 20 ppm HCHO and 10% O_2 at 25°C to gain fundamental insights into the reaction mechanism of HCHO to CO_2 via bidentate formate-mediated, carbonate-mediated, and monodentate formate-mediated (direct) reaction pathways.
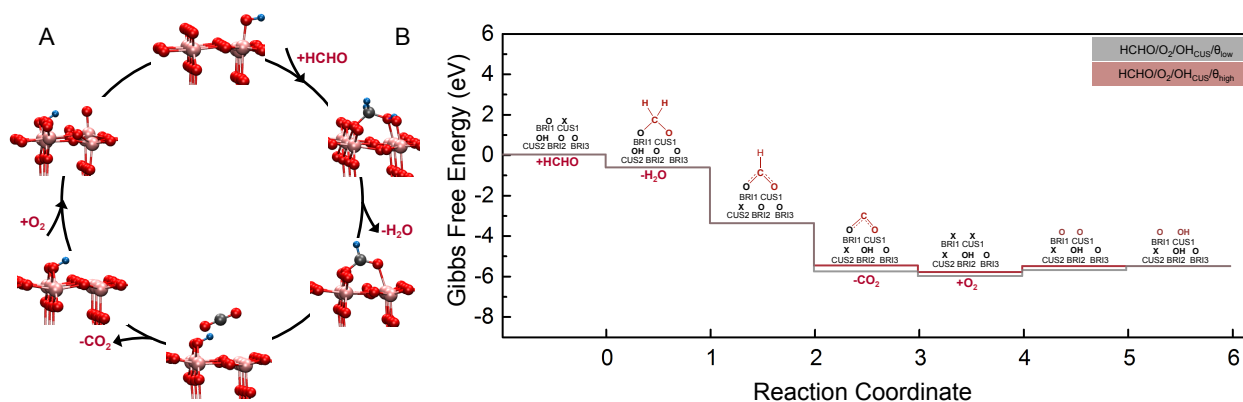
Figure 5: DFT calculated bidentate formate-mediated reaction mechanism centered on OH_{CUS}. *A) Schematic of reaction mechanism for HCHO oxidation aided by OH_{CUS} via formate-mediated reaction pathway, and B) DFT-calculated free energy diagram for formaldehyde oxidation on the (110) surface of centered on OH_{CUS}. The grey diagram shows the energy of bridge hydroxyl energy calculated in separate simulation cell to model low coverage reaction conditions (l_{ow}) and the red diagram shows the reaction energetics calculated in the same simulation cell to case to model high coverage reaction conditions (h_{igh}). Pink, manganese; blue, hydrogen; dark red, oxygen; grey, carbon, and dashed blue line indicates hydrogen bond. The equations and energetics for each step are reported in Reaction Scheme A.1.1.*

We first considered bidentate formate-mediated reaction pathway centered on OH_{CUS} reaction sites as shown in Figure 5A (OH_{CUS} formation is also aided by the presence of K+ as shown in Figure A.1.8 and Table S4) to understand the reaction mechanism under dry conditions where CO_2 formation (Fig. 2D) was noted along with decrease in OH_{CUS} peak intensity upon HCHO

adsorption (Figures A.1.13C and D). First, adsorption of HCHO on oxygen bridge sites (O_{BRI}) and the vacant Mn_{CUS} sites as DOM ($HCHO_{CUS}O_{BRI}$) was found to be downhill with -0.64 eV (Figure 5B). More favorable adsorption energy in this case was noted compared to HCHO adsorption on a stoichiometric surface as $HCHO_{CUS}O_{BRI}$ without OH_{CUS} (Figure A.1.22A) with energy of -0.50 eV (Figure A.1.22B) due to the additional hydrogen bonding of $HCHO_{CUS}O_{BRI}$ with OH_{CUS} as reported previously for birnessite.[22] Second, dehydrogenation of $HCHO_{CUS}O_{BRI}$ aided by OH_{CUS} to form formate ($HCO_{CUS}O_{BRI}$) and H_2O (Figure 5B) is favorable with Gibbs free energy of -2.75 eV. The favorable Gibbs free energy conversion of OH_{CUS} to H_2O is consistent with the decrease of intensity of OH_{CUS} upon HCHO adsorption (Figures S15C, D). Third, the dehydrogenation of $HCO_{CUS}O_{BRI}$ was found to occur by the formation of adsorbed $CO_{CUS}O_{BRI}$-like species and OH_{BRI} with Gibbs free energy of -2.11 eV for high bridge hydroxyl coverage case (-2.19 eV for low bridge hydroxyl coverage). Fourth, adsorbed $CO_{CUS}O_{BRI}$-like species desorb to form CO_2 with energy of -0.23 eV for high bridge hydroxyl coverage case (-0.32 eV for low bridge hydroxyl coverage) leading to the formation of bridge surface oxygen vacancy. Fifth, molecular oxygen adsorption on the surface to refill the bridge oxygen vacancy and form OH_{CUS} is uphill with Gibbs free energy of +0.29 eV to complete the reaction cycle. The relative Gibbs free energy of the elementary steps for low and high hydroxyl coverage cases are shown in Figure 5B and more favorable dehydrogenation energy for formate conversion to CO_2 is noted for the lower hydroxyl coverage consistent with the higher CO_2 conversion (%) observed for lower surface coverage in Fig. 2B

Another pathway centered on OH_{CUS} reaction sites is the incorporation of the hydroxyl moiety into the carbon containing intermediate moiety during the first step (Reaction Scheme S3 and Figure A.1.23A) leading to the formation of $HCHO_{CUS}OH_{CUS}$ with energy of -0.15 eV and further dehydrogenation of $HCHO_{CUS}OH_{CUS}$ to DOM ($HCHO_{CUS}O_{CUS}$) and formate ($HCO_{CUS}O_{CUS}$) as shown in Figure A.1.23B. We did not consider this pathway due to the weaker dissociate HCHO adsorption energy and as $HCHO_{CUS}OH_{CUS}$ was not observed in the DRIFTS experiments.

DFT energetics suggests that OH_{CUS} can aid HCHO adsorption via hydrogen bonding and dehydrogenation of $HCHO_{CUS}O_{BRI}$ to $CHO_{CUS}O_{BRI}$ via H_2O formation. While the dehydrogenation steps of HCHO oxidation in Figure 5 were found to be thermodynamic

favorable, the kinetics of HCHO are most likely limited by activation barriers for dehydrogenation and/or refilling of surface oxygen vacancies. The activation barrier for dehydrogenation of bidentate formate species ($HCO_{CUS}O_{BRI}$) has been reported to be high owing to the geometry of the hydrogen atom positioned perpendicular to the surface[70,71] which is further increased in the presence of adsorbed hydrogen[71]. This result is also consistent with the weaker dehydrogenation energetics in the presence of the higher bridge hydroxyl coverage as seen in Figure 5B. Thus, the reaction mechanism proposed in Figure 5 is consistent with the consumption of surface hydroxyls species observed in the DRIFTS spectrum under dry conditions along with the buildup of bidentate formate reaction intermediates leading to surface poisoning. Moreover, the uphill reaction energy for bridge vacancy refilling, as previously shown on early transition metal oxides, is rate limiting for metal oxide-based oxidation reactions[72,73]
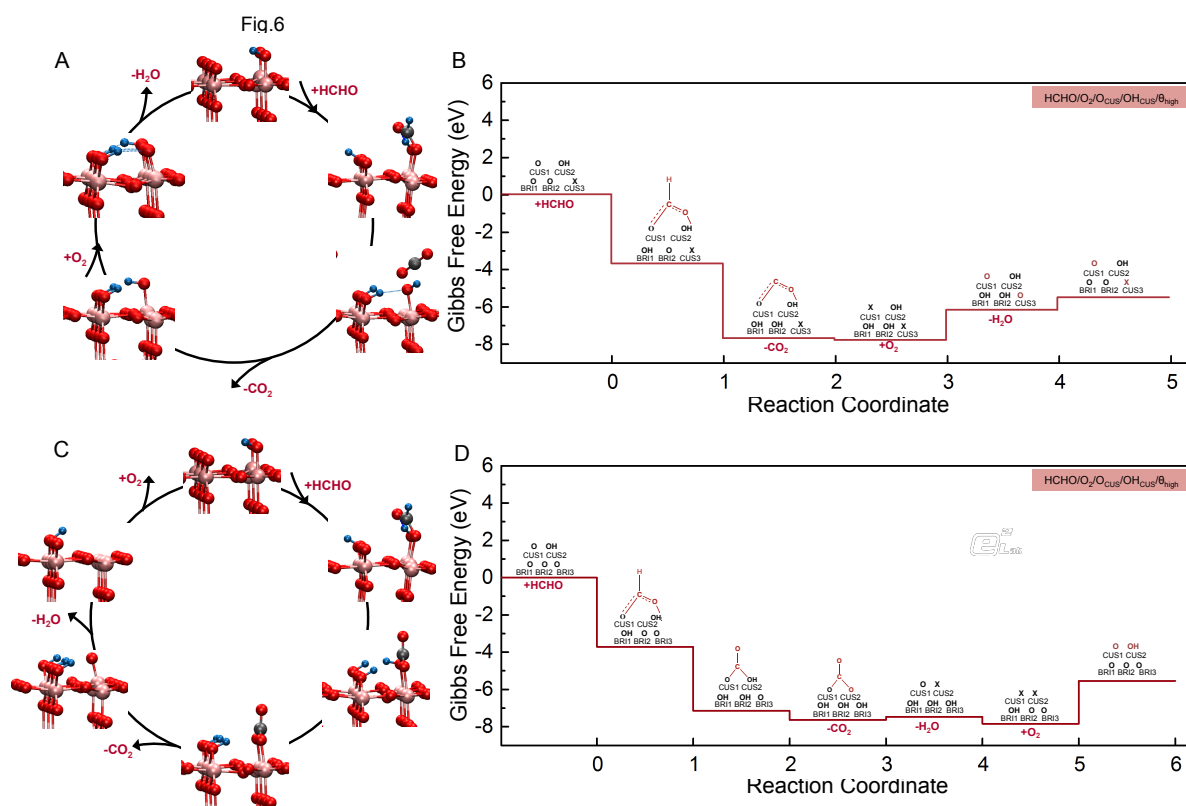
Figure 6: DFT calculated reaction mechanism for MnO₂ centered on OH_CUS and O_CUS. A) Schematic of reaction mechanism for HCHO oxidation centered on OH_CUS and O_CUS via formate-mediated reaction pathway, and B) DFT-calculated free energy diagram for formaldehyde oxidation on the (110) surface of MnO₂ centered on OH_CUS and O_CUS. The equations and energetics for each step are reported in Reaction Scheme A.1.4B, C) DFT calculated reaction

mechanism for MnO₂ centered on OH$_{CUS}$ and O$_{CUS}$ via carbonate-mediated reaction pathway D) Schematic of reaction mechanism for HCHO oxidation centered on OH$_{CUS}$ and O$_{CUS}$ via carbonate-mediated reaction pathway. Pink, manganese; blue, hydrogen; dark red, oxygen; grey, carbon. The equations and energetics for each step are reported in Reaction Scheme A.1.4A.

Next, we propose a carbonate-mediated reaction pathway for the reaction mechanism centered on OH$_{CUS}$ and O$_{CUS}$ surface sites. As the experimental DRIFTS spectrum suggested a second pathway for carbonate formation, MnO₂ (110) surface with OH$_{CUS}$ and O$_{CUS}$ was considered to model the carbonate reaction pathway (Figure 6A). First, HCHO adsorbs dissociatively to form formate (HCO$_{CUS}$O$_{CUS}$) and bridge hydroxyl (OH$_{BRI}$) without the formation of DOM with Gibbs free energy of -3.72 eV as shown in Figure 6B and described in Reaction Scheme A.1.4A. Second, dehydrogenation of HCO$_{CUS}$O$_{CUS}$ leads to bicarbonate species (HCO$_{CUS}$OH$_{CUS}$) and OH$_{BRI}$ with Gibbs free energy of -3.43 eV. Third, dehydrogenation of HCO$_{CUS}$OH$_{CUS}$ to the carbonate species (COO$_{CUS}$O$_{CUS}$) and OH$_{BRI}$ was found to have Gibbs free energy of -0.48 eV. Fourth, conversion of COO$_{CUS}$O$_{CUS}$ to CO₂ was found to have Gibbs free energy of +0.17 eV and is consistent with the buildup of carbonate reaction intermediate on the surface as observed in Figure A.1.13- A.1.15. Fifth, desorption of the two OH$_{BRI}$ and O$_{CUS}$ species as H₂O and finally molecular oxygen re-adsorption to replenish the CUS sites have Gibbs free energy of -0.37 eV and +2.30 eV respectively. Furthermore, as the carbonate reaction intermediate was the major reaction intermediate at low HCHO concentrations (Figure 3C) and the DFT results showed that the carbonate reaction intermediate is aided by OH$_{CUS}$ and O$_{CUS}$, a low coverage of OH$_{CUS}$ and O$_{CUS}$ species is suggested.

Interestingly, another competing reaction on a surface with OH$_{CUS}$ and O$_{CUS}$ is a monodentate formate reaction pathway via the conversion of formate (HCO$_{CUS}$O$_{CUS}$) directly to adsorbed CO₂-like species instead of the carbonate pathway described previously (Figure 6C), which has energy of -4.01 eV as shown in Figure 6D described in Reaction Scheme A.1.4B. Desorption of adsorbed CO₂-like species to CO₂ has an energy of -0.06 eV. The larger dehydrogenation energy in this case and the stabilization of the monodentate configuration in the presence of OH$_{CUS}$ and O$_{CUS}$ suggests that this direct dehydrogenation pathway can lead to direct HCHO oxidation to CO₂ even under dry conditions as observed in Figure 3B and Figure 3D. Finally, the adsorption of oxygen is uphill with energy of +1.61 eV and the desorption of H₂O is also uphill with +0.68

eV in this case in agreement with the trends of strong dehydrogenation energy being correlated to weaker oxygen adsorption energies in Figures A.1.24A-D. The stronger oxygen vacancy re-filling energy in the presence of bridge hydroxyl can be explained by the delocalization of the electrons donated by the OH groups to the metal atoms.[74]

We also investigated the another carbonate-mediated pathway centered only on of O_{CUS} unaided by OH_{CUS} as shown in Figure A.1.25A as previously favorable carbonate formation has been reported on rutile RuO_2 (110) along the CUS row in the presence of surface oxygen[75] and also in the presence of K^+.[76] Herein the adsorption of HCHO as $HCHO_{CUS}O_{CUS}$ was found to have energy of -1.1 eV (Figure A.1.5B and described in Reaction Scheme A.1.5). Although the HCHO adsorption energy is favorable compared to the stoichiometric surface, the larger and direct dehydrogenation energy of HCHO to $HCO_{CUS}O_{CUS}$ in the case of reaction pathway centered on both OH_{CUS} and O_{CUS} is consistent with the absence of DOM and formate species peaks that converted to the corresponding carbonate species in the DRIFTS in Figure 4C and Figure A.1.15B. Hence, we did not consider this pathway further for carbonate formation. Next, the role of water was considered to understand the decrease in lifetime in the presence of water as well as the increase in CO_2 conversion in Figure 3B and Figure 3D.

Next, as combined DRIFTS and reactor studies (Figures 4C,D) showed that the formate and carbonate reaction intermediates are converted to CO_2, in the presence of H_2O, reaction mechanism for formate and carbonate conversion to CO_2 was considered. First, we note that addition of H_2O on a CUS site adjacent (H_2O_{CUS2}) to the bidentate formate ($HCO_{BRI1}O_{CUS1}$) to maintain the BRI-CUS configuration is stable by -0.01 eV (Figure 7A). Next, H_2O adsorption on the same CUS site, (H_2O_{CUS1}, Figure 7A) leading to the formation of monodentate formate is less stable by +0.12 eV as seen in Figure 7A. As the differences in the energy amongst the bidentate and monodentate formate configurations are comparable, the bidentate formate is expected to still be a poisoning reaction intermediate with the addition of one water molecule leading to a decrease in the catalyst lifetime as H_2O now occupies the Mn_{CUS} sites. Furthermore, addition of a second molecule of H_2O on the Mn_{CUS} site (H_2O_{CUS2}) was considered to model higher concentration of water under transient reaction conditions of Figure 4C. It was seen that monodentate $HCO_{BRI1}O_{CUS1}$ is stabilized by -0.41 eV in the presence of 2 water molecules in Figure 6A. Further, dehydrogenation of monodentate $HCO_{BRI1}O_{CUS1}$ to CO_2 and OH_{BRI} is

downhill with Gibbs free energy of -1.68 eV compared to -1.48 eV for the bidentate $HCO_{BRI1}O_{CUS1}$ conversion consistent with the reported smaller barrier for monodentate $HCO_{BRI1}O_{CUS1}$ oxidation to CO_2,[71,77] The formation of OH_{BRI} is also consistent with the increase in the intensity of OH_{BRI} in the DRIFTS spectrum after the conversion of formate to CO_2 in Figure A.1.15B.

Further, we considered the conversion of $COO_{CUS1}O_{CUS2}$ to CO_2. Herein, the addition of one H_2O molecule leading to CO_2 formation (Figure 7B) was found to be favorable with an energy of -0.14 eV while CO_2 desorption energy in the presence of two water molecules was found to be -0.73 eV as seen in Figure 7B. This result further supports the early observation that carbonate reaction intermediate can be converted to CO_2 in the presence of H_2O. Next, we investigated the reaction mechanism for the role of water in decreasing the catalyst lifetime in the presence of H_2O.
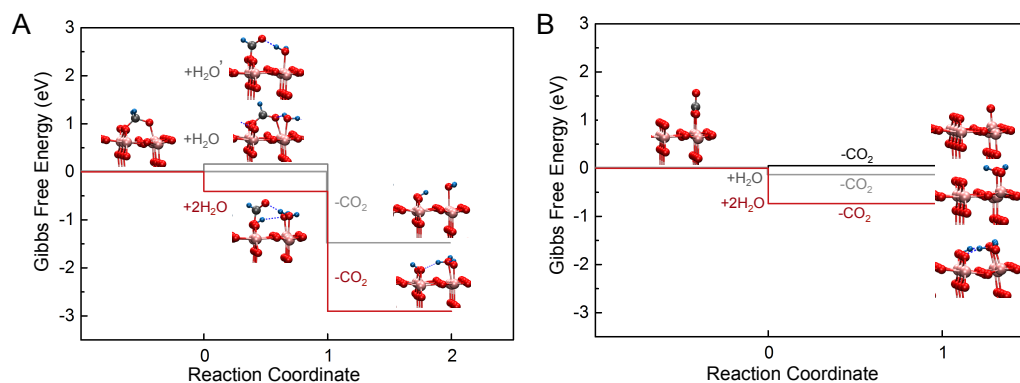
Figure 7: DFT-calculated interaction of H_2O with formate and carbonate reaction intermediates. *A) DFT–calculated energetics for dehydrogenation of bidentate formate ($HCO_{BRI1}O_{CUS}$) to CO_2 and OH_{BRI} in the presence of one co-adsorbed water on adjacent Mn_{CUS} site, same Mn_{CUS} site leading to monodentate formate configuration, in the presence of two H_2O molecules with OH_{BRI}, OH_{CUS}, and H_2O_{CUS} also leading to monodentate formate reaction intermediate prior to dehydrogenation to CO_2, B) DFT–calculated energetics of the conversion of carbonate ($COO_{CUS1}O_{CUS2}$) reaction intermediate to CO_2 in the presence of increasing zero, one and, two H_2O molecules adsorbed on Mn_{CUS} sites. Pink, manganese; blue, hydrogen; dark red, oxygen; grey, carbon and dashed blue line indicates hydrogen bond.*

To understand the decrease in catalyst lifetime during water co-adsorption in Figure 3B and Figure 3D, we first considered molecular H_2O adsorption on Mn_{CUS} sites (H_2O_{CUS} with energy of -0.20 eV (Figure A.1.26A). Next, adsorption of HCHO in a BRI-CUS configuration to form

DOM adjacent to the H_2O_{CUS2} ($HCHO_{BRI1}O_{CUS}$-H_2O_{CUS}) is favorable with energy of -0.85 eV as shown in Figure A.1.26B and described in Reaction Scheme A.1.A. Meanwhile, monodentate adsorption of HCHO on the bridge site with H_2O_{CUS} ($H_2CO_{BRI}O$-H_2O_{CUS}) which can lead to CO_2 conversion with lower barrier has a much weak adsorption energy of +0.17 eV as seen in Figure A.1.27A and Figure A.1.27B and described in Reaction Scheme A.1.B. Therefore, the more favorable adsorption energy for co-adsorption of water and HCHO in a BRI-CUS configuration ($H_2CO_{BRI1}O_{CUS1}$, H_2O_{CUS2}) leads to a decrease in the lifetime of the catalyst as Mn_{CUS} sites are now occupied by H_2O supporting earlier experimental observations in Figure 3B and Figure 3D where a decrease in lifetime is observed upon addition of water.

Finally, to understand the higher CO_2 conversion at lower HCHO coverage/concentration (Figure 2A), we propose a reaction pathway centered on O_{CUS} and H_2O_{CUS}[12,78] as shown in Figure 8A. First, direct dissociative dehydrogenation of HCHO was seen in Figure 8A to form formate ($HCO_{CUS}O-H_2O_{CUS}$) and OH_{BRI} with Gibbs free energy of -4.29 eV for the higher OH_{BRI} coverage case and -4.25 eV for the low OH_{BRI} coverage case as seen in Figure 8B and Reaction Scheme A.1.7. The strong adsorption and dehydrogenation of adsorbed HCHO for directly formed monodentate formate suggests that the direct HCHO dehydrogenation is facile in the presence of water and O_{CUS}. Second, dehydrogenation of $HCO_{CUS}O-H_2O_{CUS}$ leads to formation of CO_2 and OH_{BRI} with Gibbs free energy of -3.33 eV for the higher OH_{BRI} coverage case and -2.85 eV for the low OH_{BRI} coverage case respectively. Third, molecular oxygen re-adsorption on the Mn_{CUS} sites has Gibbs free energy of +2.15 eV and + 1.08 eV respectively for the low and high OH_{BRI} coverage cases as described in the Reaction Scheme A.1.8. Fourth, desorption of H_2O from the two OH_{BRI} species has Gibbs free energy of -0.05 and +0.48 eV respectively for the low and high OH_{BRI} coverage cases to complete the reaction cycle. The favorable HCHO dehydrogenation energy and the weak oxygen vacancy refilling energy trend reflect the opposing nature of both these effects as shown in Figure A.1.26 and reported previously.

We also considered the reaction pathway centered on OH_{CUS} and H_2O_{CUS} to model the reaction mechanism at lower HCHO coverage/concentration in the presence of H_2O as shown in Figure A.1.28A. Monodentate HCHO adsorption was found to be favorable with energy of -0.68 eV in this case as seen in Figure A.1.28B and described in Reaction Scheme A.1.8. While this reaction pathway can also lead to HCHO oxidation to CO_2 with much lower activation barrier in the

presence of H_2O due to the stabilization of the monodentate reaction intermediate, the direct dehydrogenation in the case of reaction mechanism centered on O_{CUS} and H_2O_{CUS} is more likely due to the more favorable dissociative adsorption of HCHO.
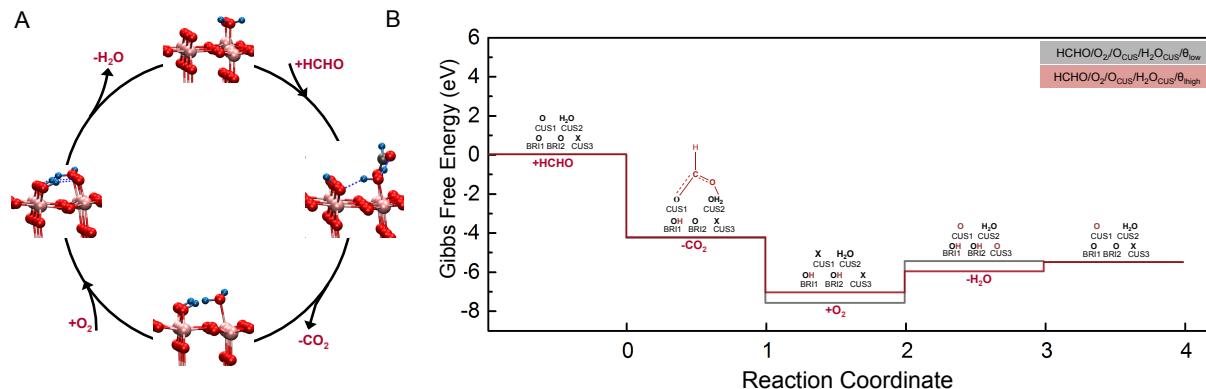
Figure 8: DFT-calculated reaction mechanism for HCHO oxidation centered on O_{CUS} and H_2O_{CUS}. *A) Schematic of reaction mechanism for HCHO oxidation centered on O_{CUS} and H_2O_{CUS} via monodentate formate-mediated reaction pathway (direct pathway), and B) DFT-calculated free energy diagram for formaldehyde oxidation on the (110) surface of MnO_2 with H_2O_{CUS} and O_{CUS}. The grey diagram showing the energy of bridge hydroxyl energy calculated in separate simulation cell to model low coverage reaction conditions (θ_{low}) and the red diagram showing the energetics in the co-adsorbed case to model high coverage reaction conditions (θ_{high}). Pink, manganese; blue, hydrogen; dark red, oxygen; grey, carbon and dashed blue line indicates hydrogen bond. The equations and energetics for each step are reported in Reaction Scheme A.1.7.*

2.6 Mechanistic insights into HCHO oxidation: Towards active site description

To understand the reaction mechanism and the active species for complete formaldehyde oxidation, we draw similarities between the current results and formic acid electro-oxidation studies where surface poisoning due to bidentate formate was understood using pH effects[79], in-situ SEIRAS[80], and DFT.[81] For formic acid oxidation (HCOOH $\rightarrow$ CO_2 + H_2) wherein bidentate formate is a surface poisoning species, the nature of the active intermediates for the reaction is unclear with both weakly adsorbed formate (HCOO⁻)[77,79,81] and direct oxidation of formic acid or a dimeric formate mechanism[82,83] being reported. While formic acid electro-oxidation studies are typically carried out on noble metal surfaces, similarities in the poisoning of the surface by bidentate formate across various material systems suggests a common underlying reaction

mechanism although gas phase oxidation of formic acid can be different from electrochemical oxidation due to solvation effects.[81,84] Typically, the role of surface hydroxyl and adsorbed water is considered in the gas phase oxidation studies and the presence of water in the gas phase can mimic solvation effects via formation of hydrogen bonds.[85] Therefore, based on the increased catalyst lifetime and complete HCHO conversion at low coverage from the experiments and the favorable adsorption for monodentate formaldehyde for the surface with OH_{CUS} and O_{CUS} species stabilized by hydrogen bonds, three different reaction pathways are proposed for formaldehyde oxidation to CO_2. (Figure A.1.29)

The first bidentate formate-mediated pathway involves formation of BRI-CUS bidentate formate from BRI-CUS DOM stabilized by OH_{CUS} that leads to surface poisoning due to the buildup of bidentate formate. (Figure A.1.29) The second carbonate-mediated pathway site involves reaction along the Mn_{CUS} row in the presence of OH_{CUS} and O_{CUS} (or only O_{CUS}) that also leads to both surface poisoning by carbonate species. Finally, the third monodentate formate-mediated pathway consists also consists of adsorption in the presence of OH_{CUS} and O_{CUS} leading to conversion of monodentate formate to CO_2 even under dry conditions. However, as carbonate was the dominant reaction intermediate only at low HCHO concentration, we expect a lower coverage of OH_{CUS} and O_{CUS} on the surface and the facile pathway to be dominant at low concentration if the bidentate formate and carbonate that poison reaction sites can be by-passed.

 Further, both experimental and theoretical results showed that the bidentate formate and carbonate reaction intermediates are not necessarily a dead end in the reaction but can be converted to CO_2 in the presence of water under transient reaction conditions in the absence of HCHO in the gas stream. As oxidation of bidentate formate and carbonate using H_2O under transient conditions has been shown to be favorable both experimentally and using DFT, a cycling methodology can be used as a practical operating procedure to regenerate a poisoned catalyst surfaces.[9] Competitive adsorption of molecular water over carbonate and formate akin to the role of water in CO oxidation[86,87] is suggested to enhance HCHO oxidation kinetics during transient experiments in H_2O/O_2 over birnessite manganese oxide. [22]

Under low HCHO concentrations and water partial pressures, the lower intensity of reaction intermediates in DRIFTS and the complete oxidation to CO_2 in the reactor measurements suggested that the reaction intermediates formed in a facile manner. DFT results also suggested

favorable adsorption of monodentate HCHO in the presence of water and oxygen stabilized by hydrogen bonding. Oxidation of monodentate formate, stabilized by hydrogen bonding, to CO_2 has been shown to much smaller barrier compared to the bidentate configuration both experimentally[77] and computationally.[71,68,88] The stabilization of monodentate formate via hydrogen bonding also supports the peak shifts observed in DRIFTS (Figure A.1.15A) along with the simultaneous generation of CO_2 under transient reactor conditions. Under practical conditions, several monolayers of water are known to exist which can provide further additional hydrogen bonding stabilization [89–91] for the oxidation of monodentate formate species. Hence, at low concentration, lifetime of the catalyst is promoted by opening up a facile reaction pathway via monodentate formate stabilization instead of the formation of bidentate formate.

Such an understanding of the role of water in conjunction with surface coverage could be extended to other oxygenates such as acetone[92] and methanol[93] where water has been shown to competitively co-adsorb. Finally, the reaction is limited by the loss of OH_{CUS} species and the buildup of bridge hydroxyls species as observed during the removal of formate and carbonate species using water and the re-adsorption of HCHO. As seen in the DFT results, re-adsorption of oxygen to refill the vacancies formed and the removal of the bridge hydroxyl as H_2O are inversely related to the dehydrogenation strength of the bridge hydrogen. Hence, the dehydrogenation ability of the bridge oxygen and the oxygen vacancy refilling energies can be used to further tune the energetics of HCHO oxidation.

2.7 Conclusions

A common underlying mechanistic understanding of the interplay between bidentate formate-carbonate-oxygen-surface hydroxyl-water adsorption has been developed to bridge the gap between the steady flow and transient reaction configurations to achieve complete oxidation of formaldehyde at room temperature. At higher surface concentration/coverage, formaldehyde oxidation on a manganese oxide catalyst occurs via three reaction pathways. The dominant reaction mechanism occurs by formation of DOM aided by OH_{CUS} via hydrogen bonding followed by the conversion of OH_{CUS} species to H_2O and form bidentate formate. The second reaction pathway involves the active site consisting of O_{CUS} and OH_{CUS} that leads to carbonate formation. Bidentate formate and carbonate can be converted to CO_2 with the formation of bridge hydroxyls species in the presence of water under transient reaction conditions. However,

when co-adsorbed with HCHO at high HCHO concentration, water competitively adsorbs with HCHO on the active CUS sites to decrease the catalyst lifetime while also converting bidentate formate and carbonate to CO_2. The third reaction pathway involves the active site consisting of O_{CUS} and OH_{CUS} which leads to CO_2 generation under both dry and wet conditions via direction dehydrogenation. On the other hand, at low concentration of HCHO, several monolayers of water are known to exist which can provide additional hydrogen bonding[89–91] for the stabilization of monodentate species. Hence, operating at low concentration, the lifetime of the catalyst is promoted by stabilizing the monodentate species (direct pathway instead of the bidentate formate and carbonate reaction intermediates.

After by-passing surface poisoning by carbonaceous species, the refilling of the formed oxygen vacancies due to CO_2 desorption and the conversion of hydroxyls to water needs to be considered. The adsorption of oxygen along with the formation of surface hydroxyl and oxygen species is endothermic at room temperature leading to the eventual deactivation of the surface at room temperature. Herein, a small addition of noble metal atoms such as Au[94] or Pt[29] also would be helpful in the activation of oxygen at low temperature to ensure longer operation time. In conclusion, the current insights into the nature of poisoning species and the active species open up pathways to realize complete oxidation of formaldehyde by tuning the reaction conditions. Such an understanding of the role of water in conjunction with surface coverage could be extended to other oxygenates such as acetone[92] and methanol[93] where water has been shown to competitively co-adsorb along with the reactant of interest as well as alter reaction kinetics for selective oxidation of larger carbon containing molecules that proceed through the formate route.[70,77]

2.8 References

(1)   Quiroz, J.; Giraudon, J.-M.; Gervasini, A.; Dujardin, C.; Lancelot, C.; Trentesaux, M.; Lamonier, J.-F. Total Oxidation of Formaldehyde over MnO $_x$ -CeO $_2$ Catalysts: The Effect of Acid Treatment. *ACS Catal.* **2015**, *5* (4), 2260–2269. https://doi.org/10.1021/cs501879j.

(2)   Adamkiewicz, G.; World Health Organization. Regional Office for Europe. *WHO Guidelines for Indoor Air Quality : Selected Pollutants.*

(3)   LI, J.; LI, Z.; LIU, B.; XIA, Q.; XI, H. Effect of Relative Humidity on Adsorption of Formaldehyde on Modified Activated Carbons. *Chinese J. Chem. Eng.* **2008**, *16* (6), 871–875. https://doi.org/10.1016/S1004-9541(09)60008-2.

(4)   László, K. Characterization and Adsorption Properties of Polymer-Based Microporous Carbons with

Different Surface Chemistry. *Microporous Mesoporous Mater.* **2005**, *80* (1–3), 205–211. https://doi.org/10.1016/J.MICROMESO.2004.12.013.

(5) Ao, C. H.; Lee, S. C.; Yu, J. Z.; Xu, J. H. Photodegradation of Formaldehyde by Photocatalyst TiO2: Effects on the Presences of NO, SO2 and VOCs. *Appl. Catal. B Environ.* **2004**, *54* (1), 41–50. https://doi.org/10.1016/J.APCATB.2004.06.004.

(6) Quiroz Torres, J.; Royer, S.; Bellat, J.-P.; Giraudon, J.-M.; Lamonier, J.-F. Formaldehyde: Catalytic Oxidation as a Promising Soft Way of Elimination. *ChemSusChem* **2013**, *6* (4), 578–592. https://doi.org/10.1002/cssc.201200809.

(7) Yusuf, A.; Snape, C.; He, J.; Xu, H.; Liu, C.; Zhao, M.; Chen, G. Z.; Tang, B.; Wang, C.; Wang, J.; Behera, S. N. Advances on Transition Metal Oxides Catalysts for Formaldehyde Oxidation: A Review. *Catal. Rev.* **2017**, *59* (3), 189–233. https://doi.org/10.1080/01614940.2017.1342476.

(8) Chen, B.-B.; Shi, C.; Crocker, M.; Wang, Y.; Zhu, A.-M. Catalytic Removal of Formaldehyde at Room Temperature over Supported Gold Catalysts. *Appl. Catal. B Environ.* **2013**, *132–133*, 245–255. https://doi.org/10.1016/J.APCATB.2012.11.028.

(9) Shi, C.; Chen, B.; Li, X.; Crocker, M.; Wang, Y.; Zhu, A. Catalytic Formaldehyde Removal by "Storage-Oxidation" Cycling Process over Supported Silver Catalysts. *Chem. Eng. J.* **2012**, *200–202*, 729–737. https://doi.org/10.1016/J.CEJ.2012.06.103.

(10) Li, Y.; Zhang, C.; Ma, J.; Chen, M.; Deng, H.; He, H. High Temperature Reduction Dramatically Promotes Pd/TiO2 Catalyst for Ambient Formaldehyde Oxidation. *Appl. Catal. B Environ.* **2017**, *217*, 560–569. https://doi.org/10.1016/J.APCATB.2017.06.023.

(11) Wang, J.; Li, J.; Jiang, C.; Zhou, P.; Zhang, P.; Yu, J. The Effect of Manganese Vacancy in Birnessite-Type MnO2 on Room-Temperature Oxidation of Formaldehyde in Air. *Appl. Catal. B Environ.* **2017**, *204*, 147–155. https://doi.org/10.1016/J.APCATB.2016.11.036.

(12) Wang, J.; Zhang, G.; Zhang, P. Layered Birnessite-Type MnO$_2$ with Surface Pits for Enhanced Catalytic Formaldehyde Oxidation Activity. *J. Mater. Chem. A* **2017**, *5* (12), 5719–5725. https://doi.org/10.1039/C6TA09793F.

(13) Li, J.; Zhang, P.; Wang, J.; Wang, M. Birnessite-Type Manganese Oxide on Granular Activated Carbon for Formaldehyde Removal at Room Temperature. *J. Phys. Chem. C* **2016**, *120* (42), 24121–24129. https://doi.org/10.1021/acs.jpcc.6b07217.

(14) Bai, B.; Arandiyan, H.; Li, J. Comparison of the Performance for Oxidation of Formaldehyde on Nano-Co3O4, 2D-Co3O4, and 3D-Co3O4 Catalysts. *Appl. Catal. B Environ.* **2013**, *142–143*, 677–683. https://doi.org/10.1016/J.APCATB.2013.05.056.

(15) Wu, Y.; Ma, M.; Zhang, B.; Gao, Y.; Lu, W.; Guo, Y. Controlled Synthesis of Porous Co$_3$O$_4$ Nanofibers by Spiral Electrospinning and Their Application for Formaldehyde Oxidation. *RSC Adv.* **2016**, *6* (104), 102127–102133. https://doi.org/10.1039/C6RA21172K.

(16) Pei, J.; Han, X.; Lu, Y. Performance and Kinetics of Catalytic Oxidation of Formaldehyde over Copper Manganese Oxide Catalyst. *Build. Environ.* **2015**, *84*, 134–141. https://doi.org/10.1016/J.BUILDENV.2014.11.002.

(17) Ma, C.; Wang, D.; Xue, W.; Dou, B.; Wang, H.; Hao, Z. Investigation of Formaldehyde Oxidation over Co$_3$O$_4$−CeO$_2$ and Au/Co$_3$O$_4$−CeO$_2$ Catalysts at Room Temperature: Effective Removal and Determination of Reaction Mechanism. *Environ. Sci. Technol.* **2011**, *45* (8), 3628–3634. https://doi.org/10.1021/es104146v.

(18) Sekine, Y. Oxidative Decomposition of Formaldehyde by Metal Oxides at Room Temperature. *Atmos. Environ.* **2002**, *36* (35), 5543–5547. https://doi.org/10.1016/S1352-2310(02)00670-2.

(19) Chen, T.; Dou, H.; Li, X.; Tang, X.; Li, J.; Hao, J. Tunnel Structure Effect of Manganese Oxides in Complete Oxidation of Formaldehyde. *Microporous Mesoporous Mater.* **2009**, *122* (1–3), 270–274. https://doi.org/10.1016/J.MICROMESO.2009.03.010.

(20) Hongmin Chen, †,§; Junhui He, *,†; Changbin Zhang, ‡ and; He‡, H. Self-Assembly of Novel Mesoporous Manganese Oxide Nanostructures and Their Application in Oxidative Decomposition of Formaldehyde. **2007**. https://doi.org/10.1021/JP076113N.

(21) Wang, J.; Li, D.; Li, P.; Zhang, P.; Xu, Q.; Yu, J. Layered Manganese Oxides for Formaldehyde-Oxidation at Room Temperature: The Effect of Interlayer Cations. *RSC Adv.* **2015**, *5* (122), 100434–100442. https://doi.org/10.1039/C5RA17018D.

(22) Wang, J.; Zhang, P.; Li, J.; Jiang, C.; Yunus, R.; Kim, J. Room-Temperature Oxidation of Formaldehyde by Layered Manganese Oxide: Effect of Water. *Environ. Sci. Technol.* **2015**, *49* (20), 12372–12379. https://doi.org/10.1021/acs.est.5b02085.

(23) Rong, S.; Zhang, P.; Yang, Y.; Zhu, L.; Wang, J.; Liu, F. MnO $_2$ Framework for Instantaneous Mineralization of Carcinogenic Airborne Formaldehyde at Room Temperature. *ACS Catal.* **2017**, *7* (2), 1057–1067. https://doi.org/10.1021/acscatal.6b02833.

(24) Zhao, D.-Z.; Shi, C.; Li, X.-S.; Zhu, A.-M.; Jang, B. W.-L. Enhanced Effect of Water Vapor on Complete Oxidation of Formaldehyde in Air with Ozone over MnOx Catalysts at Room Temperature. *J. Hazard. Mater.* **2012**, *239–240*, 362–369. https://doi.org/10.1016/J.JHAZMAT.2012.09.009.

(25) Rong, S.; Zhang, P.; Wang, J.; Liu, F.; Yang, Y.; Yang, G.; Liu, S. Ultrathin Manganese Dioxide Nanosheets for Formaldehyde Removal and Regeneration Performance. *Chem. Eng. J.* **2016**, *306*, 1172–1179. https://doi.org/10.1016/J.CEJ.2016.08.059.

(26) Zhang, C.; Liu, F.; Zhai, Y.; Ariga, H.; Yi, N.; Liu, Y.; Asakura, K.; Flytzani-Stephanopoulos, M.; He, H. Alkali-Metal-Promoted Pt/TiO2 Opens a More Efficient Pathway to Formaldehyde Oxidation at Ambient Temperatures. *Angew. Chemie Int. Ed.* **2012**, *51* (38), 9628–9632. https://doi.org/10.1002/anie.201202034.

(27) Wang, J.; Zhang, G.; Zhang, P. Layered Birnessite-Type MnO $_2$ with Surface Pits for Enhanced Catalytic Formaldehyde Oxidation Activity. *J. Mater. Chem. A* **2017**, *5* (12), 5719–5725. https://doi.org/10.1039/C6TA09793F.

(28) Huang, J.; Zhong, S.; Dai, Y.; Liu, C.-C.; Zhang, H. Effect of MnO $_2$ Phase Structure on the Oxidative Reactivity toward Bisphenol A Degradation. *Environ. Sci. Technol.* **2018**, *52* (19), 11309–11318. https://doi.org/10.1021/acs.est.8b03383.

(29) Tang, X.; Chen, J.; Huang, X.; Xu, Y.; Shen, W. Pt/MnOx–CeO2 Catalysts for the Complete Oxidation of Formaldehyde at Ambient Temperature. *Appl. Catal. B Environ.* **2008**, *81* (1–2), 115–121. https://doi.org/10.1016/J.APCATB.2007.12.007.

(30) Miao, L.; Wang, J.; Zhang, P. Review on Manganese Dioxide for Catalytic Oxidation of Airborne Formaldehyde. *Appl. Surf. Sci.* **2019**, *466*, 441–453. https://doi.org/10.1016/J.APSUSC.2018.10.031.

(31) Rong, S.; Li, K.; Zhang, P.; Liu, F.; Zhang, J. Potassium Associated Manganese Vacancy in Birnessite-Type Manganese Dioxide for Airborne Formaldehyde Oxidation. *Catal. Sci. Technol.* **2018**, *8* (7), 1799–1812. https://doi.org/10.1039/C7CY02121F.

(32) Li, Y.; Chen, X.; Wang, C.; Zhang, C.; He, H. Sodium Enhances Ir/TiO $_2$ Activity for Catalytic Oxidation of Formaldehyde at Ambient Temperature. *ACS Catal.* **2018**, *8* (12), 11377–11385. https://doi.org/10.1021/acscatal.8b03026.

(33) Chang, C.-R.; Huang, Z.-Q.; Li, J. The Promotional Role of Water in Heterogeneous Catalysis: Mechanism Insights from Computational Modeling. *Wiley Interdisc. Rev. Comput. Mol. Sci.* **2016**, *6* (6), 679–693. https://doi.org/10.1002/wcms.1272.

(34)   Rubasinghege, G.; Grassian, V. H. Role(s) of Adsorbed Water in the Surface Chemistry of Environmental Interfaces. *Chem. Commun.* **2013**, *49* (30), 3071. https://doi.org/10.1039/c3cc38872g.

(35)   Huang, H.; Leung, D. Y. C. Complete Oxidation of Formaldehyde at Room Temperature Using TiO$_2$ Supported Metallic Pd Nanoparticles. *ACS Catal.* **2011**, *1* (4), 348–354. https://doi.org/10.1021/cs200023p.

(36)   Tian, H.; He, J.; Liu, L.; Wang, D.; Hao, Z.; Ma, C. Highly Active Manganese Oxide Catalysts for Low-Temperature Oxidation of Formaldehyde. *Microporous Mesoporous Mater.* **2012**, *151*, 397–402. https://doi.org/10.1016/J.MICROMESO.2011.10.003.

(37)   Wang, Z.; Lee, S. W.; Catalano, J. G.; Lezama-Pacheco, J. S.; Bargar, J. R.; Tebo, B. M.; Giammar, D. E. Adsorption of Uranium(VI) to Manganese Oxides: X-Ray Absorption Spectroscopy and Surface Complexation Modeling. *Environ. Sci. Technol.* **2013**, *47* (2), 850–858. https://doi.org/10.1021/es304454g.

(38)   Durand, J. P.; Senanayake, S. D.; Suib, S. L.; Mullins, D. R. Reaction of Formic Acid over Amorphous Manganese Oxide Catalytic Systems: An In Situ Study. *J. Phys. Chem. C* **2010**, *114* (47), 20000–20006. https://doi.org/10.1021/jp104629j.

(39)   Sexton, B. A. Summary Abstract: Vibrational Spectra of Formate and Acetate Species on Copper (100). *J. Vac. Sci. Technol.* **1980**, *17* (1), 141–142. https://doi.org/10.1116/1.570455.

(40)   Raskó, J.; Kecskés, T.; Kiss, J. Adsorption and Reaction of Formaldehyde on TiO2-Supported Rh Catalysts Studied by FTIR and Mass Spectrometry. *J. Catal.* **2004**, *226* (1), 183–191. https://doi.org/10.1016/j.jcat.2004.05.024.

(41)   Zhu, X.; Yu, J.; Jiang, C.; Cheng, B. Catalytic Decomposition and Mechanism of Formaldehyde over Pt-Al2O3 Molecular Sieves at Room Temperature. *Phys. Chem. Chem. Phys.* **2017**, *19* (10), 6957–6963. https://doi.org/10.1039/c6cp08223h.

(42)   Ye, J.; Liu, C.; Ge, Q. DFT Study of CO$_2$ Adsorption and Hydrogenation on the in 2O 3 Surface. *J. Phys. Chem. C* **2012**, *116* (14), 7817–7825. https://doi.org/10.1021/jp3004773.

(43)   Finos, G.; Collins, S.; Blanco, G.; del Rio, E.; Cíes, J. M.; Bernal, S.; Bonivardi, A. Infrared Spectroscopic Study of Carbon Dioxide Adsorption on the Surface of Cerium–Gallium Mixed Oxides. *Catal. Today* **2012**, *180* (1), 9–18. https://doi.org/10.1016/J.CATTOD.2011.04.054.

(44)   Sophie Fritsch, †,‡; Jeffrey E. Post, §; Steven L. Suib, ‖ and; Alexandra Navrotsky*, †,⊥. Thermochemistry of Framework and Layer Manganese Dioxide Related Phases. **1998**. https://doi.org/10.1021/CM970104H.

(45)   Kakizaki, H.; Ooka, H.; Hayashi, T.; Yamaguchi, A.; Bonnet-Mercier, N.; Hashimoto, K.; Nakamura, R. Evidence That Crystal Facet Orientation Dictates Oxygen Evolution Intermediates on Rutile Manganese Oxide. *Adv. Funct. Mater.* **2018**, *28* (24), 1706319. https://doi.org/10.1002/adfm.201706319.

(46)   Andreozzi, R.; Insola, A.; Caprio, V.; Marotta, R.; Tufano, V. The Use of Manganese Dioxide as a Heterogeneous Catalyst for Oxalic Acid Ozonation in Aqueous Solution. *Appl. Catal. A Gen.* **1996**, *138* (1), 75–81. https://doi.org/10.1016/0926-860X(95)00247-2.

(47)   Thapa, A. K.; Hidaka, Y.; Hagiwara, H.; Ida, S.; Ishihara, T. Mesoporous β-MnO2 Air Electrode Modified with Pd for Rechargeability in Lithium-Air Battery. *J. Electrochem. Soc.* **2011**, *158* (12), A1483. https://doi.org/10.1149/2.090112jes.

(48)   Jiao, F.; Bruce, P. G. Mesoporous Crystalline β-MnO2—a Reversible Positive Electrode for Rechargeable Lithium Batteries. *Adv. Mater.* **2007**, *19* (5), 657–660. https://doi.org/10.1002/adma.200602499.

(49)   Yuan, H.; Chen, J.; Wang, H.; Hu, P. Activity Trend for Low-Concentration NO Oxidation at Room Temperature on Rutile-Type Metal Oxides. *ACS Catal.* **2018**, *8* (11), 10864–10870. https://doi.org/10.1021/acscatal.8b03045.

(50)   Yuan, H.; Sun, N.; Chen, J.; Jin, J.; Wang, H.; Hu, P. Insight into the NH$_3$-Assisted Selective Catalytic Reduction of NO on β-MnO$_2$ (110): Reaction Mechanism, Activity Descriptor, and Evolution from a Pristine State to a Steady State. *ACS Catal.* **2018**, *8* (10), 9269–9279. https://doi.org/10.1021/acscatal.8b02114.

(51)   Yuan, H.; Chen, J.; Guo, Y.; Wang, H.; Hu, P. Insight into the Superior Catalytic Activity of MnO$_2$ for Low-Content NO Oxidation at Room Temperature. *J. Phys. Chem. C* **2018**, *122* (44), 25365–25373. https://doi.org/10.1021/acs.jpcc.8b07330.

(52)   Li, L.; Feng, X.; Nie, Y.; Chen, S.; Shi, F.; Xiong, K.; Ding, W.; Qi, X.; Hu, J.; Wei, Z.; Wan, L.-J.; Xia, M. Insight into the Effect of Oxygen Vacancy Concentration on the Catalytic Performance of MnO$_2$. *ACS Catal.* **2015**, *5* (8), 4825–4832. https://doi.org/10.1021/acscatal.5b00320.

(53)   Tompsett, D. A.; Parker, S. C.; Islam, M. S. Rutile (β-)MnO$_2$ Surfaces and Vacancy Formation for High Electrochemical and Catalytic Performance. *J. Am. Chem. Soc.* **2014**, *136* (4), 1418–1426. https://doi.org/10.1021/ja4092962.

(54)   Tebo, B. M.; Bargar, J. R.; Clement, B. G.; Dick, G. J.; Murray, K. J.; Parker, D.; Verity, R.; Webb, S. M. BIOGENIC MANGANESE OXIDES: Properties and Mechanisms of Formation. *Annu. Rev. Earth Planet. Sci.* **2004**, *32* (1), 287–328. https://doi.org/10.1146/annurev.earth.32.101802.120213.

(55)   Chen, B.; Wu, B.; Yu, L.; Crocker, M.; Shi, C. Investigation into the Catalytic Roles of Various Oxygen Species over Different Crystal Phases of MnO2for C6H6and HCHO Oxidation. *ACS Catal.* **2020**, *10* (11), 6176–6187. https://doi.org/10.1021/acscatal.0c00459.

(56)   Wang, X.; Rui, Z.; Ji, H. DFT Study of Formaldehyde Oxidation on Silver Cluster by Active Oxygen and Hydroxyl Groups: Mechanism Comparison and Synergistic Effect. *Catal. Today* **2020**, *347*, 124–133. https://doi.org/10.1016/j.cattod.2018.06.021.

(57)   Kresse, G.; Furthmüller, J. Efficiency of Ab-Initio Total Energy Calculations for Metals and Semiconductors Using a Plane-Wave Basis Set. *Comput. Mater. Sci.* **1996**, *6* (1), 15–50. https://doi.org/10.1016/0927-0256(96)00008-0.

(58)   Kresse, G.; Hafner, J. *Ab Initio* Molecular-Dynamics Simulation of the Liquid-Metal–Amorphous-Semiconductor Transition in Germanium. *Phys. Rev. B* **1994**, *49* (20), 14251–14269. https://doi.org/10.1103/PhysRevB.49.14251.

(59)   Kresse, G.; Hafner, J. *Ab Initio* Molecular Dynamics for Liquid Metals. *Phys. Rev. B* **1993**, *47* (1), 558–561. https://doi.org/10.1103/PhysRevB.47.558.

(60)   Perdew, J. P.; Burke, K.; Ernzerhof, M. Generalized Gradient Approximation Made Simple. *Phys. Rev. Lett.* **1996**, *77* (18), 3865–3868. https://doi.org/10.1103/PhysRevLett.77.3865.

(61)   Blöchl, P. E. Projector Augmented-Wave Method. *Phys. Rev. B* **1994**, *50* (24), 17953–17979. https://doi.org/10.1103/PhysRevB.50.17953.

(62)   Kresse, G.; Joubert, D. From Ultrasoft Pseudopotentials to the Projector Augmented-Wave Method. *Phys. Rev. B* **1999**, *59* (3), 1758–1775. https://doi.org/10.1103/PhysRevB.59.1758.

(63)   Mellan, T. A.; Maenetja, K. P.; Ngoepe, P. E.; Woodley, S. M.; Catlow, C. R. A.; Grau-Crespo, R. Lithium and Oxygen Adsorption at the β-MnO2 (110) Surface. *J. Mater. Chem. A* **2013**, *1* (47), 14879. https://doi.org/10.1039/c3ta13559d.

(64)   Monkhorst, H. J.; Pack, J. D. Special Points for Brillouin-Zone Integrations. *Phys. Rev. B* **1976**, *13* (12), 5188–5192. https://doi.org/10.1103/PhysRevB.13.5188.

(65)   Wang, Y.; Cheng, H. P. Oxygen Reduction Activity on Perovskite Oxide Surfaces: A Comparative First-Principles Study of LaMnO3, LaFeO3, and LaCrO 3. *J. Phys. Chem. C* **2013**, *117* (5), 2106–2112.

https://doi.org/10.1021/jp309203k.

(66) Nørskov, J. K.; Rossmeisl, J.; Logadottir, A.; Lindqvist, L.; Kitchin, J. R.; Bligaard, T.; Jónsson, H. Origin of the Overpotential for Oxygen Reduction at a Fuel-Cell Cathode. *J. Phys. Chem. B* **2004**, *108* (46), 17886–17892. https://doi.org/10.1021/jp047349j.

(67) Loffreda, D. Theoretical Insight of Adsorption Thermodynamics of Multifunctional Molecules on Metal Surfaces. *Surf. Sci.* **2006**, *600* (10), 2103–2112. https://doi.org/10.1016/J.SUSC.2006.02.045.

(68) Miller, K. L.; Falconer, J. L.; Medlin, J. W. Effect of Water on the Adsorbed Structure of Formic Acid on TiO 2 Anatase (1 0 1). **2011**. https://doi.org/10.1016/j.jcat.2010.12.019.

(69) Zhu, X.; Jin, C.; Li, X.-S.; Liu, J.-L.; Sun, Z.-G.; Shi, C.; Li, X.; Zhu, A.-M. Photocatalytic Formaldehyde Oxidation over Plasmonic Au/TiO 2 under Visible Light: Moisture Indispensability and Light Enhancement. *ACS Catal.* **2017**, *7* (10), 6514–6524. https://doi.org/10.1021/acscatal.7b01658.

(70) Latimer, A. A.; Abild-Pedersen, F.; Nørskov, J. K. `. *ACS Catal.* **2017**, *7* (7), 4527–4534. https://doi.org/10.1021/acscatal.7b01417.

(71) Ji, Y.; Luo, Y. Structure-Dependent Photocatalytic Decomposition of Formic Acid on the Anatase TiO2(101) Surface and Strategies to Increase Its Reaction Rate. *J. Power Sources* **2016**, *306*, 208–212. https://doi.org/10.1016/J.JPOWSOUR.2015.12.002.

(72) Elias, J. S.; Stoerzinger, K. A.; Hong, W. T.; Risch, M.; Giordano, L.; Mansour, A. N.; Shao-Horn, Y. In Situ Spectroscopy and Mechanistic Insights into CO Oxidation on Transition-Metal-Substituted Ceria Nanoparticles. *ACS Catal.* **2017**, *7* (10), 6843–6857. https://doi.org/10.1021/acscatal.7b01600.

(73) Schwach, P.; Willinger, M. G.; Trunschke, A.; Schlögl, R. Methane Coupling over Magnesium Oxide: How Doping Can Work. *Angew. Chemie Int. Ed.* **2013**, *52* (43), 11381–11384. https://doi.org/10.1002/anie.201305470.

(74) L. M. Liu, †,‡; B. McAllister, ‡; H. Q. Ye, † and; P. Hu*, ‡. Identifying an O2 Supply Pathway in CO Oxidation on Au/TiO2(110): A Density Functional Theory Study on the Intrinsic Role of Water. **2006**. https://doi.org/10.1021/JA056801P.

(75) Wang, H.; Schneider, W. F. Nature and Role of Surface Carbonates and Bicarbonates in CO Oxidation over RuO2. *Phys. Chem. Chem. Phys.* **2010**, *12* (24), 6367. https://doi.org/10.1039/c001683g.

(76) Selvakumar, S.; Nuns, N.; Trentesaux, M.; Batra, V. S.; Giraudon, J.-M.; Lamonier, J.-F. Reaction of Formaldehyde over Birnessite Catalyst: A Combined XPS and ToF-SIMS Study. *Appl. Catal. B Environ.* **2018**, *223*, 192–200. https://doi.org/10.1016/J.APCATB.2017.05.029.

(77) Silbaugh, T. L.; Karp, E. M.; Campbell, C. T. Energetics of Methanol and Formic Acid Oxidation on Pt(111): Mechanistic Insights from Adsorption Calorimetry. *Surf. Sci.* **2016**, *650*, 140–143. https://doi.org/10.1016/J.SUSC.2015.12.008.

(78) Mattsson, A.; Österlund, L. Co-Adsorption of Oxygen and Formic Acid on Rutile TiO2 (110) Studied by Infrared Reflection-Absorption Spectroscopy. *Surf. Sci.* **2017**, *663*, 47–55. https://doi.org/10.1016/J.SUSC.2017.04.012.

(79) Joo, J.; Uchida, T.; Cuesta, A.; Koper, M. T. M.; Osawa, M. Importance of Acid–Base Equilibrium in Electrocatalytic Oxidation of Formic Acid on Platinum. *J. Am. Chem. Soc.* **2013**, *135* (27), 9991–9994. https://doi.org/10.1021/ja403578s.

(80) Cuesta, A.; Cabello, G.; Osawa, M.; Gutiérrez, C. Mechanism of the Electrocatalytic Oxidation of Formic Acid on Metals. *ACS Catal.* **2012**, *2* (5), 728–738. https://doi.org/10.1021/cs200661z.

(81) Gao, W.; Keith, J. A.; Anton, J.; Jacob, T. Theoretical Elucidation of the Competitive Electro-Oxidation

Mechanisms of Formic Acid on Pt(111). *J. Am. Chem. Soc.* **2010**, *132* (51), 18377–18385. https://doi.org/10.1021/ja1083317.

(82)   Xu, J.; Yuan, D.; Yang, F.; Mei, D.; Zhang, Z.; Chen, Y.-X. On the Mechanism of the Direct Pathway for Formic Acid Oxidation at a Pt(111) Electrode. *Phys. Chem. Chem. Phys.* **2013**, *15* (12), 4367. https://doi.org/10.1039/c3cp44074e.

(83)   Chen, Y. X.; Heinen, M.; Jusys, Z.; Behm, R. J. Kinetics and Mechanism of the Electrooxidation of Formic Acid—Spectroelectrochemical Studies in a Flow Cell. *Angew. Chemie Int. Ed.* **2006**, *45* (6), 981–985. https://doi.org/10.1002/anie.200502172.

(84)   Neurock, M.; Janik, M.; Wieckowski, A. A First Principles Comparison of the Mechanism and Site Requirements for the Electrocatalytic Oxidation of Methanol and Formic Acid over Pt. *Faraday Discuss.* **2009**, *140* (0), 363–378. https://doi.org/10.1039/B804591G.

(85)   Saleheen, M.; Heyden, A. Liquid-Phase Modeling in Heterogeneous Catalysis. *ACS Catal.* **2018**, *8* (3), 2188–2194. https://doi.org/10.1021/acscatal.7b04367.

(86)   Saavedra, J.; Pursell, C. J.; Chandler, B. D. CO Oxidation Kinetics over Au/TiO$_2$ and Au/Al$_2$O$_3$ Catalysts: Evidence for a Common Water-Assisted Mechanism. *J. Am. Chem. Soc.* **2018**, *140* (10), 3712–3723. https://doi.org/10.1021/jacs.7b12758.

(87)   Daté, M.; Haruta, M. Moisture Effect on CO Oxidation over Au/TiO2 Catalyst. *J. Catal.* **2001**, *201* (2), 221–224. https://doi.org/10.1006/JCAT.2001.3254.

(88)   Miller, K. L.; Lee, C. W.; Falconer, J. L.; Medlin, J. W. Effect of Water on Formic Acid Photocatalytic Decomposition on TiO$_2$ and Pt/TiO$_2$. *J. Catal.* **2010**, *275*, 294–299. https://doi.org/10.1016/j.jcat.2010.08.011.

(89)   Hassanali, A. A.; Cuny, J.; Verdolino, V.; Parrinello, M. Aqueous Solutions: State of the Art in Ab Initio Molecular Dynamics. *Philos. Trans. A. Math. Phys. Eng. Sci.* **2014**, *372* (2011), 20120482. https://doi.org/10.1098/rsta.2012.0482.

(90)   Carrasco, J.; Hodgson, A.; Michaelides, A. A Molecular Perspective of Water at Metal Interfaces. *Nat. Mater.* **2012**, *11* (8), 667–674. https://doi.org/10.1038/nmat3354.

(91)   Björneholm, O.; Hansen, M. H.; Hodgson, A.; Liu, L.-M.; Limmer, D. T.; Michaelides, A.; Pedevilla, P.; Rossmeisl, J.; Shen, H.; Tocci, G.; Tyrode, E.; Walz, M.-M.; Werner, J.; Bluhm, H. Water at Interfaces. *Chem. Rev.* **2016**, *116* (13), 7698–7726. https://doi.org/10.1021/acs.chemrev.6b00045.

(92)   Henderson, M. A. Effect of Coadsorbed Water on the Photodecomposition of Acetone on TiO2(110). *J. Catal.* **2008**, *256* (2), 287–292. https://doi.org/10.1016/J.JCAT.2008.03.020.

(93)   Chuan-yi Wang; Henning Groenzin, and; Shultz*, M. J. Comparative Study of Acetic Acid, Methanol, and Water Adsorbed on Anatase TiO2 Probed by Sum Frequency Generation Spectroscopy. **2005**. https://doi.org/10.1021/JA051996M.

(94)   Saavedra, J.; Doan, H. A.; Pursell, C. J.; Grabow, L. C.; Chandler, B. D. The Critical Role of Water at the Gold-Titania Interface in Catalytic CO Oxidation.

Chapter 3. A design descriptor approach for HCHO oxidation on manganese oxides

3.1 Introduction

Manganese oxide-based materials have applications in the fields of heterogeneous catalysis,[1] sensors,[2] and battery cathode materials.[3] Specifically, in heterogeneous catalysis, manganese oxides have been studied for the Oxygen Evolution Reaction (OER),[4] Oxygen Reduction Reaction (ORR),[5] CO_2 reduction,[6] and abatement of small molecules such as formaldehyde (HCHO), acetone (C_3H_6O), ozone (O_3), and nitric oxide (NO).[1] In particular, low temperature formaldehyde (HCHO) oxidation to carbon-dioxide (CO_2) is of interest because due to high activity and cost-effectiveness of MnO_2 catalysts.[7] Moreover, the physio-chemical properties of MnO_2 catalysts can readily be modified by changing formal valences,[5] dopant concentrations,[8] crystal structure,[9] water content,[10] and alkali cation addition.[11] This vast experimental space makes rational design of the manganese oxide catalysts challenging as surface species such as lattice oxygen, adsorbed oxygen, and surface hydroxyl have been proposed as active species for low temperature formaldehyde oxidation.[12] The nature of the oxygen involved in the reaction mechanism for CO_2 formation is unclear as both the Mars-van Krevelen mechanism involving lattice oxygen consumption[13] as well as the Eley-Rideal mechanism involving adsorbed oxygen formed on defect sites such as surface pits[14] or mediated by Mn^{3+} [15] and alkali metals such as K^+[16] have been reported. Furthermore, surface hydroxyls formed via alkali metal addition or charge compensation due to defects in the crystal structure are also known to improve the activity of manganese oxide by aiding the dehydrogenation of HCHO to dioxymethylene ($HCHOO_{oxide}$) and formate ($HCOO_{oxide}$) reaction intermediates[17,18,16,19] and also improve CO_2 conversion rate.[20] Hence, there is a need to develop a rational descriptor approach to understand the role of surface oxygen and hydroxyl species during HCHO oxidation.

Interestingly, in the field of oxygen electro catalysis manganese oxides have been extensively through descriptor-based approaches. For example, optimum e_g band filling of manganese orbitals has been used to optimize the bond strength of the Mn-O for perovskites[21] and spinel oxide catalysts [22]. Also, increasing Mn-Mn[23] bond distance to weaken Mn-O bond and Mn^{3+} in an corner-sharing octahedral environment[24] has been correlated with enhanced OER activity. Therein, the active site consists of Mn^{3+}, H_2O, OH^-, and O^- species, resembling the PS-II water oxidizing catalyst, [25] As both lowered oxygen vacancy formation energy (M-O bond strength) and the presence of surface hydroxyl have been proposed as active surface species during formaldehyde oxidation, there is an open question about the roles of surface hydroxyl and oxygen species when developing rational descriptors for formaldehyde oxidation.

In this study, we use a library of manganese oxide catalysts consisting of β-MnO_2, γ, ϵ, α, δ-MnO_x, Mn_2O_3, Mn_3O_4, and MnO to tune the surface oxygen and hydroxyl content by changing the manganese valence and water content. Next, the trends of formaldehyde adsorption and oxidation kinetics are rationalized by understanding the nature of reaction intermediates formed using in-situ DRIFTS and the structure of the manganese oxide catalysts using a combination of X-ray absorption spectroscopy (XAS), Extended X-ray Absorption Fine Structure (EXAFS), X-ray photoelectron spectroscopy (XPS), Raman spectroscopy, and thermo-gravimetric analysis (TGA) techniques. The role of surface hydroxyls in promoting HCHO adsorption was identified in low temperature CO_2 conversion. We observe that the oxidation rate of HCHO follows a volcano trend with formal valence of manganese and the surface species O/OH content defined by the mass loss in the 30-400 °C region of the TGA. Structural requirements of the active site for formaldehyde oxidation consisting of surface hydroxyl and oxygen species are proposed for three different reaction mechanisms.

3.2 Developing manganese oxide library

We first identify 8 different manganese oxide, MnO, Mn_3O_4, Mn_2O_3, α, δ, ϵ, γ, and β-MnO_2, (Fig. A.2.1A) based on manganese formal valence and surface species content. Formal valence of manganese from XAS (Fig. 1A) was estimated by fitting the first inflection point of the manganese K-edge XAS spectrum versus the formal valence (Fig. 1B and Fig. A.2.2A)[26] using

reference compounds with known manganese valence for MnO (+2), Mn_3O_4 (+2.66), Mn_2O_3 (+3), and β-MnO_2 (+4) as calibration. Manganese formal valence for α, δ, ε, and γ manganese oxides was estimated to be 3.4, 3.5, 3.65, and 3.74 respectively (Table A.2.1). The overall large window of manganese formal valence of 2 eV ensures that the binding energies of the reaction intermediates on the catalyst surface will show a notable difference for the different manganese oxide catalysts and increasing manganese valence is inferred from the inflection point (Fig. 1A). Further, Mn redox information was also inferred from the pre-edge features of the Mn K-edge spectrum in the 6535-6550 eV range. (Fig. A.2.2B) The pre-edge features primarily arises from the electronic transitions from $1s$ to the unoccupied $3d$ levels and is indicative of both the redox state as well as the symmetry around the Mn sites.[27] For the α, δ, ε, and γ manganese oxides, the pre-edge region consists of two main peaks at ~6541 and ~6543 eV indicative of the presence of both Mn(III) and Mn(IV) features in these structures.[27] and the relative intensity of the Mn (IV) feature at ~6543 eV increases from α to γ manganese oxides in the pre-edge region. Further, formal valence of manganese oxide was also estimated using the Mn $3s$ peak splitting from the XPS measurements (Fig. A.2.3A), which is proportionally to the overall spin of the manganese ion (Fig. A.2.3B and Table A.2.2).[28] Mn $3s$ peak splitting for the different catalysts was fitted against previously obtained trend of manganese formal valence versus $3s$ peak splitting for manganite compounds.[28] (Fig. A.2.3C) Good agreement is seen between the formal valence estimated using both XAS and XPS techniques, with the XAS showing higher resolution for the α, δ, ε, and γ phases in the 3.4-3.8 manganese valence regions. (Fig. A.2.4). Typically, higher manganese valence is correlated with higher oxygen content in manganese oxides[29] and we estimate the oxygen as well water content using TGA by heating the oxides in an argon atmosphere upto 600 °C (Fig. 1C). Two different weight loss regions, 30-400 °C and 400-600 °C, are identified as surface water/hydroxyl and oxygen,[10,30,31] and structural oxygen content[32] respectively (Fig. 1C). Metastable oxides such δ, α, ε, and γ-MnO_x have larger total mass loss % of 15.9, 15.7, 16.6, 11.8 wt% respectively compared to the relatively low mass loss % for the thermodynamically stable MnO (0.1%), Mn_3O_4 (2.3%), Mn_2O_3 (0.9%), and β-MnO_2 (10.2%) oxides. (Fig. 1D) A larger contribution to the overall mass loss % for the δ, α, γ, and ε- MnO_x comes from the surface O/OH species loss contribution below 400 °C (Fig. 1D) suggesting the presence of larger surface O/OH species that can aid HCHO oxidation. Next, we understand the physical origin of the O/OH species surface species for δ, α, γ, and ε- MnO_x.
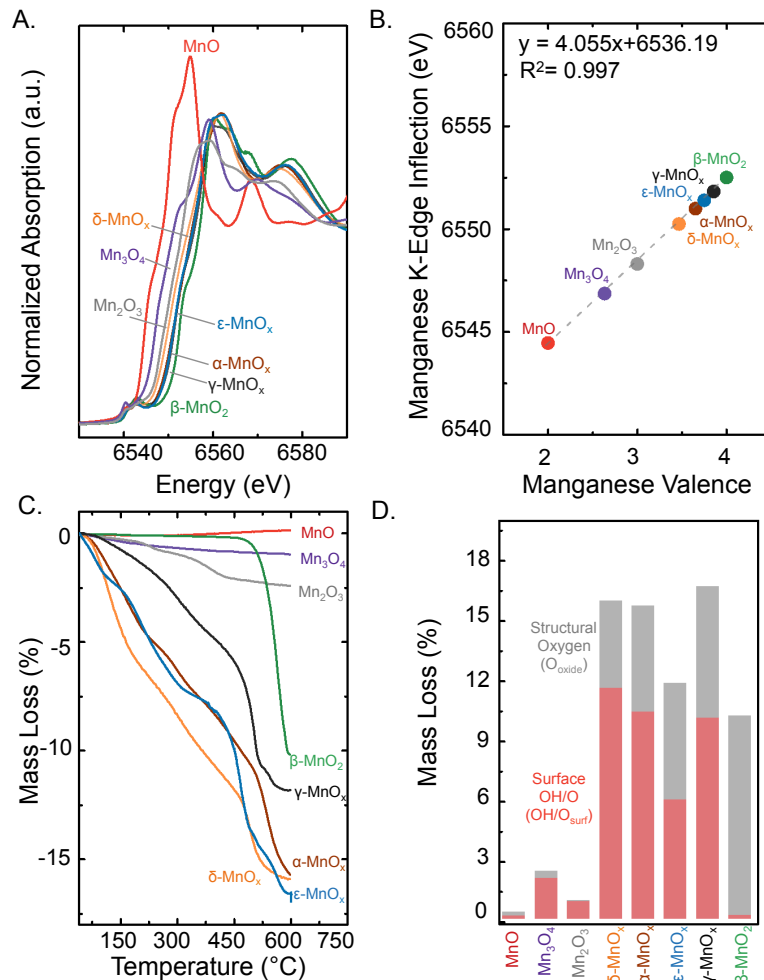
Figure 1: Characterization of manganese oxides. *A) Normalized x-ray absorption spectrum (XAS) at the manganese K-Edge region for the different catalysts, B) Manganese valence estimated by calibrating the first inflection of the Mn K-edge of the reference compounds versus known Mn valence for MnO, Mn$_3$O$_4$, Mn$_2$O$_3$ and β-MnO$_2$. Plots of the differential spectrum used to obtain the inflection points are shown in Fig. A.2.2A. C) % Mass loss for the different catalyst as a function of time from 30 °C to 600 °C used to identify surface OH/O$_{surf}$ species from 30-400 °C range and structural oxygen (O$_{oxide}$) from 400-600 °C, and D) Relative contributions of OH/O$_{surf}$ and structural oxygen (O$_{oxide}$) content to the overall mass loss percent obtained from TGA analysis. All the samples are heated to 600 °C at 5 °C min^{-1} in argon atmosphere after purging the samples at 30 °C in argon for 2 hrs to remove any weakly adsorbed species.*

Increasing structural oxygen content (O$_{oxide}$) was correlated with increasing manganese formal valence (Fig. A.2.5A). This trend is rationalized by increased oxygen stoichiometry of the oxides as the manganese valence changes from +2 for MnO to +4 for β-MnO$_2$. Next, a volcano-type trend is observed for surface OH/O species content for the catalysts as a function of manganese

formal valence (Fig. A.2.5B) that can be understood by invoking the defect structure of α, δ, ε, and γ MnO$_x$. Metastable manganese oxides such as δ, α, ε, and γ-MnO$_x$ with larger mass loss % typically contain hydroxyl ions (OH$^-$) or protons that are charge compensated by either Mn^{4+} vacancies or reduced Mn^{3+} species in the crystal structure that consists of tunnel and layers.[33,30] Both of these defects co-exist in commercially available manganese oxide catalysts[31] and DFT studies have also shown that Mn^{4+} vacancies and Mn^{3+} ions can be stabilized in the presence of OH$^-$ species.[34,35] Therefore, the volcano trend of manganese formal valence as a function of surface OH/O content with a peak at ~3.5-3.6 can be rationalized by the presence of structural water and hydroxyl species to stabilize Mn^{4+} vacancies and/or Mn^{3+} species. However, the lower surface OH/O content (11.8%) and higher manganese valence (3.74) of γ-MnO$_x$ suggests that local atomic structure needs to be further investigated to understand the defect structure.

The local atomic structure of the defective oxides containing Mn^{3+}/Mn^{4+} vacancies and OH^{-1} species was further understood by studying the relative contributions of Mn-O, Mn-Mn (corner), and Mn-Mn (edge) vectors in the manganese K-edge EXAFS (Fig. A.2.6).[36,37] Compared to the structural features of MnO, Mn$_3$O$_4$, Mn$_2$O$_3$, and β-MnO$_2$, it can be seen that all defective catalysts showed similar EXAFS vector signatures for the 3 vectors (Table A.2.3). δ-MnO$_x$ showed the lowest contribution from the corner-shared Mn-Mn vector at ~3.2 Å consistent with a defective layered structure containing larger amount of water and alkali ions for layer stablization.[27] α-MnO$_x$ and γ-MnO$_x$ possessed a similar signature but α-MnO$_x$ has a stronger contribution from the long-range vectors from 4-10 Å suggesting higher order in the crystal structure. Also, γ-MnO$_x$ and ε-MnO$_x$ with similar XRD patterns (Fig. A.2.1A) could be differentiated by the larger relative contributions of the Mn-Mn edge-shared octahedron vector and weaker long-range vectors in the 4-10 Å range for the γ-MnO$_x$ phase suggesting lower long-range order. Further structural insights into the local structures of the δ, α, ε, and γ-MnO$_x$ structures were found using Raman spectroscopy (Fig. A.2.7 and Table A.2.4), where 3 characteristic bands, ν_1 (630-650 cm^{-1}), ν_2 (570-580 cm^{-1}), and ν_3 (510-520 cm^{-1}) in the 400-700 cm^{-1} range are identified for the defective oxides.[27,38] The ~510 and 650 cm^{-1} vibrations correspond to out-of-plane Mn-O vibrations linked to the interlayer geometry[39] and a red-shift is seen for the ν_1 feature for the γ-MnO$_x$ structure suggesting contraction of the MnO$_6$ layers due to decreased repulsions.[39,40] The relative intensities of ν_2 and ν_3 peaks relative to the ν_1 peak was

also lower for γ-MnO_x compared to δ, α, ϵ-MnO_x suggesting smaller tunnel features.[41] The lack of bands in the 500-650 cm^{-1} region for the MnO, Mn_2O_3, and β-MnO_2 suggest that the Mn-O-Mn symmetric bonds corresponding to the longer and active bonds around Mn^{3+} are absent[24] suggesting that these oxides could have lower HCHO oxidation activity. Moreover, the ν_2 peak which is absent for MnO, Mn_3O_4, Mn_2O_3, and β-MnO_2 is attributed to a characteristic feature of the layers/tunnel of the defective oxides.[41] β-MnO_2 contains characteristics peaks at 665 and 535 cm^{-1} corresponding to the E_g mode (in plane) and A_{1g} mode (out of plane) vibrations of the MnO_6 octahedron, which are similar to the ν_1 and ν_2 vibrations of δ, α, ϵ, and γ-MnO_x. To understand the role of Mn^{3+} and the surface hydroxyl, oxygen species in altering the reaction kinetics, the activity of the manganese oxide catalysts was studied for formaldehyde adsorption/oxidation to CO_2.

3.3 Room temperature HCHO adsorption and oxidation to CO_2

HCHO can be both adsorbed dissociatively and oxidized to CO_2 at room temperature. Typical room temperature behavior for all catalysts upon exposure to formaldehyde and oxygen gas stream of 20 ppm_{HCHO}/10%$_{O2}$/Balance$_{N2}$ consisted of formaldehyde adsorption (Fig. 2A) and simultaneous conversion to CO_2 (Fig. 2B) until the breakthrough of HCHO at which point a decrease in the CO_2 conversion is observed for the δ, α, ϵ, and γ-MnO_x with the highest conversion of HCHO to CO_2 (~17%) being noted for γ-MnO_x. For Mn_2O_3 and Mn_3O_4, HCHO adsorption was observed without any CO_2 generation suggesting surface poisoning while for MnO and β-MnO_2 negligible HCHO adsorption and CO_2 generation was seen which could be attributed to the lack of surface sites for HCHO adsorption. Surface area normalized total CO_2 converted and HCHO adsorbed showed a volcano trend with the formal valence of manganese. (Fig. 2C) Also, a volcano-trend was observed for the surface area-normalized CO_2 generated as a function of the surface OH/O content with maximum adsorption at optimal surface species of ~6% (Fig. A.2.8A). The volcano trend of CO_2 converted with manganese valence and OH/O surface species can be explained by prohibitive reaction pathways at higher OH/O ratios.[20] The observation of CO_2 at room temperature for oxides containing surface species suggests that both surface oxygen and hydroxyl species are involved in the direct conversion of HCHO to CO_2. Also, a clear trend was not observed for formaldehyde adsorption as a function of surface OH/O

species (Fig. A.2.8B). Next, to understand the role of surface OH/O for HCHO adsorption and CO_2 conversion at room temperature, in situ DRIFTS was carried under reaction conditions.
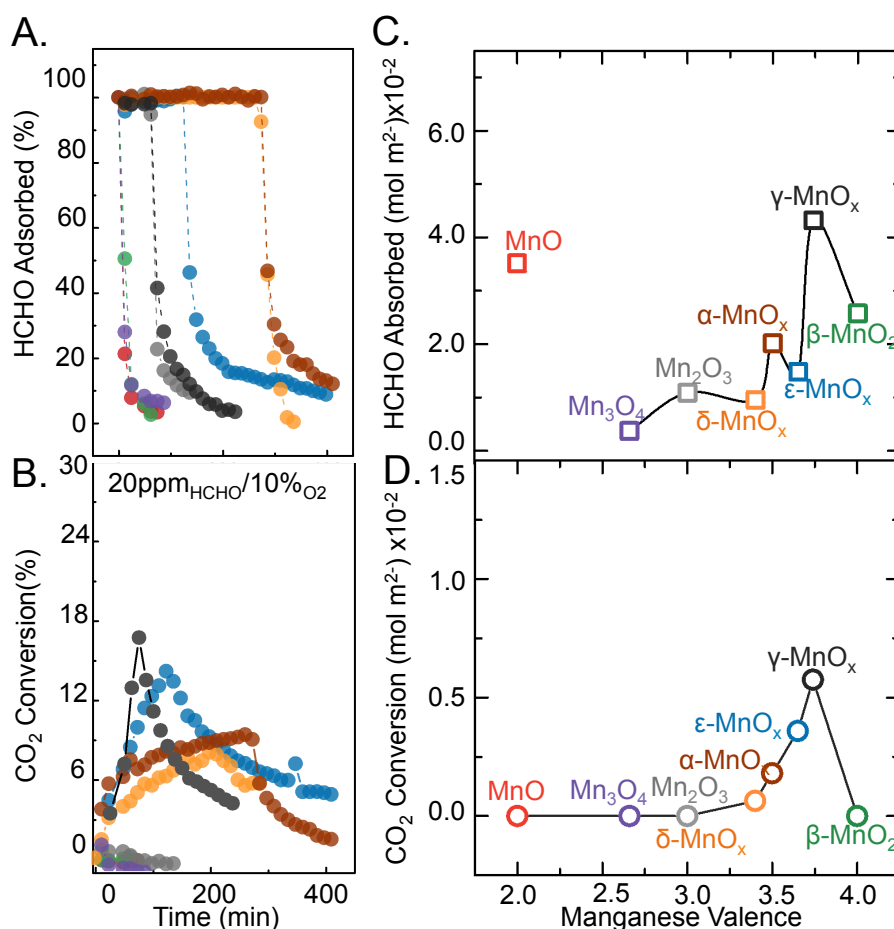
Figure 2: Room temperature HCHO adsorption and CO₂ conversion. *Room temperature formaldehyde A) adsorption behavior showing % HCHO adsorption and breakthrough as a function of time, and B) CO₂ generation behavior with increasing % CO₂ conversion until HCHO breakthrough after which a gradual decrease is observed. Trends of surface area normalized C) total HCHO adsorbed (mol m⁻²) and D) total CO₂ converted (mol m⁻²) as a function of manganese formal valence of the catalyst estimated by XAS manganese valence obtained in Table S1. CO₂ converted and HCHO adsorbed were calculated by integrating the area under the profiles in Figs. 2A, B respectively and normalizing by the BET surface area. For all the measurements, inlet HCHO gas composition of 20 ppm HCHO and 10% O₂ with a flow rate of 200 ml min⁻¹ was used at room temperature and catalyst loading of 25 mg. MnO was not included in the trend for HCHO due to low surface area and low HCHO adsorbed. BET surface area is reported in Table A.2.6.*

All the oxides showed the formation and growth of dioxymethylene (DOM, $HCHOO_{oxide}$) species while bidentate formate ($HCOO_{oxide}$) was observed for all the oxides except for MnO, and carbonate (COO_{2oxide}) was only observed for δ, α, ε, and γ-MnO_x (Fig. 3A and Figs. A.2.11A-H) upon exposure to 20 $ppm_{HCHO}/10\%_{O2}/Balance_{N2}$. The peak ranging from 1565 cm^{-1}-1585 cm^{-1} was identified as bidentate formate ($HCOO_{oxide}$) reaction intermediate while the 1500-1520 cm^{-1} ranged peak was assigned to the carbonate (COO_{2oxide}) reaction intermediate, and the peaks in the 900-1200 cm^{-1} region were identified as dioxymethylene (DOM, $HCHOO_{oxide}$) reaction intermediate.[17,43] The formation of carbonaceous reaction intermediates suggests the presence of surface oxygen/hydroxyl species as a source of oxygen to convert HCHO to $HCHOO_{oxide}$, $HCOO_{oxide}$, and further into CO_2 or COO_{2oxide}.[14,42] This suggests that the HCHO oxidation proceeds via HCHO conversion to $HCHOO_{oxide}$ (e.g. HCHO+ $2O_{oxide}$-→ $HCHOO_{oxide}$ + HO_{oxide}), followed by dehydrogenation to $HCOO_{oxide}$ (e.g. $HCHOO_{oxide}$ + $H-O_{oxide}$-→ $HCOO_{oxide}$ + H_2O) and COO_{2oxide} (e.g. $HCOO_{oxide}$ + $2O_{oxide}$→ COO_{2oxide} + $H-O_{oxide}$). The spectral region between 1500-1600 cm^{-1} consisting of $HCOO_{oxide}$ and COO_{2oxide} reaction intermediates was further de-convoluted to obtain the relative fractions of the two reaction intermediates (Fig. A.2.9). The fraction of COO_{2oxide} intermediate showed a volcano-type trend with manganese formal valence and maximized at intermediate valence of ~3.5 for α-MnO_x (Fig. 3C) and increased linearly as function of the surface O/OH species (Fig. A.2.10). The linear trend of increasing carbonate coverage with increasing surface O/OH species can be explained with increased adsorbed O/OH that aid in carbonate formation.[42] Further support comes from the examination of the hydroxyl region (2600-3700 cm^{-1}) which revealed the loss of intensity in the surface/CUS hydroxyl region (3550-3700 cm^{-1})[44] for δ, α, ε, and γ-MnO_x as well as the build-up of lattice/bridge hydroxyl region (2900-3300 cm^{-1})[44] for MnO, Mn_3O_4, Mn_2O_3, δ, α, ε, and γ-MnO_x with time (Fig. 3B and Figs. A.2.12A-H). This observation suggests the role of lattice and surface hydroxyl in aiding HCHO adsorption and dehydrogenation to $HCOO_{oxide}$ and COO_{2oxide} (For example, HCHO+ $H-O_{oxide}$ + O_{oxide} → $HCOO_{oxide}$+ H_2O, $HCOO_{oxide}$ + $H-O_{oxide}$+O_{oxide} → COO_{2oxide}+ H_2O + $H-O_{oxide}$) as well as conversion to CO_2. Interestingly, catalysts showing loss of surface hydroxyl species, δ, α, ε, γ-MnO_x also showed CO_2 conversion at room temperature (Fig. 2A and Fig. 3B). We also have previously shown for δ-MnO_x that CUS/surface hydroxyl and adsorbed oxygen species aid in HCHO adsorption and direct dehydrogenation via stabilization of monodentate formate reaction intermediates using extensive DFT calculations and DRIFTS

measurements. (For example, $HCHO + H\text{-}O_{oxide} + 2O_{oxide} \rightarrow CO_2 + H_2O + 2H\text{-}O_{oxide}$). Lattice hydroxyl formation was observed for the Mn_2O_3 and Mn_3O_4 that did not show CO_2 generation at room temperature (Figure 3B). This suggests that lattice hydroxyls are involved only in $HCOO_{oxide}$ formation but not the generation of CO_2 for these oxides ($HCHOO_{oxide} + O_{oxide} \rightarrow HCOO_{oxide} + H\text{-}O_{oxide}$) leading to surface poisoning at room temperature. In order to overcome the limitations of surface poisoning at room temperature, low temperature oxidation was carried out under $20\ ppm_{HCHO}/10\%_{O2}/Balance_{N2}$ after room temperature HCHO adsorption.
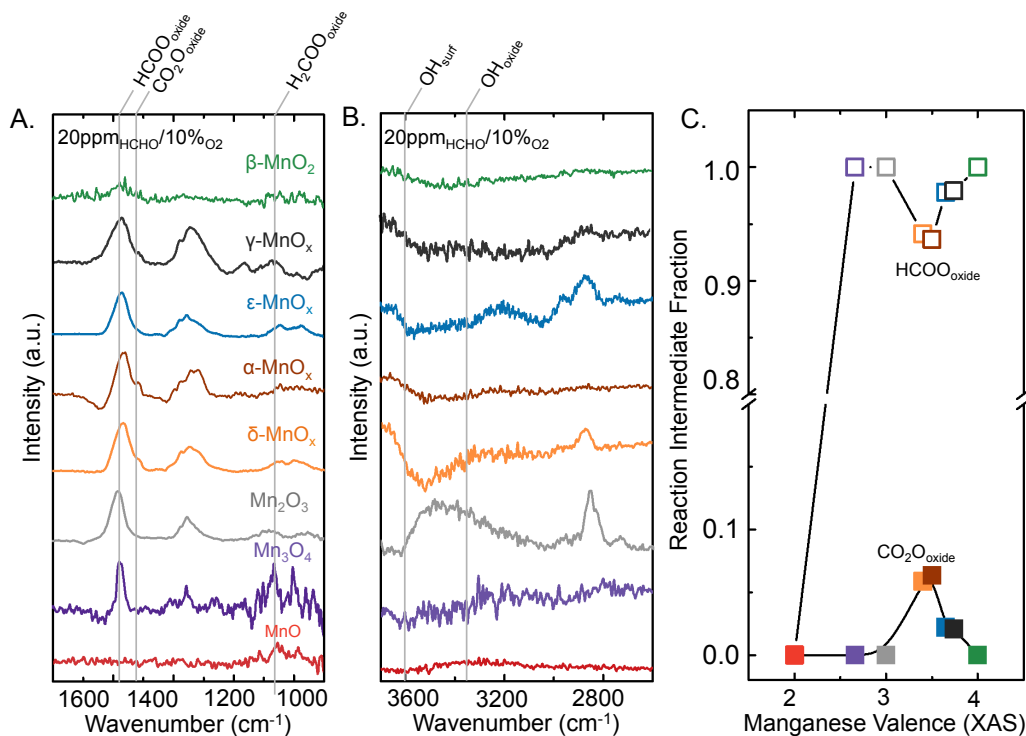
Figure 3: Reaction intermediates during HCHO adsorption. *A) DRIFTS of manganese oxides upon exposure to 20 ppm HCHO and 10% O_2 at room temperature in the A) 900-1900 cm^{-1} region showing the formation of DOM ($HCHOO_{oxide}$, 900-1200 cm^{-1}), carbonate (COO_{2oxide}, 1500-1520 cm^{-1}), and bidentate formate ($HCOO_{oxide}$, 1565-1585 cm^{-1}) reaction intermediates, and B) 2600-3700 cm^{-1} region showing the decrease in intensity of surface hydroxyl (HO_{surf}, 3500-3700 cm^{-1}) indicated by the loss of intensity relative to the background and the formation of a lattice oxygen-related hydroxyl (HO_{oxide}, 3000-3300 cm^{-1}), and C) Relative fraction of $HCOO_{oxide}$ and COO_{2oxide} reaction intermediates obtained from Fig. A.2.9 by de-convoluting the $HCOO_{oxide}$ and COO_{2oxide} peaks in Fig. 3A as a function of the manganese valence obtained from XAS in Table S1. For all the measurements, inlet HCHO gas composition of 20 ppm HCHO and 10% O_2 with a flow rate of 200 ml min^{-1} was used at room temperature and catalyst loading of 25 mg. DRIFTS spectra are recorded at the breakthrough point for each of the catalyst. The time dependent spectra for both the regions are shown in Figs. S11A-H and Figs A.2.12A-H respectively.*

3.4 Low temperature complete HCHO oxidation to CO_2

Light off curves for HCHO oxidation showed complete HCHO oxidation at ~100°C for δ, α, ε, and γ-MnO_x catalysts while MnO was least active with complete conversion at 225 °C (Fig. 4A). Surface-area normalized HCHO reaction rates at 30 °C, 45 °C, and 60 °C obtained by linear interpolation of Arrhenius-type reaction rate plots in Fig. 4B showed a volcano-trend with manganese valence (Fig. 4C) and surface OH/O species content (Fig. A.2.14, mass normalized reaction rates are shown in Fig. A.2.13). A volcano-trend with manganese valence can be attributed to optimal Mn-O bond strength to tune oxygen vacancy formation energy[5,21] as previously observed for manganese-based perovskite catalysts for OER and ORR. For the lower valent manganese oxide catalysts such as MnO, Mn_3O_4, and Mn_2O_3 as well as β-MnO_2 with no surface hydroxyls on the surface, we propose a reaction pathway centered on lattice oxygen. (Bidentate formate-mediated pathway, Fig. 5A) The bidentate formate pathway involves the adsorption of HCHO on lattice oxygen sites as $HCHOO_{oxide}$, and conversion of $HCHOO_{oxide}$ to $HCOO_{oxide}$ and lattice OH species at low temperature leading to surface poisoning by $HCOO_{oxide}$ without CO_2 formation. (Figs. 3-5A). The lack of CO_2 conversion at room temperature can be attributed to the buildup of $HCOO_{oxide}$, which has high activation barrier for conversion to CO_2.[45] At higher temperature, $HCOO_{oxide}$ is converted to CO_2 and lattice OH to H_2O ($HCOO_{oxide} + O_{oxide} \rightarrow CO_2 + H\text{-}O_{oxide},$ $2H\text{-}O_{oxide} \rightarrow H_2O + O_{vac}$) with the resulting oxygen vacancies refilled by molecular oxygen, which can also be the rate limiting step (Fig. 5A).
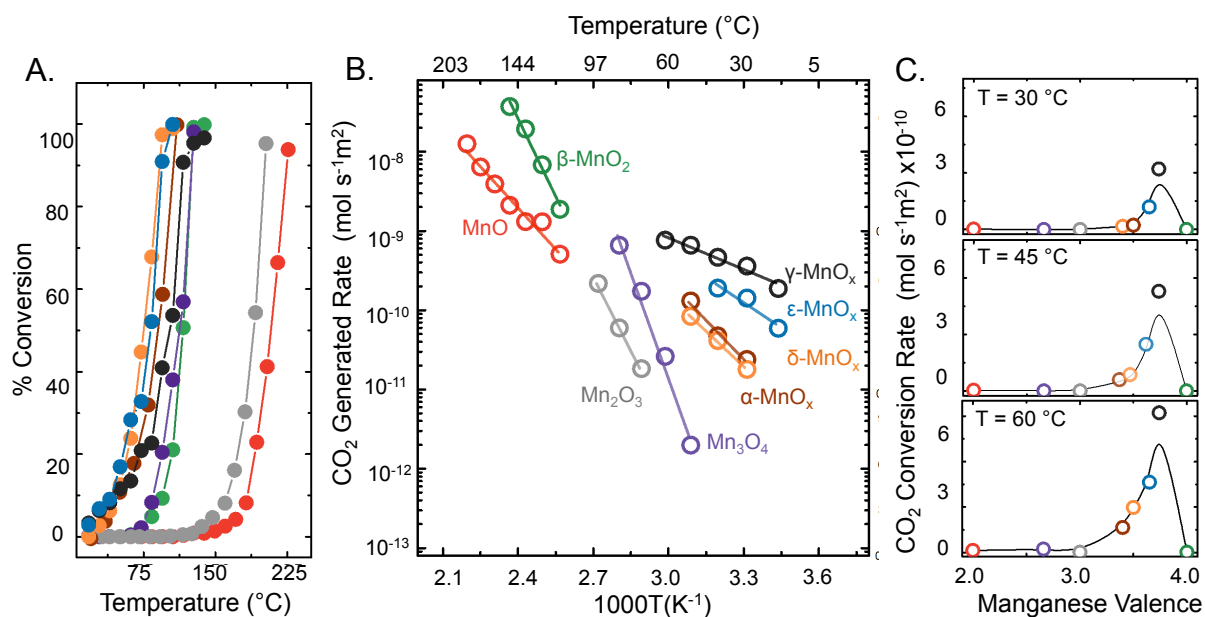
Figure 4: Low temperature HCHO oxidation activity. *A) Light off curves for CO₂ generation for the manganese oxide catalysts. B) Surface area normalized reaction rates for the different catalysts obtained from the light off curves for overall conversion less than 12.5%. C) Trends for surface area normalized CO₂ generation rate as a function of manganese formal valence obtained from XAS for 30 °C, 45 °C and 60 °C. For all the measurements, inlet HCHO gas composition of 20 ppm HCHO and 10% O₂ with a flow rate of 200 ml min⁻¹ was used at room temperature and catalyst loading of 25 mg. The catalyst was first exposed to 20 ppm HCHO and 10 % O₂ at room temperature until breakthrough was achieved prior to heating up the sample. BET surface area for all the catalysts are reported in Table. A.2.6. Reaction rates are obtained from extrapolation of the linear fits shown in Figure 4B to 30 °C, 45 °C and 60 °C.*

3.5 Reaction mechanisms for HCHO oxidation to CO_2

Two different reaction pathways are proposed in the presence of surface O/OH species leading to COO_{2oxide} and CO_2 formation for δ, α, ε, and γ-MnO_x. In the presence of surface oxygen and hydroxyl species, the decrease in intensity of surface hydroxyl and increase in intensity of lattice hydroxyls (Fig. 3B) and the simultaneous generation of CO_2 for the oxides containing surface hydroxyls species (Fig. 2B) suggests that surface oxygen and hydroxyl species aid in conversion of HCHO to CO_2 as well as to COO_{2oxide}. The build-up of carbonate reaction intermediates with time in Figs. S11A-H suggests that carbonate formation is also aided by surface hydroxyl and oxygen but does not lead to CO_2 generation at room temperature. Therefore, for the carbonate pathway, HCHO adsorption is aided by surface hydroxyl and oxygen species leading to dissociative adsorption of HCHO to form monodentate $HCOO_{oxide}$ and $H-O_{oxide}$ species as shown

in Fig. 5B. Next, monodentate $HCOO_{oxide}$ is converted into COO_{2oxid} due to the availability of surface oxygen on these catalysts. COO_{2oxid} species can be converted into CO_2 at high temperature as shown previously[48] and the surface regeneration occurs via lattice hydroxyl converting to H_2O and oxygen vacancy re-filling steps. The second pathway involves a facile direct reaction pathway[46,47] for HCHO oxidation to CO_2 is proposed via the stabilization of monodentate formate reaction intermediates by both surface oxygen and hydroxyl as shown previously for birnessite manganese oxide leading to direct dehydrogenation of HCHO to CO_2 (Fig. 5C). The direct dehydrogenation pathway is also consistent with the increasing CO_2 conversion with time in Fig. 2C until HCHO breakthrough at where CO_2 conversion also decreases. Surface hydroxyls provide alternate pathway for formaldehyde oxidation and improve the concentration of Mn^{3+} ions in the catalysts that also lead to the weakening of the Mn-O bond relative to Mn-O bonds associated with Mn^{4+}.[33] Mn^{3+} is also present in Mn_3O_4 and Mn_2O_3 but do not show high activity due to the lack of surface hydroxyls. Pt-based catalyst surface hydroxyls have also shown to open an alternate reaction pathway for CO_2 formation via conversion of formate to CO_2.[18] Based on these results, we propose the requirements for active site for low temperature formaldehyde oxidation are optimal valence of manganese of ~3.75 with surface specie content of ~6%. We also propose that the electronic structure descriptor of manganese valence and the structural requirement of surface hydroxyls are closely related due to the charge compensation required to generate sufficient Mn^{4+} vacancies and Mn^{3+} species to accommodate surface hydroxyls.

A.   Formate Pathway

B.   Carbonate Pathway

C.   Direct Pathway
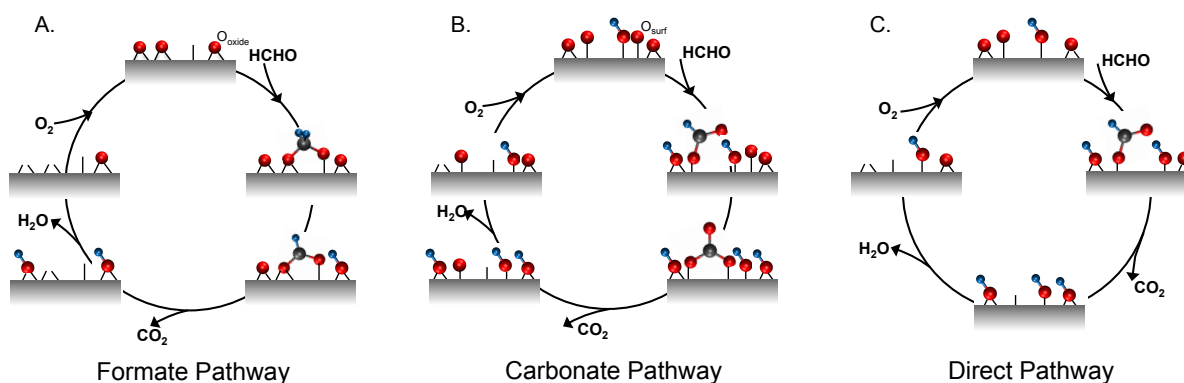
Figure 5: Reaction pathways for formaldehyde oxidation. A) Bidentate formate-mediated reaction pathway centered on lattice oxygen (O_{oxide}) showing the adsorption of HCHO on lattice oxygen sties as H_2COO_{oxide}, dehydrogenation of H_2COO_{oxide} to from $HCOO_{oxide}$ and HO_{oxide}, conversion of $HCOO_{oxide}$ to CO_2 and HO_{oxide}, H_2O desorption leading to O_{vac} formation, and

adsorption of O_2 to regenerate the catalyst surface, B) Carbonate-mediated reaction pathway centered on surface hydroxyl (HO_{surf}) and surface oxygen (O_{surf}) showing the direct formation of $HCOO_{oxide}$ and HO_{oxide}, conversion of $HCOO_{oxide}$ to COO_{2oxide} and HO_{oxide} via consumption of HO_{surf}, conversion of COO_{2oxide} to CO_2, H_2O desorption leading to O_{vac} formation, and adsorption of O_2 to regenerate the catalyst surface, and C) Direct dehydrogenation pathway centered on surface hydroxyl (HO_{surf}) and surface oxygen (O_{surf}) leading to the formation of monodentate formate leading via dehydrogenation of HCHO, conversion of $HCOO_{oxide}$ to CO_2 and HO_{oxide}, H_2O desorption leading to O_{vac} formation, and adsorption of O_2 to regenerate the catalyst surface.

3.6 Conclusions

In this work we showed that formaldehyde oxidation reaction kinetics could be tuned by the manganese formal valence and surface species content for manganese oxides. We rationalized the dependence of oxidative activity on surface hydroxyl/oxygen content and manganese formal valence by the change in reaction mechanism aided from being centred on lattice oxygen to being centred on surface hydroxyls, and oxygen species due to the stabilization of Mn^{3+} species by the replacement of lattice oxygen by hydroxyl species on the surface and in the bulk lattice for charge compensation. While $HCHOO_{oxide}$, $HCHO_{Ooxide}$, and COO_{2oxide} reaction intermediates were identified for the manganese oxide catalysts, HCHO adsorption and CO_2 conversion rate was attributed to the direct dehydrogenation reaction mechanism at low temperature stabilized by the surface hydroxyl and oxygen species that providing an alternate pathway along with the formation of bidentate formate and carbonate that lead to surface poisoning.

3.7 Experimental methods

Materials

Commercial birnessite manganese oxide (δ-MnO_x), alpha manganese oxide (α-MnO_x), and Mn_3O_4 were procured from BASF Corporation. Gamma manganese oxide (γ-MnO_x) was a commercial EMD material obtained from Erachem Comilog and commercial Mn_2O_3 was obtained from Sigma Aldrich. Epsilon manganese oxide (ϵ-MnO_x) was synthesized using an acid leaching technique while MnO and β-MnO_2 were purchased from Alfa Aesar. Complete preparation details are included in the Supplementary Information

Raman Spectroscopy

Raman spectroscopy was collected out using a 514.5 cm^{-1} wavelength in the rage of 200-1000 cm^{-1} at room temperature. Each Raman spectrum is averaged using 15 acquisitions using a low laser power of 0.1% to avoid any sample damage.

TGA Measurements

TGA measurements were conducted in a NETZCSH STA instrument. The samples (~10-40 mg) were heated to 600 °C in an argon atmosphere after purging the sample at 30 °C for 2 hr to remove any weakly adsorbed surface species prior to the heating step.

X-ray Absorption Spectroscopy (XAS) and Extended X-ray Absorption Fine Structure (EXAFS)

Mn K-edge X-ray absorption measurements were performed at Beamline 8-ID of National Synchrotron light source II (NSLS-II) at the Brookhaven National Laboratory. All data were collected at transmittance mode, and the measurements were conducted at room temperature. EXAFS spectra were obtained by the k^3-weighted Fourier transform of the XAS results.

X-ray Photoelectron Spectroscopy (XPS)

XPS measurements were conducted using the Thermo Scientific K-Alpha+ system with Al monochromator.

X-Ray Diffraction (XRD)

XRD was conducted using a PANalytical XRD system with copper Kα X-ray source generated at 45 kV and 40 mA with a 2θ range of 0 to 30 degrees. X-Ray diffraction patterns of the manganese oxide catalysts (Figure S1B) are consistent with previously reported structures.[32,49]

BET Surface Area

Single point BET measurements were conducted using the Quantchrome instrument without any drying prior to measurement.

Plug flow reactor measurements

25 mg of the powder catalyst was mixed with oven-dried SiO_2 sand (2.5 g) and loaded into a quartz tube (3.81 mm inner diameter) with a total flow rate of 200 ml min^{-1}. The flow rate of individual gases, HCHO (Ultra High Purity, 50 ppm in balance N_2), O_2 (Ultra High Purity, 25% by volume in balance N_2), and pure N_2 (Ultra High Purity), was controlled using dedicated mass flow controllers to achieve the desired gas concentration of 20 ppm HCHO and 10% O_2 balanced with N_2. The gas composition was analyzed using a PIKE FTIR gas cell attached to a Bruker Vertex 70 FT-IR spectrophotometer. Background spectrum was collected under a pure stream of N_2 prior to spectra collection. The percentage conversion of HCHO oxidation to CO_2 was calculated by determining the percentage of inlet HCHO reacted during the course of the reaction, which can be calculated by the formula,

$$\% \text{ conversion} = 100*(CO_{2ppm,out}/HCHO_{ppm,in}),$$

where $HCHO_{ppm,in}$ is the concentration of the inlet HCHO and $CO_{2ppm,out}$ is the concentration of CO_2 observed after reaction of HCHO with the catalyst.

Total CO_2 converted was calculated by integrating the area under the CO_2 conversion profile and normalizing by the flow rate and the BET surface area using the formula,

$$CO_{2flux} = \left(10^{-3} * 10^{-6} * CO_{2Area} * F_{HCHO} * 10^3\right) \Big/ \left(V_m * A_{cat} * m_{cat}\right)$$

Where CO_{2area} is the area under the CO_2 conversion profile as a function of time, F_{HCHO} is the flow rate of HCHO gas (l mol^{-1}), V_m is the molar volume (mol g^{-1}), A_{cat} is the BET surface area (m^{2}g^{-1}) and m_{cat} is the catalyst loading (mg).

Total HCHO adsorbed was calculated subtracting the contribution from the CO_2 generated from HCHO adsorbed using the formula,

$$HCHO_{adsorbed} = \left(10^{-3} * 10^{-6} * (HCHO_{Area} - CO2_{Area}) * F_{HCHO} * 10^3\right) \Big/ \left(V_m * A_{cat} * m_{cat}\right)$$

Reaction rates were calculated by first calculating the mass-normalized reaction rates and then estimated the specific reactions rates by normalizing the mass reaction rates with BET surface area using the formulae,

$$r_{mass=} \left(\frac{\%conversion}{100} * F_{HCHO} * 10^3 * 10^{-6} \right) \Big/ (V_m * 60 * m_{cat})$$

$$r_{area=} (r_{mass}) \Big/ (A_{cat})$$

Where %conversion below 15% is obtained from the light off curves, F_{HCHO} is the flow rate of HCHO (ml min^{-1}), V_m is the molar volume (l mol^{-1}), A_{cat} is the BET surface area (m^{2}g^{-1}) and m_{cat} is the catalyst loading (mg).

In-situ DRIFTS

In-situ Diffuse Reflectance Infrared Fourier Transmission Spectroscopy (DRIFTS) measurements were carried out using the Praying Mantis setup (Harrick) in an environmental chamber with KBr windows at room temperature. 25 mg of manganese oxide catalyst was mixed with 25 mg of KBr. The catalysts were purged with N_2 at room temperature prior to collection of DRIFTS spectrum to remove any weakly adsorbed contaminants prior to obtaining a background spectrum. Gas compositions and flow rates were similar to the plug-flow reactor conditions.

3.8 References

1. Xu, H. *et al*. Gaseous Heterogeneous Catalytic Reactions over Mn-Based Oxides for Environmental Applications: A Critical Review. *Environ. Sci. Technol.* **51**, 8879–8892 (2017).

2. Lima, A., Bocchi, N., Gomes, H. & Teixeira, M. F. An Electrochemical Sensor Based on Nanostructured Hollandite-type Manganese Oxide for Detection of Potassium Ions. *Sensors* **9**, 6613–6625 (2009).

3. Dessie, Y., Tadesse, S., Eswaramoorthy, R. & Abebe, B. Recent developments in manganese oxide based nanomaterials with oxygen reduction reaction functionalities for energy conversion and storage applications: A review. *J. Sci. Adv. Mater. Devices* **4**, 353–369 (2019).

4. Huynh, M., Shi, C., Billinge, S. J. L. & Nocera, D. G. Nature of Activated Manganese Oxide for Oxygen Evolution. *J. Am. Chem. Soc.* **137**, 14887–14904 (2015).

5. Stoerzinger, K. A., Risch, M., Han, B. & Shao-Horn, Y. Recent Insights into Manganese Oxides in Catalyzing Oxygen Reduction Kinetics. *ACS Catal.* **5**, 6021–6031 (2015).

6. Zhang, B. *et al*. Manganese acting as a high-performance heterogeneous electrocatalyst in carbon dioxide reduction. *Nat. Commun.* **10**, 2980 (2019).

7. Miao, L., Wang, J. & Zhang, P. Review on manganese dioxide for catalytic oxidation of airborne formaldehyde. *Appl. Surf. Sci.* **466**, 441–453 (2019).

8. Ma, J., Wang, C. & He, H. Transition metal doped cryptomelane-type manganese oxide catalysts for ozone decomposition. *Appl. Catal. B Environ.* **201**, 503–510 (2017).

9. Post, J. E. Manganese oxide minerals: Crystal structures and economic and environmental significance. *Proc. Natl. Acad. Sci.* **96**, 3447–3454 (1999).

10. Wang, J. *et al*. Room-Temperature Oxidation of Formaldehyde by Layered Manganese Oxide: Effect of

Water. *Environ. Sci. Technol.* **49**, 12372–12379 (2015).

11.   Kang, Q. *et al.* Effect of Interlayer Spacing on the Activity of Layered Manganese Oxide Bilayer Catalysts for the Oxygen Evolution Reaction. (2017). doi:10.1021/JACS.6B09184

12.   Miao, L., Wang, J. & Zhang, P. Review on manganese dioxide for catalytic oxidation of airborne formaldehyde. *Appl. Surf. Sci.* **466**, 441–453 (2019).

13.   Zhang, J., Li, Y., Wang, L., Zhang, C. & He, H. Catalytic oxidation of formaldehyde over manganese oxides with different crystal structures. *Catal. Sci. Technol.* **5**, 2305–2313 (2015).

14.   Wang, J., Zhang, G. & Zhang, P. Layered birnessite-type MnO₂ with surface pits for enhanced catalytic formaldehyde oxidation activity. *J. Mater. Chem. A* **5**, 5719–5725 (2017).

15.   Fang, R. *et al.* Efficient MnOx supported on coconut shell activated carbon for catalytic oxidation of indoor formaldehyde at room temperature. *Chem. Eng. J.* **334**, 2050–2057 (2018).

16.   Rong, S., Li, K., Zhang, P., Liu, F. & Zhang, J. Potassium associated manganese vacancy in birnessite-type manganese dioxide for airborne formaldehyde oxidation. *Catal. Sci. Technol.* **8**, 1799–1812 (2018).

17.   Rong, S. *et al.* MnO₂ Framework for Instantaneous Mineralization of Carcinogenic Airborne Formaldehyde at Room Temperature. *ACS Catal.* **7**, 1057–1067 (2017).

18.   Zhang, C. *et al.* Alkali-Metal-Promoted Pt/TiO2 Opens a More Efficient Pathway to Formaldehyde Oxidation at Ambient Temperatures. *Angew. Chemie Int. Ed.* **51**, 9628–9632 (2012).

19.   Chen, X. *et al.* Identification of a Facile Pathway for Dioxymethylene Conversion to Formate Catalyzed by Surface Hydroxyl on TiO2-Based Catalyst. *ACS Catal.* **10**, 9706–9715 (2020).

20.   Bo, Z. *et al.* Mutualistic decomposition pathway of formaldehyde on O-predosed δ-MnO2. *Appl. Surf. Sci.* **498**, 143784 (2019).

21.   Suntivich, J., May, K. J., Gasteiger, H. A., Goodenough, J. B. & Shao-Horn, Y. A perovskite oxide optimized for oxygen evolution catalysis from molecular orbital principles. *Science* **334**, 1383–5 (2011).

22.   Wei, C. *et al.* Cations in Octahedral Sites: A Descriptor for Oxygen Electrocatalysis on Transition-Metal Spinels. *Adv. Mater.* **29**, 1606800 (2017).

23.   Robinson, D. M. *et al.* Photochemical Water Oxidation by Crystalline Polymorphs of Manganese Oxides: Structural Requirements for Catalysis. *J. Am. Chem. Soc.* **135**, 3494–3501 (2013).

24.   Smith, P. F. *et al.* Coordination Geometry and Oxidation State Requirements of Corner-Sharing MnO₆ Octahedra for Water Oxidation Catalysis: An Investigation of Manganite (γ-MnOOH). *ACS Catal.* **6**, 2089–2099 (2016).

25.   Vinyard, D. J., Ananyev, G. M. & Charles Dismukes, G. Photosystem II: The Reaction Center of Oxygenic Photosynthesis. *Annu. Rev. Biochem.* **82**, 577–606 (2013).

26.   Risch, M. *et al.* Redox Processes of Manganese Oxide in Catalyzing Oxygen Evolution and Reduction: An *in Situ* Soft X-ray Absorption Spectroscopy Study. *J. Phys. Chem. C* **121**, 17682–17692 (2017).

27.   Kyung-Wan Nam, †,‖, Min Gyu Kim, ‡ and & Kwang-Bum Kim†, §,*. In Situ Mn K-edge X-ray Absorption Spectroscopy Studies of Electrodeposited Manganese Oxide Films for Electrochemical Capacitors. (2006). doi:10.1021/JP063130O

28.   Galakhov, V. R. *et al.* Mn 3s exchange splitting in mixed-valence manganites. doi:10.1103/PhysRevB.65.113102

29.   Tang, Q., Jiang, L., Liu, J., Wang, S. & Sun, G. Effect of Surface Manganese Valence of Manganese Oxides on the Activity of the Oxygen Reduction Reaction in Alkaline Media. *ACS Catal.* **4**, 457–463 (2014).

30.   Ruetschi, P. & Giovanoli, R. Cation Vacancies in MnO[sub 2] and Their Influence on Electrochemical Reactivity. *J. Electrochem. Soc.* **135**, 2663 (1988).

31.   Abbas, H. & Nasser, S. A. Hydroxyl as a defect of the manganese dioxide lattice and its applications to the dry cell battery. *J. Power Sources* **58**, 15–21 (1996).

32.   Meng, Y. *et al*. Structure–Property Relationship of Bifunctional MnO$_2$ Nanostructures: Highly Efficient, Ultra-Stable Electrochemical Water Oxidation and Oxygen Reduction Reaction Catalysts Identified in Alkaline Media. *J. Am. Chem. Soc.* **136**, 11452–11464 (2014).

33.   Ruetschi, P. Influence of Cation Vacancies on the Electrode Potential of MnO[sub 2]. *J. Electrochem. Soc.* **135**, 2657 (1988).

34.   Kitchaev, D. A., Dacek, S. T., Sun, W. & Ceder, G. Thermodynamics of Phase Selection in MnO$_2$ Framework Structures through Alkali Intercalation and Hydration. *J. Am. Chem. Soc.* **139**, 2672–2681 (2017).

35.   Balachandran, D., Morgan, D. & Ceder, G. First Principles Study of H-insertion in MnO2. *J. Solid State Chem.* **166**, 91–103 (2002).

36.   Zaharieva, I. *et al*. Electrosynthesis, functional, and structural characterization of a water-oxidizing manganese oxide. *Energy Environ. Sci.* **5**, 7081 (2012).

37.   Anne-Claire Gaillot, † *et al*. Structure of Synthetic K-rich Birnessite Obtained by High-Temperature Decomposition of KMnO4. I. Two-Layer Polytype from 800 °C Experiment. (2003). doi:10.1021/CM021733G

38.   Chen, D. *et al*. Probing the Charge Storage Mechanism of a Pseudocapacitive MnO$_2$ Electrode Using *in Operando* Raman Spectroscopy. *Chem. Mater.* **27**, 6608–6619 (2015).

39.   Morgan Chan, Z. *et al*. Electrochemical trapping of metastable Mn3+ ions for activation of MnO2 oxygen evolution catalysts. *Proc. Natl. Acad. Sci. U. S. A.* **115**, E5261–E5268 (2018).

40.   Julien, C. *et al*. Raman spectra of birnessite manganese dioxides. *Solid State Ionics* **159**, 345–356 (2003).

41.   Abrashev, M. V. *et al*. Origin of the heat-induced improvement of catalytic activity and stability of MnO$_2$ electrocatalysts for water oxidation. *J. Mater. Chem. A* **7**, 17022–17036 (2019).

42.   Hwang, J. *et al*. CO$_2$ Reactivity on Cobalt-Based Perovskites. *J. Phys. Chem. C* acs.jpcc.8b06104 (2018). doi:10.1021/acs.jpcc.8b06104

43.   Wang, J., Zhang, G. & Zhang, P. Layered birnessite-type MnO$_2$ with surface pits for enhanced catalytic formaldehyde oxidation activity. *J. Mater. Chem. A* **5**, 5719–5725 (2017).

44.   Zhang, C. *et al*. Alkali-Metal-Promoted Pt/TiO2 Opens a More Efficient Pathway to Formaldehyde Oxidation at Ambient Temperatures. *Angew. Chemie Int. Ed.* **51**, 9628–9632 (2012).

45.   Ji, Y. & Luo, Y. Structure-dependent photocatalytic decomposition of formic acid on the anatase TiO2(101) surface and strategies to increase its reaction rate. *J. Power Sources* **306**, 208–212 (2016).

46.   Xu, J. *et al*. On the mechanism of the direct pathway for formic acid oxidation at a Pt(111) electrode. *Phys. Chem. Chem. Phys.* **15**, 4367–4376 (2013).

47.   Joo, J., Uchida, T., Cuesta, A., Koper, M. T. M. & Osawa, M. Importance of Acid–Base Equilibrium in Electrocatalytic Oxidation of Formic Acid on Platinum. *J. Am. Chem. Soc.* **135**, 9991–9994 (2013).

48.   Selvakumar, S. *et al*. Reaction of formaldehyde over birnessite catalyst: A combined XPS and ToF-SIMS study. *Appl. Catal. B Environ.* **223**, 192–200 (2018).

49.   Gorlin, Y. *et al*. In Situ X-ray Absorption Spectroscopy Investigation of a Bifunctional Manganese Oxide Catalyst with High Activity for Electrochemical Water Oxidation and Oxygen Reduction. *J. Am. Chem. Soc.* **135**, 8525–8534 (2013).

Chapter 4. Revealing the electronic structure origin to low temperature activation of small molecules on iridium oxides

4.1 Introduction

Due to the inert nature of C-H bond, selective low-temperature activation of small hydrocarbon molecules is a holy grail in the field of heterogeneous catalysis.[1,2,3] Recently, oxygen-promoted rutile $IrO_2(110)$ with partially filled under-coordinated surface oxygen (O_{CUS}) was predicted to have the highest C-H activation rate[4] amongst the studied rutiles, perovskites, metals, oxide supported metal catalysts, and layered materials.[4] This prediction has motivated the exploration of $IrO_2(110)$ for the selective conversion of methane to methanol and formaldehyde. Weaver et al. showed that methane activation could indeed take place at 88 K, to release CO_2, CO, and H_2O at mild temperatures (400 - 750 K), via the molecularly adsorbed, strongly bound precursor mechanism[5]. Consequently, several works on the reactivity of IrO_2 (110) for hydrogen abstraction from small molecules such as H_2,[6] C_2H_6[7], and C_3H_8[8] have been reported. However, the nature of the active species and the reaction mechanism responsible for low-temperature C-H activation remains an open question. Motivated to study the role of O_{CUS} on $IrO_2(110)$, as has been done for the OER using both experimental[9,10] and theoretical[11] methods, we here report the investigation of how $IrO_2(110)$ activates methane and methanol through its O_{CUS} species. We use this finding to advance our understanding of the small-molecule activation mechanism and how it connects to the surface chemistry and electronic structure of oxides.

The nature of the active species in IrO_2 catalysts has historically been of interest in the OER field. Several IrO_2-based chemistries such as Ti-doped IrO_2[12], amorphous Iridium oxide[13], and leached IrO_2[14] have shown higher mass specific activity compared to monolithic rutile IrO_2 crystal structure. The origin of enhanced activity of these different IrO_2-based catalysts has been attributed to O_{CUS} formed during the water activation using both DFT and experimental methods.[15] These O_{CUS} in IrO_2-based catalysts was correlated to the low binding energy feature

at ~528.4 eV in the O 1*s* spectrum in X-ray Photoelectron Spectroscopy (XPS)[16] and ~529 eV feature of the O K-edge in X-ray Absorption Spectroscopy (XAS.)[17] This observation has also been referred to as the electrophilic oxygen (O^{I-}).[18,19] and shown to be active for CO oxidation.[20] More recently, in situ XPS measurements of IrO_2 (110) have identified the low binding energy feature of the O 1*s* spectra as O_{CUS}[21] and O_{BRI}[22] species along with the corresponding Ir species in the Ir 4*f* spectrum. These observations suggest that the under-coordinated oxygen species (O_{CUS}) can be active under oxygen atmosphere of 0.5-1 Torr at 320 K. The driver of this work is to probe the nature of IrO_2 under the reaction conditions to understand the surface oxygen responsible for the C-H activation.

We present evidence for the formation of O_{CUS} and iridium species under the oxidizing conditions using in situ AP-XPS and density of states (DOS) calculations for IrO_2 (110). We identify the O_{CUS}/Ir_{CUS} species on IrO_2 (110) as the active species by observing how the surface core level shifts in the O 1*s* and Ir 4*f* spectra as well as the valence band spectra under reaction conditions of methane and methanol oxidation. Moreover, we show that room temperature selective methanol oxidation to methyl formate as well as methane oxidation to CO_2 can be achieved by increasing the coverage of O_{CUS}/Ir_{CUS} species using plug flow reactor measurements. Finally, we propose reaction mechanisms for methanol and methane oxidation on IrO_2 by understanding the nature of carbonaceous reaction intermediates using AP-XPS and diffuse reflectance infrared fourier transmission spectroscopy (DRIFTS).

4.2 Formation of CUS oxygen (O_{CUS}) and CUS Iridium (Ir_{CUS})

AP-XPS measurements were performed on the epitaxial thin films of IrO_2 with the (110)

termination, grown on $TiO_2(110)$ single crystals using molecular beam epitaxy (MBE) to investigate the $C_xH_yO_z$ -type species as well as the Ir $4f$ core states and valence band in the presence of 100 mTorr O_2. The as-prepared thin film was heated at 250 °C under 100 mTorr of O_2 to remove carbonaceous impurities (Fig. A.3.1) and cooled back to room temperature to study surface speciation for methanol and methane oxidation (Fig. A.3.2).

Surface core level shift[23] was noted for both the O $1s$ and Ir $4f$ spectra for a cleaned sample at room temperature. We observed a surface core level shift[23] of 1.1 eV in the O $1s$ spectrum indicated by the increase of intensity at 529.1 eV (Fig. 1A) and 0.5 eV in Ir $4f$ spectrum indicated by the increase of intensity at 62.3 eV (Fig. 1B) The surface core level shifts towards lower binding energy for the O $1s$ spectrum due to the formation of a new feature at 528.9 eV (O_{CUS}, Fig. 1A), which can be attributed to the formation of surface oxygen species.[21] On the other hand, the Ir $4f$ peaks (Ir_{CUS}, Fig. 1B) shift towards higher binding energy with an increase in intensity in the 61-63 eV region, which could be assigned to surface iridium species.[21] Moreover, the valence band spectrum of the cleaned sample also an increase in intensity of the sharp feature close to the Fermi edge as well as the loss of intensity further away from the Fermi edge when compared to the as-prepared sample as shown in Fig. 1C. No other obvious changes in speciation were observed in the cleaned sample as seen in the survey spectrum (Fig. A.3.3). Finally, we also observed a decrease in intensity in the higher binding regions of the O $1s$ spectrum from 531-534 eV upon cleaning, which was attributed to the loss of surface hydroxyls ($OH_{BRI,}$ 531.2 eV and $OH_{CUS,}$ 532.2 eV)[24] and carbonaceous species such as CH_3O (531.2 eV),[25] HCOO (532.2 eV)[25] and adsorbed CO_2 (b-CO_2, 533.9 eV).[26] The peak assignment for the clean surface for the O $1s$ and Ir $4f$ spectra based on the formation of O_{CUS} and Ir_{CUS} species are shown in Figs. 1A and S4 and the fitting parameters[16,17] are reported in Tables A.3.1 and A.3.2 respectively. We next

understand the physical origin of the changes in the O 1*s*, Ir 4*f*, and the valence band spectra using DFT.
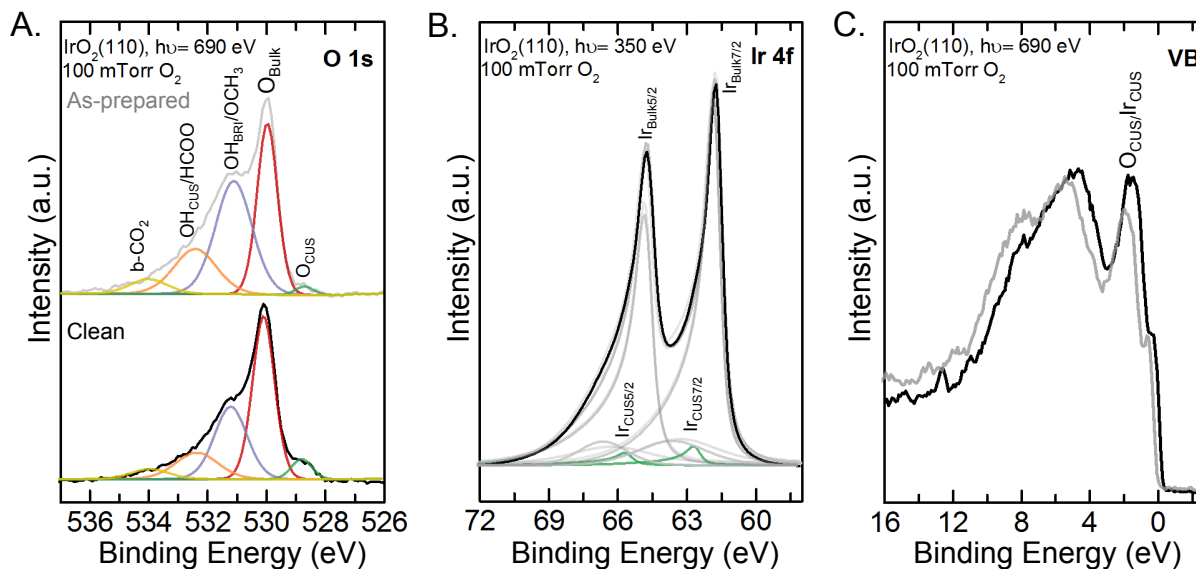
Figure 1: AP-XPS at room temperature before and after cleaning. *AP-XPS under 100 mTorr O_2 for the as-prepared (grey) and clean sample (black) prepared by heating the sample to 250 °C in 100 mTorr O_2 and cooled to room temperature showing A) O 1s spectrum with surface core level shift due to formation of O_{CUS} (528.9 eV), and a decrease in the intensity of surface bridge hydroxyl/methoxy (OH_{BRI}/CH_3O, 531.2 eV), surface CUS hydroxyl/formate ($OH_{CUS}/HCOO$, 532.2 eV), and adsorbed CO_2 species (b-CO_2, 533.9 eV), B) Ir 4f spectrum with surface core level shift leading to the formation of a shoulder at the higher binding energy side compared to the $Ir_{Bulk}(Ir_{Bulk5/2}$, 61.8 eV and $Ir_{Bul7/2}$, 64.8 eV) indicating the formation of Ir_{CUS} species ($Ir_{CUS5/2}$, 62.3 eV and $Ir_{CUS7/2}$, 65.2 eV). The corresponding satellite features are assigned to the peaks at 63.3 eV ($Ir_{Bulk7/2\ (Sat)}$) and 66.1 eV ($Ir_{Bulk5/2\ (Sat)}$), and C) valence band spectrum showing the loss of intensity at higher binding region around ~12.5 eV and gain of new intensity closer to the Fermi level after heating IrO$_2$(110) under 100 m Torr O_2 at 250 °C and cooling back to room temperature. C 1s spectrum showing minimum surface contamination from carbonaceous species for the clean surface when compared to the as-prepared surface is shown in Fig. A.3.2. Source energy of 690 eV was used for the O 1s spectrum, while 350 eV was used for Ir 4f spectrum and the valence band spectrum. O 1s and Ir 4f spectra are plotted after normalizing to O_{Bulk} (530 eV) and Ir_{Bulk} (61.8 eV) intensities respectively while valence band spectrum is plotted without normalization after background subtraction.*

The origin of the surface core level shift of 0.5 eV in Ir 4*f* spectrum (increase in intensity at 62.3 eV) and 1.1 eV in the O 1*s* spectrum (increase in intensity at 528. 9 eV) can be attributed to the

surface coordination and the density of states closer to the Fermi edge respectively.[27,28] Previous surface core level shift calculations for a closely related catalyst system, rutile $RuO_2(110)$, suggested that the Ru coordination (e.g., bond distance) dictates the core level shift for the Ru $3d$ spectra while the density of states closer to the Fermi edge dictates the core level shift in the O $1s$ spectrum due to enhanced screening.[29] To understand the observed changes in the surface core level and the valence band under oxygen atmosphere (100 mTorr) for the O $1s$ and Ir $4f$ spectrum, we modeled $IrO_2(110)$ using DFT with bulk Ir_{Bulk}/O_{Bulk} (red), surface bridge Ir_{BRI}/O_{BRI} (violet), and surface co-ordinatively under-coordinated Ir_{CUS}/O_{CUS} (green) species (Fig. 2A). The surface-core-level shift towards lower binding in O $1s$ (Fig. 1A) is attributed to enhanced screening due to larger oxygen partial density of states (pDOS) closer to the Fermi edge upon O_{CUS} formation (Figs. 2B and C). Furthermore, the Ir-O bond distances decreases from the bulk atoms (2.01 Å) to the bridge species (BRI, 1.98 Å), and finally to the CUS (1.78 Å) species (Fig. 2D). The under-coordinated bonds of $Ir_{CUS}-O_{CUS}$ species are thus expected to have higher binding energy in the Ir $4f$ spectra due to the shortening of the Ir-O bond. Therefore, the core level shift of 1.1 eV in O $1s$ spectra and 0.6 eV in the Ir $4f$ spectra is attributed to the formation of O_{CUS} and Ir_{CUS} species respectively.

To understand the observed changes in the valence band spectrum, we computed the pDOS of O_{CUS} (Fig. 2B) and Ir_{CUS} (Fig. A.3.5) species of $IrO_2(110)$. O_{CUS} in particular manifests a feature at ~-2 eV from the Fermi level. This feature is closer to the Fermi edge compared to the pDOS of O_{Bulk} and O_{BRI}. In addition, a loss of intensity was observed at ~-5.3 eV for O_{CUS} when compared to O_{BRI} and O_{Bulk}. These changes suggest that the electron density shifts closer to the Fermi edge with the O_{CUS} formation, which is consistent with the changes observed in the valence band spectrum from AP-XPS in Fig. 1C. Moreover, the computed iridium pDOS (Fig. A.3.5) revealed

an increase in the pDOS closer to the Fermi edge for Ir_{CUS} compared to Ir_{BRI} and Ir_{Bulk}, which is consistent with the observed changes in the valence band in Fig. 1C. The identification of the fingerprint of the O_{CUS}/Ir_{CUS} species closer to the Fermi edge using pDOS and the changes in the valence band further suggests the formation of Ir_{CUS}/O_{CUS} species after cleaning at room temperature using AP-XPS. Next, we investigated the role of O_{CUS} and Ir_{CUS} species during the methanol and methane oxidation using AP-XPS.
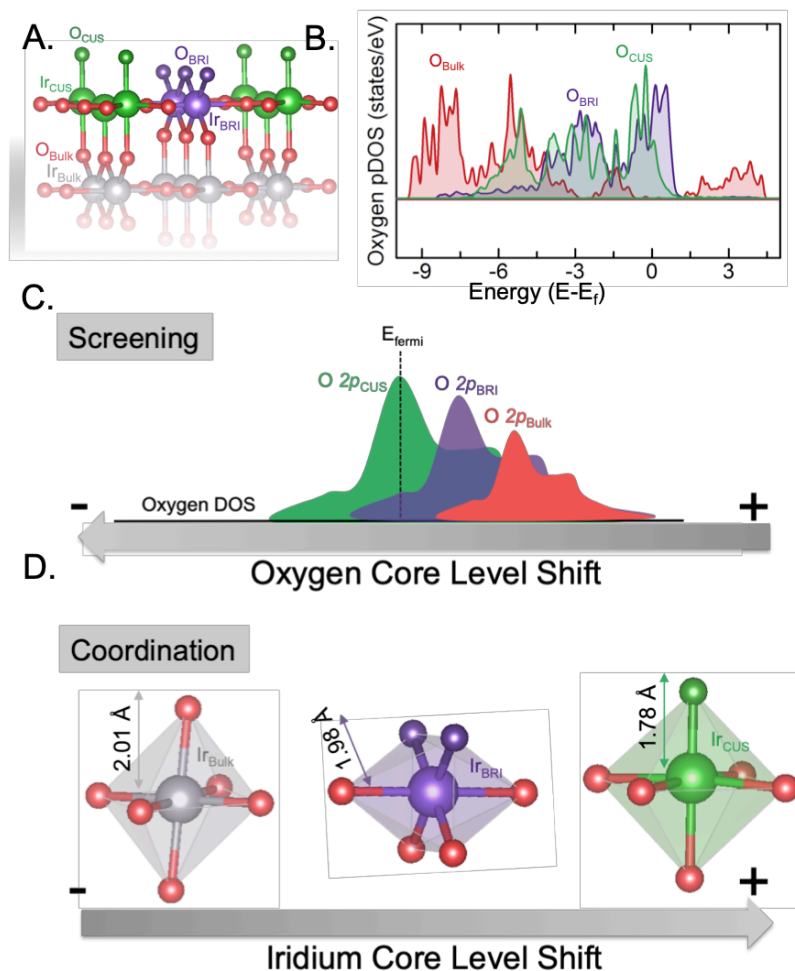
Figure 2: ***Origin of surface core level shift for IrO$_2$(110).*** *A) Surface structure of the IrO$_2$(110) showing the bridge (BRI, Ir$_{BRI}$, O$_{BRI}$, violet), co-ordinatively under-saturated (CUS, Ir$_{CUS}$, O$_{CUS}$, green), and bulk (Ir$_{Bulk}$, O$_{Bulk}$, grey) iridium and oxygen species, B) pDOS of the valence band of oxygen states for O$_{BRI}$, O$_{CUS}$, and O$_{Bulk}$ species showing increase in intensity closer to the Fermi level for O$_{BRI}$ and O$_{CUS}$ atoms. Oxygen pDOS are calculated by summing up the oxygen 2p orbitals of the respective surface species. Schematic of C) negative shift for the O 1s core level as a function of increasing pDOS at the Fermi level for the bridge and CUS oxygen species*

leading to increased screening when compared to the bulk oxygen species, and schematic of D) positive core level shift for the Ir 4f core level as a function of shortening bond length of Ir-O bonds for the bulk (2.01 Å), bridge (1.98 Å), and CUS (1.78 Å) Ir species.

4.3 Role of CUS oxygen in low temperature methanol oxidation

AP-XPS measurements were performed to investigate the surface speciation of $C_xH_yO_z$ reaction intermediates on $IrO_2(110)$ films in the presence of 25 mTorr CH_3OH and 200 mTorr O_2. O 1s, Ir 4f, and C 1s spectra were collected from epitaxial-grown thin films under isobaric conditions of pCH_3OH = 25 mTorr and pO_2 = 200 mTorr. We focus on the temperature range of 25-250 °C following heating to 250 °C and cooling to room temperature in 100 mTorr O_2 (C 1s spectra in Fig. A.3.2). Representative O 1s, Ir 4f, C 1s, and valence band spectra of IrO_2 before and after 25 mTorr CH_3OH and 200 mTorr O_2 exposure at room temperature are shown in Figs. 3A-D. Relative intensities of O_{CUS} in O 1s spectra (528.9 eV[21], Fig. 3A) and Ir_{CUS} in Ir 4f spectra (62.3 eV[21], Fig. 3B) were observed to decrease after normalizing the intensities with respect to O_{Bulk} intensity (Table A.3.3). In addition, an increase in C 1s intensity was observed in Fig. 3C due to the formation of CH_x (284.8 eV),[30] CH_3O (286.1 eV),[31] HCOO (287.2 eV),[32] and b-CO_2 (288.2 eV)[32] reaction intermediates.

In order to obtain the corresponding intensities of the carbonaceous species in the O 1s spectra, we first estimated the relative sensitivity factor (RSF) as 0.9 using the intensities of CO_2 gas measured at source energy of 490 eV and 690 eV (Fig. A.3.6). We then assign the peak at 531.2 eV to both surface hydroxyl (OH_{BRI})[24,33] and methoxy (CH_3O)[33] species as the peak intensity ratio of CH_3O in C 1s spectra to the 531.2 eV peak in the O 1s spectra is greater than 1. A ratio greater than 1 suggests that the additional intensity could arise from a non-carbonaceous species

such as hydroxyl species.[24,25] Next, we assign the 532.2 eV peak to both $OH_{CUS}/HCOO^{24}$ species, as the intensity ratio of this peak to the $OH_{CUS}/HCOO$ peak in the C 1*s* spectra is larger than 1 (1.47) consistent with stoichiometry of HCOO. However, we also assign this feature to OH_{CUS}^{24} as surface hydroxyl is a known reaction intermediate during methanol oxidation. Finally, we assign the 534.9 eV peak to adsorbed CO_2 (b-CO_2) but the intensity of this peak is too small to make any ratio evaluation meaningful. Moreover, a decrease in intensity closer to the Fermi level and a slight increase in intensity away from the Fermi level was observed in the valence band in Fig. 3D. Spectral changes in Figs. 3A-D upon CH_3OH adsorption at room temperature suggest that O_{CUS}^{33} and Ir_{CUS} species are consumed leading to the formation of the different carbonaceous reaction intermediates species (for example, $CH_3OH + O_{CUS} + Ir_{CUS} \rightarrow CH_3O\text{-}Ir_{CUS} + HO_{CUS}$).
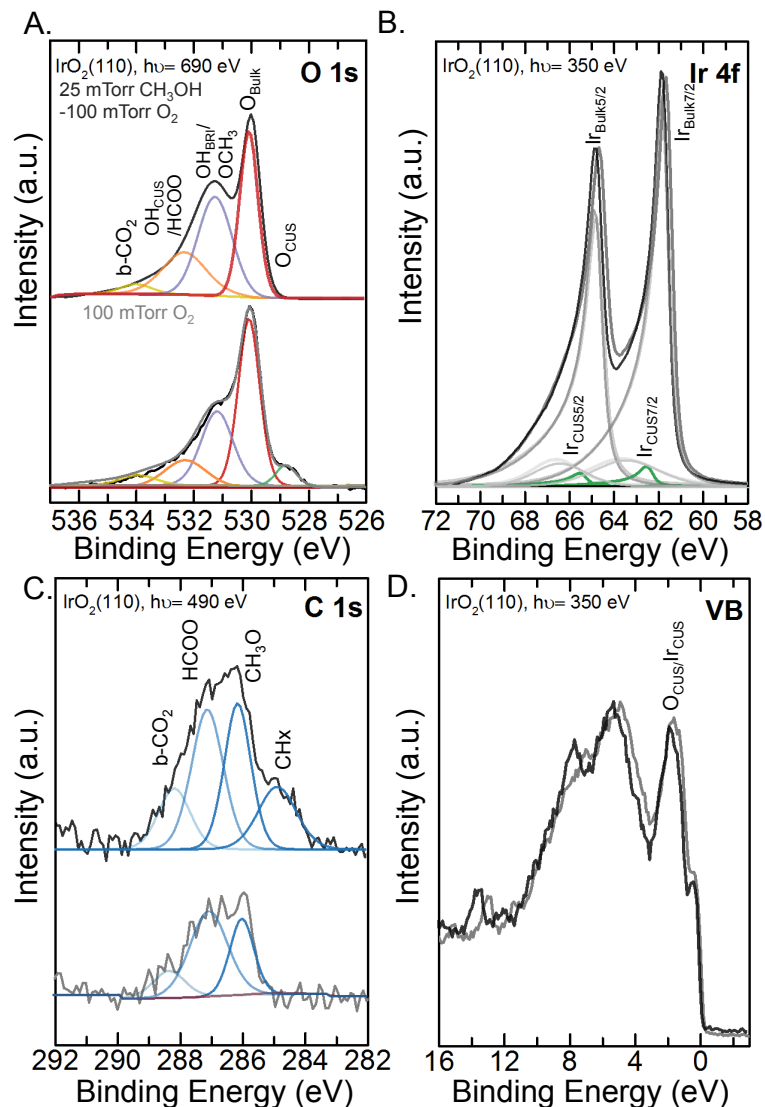
Figure 3: Methanol adsorption at room temperature using AP-XPS. *Comparison of spectra of the clean surface under 100 mTorr O_2 and 25 mTorr CH_3OH/200 mTorr O_2 at room temperature showing A) O 1s spectrum showing decrease in intensity of O_{CUS} (528.9 eV) and increase in intensity of OH_{BRI}/CH_3O (531.1 eV), OH_{CUS}/HCOO (532.1 eV), and b-CO_2 (533.8 eV) species, B) Ir 4f spectrum showing decrease in Ir_{CUS} (62.3 eV) intensity, C) C 1s spectrum showing increase in intensity of CH_x (284.8 eV), CH_3O (286.2 eV), HCOO (287.2 eV), and b-CO_2 (288.2 eV) species, and D) valence band spectrum showing decrease in intensity closer to the Fermi level (O_{CUS}/Ir_{CUS}) and increase of intensity away from the Fermi level. Source energy of 690 eV was used for the O 1s spectrum, 490 eV was used for the C 1s spectrum, and 350 eV was used for Ir 4f and valence band spectra. The O 1s and Ir 4f spectra are normalized to O_{Bulk} (530 eV) and Ir_{Bulk} (61.8 eV) species respectively while no normalization was done for the C 1s and valence band spectra. All intensities were fitted after background subtraction and fitting parameters for AP-XPS spectra are shown in Tables A.3.1, A.3.2, and A.3.4.*

The C $1s$ spectrum (Fig. 4A) revealed the loss of intensity of the CH_X(284.8 eV),[30] CH_3O (286.1 eV),[31], HCOO (287.2 eV),[32] and b-CO_2 (288.2 eV)[32] reaction intermediates upon heating from 25°C to 250 °C (Fig. 4D).We also note the intensities of CH_3O/OH_{BRI} decreases with increasing temperature (Fig. 4D) suggesting the conversion of OH_{BRI} to H_2O. Also, the intensities of HCOO (532.2 eV) and b-CO_2 (533.2 eV) species in the O $1s$ spectra (Fig. A.3.7) follow similar trends to the intensities calculated using the C 1s spectra (Fig. 3D) further supporting the peak assignments. In addition, the intensity of the O_{CUS} species in the O $1s$ spectra (Fig. 4B) increases with temperature (Fig. 4D)[29] suggesting that the O_{CUS} species can be replenished under 25 mTorr CH_3OH and 200 mTorr O_2 at 125 °C. Further support comes from the Ir $4f$ spectra (Fig. 4C)[29] where an increase in the intensity of the Ir_{CUS} species at 62.3 eV (Fig. 4D) was observed, implying the formation of the O_{CUS} species. The normalized raw and difference spectra for the O $1s$ and Ir $4f$ regions in the range of 25 °C to 250 °C also revealed the formation of O_{CUS} and Ir_{CUS} species (Figs. A.3.8A and B respectively). We discuss how the O_{CUS}/Ir_{CUS} species affect the product selectivity for the methanol oxidation in a later section. First, we discuss the role of O_{CUS} and Ir_{CUS} species during the methane oxidation using AP-XPS.

Fig. 4
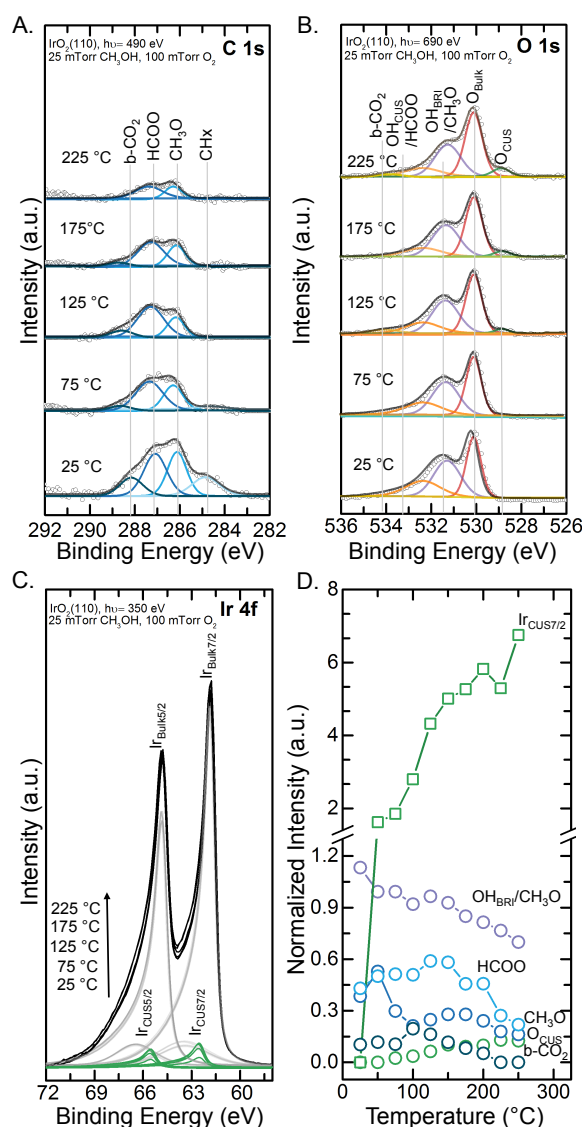
Figure 4: Low temperature methanol oxidation using AP-XPS. AP-XPS of A) C 1s spectrum showing decrease in intensity of CH_x (284.8 eV), CH_3O (286.1 eV), HCOO (287.2 eV), and b-CO_2 (288.2 eV), species, B) appearance and growth of O_{CUS} (528.8 eV) species from 125 °C to 225 °C as well as the decrease in the intensity of OH_{BRI}/CH_3O (531.2 eV), and OH_{CUS}/HCOO (532.2 eV) species in the O 1s spectrum, C) appearance and growth of Ir_{CUS} species (63.2 eV) from 25°C to 225 °C in the Ir 4f spectrum, D) trends in relative intensities of Ir_{CUS}, OH_{BRI}/CH_3O, HCOO, O_{CUS}, and b-CO_2 normalized to the corresponding O_{Bulk} intensity as a function of temperature from 25-225 °C under 20 mTorr CH_3OH and 100 mTorr O_2. The O 1s and Ir 4f spectra are normalized to O_{Bulk} (530 eV) and Ir_{Bulk} (61.8 eV) species respectively while no normalization was done for the C 1s spectra. Source energy of 690 eV was used for O 1s spectra, while 350 eV was used for Ir 4f spectra and 490 eV was used for the C 1s spectra collection. All intensities were fitted after background subtraction and fitting parameters for AP-XPS spectra are shown in Tables A.3.1, A.3.2, and A.3.4.

112

4.4 Role of CUS oxygen in low temperature methane oxidation

We have identified 125 °C to be the optimum temperature for dosing the methane-oxygen gas mixture of 1 and 10 mTorr of CH_4 and O_2 respectively. The formation of the background carbonaceous species from surface contamination from the AP-XPS chamber[34] and sample reduction can interfere with the intermediates of methane activation (Fig. A.3.9A and Fig. A.3.9B). Our dosing condition minimizes this impact CH_4-10 mTorr O_2, a small increase in the intensity of the C 1s spectrum was observed which was attributed to background chamber contamination (Fig. A.3.10). Further increasing the temperature to 175 °C, led to an increase in intensity in the C 1s spectra which could be associated to the formation of CH_3O (286.3 eV) and HCOO (288.1 eV) reaction intermediates (Fig. 5A) from the activation of methane (e.g., CH_4+ O_{CUS}+O_{BR} → CH_3-O_{CUS}+−OH_{BRI}). Further support comes from the observation that similar spectra collected under only 10 mTorr O_2 in the same temperature range does not show an increase in the C 1s spectrum (Fig. A.3.11A). Total intensities of the C 1s reaction intermediates for the reaction conditions with and without CH_4 are compared in Fig. A.3.11B where an increase in the C 1s intensity was observed only when having CH_4 in the gas stream. We also note that the intensities of the OH_{CUS}/HCOO (532.2 eV) peaks follows a similar trend as the intensity of HCOO (288.1 eV) peak intensity in C 1s spectrum after normalization. (Fig. A.3.12) Moreover, the O 1s and Ir 4f spectra showed an increase in intensity of O_{CUS} (528.9 eV, Fig. 5B) and Ir_{CUS} species (62.3 eV, Fig. 5C) upon heating and in the difference spectra in Figs. S13A and B respectively. This finding suggests that CUS-species can be the active surface species during the methane activation. In addition, the formation of CO_2 was detected at 225 °C and higher temperature in the mass spectrometer (Fig. 5D) suggesting that the reaction intermediates of CH_4 activation are converted to CO_2 at this temperature (for example, HCO-O_{CUS} + O_{BRI} → CO_2 +

OH_{BRI}). Furthermore, a decrease in the CH_3O/OH_{BRI} intensity with increasing temperature (Fig. 5C and Fig. A.3.12) along with H_2O formation with increasing temperature suggesting that the OH_{BRI} formed are converted to H_2O at higher temperature (For example, $OH_{BRI} + OH_{BRI} \rightarrow O_{BRI} + O_{BRI\_vac} + H_2O$). Lastly, the valence band spectrum also showed a decrease in the intensity away from the Fermi edge and increase in intensity closer to the Fermi edge in Fig. A.3.14 further supporting the hypothesis that O_{CUS} are replenished under reaction conditions. Next, we investigated the role of O_{CUS} for product selectivity and reaction kinetics for CH_3OH and CH_4 oxidation on IrO_2.
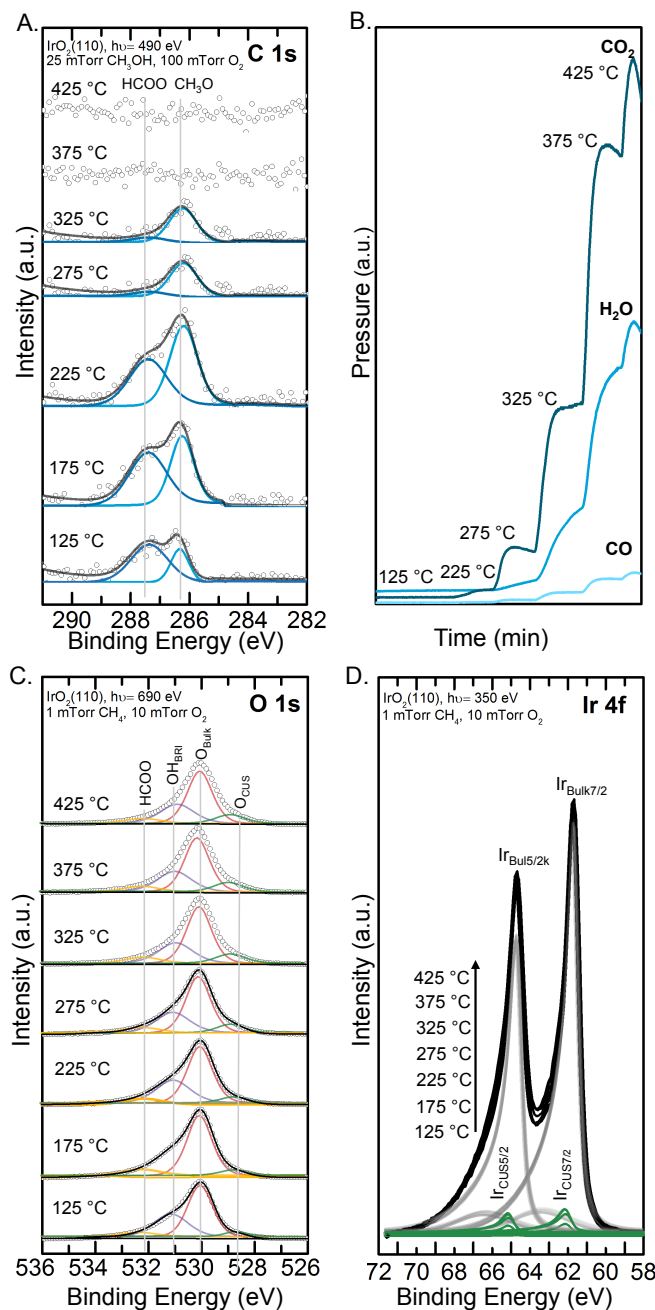
Figure 5: Low temperature methane oxidation using AP-XPS. *AP-XPS of A) C 1s spectra showing the increase in intensity of CH_3O (286.1 eV) and HCOO (287.2 eV) reaction intermediates between 125 °C to 225 °C followed by a decrease in intensity between 225 °C to 425 °C, B) corresponding mass spectroscopy showing the generation of CO, CO_2, and H_2O gases as a function of time at different temperatures (125, 225, 275, 325, 375, and 425 °C), C) O 1s spectrum showing increase in O_{CUS} (528.9 eV) intensity as a decrease in intensity in OH_{BRI}/CH_3O (531.2 eV) between 125 °C to 425 °C and D) Ir 4f spectrum showing increase in the intensity of Ir_{CUS} (62.3 eV) species (62.3 eV) from 125 °C to 425 °C. Source energy of 690 eV was used for the O 1s spectra, while 350 eV was used for Ir 4f spectra, and 490 eV was used for C 1s spectra collection. The O 1s and Ir 4f spectra are normalized to the O_{Bulk} (530 eV) and*

Ir$_{Bulk}$ (61.8 eV) peaks respectively while no normalization was done for the C 1s spectra. All intensities are fitted after background subtraction and fitting parameters for AP-XPS spectra are shown in Table A.3.1, A.3.2, and A.3.4.

4.5 Role of surface oxygen activity for conversion of CH$_3$OH to HCOOCH$_3$, HCHO, and CO$_2$ and CH$_4$ to CO$_2$

We examined the role of Ir$_{CUS}$/O$_{CUS}$ in CH$_3$OH oxidation to HCOOCH$_3$, HCHO, and CO$_2$ as well as CH$_4$ oxidation to CO$_2$ by examining three IrO$_2$ catalysts with different Ir$_{CUS}$. XRD pattern shown in Fig. A.3.15A also showed rutile structure for IrO$_2$ (Sigma Aldrich) and an amorphous structure for IrO$_2$·0.5H$_2$O (Alfa Aesar, Premion 84%) and amorphous IrO$_2$·1.5H$_2$O (Alfa Aesar, Premion 73%). Ir 4f spectra collected using lab scale XPS showed higher Ir$_{CUS}$ intensity for IrO$_2$·0.5H$_2$O and IrO$_2$·1.5H$_2$O compared to rutile IrO$_2$ in Fig. A.3.15B. The O 1s spectra showed the larger carbonaceous and hydroxyl species for the IrO$_2$·0.5H$_2$O and IrO$_2$·1.5H$_2$O when compared to the rutile IrO$_2$ (Fig. A.3.15C) consistent with the larger water content in these oxides as revealed by thermogravimetric analysis (TGA) in Fig. A.3.15D.

First, we flowed ~70 ppm CH$_3$OH/280 ppm O$_2$ at room temperature with a gas ratio (1:4) similar to AP-XPS measurements to understand product selectivity during methanol oxidation prior to heating up. We observed the formation of methyl formate (HCOOCH$_3$) and carbon dioxide (CO$_2$) for IrO$_2$·0.5H$_2$O and IrO$_2$·1.5H$_2$O with higher conversion of 70% noted for IrO$_2$.0.5H$_2$O (Figs. A.3.16A and B) while rutile IrO$_2$ was only active at higher temperature. Moreover, for both IrO$_2$·0.5H$_2$O and IrO$_2$·1.5H$_2$O, we observed an initial increase in the CO$_2$ conversion followed by the HCOOCH$_3$ formation, at which point CO$_2$ conversion started decreasing with time at room temperature (Figs. A.3.16A and B). In addition, no formaldehyde (HCHO)

formation was observed at room temperature for $IrO_2 \cdot 0.5H_2O$ and $IrO_2 \cdot 1.5H_2O$ suggesting higher

O_{CUS}/Ir_{CUS} is correlated with methyl formate ($HCOOCH_3$) and carbon dioxide (CO_2) formation.

Upon heating the powders, $IrO_2 \cdot 0.5H_2O$ and $IrO_2 \cdot 1.5H_2O$ showed selectivity towards $HCOOCH_3$

and HCHO (Figs. 6A,B) while the rutile IrO_2 was selective only towards HCHO formation (Fig.

6C) suggesting HCHO formation is correlated with lower O_{CUS}/Ir_{CUS}. Also, similar high

temperature product selectivity observed for $IrO_2 \cdot 0.5H_2O$ and $IrO_2 \cdot 1.5H_2O$ suggested that the

structural water content does not change product selectivity. Finally, heating the catalysts to

higher temperature (>120 °C) led to complete oxidation of CH_3OH to CO_2 for all the catalysts

(Figs. A.3.17A-C). Interestingly, the addition of 0.3% water vapor (Figs. 6C) to the gas stream

containing ~70 ppm CH_3OH/280 ppm O_2 led to a slight decrease in the activity for the IrO_2

catalyst while the selectivity remained the same, suggesting that the origin of the higher activity

and selectivity for $IrO_2 \cdot 0.5H_2O$ and $IrO_2 \cdot 1.5H_2O$ is due to the higher O_{CUS}/Ir_{CUS} species and not

due to the water content.

The higher conversion for the $IrO_2 \cdot 0.5H_2O$ and $IrO_2 \cdot 1.5H_2O$ (Figs. S17A and B) as well the

selectivity towards $HCOOCH_3$ (Figs. 6A,B) is attributed to the higher O_{CUS}/Ir_{CUS} coverage as

previously proposed for RuO_2.[35] Herein, we propose a reaction mechanism center on the idea

that the O_{CUS}/Ir_{CUS} (Fig. A.3.18A) species are responsible for the selective methanol oxidation on

iridium oxides. First, CH_3OH dissociative adsorbs as CH_3O-Ir_{CUS} and $O_{CUS}H$ (Step 1), followed

by dehydrogenation of CH_3O-Ir_{CUS} to form CH_2O-Ir_{CUS} (Step 2). Next, in the case of higher

coverage of O_{CUS}/Ir_{CUS} species, a second CH_3OH molecule and react with the adsorbed CH_2O-

Ir_{CUS} to form $HCOOCH_3$ (Step 3). However, in the presence of lower O_{CUS}/Ir_{CUS} coverage for

rutile IrO_2, only HCHO is desorbed as seen in Step 3' of Fig. A.3.18B. Finally, oxygen

adsorption occurs to desorb H_2O and replenish the active O_{CUS} sites (Steps 4,4' in Figs. A.3.18A and B). Further support for this mechanism comes from *in situ* DRIFTS (Fig. A.3.19), where initial lower peak intensity of CH_3O and HCOO species is correlated with complete oxidation to CO_2 (Fig. A.3.15) and the higher coverage of CH_3O with increasing time is correlated to $HCOOCH_3$ formation (Fig. A.3.15) in the reactor experiments.
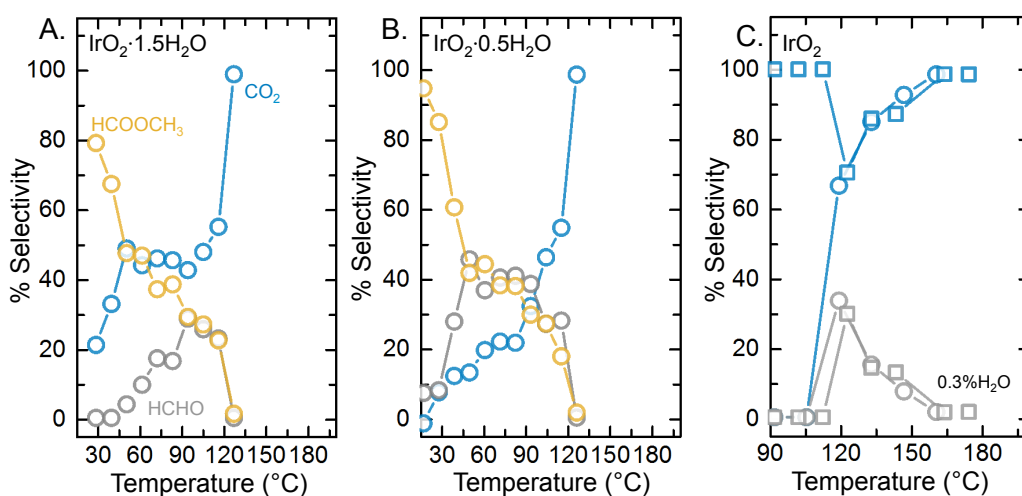
Figure 6: Selectivity of CH_3OH oxidation to $HCOOCH_3$, $HCHO$, and CO_2. *CH_3OH selectivity% towards $HCOOCH_3$ (yellow, circle), HCHO (circle, grey), and CO_2 (circle, blue) for A) $IrO_2 \cdot 0.5H_2O$, B) $IrO_2 \cdot 1.5H_2O$, and C) rutile IrO_2 with (square) and without water (circle) in the gas stream as a function of temperature measured using plug flow reactor. %Selectivity to CO_2 is defined as $100*(CO_{2ppm,out}/HCHO_{ppm,out}+CO_{2ppm,out}+ HCOOCH_{3ppm,out})$;%Selectivity to HCHO is defined as %selectivity$_{HCHO}$ $=100*(HCHO_{ppm,out}/HCHO_{ppm,out}+CO_{2ppm,out}+ HCOOCH_{3ppm,out})$ and %Selectivty to CH_3OCH_3OH is defined as %selectivity$_{HCOOCH3}$=$100*(HCOOCH_{3ppm,out}/HCHO_{ppm,out}+CO_{2ppm,out}+ HCOOCH_{3ppm,out})$; Catalyst loading of 50 mg, flow rate of 150 ml min^{-1}, and gas concentration of 70 ppm CH_3OH/280 ppm O_2 with no added water or 0.3% H_2O was used for all the measurements.*

Next, we investigated methane oxidation using a gas ratio similar to AP-XPS (1:10) measurements by flowing 35 ppm CH_4/350 ppm O_2, over the three powder catalysts. First, at room temperature, we observed CO_2 formation for the $IrO_2 \cdot 0.5H_2O$ (red, Fig. 7A) and $IrO_2 \cdot 1.5H_2O$ (blue, Fig. 7A) while the rutile IrO_2 showed no CO_2 formation (grey, Fig. 7A). As $IrO_2 \cdot 0.5H_2O$ and $IrO_2 \cdot 1.5H_2O$ show higher O_{CUS}/Ir_{CUS} ratio than the rutile, our result suggests

that IrO_2 catalysts with higher O_{CUS}/Ir_{CUS} are more active for the CH_4 activation. Further support

comes from in situ DRIFTS (Fig. A.3.20), where HCOO reaction intermediate is observed at 25

°C and higher temperatures consistent with previous DRIFTS measurements on IrO_x

nanopowders showing the formation of CH_xO-type reaction intermediates at 25 °C upon

methane exposure.[36] Room temperature oxidation of CH_4 to CO_2 shows that $IrO_2 \cdot xH_2O$ are

highly promising active catalysts for the C-H bond dissociation. Very few catalysts such as

FeN$_4$/Graphene nanosheets[37], Ni/TiC[38], M/CeO$_2$ (M = Ni, Pt, Co)[39], CeO$_2$/Cu$_2$O/Cu[40]catalysts

have been shown to activate methane at room temperature. Next, light off curve for CH_4

conversion to CO_2 also showed that $IrO_2 \cdot 0.5H_2O$ and $IrO_2 \cdot 1.5H_2O$ catalysts with higher

O_{CUS}/Ir_{CUS} are active at low temperature compared to the rutile IrO_2 (Fig. 7B) with complete

conversion noted at 225 °C while rutile IrO_2 showed only 10% conversion at the same

temperature (Fig. A.3.21A). Furthermore, adding water vapor (0.3%) to the gas stream for rutile

IrO_2 showed a small decrease in the activity (Fig. 7C) suggesting that the higher activity of

$IrO_2 \cdot 0.5H_2O$ and $IrO_2 \cdot 1.5H_2O$ is not due to the water content in these catalysts but due to the

higher coverage of O_{CUS}/Ir_{CUS} sites. Based on the AP-XPS observations, we propose a reaction

mechanism for the methane oxidation centered on the O_{CUS}/Ir_{CUS} sites (Fig. A.3.22). First, CH_4

adsorbs dissociatively on O_{CUS} sites as CH_3O_{CUS} along with the formation of $O_{BRI}H$ (Step 1),

followed by a series of dehydrogenation of CH_3O_{CUS} to $CH_2O_{CUS}O_{oxide}$ (Step 2), $HCO_{CUS}O_{oxide}$

(Step 3), and $CO_{CUS}O_{2oxide}$ (Step 4) along with the formation of the corresponding $O_{BRI}H$ species.

Finally, oxygen adsorption leads to H_2O desorption and conversion of $CO_{CUS}O_{BRI}$ to CO_2 (Step

5) to complete the catalytic cycle. Therefore, combined AP-XPS, DFT, and kinetic results of

IrO_2 catalysts suggest towards increasing O_{CUS}/Ir_{CUS} species to achieve low temperature CH_3OH

conversion to $HCOOCH_3$ and CH_4 oxidation to CO_2.
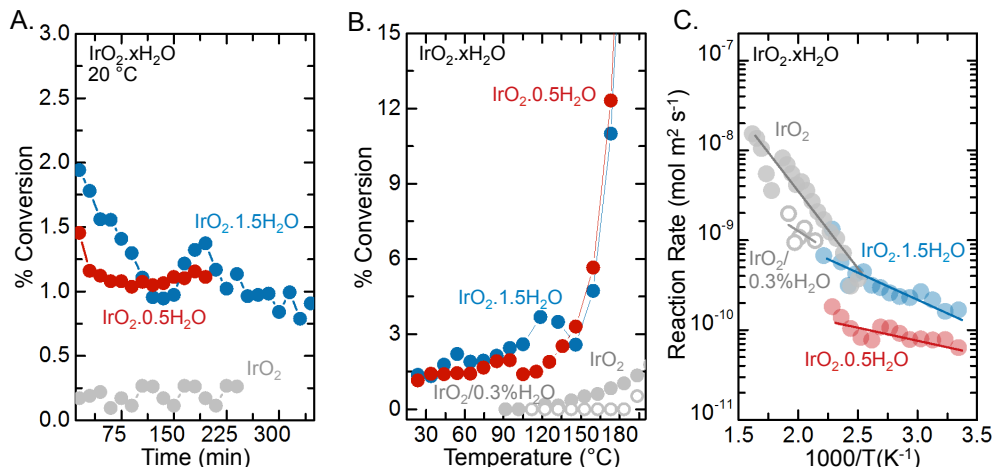
Figure 7: Low temperature methane oxidation. *Methane conversion % to CO_2 at A) room temperature showing CO_2 generation for $IrO_2.0.5H_2O$ (filled, red) and $IrO_2.1.5H_2O$ (filled, blue) and no CO_2 conversion for rutile IrO_2 (filed, grey), B) light off curves at low temperature showing CH_4 conversion to CO_2 for $IrO_2·0.5H_2O$ (filled, red), $IrO_2·1.5H_2O$ (filled, blue), and rutile IrO_2 with (filled, grey) and without 0.3%H_2O (empty, grey) added to the gas stream, and C) Arrhenius-type surface area normalized CH_4 oxidation reaction rates for $IrO_2·0.5H_2O$ (filled, red), $IrO_2·1.5H_2O$ (filled, red), and rutile IrO_2 with (filled grey) and without (unfilled, grey) 0.3%H_2O added to the gas stream. Complete lights-off curves are shown in Fig. A.3.21A, mass normalized reaction rates are reported in Fig. A.3.21B, and BET surface areas are reported in Table A.3.5. Catalyst loading of 50 mg, flow rate of 150 ml min^{-1}, and gas concentration of 35 ppm CH_3OH/350 ppm O_2 with no added H_2O or 0.3% added H_2O was used for all the measurements.*

4.6 Conclusions

We report the AP-XPS measurements, DFT calculations, and plug flow reactor measurements to study the C-H activation on IrO_2. We identify the O_{CUS} species on iridium oxide as the active species for the CH_4 and CH_3OH oxidation. Using single crystal (110)-oriented epitaxial thin films for AP-XPS studies under reaction conditions, we were able to identify trends in the O_{CUS} and Ir_{CUS} formation. We use this experiment to understand the reaction intermediate, along with the role of temperature along with the formation of carbonaceous reaction intermediates such as methoxy, formate, and adsorbed CO_2. The observation of O_{CUS} as the active species for CH_3OH and CH_4 oxidation is consistent with the plug-flow reactor studies of CH_3OH and CH_4

conversion on $IrO_2·0.5H_2O$ and $IrO_2·1.5H_2O$, which have higher O_{CUS}/Ir_{CUS} species and are thus more active for the C-H activation than rutile IrO_2. We find that IrO_2 catalysts with higher O_{CUS}/Ir_{CUS} (e.g., $rO_2·0.5H_2O$ and $IrO_2·1.5H_2O$) can oxidize CH_4 to CO_2 and CH_3OH to CO_2 and $HCOOCH_3$ even at room temperature. By providing this critical link between surface chemistry, electronic structure, and C-H activation ability, these insights provide guiding principles for the selection of next-generation materials chemistries for catalytic CH_x abatement technologies, where multiple catalytic processes are tuned for selective generation of value-added products.

4.7 Experimental and computational methods

4.7.1 Thin Film Fabrication and Characterization

Epitaxial (110)-oriented thin films of the IrO_2 were prepared using molecular beam epitaxy as previously described.[41] Briefly, the oxide films were synthesized using reactive oxide molecular beam epitaxy on single-crystal TiO_2(110) substrates at a substrate temperature of 300 C. Ir was supplied by an electron beam evaporator and a background pressure of 10^{-6} Torr distilled ozone (80% O_3 + 20% O_2) was used. The success of the synthesis was characterized using in-situ reflective high-energy electron diffraction (RHEED) including RHEED oscillations to monitor the growth rate, in-situ low-energy electron diffraction (LEED), atomic force microscopy (AFM),[42] and X-ray diffraction (XRD.)[41] and ARPES.[43] These measurements demonstrate that the samples are phase-pure, single crystal IrO_2(110) films with properties consistent with bulk single crystals.

4.7.2 Ambient Pressure XPS

Beamline 9.3.2 and Beamline 11.3.2 at the Advanced Light Source at Lawrence Berkeley

National Laboratory was used for conducting the AP-XPS measurements.[44] To account for effects of surface charging during the AP-XPS measurements, the binding energy (BE) of all XPS spectra is adjusted to the known BE position of the lattice oxygen peak at 530 eV for the O 1s spectra, adventious carbon at 284.8 eV for the C 1s peak, and Ir 4f peak at 61.7 eV. As the as-prepared sample surface contained several oxo-carbonaceous species, these were removed from the surface by heating the sample to 250 °C under 100 mTorr O_2.[45,46]

To monitor the surface chemistry and reaction intermediate formation under CH_3OH and CH_4 conversion conditions, the sample was cooled to room temperature for the methanol experiments post the cleaning procedure followed by introduction of 25 mTorr of CH_3OH-200 mTorr of O_2 while for the methane oxidation experiments the sample was cooled to 125 °C prior to the introduction of 1 mTorr of CH_4 and 10 mTorr of O_2. Isobar measurements were conducted from room temperature for CH_3OH oxidation (/125 °C for CH_4 oxidation) to 250 °C (/425°C for CH_4 oxidation), where C 1s and O 1s spectra were measured every 25 °C and the metal core level and valence band spectra were measured at regular intervals. Quantification of beam damage under the conditions of this study were done by comparing several C 1s spectra taken as a function of time at the same sample spot upon dosing 1 mTorr of CH_4-10 mTorr of O_2 at 125°C (Fig. A.3.20), and the lack of changes of spectral features indicate that beam damage effects are negligible under our experimental conditions.

Analysis of the XPS spectra was performed by the software package CasaXPS to quantify the photoemission peak areas and positions. All spectra were fit using Gaussian-Lorentzian peaks after a Shirley-type background subtraction. The range of full-width half maximums and binding

energy values of the peaks were constrained to 0.2 eV. These peak fitting parameters and constraints for the O 1s, C 1s, and Ir 4f spectra are summarized in Table S1, Table S2, and Table S3 respectively. The binding peak assignments of C 1s and O 1s are in agreement with previous experimental work[30,31,32] while the Ir 4f peak assignments have been adopted from experimental and computational work on IrO_2 oxides.[16,45]

4.7.3 Lab Scale XPS

Thermo Scientific K-Alpha ESCA spectrometer was used for lab scale XPS was performed. Monochromatic Al Kα radiation (1486.6 eV) and low energy flood gun was used as a neutralizer.

4.7.4 Powder catalyst Characterization

Powder IrO_2 catalysts of were obtained from Sigma Aldrich (rutile) and Alfa Aesar (amorphous, Premion 73%, Premion 84%). The as-labeled commercial catalyst with 73% Ir is referred to as $IrO_2 \cdot 1.5H_2O$ and with 84% Ir is referred to as $IrO_2 \cdot 0.5H_2O$ based on the water content obtained from TGA in Fig. A.3.15C. Lab scale XPS, and XRD patterns of the catalyst powders are shown in Figs. S15A,B,D. BET surface area is reported in Table A.3.5.

4.7.5 CH$_4$/CH$_3$OH Oxidation Activity Measurements

50 mg of the powder catalyst was mixed with oven-dried SiO_2 sand (2.5 g) and loaded into a quartz tube (3.81 mm inner diameter). Total flow rate of 150 ml min^{-1} was used for all the plug flow reactor experiments and the flow rate of individual gases, CH_4, (100 ppm by volume CH_4 in balance Ar), CH_3OH (150 ppm by volume in balance N_2), O_2 (2% and 1000 ppm by volume in balance N_2), and pure N_2, was controlled using dedicated mass flow controllers to obtain the desired gas concentration of 70 ppm CH_3OH- 280 ppm O_2 and 35 ppm CH_4 −350 ppm O_2 which

is similar to the gas ratios used in the AP-XPS study. Further, water vapor was introduced into the gas mixture by means of a water bubbler connected to the nitrogen gas line. The gas composition was analyzed using a PIKE FTIR gas cell attached to a Bruker Vertex 70 FT-IR spectrophotometer. 32 scans were collected at a resolution of 4 cm^{-1} every 12.5 min. A background spectrum was collected under a pure stream of N_2.

For the CH_3OH oxidation measurements, inlet reaction gas mixture of 70 ppm of CH_3OH-280 ppm of O_2 by volume, and N_2 balance was used for all the experiments. The percentage conversion and selectivity of CH_3OH oxidation to $HCOOCH_3$, $HCHO$, and CO_2 was calculated by determining the percentage of outlet $HCOOCH_3$, $HCHO$, CO_2 concentrations, which was calculated by the formula,

%conversion$_{CO2}$=100*($CO_{2ppm,out}$/$CH_3OH_{ppm,in}$);

%selectivity$_{CO2}$=100*($CO_{2ppm,out}$/$HCHO_{ppm,out}$+$CO_{2ppm,out}$+ $HCOOCH_{3ppm,out}$);

%conversion$_{HCHO}$=100*($HCHO_{ppm,out}$/$CH_3OH_{ppm,in}$);

%selectivity$_{HCHO}$=100*($HCHO_{ppm,out}$/$HCHO_{ppm,out}$+$CO_{2ppm,out}$+ $HCOOCH_{3ppm,out}$);

%conversion$_{HCOOCH3}$=100*($HCOOCH_{3ppm,out}$/$CH_3OH_{ppm,in}$);

%selectivity$_{HCOOCH3}$=100*($HCOOCH_{3ppm,out}$/$HCHO_{ppm,out}$+$CO_{2ppm,out}$+ $HCOOCH_{3ppm,out}$);

where $CH_3OH_{ppm,in}$ was the total concentration of the initial CH_3OH reactant and

$HCOOCH_{3ppm,out}$, $HCHO_{ppm,out}$ and $CO_{2ppm,out}$ was the concentration of $HCOOCH_3$, $HCHO$,

and CO_2 observed after reaction with the catalyst.

For the CH_4 oxidation measurements, inlet reaction gas mixture of 35 ppm of CH_4 with 350 ppm

of O_2 by volume, and N_2 balance was used for all the experiments. The percentage conversion of CH_4 oxidation to CO_2 was calculated by determining the percentage of outlet CO_2 reacted during the course of the reaction, which can be calculated by the formula,

$$\% \text{ conversion} = 100*(CO_{2ppm,out}/CH_{4ppm,in}),$$

where $CH_{4ppm,in}$ was the total concentration of the inlet CH_4 and $CO_{2ppm,out}$ was the concentration of CO_2 observed after reaction with the catalyst. Mass normalized reaction rates are calculated using the formula,

$$r_{mass=} \left(\frac{\%conversion}{100} * F_{HCHO} * 10^3 * 10^{-6} \right) \Big/ (V_m * 60 * m_{cat})$$

Surface area normalized reaction rates are calculated using the formula

$$r_{area=} (r_{mass}) \Big/ (A_{cat})$$

Where %conversion below 12.5% is obtained from the light off curves, F_{HCHO} is the flow rate of CH_3OH (ml min^{-1}), V_m is the molar volume (l mol^{-1}), A_{cat} is the BET surface area (m^{2}g^{-1}) reported in Table S4, and m_{cat} is the catalyst loading (mg).

4.7.6 Density Functional Theory Calculations

Density functional theory (DFT) calculations were performed with the Vienna Ab-initio Simulation Package (VASP) using the Projector-Augmented plane-wave method with the Perdew-Burke-Ernzerhof Generalized Gradient Approximation (GGA). Fully relaxed bulk calculations of IrO_2 were performed with $2\times2\times2$ supercells and a ferromagnetic state is assumed to have a consistent set of magnetic structures. Further, the $IrO_2(110)$ surface was generated using the completely relaxed bulk cell and relaxing the bottom 2 layers of the surface slab.

4.7 *In situ* Diffuse Reflectance Infrared Fourier Transmission Spectroscopy (DRIFTS)

In situ DRIFTS measurements were carried out using the Praying Mantis setup (Harrick) in an environmental chamber with KBr windows at room temperature. 25 mg of $IrO_2 \cdot 0.5H_2O$ catalyst was mixed with 25 mg of KBr.

4.8 References

(1)   Horn, R.; Schlögl, R. Methane Activation by Heterogeneous Catalysis. *Catal. Letters* **2015**, *145* (1), 23–39. https://doi.org/10.1007/s10562-014-1417-z.

(2)   Junrong, H.; Min, Y.; Chuan, D.; Yajun, Z.; Huilong, F.; Lizhi, Z.; Feng, Y.; Zigang, L. Novel Strategies in C-H Oxidations for Natural Product Diversification—A Remote Functionalization Application Summary. *Front. Chem.* **2021**, *9*, 836. https://doi.org/10.3389/FCHEM.2021.737530/BIBTEX.

(3)   Arndtsen, B. A.; Bergman, R. G.; Mobley, T. A.; Peterson, T. H. Selective Intermolecular Carbon-Hydrogen Bond Activation by Synthetic Metal Complexes in Homogeneous Solution. *Acc. Chem. Res.* **1995**, *28* (3), 154–162. https://doi.org/10.1021/ar00051a009.

(4)   Latimer, A. A.; Kulkarni, A. R.; Aljama, H.; Montoya, J. H.; Yoo, J. S.; Tsai, C.; Abild-Pedersen, F.; Studt, F.; Nørskov, J. K. Understanding Trends in C–H Bond Activation in Heterogeneous Catalysis. *Nat. Mater.* **2017**, *16* (2), 225–229. https://doi.org/10.1038/nmat4760.

(5)   Liang, Z.; Li, T.; Kim, M.; Asthagiri, A.; Weaver, J. F. Low-Temperature Activation of Methane on the IrO2 (110) Surface. *Science (80-.).* **2017**, *356* (6335), 299–303. https://doi.org/10.1126/science.aam9147.

(6)   Li, T.; Kim, M.; Liang, Z.; Asthagiri, A.; Weaver, J. F. Hydrogen Oxidation on Oxygen-Rich IrO2(110). *Catal. Struct. React.* **2018**, *4* (4), 1–13. https://doi.org/10.1080/2055074X.2018.1565002.

(7)   Bian, Y.; Kim, M.; Li, T.; Asthagiri, A.; Weaver, J. F. Facile Dehydrogenation of Ethane on the IrO2(110) Surface. *J. Am. Chem. Soc.* **2018**, *140* (7), 2665–2672. https://doi.org/10.1021/jacs.7b13599.

(8)   Martin, R.; Kim, M.; Franklin, A.; Bian, Y.; Asthagiri, A.; Weaver, J. F. Adsorption and Oxidation of Propane and Cyclopropane on IrO2(110). *Phys. Chem. Chem. Phys.* **2018**, *20* (46), 29264–29273. https://doi.org/10.1039/c8cp06125d.

(9)   Geiger, S.; Kasian, O.; Shrestha, B. R.; Mingers, A. M.; Mayrhofer, K. J. J.; Cherevko, S. Activity and Stability of Electrochemically and Thermally Treated Iridium for the Oxygen Evolution Reaction. *J.*

Electrochem. Soc. **2016**, *163* (11), F3132. https://doi.org/10.1149/2.0181611JES.

(10)   Trasatti, S. Electrocatalysis in the Anodic Evolution of Oxygen and Chlorine. *Electrochim. Acta* **1984**, *29*

(11), 1503–1512. https://doi.org/10.1016/0013-4686(84)85004-5.

(11)   Man, I. C.; Su, H.-Y.; Calle-Vallejo, F.; Hansen, H. A.; Martínez, J. I.; Inoglu, N. G.; Kitchin, J.; Jaramillo,

T. F.; Nørskov, J. K.; Rossmeisl, J. Universality in Oxygen Evolution Electrocatalysis on Oxide Surfaces.

ChemCatChem **2011**, *3* (7), 1159–1165. https://doi.org/10.1002/CCTC.201000397.

(12)   Oakton, E.; Lebedev, D.; Povia, M.; Abbott, D. F.; Fabbri, E.; Fedorov, A.; Nachtegaal, M.; Copéret, C.;

Schmidt, T. J. IrO2-TiO2: A High-Surface-Area, Active, and Stable Electrocatalyst for the Oxygen

Evolution Reaction. *ACS Catal.* **2017**, *7* (4), 2346–2352. https://doi.org/10.1021/acscatal.6b03246.

(13)   Willinger, E.; Massué, C.; Schlögl, R.; Willinger, M. G. Identifying Key Structural Features of IrOx Water

Splitting Catalysts. *J. Am. Chem. Soc.* **2017**, *139* (34), 12093–12101. https://doi.org/10.1021/jacs.7b07079.

(14)   Kasian, O.; Geiger, S.; Li, T.; Grote, J. P.; Schweinar, K.; Zhang, S.; Scheu, C.; Raabe, D.; Cherevko, S.;

Gault, B.; Mayrhofer, K. J. J. Degradation of Iridium Oxides via Oxygen Evolution from the Lattice:

Correlating Atomic Scale Structure with Reaction Mechanisms. *Energy Environ. Sci.* **2019**, *12* (12), 3548–

3555. https://doi.org/10.1039/c9ee01872g.

(15)   Saveleva, V. A.; Wang, L.; Teschner, D.; Jones, T.; Gago, A. S.; Friedrich, K. A.; Zafeiratos, S.; Schlögl,

R.; Savinova, E. R. Operando Evidence for a Universal Oxygen Evolution Mechanism on Thermal and

Electrochemical Iridium Oxides. *J. Phys. Chem. Lett.* **2018**, *9* (11), 3154–3160.

https://doi.org/10.1021/acs.jpclett.8b00810.

(16)   Martin, R.; Kim, M.; Lee, C. J.; Mehar, V.; Albertin, S.; Hejral, U.; Merte, L. R.; Asthagiri, A.; Weaver, J.

F. Isothermal Reduction of IrO $_2$ (110) Films by Methane Investigated Using In Situ X-Ray Photoelectron

Spectroscopy. *ACS Catal.* **2021**, *11* (9), 5004–5016. https://doi.org/10.1021/acscatal.1c00702.

(17)   Pfeifer, V.; Jones, T. E.; Velasco Vélez, J. J.; Arrigo, R.; Piccinin, S.; Hävecker, M.; Knop-Gericke, A.;

Schlögl, R. In Situ Observation of Reactive Oxygen Species Forming on Oxygen-Evolving Iridium

Surfaces. *Chem. Sci.* **2017**, *8* (3), 2143–2149. https://doi.org/10.1039/c6sc04622c.

(18)   Nong, H. N.; Falling, L. J.; Bergmann, A.; Klingenhof, M.; Tran, H. P.; Spöri, C.; Mom, R.; Timoshenko, J.;

Zichittella, G.; Knop-Gericke, A.; Piccinin, S.; Pérez-Ramírez, J.; Cuenya, B. R.; Schlögl, R.; Strasser, P.;

Teschner, D.; Jones, T. E. Key Role of Chemistry versus Bias in Electrocatalytic Oxygen Evolution. *Nat.*

2020 5877834 **2020**, *587* (7834), 408–413. https://doi.org/10.1038/s41586-020-2908-2.

(19)   Rao, R. R.; Stephens, I. E. L.; Durrant, J. R. Understanding What Controls the Rate of Electrochemical

Oxygen Evolution. *Joule* **2021**, *5* (1), 16–18. https://doi.org/10.1016/J.JOULE.2020.12.017.

(20)   Pfeifer, V.; Jones, T. E.; Wrabetz, S.; Massué, C.; Velasco Vélez, J. J.; Arrigo, R.; Scherzer, M.; Piccinin,

S.; Hävecker, M.; Knop-Gericke, A.; Schlögl, R. Reactive Oxygen Species in Iridium-Based OER Catalysts.

Chem. Sci. **2016**, *7* (11), 6791–6795. https://doi.org/10.1039/c6sc01860b.

(21)   Abb, M. J. S.; Weber, T.; Langsdorf, D.; Koller, V.; Gericke, S. M.; Pfaff, S.; Busch, M.; Zetterberg, J.;

Preobrajenski, A.; Grönbeck, H.; Lundgren, E.; Over, H. Thermal Stability of Single-Crystalline IrO2(110)

Layers: Spectroscopic and Adsorption Studies. *J. Phys. Chem. C* **2020**, *124* (28), 15324–15336.

https://doi.org/10.1021/acs.jpcc.0c04373.

(22)   Martin, R.; Kim, M.; Lee, C. J.; Mehar, V.; Albertin, S.; Hejral, U.; Merte, L. R.; Lundgren, E.; Asthagiri,

A.; Weaver, J. F. High-Resolution X-Ray Photoelectron Spectroscopy of an IrO2(110) Film on Ir(100). *J.

Phys. Chem. Lett.* **2020**, *11* (17), 7184–7189. https://doi.org/10.1021/acs.jpclett.0c01805.

(23)   Mårtensson, N.; Nilsson, A. High-Resolution Core-Level Photoelectron Spectroscopy of Surfaces and

Adsorbates. In *Springer Series in Surface Sciences*; W. Eberhardt, 1995; Vol. 35, pp 65–126.

https://doi.org/10.1007/978-3-642-79024-9_3.

(24)   Rao, R. R.; Kolb, M. J.; Hwang, J.; Pedersen, A. F.; Mehta, A.; You, H.; Stoerzinger, K. A.; Feng, Z.; Zhou,

H.; Bluhm, H.; Giordano, L.; Stephens, I. E. L.; Shao-Horn, Y. Surface Orientation Dependent Water

Dissociation on Rutile Ruthenium Dioxide. *J. Phys. Chem. C* **2018**, *122* (31), 17802–17811.

https://doi.org/10.1021/ACS.JPCC.8B04284.

(25)   Goodacre, D.; Blum, M.; Buechner, C.; Jovic, V.; Franklin, J. B.; Kittiwatanakul, S.; Söhnel, T.; Bluhm, H.;

Smith, K. E. Methanol Adsorption on Vanadium Oxide Surfaces Observed by Ambient Pressure X-Ray

Photoelectron Spectroscopy. *J. Phys. Chem. C* **2021**, *125* (42), 23192–23204.

https://doi.org/10.1021/ACS.JPCC.1C07403/SUPPL_FILE/JP1C07403_SI_001.PDF.

(26)   Stoerzinger, K. A.; Hong, W. T.; Azimi, G.; Giordano, L.; Lee, Y.-L.; Crumlin, E. J.; Biegalski, M. D.;

Bluhm, H.; Varanasi, K. K.; Shao-Horn, Y. Reactivity of Perovskites with Water: Role of Hydroxylation in

Wetting and Implications for Oxygen Electrocatalysis. *J. Phys. Chem. C* **2015**, *119* (32), 18504–18512.

https://doi.org/10.1021/ACS.JPCC.5B06621.

(27)   Lizzit, S.; Baraldi, A.; Groso, A.; Reuter, K.; Ganduglia-Pirovano, M. V.; Stampfl, C.; Scheffler, M.;

Stichler, M.; Keller, C.; Wurth, W.; Menzel, D. Surface Core-Level Shifts of Clean and Oxygen-Covered

Ru(0001). *Phys. Rev. B - Condens. Matter Mater. Phys.* **2001**, *63* (20), 205419.

https://doi.org/10.1103/PhysRevB.63.205419.

(28)   Reuter, K.; Scheffler, M. Surface Core-Level Shifts at an Oxygen-Rich Ru Surface: O/Ru(0001) vs.

RuO2(110). *Surf. Sci.* **2001**, *490* (1–2), 20–28. https://doi.org/10.1016/S0039-6028(01)01214-6.

(29)   Reuter, K.; Scheffler, M. Surface Core-Level Shifts at an Oxygen-Rich Ru Surface: O/Ru(0 0 0 1) vs.

RuO2(1 1 0). *Surf. Sci.* **2001**, *490* (1–2), 20–28. https://doi.org/10.1016/S0039-6028(01)01214-6.

(30)   Hwang, J.; Rao, R. R.; Katayama, Y.; Lee, D.; Wang, X. R.; Crumlin, E.; Venkatesan, T.; Lee, H. N.; Shao-

Horn, Y. CO $_2$ Reactivity on Cobalt-Based Perovskites. *J. Phys. Chem. C* **2018**, acs.jpcc.8b06104.

https://doi.org/10.1021/acs.jpcc.8b06104.

(31)   Trotochaud, L.; Head, A. R.; Büchner, C.; Yu, Y.; Karslıoğlu, O.; Tsyshevsky, R.; Holdren, S.; Eichhorn,

B.; Kuklja, M. M.; Bluhm, H. Room Temperature Decomposition of Dimethyl Methylphosphonate on

Cuprous Oxide Yields Atomic Phosphorus. *Surf. Sci.* **2019**, *680*, 75–87.

https://doi.org/10.1016/j.susc.2018.10.003.

(32)   Favaro, M.; Xiao, H.; Cheng, T.; Goddard, W. A.; Crumlin, E. J. Subsurface Oxide Plays a Critical Role in

CO2 Activation by Cu(111) Surfaces to Form Chemisorbed CO2, the First Step in Reduction of CO2. *Proc.

Natl. Acad. Sci. U. S. A.* **2017**, *114* (26), 6706–6711. https://doi.org/10.1073/pnas.1701405114.

(33)   Knapp, M.; Crihan, D.; Seitsonen, A. P.; Lundgren, E.; Resta, A.; Andersen, J. N.; Over, H. Complex

Interaction of Hydrogen with the RuO2(110) Surface. *J. Phys. Chem. C* **2007**, *111* (14), 5363–5373.

https://doi.org/10.1021/jp0667339.

(34)   Comini, N.; Huthwelker, T.; Diulus, J. T.; Osterwalder, J.; Novotny, Z. Factors Influencing Surface Carbon

Contamination in Ambient-Pressure x-Ray Photoelectron Spectroscopy Experiments. *J. Vac. Sci. Technol. A

Vacuum, Surfaces, Film.* **2021**, *39* (4), 043203. https://doi.org/10.1116/6.0001013.

(35)   Li, W.; Liu, H.; Iglesia, E. Structures and Properties of Zirconia-Supported Ruthenium Oxide Catalysts for

the Selective Oxidation of Methanol to Methyl Formate. *J. Phys. Chem. B* **2006**, *110* (46), 23337–23342.

https://doi.org/10.1021/jp0648689.

(36)   Liu, Y. C.; Yeh, C. H.; Lo, Y. F.; Nachimuthu, S.; Lin, S. D.; Jiang, J. C. In Situ Spectroscopic and

Theoretical Investigation of Methane Activation on IrO2 Nanoparticles: Role of Ir Oxidation State on C-H Activation. *J. Catal.* **2020**, *385*, 265–273. https://doi.org/10.1016/j.jcat.2020.03.018.

(37)   Cui, X.; Li, H.; Wang, Y.; Hu, Y.; Hua, L.; Li, H.; Han, X.; Liu, Q.; Yang, F.; He, L.; Chen, X.; Li, Q.; Xiao, J.; Deng, D.; Bao, X. Room-Temperature Methane Conversion by Graphene-Confined Single Iron Atoms. *Chem* **2018**, *4* (8), 1902–1910. https://doi.org/10.1016/j.chempr.2018.05.006.

(38)   Prats, H.; Gutiérrez, R. A.; Pinero, J. J.; Vines, F.; Bromley, S. T.; Ramírez, P. J.; Rodriguez, J. A.; Illas, F. Room Temperature Methane Capture and Activation by Ni Clusters Supported on TiC(001): Effects of Metal-Carbide Interactions on the Cleavage of the C-H Bond. *J. Am. Chem. Soc.* **2019**, *141* (13), 5303–5313. https://doi.org/10.1021/jacs.8b13552.

(39)   Lustemberg, P. G.; Zhang, F.; Gutiérrez, R. A.; Ramírez, P. J.; Senanayake, S. D.; Rodriguez, J. A.; Ganduglia-Pirovano, M. V. Breaking Simple Scaling Relations through Metal-Oxide Interactions: Understanding Room-Temperature Activation of Methane on M/CeO2(M = Pt, Ni, or Co) Interfaces. *J. Phys. Chem. Lett.* **2020**, 9131–9137. https://doi.org/10.1021/acs.jpclett.0c02109.

(40)   Zuo, Z.; Ramírez, P. J.; Senanayake, S. D.; Liu, P.; Rodriguez, J. A. Low-Temperature Conversion of Methane to Methanol on CeOx/Cu2O Catalysts: Water Controlled Activation of the C-H Bond. *J. Am. Chem. Soc.* **2016**, *138* (42), 13810–13813. https://doi.org/10.1021/jacs.6b08668.

(41)   Kuo, D. Y.; Kawasaki, J. K.; Nelson, J. N.; Kloppenburg, J.; Hautier, G.; Shen, K. M.; Schlom, D. G.; Suntivich, J. Influence of Surface Adsorption on the Oxygen Evolution Reaction on IrO2(110). *J. Am. Chem. Soc.* **2017**, *139* (9), 3473–3479. https://doi.org/10.1021/jacs.6b11932.

(42)   Nelson, J. N.; Ruf, J. P.; Lee, Y.; Zeledon, C.; Kawasaki, J. K.; Moser, S.; Jozwiak, C.; Rotenberg, E.; Bostwick, A.; Schlom, D. G.; Shen, K. M.; Moreschini, L. Dirac Nodal Lines Protected against Spin-Orbit Interaction in IrO2. *Phys. Rev. Mater.* **2019**, *3* (6), 064205. https://doi.org/10.1103/PHYSREVMATERIALS.3.064205/FIGURES/3/MEDIUM.

(43)   Kawasaki, J. K.; Uchida, M.; Paik, H.; Schlom, D. G.; Shen, K. M. Evolution of Electronic Correlations across the Rutile, Perovskite, and Ruddelsden-Popper Iridates with Octahedral Connectivity. *Phys. Rev. B* **2016**, *94* (12), 121104. https://doi.org/10.1103/PHYSREVB.94.121104/FIGURES/4/MEDIUM.

(44)   Grass, M. E.; Karlsson, P. G.; Aksoy, F.; Lundqvist, M.; Wannberg, B.; Mun, B. S.; Hussain, Z.; Liu, Z. New Ambient Pressure Photoemission Endstation at Advanced Light Source Beamline 9.3.2. *Rev. Sci.*

Instrum. **2010**, *81* (5), 053106. https://doi.org/10.1063/1.3427218.

(45)   Pfeifer, V.; Jones, T. E.; Velasco Vélez, J. J.; Massué, C.; Arrigo, R.; Teschner, D.; Girgsdies, F.; Scherzer, M.; Greiner, M. T.; Allan, J.; Hashagen, M.; Weinberg, G.; Piccinin, S.; Hävecker, M.; Knop-Gericke, A.; Schlögl, R. The Electronic Structure of Iridium and Its Oxides. *Surf. Interface Anal.* **2016**, *48* (5), 261–273. https://doi.org/10.1002/sia.5895.

(46)   Stoerzinger, K. A.; Hong, W. T.; Crumlin, E. J.; Bluhm, H.; Shao-Horn, Y. Insights into Electrochemical Reactions from Ambient Pressure Photoelectron Spectroscopy. *Acc. Chem. Res.* **2015**, *48* (11), 2976–2983. https://doi.org/10.1021/acs.accounts.5b00275.

Chapter 5. Regulating oxygen activity of perovskites to promote activity and selectivity for methanol oxidation to formaldehyde

5.1 Introduction

Selective oxidation of methanol (CH_3OH) to formaldehyde (HCHO) is the predominant methodology for HCHO generation in the automotive, chemical, and construction industries.[1] HCHO is used in the production of industrial chemicals such as urea resins, melamine resins, phenol resins, and methylene diphenyl di-isocyante (MDI)[1] as well as being a key reaction intermediate during methane partial oxidation[2] with an annual turnover of 5 million tons.[3] Typically, Ag-based catalysts are used for selective oxidation of CH_3OH to HCHO at intermediate temperatures ($T \sim 600$–650 °C), which are expensive and sensitive to environmental contamination.[1,4,5] Recent efforts have focused on replacing Ag-based catalysts with more economically viable catalysts.[5,6,7] For example, iron-molybdenum oxides have higher reaction yields compared to the Ag-based catalysts and higher catalytic activity at reduced temperatures ($T \sim 300$ °C).[5,6,8,9] More recently, oxide chemistries such as V_2O_5,[10,11] ZnO,[12] and CeO_2[12] have been investigated for selective synthesis of HCHO. However, HCHO % selectivity typically decreases with increasing CH_3OH %conversion,[13] so there is a need to understand the reaction mechanism.

To promote HCHO synthesis from CH_3OH, the reaction mechanism for HCHO formation on oxides needs to be understood and controlled to prevent complete oxidation of CH_3OH to produce CO_2. By catalyzing CH_3OH oxidation on oxides, it has been suggested that CO and CO_2 are formed on strong basic sites (oxygen), CH_3OHCH_3 and $(CH_3O)_2CH_2$ are formed on strong acid sites (metal), while HCHO is formed on weak bi-functional acid-base sites.[14] In addition, studies have shown more favorable HCHO desorption for CeO_2 with more facile oxygen vacancy formation energy.[15] Moreover, a linear correlation has been established between HCHO desorption energy and a descriptor for selective methanol oxidation to HCHO based on redox character (indicated by the energy difference between the starting surface and the reduced surface upon the addition of one electron), geometric site area, and oxygen basicity (indicated by the O $2p$-band center) for CeO_2-based catalysts.[16] Furthermore, several works have examined the reactivity of CH_3OH on model oxide surfaces experimentally (SrO,[17] TiO_2,[18] and $SrTiO_3$[19]) and theoretically (Co_3O_4,[20] TiO_2,[18] and MoO_3[7]) to reveal the nature of reaction intermediates. Both experimental and theoretical studies have revealed the formation of methoxy (CH_3O-),[16,18,19] formate (HCOO-),[16,21,22] and carbonate

$(CO_3-)^{17,23}$ reaction intermediates upon CH_3OH adsorption. Unfortunately, an understanding of selective HCHO formation through an analysis of the reaction intermediates such as CH_3O- has remained limited.[,24]

Perovskites (ABO_3) with tuneable physio-chemical properties and catalytic activities provide rich opportunities to investigate the oxidation of small carbon molecules.[25,26,27] Surface heat of reaction defined as the difference between the adsorption energy of acetone, hydrogen and propanol, has been shown to correlate with 2-propanol conversion rate to acetone for $BaTiO_3$, $BaZrO_3$, and $SrTiO_3$.[28] In addition, surface acidity, quantified by experimental NH_3 adsorption for $SrTiO_3$-based (STO) chemistries,[29] is correlated negatively with selective 2-propanol conversion rate to propene while surface basicity quantified by 2-propanol adsorption is seen to correlate positively with ethanol selectivity% to 1-butanol and 2-pentatnone for $LaFeO_3$.[30] Surface oxygen content, measured using temperature programmed desorption (TPD), correlated with CO_2 generation rate during methanol oxidation for $LaBO_3$ (B = Co, Mn, Fe).[23] Moreover, optimal e_g filling of 1.2 has been attributed to maximized acetone %selectivity and %conversion during isopropanol conversion by B-site tuning in layered $Sr_2Sn_{1-x}Ru_xO_4$ perovskites.[31] Furthermore, C2 product selectivity% involving C-C coupling during methane oxidation has been correlated with oxygen vacancy formation and CH_3 adsorption energy for STO-doped perovskites[32] while the selectivity% of acetic acid to ketene in $La_{1-x}Sr_xMnO_3$ is shown to decrease in the presence of oxygen vacancies.[33] The O $2p$-band centre descriptor,[41,42] described by the centroid of the oxygen projected electronic density of states relative to the Fermi level has been used to describe relevant catalytic properties, such as oxygen vacancy formation energy,[43] surface acid-base properties [44,45] oxygen binding energy[26], OER reaction kinetics[43], small molecule oxidative dehydrogenation,[46] carbonate formation[47], and CH_4 selectivity during CO_2 reduction,[48] NO oxidation,[27] suggesting that O $2p$-band descriptor-based approach can be a unifying physical parameter used to describe methanol oxidation kinetics.

In this study, we show the critical role of surface oxygen activity, measured by the position of the surface O $2p$-band center with respect to the Fermi level (Fig. 1A), in catalyzing the CH_3OH oxidation reaction, with oxides having an intermediate surface oxygen activity in

La$_{1-x}$Sr$_x$CoO$_3$ (LSC) catalysts demonstrating the maximum selectivity% towards HCHO by simultaneously enhancing CH$_3$OH adsorption and oxygen adsorption/H$_2$O formation energetics while maximizing methoxy (CH$_3$O-O$_{vac}$) reaction intermediate and minimizing surface poisoning by carbonate (B-CO$_2$-O$_{oxide}$) reaction intermediate. We employ the tunable surface electronic structure of La$_{1-x}$Sr$_x$CoO$_3$ to control surface oxygen vacancy concentration, where increasing the oxidation states of cobalt ions upon Sr^{2+} substitution of La^{3+} shifts the Fermi level towards the O $2p$ states. Increasing oxygen vacancies concentration for perovskite chemistries by having more strontium substitution of lanthanum in LaCoO$_3$ enhances adsorption of CH$_3$OH on surface oxygen vacancies but adsorption on transition metal site remains the same. On the other hand, having high surface oxygen activity leads to strong binding of B-CO$_2$-O$_{oxide}$ reaction intermediates on surface oxygen sites, resulting in surface poisoning and a large energetic barrier for HCHO and CO$_2$ formation. Therefore, the high activity of La$_{0.6}$Sr$_{0.4}$CoO$_3$ for CH$_3$OH oxidation and selectivity rates towards HCHO can be attributed to optimal adsorption energetics for CH$_3$OH and optimal energetic penalty for oxygen adsorption and water desorption energy.

5.2 Role of surface-oxygen-activity of La$_{1-x}$Sr$_x$CoO$_3$ on CH$_3$OH adsorption energetics

Increasing A-site strontium substitution of lanthanum in CoO$_2$-termniated (001) La$_{1-x}$Sr$_x$CoO$_3$ (x= 0.0, 0.25, 0.50, 0.75, and 1.00) was found to greatly increase the dissociative adsorption energetics of CH$_3$OH (Co/B-OHCH$_2$-O$_{oxide}$, dark brown, Fig. A.4.1A and Table A.4.1 and CH$_3$O-O$_{oxide}$, dark orange, Fig. A.4.1A and Table A.4.1) on surface oxygen of perovskites which was accompanied with the formation of H-O$_{oxide}$. Greater dissociative adsorption strength was correlated with moving the Fermi level closer to the surface O $2p$-band center. On the other hand, CH$_3$OH adsorption energetics on surface cobalt sites (CH$_3$O-B, dark green, Fig. 1A and Table A.4.1) is largely unchanged for La$_x$Sr$_{1-x}$CoO$_3$ and the surface O $2p$-band center. For example, for LaCoO$_3$, CH$_3$OH adsorbs more strongly via the C-H bond scission in the bidentate configuration on surface Co and oxygen sites (B-OHCH$_2$-O$_{oxide}$, dark brown, Fig. A.4.1A) with energy of -2.39 eV rather than the O-H bond scission on surface Co sites (CH$_3$O-B, dark green, Fig. 1A) with energy of -0.20 eV or surface oxygen sites

(CH_3O-O_{oxide}, dark orange, Fig. A.4.1A) with energy of +0.64 eV or C-O bond scission (CH_3-*B*, blue,, Fig. A.4.1A and Table A.4.1) on surface cobalt sites with energy of +1.60 eV. Similar to $LaCoO_3$, $SrCoO_3$, showed strongest dissociative adsorption in the *B*-$OHCH_2$-O_{oxide} configuration (dark brown, Fig. A.4.1A) with energy of -3.04 eV and the weakest adsorption as CH_3O-*B* (dark green, Fig. A.4.1A) with energy of -0.40 eV. These results are in agreement with previous results showing favorable methanol adsorption via C-H bond scission for MoO_3[49] and Pt/TiO_2.[18] We did not consider physisorbed or non-dissociative CH_3OH adsorption, as previous studies on TiO_2[50] and CeO_2[51] showed that molecular adsorbed CH_3OH species either convert favorably or are thermo neutral to convert to dissociated CH_3OH species. More interestingly, increasing dissociative adsorption strength of CH_3OH (*B*-$OHCH_2$-O_{oxide}, dark brown, Fig A.4.1A and CH_3O-O_{oxide}, dark orange, Fig A.4.1A) with lowered Fermi level into the O 2*p*-band center was correlated with reduced surface oxygen vacancy formation energy (grey, Fig. 1B) as well as increased hydrogen adsorption energy (black, Fig. 1B), similar to previous works.[46] As surface binding energetics of different adsorbed species are largely dictated by the degree of coupling between surface electronic states and frontier orbitals of CH_3OH (Fig. 1A), we explain the strong dependence of CH_3OH adsorption energetics upon dissociate adsorption or the formation of oxygen vacancy on the surface by the large charge transfer for the strongly adsorbed species[27,52,42] in Table A.4.2.

We further show that direct removal of two hydrogens from gas phase methanol is more energetically favorable. The direct dehydrogenation of methanol on surface cobalt sites via O-H and C-H bond scission, CH_2O-*B*, (medium green, Fig. A.4.2A and Table A.4.3) and both surface cobalt and oxygen sites via C-H and O-H bond scission in the bidentate configuration to form *B*-OCH_2-O_{oxide} (medium brown, Fig. 1B and Table A.5.3) were found to be favorable with adsorption energy of -1.8 eV and -2.1 eV, for $LaCoO_3$ respectively. In addition, the adsorption strength of both CH_2O-*B* (medium green, Fig. A.42A) and *B*-OCH_2-O_{oxide} (medium brown, Fig. A.4.2A) reaction intermediates were found to increase with lowered Fermi level into the surface O 2*p*-band center. Interestingly, the CH_2O-O_{oxide} configuration, formed via O-H and C-H bond scission on the surface oxygen site, (medium orange, Fig. A.4.2A and Table A.4.3) was only stable for $LaCoO_3$ while HCHO desorption was observed for the $La_{0.75}Sr_{0.25}CoO_3$, $La_{0.5}Sr_{0.5}CoO_3$, $La_{0.25}Sr_{0.75}CoO_3$ catalysts, and will be

addressed in detail later. Here, we find that the adsorption energy trends for the direct dissociation of two hydrogens follows the trend for the adsorption energy via dissociation of only one hydrogen from CH_3OH and the dissociation of two hydrogens is more favorable compared to dissociation of one hydrogen on the (001) surface of $La_{1-x}Sr_xCoO_3$.

We next show that further direct dehydrogenation of CH_3OH via dissociation of three and four hydrogens is favorable for all the chemistries investigated. The dissociative adsorption energy for direct removal of three and four hydrogens from gas phase CH_3OH to form B-OCH-O_{oxide} via O-H and two C-H bond dissociation on surface cobalt and oxygen sites (dark purple, Fig. A.4.A, and Table A.4.4), B-OCH-O_{oxide} via O-H and two C-H bond dissociations on surface cobalt and oxygen sites (dark yellow, Fig. 1B and Table S4), and B-CO_2-O_{oxide} via O-H and three C-H bond dissociations on surface cobalt and oxygen sites (dark red, Fig. 1B and Table A.5.4) was found to be of -4.00 eV, -6.80 eV, and -7.10 eV respectively for $LaCoO_3$ (Fig. 1B). In addition, the adsorption energy for B-OCH-O_{oxide}, B-$OCOH$-O_{oxide}, and B-CO_2O_{oxide} increased with the lowering of the Fermi level into the surface O $2p$-band center (Fig. 1B). The CH-B configuration (light blue, Fig. A.4.3B and Table A.4.4) formed via C-O and two C-H bond dissociation of CH_3-B (blue, Fig. A.5.1A) is only stable for $LaCoO_3$ while for the remaining catalyst surfaces the CH-B configuration converts to B-CH-O_{oxide}-type reaction intermediate (dark purple, Fig. A.5.3B), indicating the increased reactivity of surface oxygen with surface O $2p$-band center closer to the Fermi level. Here, we find that the adsorption energy trends for the direct dissociation of three, four hydrogens follow the trend for the adsorption energy via dissociation of only one hydrogen from CH_3OH and the dissociation of three, four hydrogens is more favorable compared to removal of one or two hydrogens.

The presence of surface oxygen vacancies can greatly influence the adsorption energetics of CH_3OH on the CoO_2 termination of stoichiometric (001) $La_{1-x}Sr_xCoO_3$. The dissociative adsorption of CH_3OH via O-H bond scission on under-coordinated Co sites, defined as surface Co sites adjacent to oxygen vacancy (B_{uc} or Co_{uc}), (CH_3O-B_{uc}, green , Fig. A.4.1B and Table A.4.1) was found stronger than that bound to fully coordinated Co sites (CH_3O-B, dark green, Fig. A.4.1A) for the Sr-substituted oxides where the Fermi level is much closer to

the surface O 2p-band center. For example, CH$_3$O-B_{uc} binding on an under-coordinated Co site for SrCoO$_3$ was more favorable than CH$_3$O-B on a fully coordinated Co site by -0.86 eV (Fig. A.4.1B), which could be attributed to energy gain in filling the oxygen vacancy and less charge transfer to oxidize surface metal sites with carbon down on surface metal sites. We next consider dissociative O-H adsorption of CH$_3$OH on surface oxygen vacancy sites (CH$_3$O-O$_{vac}$, orange, Fig. 1B and Table A.4.1) which has the same stoichiometry as the CH$_3$O-B_{uc} but different surface configuration (Fig. A.4.1B). A similar trend was found for CH$_3$O-O$_{vac}$ (Fig. 1B), where adsorption on LaCoO$_3$ was found to be +0.35 eV less favorable while for SrCoO$_3$ it was found to be –0.32 eV more favorable when compared to adsorption on the oxygen site (CH$_3$O-O$_{oxide}$, dark orange, Fig. A.4.1A). Moreover, we studied the dissociative adsorption of CH$_3$OH via C-O scission on under-coordinated Co sites as CH$_3$-B_{uc} (dark blue, Fig. A.4.1B and Table A.5.1), where more favorable dissociative adsorption was observed with oxides having O 2p-band center closer to the Fermi level. Similarly, adsorption energetics of the CH$_3$-B_{uc} reaction intermediates (dark blue, Fig. 1B) are more favorable than the corresponding CH$_3$-B reaction intermediate (blue, Fig. A.4.1A) for all the oxide chemistries except for SrCoO$_3$. Furthermore, CH$_3$OH adsorption via C-H bonds dissociation on surface oxygen and under-coordinated Co sites (brown, B_{uc}-OHCH$_2$-O$_{oxide}$, Fig. A.4.1B and Table A.4.1) and the adsorption energy for all the catalysts was more favorable for the case of dissociative CH$_3$OH adsorption on stoichiometric surface (B-OHCH$_2$-O$_{oxide}$) compared to the surface containing oxygen vacancies. We find that dissociative CH$_3$OH adsorption on the oxygen vacancy sites is more favorable for CH$_3$O-O$_{vac}$ configuration compared to adsorption on stoichiometric sites (CH$_3$O-B, CH$_3$O-O$_{oxide}$) while in the case of CH$_3$OH adsorption on both Co and oxygen surface sites (B-OHCH$_2$-O$_{oxide}$), adsorption on the stoichiometric site is more favorable.

We further find that adsorption energy for direct dehydrogenation of CH$_3$OH via dissociation of two; three, and four hydrogens are favorable in the presence of oxygen vacancies. First, dissociation of two hydrogens of CH$_3$OH via O-H and C-H bond scission on under-coordinated cobalt sites to form CH$_2$O-B_{uc} (light green, Fig. A.4.2B and Table A.5.3), via O-H and C-H bond scission at oxygen vacancy sites to form CH$_2$O-O$_{vac}$ (light orange, Fig. A.4.2B and Table A.4.3), via C-H and O-H bond scission in a bidentate configuration on

under-coordinated cobalt and oxygen surface sites, B_{uc}-CH$_2$OH-O$_{oxide}$ (light brown, Fig. A.4.2B and Table A.4.3) became more favorable with lowering O $2p$-band center. Also, HCHO can desorb from CH$_2$O-O$_{vac}$ or CH$_2$O-B_{uc} to leave behind a surface oxygen vacancy. Moreover, compared to adsorption in the stoichiometric case, the adsorption energy for B_{uc}-CH$_2$OH-O$_{oxide}$ and CH$_2$O-B_{uc} are less favorable or comparable to B-CH$_2$OH-O$_{oxide}$ and CH$_2$O-B respectively. In addition, dissociative adsorption energy of B_{uc}-OCH-O$_{oxide}$ (light purple, Fig. A.5.3A and Table A.5.4), and B_{uc}-CO$_2$-O$_{oxide}$ (light red, Fig. A.4.3A and Table A.4.4) were found to be weaker than the corresponding adsorption energy for stoichiometric LaCoO$_3$ by +0.10 eV and +0.68 eV, and by +1.20 and +0.20 eV for SrCoO$_3$, respectively (Fig. A.4.3A). These results indicate that for these reaction intermediates the adsorption energy for multiple dehydrogenation steps is dictated by the formation of carbonaceous and H-O$_{oxide}$ species instead of energy arising from oxygen vacancy formation energy. (Table. A.4.5) Therefore, the surface electronic structure feature, namely the surface O $2p$-band center relative to the Fermi level, dictates the oxygen vacancy formation energy and adsorption energetics of CH$_3$OH and O$_2$ on surface metal and oxygen sites (Fig. 1B), which
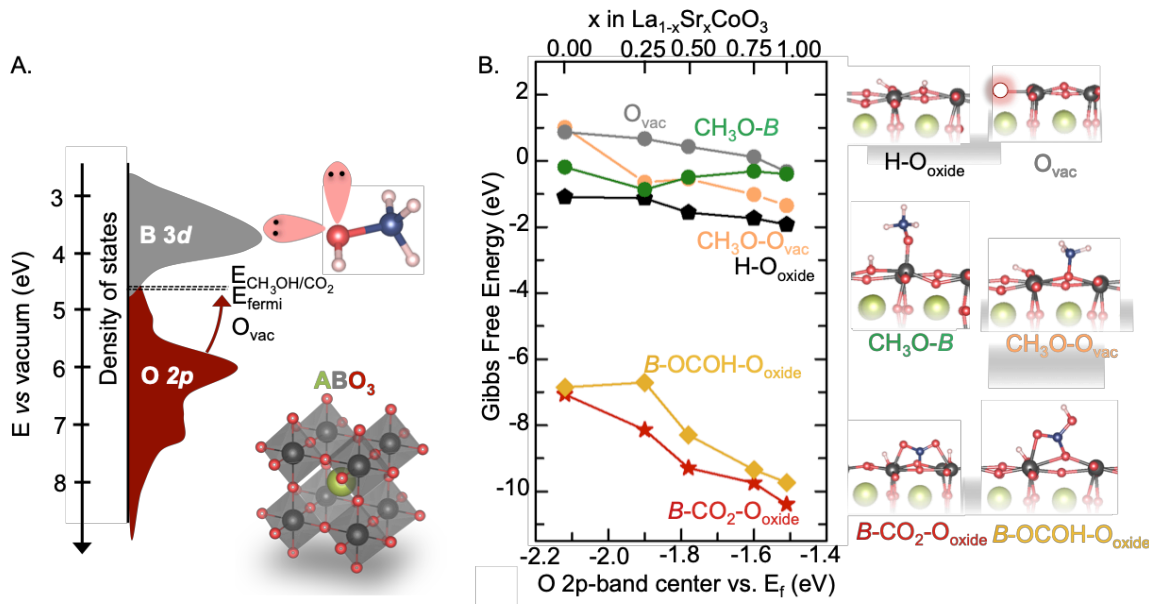
can greatly influence the CH$_3$OH oxidation kinetics on these perovskite surfaces.

Figure 1. Dissociative adsorption of CH$_3$OH on La$_{1-x}$Sr$_x$CoO$_3$. *A) Schematic electronic structure of perovskite metal oxide on an absolute energy scale referenced to vacuum and CH$_3$OH molecule showing the lone pairs on the oxygen atom aligned to the oxidation potential of CH$_3$OH to CO$_2$. B) Correlation between surface oxygen vacancy formation energy (O$_{vac}$, grey, BO$_2 \rightarrow$ BO$_{2-}$ $_x$ + ½O$_2$), hydrogen adsorption energy (black, H-O$_{oxide}$, ½H$_2$ + BO$_2 \rightarrow$ H-O$_{oxide}$,), dissociative*

adsorption energy of CH₃OH on surface oxygen vacancy site via O-H bond scission to form CH₃O-O_vac (orange, BO₂ + CH₃OH → CH₃O-O_vac + H-O_oxide + ½O₂), surface Co surface site via C-O bond scission to form CH₃-B (dark green, BO₂ + CH₃OH → CH₃-B + H-O_oxide), complete dehydrogenation leading to B-OCOH-O_oxide via three C-H bond dissociations on surface Co and oxygen sites (dark yellow, BO₂ + CH₃OH→ B-OCOH-O_oxide + 2H-O_oxide + 2H-O_oxide), and B-CO₂-O_oxide via O-H and three C-H bond dissociations on surface Co and oxygen sites (dark red, BO₂ + ½O₂ + CH₃OH→ B-CO₂O_oxide + 2H-O_oxide + 2H-O_oxide*) as a function of the surface O 2p-band center relative to the Fermi level. Data points were obtained from the BO₂-terminated-(001) surface of La₁₋ₓSrₓCoO₃ with increasing Sr (x = 0.00, 0.25, 0.50, 0.75, and 1.00), calculated by DFT with the optimized binding configurations of CH₃OH on the metal and oxygen site shown here. Adsorption free energy is calculated with respect to the stoichiometric BO₂ surface, CH₃OH, H₂, and O₂ in the gas phase (T = 100 °C, pCH₃OH = 100 mTorr, pH₂ = 1 mTorr, and pO₂ = 20 mTorr). Oxygen: red, cobalt: grey, lanthanum: green, carbon: dark blue, hydrogen: white and red square indicates surface oxygen vacancy.* indicates that the adsorption energy of the H-O_oxide reaction intermediate was calculated on a separate unit cell.*

5.3 Role of surface-oxygen-activity of La₁₋ₓSrₓCoO₃ on carbonaceous speciation

AP-XPS measurements were performed to investigate the surface speciation of carbonaceous reaction intermediates in presence of CH_3OH and O_2 on epitaxial thin films of (001)-oriented $La_{1-x}Sr_xCoO_3$. Increasing Sr content (estimated using La 4d in Fig. A.5.4A and Sr 3d intensities in Fig. A.4.4B) in accordance with increasing Sr substitution (Fig. A.4.4C) Excellent agreement was observed for estimated Sr content in $La_{0.2}Sr_{0.8}CoO_3$ and $La_{0.6}Sr_{0.4}CoO_3$ when compared to the expected nominal Sr content. We also note a slightly higher estimated Sr content (~0.71) from AP-XPS for $La_{0.4}Sr_{0.6}CoO_3$ than the nominal composition (0.6) due to surface segregation of Sr and/or formation of SrO_x phase in agreement with previous works.[53,54] C 1s spectra were collected from epitaxially-grown $La_{1-x}Sr_xCoO_3$ thin films under isobaric conditions of pCH_3OH = 100 mTorr and pO_2 = 20 mTorr for the temperature range of ~25-300 °C (Fig. 2A) following the removal of most adventious carbon species by heating to 250 °C in O_2 (C 1s spectra in Fig. A.4.5 and survey spectrum in Fig. A.4.6). Representative C 1s spectra of $La_{0.6}Sr_{0.4}CoO_3$ as a function of temperature are shown in Fig. 2A and the other $La_xSr_{1-x}CoO_3$ (x = 0, 0.20, 0.40) are shown in Figs. A.4.7-S9. The C 1s peaks were fitted with the Gaussian-Lorentzian line shape (Fig. 2B, fitting parameters in Table A.5.2), and deconvoluted to include adventitious carbon (CH_x-like

species, 284.8 eV),[47] methoxy (CH$_3$O-, 286.1 eV),[18,55] carbonate (CO$_3$-, 288.3 eV),[47] and bicarbonate (HCO$_3$-, 290.1 eV)[47] species based on previous work from CO$_2$,[47] CH$_3$OH,[18] and dimethyl methylphosphonate[55] adsorption on oxide surfaces (Fig. A.4.10). Considering the most energetically favorable adsorbates on La$_x$Sr$_{1-x}$CoO$_3$ from DFT results, we assign the ~284.8 eV peak in Fig. 2B to CH$_3$-B_{uc} (adventious, dark blue in Fig. A.5.1B), 286.1 eV peak in Fig. 2B to CH$_3$O-O$_{vac}$ (methoxy, orange in Fig. 1B), and 288.3 eV peak in Fig. 2B to B-CO$_2$-O$_{oxide}$ species (carbonate, dark red in Fig. 1B). Also, as the CH$_3$OH adsorption energy for under-coordinated metal-site (CH$_3$O-B_{uc}, light green, Fig. A.4.1B) is similar to that of on oxygen vacancy sites (CH$_3$O-O$_{vac}$, orange, Fig. 1B), the peak at 286.1 eV could also be assigned to CH$_3$O–B_{uc} species. Beyond these three major components, minor species at higher binding energy at 290.1 eV in Fig. 2B were observed which was attributed to B-OCOH-O$_{oxide}$ reaction intermediate (bicarbonate, dark yellow in Fig. 1B). However, we did not consider this reaction intermediate in further discussion due to the lower relative intensity compared to the other reaction intermediates. Further, the low-binding component at 284.8 eV, CH$_3$-B_{uc} (adventious, blue, Fig. 3A) was found to have a decreasing intensity trend with lowered surface O $2p$-band center relative to Fermi level of La$_{1-x}$Sr$_x$CoO$_3$. While a similar trend of reducing CH$_x$ intensity with lowering O $2p$-band center was observed for Co-based perovskite surfaces upon CO$_2$ adsorption in the absence of CH$_3$OH at room temperature,[47] adventious carbon in the AP-XPS chamber[56] may contribute to the peak feature, which will not be considered further. Finally, we also note that while B-OHCH$_2$-O$_{oxide}$, B_{uc}-OHCH$_2$-O$_{oxide}$, B-OCH$_2$-O$_{oxide}$, B_{uc}-OCH$_2$-O$_{oxide}$, B-OCH-O$_{oxide}$, and B_{uc}-OCH-O$_{oxide}$ reaction intermediates have favorable adsorption energy (Figs. A.4.1, A.4.2), we do not assign any of the AP-XPS features to these reaction intermediates due to the relatively larger adsorption energy for B-CO$_2$-O$_{oxide}$ and B_{uc}-CO$_2$-O$_{oxide}$ arising from further dehydrogenation of such reaction intermediates and also the strong overlap in the XPS peak regions of B-CO$_2$-O$_{oxide}$ (CO$_3$-) and B-OCH-O$_{oxide}$ (HCOO-) reaction intermediates from previous studies. (Fig. A.4.10)

The B-CO$_2$-O$_{oxide}$ (dark red, Fig. 2C) and CH$_3$O-O$_{vac}$ (orange, Fig. 2C) species were found to dominate at temperatures lower than 200 °C for La$_{0.6}$Sr$_{0.4}$CoO$_3$, (dark red, Fig. 2C), where the intensity of B-CO$_2$-O$_{oxide}$ species first increased and then decreased with increasing

temperature (Figs. A.4.7B-9B) attributed to the conversion of CH_3O-type reaction intermediates to B-CO_2-O_{oxide}. In contrast to B-CO_2-O_{oxide}, the intensity of CH_3O-O_{vac} (orange, Fig. 2C), CH_3-B_{uc} (dark blue, Fig. 2C), and B-$OCOH$-O_{oxide} (dark yellow, Fig. 2C) reaction intermediates decreased with increased temperature, but the CH_3O-O_{vac} (orange, Fig. 2C) reaction intermediate became dominant at high temperatures greater than 200 C°. The changes of the O 1s spectra collected at 25 °C, 100 °C, and 200 °C for $La_{1-x}Sr_xCoO_3$ (x = 0, 0.2, 0.4, and 0.6) in Figs. A.4.11A-C was consistent with the observation of the C 1s spectra. The O 1s also a decrease in the relative intensity of B-CO_2-O_{oxide} (dark red, 533 eV),[57,58] and CH_3O-O_{vac} (orange, 532 eV)[53.31] species with increasing temperature in agreement with the observation in the C 1s spectra indicating the oxidation of methanol reaction intermediates to HCHO, CO_2, and H_2O.[59,60] Also, surface Sr species (531.9 eV)[61], SrO (529.7 eV)[62], and $Sr(OH)_2$ (533 eV)[62] have been reported in the O 1s spectra previously but have not been considered here.
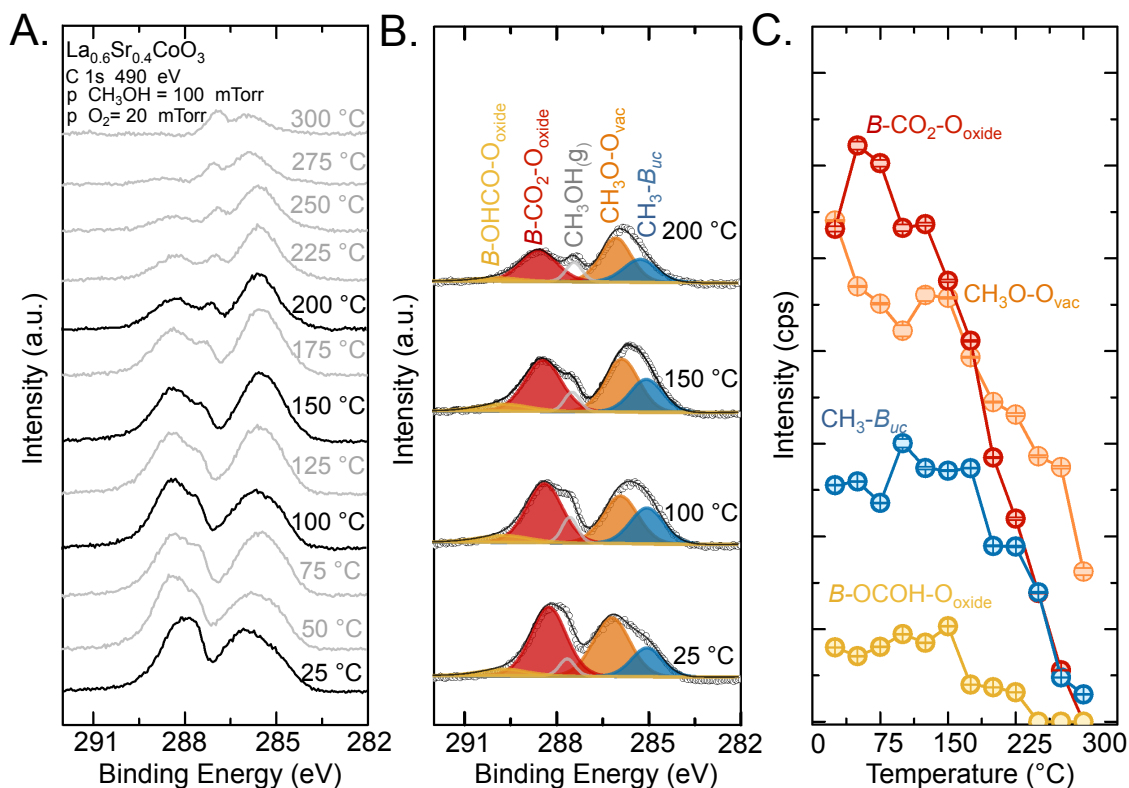
Figure 2. AP-XPS of $La_{0.6}Sr_{0.4}CoO_3$ thin film exposed to CH_3OH and O_2. *A) Raw isobar spectrum of C 1s collected at 490 eV incident photon energy under pCH$_3$OH = 100 mTorr and pO$_2$ = 20 mTorr from T = 25 °C – 300 °C. B) Representative de-convolution of the C 1s 490 eV spectrum collected at 25, 100, 150, and 200 °C. C) Evolution of integrated areas as a*

function of increasing temperature, where CH$_3$-B$_{uc}$ (adventious, 285 eV, dark blue), CH$_3$O-O$_{vac}$ (methoxy, 286.1 eV, orange), B-CO$_2$-O$_{oxide}$ (carbonate, 288.34 eV, dark red), and B-OCOH-O$_{oxide}$ (bicarbonate, 290 eV, dark yellow) species are initially formed at 25 °C and whose quantity decreases upon increasing temperature. Overall carbonaceous species were found at lower temperature in more significant quantities and the intensities decrease with temperature. All spectra and intensities are plotted after background subtraction without any normalization. AP-XPS integrated intensities error bars (standard deviations) were calculated by Monte Carlo simulation of the peak fitting. Peak width of 0.3 eV and FWHM of 0.2 eV were used for the peak fittings and are reported in Table A.4.2.

The assignment of these major components derived from CH$_3$OH adsorption on (001) La$_{1-x}$Sr$_x$CoO$_3$ was further supported by Sr-dependent changes in the C 1s spectra of La$_{1-x}$Sr$_x$CoO$_3$ (x = 0, 0.2, 0.4, and 0.6) collected at 100 °C, as shown in Fig. 3A (temperature dependent spectra in Figs. A.4.12-A.5.15). The intensity of CH$_3$O-O$_{vac}$ reaction intermediate (orange, Fig. 3A) was seen to first increase and then decreases with lowered Fermi level into O 2p-band center of La$_{1-x}$Sr$_x$CoO$_3$, which is in contrast with the monotonic increase in the computed adsorption energy of this CH$_3$O-O$_{vac}$ species (orange, Fig. 1B). Such a different trend can be attributed to favorable Gibbs free energy gain for the formation of CH$_3$O-O$_{vac}$ and H-O$_{oxide}$ reaction intermediates due to dehydrogenation of CH$_3$OH on a surface oxygen vacancy site at low strontium concentrations versus the conversion of CH$_3$O-O$_{vac}$ to HCHO and *B*-CO$_2$-O$_{oxide}$ at high strontium concentrations in La$_{1-x}$Sr$_x$CoO$_3$. In addition, with increasing temperature, CH$_3$O-O$_{vac}$ intensity was observed to decrease (Fig. 3B), which could be attributed to the conversion of CH$_3$O-O$_{vac}$ to HCHO and *B*-CO$_2$-O$_{oxide}$. Moreover, unlike the trends observed for CH$_3$O-O$_{vac}$, *B*-CO$_2$-O$_{oxide}$ (dark red, Fig. 3A) was found to significantly increase with Fermi level closer to surface O 2p-band center of La$_{1-x}$Sr$_x$CoO$_3$ for all temperatures in Fig. 3C, which is consistent with increasing adsorption energy of the carbonate species on surface oxygen as shown in Fig. 1B (dark red) in agreement with previous work on CO$_2$ adsorption on perovskite thin films.[47] Also, with increasing temperature, the B-CO$_2$-O$_{oxide}$ intensity was observed between 25-100 °C (Fig. 3C), which could be attributed to the conversion of CH$_3$O-type intermediates to *B*-CO$_2$-O$_{oxide}$. Upon further increasing temperature the *B*-CO$_2$-O$_{oxide}$ intensity was seen to decrease suggesting the conversion of *B*-CO$_2$-O$_{oxide}$ to CO$_2$. Furthermore, the intensity of all surface species, including CH$_3$-B$_{uc}$ (Fig. A.4.16A) and *B*-OHCO-O$_{oxide}$ (Fig. A.4.16B) decreased at higher temperature consistent with the overall oxidation of reaction intermediates. Also, a decrease

in the Sr-segregation on the surface was observed with increasing temperature as seen in the Sr $3d$ spectra in Figs. A.4.17A-C. The largest Sr segregation was noted for $La_{0.6}Sr_{0.4}CoO_3$ (Fig. A.4.17C) and we address the extent of Sr segregation in $La_{0.6}Sr_{0.4}CoO_3$ by developing a surface Sr segregation model (Supplementary Information) based on the estimated Sr content (Fig. A.4.4C) and the inelastic mean free path (IMFP) of the photoelectrons in AP-XPS (~1.5 nm for 735 eV). We find that the average $Sr_{Surface}$ content to be 0.75 (Fig. A.4.18A) and estimate the $Sr_{Surface}$ O $2p$-band center to be -1.63 eV based on the linear correlation between surface O $2p$-band center and Sr content (Fig. A.4.18B). Therefore, the trends of intensities of the major reaction intermediates CH_3O-O_{vac} (orange, Fig. 3B) and $B-CO_2-O_{oxide}$ (dark red, Fig. 3C) with respect to the $Sr_{Surface}$ content (Fig. A.4.19A and B) would be the same as previously described since the O $2p$-band center computed for $La_{0.25}Sr_{0.75}CoO_3$ was used for the experimental $La_{0.6}Sr_{0.4}CoO_3$ thin film. The similar trend in the reaction intermediate intensity result suggests that the surface Sr-enrichment and/or formation of SrO_x-type phases are not significant enough to alter the observed trends in intensities of reaction intermediates. We also note that $Sr_{Surface}$ layer could contain SrO, $SrCO_3$, and $Sr(OH)_2$ species whose relative contributions are difficult to discern due to their overlapping features in the Sr $3d$ spectra[61] and the presence of carbonaceous species in the O 1s spectra. Moreover, we also show that SrO (if present) is inactive towards CH_3OH oxidation with no HCHO or CO_2 conversion being observed upto 200 °C (Fig. A.4.19)

The O 1s spectra also revealed similar trends as the C 1s spectra with a volcano-like trend for the CH_3O-O_{vac} intensity and increased $B-CO_2-O_{oxide}$ intensity with increasing O $2p$-band center in Figs. A.4.11A-C. Therefore, the AP-XPS results revealed that increasing strontium substitution in $La_xSr_{1-x}CoO_3$ can enhance CH_3OH adsorption on oxygen vacancies, and on surface oxygen and cobalt sites in agreement with DFT results (Fig. 1B), where the intensity decreases with increasing temperature due to desorption. Next, we discuss how different reaction intermediates can affect the kinetics of CH_3OH conversion to HCHO and CO_2.
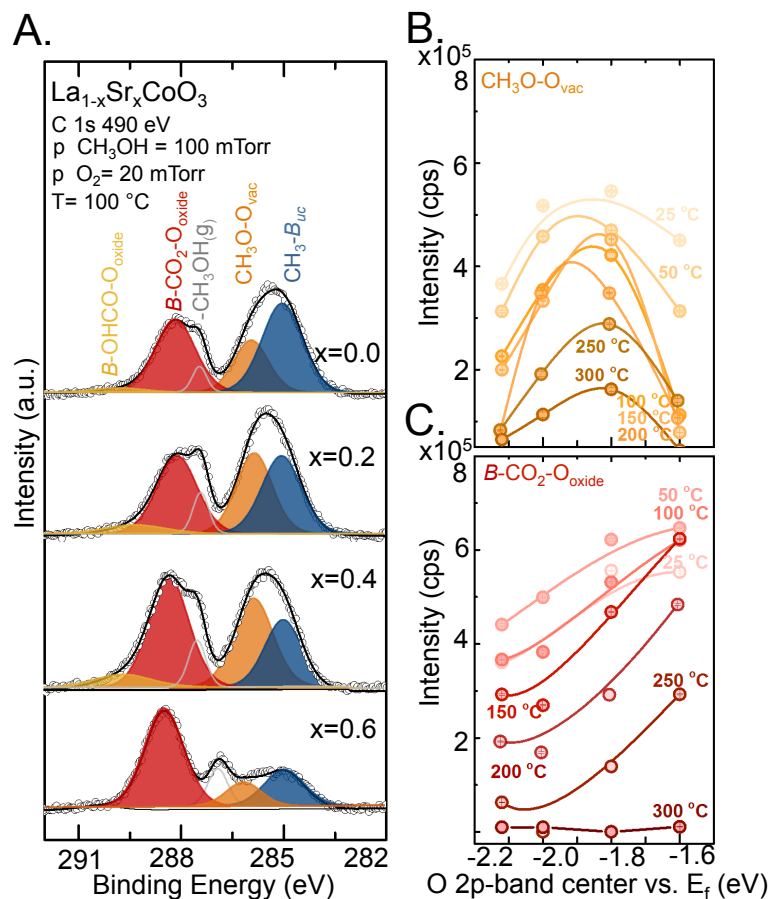
Figure 3: Role of Sr-substitution on AP-XPS surface speciation. *A) C 1s 490 eV spectra at 100 °C for the $La_{1-x}Sr_xCoO_3$ thin films (x = 0, 0.2, 0.4, and 0.6). Surface quantity of B) CH_3O-O_{vac} (methoxy, orange), C) B-CO_2-O_{oxide} (carbonate, dark red), reaction intermediates as a function of surface O 2p-band center, where surface species quantity was determined by the counts per second (cps) after background subtraction without any normalization for a range of temperatures. (T = 25, 50, 100, 150, 200, 250, and 300 °C) AP-XPS integrated intensities error bars (standard deviations) were calculated by Monte Carlo simulation of the peak fitting. O 2p-band center values for the experimental thin films were obtained from the DFT calculations of the surface slab with the closest Sr content.*

5.4 Role of surface oxygen activity on the selective oxidation kinetics of CH$_3$OH to HCHO

We examined the catalytic activity of CH_3OH oxidation to HCHO (Fig. A.4.20A) and CO_2 (Fig. A.4.20B) on $La_{1-x}Sr_xCoO_3$ (x = 0, 0.2, 0.4 and 0.6) powders samples, which were

measured in a plug flow reactor by introducing 70 ppm CH_3OH under a flow rate of 150 mL min^{-1} with varying oxygen concentration of 20 ppm-8% O_2. We first investigated CH_3OH conversion under the same O_2:CH3OH gas ratio as the AP-XPS reaction conditions (1:5) and observed abrupt formation of CO_2 (Fig. A.4.20A) and CO (Fig. A.4.20C) at 120 °C for $LaCoO_3$ suggesting that the catalyst was likely reduced due to insufficient oxygen in the gas stream.[63]Since no sample reduction was observed in Co $3p$ spectrum (Figs. A.4.21A-D) in the relevant temperature range under AP-XPS reaction conditions, we investigated methanol conversion at higher oxygen gas concentration (8% O_2) to avoid sample reduction.

We next studied CH_3OH oxidation by heating the catalysts in the presence of 70 ppm CH_3OH-8% O_2 and measuring CH_3OH conversion to HCHO (Fig. 4A) and CO_2 (Fig. A.4.22A) as a function of temperature. HCHO formation kinetics described by HCHO turnover frequency (TOF, Fig. 4B, surface area normalized reaction rates in Fig. A.5.23A) and HCHO selectivity% (Fig. A.4.23B) was found to increase from $LaCoO_3$ to $La_{0.8}Sr_{0.2}CoO_3$ and $La_{0.6}Sr_{0.4}CoO_3$ and then decrease for $La_{0.4}Sr_{0.6}CoO_3$ This volcano trend with the surface O $2p$-band center relative the Fermi level is similar to the trends observed for the CH_3O-O_{vac} reaction intermediate using AP-XPS in Fig. 3B. %HCHO selectivity decreased with increasing temperature (Fig. A.4.23B), suggesting that the thermodynamically favorable reaction of complete CH_3OH oxidation to CO_2 (ΔG = -8.25 eV for CO_2 compared to ΔG = -2.30 eV for HCHO at T = 100 °C and pCH_3OH = 100m Torr, pO_2= 25 mTorr, pCO_2 = 1 mTorr, $pHCHO$ =1 mTorr, pH_2O = 1mTorr) becomes more favorable at higher temperatures. Meanwhile, CO_2 TOF showed a volcano trend with the surface O $2p$-band center in Fig. 5A (surface area-normalized CO_2 formation rate in Fig. A.4.22B) and %CO_2 selectivity was found to follow an inverted volcano type trend at various temperatures as shown in Fig. A.4.22C. Finally, CH_3OH consumption rate with increasing temperature function of temperature (Fig. A.4.24A and B) showed a volcano trend with surface O $2p$-band center relative to the Fermi level. Of significance note is that $La_{0.6}Sr_{0.4}CoO_3$ showing the highest consumption rate at temperatures much lower than the Ag,[64] BCN,[65] and Fe-Mo oxide catalysts.[66,67]
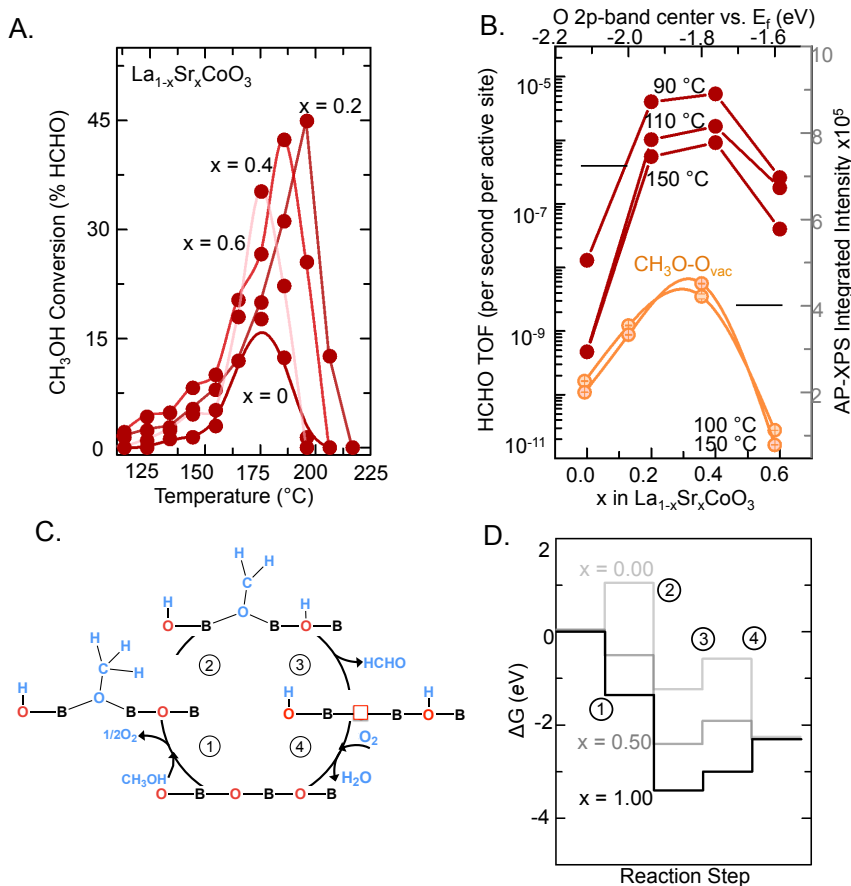
Figure 4. Selective oxidation kinetics of CH₃OH to HCHO. *A) CH₃OH oxidation activity shown as conversion to HCHO as a function of temperature for the La₁₋ₓSrₓCoO₃ (x = 0-0.6) series conducted in a flow reactor, B) Turnover frequency (TOF) values for CH₃OH oxidation to HCHO at T = 90, 110 and 150 °C and integrated peak intensities for CH₃O-O_vac (orange) at 100 and 150 °C (Fig. 3A) as a function of the surface O 2p-band center. HCHO formation rate as a function of the surface O 2p-band center, where the activity metric was chosen at T = 90, 110, and 150 °C from the Arrhenius type plot in Fig. A.4.20A. The percentage conversion of CH₃OH oxidation to HCHO was calculated by determining the percentage of inlet CH₃OH reacted during the reaction, which can be calculated by the formula, % conversion=100*((HCHO_{ppm, out})/CH₃OH_{ppm, in}), where CH₃OH_{ppm, in} was the concentration of the initial CH₃OH reactant, HCHO_{ppm, out} and CO₂_{ppm, out} were the concentrations of HCOH and CO₂ gases observed after reaction with the catalyst. HCHO formation rate was determined using the formula, $r_{formation} = \frac{r_{mass} \cdot 10^{-6}}{A_S}$ $\{\frac{ml. \ min^{-1}}{l. \ mol^{-1}. \ g. \ m^2. g^{-1}}\}$, Where mass activity was estimated using the formula, $r_{mass} = \frac{\% \ conversion. F_{CH3OH}}{6. V_m. m_{cat}}$ $\{\frac{ml. \ min^{-1}}{l. \ mol^{-1}. \ g}\}$, For %CH₃OH conversion less than 12.5% obtained for the La₁₋ₓSrₓCoO₃ (x = 0-0.6) series conducted in a flow reactor. Finally, the TOF are reported using the formula, $TOF = \frac{r_f. N_a}{PD_{100}} = (\frac{mol^{+1}. mol^{-1}}{m^{+2} . s^{-1}. m^{-2}})$ With N_a being the Avogadro's numbers, and PD₁₀₀ planar density of the surface oxygen atoms on 100 BO₂-type termination*

of the pseudo-cubic perovskite catalysts as obtained from DFT ($PD_{100} = 1.34*10^{19}$ O_{oxide}/m^2. Catalyst loading of 750 mg, inlet CH_3OH flow rate of 150 ml min^{-1} and gas concentration of 70 ppm CH_3OH-8% O_2 was used for all the measurements. AP-XPS integrated intensities error bars (standard deviations) were calculated by Monte Carlo simulation of the peak fitting. C) Oxygen vacancy mediated CH_3OH oxidation to HCHO via O-H bond scission of CH_3OH to form CH_3O-O_{vac} after oxygen vacancy formation (step 1), followed by dehydrogenation of CH_3O-O_{vac} to adsorbed CH_2O-O_{vac} (step 2), desorption as HCHO (step 3), and oxygen adsorption and H_2O desorption to complete the catalytic cycle (step 4), where oxygen vacancy is denoted by an open red square. Adsorption and desorption free energy are calculated with respect to the BO_2 surface CH_3OH, HCHO, H_2O, and O_2 in the gas phase (T = 100 °C, pCH_3OH = 100 mTorr, pO_2 = 20 mTorr, pCO_2 = 1 mTorr, $pHCHO$ = 1 mTorr, and pH_2O= 1 mTorr), D) Gibbs free energy profile on $La_{1-x}Sr_xCoO_3$ (x = 0.00, 0.50, and 1.00) for the vacancy mediated reaction mechanism, which shows CH_3OH adsorption being rate limiting for x = 0.00, desorption of HCHO being limiting for x = 0.50 and oxygen adsorption and H_2O desorption being limiting for x = 1.00.

Here we propose redox reaction mechanisms of CH_3OH, specifically selective CH_3OH oxidation to HCHO, centered on surface oxygen vacancies (CH_3O-O_{vac}, Fig. 4C), where the kinetics can be regulated by surface oxygen activity as described by the surface O $2p$-band center relative to the Fermi level. The reaction mechanism on the surface oxygen vacancy was found more favorable than the reaction mechanism on surface metal sites or surface oxygen sites (CH_3O-B in Fig. A.4.25A, CH_3O-O_{oxide} in Fig. A.4.26A, or B-$HOCH_2$-O_{oxide} in Fig. A.4.27A). The proposed reaction mechanisms are supported by the energetics of each reaction step computed from DFT (Fig. A.4.28) and AP-XPS observations (Figs. 2 and 3), and the following steps discussed below.

First, dissociative CH_3OH adsorption occurs at the surface oxygen vacancy site (CH_3O-O_{vac}) as reported previously[49,68] rather than the transition metal site (CH_3O-B) or an oxygen site (CH_3O-O_{oxide}) along with the formation of H-O_{oxide} (Fig. 4C). Although the B-$HOCH_2$-O_{oxide} reaction pathway has the most favorable CH_3OH dissociation energy, we did not consider the B-$HOCH_2$-O_{oxide} pathway here as CH_3O-O_{vac} species were observed in the AP-XPS spectra (orange, Figs. 2-3) and have been reported previously on $SrTiO_3$ after CH_3OH adsorption.[19] Second, CH_3O-O_{vac} reaction intermediate undergoes dehydrogenation by second surface oxygen to form CH_2O-O_{vac} and H-O_{oxide}. Third, CH_2O-O_{vac} desorbs as HCHO to leave behind a surface oxygen vacancy. Finally, oxygen adsorption occurs to refill the oxygen vacancy along with desorption of H_2O from H-O_{oxide}. The free energy of CH_3OH adsorption on the

oxygen vacancy sites of $LaCoO_3$ was found to be uphill with energy of +0.13 eV, and this step became more energetically favorable with moving the Fermi level closer to the surface oxygen $2p$-band center, where the step was downhill by -1.02 eV on the surface vacancy site of $SrCoO_3$ (Fig. 4D). Further, Gibbs free energy for CH_3OH adsorption as CH_3O-O_{vac} and oxygen adsorption/H_2O desorption were seen to have opposite trends as a function of the surface O $2p$-band center relative to the Fermi level (Fig. A.5.28), leading to the formation of the volcano-like trend observed for the CH_3O-O_{vac} intermediate in AP-XPS in Fig. 3B. For the surfaces with O $2p$-band away from the Fermi level, we find that the reaction is likely to be limited by C-H bond dehydrogenation or HCHO desorption while for surfaces with O $2p$-band closer to the Fermi level, the reaction is likely to be limited by oxygen adsorption and water desorption (Fig. 4D) leading to the observed volcano-type correlation for HCHO TOF and CH_3O-O_{vac} integrated intensity (Fig. 4B). We also note that the energetics for an under-coordinated metal-based CH_3OH oxidation pathway (CH_3O-B_{uc}, Fig. A.4.29A) is similar to that of the oxygen vacancy-based CH_3OH oxidation pathway and this reaction mechanism cannot be ruled out. The corresponding free energy diagrams for $LaCoO_3$ (x = 0), $La_{0.5}Sr_{0.5}CoO_3$ (x = 0.5), and $SrCoO_3$ (x = 1) surfaces are reported in Fig. A.4.29B and the Gibbs free energy for the CH_3OH adsorption step on under-coordinated Co sites (CH_3O-B_{uc}) and the steps for H_2O desorption and oxygen adsorptions show opposite trends (Fig. A.4.29C) similar to the surface oxygen vacancy pathway. This result is consistent with previous investigations that have shown that methoxy species (CH_3O-) decomposition temperature correlated with HCHO formation rates.[35]

We further verified the proposed reaction mechanism involving CH_3OH adsorption on the oxygen vacancy sites by measuring the HCHO formation rate (Fig. A.4.30A), CO_2 formation rate (Fig. A.4.30B), as well as CH_3OH conversion rate (Fig. A.4.30C) by varying the oxygen partial pressure from 20 ppm to 8% O_2 for $La_xSr_{1-x}CoO_3$ (x = 0.0, x = 0.6). We observed volcano type dependence as a function of the oxygen concentration for HCHO and CO_2 formation rate which can be understood by invoking a micro-kinetic model in the low and high oxygen concentrations regimes based on previously developed models for methanol oxidation on MoO_3[50] and Pd clusters[49,69] (Table A.5.7). First, under low oxygen concentration (pressure), we rationalize the trend of increasing reaction rate with increasing

oxygen concentration by the limited C-H dehydrogenation at low oxygen partial pressure due to the presence of a large number of oxygen vacancies and non-availability of surface oxygen species to form surface hydroxyl species. Hence, the methanol conversion rate increases with increasing oxygen partial pressure in this region. On the other hand, at higher oxygen partial pressure, with surface oxygen species being the dominant surface species, the reaction is limited by oxygen vacancy formation and the reaction rate decreases with increasing oxygen partial pressure.[49]
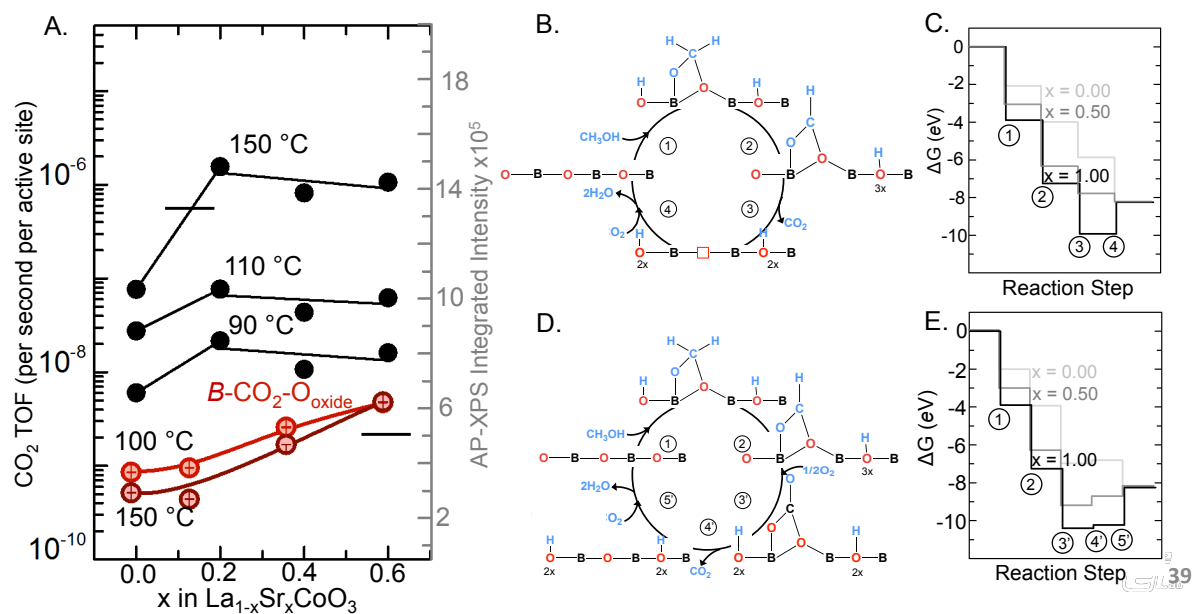
Figure 5. Selective oxidation kinetics of CH₃OH to CO₂. *A) TOF values for CH_3OH oxidation to CO_2 at T = 90, 110, and 150 °C and integrated peak intensities for B-CO₂-O_oxide reaction intermediate at 100 and 150 °C (dark red, Fig. 3C) as a function of the surface O 2p-band center, where the activity metric was chosen from the Arrhenius type plot in Fig. A.4.20A. The percentage conversion of CH_3OH oxidation to CO_2 was calculated by the formula, %conversion=100*(CO₂ₚₚₘ, ₒᵤₜ)/CH₃OHₚₚₘ, ᵢₙ, where $CH_3OH_{ppm, in}$ was the concentration of the initial CH_3OH reactant, and $CO_{2ppm, out}$ was the concentration of CO_2 gas observed after reaction with the catalyst. CO_2 formation rate was determined using the formula, $r_{formation} = \frac{r_{mass} \cdot 10^{-6}}{A_S} \{\frac{ml. \, min^{-1}}{l. \, mol^{-1}. \, g. \, m^2. g^{-1}}\}$, Where mass activity was estimated using the formula, $r_{mass} = \frac{\% \, conversion. F_{CH3OH}}{6. \, V_m. \, m_{cat}} \{\frac{ml. \, min^{-1}}{l. \, mol^{-1}. \, g}\}$, For %CH₃OH conversion less than 12.5% obtained for the $La_{1-x}Sr_xCoO_3$ (x=0-0.6) series conducted in a flow reactor. Catalyst loading of 750 mg, inlet CH_3OH flow rate of 150 ml min⁻¹ and gas concentration of 70 ppm CH₃OH-8% O_2 were used for all the measurements. Finally, the TOF are reported using the formula, $TOF = \frac{r_f. N_a}{PD_{100}} = (\frac{mol^{+1}. mol^{-1}}{m^{+2}. s^{-1}. m^{-2}})$ With N_a being the Avogadro's numbers, and PD_{100} planar density of the surface oxygen atoms on 100 BO_2-type termination of the*

pseudo-cubic perovskite catalysts as obtained from DFT ($PD_{100} = 1.34*10^{19} O_{oxide}/m^2$. AP-XPS integrated intensities error bars (standard deviations) were calculated by Monte Carlo simulation of the peak fitting. B) Oxygen vacancy mediated CH_3OH oxidation to CO_2 via O-H and C-H bond scissions of CH_3OH to form B-OCH_2-O_{oxide} (step 1), followed by dehydrogenation of B-OCH_2-O_{oxide} to B-OCH-O_{oxide} (step 2), conversion of B-OCH-O_{oxide} to CO_2 leading to oxygen vacancy formation (step 3), and oxygen adsorption and H_2O desorption to complete the catalytic cycle (step 4), where oxygen vacancy is denoted by an open red square. C) Gibbs free energy profile on $La_{1-x}Sr_xCoO_3$ (x = 0.00, 0.50, and 1.00) for the vacancy mediated reaction mechanism, D) Carbonate mediated CH_3OH oxidation to CO_2 via conversion of B-OCH-O_{oxide} to B-CO_2-O_{oxide} (step 3'), followed by desorption of CO_2 from B-CO_2-O_{oxide} (step 4'), and oxygen adsorption and H_2O desorption to complete the catalytic cycle (step 5'). E) Gibbs free energy profile on $La_{1-x}Sr_xCoO_3$ (x = 0.00, 0.50, and 1.00) for the carbonate mediated reaction mechanism.

In contrast to the oxygen vacancy-based CH_3OH oxidation pathways, the transition metal-based CH_3OH oxidation pathway (Fig. A.4.25A) is rather unlikely without the involvement of the surface oxygen. The adsorption of CH_3OH on surface metal sites (CH_3O-B) and subsequent desorption of CH_2O-B in Fig. A.4.25B are energetically unfavorable (Fig. A.5.25C). A high-energy penalty for CH_3OH adsorption not strongly dependent on neither oxide-chemistry nor strontium concentration in $La_{1-x}Sr_xCoO_3$ (Fig. A.4.25C) is in contrast to pronounced changes in the C $1s$ speciation observed in AP-XPS (Fig. 3) and distinctive kinetics of CH_3OH to HCHO conversion found for different concentrations of Sr in $La_{1-x}Sr_xCoO_3$ (Fig. 4B) suggesting that the transition metal-based reaction mechanism is unlikely. Next, we also considered the reaction mechanism for CH_3OH adsorption on the oxygen sites (Fig. A.4.26A) leading to the formation of CH_3O-O_{oxide}. Here we observed that the dehydrogenation of CH_3O-O_{oxide} to form HCHO was found to be energetically favorable for all the oxide chemistries. (Figs. A.4.26B and C) However, as the surface oxygen site is the active reaction site in this case, increasing oxygen pressure in this case would lead to linearly increasing reaction rate which is in contrast to the volcano type behavior observed in the reaction order measurements (Fig. A.4.30).

We next considered CH_3OH adsorption on both the surface oxygen and cobalt sites in a bidentate configuration (B-$OHCH_2$-O_{oxide}, Fig. A.4.27A), which was found to have strong adsorption for all the catalysts (Fig. A.4.27B). This reaction mechanism is unlikely for HCHO formation due to the high activation barrier for bidentate B-OCH_2-O_{oxide} conversion to HCHO[70] and the uphill free energy for HCHO desorption (Fig. A.4.27C). Moreover, as

bidentate reaction intermediates are thermodynamically favored reaction intermediates *(B-CH₂OH-O$_{oxide}$*, and B-CH₂O-O$_{oxide}$, dark brown in Fig. A.4.1B and Fig. A.4.2B respectively) as seen previously for CeO_2,[16] we consider this pathway to understand the reaction mechanism for CO_2 formation which is the thermodynamically favored product. We justify this consideration by noting it is energetically favorable for monodentate reaction intermediates adsorbed only on the surface Co sites (CH₃-*B*, CH₃-*B*$_{uc}$) or surface oxygen sites (CH₃O-O$_{oxide}$, CH₃O-O$_{vac}$), to convert to the respective bidentate configurations of *B*-OH₂C-O$_{oxide}$ and *B*$_{uc}$-OH₂C-O$_{oxide}$ (Fig. A.4.31). Moreover, both *B*$_{uc}$-OH₂C-O$_{oxide}$ and *B*$_{uc}$-CO₂-O$_{oxide}$ have favorable adsorption energy, but we did not consider these reaction intermediates for CO_2 formation reaction pathway due to the more favorable adsorption energy for the corresponding *B*-OH₂C-O$_{oxide}$ and *B*-CO₂-O$_{oxide}$ reaction intermediates (Figs. A.4.2A and B and A.4.3A). To explain the volcano trend of CO_2 TOF as a function of the surface O 2*p*-band center (Fig. 5A), we understand the trends in the adsorption energetics of *B*-CO₂-O$_{oxide}$, and desorption of CO_2 using the reaction mechanisms centered on both the surface oxygen and cobalt sites proposed in Figs. 5B,D. Firstly, for the vacancy-mediated mechanism (Fig. 5B), we consider direct dehydrogenation of two hydrogens of CH₃OH to form *B*-OH₂C-O$_{oxide}$ and 2H-O$_{oxide}$ (Step 1). The second step involves the formation of *B*-OHC-O$_{oxide}$ and H-O$_{oxide}$ from *B*-OH₂C-O$_{oxide}$ (Step 2) followed by the third step of CO_2 desorption from *B*-OHC-O$_{oxide}$ to form surface oxygen vacancies (Step 3). The fourth step involves oxygen adsorption leading to vacancy refilling and water desorption from H-O$_{oxide}$ (Step 4). Furthermore, carbonate mediated pathway for CO_2 formation is also proposed via carbonate (*B*-CO₂-O$_{oxide}$) formation (Fig. 5D) wherein the *B*-OHC-O$_{oxide}$ converts to *B*-CO₂-O$_{oxide}$ via oxygen adsorption (Step 3') instead of converting to CO_2 as described previously. Next, *B*-CO₂-O$_{oxide}$ is converted to CO_2 (Step 4'), and finally, oxygen adsorption occurs leading to H₂O desorption from H-O$_{oxide}$ (Step 5').

We considered the adsorption energy trends for each of the reaction steps for both the vacancy mediated and carbonate mediated reaction pathways where the energetics for *B*-OHC-O$_{oxide}$ formation (Step 1, 2) and CO_2 desorption (Step 3) become favorable as the Fermi level moves closer to the oxygen 2*p*-band center (Fig. A.4.32). In addition, the Gibbs free energy for oxygen adsorption and H₂O desorption (Step 4) trends in the opposite direction to

that of the CO_2 formation energy. Interestingly, the energetics for conversion of B-OHC-O_{oxide} to B-CO_2-O_{oxide} (Step 3') is highly favorable for $LaCoO_3$ (x = 0.0) with energy of -3.07 eV and does not change significantly for $SrCoO_3$ (x = 1.0) with energy of -3.15 eV. Moreover, the conversion of B-CO_2-O_{oxide} to CO_2 is not favorable (+0.16 eV for $LaCoO_3$ and +0.17 eV for $SrCoO_3$ in Fig. 5E) compared to the conversion of B-HCO-O_{oxide} to CO_2 (-1.90 eV for $LaCoO_3$ and -2.67 eV for $SrCoO_3$ in Fig. 5C) suggesting that the carbonate mediated pathway (B-CO_2-O_{oxide}) is not an active pathway for CO_2 formation at low temperature (Step 4'). Hence, we propose for the lower Sr substituted catalysts, CO_2 formation is limited by C-H bond dissociation while for the higher Sr substituted catalysts, the reaction is limited by CO_2 desorption from the B-CO_2-O_{oxide} sites leading to the volcano-type trend for CO_2 formation as a function of the O $2p$-band center in Fig. 5A. We further verify the reaction mechanism for CO_2 formation by understanding the volcano trend of CO_2 formation rate with increasing oxygen concentration (Fig. A.4.30B) by proposing that at low oxygen concentration not enough surface oxygen sites are available for B-HCO-O_{oxide} dehydrogenation to CO_2 while at higher oxygen concentration increasing carbonate formation leads to surface poisoning by carbonate (B-CO_2-O_{oxide}) which decreases CO_2 formation rate.

This investigation on perovskite catalysts with a significant range of O $2p$-band centers highlights that the CH_3OH oxidation activity peaks at optimal oxygen vacancy formation energy. For an optimal oxygen vacancy formation exhibited by $La_{0.5}Sr_{0.5}CoO_3$, both the CH_3OH adsorption (Fig. 1B, ΔG = -0.98 eV) and H_2O desorption-oxygen vacancy filling (Step 4 in Fig. 4D, ΔG = -0.91 eV) are facile for the oxygen vacancy pathway, and a not too high thermodynamic barrier for B-CO_2-O_{oxide} removal is observed (Step 4' in Fig. 5D, ΔG = +0.50 eV), thus preventing poisoning of the active surface oxygen sites. Such a reaction mechanism is in contrast to previous reaction mechanisms for selective HCHO formation proposed on metal sites[71,72,73,74] and is in agreement with previous studies indicating the importance of oxygen vacancies[75,15] for selective HCHO formation. Our proposed mechanism is further supported by the AP-XPS measurements, which show that the intensity of the peak corresponding to CH_3OH adsorption on oxygen vacancy sites as CH_3O-O_{vac} is the highest for $La_{0.6}Sr_{0.4}CoO_3$, beyond which the presence of surface adsorbed carbonates

increases at the expense of these species, suggesting the dominance of the surface-poisoning carbonate pathway. The initial increase HCHO selectivity upon Sr substitution of $LaCoO_3$ to ~$La_{0.8}Sr_{0.2}CoO_3$ and $La_{0.6}Sr_{0.4}CoO_3$ originates from the enhancement of the initial CH_3OH adsorption on the perovskite surface to enhance kinetics, as shown experimentally in the AP-XPS (Fig. 3B, orange, CH_3O-O_{vac}) and DFT (Fig. 4D). Yet, further increasing of Sr substitution, manifesting as an increase in O $2p$-band center and increased surface oxygen activity, results in the predominance of the carbonate-mediated mechanism, where B-CO_2-O_{oxide} desorption limits CH_3OH oxidation kinetics, similarly supported by AP-XPS (Fig. 3C) and the DFT calculations (Fig. 5D). In this manner, the surface electronic structure parameter, O $2p$-band center, serves as a useful descriptor for CH_3OH oxidation and selectivity kinetics across different perovskite oxide chemistries.

5.5 Conclusions

In this study, we undertook AP-XPS, reactor activity measurements, and DFT studies to identify the critical role of surface oxygen activity for cobalt-based perovskite oxides in dictating CH_3OH surface energetics and the kinetics of CH_3OH selective oxidation to HCHO and complete oxidation to CO_2. By developing well-defined materials systems of (100)-oriented epitaxial perovskite thin films for AP-XPS studies under catalytically-relevant pressures of CH_3OH and O_2, we were able to systematically elucidate trends in surface speciation of carbonaceous reaction intermediates as a function of O $2p$-band center for the of $La_{1-x}Sr_xCoO_3$ series. We have established a relation between metal oxide chemistry, methoxy reaction intermediate surface reactivity, and product selectivity using such a combined approach. This study provides a critical link and scientific understanding for attempts to discover new catalyst materials through material property-activity relationships for the small carbon molecule reaction network. We identify that chemistries with intermediate surface O $2p$-band center that exhibit the highest intrinsic CH_3OH conversion for selective generation of HCHO at lower temperatures compared to the commercial catalysts, where the surface O $2p$-band relative to the Fermi level is neither too low (so as to limit the adsorption of CH_3OH species) nor too high (limit oxygen vacancy refilling and water desorption energy from surface oxygen sites, triggering carbonate poisoning).

Furthermore, we find that highly covalent oxides, with O 2*p*-band centers close to the Fermi level are well suited for carbonate storage. These insights provide guiding principles for the selection of next-generation materials chemistries for catalytically complex small molecule conversion, where multiple catalytic processes have to be tuned.

5.6 Experimental and Computational Methods

Thin Film Fabrication and Characterization

Epitaxial (001)-oriented thin films of the $La_xSr_{1-x}CoO_3$ (x = 0, 0.2, 0.4 and 0.6) were prepared using pulsed laser deposition as previously described.[27] Briefly, targets synthesized using solid-state reaction were deposited using KrF excimer laser (λ = 248 nm). Film surface was characterized by atomic force microscopy (AFM, Bruker Dimension Icon) and high-resolution x-ray diffraction (HRXRD, Panalytical).[27]

Ambient Pressure XPS

Beamline 9.3.2 at the Advanced Light Source at Lawrence Berkeley National Laboratory was used for conducting the AP-XPS measurements. To account for effects of surface charging during the AP-XPS measurements, the binding energy (BE) axis in all XPS spectra is adjusted to the known BE position of the lattice oxygen peak at 530 eV for the O 1*s* spectra and adventious carbon at 284.8 eV for the C 1*s* peak. As the pristine sample surface contained several oxo-carbonaceous species, these were removed from the surface by heating the sample to 300 °C under 100 mTorr O_2.

To monitor the surface chemistry and reaction intermediate formation under CH_3OH conversion conditions, the sample was cooled to room temperature post the cleaning procedure followed by introduction of 100 mTorr of CH_3OH and 20 mTorr of O_2. Isobar measurements were conducted from room temperature (~25 °C) to 300 °C, where C 1*s*, and O 1*s* spectra were measured every 25 °C and the metal core level spectra were measured periodically. The O 1*s*, Co 3*p*, and Sr 3*d* core level spectra were measured with incident

photon energy of 735 eV while C 1s was measured using 490 eV.

Analysis of the XPS spectra was performed by the software package CasaXPS to quantify the photoemission peak areas and positions. All spectra were fit using Gaussian-Lorentzian peaks after a Shirley-type background subtraction. The range of full-width half maximums and binding energy values of the peaks were constrained to 0.3 eV and 0.2 eV, respectively. These peak fitting parameters are summarized in Table A.4.2. The binding peak assignments of C 1s are in agreement with previous experimental and computational work on metal oxide surfaces (Fig. A.4.6). The effect of bulk or near surface reduction in influencing the surface reactivity could be ruled out based on the unchanged Co 3d spectra (Fig. A.4.15).

CH$_3$OH Oxidation Activity Measurements

Powder catalysts of La$_x$Sr$_{1-x}$CoO$_3$ (x = 0, 0.2, 0.4, and 0.6) were prepared by solid-state route as described previously until phase pure is obtained. X-Ray Diffraction (XRD) and Brunauer-Emmett-Teller (BET) surface area of synthesized powders is available from our previous work.[27] 750 mg of the powder catalyst was mixed with oven-dried SiO$_2$ sand (2.5 g) and loaded into a quartz tube (3.81 mm inner diameter). A total flow rate of 150 ml min^{-1} was used for all the plug flow reactor experiments and the flow rate of individual gases, CH$_3$OH (150 ppm in balance N$_2$), O$_2$ (100 ppm-25% by volume in balance N$_2$), and pure N$_2$, was controlled using dedicated mass flow controllers. The gas composition was analyzed using a PIKE FTIR gas cell attached to a Bruker Vertex 70 FT-IR spectrophotometer. 32 scans were collected at a resolution of 4 cm^{-1} every 12.5 min. A background spectrum was collected under a pure stream of N$_2$. Prior to flowing the reaction gas mixture, the catalyst was purged with pre-treated in pure O$_2$ at 450 °C for 5 hours to remove any carbonaceous species. For the CH$_3$OH oxidation measurements, inlet reaction gas mixture of 70 ppm of CH$_3$OH with 20 ppm - 8% of O$_2$ by volume, and N$_2$ balance was used for all the experiments. The percentage conversion of CH$_3$OH oxidation to HCHO and CO$_2$ was calculated by determining the percentage of outlet HCHO, CO$_2$ reacted during the reaction, which can be calculated by the formula,

% Conversion (CH$_3$OH) = 100*(HCHO$_{ppm, out}$ +CO$_{2ppm, out}$)/(CH$_3$OH$_{ppm, in}$),

% Conversion (CO_2) = $100*(CO_{2ppm,\ out}/CH_3OH_{ppm,\ in})$,

% Conversion (HCHO) = $100*(HCHO_{ppm,\ out}/CH_3OH_{ppm,\ in})$,

% Selectivity (HCHO) = $100*(HCHO_{ppm,\ out})/(HCHO_{ppm,\ out} + CO_{2ppm,\ out})$,

% Selectivity (CO_2) = $100*(CO_{2ppm,\ out})/(HCHO_{ppm,\ out} + CO_{2ppm,\ out})$,

Where $CH_3OH_{ppm,\ in}$ was the concentration of the initial CH_3OH reactant, $CO_{2ppm,\ out}$ and $HCHO_{ppm,\ out}$ was the concentration of CO_2 and HCHO observed after reaction with the catalyst.

%Conversion of less than 12.5% was used to calculate specific area normalized reaction rates and turnover frequencies (TOF).

$$r_{formation} = \frac{\left(\%\frac{conversion}{100}\right).\ r_{CH3OH}\cdot 10^{+3}.\ 10^{-6}}{V_m\cdot 60.\ m_{cat}\cdot A_S} = \left(\frac{ml.\ min^{-1}}{l.\ mol^{-1}.\ g\ .\ m^{+2}.g^{-1}}\right)$$

Where r_{CH3OH} is the inlet volumetric flow rate of CH_3OH of the gas stream (150 mL min^{-1}), V_m is the molar volume assuming ideal gas behavior, A_s is the BET surface area[27], and m_{cat} is catalyst loading (750 mg). Finally, the TOF are reported using the formula,

$$TOF = \frac{r_f.\ N_a}{PD_{100}} = \left(\frac{mol^{+1}.mol^{-1}}{m^{+2}.\ s^{-1}.\ m^{-2}}\right)$$

With N_a being the Avogadro's numbers, and PD_{100} planar density of the surface oxygen atoms on 100 BO_2-type termination of the pseudo-cubic perovskite catalysts as obtained from DFT ($PD_{100} = 1.34*10^{19}\ O_{oxide}/m^2$

Density Functional Theory Calculations

Density functional theory (DFT) calculations were performed with the Vienna Ab-initio Simulation Package (VASP)[76,77] using the Projector-Augmented plane-wave method with the Perdew-Burke-Ernzerhof (PBE) Generalized Gradient Approximation (GGA) plus Hubbard U method to treat the exchange-correlation interactions,[78,79] where the *U* value was optimized by fitting the formation enthalpies of oxides (U_{eff} = 3.3 eV for Co).[80,81] Fully relaxed bulk perovskite calculations of $La_xSr_{1-x}CoO_3$ (x = 0.00, 0.25, 0.50, 0.75, and 1.00) were performed with 2×2×2 perovskite supercells and a ferromagnetic state is assumed to have a consistent set of magnetic structures.[80,82] We considered a (001)-*BO*$_2$ terminated slab model, where the CoO_2-terminated surface was described by a seven-layer symmetric slab constructed from the 2 × 2 × 2 pseudocubic perovskite cell, as previous first-principles thermodynamics

studies showed that the (001) CoO_2 and LaO terminations are most preferred at high temperature under oxidizing conditions. [41] The slabs were separated by a vacuum space of at least 10 Å and a (2 × 2 × 1) *k*-point sampling was used for the slab models. After performing an internal relaxation of coordinates for the clean slab, the bottom two layers were then kept fixed. The reaction intermediates were adsorbed on one side of the slab. The surface O 2*p*-band was determined by taking the centroid of the projected density of states of O 2*p* states (both occupied and unoccupied) relative to the Fermi level of surface oxygen atoms. Thermodynamic tables[83] were used for conversion of calculated DFT adsorption energy to Gibbs free energy for gas phase species, while the zero point energy and vibrational entropy contributions of adsorbed species were estimated from vibrational analysis.[67]

5.7 References

(1)   Kowatsch, S. Formaldehyde. In *Phenolic Resins: A Century of Progress*; Springer Berlin Heidelberg, 2010; pp 25–40. https://doi.org/10.1007/978-3-642-04714-5_3.

(2)   Akiyama, T.; Sei, R.; Takenaka, S. Partial Oxidation of Methane to Formaldehyde over Copper–Molybdenum Complex Oxide Catalysts. *Catal. Sci. Technol.* **2021**, *11* (15), 5273–5281. https://doi.org/10.1039/D1CY00511A.

(3)   Yuan, S.; Li, Y.; Peng, J.; Questell-Santiago, Y. M.; Akkiraju, K.; Giordano, L.; Zheng, D. J.; Bagi, S.; Román-Leshkov, Y.; Shao-Horn, Y. Conversion of Methane into Liquid Fuels—Bridging Thermal Catalysis with Electrocatalysis. *Advanced Energy Materials*. Wiley-VCH Verlag October 1, 2020, p 2002154. https://doi.org/10.1002/aenm.202002154.

(4)   Franz, A. W.; Kronemayer, H.; Pfeiffer, D.; Pilz, R. D.; Reuss, G.; Disteldorf, W.; Gamer, A. O.; Hilt, A. Formaldehyde. In *Ullmann's Encyclopedia of Industrial Chemistry*; Wiley-VCH Verlag GmbH & Co. KGaA: Weinheim, Germany, 2016; pp 1–34. https://doi.org/10.1002/14356007.a11_619.pub2.

(5)   Vieira Soares, A. P.; Farinha Portela, M.; Kiennemann, A. Methanol Selective Oxidation to Formaldehyde over Iron-Molybdate Catalysts. *Catalysis Reviews - Science and Engineering*. Taylor and Francis Inc. 2005, pp 125–174. https://doi.org/10.1081/CR-200049088.

(6)   Lafyatis, D. S.; Creten, G.; Froment, G. F. TAP Reactor Study of the Partial Oxidation of Methanol to Formaldehyde Using an Industrial Fe-Cr-Mo Oxide Catalyst. *Appl. Catal. A, Gen.* **1994**, *120* (1), 85–103. https://doi.org/10.1016/0926-860X(94)80335-8.

(7)   Rellán-Piñeiro, M.; López, N. The Active Molybdenum Oxide Phase in the Methanol Oxidation to Formaldehyde (Formox Process): A DFT Study. *ChemSusChem* **2015**, *8* (13), 2231–2239. https://doi.org/10.1002/cssc.201500315.

(8)   Adkins, H.; Peterson, W. R. THE OXIDATION OF METHANOL WITH AIR OVER IRON, MOLYBDENUM, AND IRON-MOLYBDENUM OXIDES. *J. Am. Chem. Soc.* **2002**, *53* (4), 1512–1520. https://doi.org/10.1021/JA01355A050.

(9)   Millar, G. J.; Collins, M. Industrial Production of Formaldehyde Using Polycrystalline Silver Catalyst.

Industrial and Engineering Chemistry Research. American Chemical Society August 23, 2017, pp 9247–9265. https://doi.org/10.1021/acs.iecr.7b02388.

(10)   Jehng, J.-M. Dynamic States of V2O5 Supported on SnO2/SiO2 and CeO2/SiO2 Mixed-Oxide Catalysts during Methanol Oxidation. *J. Phys. Chem. B* **1998**, *102* (30), 5816–5822. https://doi.org/10.1021/JP980622V.

(11)   Chen, Y.; Wachs, I. E. Tantalum Oxide-Supported Metal Oxide (Re2O7, CrO3, MoO3, WO3, V2O5, and Nb2O5) Catalysts: Synthesis, Raman Characterization and Chemically Probed by Methanol Oxidation. *J. Catal.* **2003**, *217* (2), 468–477. https://doi.org/10.1016/S0021-9517(03)00065-4.

(12)   Vohs, J. M. Site Requirements for the Adsorption and Reaction of Oxygenates on Metal Oxide Surfaces. *Chemical Reviews*. American Chemical Society June 12, 2013, pp 4136–4163. https://doi.org/10.1021/cr300328u.

(13)   Bowker, M.; Holroyd, R.; House, M.; Bracey, R.; Bamroongwongdee, C.; Shannon, M.; Carley, A. The Selective Oxidation of Methanol on Iron Molybdate Catalysts. *Top. Catal. 2008 481* **2008**, *48* (1), 158–165. https://doi.org/10.1007/S11244-008-9058-3.

(14)   Tatibouët, J. M. Methanol Oxidation as a Catalytic Surface Probe. *Applied Catalysis A: General*. Elsevier January 2, 1997, pp 213–252. https://doi.org/10.1016/S0926-860X(96)00236-0.

(15)   Kropp, T.; Paier, J. Activity versus Selectivity of the Methanol Oxidation at Ceria Surfaces: A Comparative First-Principles Study. *J. Phys. Chem. C* **2015**, *119* (40), 23021–23031. https://doi.org/10.1021/acs.jpcc.5b07186.

(16)   Capdevila-Cortada, M.; López, N. Descriptor Analysis in Methanol Conversion on Doped CeO2(111): Guidelines for Selectivity Tuning. *ACS Catal.* **2015**, *5* (11), 6473–6480. https://doi.org/10.1021/acscatal.5b01427.

(17)   Aas, N.; Pringle, T. J.; Bowker, M. Adsorption and Decomposition of Methanol on TiO2, SrTiO3 and SrO. *J. Chem. Soc. Faraday Trans.* **1994**, *90* (7), 1015–1022. https://doi.org/10.1039/FT9949001015.

(18)   Setvin, M.; Shi, X.; Hulva, J.; Simschitz, T.; Parkinson, G. S.; Schmid, M.; Di Valentin, C.; Selloni, A.; Diebold, U. Methanol on Anatase TiO2 (101): Mechanistic Insights into Photocatalysis. *ACS Catal.* **2017**, *7* (10), 7081–7091. https://doi.org/10.1021/acscatal.7b02003.

(19)   Zhang, Y.; Savara, A.; Mullins, D. R. Ambient-Pressure XPS Studies of Reactions of Alcohols on SrTiO3(100). *J. Phys. Chem. C* **2017**, *121* (42), 23436–23445. https://doi.org/10.1021/acs.jpcc.7b06319.

(20)   Lv, C. Q.; Liu, C.; Wang, G. C. A DFT Study of Methanol Oxidation on Co3O4. *Catal. Commun.* **2014**, *45*, 83–90. https://doi.org/10.1016/j.catcom.2013.10.039.

(21)   Huttunen, P. K.; Labadini, D.; Hafiz, S. S.; Gokalp, S.; Wolff, E. P.; Martell, S. M.; Foster, M. DRIFTS Investigation of Methanol Oxidation on CeO2 Nanoparticles. *Appl. Surf. Sci.* **2021**, *554*, 149518. https://doi.org/10.1016/J.APSUSC.2021.149518.

(22)   Wang, X.; Wu, J.; Wang, J.; Xiao, H.; Chen, B.; Peng, R.; Fu, M.; Chen, L.; Ye, D.; Wen, W. Methanol Plasma-Catalytic Oxidation over CeO2 Catalysts: Effect of Ceria Morphology and Reaction Mechanism. *Chem. Eng. J.* **2019**, *369*, 233–244. https://doi.org/10.1016/J.CEJ.2019.03.067.

(23)   Levasseur, B.; Kaliaguine, S. Methanol Oxidation on LaBO3 (B=Co, Mn, Fe) Perovskite-Type Catalysts Prepared by Reactive Grinding. *Appl. Catal. A Gen.* **2008**, *343* (1–2), 29–38. https://doi.org/10.1016/j.apcata.2008.03.016.

(24)   Deo, G.; Wachs, I. E. Reactivity of Supported Vanadium Oxide Catalysts: The Partial Oxidation of

Methanol. *J. Catal.* **1994**, *146* (2), 323–334. https://doi.org/10.1006/JCAT.1994.1071.

(25)   Hwang, J.; Rao, R. R.; Giordano, L.; Katayama, Y.; Yu, Y.; Shao-Horn, Y. Perovskites in Catalysis and Electrocatalysis. *Science* **2017**, *358* (6364), 751–756. https://doi.org/10.1126/science.aam7092.

(26)   Jacobs, R.; Hwang, J.; Shao-Horn, Y.; Morgan, D. Assessing Correlations of Perovskite Catalytic Performance with Electronic Structure Descriptors. *Chem. Mater.* **2019**, *31* (3), 785–797. https://doi.org/10.1021/acs.chemmater.8b03840.

(27)   Hwang, J.; Rao, R. R.; Giordano, L.; Akkiraju, K.; Wang, X. R.; Crumlin, E. J.; Bluhm, H.; Shao-Horn, Y. Regulating Oxygen Activity of Perovskites to Promote NOx Oxidation and Reduction Kinetics. *Nat. Catal. 2021* **2021**, 1–11. https://doi.org/10.1038/s41929-021-00656-4.

(28)   Foo, G. S.; Polo-Garzon, F.; Fung, V.; Jiang, D. E.; Overbury, S. H.; Wu, Z. Acid-Base Reactivity of Perovskite Catalysts Probed via Conversion of 2-Propanol over Titanates and Zirconates. *ACS Catal.* **2017**, *7* (7), 4423–4434. https://doi.org/10.1021/acscatal.7b00783.

(29)   Polo-Garzon, F.; Yang, S.-Z.; Fung, V.; Foo, G. S.; Bickel, E. E.; Chisholm, M. F.; Jiang, D.; Wu, Z. Controlling Reaction Selectivity through the Surface Termination of Perovskite Catalysts. *Angew. Chemie* **2017**, *129* (33), 9952–9956. https://doi.org/10.1002/ANGE.201704656.

(30)   Tesquet, G.; Faye, J.; Hosoglu, F.; Mamede, A.-S.; Dumeignil, F.; Capron, M. Ethanol Reactivity over La1+x FeO3+δ Perovskites. *Appl. Catal. A Gen.* **2016**, *511*, 141–148. https://doi.org/10.1016/j.apcata.2015.12.005.

(31)   Tan, S.; Sayed, F.; Yang, S.; Li, Z.; Wu, J.; Ajayan, P. M. Strong Effect of B-Site Substitution on the Reactivity of Layered Perovskite Oxides Probed via Isopropanol Conversion. *ACS Mater. Lett.* **2019**, *1* (2), 230–236. https://doi.org/10.1021/acsmaterialslett.9b00095.

(32)   Lim, S.; Choi, J.-W.; Suh, D. J.; Song, K. H.; Ham, H. C.; Ha, J.-M. Combined Experimental and Density Functional Theory (DFT) Studies on the Catalyst Design for the Oxidative Coupling of Methane. *J. Catal.* **2019**, *375*, 478–492. https://doi.org/10.1016/j.jcat.2019.04.008.

(33)   Zhang, Y.; Mullins, D. R.; Savara, A. Surface Reactions and Catalytic Activities for Small Alcohols over LaMnO 3 (100) and La 0.7 Sr 0.3 MnO 3 (100): Dehydrogenation, Dehydration, and Oxidation . *J. Phys. Chem. C* **2020**, *124* (6), 3650–3663. https://doi.org/10.1021/acs.jpcc.9b10797.

(34)   Polo-Garzon, F.; Fung, V.; Liu, X.; Hood, Z. D.; Bickel, E. E.; Bai, L.; Tian, H.; Foo, G. S.; Chi, M.; Jiang, D.; Wu, Z. Understanding the Impact of Surface Reconstruction of Perovskite Catalysts on CH 4 Activation and Combustion. *ACS Catal.* **2018**, *8* (11), 10306–10315. https://doi.org/10.1021/acscatal.8b02307.

(35)   Badlani, M.; Wachs, I. E. Methanol: A "Smart" Chemical Probe Molecule. *Catal. Letters* **2001**, *75* (3–4), 137–149. https://doi.org/10.1023/A:1016715520904.

(36)   Kubokawa, Y. DETERMINATION OF ACIDITY OF SOLID CATALYSTS BY AMMONIA CHEMISORPTION. *J. Phys. Chem.* **2002**, *67* (4), 769–771. https://doi.org/10.1021/J100798A011.

(37)   Kester, P. M.; Miller, J. T.; Gounder, R. Ammonia Titration Methods To Quantify Brønsted Acid Sites in Zeolites Substituted with Aluminum and Boron Heteroatoms. *Ind. Eng. Chem. Res.* **2018**, *57* (19), 6673–6683. https://doi.org/10.1021/ACS.IECR.8B00933.

(38)   Hattori, H. Solid Base Catalysts: Generation, Characterization, and Catalytic Behavior of Basic Sites. *J. Japan Pet. Inst.* **2004**, *47* (2), 67–81. https://doi.org/10.1627/JPI.47.67.

(39)   A. Aziz, M. A.; A. Jalil, A.; S. Wongsakulphasatch; N. Vo, D.-V. Understanding the Role of Surface Basic Sites of Catalysts in CO 2 Activation in Dry Reforming of Methane: A Short Review. *Catal. Sci. Technol.* **2020**, *10* (1), 35–45. https://doi.org/10.1039/C9CY01519A.

(40)   Polo-Garzon, F.; Wu, Z. Acid–Base Catalysis over Perovskites: A Review. *J. Mater. Chem. A* **2018**, *6* (7), 2877–2894. https://doi.org/10.1039/C7TA10591F.

(41)   Lee, Y.-L.; Kleis, J.; Rossmeisl, J.; Shao-Horn, Y.; Morgan, D. Prediction of Solid Oxide Fuel Cell Cathode Activity with First-Principles Descriptors. *Energy Environ. Sci.* **2011**, *4* (10), 3966–3970. https://doi.org/10.1039/C1EE02032C.

(42)   Livia Giordano, Karthik Akkiraju, Ryan Jacobs, Daniele Vivona, Dane Morgan, Y. S.-H. Electronic Structure-Based Descriptors for Oxide Properties and Functions. *Under Review*.

(43)   Grimaud, A.; Diaz-Morales, O.; Han, B.; Hong, W. T.; Lee, Y.-L.; Giordano, L.; Stoerzinger, K. A.; Koper, M. T. M.; Shao-Horn, Y. Activating Lattice Oxygen Redox Reactions in Metal Oxides to Catalyse Oxygen Evolution. *Nat. Chem.* **2017**, *9* (5), 457–465. https://doi.org/10.1038/nchem.2695.

(44)   Hong, W. T.; Stoerzinger, K. A.; Lee, Y.-L.; Giordano, L.; Grimaud, A.; Johnson, A. M.; Hwang, J.; Crumlin, E. J.; Yang, W.; Shao-Horn, Y. Charge-Transfer-Energy-Dependent Oxygen Evolution Reaction Mechanisms for Perovskite Oxides. *Energy Environ. Sci.* **2017**, *10* (10), 2190–2200. https://doi.org/10.1039/C7EE02052J.

(45)   Kuznetsov, D. A.; Han, B.; Yu, Y.; Rao, R. R.; Hwang, J.; Román-Leshkov, Y.; Shao-Horn, Y. Tuning Redox Transitions via Inductive Effect in Metal Oxides and Complexes, and Implications in Oxygen Electrocatalysis. *Joule* **2018**, *2* (2), 225–244. https://doi.org/10.1016/J.JOULE.2017.11.014.

(46)   Giordano, L.; Østergaard, T. M.; Muy, S.; Yu, Y.; Charles, N.; Kim, S.; Zhang, Y.; Maglia, F.; Jung, R.; Lund, I.; Rossmeisl, J.; Shao-Horn, Y. Ligand-Dependent Energetics for Dehydrogenation: Implications in Li-Ion Battery Electrolyte Stability and Selective Oxidation Catalysis of Hydrogen-Containing Molecules. *Chem. Mater.* **2019**, *31* (15), 5464–5474. https://doi.org/10.1021/acs.chemmater.9b00767.

(47)   Hwang, J.; Rao, R. R.; Katayama, Y.; Lee, D.; Wang, X. R.; Crumlin, E.; Venkatesan, T.; Lee, H. N.; Shao-Horn, Y. CO$_2$ Reactivity on Cobalt-Based Perovskites. *J. Phys. Chem. C* **2018**, acs.jpcc.8b06104. https://doi.org/10.1021/acs.jpcc.8b06104.

(48)   Hwang, J.; Akkiraju, K.; Corchado-García, J.; Shao-Horn, Y. A Perovskite Electronic Structure Descriptor for Electrochemical CO2 Reduction and the Competing H2 Evolution Reaction. *J. Phys. Chem. C* **2019**, *123* (40). https://doi.org/10.1021/acs.jpcc.9b04120.

(49)   Choksi, T.; Greeley, J. Partial Oxidation of Methanol on MoO3 (010): A DFT and Microkinetic Study. *ACS Catal.* **2016**, *6* (11), 7260–7277. https://doi.org/10.1021/acscatal.6b01633.

(50)   R. Sánchez de Armas; J. Oviedo, *; M. A. San Miguel, and; Sanz, J. F. Methanol Adsorption and Dissociation on TiO2(110) from First Principles Calculations. *J. Phys. Chem. C* **2007**, *111* (27), 10023–10028. https://doi.org/10.1021/JP0717701.

(51)   Beste, A.; Mullins, D. R.; Overbury, S. H.; Harrison, R. J. Adsorption and Dissociation of Methanol on the Fully Oxidized and Partially Reduced (1 1 1) Cerium Oxide Surface: Dependence on the Configuration of the Cerium 4f Electrons. *Surf. Sci.* **2008**, *602* (1), 162–175. https://doi.org/10.1016/J.SUSC.2007.10.024.

(52)   Li, Y.; Cheng, W.; Sui, Z. J.; Zhou, X. G.; Chen, D.; Yuan, W. K.; Zhu, Y. A. Origin of Chemisorption Energy Scaling Relations over Perovskite Surfaces. *J. Phys. Chem. C* **2019**, *123* (46), 28275–28283. https://doi.org/10.1021/acs.jpcc.9b08741.

(53)   Gao, R.; Fernandez, A.; Chakraborty, T.; Luo, A.; Pesquera, D.; Das, S.; Velarde, G.; Thoréton, V.; Kilner, J.; Ishihara, T.; Nemšák, S.; Crumlin, E. J.; Ertekin, E.; Martin, L. W. Correlating Surface Crystal Orientation and Gas Kinetics in Perovskite Oxide Electrodes. *Adv. Mater.* **2021**, *33* (20), 2100977. https://doi.org/10.1002/ADMA.202100977.

(54)   Crumlin, E. J.; Mutoro, E.; Liu, Z.; Grass, M. E.; Biegalski, M. D.; Lee, Y.-L.; Morgan, D.; Christen, H. M.; Bluhm, H.; Shao-Horn, Y. Surface Strontium Enrichment on Highly Active Perovskites for Oxygen Electrocatalysis in Solid Oxide Fuel Cells. *Energy Environ. Sci.* **2012**, *5* (3), 6081–6088. https://doi.org/10.1039/C2EE03397F.

(55)   Trotochaud, L.; Head, A. R.; Büchner, C.; Yu, Y.; Karslıoğlu, O.; Tsyshevsky, R.; Holdren, S.; Eichhorn, B.; Kuklja, M. M.; Bluhm, H. Room Temperature Decomposition of Dimethyl Methylphosphonate on Cuprous Oxide Yields Atomic Phosphorus. *Surf. Sci.* **2019**, *680*, 75–87. https://doi.org/10.1016/j.susc.2018.10.003.

(56)   Comini, N.; Huthwelker, T.; Diulus, J. T.; Osterwalder, J.; Novotny, Z. Factors Influencing Surface Carbon Contamination in Ambient-Pressure x-Ray Photoelectron Spectroscopy Experiments. *J. Vac. Sci. Technol. A Vacuum, Surfaces, Film.* **2021**, *39* (4), 043203. https://doi.org/10.1116/6.0001013.

(57)   Stoerzinger, K. A.; Hong, W. T.; Azimi, G.; Giordano, L.; Lee, Y. L.; Crumlin, E. J.; Biegalski, M. D.; Bluhm, H.; Varanasi, K. K.; Shao-Horn, Y. Reactivity of Perovskites with Water: Role of Hydroxylation in Wetting and Implications for Oxygen Electrocatalysis. *J. Phys. Chem. C* **2015**, *119* (32), 18504–18512. https://doi.org/10.1021/acs.jpcc.5b06621.

(58)   Domingo, N.; Pach, E.; Cordero-Edwards, K.; Pérez-Dieste, V.; Escudero, C.; Verdaguer, A. Water Adsorption, Dissociation and Oxidation on SrTiO3 and Ferroelectric Surfaces Revealed by Ambient Pressure X-Ray Photoelectron Spectroscopy. *Phys. Chem. Chem. Phys.* **2019**, *21* (9), 4920–4930. https://doi.org/10.1039/c8cp07632d.

(59)   Prosvirin, I. P.; Bukhtiyarov, A. V.; Bluhm, H.; Bukhtiyarov, V. I. Application of near Ambient Pressure Gas-Phase X-Ray Photoelectron Spectroscopy to the Investigation of Catalytic Properties of Copper in Methanol Oxidation. *Appl. Surf. Sci.* **2016**, *363*, 303–309. https://doi.org/10.1016/J.APSUSC.2015.11.258.

(60)   Gamba, O.; Hulva, J.; Pavelec, J.; Bliem, R.; Schmid, M.; Diebold, U.; Parkinson, G. S. The Role of Surface Defects in the Adsorption of Methanol on Fe3O4(001). *Top. Catal. 2016 606* **2016**, *60* (6), 420–430. https://doi.org/10.1007/S11244-016-0713-9.

(61)   Hong, W. T.; Stoerzinger, K. A.; Crumlin, E. J.; Mutoro, E.; Jeen, H.; Lee, H. N.; Shao-Horn, Y. Near-Ambient Pressure XPS of Higherature Surface Chemistry in Sr2Co2O5 Thin Films. *Top. Catal.* **2016**, *59* (5–7), 574–582. https://doi.org/10.1007/S11244-015-0532-4/FIGURES/6.

(62)   Opitz, A. K.; Rameshan, C.; Kubicek, M.; Rupp, G. M.; Nenning, A.; Götsch, T.; Blume, R.; Hävecker, M.; Knop-Gericke, A.; Rupprechter, G.; Klötzer, B.; Fleig, J. The Chemical Evolution of the La0.6Sr0.4CoO3−Δ Surface Under SOFC Operating Conditions and Its Implications for Electrochemical Oxygen Exchange Activity. *Top. Catal.* **2018**, *61* (20), 2129–2141. https://doi.org/10.1007/S11244-018-1068-1/FIGURES/10.

(63)   Kozokaro, V. F.; Addo, P. K.; Ansari, H. M.; Birss, V. I.; Toroker, M. C. Optimal Oxygen Vacancy Concentration for CO2 Reduction in LSFCr Perovskite: A Combined Density Functional Theory and Thermogravimetric Analysis Measurement Study. *J. Phys. Chem. C* **2020**, *124* (50), 27453–27466. https://doi.org/10.1021/ACS.JPCC.0C07097.

(64)   Beuhler, R. J.; Rao, R. M.; Hrbek, J.; White, M. G. Study of the Partial Oxidation of Methanol to Formaldehyde on a Polycrystalline Ag Foil. *J. Phys. Chem. B* **2001**, *105* (25), 5950–5956. https://doi.org/10.1021/jp010134e.

(65)   Zhang, X.; Yan, P.; Xu, J.; Li, F.; Herold, F.; Etzold, B. J. M.; Wang, P.; Su, D. S.; Lin, S.; Qi, W.; Xie, Z. Methanol Conversion on Borocarbonitride Catalysts: Identification and Quantification of Active Sites. *Sci. Adv.* **2020**, *6* (26), 5778–5802. https://doi.org/10.1126/sciadv.aba5778.

(66)   Deshmukh, S. A. R. K.; Van Sint Annaland, M.; Kuipers, J. A. M. Kinetics of the Partial Oxidation of Methanol over a Fe-Mo Catalyst. *Appl. Catal. A Gen.* **2005**, *289* (2), 240–255. https://doi.org/10.1016/j.apcata.2005.05.005.

(67)   Soares, A. P. V.; Portela, M. F.; Kiennemann, A. Kinetics of the Main and Side Reactions of the Methanol Oxidation over Iron Molybdates. In *Studies in Surface Science and Catalysis*; Elsevier Inc., 2001; Vol. 133, pp 489–494. https://doi.org/10.1016/s0167-2991(01)82000-0.

(68)   Chung, J. S.; Miranda, R.; Bennett, C. O. Mechanism of Partial Oxidation of Methanol over MoO3. *J. Catal.* **1988**, *114* (2), 398–410. https://doi.org/10.1016/0021-9517(88)90043-7.

(69)   Tu, W.; Chin, Y. H. Catalytic Consequences of Chemisorbed Oxygen during Methanol Oxidative Dehydrogenation on Pd Clusters. *ACS Catal.* **2015**, *5* (6), 3375–3386. https://doi.org/10.1021/acscatal.5b00068.

(70)   Latimer, A. A.; Abild-Pedersen, F.; Nørskov, J. K. `. *ACS Catal.* **2017**, *7* (7), 4527–4534. https://doi.org/10.1021/acscatal.7b01417.

(71)   Vining, W. C.; Strunk, J.; Bell, A. T. Investigation of the Structure and Activity of VOx/CeO2/SiO2 Catalysts for Methanol Oxidation to Formaldehyde. *J. Catal.* **2012**, *285* (1), 160–167. https://doi.org/10.1016/J.JCAT.2011.09.024.

(72)   and, J. L. B.; Bell*, A. T. Mechanistic Studies of Methanol Oxidation to Formaldehyde on Isolated Vanadate Sites Supported on MCM-48. *J. Phys. Chem. C* **2006**, *111* (1), 420–430. https://doi.org/10.1021/JP0653149.

(73)   Pala, R. G. S.; Metiu, H. Selective Promotion of Different Modes of Methanol Adsorption via the Cation Substitutional Doping of a ZnO(101¯0) Surface. *J. Catal.* **2008**, *254* (2), 325–331. https://doi.org/10.1016/J.JCAT.2008.01.014.

(74)   González-Navarrete, P.; Gracia, L.; Calatayud, M.; Andrés, J. Unraveling the Mechanisms of the Selective Oxidation of Methanol to Formaldehyde in Vanadia Supported on Titania Catalyst. *J. Phys. Chem. C* **2010**, *114* (13), 6039–6046. https://doi.org/10.1021/JP911528Q.

(75)   Kropp, T.; Paier, J.; Sauer, J. Support Effect in Oxide Catalysis: Methanol Oxidation on Vanadia/Ceria. *J. Am. Chem. Soc.* **2014**, *136* (41), 14616–14625. https://doi.org/10.1021/JA508657C.

(76)   Kresse, G.; Furthmüller, J. Efficiency of Ab-Initio Total Energy Calculations for Metals and Semiconductors Using a Plane-Wave Basis Set. *Comput. Mater. Sci.* **1996**, *6* (1), 15–50. https://doi.org/10.1016/0927-0256(96)00008-0.

(77)   Kresse, G.; Hafner, J. *Ab Initio* Molecular Dynamics for Liquid Metals. *Phys. Rev. B* **1993**, *47* (1), 558–561. https://doi.org/10.1103/PhysRevB.47.558.

(78)   Dudarev, S. L.; Botton, G. A.; Savrasov, S. Y.; Humphreys, C. J.; Sutton, A. P. Electron-Energy-Loss Spectra and the Structural Stability of Nickel Oxide: An LSDA U Study. *Phys. Rev. B* **1998**, *57* (3), 1505. https://doi.org/10.1103/PhysRevB.57.1505.

(79)   Wang, L.; Maxisch, T.; Ceder, G. Oxidation Energies of Transition Metal Oxides within the <span Class. *Phys. Rev. B* **2006**, *73* (19), 195107. https://doi.org/10.1103/PhysRevB.73.195107.

(80)   Lee, Y.-L.; Kleis, J.; Rossmeisl, J.; Morgan, D. Ab Initio Energetics of LaBO3(001) (B=Mn,Fe,CO, and Ni) for Solid Oxide Fuel Cell Cathodes. *Phys. Rev. B* **2009**, *80* (22), 224101. https://doi.org/10.1103/PhysRevB.80.224101.

(81)   Balachandran, D.; Morgan, D.; Ceder, G. First Principles Study of H-Insertion in MnO2. *J. Solid State Chem.* **2002**, *166* (1), 91–103. https://doi.org/10.1006/jssc.2002.9564.

(82)   Stoerzinger, K. A.; Hong, W. T.; Azimi, G.; Giordano, L.; Lee, Y.-L.; Crumlin, E. J.; Biegalski, M. D.; Bluhm, H.; Varanasi, K. K.; Shao-Horn, Y. Reactivity of Perovskites with Water: Role of Hydroxylation in Wetting and Implications for Oxygen Electrocatalysis. *J. Phys. Chem. C* **2015**, *119* (32), 18504–18512. https://doi.org/10.1021/ACS.JPCC.5B06621.

(83)   NIST-JANAF Thermochemical Tables https://janaf.nist.gov/ (accessed Sep 13, 2021).

(84)   Towns, J.; Cockerill, T.; Dahan, M.; Foster, I.; Gaither, K.; Grimshaw, A.; Hazlewood, V.; Lathrop, S.; Lifka, D.; Peterson, G. D.; Roskies, R.; Scott, J. R.; Wilkens-Diehr, N. XSEDE: Accelerating Scientific Discovery. *Comput. Sci. Eng.* **2014**, *16* (5), 62–74. https://doi.org/10.1109/MCSE.2014.80.

Chapter. 6 Regulating oxygen activity of perovskites to promote activity and selectivity during propane oxidative dehydrogenation

6.1 Introduction

Alkanes such as methane, ethane, and propane constitute a major component of natural gas and are routinely converted to value-added products in the chemical industry. Specifically, in the petrochemical industry, propylene generated from propane is used in the synthesis of polypropylene, acrylonitrile, acrylic acid, cumene, and propylene oxide.[1] Typically, platinum-based catalysts have been used for the commercial production of propylene and hydrogen via dehydrogenation (DH) of propane.[2] However, widespread usage of this method is limited due to the endothermic nature of the reaction requiring high operating temperature. More recently, catalytic oxidative dehydrogenation (ODH) of propane to propene has become more popular due to the lower operating temperature and the exothermic nature of the reaction.[1] Vanadium and molybdenum-based catalysts have been studied for propane ODH reaction to understand the role of size of the catalyst cluster,[3] nature of support and alkali metal additions.[4] Further, *in situ* DRIFTS measurements have revealed the formation of oxygenated reaction intermediates[5] but structure-activity relationships via the understanding of the reaction mechanism have been limited.[6]

Perovskites (ABO$_3$) with tuneable physio-chemical properties, have been extensively investigated to develop structure-activity relationships through an understanding of the reaction mechanism. For example, electronic structure parameters such as e$_g$ occupancy,[7] d electron count,[8] charge-transfer energy,[9] and O $2p$-band centre[10] have been shown to correlated with catalytic activity metrics. More recently, the O $2p$-band centre descriptor has been used to not only describe relevant material properties such as oxygen vacancy formation energy,[11] surface basicity,[12] oxygen diffusion coefficients,[13] and work function but adsorption energies of important reaction intermediates such as O, OH, CO$_2$. These results suggest that the O $2p$-band descriptor based approach can be used to describe selective oxidation kinetics.

In this study, we show the role of surface oxygen sites in catalyzing the C$_3$H$_8$ oxidation to C$_3$H$_6$ with oxides having higher surface oxygen activity for ABO$_3$ perovskites demonstrating higher propene formation rate. We employ tunable surface electronic structure of ABO$_3$-type perovskites to control surface oxygen vacancy formation energy, where TM substitution from Cr to Ni shifts the O $2p$ states closer to the Fermi level. Our DFT results show that C$_3$H$_8$ adsorbs more strongly

via C-H bond scission on the oxygen sites, where binding strength is dependent on the surface electronic structure of perovskites, specifically the O $2p$-band center relative to the Fermi level. We further show that the adsorption energy of reaction intermediates trends with the O 2p-band center descriptor, and the rate-limiting step changes from dehydrogenation of C_3H_7 to desorption of H_2O and O_2 adsorption on the surface oxygen sites. Oxides with higher surface O $2p$-band center such as Bi-SrCoO$_3$ and La$_{0.6}$Sr$_{0.4}$CoO$_3$ were shown to have the highest C_3H_6 formation rate.

6.2 Trends in adsorption energetics of reaction intermediates for C_3H_8 ODH reaction

We propose a reaction scheme for propane ODH to propene on oxide catalyst in based on previously described MvK-type reaction mechanisms on oxide catalysts, (Fig. 1A), occurring on the surface oxygen site via terminal C-H bond scission of C_3H_8 to form C_3H_7-O$_{oxide}$ (Step 1), followed by dehydrogenation of C_3H_7-O$_{oxide}$ to C_3H_6-O$_{oxide}$ (Step 2), desorption of C_3H_6-O$_{oxide}$ as C_3H_6 (Step 3) and finally, oxygen re-fadsorption leading to H_2O desorption to complete the reaction cycle (Step 4). First, we first show that C_3H_8 can dissociatively adsorb either via terminal (Fig. A.5.1A) or allylic C-H (Fig. A.5.1B) bond scission on the surface oxygen sites of both AO-(100) and BO$_2$-(100) termination of ABO_3–type perovskites. For both the reaction configurations (Fig. 1A and Fig. A.5.2A), transition metal substitution on the B-site was found to greatly increase the dissociative adsorption energetics of C_3H_8 (BO_2+ C_3H_8 → B-C_3H_7-O$_{oxide}$ + H-O$_{oxide}$) on the surface oxygen of perovskites, which was correlated with moving the Fermi level closer to the surface O $2p$-band center (red, Fig. 1B and light red, Fig. A.5.2B). Moreover, the dissociative adsorption energetics via terminal and allylic C-H bond dissociation were found to be comparable suggesting that both reaction pathways can simultaneously occur. The trend of more favorable C_3H_8 dehydrogenation energy with O $2p$-band center moving closer to the Fermi level also follows the trend of increasing hydrogen adsorption energy with the O $2p$-band center moving closer to the Fermi level (blue, Fig. A.5.3A), and is consistent with previous adsorption trends on perovskite and layered oxides. Second, the dehydrogenation energy of B-C_3H_7-O$_{oxide}$ to form B-C_3H_6-O$_{oxide}$ (B-C_3H_7-O$_{oxide + }$H-O$_{oxide}$ → B-C_3H_6-O$_{oxide}$ + 2H-O$_{oxide}$) also correlated with

moving the Fermi level closer to the surface O $2p$-band center (green in Fig. 1C, light green in Fig. A.5.2C) while being more favorable for the BO_2-terminated perovskite surfaces compared to the AO-terminated surfaces. Also, a similar trend was observed for the direct dehydrogenation of C_3H_8 via 2 C-H terminal (Fig. A.5.3B) or allylic bond scissions ($BO_2 + C_3H_8 \rightarrow B$-$C_3H_6$-$O_{oxide} + 2H$-$O_{oxide}$) to from B-C_3H_6-O_{oxide}. Third, desorption of C_3H_6 from B-C_3H_6-O_{oxide} (B-C_3H_6-$O_{oxide} + 2H$-$O_{oxide} \rightarrow BO_{2oxide} + C_3H_6 + 2H$-$O_{oxide}$) showed a weaker trend as a function of the O $2p$-band center propene desorption becoming less favorable with moving the Fermi level closer to the surface O $2p$-band center (blue in Fig. 1D and light blue in Fig. A.5.2D). Fourth, we considered the recovery of the stoichiometric surface via conversion of adsorbed hydroxyls ($2H$-O_{oxide}) to H_2O after oxygen adsorption ($2H$-$O_{oxide} + 0.5O_2 \rightarrow BO_2 + H_2O$), and the reaction energetics become less favorable as the O $2p$-band center moves closer to the Fermi level (orange in Fig. 1E and light orange in Fig. A.5.2E). We also considered a two-step pathway for the removal of surface hydroxyl via oxygen vacancy formation (Fig. A.5.4A). Herein, a clear trend was not observed for H_2O desorption ($2H$-$O_{oxide} \rightarrow O_{vac} + H_2O$, Fig. A.5.3B), while oxygen vacancy re-filling energy was found to decrease (Fig. A.5.3C) as a function of the O $2p$-band relative to the Fermi level. As the trends in the adsorption energies are dictated by the position of the surface O-$2p$ band center relative to the Fermi level, we next considered the co-adsorption of water to understand the adsorption energy trends under wet reaction conditions.
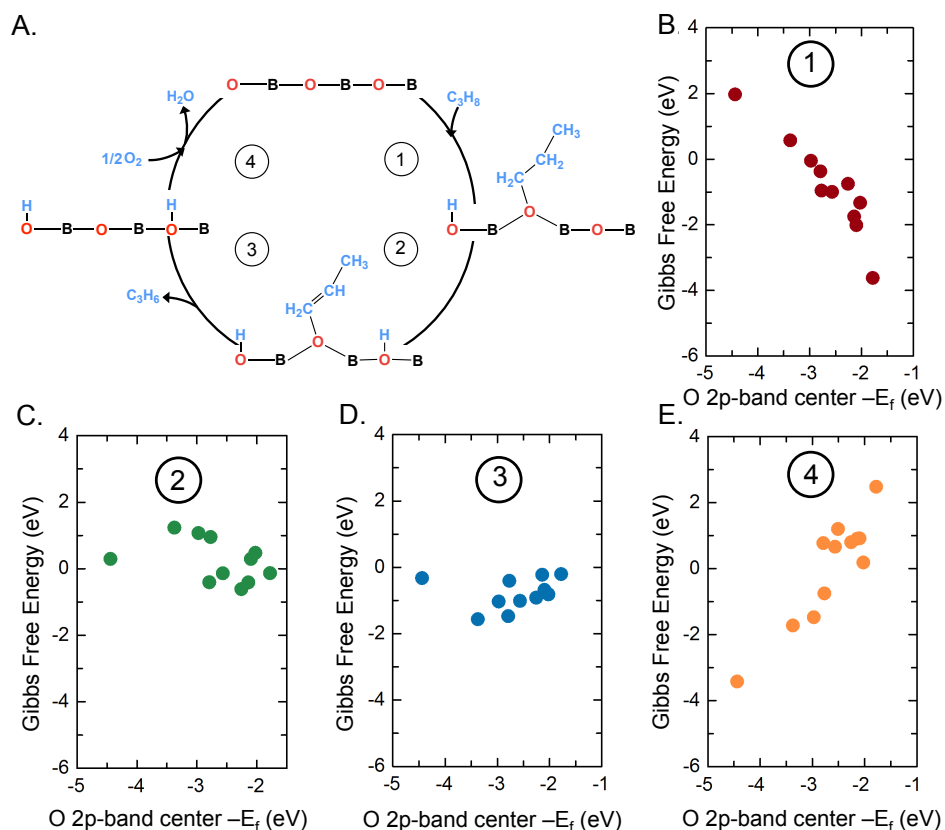
Figure 1: Reaction mechanism for selective propene generation under dry conditions. *A)
Proposed reaction mechanism for C_3H_8 selective oxidation to C_3H_6 occurring on the surface
oxygen site via terminal C-H bond scission of C_3H_8 to form C_3H_7-O_{oxide} and O_{oxide}-H (Step 1),
followed by dehydrogenation of C_3H_7-O_{oxide} to C_3H_6-O_{oxide} and O_{oxide}-H (Step 2), desorption of
C_3H_6-O_{oxide} as C_3H_6 (Step 3), oxygen re-adsorption leading to H_2O desorption to complete the
reaction cycle (Step 4), B) Correlation between first dehydrogenation adsorption energy of C_3H_8
on the surface oxygen surface site (C_3H_7-O_{oxide}, red), C) dehydrogenation adsorption energy of
C_3H_8 on the surface oxygen surface site (C_3H_6-O_{oxide}, green), D) C_3H_6 desorption energy from
the C_3H_6-O_{oxide} adsorbed on surface oxygen sites (blue), E) oxygen adsorption and H_2O
desorption energy from the 2H-O_{oxide} adsorbed on surface oxygen sites (orange), as a function of
the surface O 2p-band center relative to the Fermi level for ABO_3 perovskites. Data points were
obtained from the AO and BO_2-terminated-(100) surface of ABO_3 (A = La, Sm; B = Cr, Co, Mn,
Fe, and Ni), calculated by DFT with the binding configurations C_3H_8 on the surface oxygen sites
with reference to C_3H_8 and O_2 in the gas phase (T = 300 °C)*

Next, we considered the reaction mechanism for selective propene formation under wet

conditions (Fig. 2A). Herein, H_2O dissociatively adsorbs on the surface oxygen and metal sites

(Step 1), followed up C_3H_8 adsorption to form C_3H_7-O_{oxide} and O_{oxide}-H in the presence of

dissociated water (Step 2), dehydrogenation of C_3H_7-O_{oxide} to C_3H_6-O_{oxide} and O_{oxide}-H (Step 3),

desorption of C_3H_6-O_{oxide} as C_3H_6 (Step 4), and oxygen adsorption to form H_2O (Step 5) to complete the reaction cycle. We did not consider molecular adsorption of H_2O as previous in situ AP-XPS showed higher coverage of OH species during propane oxidation on $LaMnO_3$. First, dissociation energy of H_2O (BO_2 +H2O → B-OH + H-O_{oxide}) and hydroxyl formation energy (computed using ΔG(H_2O)- ΔG(H)) was found to have decreasing adsorption energy as a function of the O $2p$-band center relative to the Fermi level (Fig. 2B) consistent with previous trends on ABO_3 perovskites. Second, C_3H_8 dissociatively adsorbs on the surface oxygen site via terminal C-H bond scission adjacent to the dissociated water sites (red, Fig. 2A) and a trend of increasing adsorption energy with the surface O $2p$-band center moving closer to the Fermi level similar to the trend seen in the absence of H_2O (red, Fig. 1B). Herein too, the adsorption energy was also found to correlate with the adsorption of hydrogen in the presence of dissociated water (Fig. A.5.3A). The adsorption energy for C_3H_8 in the presence of the dissociated H_2O was found to be similar to the adsorption energy without dissociated water. Interestingly, the dissociative co-adsorption of C_3H_8 and H_2O (BO_2+ C_3H_8 +H_2O → B-C_3H_7-O_{oxide} + OH-B + 2H-O_{oxide}) was found to be more favorable compared to the dissociative adsorption of C_3H_8 without H_2O. (Fig. A.5.5) Third, dehydrogenation energy of C_3H_7-O_{oxide} to form C_3H_6-O_{oxide} and H-O_{oxide}, was found to increase with increasing O $2p$-band center closer to the Fermi level (blue, Fig. 2D). Next, the desorption of C_3H_6 showed a weaker trend as a function of the O $2p$-band center propene desorption becoming less favorable with moving the Fermi level closer to the surface O $2p$-band center (blue, Fig. 2E). Finally, we considered the recovery of the stoichiometric surface via conversion of adsorbed hydroxyls (OH-B and 3H-O_{oxide}) to 2H_2O after oxygen adsorption (2H-O_{oxide} + OH-B + O_2 → BO_2 + 2H_2O), and the reaction energetics become less favorable as the O $2p$-band center moves closer to the Fermi level (orange, Fig. 2F). We also considered a two-step pathway for the removal of surface hydroxyl via oxygen vacancy formation (Fig. A.5.6A) Herein, H_2O desorption (2H-O_{oxide} → O_{vac} + H_2O, Fig. A.5.6B), while oxygen vacancy re-filling energy in the presence of dissociated water (OH-B +H-O_{oxide} + O_{vac} → BO_2), was found to decrease (Fig. A.5.6C) as a function of the O $2p$-band relative to the Fermi level (Fig. A.5.6C). Therefore, Gibbs free energy of adsorption of C_3H_8, formation of C_3H_6, H_2O, and adsorption of O_2 are dictated by the position of the O $2p$-band center relative to the Fermi level for the dry and wet reaction condition. Next, we investigated the trends in reaction kinetics for C_3H_8 to C_3H_6 and CO_2 conversion for ABO_3-type perovskites for using plug flow reactor measurements.
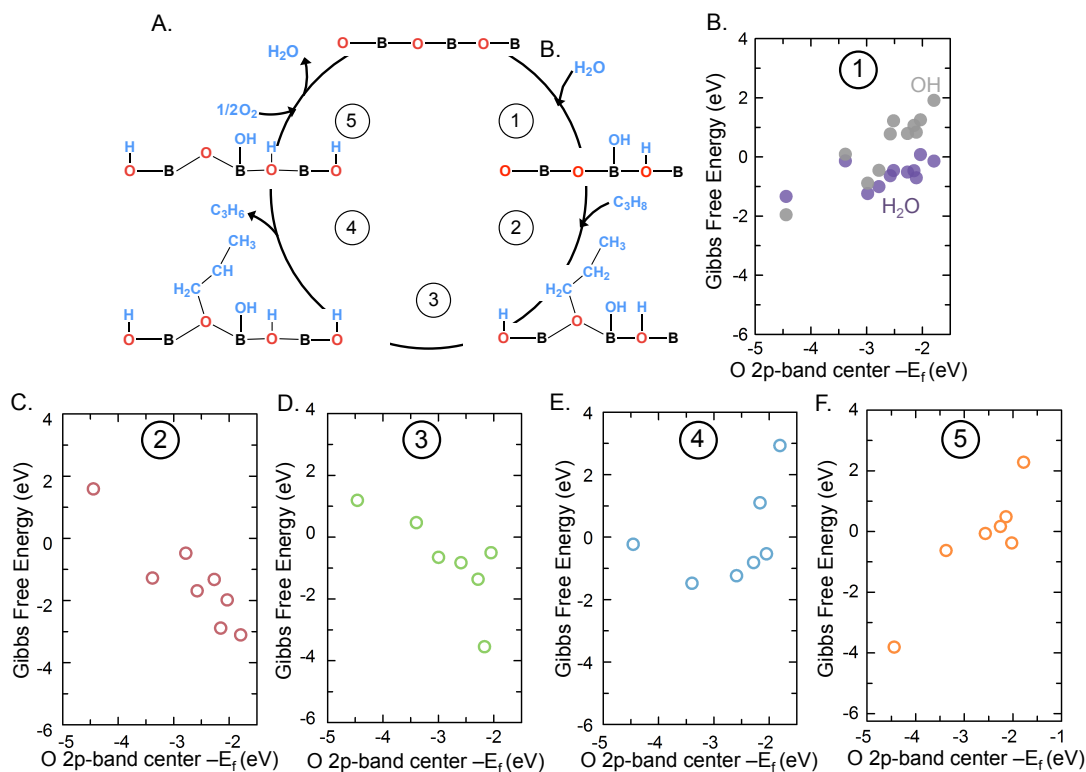
Figure 2: Reaction mechanism for selective propene generation under wet conditions A) *Proposed reaction mechanism for C_3H_8 selective oxidation to C_3H_6 occurring on the oxygen sites via terminal C-H bond scission with dissociative H_2O adsorption (Step 1), followed up C_3H_8 adsorption to form C_3H_7-O_{oxide} and O_{oxide}-H in the presence of dissociated water (Step 2), followed by dehydrogenation of C_3H_7-O_{oxide} to C_3H_6-O_{oxide} and O_{oxide}-H (Step 3) and desorption of C_3H_6-O_{oxide} as C_3H_6 (Step 4). Following desorption of C_3H_6, oxygen adsorption occurs to H_2O desorption to complete the reaction cycle (Step 5), Correlation between B) H_2O dissociation (purple) and OH (grey) formation energy, C) first dehydrogenation adsorption energy of C_3H_8 on the oxygen surface site (C_3H_7-O_{oxide}, red), D) second dehydrogenation adsorption energy of C_3H_8 on the surface oxygen site (C_3H_6-O_{oxide}, green), E) C_3H_6 desorption energy from the C_3H_6-O_{oxide} surface oxygen sites (blue), F) oxygen adsorption and H_2O desorption energy from the O_{oxide}-H surface sites (orange), as a function of the surface O 2p-band center relative to the Fermi level. Data points were obtained from the AO and BO_2-terminated-(100) surface of ABO_3 (A = La, Sm; B = Cr, Co, Mn, Fe, Ni) with respect to the AO and BO_2 surface and C_3H_8 and O_2 in the gas phase (T = 300 °C)*

6.3 Role of surface oxygen activity for conversion of C_3H_8 to C_3H_6 and CO_2

We next examined the catalytic activity of C_3H_8 conversion to C_3H_6 and CO_2 under both dry (5 C_3H_8/10O_2/85N_2) and wet (5C_3H_8/10O_2/4H_2O/85N_2) reaction conditions on ABO_3 perovskite powder (A = La, Sm; B = Cr, Co, Mn, Fe, Ni). First, we note that under dry conditions, C_3H_6 and CO_2 formation rates were seen to correlate with C_3H_8 consumption rate (Fig. 3A) suggesting that

similar reaction sites are responsible for C_3H_6 and CO_2 formation. Moreover, the same trend was seen for the reaction rates under wet conditions (Fig. 3A) although all the reaction rates were found to be lower under wet conditions when compared to the dry conditions which can be attributed to the site poisoning due to stronger adsorption energetics in the co-adsorbed case (Fig. A.5.5). Next, we observed that C_3H_6 (Fig. 3C) and CO_2 (Fig. 3D) formation rate increased with the O 2p-band center with a range of three orders of magnitude. The trend was much stronger for the propene generation compared to the CO_2 generation and propane consumption rates. Based on this observation, we predict that oxides with surface O 2p-band closer to the Fermi level to have higher C_3H_6 formation rate. We verified this prediction by showing that Bi-SrCoO$_3$ and Ba$_{0.5}$Sr$_{0.5}$Co$_{0.8}$Fe$_{0.2}$O$_{3-\delta}$ (BSCF) have relatively higher C_3H_6 formation rate (Fig. 3C) Interestingly, similar trends of increasing reaction rates was observed with C_3H_8 dehydrogenation energy (Fig. A.5.7), charge transfer energy (Fig. A.5.8), oxygen vacancy re-filling energy (Fig. A.5.9), while a M-type trend was observed with the number of TM d electrons. (Fig. A.5.10)
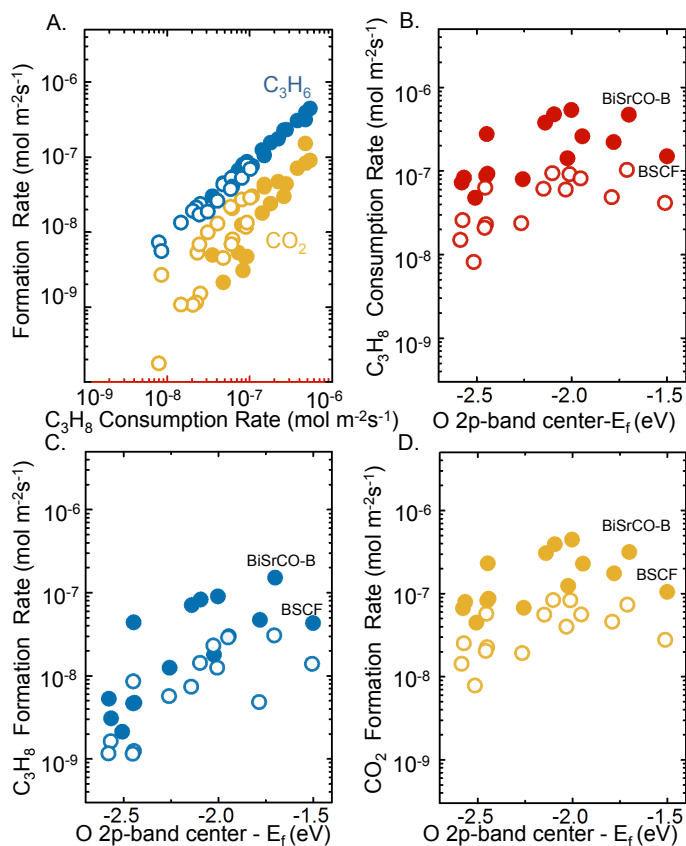
Figure 3: Reaction kinetics for C_3H_8 conversion to C_3H_6 and CO_2. *A) Surface-area normalized*

C₃H₆ and CO₂ formation rate (mol m² s⁻¹) shown as a function of C₃H₈ consumption rate under wet (unfilled) and dry (filled) reaction conditions for ABO₃ perovskites series conducted in a flow reactor, B) Surface-area normalized C₃H₈ consumption rate (mol m² s⁻¹), C) Surface-area normalized C₃H₆ formation rate (mol m² s⁻¹), D) Surface-area normalized CO₂ formation rate (mol m² s⁻¹) under wet (unfilled) and dry (filled) reaction conditions as function of the surface O 2p-band center, where the activity metric was chosen at T = 280 °C, obtained from the Arrhenius type fitting. Gas concentration of 5%C₃H₈-10%O₂ was used for the dry measurements while of 5%C₃H₈-10%O₂-H₂O was used for the wet measurements.

6.4 Reaction mechanism for propane ODH to propene

We rationalize the trend of increasing C_3H_6 formation rate with the O 2p-band center descriptor by understanding the reaction energetics for each of the reaction steps of the catalytic cycle in Fig. 4A. We observe that the reaction is likely to be limited by the dehydrogenation of C_3H_7 to form C_3H_6 and OH for all the oxide composition with surface oxygen 2p-band center less than -1.7 eV while for the oxides with surface O 2p-band center greater than -1.7 eV the reaction is likely to be limited by the re-generation of the stoichiometric surface via oxygen re-adsorption and water desorption. Hence, a linear trend or a weak volcano trend centered at ~1.7 eV is expected for the reaction rate as a function of the surface O 2p-band center. Further support come from the estimated activation energy which showed a decreasing energy with the O 2p-band center (Fig. 4B) for both the wet and dry reaction conditions consistent with the increase in reaction rate with the O 2p-band center moving closer to the Fermi level.
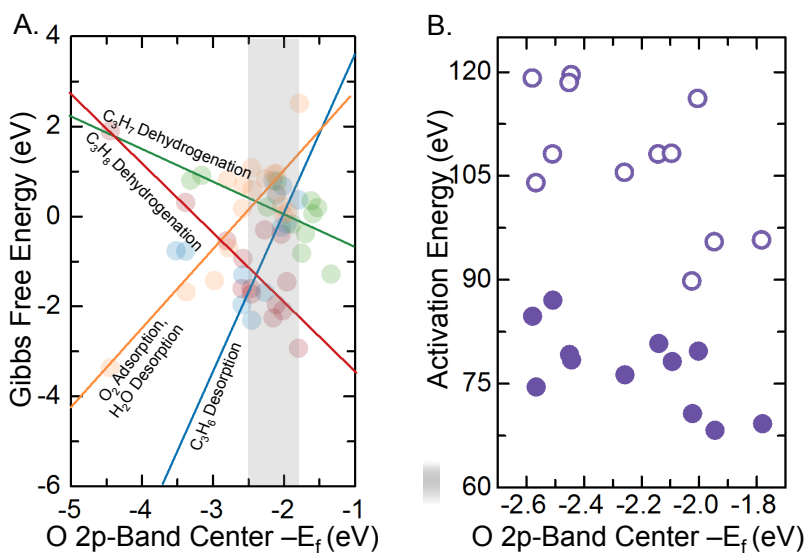
***Figure 4: Propane ODH reaction kinetics.** A) Relative Gibbs free energy trends for C_3H_6 formation from C_3H_8 and B) activation energy trends for C_3H_8 conversion to C_3H_6 and CO₂ as a*

function of the surface O 2p-band under wet (unfilled) and dry (filled) reaction conditions for ABO₃ perovskites (A = La, Sm; B = Cr, Co, Mn, Fe, Ni) series conducted in a flow reactor. Gas concentration of 5%C₃H₈-10%O₂ was used for the dry measurements while of 5%C₃H₈-10%O₂-H₂O was used for the wet measurements.

6.5 Conclusions

In this study, we undertook reactor activity measurements, and DFT studies to identify the critical role of surface oxygen vacancies for ABO_3 perovskite oxides in dictating C_3H_8 surface energetics and the kinetics of C_3H_8 selective oxidation to C_3H_6 and complete oxidation to CO_2. This study provides a critical link and scientific understanding for attempts to discover new catalyst materials through material property-activity relationships for the small carbon molecule reaction network. We identify that chemistries with high metal-oxygen covalency exhibit highest intrinsic C_3H_8 conversion for selective generation of C_3H_8 at lower temperatures compared to the commercial catalysts, where the surface O 2p-band relative to the Fermi level is neither too low (so as to limit the adsorption of C_3H_6 nor too high (limit oxygen vacancy refilling and water desorption energy from surface oxygen sites). These insights provide guiding principles for the selection of next-generation materials chemistries for catalytically complex small molecule conversion, where multiple catalytic processes have to be tuned.

6.7 Computational methods

Density functional theory (DFT) calculations were performed with the Vienna Ab-initio Simulation Package (VASP) using the Projector-Augmented plane-wave method with the Perdew-Burke-Ernzerhof Generalized Gradient Approximation (GGA) plus Hubbard U method to treat the exchange–correlation interactions, where the U value was optimized by fitting the formation enthalpies of oxides (U_{eff} = 3.3 eV for Co). Fully relaxed bulk perovskite calculations of ABO3 (A = La, Sm; B = Cr, Co, Mn, Fe, Ni) were performed with $2 \times 2 \times 2$ perovskite supercells and a ferromagnetic state is assumed to have a consistent set of magnetic structures. We considered both (001)-AO and BO₂-terminated slab model, where the AO, BO₂-terminated surface was described by a seven-layer symmetric slab constructed from the $2 \times 2 \times 2$ pseudocubic perovskite cell. The slabs were separated by a vacuum space of at least 10 Å and a $(2 \times 2 \times 1)$ k-point sampling was used for the slab models. After performing an internal relaxation of coordinates for the clean slab, the bottom two layers were then kept fixed. The

reaction intermediates where adsorbed on one side of the slab. The surface O 2*p*-band was determined by taking the centroid of the projected density of states of O 2*p* states (both occupied and unoccupied) relative to the Fermi level of surface oxygen atoms. Thermodynamic tables were used for conversion of calculated DFT adsorption energies to Gibbs free energies for gas phase species, while the zero point energies and vibrational entropy contributions of adsorbed species were estimated from vibrational analysis. The Bader charge decomposition scheme was used to estimate the charges of adsorbed species.

6.6 References

(1)   Carrero, C. A.; Schloegl, R.; Wachs, I. E.; Schomaecker, R. Critical Literature Review of the Kinetics for the Oxidative Dehydrogenation of Propane over Well-Defined Supported Vanadium Oxide Catalysts. *ACS Catal.* **2014**, *4* (10), 3357–3380. https://doi.org/10.1021/cs5003417.

(2)   Biloen, P.; Dautzenberg, F. M.; Sachtler, W. M. H. Catalytic Dehydrogenation of Propane to Propene over Platinum and Platinum-Gold Alloys. *J. Catal.* **1977**, *50* (1), 77–86. https://doi.org/10.1016/0021-9517(77)90010-0.

(3)   Rozanska, X.; Fortrie, R.; Sauer, J. Size-Dependent Catalytic Activity of Supported Vanadium Oxide Species: Oxidative Dehydrogenation of Propane. *J. Am. Chem. Soc.* **2014**, *136* (21), 7751–7761. https://doi.org/10.1021/JA503130Z/SUPPL_FILE/JA503130Z_SI_001.PDF.

(4)   Lemonidou, A. A.; Nalbandian, L.; Vasalos, I. A. Oxidative Dehydrogenation of Propane over Vanadium Oxide Based Catalysts: Effect of Support and Alkali Promoter. *Catal. Today* **2000**, *61* (1–4), 333–341. https://doi.org/10.1016/S0920-5861(00)00393-X.

(5)   Shee, D.; Deo, G. In Situ DRIFT Studies of Alkane Adsorption on Vanadia Supported Titania-Doped Catalysts. *Catal. Today* **2019**, *325*, 25–32. https://doi.org/10.1016/J.CATTOD.2018.06.003.

(6)   Dixit, M.; Kostetskyy, P.; Mpourmpakis, G. Structure–Activity Relationships in Alkane Dehydrogenation on γ-Al$_2$O$_3$: Site-Dependent Reactions. *ACS Catal.* **2018**, *8* (12), 11570–11578. https://doi.org/10.1021/acscatal.8b03484.

(7)   Suntivich, J.; May, K. J.; Gasteiger, H. A.; Goodenough, J. B.; Shao-Horn, Y. A Perovskite Oxide Optimized for Oxygen Evolution Catalysis from Molecular Orbital Principles. *Science* **2011**, *334* (6061), 1383–1385. https://doi.org/10.1126/science.1212858.

(8)   Stoerzinger, K. A.; Hong, W. T.; Azimi, G.; Giordano, L.; Lee, Y.-L.; Crumlin, E. J.; Biegalski, M. D.; Bluhm, H.; Varanasi, K. K.; Shao-Horn, Y. Reactivity of Perovskites with Water: Role of Hydroxylation in Wetting and Implications for Oxygen Electrocatalysis. *J. Phys. Chem. C* **2015**, *119* (32), 18504–18512. https://doi.org/10.1021/ACS.JPCC.5B06621.

(9)   Hong, W. T.; Stoerzinger, K. A.; Lee, Y.-L.; Giordano, L.; Grimaud, A.; Johnson, A. M.; Hwang, J.; Crumlin, E. J.; Yang, W.; Shao-Horn, Y. Charge-Transfer-Energy-Dependent Oxygen Evolution Reaction Mechanisms for Perovskite Oxides. *Energy Environ. Sci.* **2017**, *10* (10), 2190–2200. https://doi.org/10.1039/C7EE02052J.

(10)   Lee, Y.-L.; Kleis, J.; Rossmeisl, J.; Shao-Horn, Y.; Morgan, D. Prediction of Solid Oxide Fuel Cell Cathode

Activity with First-Principles Descriptors. *Energy Environ. Sci.* **2011**, *4* (10), 3966–3970. https://doi.org/10.1039/C1EE02032C.

(11)   Grimaud, A.; Diaz-Morales, O.; Han, B.; Hong, W. T.; Lee, Y.-L.; Giordano, L.; Stoerzinger, K. A.; Koper, M. T. M.; Shao-Horn, Y. Activating Lattice Oxygen Redox Reactions in Metal Oxides to Catalyse Oxygen Evolution. *Nat. Chem.* **2017**, *9* (5), 457–465. https://doi.org/10.1038/nchem.2695.

(12)   Hwang, J.; Rao, R. R.; Katayama, Y.; Lee, D.; Wang, X. R.; Crumlin, E.; Venkatesan, T.; Lee, H. N.; Shao-Horn, Y. CO$_2$ Reactivity on Cobalt-Based Perovskites. *J. Phys. Chem. C* **2018**, acs.jpcc.8b06104. https://doi.org/10.1021/acs.jpcc.8b06104.

(13)   Jacobs, R.; Hwang, J.; Shao-Horn, Y.; Morgan, D. Assessing Correlations of Perovskite Catalytic Performance with Electronic Structure Descriptors. *Chem. Mater.* **2019**, *31* (3), 785–797. https://doi.org/10.1021/acs.chemmater.8b03840.

(14)   Giordano, L.; Østergaard, T. M.; Muy, S.; Yu, Y.; Charles, N.; Kim, S.; Zhang, Y.; Maglia, F.; Jung, R.; Lund, I.; Rossmeisl, J.; Shao-Horn, Y. Ligand-Dependent Energetics for Dehydrogenation: Implications in Li-Ion Battery Electrolyte Stability and Selective Oxidation Catalysis of Hydrogen-Containing Molecules. *Chem. Mater.* **2019**, *31* (15), 5464–5474. https://doi.org/10.1021/acs.chemmater.9b00767.

(15)   Hwang, J.; Akkiraju, K.; Corchado-García, J.; Shao-Horn, Y. A Perovskite Electronic Structure Descriptor for Electrochemical CO2 Reduction and the Competing H2 Evolution Reaction. *J. Phys. Chem. C* **2019**, *123* (40). https://doi.org/10.1021/acs.jpcc.9b04120.

Chapter 7 – Summary and perspectives

7.1 Summary

This thesis explored the reactivity of C-H bond containing small molecules on oxide catalysts to study trends in overall activity and product selectivity. The theme for the thesis was to identify trends in adsorption energies of reaction intermediates to maximize activity as well as selectivity towards the desired product. We have identified reaction conditions for HCHO and CH_4 oxidation to maximize oxidation kinetics as well as predict more active catalysts for selective CH_3OH and C_3H_8 oxidation.

In chapter 2, we investigated the reaction mechanism for HCHO conversion to CO_2 under practical operating conditions for a commercial manganese oxide catalyst. We showed that the lifetime of the catalyst was prolonged under relative humidity (1.87%) and low HCHO concentration (0.5 ppm) reaction conditions. Using DRIFTS and DFT, we identified the reaction mechanism for HCHO conversion to CO_2 to proceed via carbonate, bidentate formate, and monodentate formate (direct) reaction pathways. However, there is an unanswered avenue which we have not comprehensively investigated is the catalyst deactivation after prolonged use due to the buildup of surface hydroxyl and inability to re-fill oxygen vacancies at room temperature. Hence, it is not surprising that typical industrial catalysts employ precious metal catalysts where oxygen activation is much facile at lower temperatures compared to transition metal oxides. There is need to explore catalysts with more favorable oxygen dissociation energies while also having strong C-H dehydrogenation energy as both these factors are competing.

In chapter 3, we used our learning about the reaction mechanism for HCHO oxidation from Chapter 2 to investigate a library of manganese oxides to optimize HCHO oxidation rates. Herein, we identified manganese formal valence and water content as activity descriptors for HCHO reaction by showing the reaction rate varied over 3 orders of magnitude. We also showed how the activity enhancement in due to the presence of surface hydroxyls by studying the reaction intermediates using DRIFTS. An interesting aspect that we have not comprehensively investigated is the role of water in the gas steam in alerting the reaction kinetics as we had studied in Chapter 2.

In chapter 4, we investigated the dehydrogenation the stronger C-H bond of methane to lower the temperature for methane oxidation to CO_2 as well as the selective methanol oxidation using iridium oxide catalysts. Herein, we were able to identify the CUS species of IrO_2 as the active surfaces species for low temperature oxidation of both HCHO and CH_3OH using AP-XPS and DFT. We further leveraged this conclusion to achieve room temperature CH_4 oxidation to CO_2 as well as increase the selectivity towards methyl formate during CH_3OH oxidation using catalyst with higher CUS species. An interesting extension of this research would be the investigation of room temperature selective CH_4 oxidation to CH_3OH instead of CO_2 by lowering the catalytic activity using iridium oxide clusters or a composite of iridium oxide and a lesser active catalyst.

In chapter 5, we improve upon the descriptor approach for selective CH_3OH oxidation developed in chapter 4 by developing a robust descriptor approach using a larger family of inexpensive perovskite catalysts. Here, using a combined AP-XPS, DFT, and reactor studies we showed that catalysts with intermediate O $2p$-band center relative to the Fermi level showed the highest selectivity towards HCHO. We identified methoxy species adsorbed on surface oxygen vacancy sites as the active reaction intermediate whose coverage correlated with the HCHO selectivity and developed a DFT-micro-kinetic model to explain the trends in reactivity rates as a function of both catalyst composition and oxygen partial pressure. While our study is a big step towards a descriptor approach to describe product selectivity, there is a need to increase the throughput of such a combined experimental-computational effort.

Finally, in chapter 6, we extend the O $2p$-band descriptor approach that we developed for selective C_3H_8 oxidative dehydrogenation to C_3H_6 on ABO$_3$-type perovskites. Herein, using a larger library of perovskite catalysts we showed that the C_3H_8 consumption rates as well as C_3H_6 generation rates correlated linearly with the surface O $2p$-band center.

In summary, we have shown that a descriptor-based approach can be used to selectively tune HCHO complete oxidation rates (Chapter 3), product selectivity (Chapter 4) as well as selective formate rate for HCHO (Chapter 5) and C_3H_6 (Chapter 6). First, in the context of HCHO oxidation, we showed that manganese oxide could be used for room temperature HCHO oxidation after extensive optimization of reaction conditions. This offers a chance to replace

current expensive noble metal catalysts for HCHO oxidation reactions while also opening up opportunities for air purification applications such as acetaldehyde and acetone oxidation. Second, for the selective oxidation reactions using perovskites, we find that perovskites are active at lower temperatures compared to the traditionally used catalysts in the chemical industry. The results here for CH_3OH and C_3H_8 selective oxidation along with previously studies for NO_x elimination show that perovskites are exciting prospects to replace the more expensive catalysts in the chemical industry. However, we do note that CO_2 formation rate also correlated with the formation rate of the selective reaction product for both CH_3OH and C_3H_8 selective oxidation reactions. This result suggested that the active reaction site(s) for selective formation of HCHO or C_3H_6 could also be responsible for the undesirable complete oxidation reaction to CO_2. Hence, there is a need to further investigate methods to decouple the two reaction mechanisms to promote selective oxidation. Approaches to break the scaling relationships between reaction steps is an active area of research in heterogeneous catalysis,[1] the O $2p$-(ligand) band center, especially when defined by the local site geometry,[2,3] can also be used as a design criteria to further optimize the selective oxidation mechanism. However, this additional fine-tuning of the local structure would increase the overall computational or experimental cost. Therefore, there is a trade-off between screening for potential catalysts using simple descriptors such as the bulk or surface O $2p$-band center and an in-depth investigation of the local surface structure. While the first approach was used in this thesis, there is a lot of scope to further engineer the local surface structure via surface decoration, site-blocking methods. Next, we discuss the improvements that can be made for the O 2p-band center descriptor approach.

7.2 Perspective for descriptor-based approaches

The O $2p$-band center provides a proxy measurement of the overall M-O bond strength of the oxide material, the nature of the M-O bonding (e.g. degree of hybridization), and the position of band levels relevant for materials redox. We hypothesize that the results summarized in this work suggest could be generalized to other anions as a more widely applicable "anion p-band center". The anion p-band center of either a bulk, surface, or adsorbate might play a parallel role to the oxygen $2p$-band center, correlating with defect, migration, adsorption, redox and work function energies, and overall catalytic processes. If such a generalization is successful, the anion p-band center could be used to understand trends of material properties and functions not only in

different oxide structural families but also for different materials chemistries beyond oxides, for example fluorides, sulfides, phosphides, and more. We expect the use of the anion p-band center to find relevance in numerous materials design applications and to provide new insights relating trends in materials properties and functions to the underlying materials chemistry outside of oxides and oxygen adsorbates.

The use of descriptors such as the O $2p$-band center provides a powerful method for the accelerated discovery and design of new catalyst materials. Given these correlations, high-throughput density functional theory calculation studies can be conducted, and the predicted quantities of interest can be obtained from calculation of the O $2p$-band center for each screened material.[4] This would be similar to the approach we attempted in Chapter 6 but with a bigger database. The correlations developed would also enable improved understanding of materials trends, which, coupled with domain-specific knowledge, can be used to guide new efforts by proposing sensible composition or structure spaces to focus a materials search, or provide rational strategies toward targeted design spaces of interest.

The acceleration of such materials discovery and design efforts are enabled by the fact that the O $2p$-band center can be obtained from a single bulk DFT calculation,[5] typically requiring less than one day of combined human and computer time per system. This time scale of obtaining at least a qualitative sense of whether a material is of interest for a particular application is likely 1-3 orders of magnitude faster than explicitly synthesizing the material, confirming its structure and composition, and then measuring the quantity of interest. Given the increased prevalence of large materials databases of computed data, together with rapidly increased adoption of machine learning methods in materials science, there is an opportunity to further develop the descriptor-based approach of catalyst discovery and design with the aid of modern data science and machine learning techniques.

In addition, from a materials discovery perspective, we have repeatedly seen in this thesis that a fundamental understanding of the reaction mechanism using in situ techniques needs to be combined with DFT methods to predict new materials with improved activity and selectivity. However, we also have seen that reaction conditions also need to be simultaneously optimized, thus adding more complexity to the materials discovery process. Such an intuition-driven method

of materials discovery provides in-depth insights of the reaction mechanism but is inherently slow due to the lack of automation. (Figure 7.1) Fortunately, many data-driven approaches have been used to develop better descriptors and utilize these design principles to enable more efficient materials screening. Herein, multi-dimensional descriptors can be developed to increase the prediction accuracy. Numerous funnel-like screening pipelines have been developed using high throughput virtual screening (HTVS) and high throughput experimental (HTE) to narrow down and test out material candidates based on existing descriptors. While the screening efficiency of this type of brute-force approach is still constrained by the throughput of HTVS, there is also the challenge of transferability across different material systems.

Furthermore, the search space in high-throughput studies can be extended beyond a single pre-defined, limited candidate space to several new strategies. For example, functionality-driven inverse design is an alternative approach aimed at taking desired properties as inputs to identify the best material compounds. Ideally, only a small fraction of chemistries would need to be sampled because optimization methods would actively learn the structure-property landscape and researchers to the optimal solution. Indeed, the spirit of inverse design dates back to the late 1990s.[6] Early inverse design studies used first-principles calculations and evolutionary algorithms to successfully reverse engineered optical and electronic properties of complex inorganic compounds.[6–10] In many areas like machine vision, natural language processing, or speech recognition and generation, the combination of large datasets available, the efficient deep learning algorithms and the powerful hardware have allowed to apply to transition from hand-tuned features based on intuition to fully learned representations. Graph based neural network tools can be trained of vary basic features (atomic numbers and geometries) and autonomously learn the key representations that are connected to performance. These types of approaches moves away from the Edisonian approach of feature engineering to a more full-stack learning approach. Modern inverse design strategies combine large materials databases with artificial intelligence and uses machine learning to further accelerate functional materials discovery. Machine learning approaches have the potential to introduce new chemical insights free of *a priori* assumptions.

Recently adaptive learning techniques for prediction of materials are becoming popular outside the existing repository by navigating the parameter space more efficiently to minimize the

number of experiments and computations needed to achieve the required yields.[11,12]A fully mature machine learning materials discovery infrastructure would seamlessly link autonomous computational and experimental frameworks to realize desired functionality. (Figure 7.1)
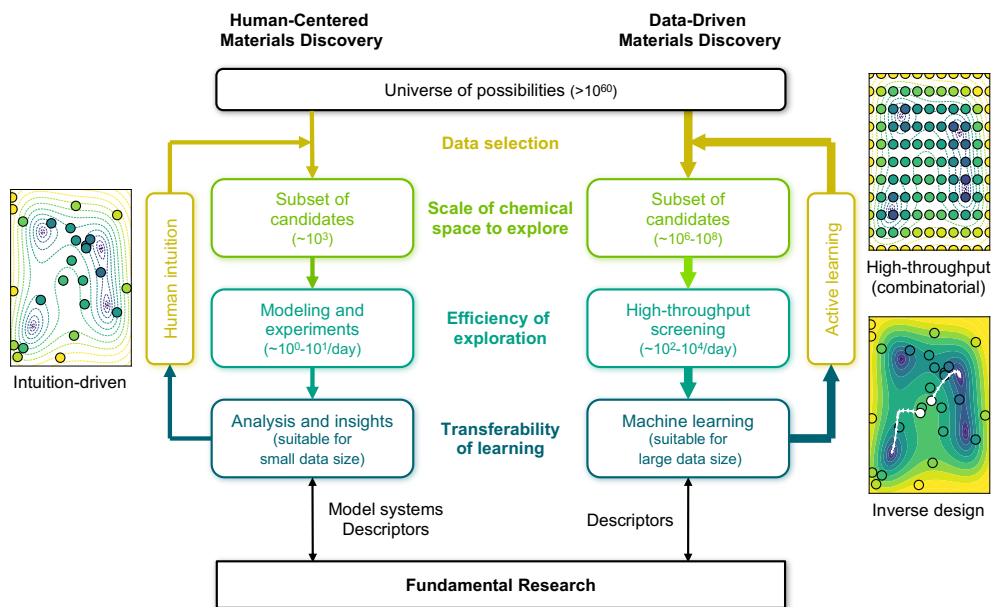
Figure 7.1. *Comparison of intuition–driven and data-driven materials discovery paradigms.*[13]

7.3 Towards a more sustainable and equitable future

Another facet of the sustainable future while meeting energy and environmental challenges is the integration of solutions developed in this thesis and elsewhere with socio-economic factors. For example, *how does society, with its heterogeneity of economic and cultural norms, interact with energy and environmental solutions to tackle climate change?*
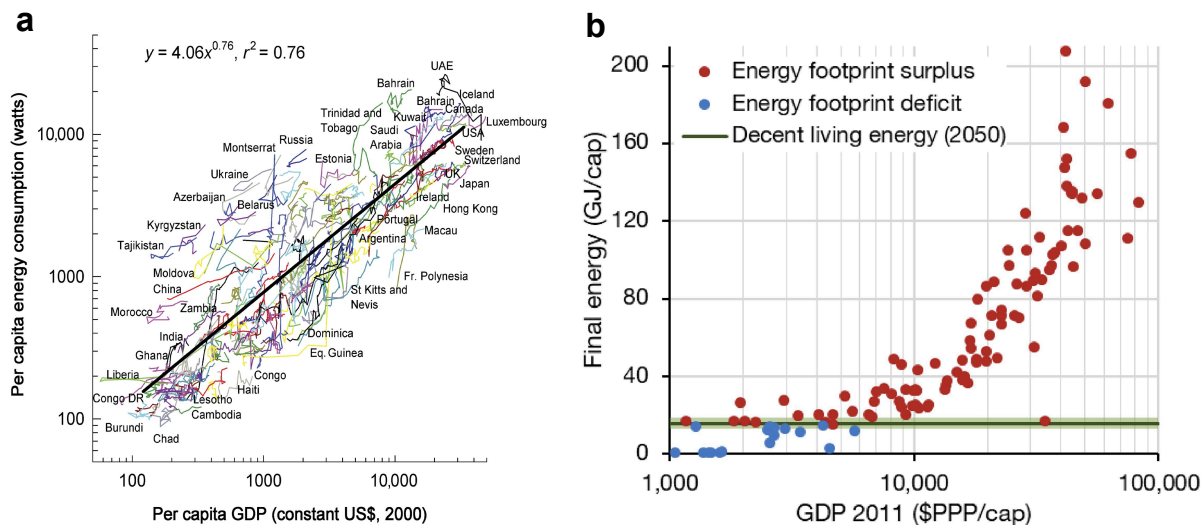
Figure 7.2 (a) *The relationship between per capita energy use and per capita gross domestic product (GDP; in US dollars) of countries, plotted on logarithmic axes, from 1980 to 2003. Figure is reproduced with permission from ref.[14], Copyright Oxford Press 2011. **(b)** Final energy consumption for 119 countries in the GTAP database calculated using input–output analysis, for 2011. For the same countries, decent living energy estimates are shown. Figure is used from ref.[15] with permission, Copyright Elsevier 2020.*

The interaction of technology and society is an ever-evolving goal post with the combined challenge of improving the standard of living across the globe while addressing climate change concerns. And as Norbert Weiner says, "change comes most of all from the unvisited no-man's land between the disciplines", and this core spirit are required for a more equitable and sustainable future. This thesis addressed the technological aspect by rational design of catalysts for cleaner environment and efficient generation of clean energy on wide-ranging applications including air pollution, electrochemical energy storage, and chemical production with the over-arching theme of developing activity descriptors that correlate macroscopic performance metrics to microscopic material properties via investigating the underlying reaction mechanism

The deployment of novel energy storage and carbon neutral technologies using macro-economic trends projected by IPCC is an up and coming field of study. Many such cost benefit analysis and cost-effectiveness methodologies often capture only a narrow set of aggregated parameters while not addressing the consumer side to the energy equation. For example, it is known that different countries as well as populations in the country are affected differently by climate change with the low-income households facing the direst consequences. Hence, there is a need to address the

adaption of carbon neutral technologies while considering the social heterogeneities and preferences in lifestyles, social norms, and well being that exist in in aggregated data. (Figure 7a) For example, the current energy consumption far exceeds the needs for a decent living standard for a large number of countries with higher GDPs.[15] (Figure 7b) Hence, there is a need to address underlying aspects of energy transition that include energy demand, acquisition of new technologies, perceived risks, decision-making, and energy ethics which would require solutions at the home and local community level. Finally, there is a twofold challenge in energy distribution wherein income distribution of the households and more equitable growth need to be balanced in light of CO_2 emissions. In summary, we need to broaden the techno-economic investigation by including a social science component to address the grand challenge of climate science.

7.4 References

(1)   Zhao, Z.-J.; Liu, S.; Zha, S.; Cheng, D.; Studt, F.; Henkelman, G.; Gong, J. Theory-Guided Design of Catalytic Materials Using Scaling Relationships and Reactivity Descriptors. *Nat. Rev. Mater.* **2019**, *4* (12), 792–804. https://doi.org/10.1038/s41578-019-0152-x.

(2)   Dickens, C. F.; Montoya, J. H.; Kulkarni, A. R.; Bajdich, M.; Nørskov, J. K. An Electronic Structure Descriptor for Oxygen Reactivity at Metal and Metal-Oxide Surfaces. *Surf. Sci.* **2019**, *681*, 122–129. https://doi.org/10.1016/j.susc.2018.11.019.

(3)   Rao, R. R.; Kolb, M. J.; Giordano, L.; Pedersen, A. F.; Katayama, Y.; Hwang, J.; Mehta, A.; You, H.; Lunger, J. R.; Zhou, H.; Halck, N. B.; Vegge, T.; Chorkendorff, I.; Stephens, I. E. L.; Shao-Horn, Y. Operando Identification of Site-Dependent Water Oxidation Activity on Ruthenium Dioxide Single-Crystal Surfaces. *Nat. Catal.* **2020**, *3* (6), 516–525. https://doi.org/10.1038/s41929-020-0457-6.

(4)   Jacobs, R.; Mayeshiba, T.; Booske, J.; Morgan, D. Material Discovery and Design Principles for Stable, High Activity Perovskite Cathodes for Solid Oxide Fuel Cells. *Adv. Energy Mater.* **2018**, *8* (11), 1702708. https://doi.org/10.1002/aenm.201702708.

(5)   Lee, Y.-L.; Kleis, J.; Rossmeisl, J.; Shao-Horn, Y.; Morgan, D. Prediction of Solid Oxide Fuel Cell Cathode Activity with First-Principles Descriptors. *Energy Environ. Sci.* **2011**, *4* (10), 3966–3970. https://doi.org/10.1039/C1EE02032C.

(6)   Franceschetti, A.; Zunger, A. The Inverse Band-Structure Problem of Finding an Atomic Configuration with given Electronic Properties. *Nature* **1999**, *402* (November), 60–63. https://doi.org/10.1038/46995.

(7)   Gautier, R.; Zhang, X.; Hu, L.; Yu, L.; Lin, Y.; Sunde, T. O. L.; Chon, D.; Poeppelmeier, K. R.; Zunger, A. Prediction and Accelerated Laboratory Discovery of Previously Unknown 18-Electron ABX Compounds. *Nat. Chem.* **2015**, *7*, 308.

(8)   Franceschetti, A.; Dudiy, S. V; Barabash, S. V; Zunger, A.; Xu, J.; van Schilfgaarde, M. First-Principles Combinatorial Design of Transition Temperatures in Multicomponent Systems: The Case of Mn in GaAs. *Phys. Rev. Lett.* **2006**, *97* (4), 47202. https://doi.org/10.1103/PhysRevLett.97.047202.

(9)   Dudiy, S. V; Zunger, A. Searching for Alloy Configurations with Target Physical Properties: Impurity Design via a Genetic Algorithm Inverse Band Structure Approach. *Phys. Rev. Lett.* **2006**, *97* (4), 46401. https://doi.org/10.1103/PhysRevLett.97.046401.

(10)   Zhang, L.; Luo, J.-W.; Saraiva, A.; Koiller, B.; Zunger, A. Genetic Design of Enhanced Valley Splitting towards a Spin Qubit in Silicon. *Nat. Commun.* **2013**, *4*, 2396.

(11)   Silver, D.; Huang, A.; Maddison, C. J.; Guez, A.; Sifre, L.; van den Driessche, G.; Schrittwieser, J.; Antonoglou, I.; Panneershelvam, V.; Lanctot, M.; Dieleman, S.; Grewe, D.; Nham, J.; Kalchbrenner, N.; Sutskever, I.; Lillicrap, T.; Leach, M.; Kavukcuoglu, K.; Graepel, T.; Hassabis, D. Mastering the Game of

Go with Deep Neural Networks and Tree Search. *Nature* **2016**, *529* (7587), 484–489. https://doi.org/10.1038/nature16961.

(12) Silver, D.; Schrittwieser, J.; Simonyan, K.; Antonoglou, I.; Huang, A.; Guez, A.; Hubert, T.; Baker, L.; Lai, M.; Bolton, A.; Chen, Y.; Lillicrap, T.; Hui, F.; Sifre, L.; van den Driessche, G.; Graepel, T.; Hassabis, D. Mastering the Game of Go without Human Knowledge. *Nature* **2017**, *550* (7676), 354–359. https://doi.org/10.1038/nature24270.

(13) J. Peng, D. S. Koda, K. Akkiraju,.., J. C. Grossman, K. Reuter, R. Gomez-Bombarelli, and Y, S.-H. Human- and Machine-Centered Design of Molecules and Materials for Chemical Transformations and Energy Storage,. *Under Rev.* **2021**.

(14) Brown, J. H.; Burnside, W. R.; Davidson, A. D.; Delong, J. R.; Dunn, W. C.; Hamilton, M. J.; Mercado-Silva, N.; Nekola, J. C.; Okie, J. G.; Woodruff, W. H.; Zuo, W. Energetic Limits to Economic Growth. *Bioscience* **2011**, *61* (1), 19–26. https://doi.org/10.1525/BIO.2011.61.1.7.

(15) Millward-Hopkins, J.; Steinberger, J. K.; Rao, N. D.; Oswald, Y. Providing Decent Living with Minimum Energy: A Global Scenario. *Glob. Environ. Chang.* **2020**, *65*, 102168. https://doi.org/10.1016/J.GLOENVCHA.2020.102168.

A.1: Supplementary Data for Chapter 2
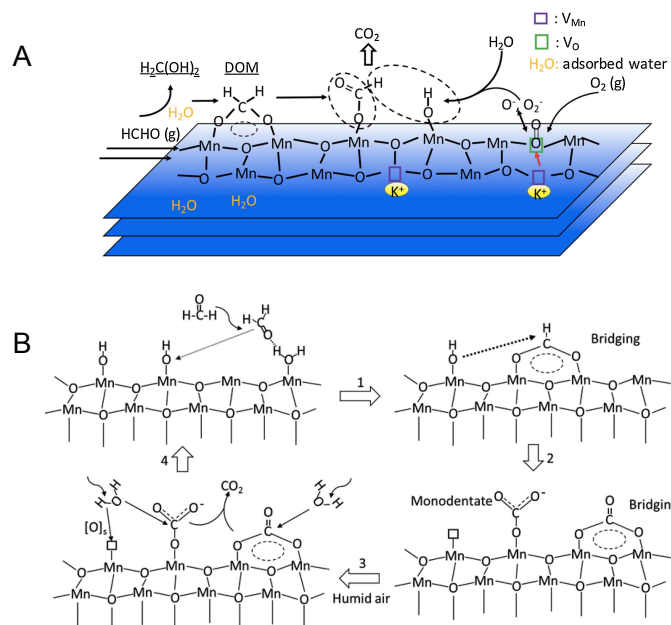
Figure A.1.1: Reaction mechanism for formaldehyde oxidation on birnessite manganese oxide. Schematics of reaction mechanism via A) formation of DOM (H_2COO_{Oxide}) and formate ($HCOO_{oxide}$) reaction intermediates[1] and B) formate ($HCOO_{oxide}$) and carbonate (CO_2O_{oxide}) reaction intermediates[2] aided by surface oxygen, hydroxyl, and adsorbed water. Figures are used with permission from References [1,2], Copyright American Chemical Society 2015 and Elsevier 2017.
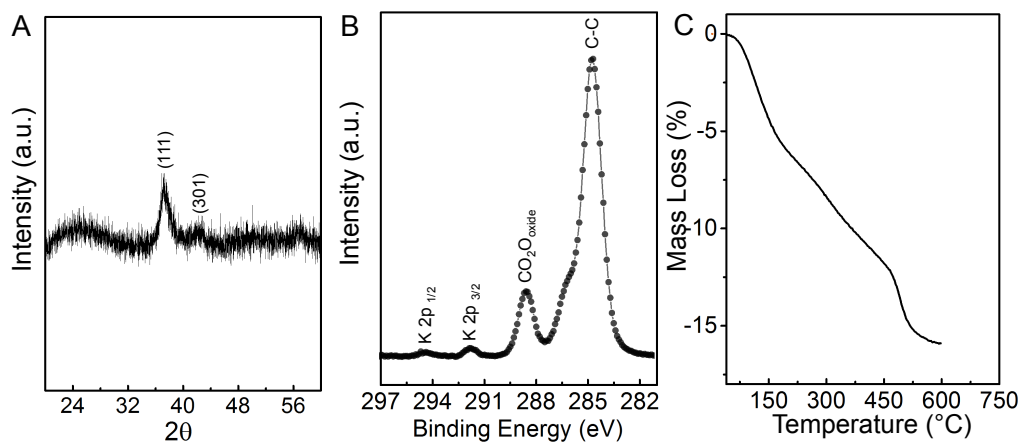
Figure A.1.2: Characterization of MnO$_x$ catalyst. A) XRD pattern of the MnO$_x$ catalyst which can be described by a birnessite phase, B) X-ray Photoelectron Spectrum showing K 2p and C1s region of the MnO$_x$ catalyst used in this study. We show that the addition of potassium enhances adsorption of oxygen and dissociation of water dissociation as shown in the Table S4 and Figure S9, and C) thermo gravimetric (TG) mass loss curve showing the loss of surface hydroxyl, oxygen, and structural water from the catalyst as a function of temperature.[1]
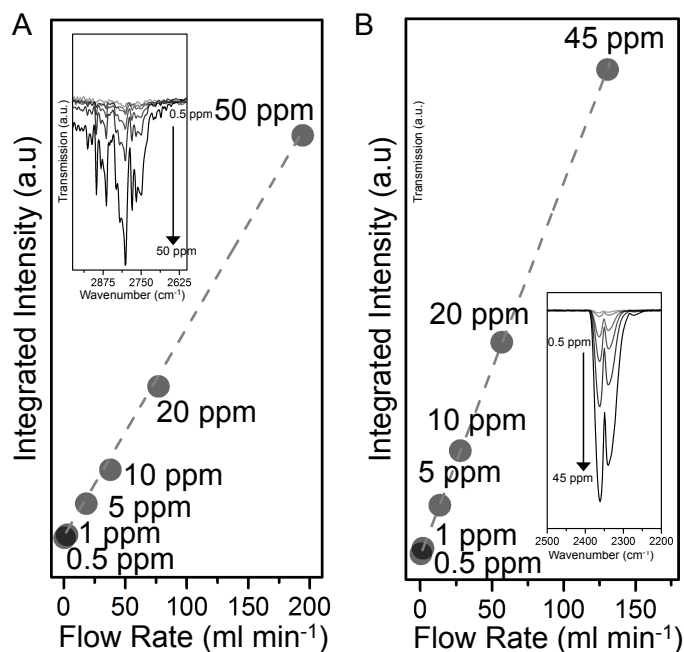
Figure A.1.3: Sensitivity of FTIR gas-cell for HCHO and CO$_2$ detection. Sensitivity of A) HCHO and B) CO$_2$ gases showing the FTIR spectral region and the integrated intensities for gas concentrations of 50-0.5 ppm/Balance$_{N2}$ obtained by changing the flow rates of the HCHO and CO$_2$ gases with a balance of N$_2$ gas using dedicate mass flow controllers. A total flow rate of 200 ml min^{-1} was used for all the measurements.

188
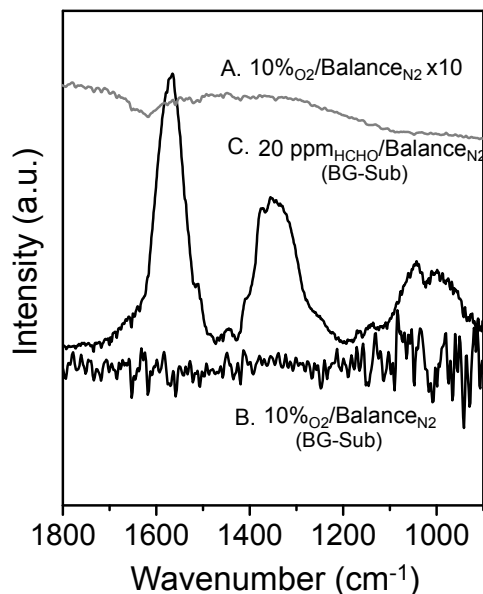
Figure A.1.4: DRIFTS spectrum before and after background subtraction. DRIFTS spectrum showing the spectrum A) taken prior to background subtraction in 10%$_{O2}$/Balance$_{N2}$ and after background subtraction B) in 10%$_{O2}$/Balance$_{N2}$ and, C) after flowing 20ppm$_{HCHO}$/Balance$_{N2}$. 25 mg MnO$_x$ catalyst was mixed with 25 mg KBr and the total gas flow rate was 200 ml min^{-1} for the DRIFTS measurements.

Table A.1.1: Reaction conditions for identifying reaction intermediates using DRIFTS

Catalyst Loading (mg)	Inlet Gas Composition (xx ppm$_{HCHO}$/10%$_{O2}$/Balance$_{N2}$)	Flow Rate (ml min^{-1})
5	20 ppm	250
50	2 ppm	100
50	0.5 ppm	50
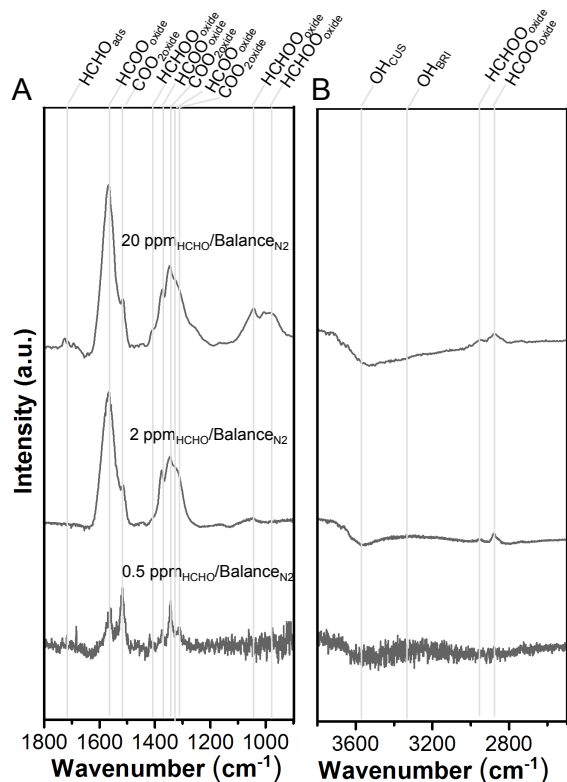
Figure A.1.5: Identification of reaction intermediates using DRIFTS. DRIFTS collected under 20 ppm_{HCHO}, 2 ppm_{HCHO}, 0.5ppm_{HCHO} (balanced with nitrogen) with 5 mg, 50 mg, 50 mg of MnO_x catalyst at a flow rate of 250, 100, 50 ml/min respectively A) in the 900-1800 cm^{-1} region showing major carbonate reaction intermediate (COO_{2oxide}) at low concentration of 0.5 ppm_{HCHO}/$Balance_{N2}$, major bidentate formate reaction intermediate ($HCOO_{Oxide}$) at higher concentration of 20 ppm_{HCHO}/$Balance_{N2}$ with peaks corresponding to DOM ($HCHOO_{oxide}$) only seen in the highest concentration of 20ppm_{HCHO}/$Balance_{N2}$ case, and B) in the 2600-3700 cm^{-1} region showing terminal/CUS hydroxyl (OH_{CUS}), lattice/bridge hydroxyl (OH_{BRI}), and bidentate formate ($HCOO_{Oxide}$) related peaks. 25 mg MnO_x catalyst was mixed with 25 mg KBr and the total gas flow rate was 200 ml min^{-1} for the DRIFTS measurements.
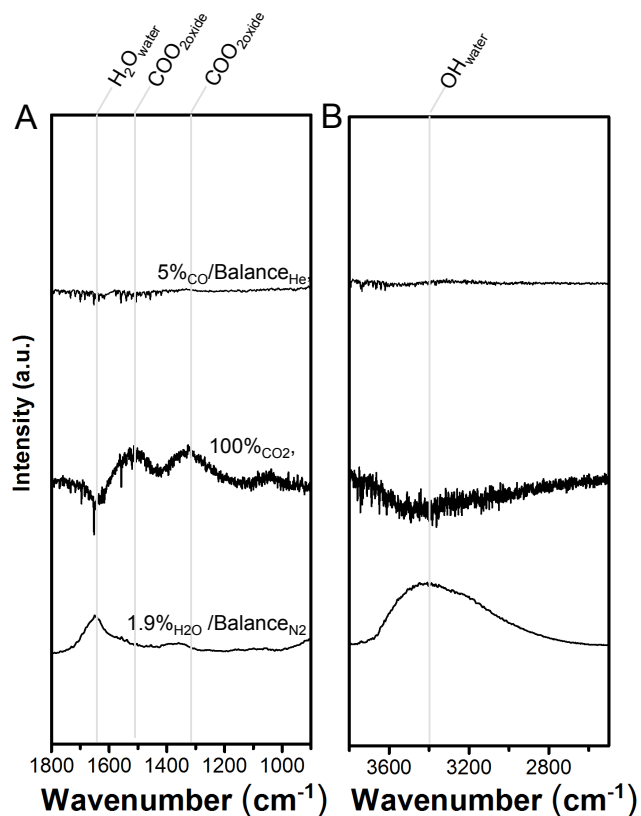
Figure A.1.6: Identification of reaction intermediates using DRIFTS. DRIFTS collected under $5\%_{CO}$/Balance $_{He}$, $100\%_{CO2}$, and $1.9\%_{H2O}$/Balance$_{N2}$ A) in the 900-1800 cm^{-1} region showing the no CO related adsorption species, carbonate (COO$_{2oxide}$) peaks related peaks at 1512 and 1324 cm^{-1} and water related peaks (H$_2$O$_{water}$) at 1647 cm^{-1} and while the B) 2600-3700 cm^{-1} region showing no peaks for CO, CO$_2$ adsorption while a broader peak corresponding to O-H stretching of water (OH$_{water}$) was observed. 25 mg MnO$_x$ catalyst was mixed with 25 mg KBr and the total gas flow rate was 200 ml min^{-1} for the DRIFTS measurements.

Table A.1.2: Comparison of the experimental and DFT computed wavenumber of the reaction intermediates observed during HCHO oxidation

Species	DFT Computed	DFT Reference	Experimental	Experimental Reference
$HCHOO_{oxide}$	2961, 2950, 1405, 1327, 1206,1020	2372, 2211, 1342, 1321, 1229, 1018, 979;[3] 3958,2884,1394,1340, 1207, 999[4]	1420, 1054,969	~1473,1302,1186,1138,1114,1086,858; 1412[5]
$HCOO_{oxide}$	2998, 1503,1342,1218,	2968, 1497, 1381, 1169;[3] 3012, 1453, 1384, 1294[4]	2955, 2882, 1567, 1384, 1354, 1320	2951,2872,2735,1562,1385,1365,1322[5]
CO_2O_{oxide}	1387, 1204	1301, 1254[6] ;1537,1302	1512, 1340	1503,1324,1220[1]

Table A.1.3: Surface energies of commonly encountered facets of rutile

Surface Facet	Surface Energy (kJ/m^2)
001	1.69
100	1.26
111	0.94
101	2.57
110	0.7

A

B
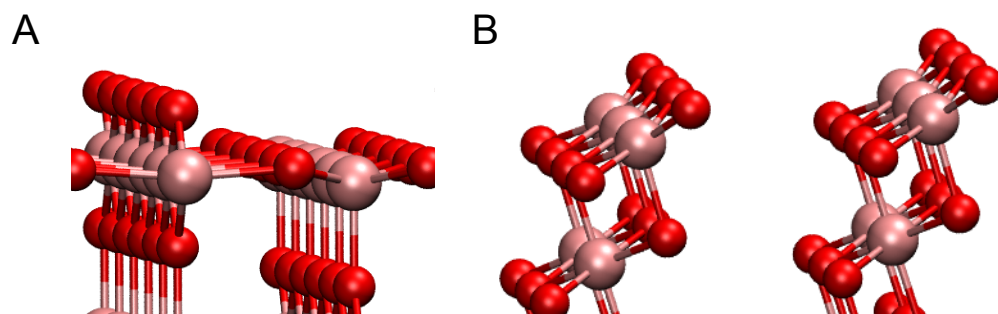
Figure A.1.7: Comparison of the surface structure of manganese oxides. Structure of A) (110) facet of rutile MnO_2 and B) (101) facet of δ-MnO_2 (birnessite).
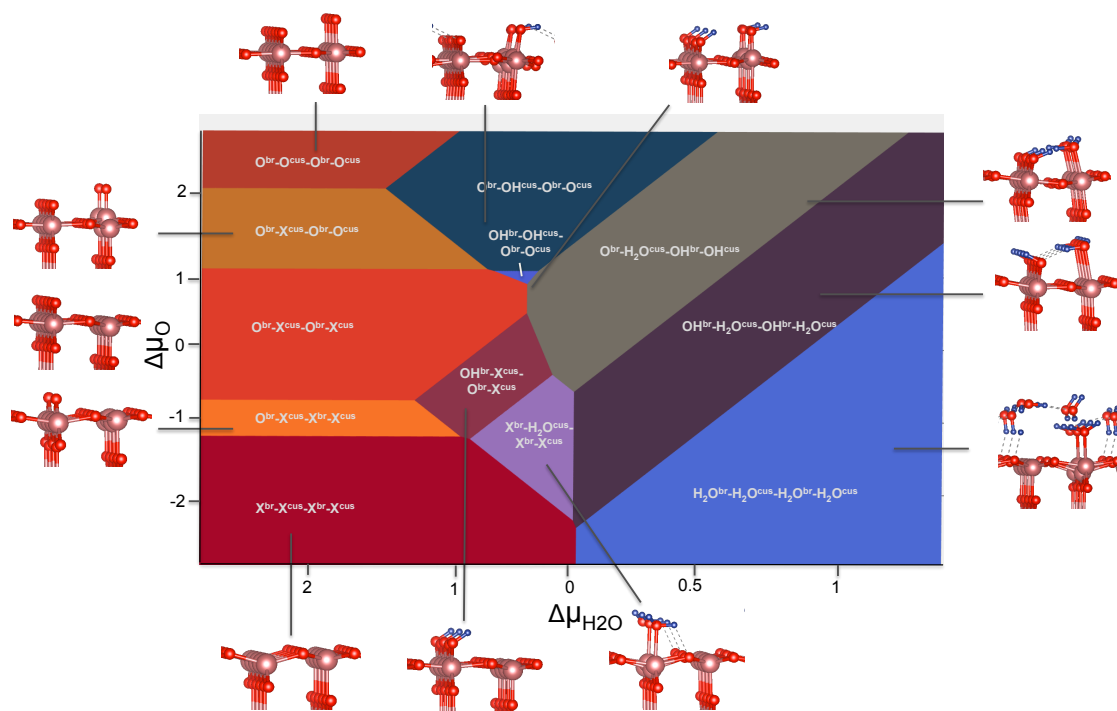
Figure A.1.8: Surface phase diagram for the MnO$_2$ surface (110) in the presence of O$_2$ and H$_2$O chemical potentials showing the different surface structures.
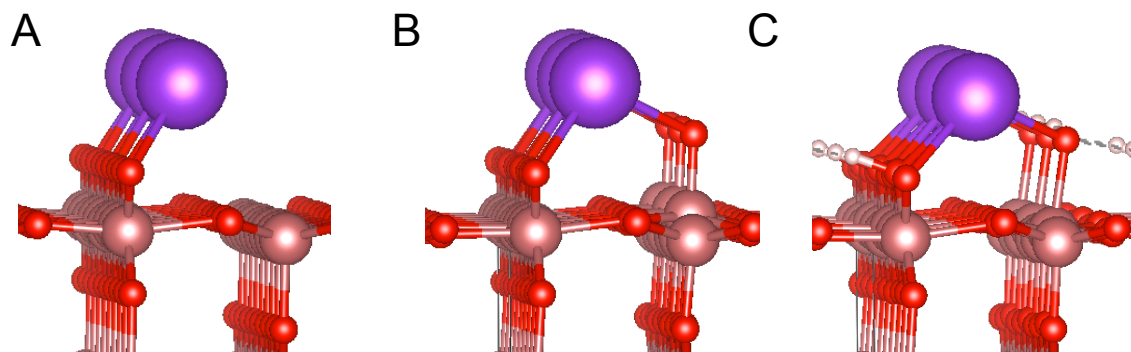
Figure A.1.9: Optimized adsorption geometries for K adsorption. A) Potassium ad-atom adsorption similar to the configuration reported for K adsorption on TiO$_2$ (110)[8], B) adsorbed O$_{CUS}$ and C) dissociated H$_2$O on MnO$_2$(110) with potassium ad-atom.

Table A.1.4: Adsorption energy of water and oxygen atom compared for the cases of with and without K ad-atom.

Adsorbed Species	Without K (eV)	With K (eV)
Oxygen	+1.07	+0.63
Dissociated Water	-0.36	-0.56
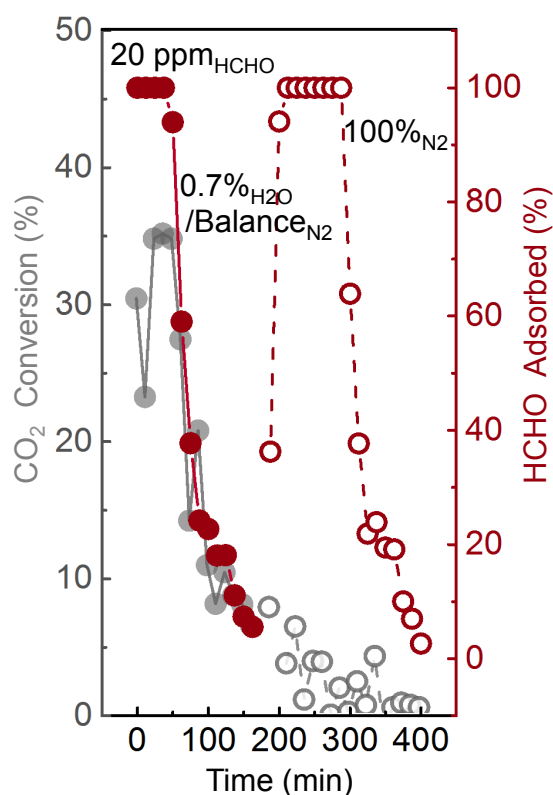
Figure A.1.10: Increase in catalyst lifetime upon switching from wet to dry conditions. Reactor studies for inlet concentration of 20 ppm$_{HCHO}$/Balance$_{N2}$ showing HCHO adsorption for additional 100 min after achieving HCHO breakthrough under flow of 20 ppm$_{HCHO}$/0.7%$_{H2O}$/Balance$_{N2}$. However, no additional CO_2 was generated after switching the gas from 20 ppm$_{HCHO}$/0.7%$_{H2O}$/10%$_{O2}$/Balance$_{N2}$ to 20 ppm$_{HCHO}$/Balance$_{N2}$. Catalyst loading was 25 mg MnO$_x$ while and total gas flow rate was 200 ml min^{-1} was used for all the measurements.

Table A.1.5: CO_2 converted under different reaction conditions until 50 min in Figure 2A and Figure 2C

Reaction Condition/Loading	Total CO_2 Converted (mmol/gcat)
20 ppm$_{HCHO}$ /Balance$_{N2}$/25 mg	0.084
20 ppm$_{HCHO}$/10%$_{O2}$/Balance$_{N2}$/25 mg	0.082
20 ppm$_{HCHO}$/0.7%$_{H2O}$/Balance$_{N2}$/100 mg	0.070
20 ppm$_{HCHO}$/10%$_{O2}$/0.7%$_{H2O}$/Balance$_{N2}$/100 mg	0.071
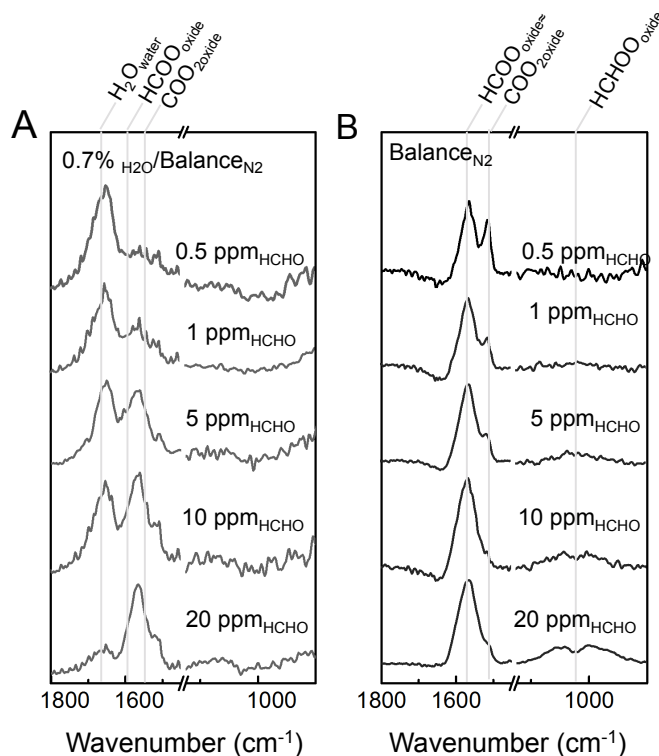
Figure A.1.11: DRIFTS spectrum with bidentate formate and carbonate reaction intermediates . A) DRIFTS in the 900-1800 cm^{-1} region for 0.5-20ppm$_{HCHO}$/0.7%$_{H2O}$/Balance$_{N2}$ at 120 min showing water, bidentate formate (HCOO$_{oxide}$), and carbonate (COO$_{2oxide}$), related peaks and no DOM (HCHOO$_{oxide}$), peaks in any of the spectra. B) DRIFTS in the 900-1800 cm^{-1} region for 0.5-20ppm$_{HCHO}$/Balance$_{N2}$ at 120 min showing that DOM, HCOO$_{oxide}$, and COO$_{2oxide}$ reaction intermediates with the dominant surface species changing from carbonate to HCOO$_{oxide}$ and HCHOO$_{oxide}$ reaction

intermediates with increasing HCHO concentration 25 mg MnO_x catalyst was mixed with 25 mg KBr for the DRIFTS measurements and total gas flow rate was 200 ml min^{-1}.
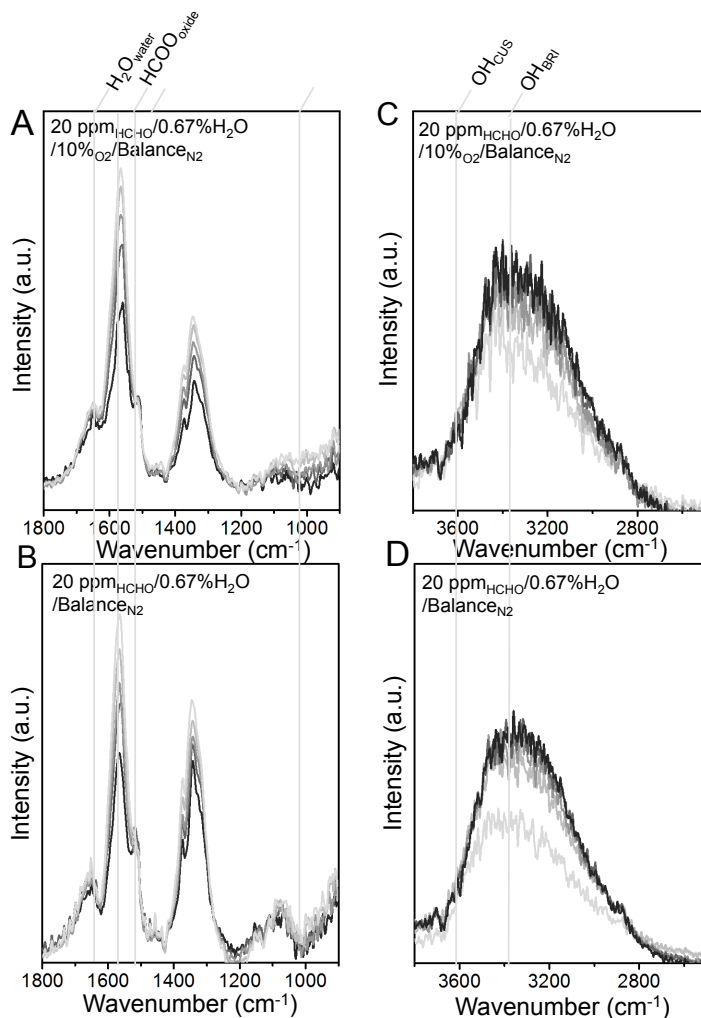
Figure A.1.12: DRIFTS collected under HCHO and H_2O with and without oxygen in gas stream. DRIFTS in the 900-1800 cm^{-1} region collected under A) 20 ppm_{HCHO}/ 0.7%$_{H2O}$/10%$_{O2}$/Balance$_{N2}$ and B) 20 ppm_{HCHO}/0.7%$_{H2O}$/Balance$_{N2}$ showing bidentate formate ($HCOO_{oxide}$), carbonate (COO_{2oxide}), and adsorbed water (H_2O_{water}) reaction intermediates. DRIFTS in the 2700-3700 cm^{-1} region collected under C) 20 ppm_{HCHO}/ 0.7%$_{H2O}$/10%$_{O2}$/Balance$_{N2}$ and D) 20 ppm_{HCHO}/0.7%$_{H2O}$/Balance$_{N2}$ showing adsorbed water reaction (H_2O_{water}) intermediates. The 5 spectra (light to dark) in each case were collected at collected at 6, 12, 24, 72, and 120 min. 25 mg MnO_x catalyst was mixed with 25 mg KBr for the DRIFTS measurements and a total gas flow rate was 200 ml min^{-1}.
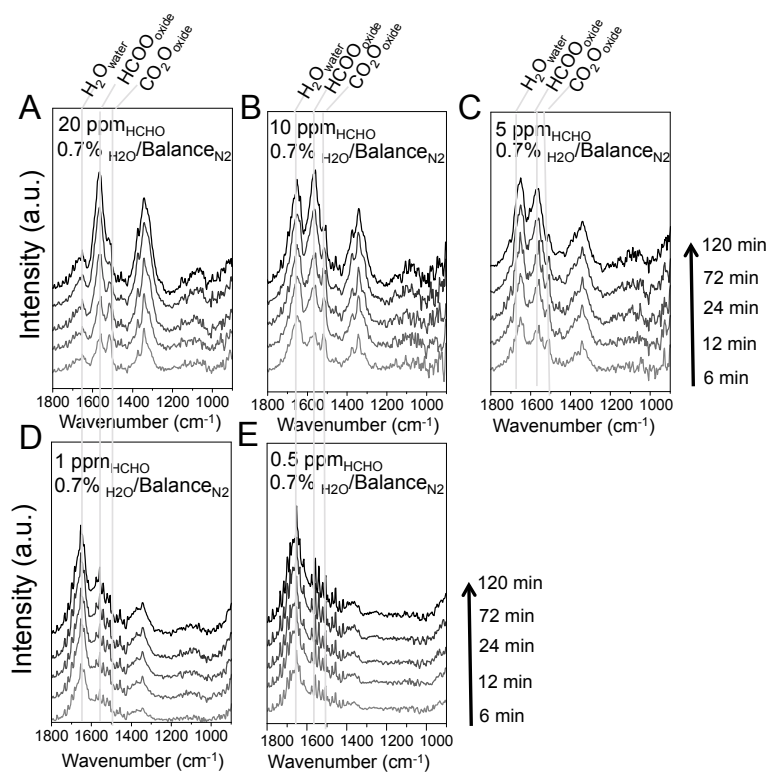
Figure A.1.13: DRIFTS evolution of reaction intermediates with time. DRIFTS showing bidentate formate (HCOO$_{oxide}$), and carbonate reaction (COO$_{2oxide}$) reaction intermediates for inlet concentration of A) 20 ppm $_{HCHO}$, B) 10 ppm $_{HCHO}$ C) 5 ppm $_{HCHO}$ D) 1ppm $_{HCHO}$ E) 0.5 ppm$_{HCHO}$ with balance gas of 0.7%$_{H2O}$Balance$_{N2}$ collected at 6, 12, 24,72, and 120 min after flowing the gas mixture. Catalyst loading was 25 mg MnO$_x$ and total gas flow rate was 200 ml min^{-1}.
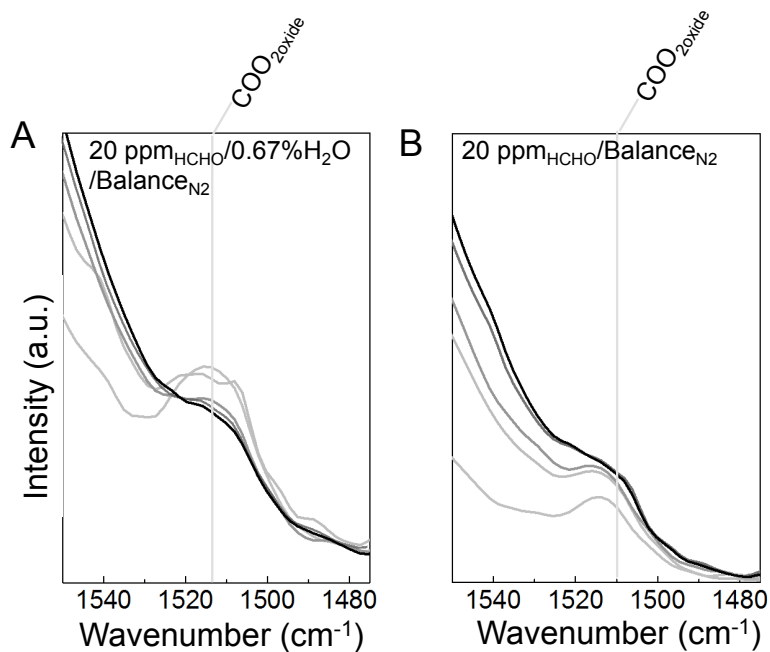
Figure A.1.14: DRIFTS in the carbonate region. DRIFTS in the 900-1800 cm^{-1} region collected under A) 20 ppm$_{HCHO}$/ 0.7%$_{H2O}$/Balance$_{N2}$ and B) 20 ppm$_{HCHO}$/Balance$_{N2}$ showing carbonate (COO$_{2oxide}$) reaction intermediate. The 5 spectra (light to dark) in each case were collected at 40 80, 120, 150, and 180 min under gas flow. 25 mg MnO$_x$ catalyst was mixed with 25 mg KBr for the DRIFTS measurements and a total gas flow rate was 200 ml min^{-1}.
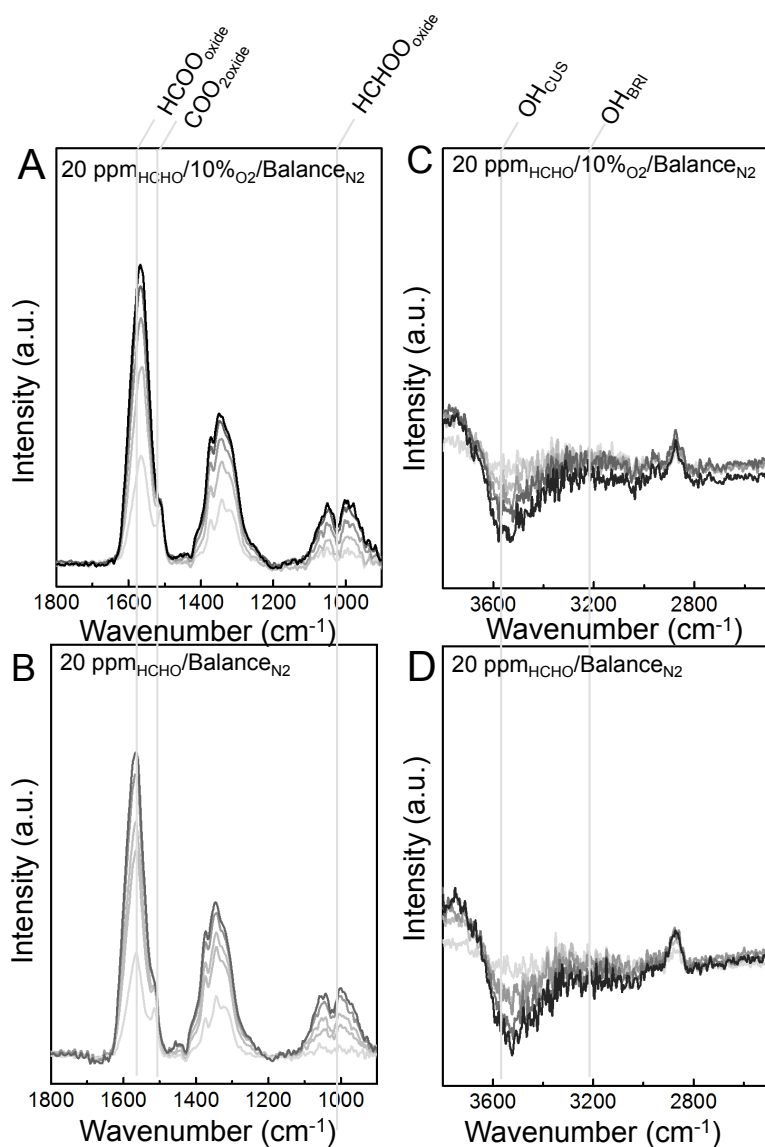
Figure A.1.15: DRIFTS collected under HCHO with and without oxygen in gas stream. DRIFTS in the 900-1800 cm^{-1} region collected under A) 20 ppm_{HCHO}/ 0.7%$_{H2O}$/10%$_{O2}$/Balance$_{N2}$ and B) 20 ppm_{HCHO}/0.7%$_{H2O}$/Balance$_{N2}$ showing DOM (HCHOO$_{oxide}$), bidentate formate (HCOO$_{oxide}$), carbonate (COO$_{2oxide}$), DRIFTS in the 2600-3700 cm^{-1} region collected under A) 20 ppm_{HCHO}/ 0.7%$_{H2O}$/10%$_{O2}$/Balance$_{N2}$ and B) 20 ppm_{HCHO}/0.7%$_{H2O}$/Balance$_{N2}$ showing a decrease in the intensity of CUS hydroxyl species (OH$_{CUS}$) and slight increase in the intensity of the bridging hydroxyl (OH$_{BRI}$). The 5 spectra (light to dark) in each case were collected at 40 80, 120, 150, and 180 min under gas flow. 25 mg MnO$_x$ catalyst was mixed with 25 mg KBr for the DRIFTS measurements and a total gas flow rate was 200 ml min^{-1}.
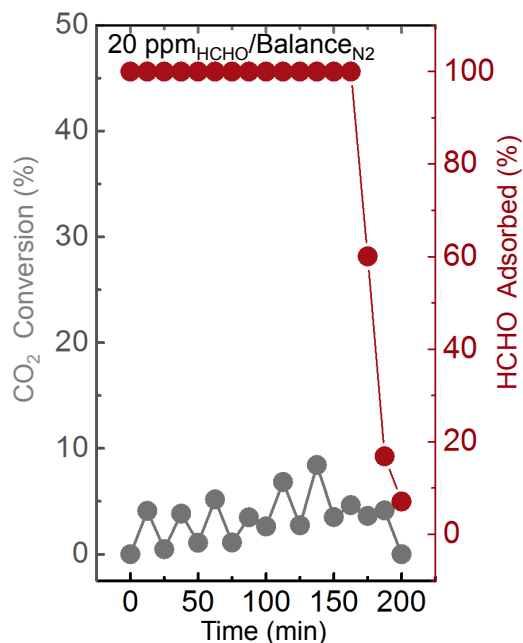
Figure A.1.16: Series of repeated measurements showing HCHO breakthrough and CO₂ conversion for the catalyst when exposed A) to 20 ppm$_{HCHO}$/Balance$_{N2}$ initially and purging with 1.9%$_{H2O}$/Balance$_{N2}$ and re-adsorption of HCHO, B) to 20 ppm$_{HCHO}$/10%$_{O2}$/Balance$_{N2}$ and purging with 1.9%$_{H2O}$/10%$_{O2}$/Balance$_{N2}$ and re-adsorption of HCHO. A gradual decrease in the lifetime is observed for the second and third re-adsorption of HCHO. Catalyst loading was 25 mg MnO$_x$ while and total gas flow rate was 200 ml min^{-1}.

Figure A.1.17: DRIFTS collected under transient reaction conditions with and without H₂O in gas stream after flowing HCHO. DRIFTS collected under transient reaction conditions without HCHO in the gas stream in the 900-1800 cm^{-1} region with A) $100\%_{N2}$ after flowing 20 ppm_{HCHO}/ Balance$_{N2}$ and B) $0.7\%_{H2O}$/Balance$_{N2}$ after flowing 20 ppm_{HCHO}/$0.7\%_{H2O}$/Balance$_{N2}$, in the 2600-3700 cm^{-1} region for C) $100\%_{N2}$ after flowing 20 ppm_{HCHO}/Balance$_{N2}$ and D) $0.7\%_{H2O}$/Balance$_{N2}$ after flowing 20 ppm_{HCHO}/ $0.7\%_{H2O}$/Balance$_{N2}$. Spectra (dark to light) were collected at 6, 12, 24, 72, and 120 min. 25 mg MnO$_x$ catalyst was mixed with 25 mg KBr for the DRIFTS measurements and a total gas flow rate was 200 ml min^{-1}.
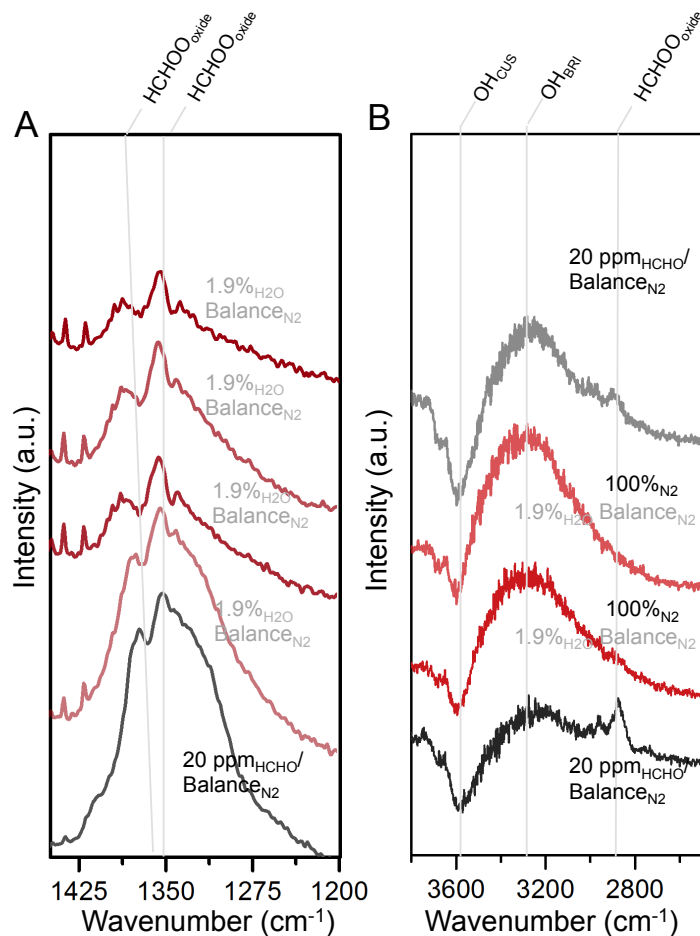
Figure A.1.18: Influence of water on the stability of reaction intermediates. A) DRIFTS spectra of the bidentate formate ($HCOO_{oxide}$) peak in the 1200-1400 cm^{-1} region showing a red shift of the –OCO stretching of the formate reaction intermediate while flowing 1.9%$_{H2O}$/Balance$_{N2}$ collected after flowing 20 ppm$_{HCHO}$/Balance$_{N2}$ B) DRIFTS in the 2700-3700 cm^{-1} region collected after flowing 20 ppm$_{HCHO}$/Balance$_{N2}$ (black) showing a decrease in the surface hydroxyl peak at 3590 cm^{-1} and the formation of a OH_{BRI} between 2800-3600 cm^{-1} followed by flowing 1.9%$_{H2O}$/Balance$_{N2}$ for 90 min and 100%$_{N2}$ for 300 min (red), showing an increase in the intensity of the broader OH_{BRI} peak. Further, flowing 1.9%$_{H2O}$/Balance$_{N2}$ for 120 min and 100%$_{N2}$ for 240 min (red) revealed further increase in the intensities of lattice hydroxyl peak. Re-adsorption of 20 ppm$_{HCHO}$/Balance$_{N2}$ after the complete removal of the carbonaceous species in Figure 4C showed a further decrease in intensity of OH_{CUS} peak at 3590 cm^{-1} while the OH_{BRI} intensity did not change for the spectra collected after 180 min.
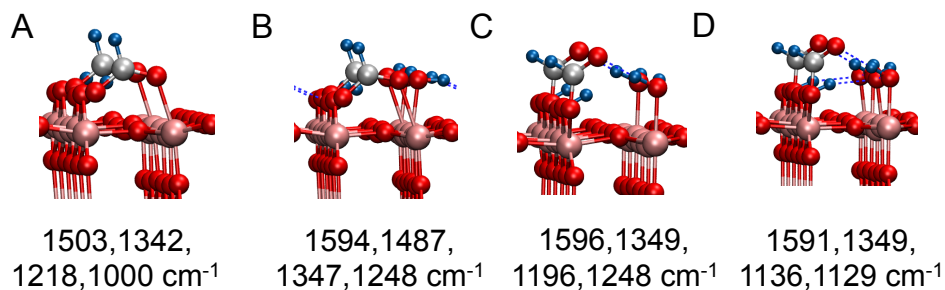
Figure A.1.19: DFT-calculated structures for water interaction with formate (HCO$_{BRI}$O$_{CUS}$). Computed DFT structures and wavenumbers for the different configurations of formate reaction intermediate for A) bidentate formate in BRI-CUS geometry, B) bidentate formate in BRI-CUS geometry with co-adsorbed water on the Mn$_{CUS}$ site, C) monodentate formate adsorbed on OH hydroxyl on the Mn$_{CUS}$ site with co-adsorbed water on the adjacent Mn$_{CUS}$ site, and D) monodentate formate geometry adsorbed on H$_2$O on the CUS site with OH on Mn$_{CUS}$ site. Pink, manganese; blue, hydrogen; dark red, oxygen; grey, carbon.
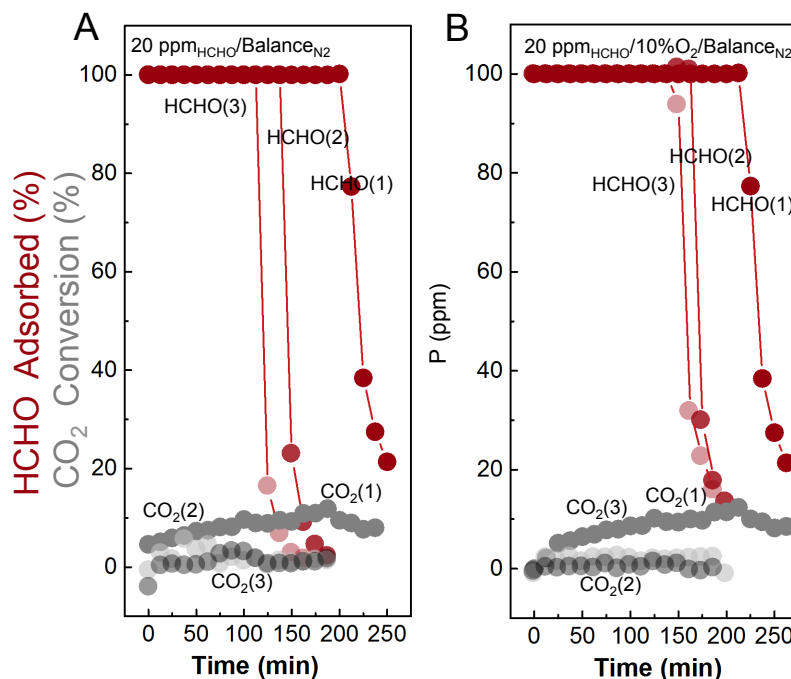
Figure A.1.20: Series of repeated measurements showing HCHO breakthrough and CO$_2$ conversion for the catalyst when exposed A) to 20 ppm$_{HCHO}$/Balance$_{N2}$ initially and purging with 1.9%$_{H2O}$/Balance$_{N2}$ and re-adsorption of HCHO, B) to 20 ppm$_{HCHO}$/10%$_{O2}$/Balance$_{N2}$ and purging with 1.9%$_{H2O}$/10%$_{O2}$/Balance$_{N2}$ and re-adsorption of HCHO. A gradual decrease in the lifetime is observed for the second and third re-adsorption of HCHO. Catalyst loading was 25 mg MnO$_x$ while and total gas flow rate was 200 ml min^{-1}.

Figure A.1.21: Conversion of bidentate formate (HCOO$_{oxide}$) and carbonate (COO$_{2oxide}$) reaction intermediates. A) DRIFTS collected after flowing 20 ppm$_{HCHO}$/Balance$_{N2}$ for 12 min of followed by flowing 100%$_{N2}$ for 30 min, 80 min, and 130 min (dark-light grey) in the 900-1800 cm^{-1} region showing the formation of bidentate formate (HCOO$_{oxide}$) and carbonate (COO$_{2oxide}$) reaction intermediates at 12 min and a slight decrease in the intensity of the HCOO$_{oxide}$ and COO$_{2oxide}$ peaks with increasing time. Introduction of 0.7%$_{H2O}$/Balance$_{N2}$ for 0 min (red) showed a decrease in the intensities of the carbonaceous intermediates while continued exposure to 1.2%$_{H2O}$/Balance$_{N2}$ for 0 min, 1.9%$_{H2O}$/Balance$_{N2}$ for 0 min (red), and 1.9%$_{H2O}$/Balance$_{N2}$ for 30 min (red) and 120 min (red) leads to complete removal of the HCOO$_{oxide}$ and COO$_{2oxide}$ peaks, B) The corresponding hydroxyl region from 2700-3700 cm^{-1} showing a decrease in intensity of OH$_{CUS}$ peaks at 3590 cm^{-1} under the dry conditions (grey) while the addition of water leads to the formation of a broader hydroxyl peak (OH$_{water}$) from 2900-3500 cm^{-1}. C) Decrease in intensities of both COO$_{2oxide}$ and HCOO$_{oxide}$ peak upon introduction of increasing amounts of water (0.7%$_{H2O}$-1.9%$_{H2O}$). Also, the amount of decrease of the intensity was the same for both the intermediates and the relative peak ratios of formate and carbonate remained the same at ~2.5 suggesting that the HCOO$_{oxide}$ did not transform into COO$_{2oxide}$ after the initial COO$_{2oxide}$ had been converted to CO$_2$.
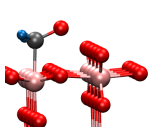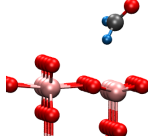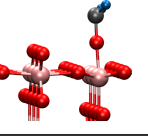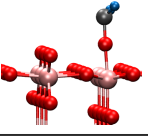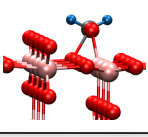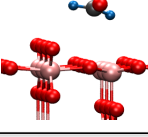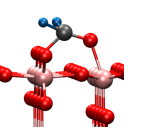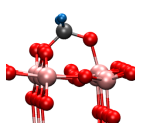
	Initial	Final	ΔG (eV)
A			+0.43
B			+0.02
C			+0.41
D			-0.51

Table A.1.6: Computed adsorption energies for HCHO adsorption on the stoichiometric surface showing initial and final configuration for A) C-down adsorption on the Mn_{CUS} site with energy of +0.43 eV, B) C-down adsorption on the Mn_{CUS} site with +0.02 eV energy, C) bidentate adsorption along the Mn_{CUS} row sites with +0.41 eV, and D) bidentate configuration with adsorption on both the Mn_{CUS} and oxygen bridge sites (O_{BRI}) with energy of -0.51 eV. Pink, manganese; blue, hydrogen; dark red, oxygen; grey, carbon.

Reaction Scheme A.1.1: Energetics of reaction of HCHO and O_2 assisted by OH_{CUS} to form CO_2 and H_2O surface with hydrogen adsorption on the bridge site (OH_{BRI}) computed using the same unit cell in red and different unit cells in grey to model high and low coverage scenarios.

$$HCHO + OH_{CUS2} + O_{CUS1}^{vac} + O_{BRI1} \rightarrow H_2CO_{BRI1}O_{CUS1} + OH_{CUS2} \ (G_1 = -0.64 \text{ eV})$$

$$H_2CO_{BRI1}O_{CUS1} + OH_{CUS2} \rightarrow HCO_{BRI1}O_{CUS1} + H_2O + O_{CUS2}^{vac} (G_2 = -2.75 \text{ eV})$$

$$HCO_{BRI1}O_{CUS1} + O_{BRI2} \rightarrow CO_{BRI1}O_{CUS1} + OH_{BRI2} \ (G_3 = -2.19 \text{ eV}, G_3 = -2.10 \text{ eV})$$

$$CO_{BRI1}O_{CUS1} \rightarrow CO_2 + O_{BRI1}^{vac} + O_{CUS1}^{vac} \ (G_4 = -0.23 \text{ eV}, G_4 = -0.32 \text{ eV})$$

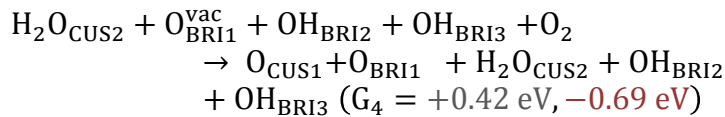$$O_{BRI1}^{vac} + O_{CUS2}^{vac} + OH_{BRI2} + O_2 \rightarrow O_{BRI1} + OH_{CUS2} + O_{BRI2} \ (G_5 = +0.29 \text{eV})$$
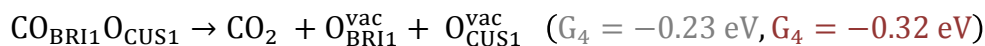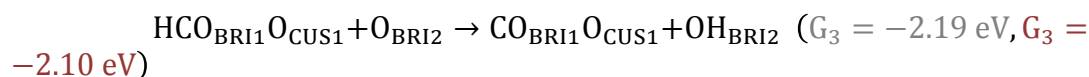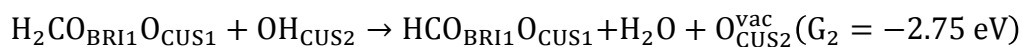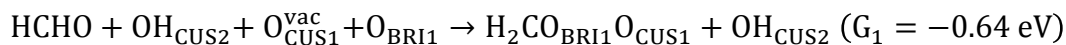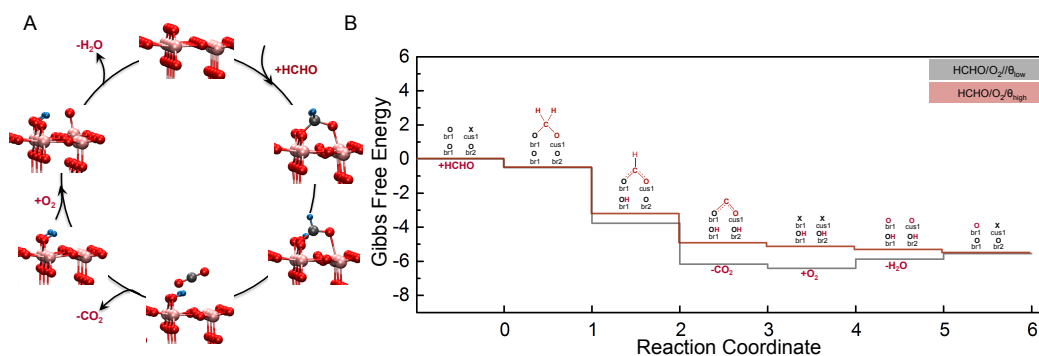
Figure A.1.22: DFT calculated reaction mechanism for stoichiometric MnO₂ surface.
A) Schematic of reaction mechanism for HCHO oxidation on a stoichiometric surface via formate reaction pathway and B) DFT-calculated free energy diagram of formaldehyde oxidation on the stoichiometric (110) surface of MnO_2 surface where the grey diagram shows the energy of bridging hydroxyl energy calculated in separate simulation cell to model low coverage reaction conditions (θ_{low}) and the red diagram showing the energetics calculated in the same simulation cell to case to model high coverage reaction conditions (θ_{high}). First, the adsorption of HCHO was found to be most favorable in a bidentate BRI-CUS geometry on the stoichiometric surface (Table A.1.5) as dioxymethylene (DOM, $H_2CO_{BRI1}O_{CUS1}$), with adsorption energy of -0.51 eV. Second, dehydrogenation of DOM by a bridge oxygen (O_{BRI2}) can lead to the formation of bidentate formate in a BRI-CUS geometry ($HCO_{BRI1}O_{CUS1}$) and a bridge hydroxyl (OH_{BRI2}) in Figure S19A, which was found thermodynamically downhill with -2.74 eV for having OH_{BRI2} in the same unit cell (or -3.26 eV for having the co-adsorbed hydroxyl in a different unit cell from $HCO^{BRI1}O^{cus1}$, representing lower coverage). Third, dehydrogenation of bidentate formate can lead to the formation of a second hydroxyl (OH_{BRI3}), with Gibbs free energy of -1.71 eV (-2.40 eV for the lower coverage case), and an adsorbed CO_2 -like species in a BRI–CUS geometry, with Gibbs free energy of -0.22 eV (-0.24 eV for the lower coverage). Fourth, the CO_2-like species can desorb as CO_2, leaving behind an oxygen vacancy on the bridge site (O_{BRI1}^{vac}). Fifth, refilling of the vacancy on the cus site (O_{CUS1} by molecular oxygen is thermodynamically uphill, with Gibbs free energy penalty of +0.53 eV, which could become favorable (-0.17 eV) in the presence of co-adsorbed hydroxyl. This result is in agreement with previous work that OH coverage can aid oxygen adsorption due to the delocalization of donated electrons along the CUS row of atoms.[9] Sixth, the two bridge hydroxyls (OH_{BRI2}, OH_{BRI3}) can combine with the dissociated oxygen on the cus site (O_{CUS1}) to desorb as H_2O with -0.19 eV (with an energy penalty of +0.33 eV for the lower coverage). Pink, manganese; blue, hydrogen; dark red, oxygen; grey, carbon. The equations and energetics for each step are reported in Reaction Scheme A.1.2.

Reaction Scheme A.12: Energetics of reaction of HCHO and O_2 on a stoichiometric surface with hydrogen adsorption on the bridge site (OH_{BRI}) computed using the same unit cell in red and different unit cells in grey to model high and low coverage scenarios.
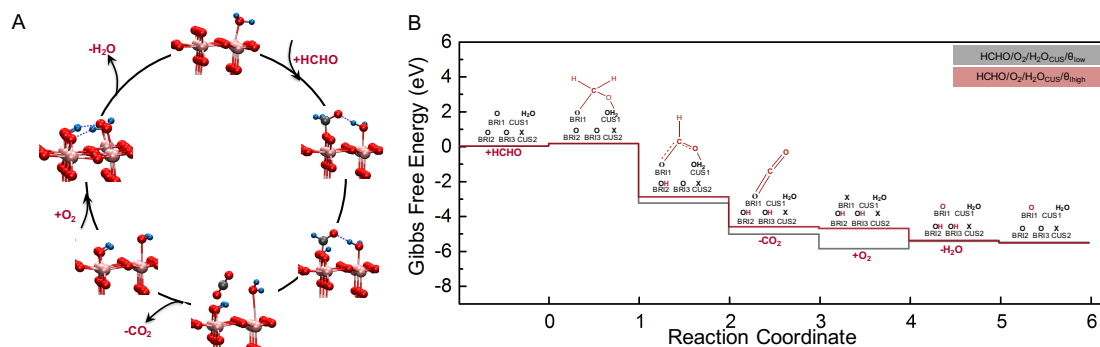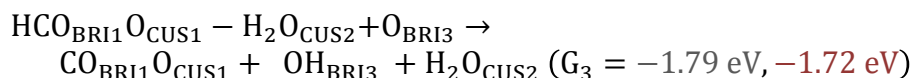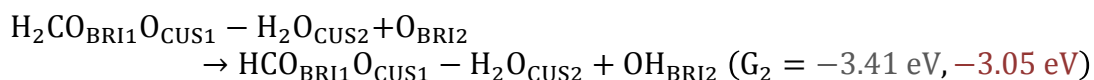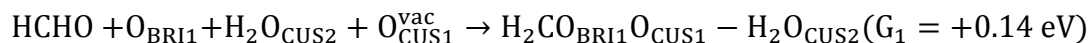
$$HCHO + O_{BRI1} + O_{CUS1}^{vac} \rightarrow H_2CO_{BRI1}O_{CUS1}\ (G_1 = -0.51\ eV, -0.51\ eV)$$

$$H_2CO_{BRI1}O_{CUS1}+O_{BRI1} \rightarrow HCO_{BRI1}O_{CUS1} + +OH_{BRI2} \ (G_2 = -3.05 \text{ eV}, -2.74 \text{ eV})$$

$$HCO_{BRI1}O_{CUS1}+O_{BRI3} \rightarrow CO_{BRI1}O_{CUS1} + +OH_{BRI3} \ (G_3 = -2.19 \text{ eV}, -1.71 \text{ eV})$$

$$CO_{BRI1}O_{CUS1} \rightarrow CO_2 + O_{BRI1}^{vac} + O_{CUS1}^{vac} (G_4 = -0.24\text{eV}, -0.22 \text{ eV})$$

$$O_{BRI1}^{vac} + O_{CUS1}^{vac}+O_2 \rightarrow O_{CUS1} +O_{BRI1} \ (G_5 = +0.53 \text{ eV}, -0.17 \text{ eV})$$

$$O_{CUS1} + OH_{BRI2}+OH_{BRI3} \rightarrow H_2O +O_{BRI1}+O_{BRI2} + O_{CUS1}^{vac}(G_6 = -0.07 \text{ eV}, -0.19 \text{ eV})$$
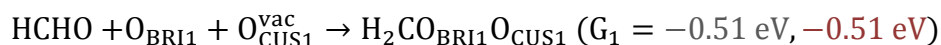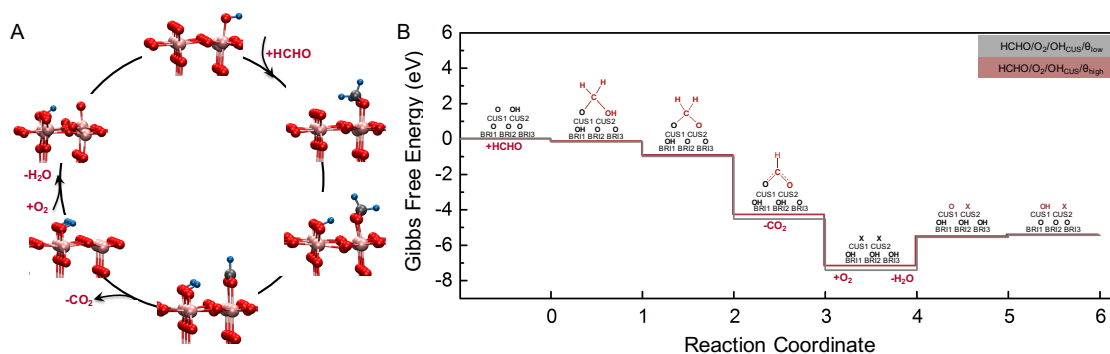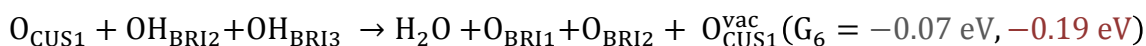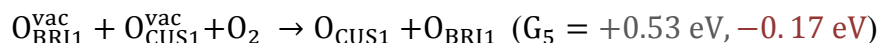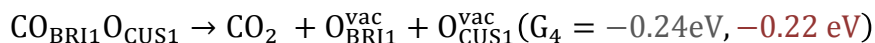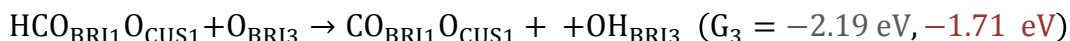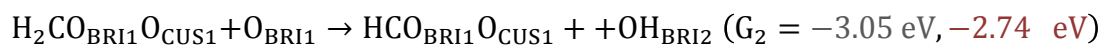
Figure A.1.23: DFT calculated reaction mechanism for MnO$_2$ with OH$_{CUS}$. A) Reaction mechanism for HCHO oxidation aided by OH$_{CUS}$ via formate reaction intermediate, and B) DFT-calculated free energy diagram for formaldehyde oxidation on the (110) surface of MnO$_2$ surface with OH$_{CUS}$. The grey diagram showing the energy of bridging hydroxyl energy calculated in separate simulation cell to model low coverage reaction conditions (θ_{low}) and the red diagram showing the energetics in the co-adsorbed case to model high coverage reaction conditions (θ_{high}). The equations and energetics for each step are reported in Reaction Scheme S3.

Reaction Scheme A.13: Energetics of reaction of HCHO and O$_2$ assisted by OH$_{CUS}$ to form CO$_2$ and H$_2$O computed with hydrogen adsorption on the bridge site (OH$_{BRI}$) computed using the same unit cell in red and different unit cells in grey to model high and low coverage scenarios.
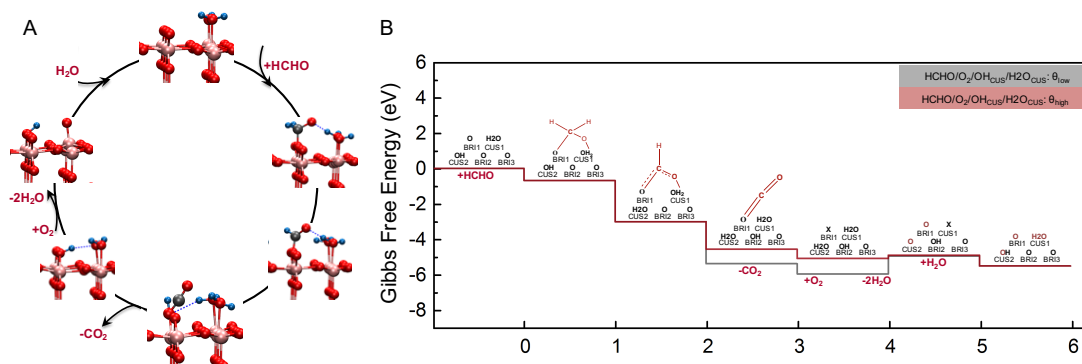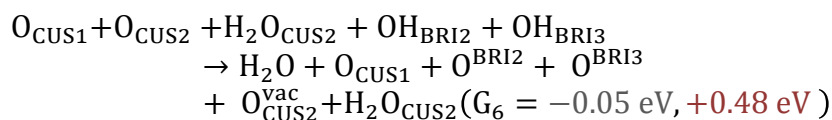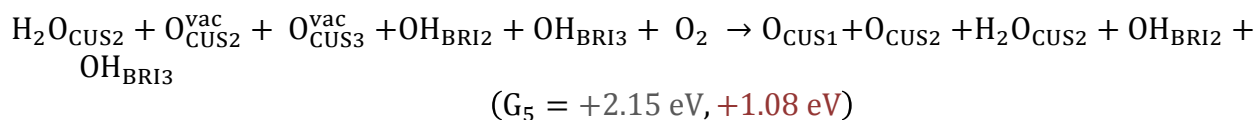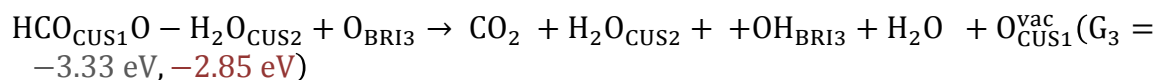
$$HCHO + OH_{CUS2}+O_{CUS1}^{vac} \rightarrow H_2CO_{CUS1}OH_{CUS2} \ (G_1 = -0.15 \text{ eV})$$

$$H_2CO_{CUS1}OH_{CUS2}+O_{BRI2} \rightarrow H_2CO_{CUS1}O_{CUS2}+OH_{BRI1}(G_2 = -0.82 \text{ eV}, G_2 = -0.78 \text{ eV})$$

$$H_2CO_{CUS1}O_{CUS2}+O_{BRI2} \rightarrow HCO_{CUS1}O_{CUS2}+OH_{BRI2} \ (G_3 = -3.55 \text{ eV}, G_3 = -3.36 \text{ eV})$$

$$HCO_{CUS1}O_{CUS2}+O_{BRI3} \rightarrow CO_2 + O_{CUS1}^{vac} + O_{CUS2}^{vac} + OH_{BRI3} \ (G_4 = -2.88 \text{ eV}, G_4 = -2.90 \text{ eV})$$

$$O_{CUS1}^{vac} + \ + OH_{BRI1} + OH_{BRI2} + O_2$$
$$\rightarrow O_{CUS2} + O_{BRI1} + O_{BRI2} + H_2O \ (G_5 = +1.86 \text{ eV}, G_5 = +1.67 \text{ eV})$$
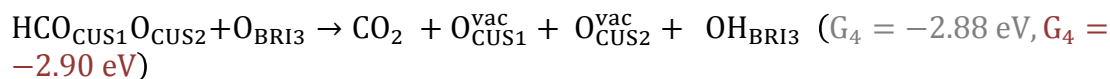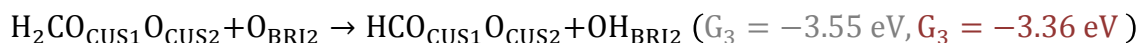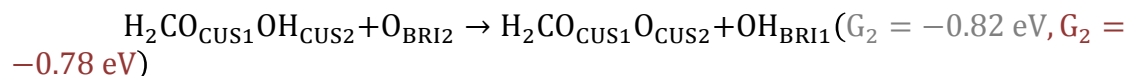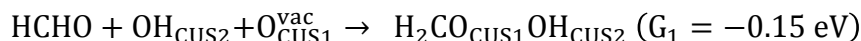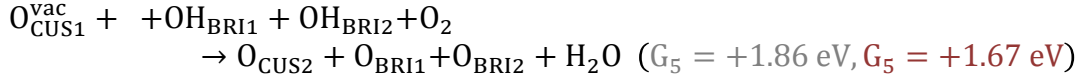
Reaction Scheme A.14A: Energetics of reaction of HCHO and O_2 assisted by OH_{CUS} and O_{CUS} to form CO_2 and H_2O via carbonate reaction intermediate with hydrogen adsorption on the bridge site (OH_{BRI}) computed using the same unit cell in red and different unit cells in grey to model high and low coverage scenarios.

$$HCHO + O_{CUS1} + O_{BRI1} + O_{BRI2} + OH_{CUS2} + O_{BRI1}$$
$$\rightarrow HCO_{CUS1}O - OH_{CUS2} + OH_{BRI1} (G_2 = -3.72 \text{ eV})$$

$$HCO_{CUS1}O - OH_{CUS2} + O_{BRI2} \rightarrow COO_{CUS1}OH_{CUS2} + OH_{BRI2} \ (G_2 = -3.43 \text{ eV})$$

$$COO_{CUS1}OH^{CUS2} + O^{BRI3} \rightarrow COO_{CUS1}O_{CUS2} + OH_{BRI3} \ (G_3 = -0.48 \text{ eV})$$

$$COO_{CUS1}O_{CUS1} \rightarrow CO_2 \ + O_{CUS1} + O_{CUS2}^{vac} \ (G_3 = +0.17 \text{ eV})$$

$$O_{CUS1} + OH_{BRI1} + OH_{BRI2} \rightarrow H_2O + O_{BRI1} + O_{BRI2} + O_{CUS1}^{vac} (G_5 = -0.37 \text{ eV})$$

$$O_{CUS1}^{vac} + O_{CUS2}^{vac} + OH_{BRI3} + O_2 \rightarrow O_{CUS1} + OH_{CUS2} (G_6 = +2.30 \text{ eV})$$
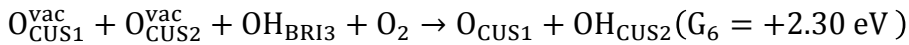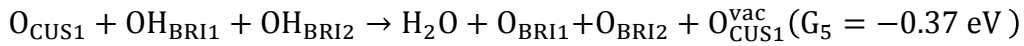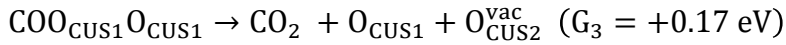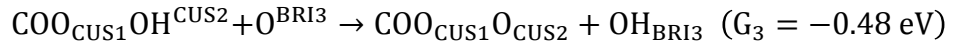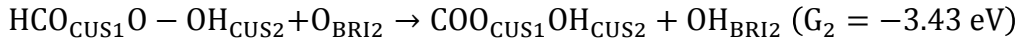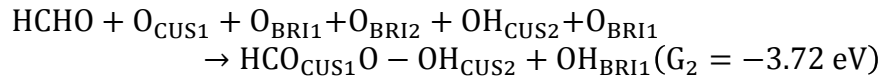
Reaction Scheme A.14B: Reaction of HCHO and O_2 assisted by OH_{CUS} and O_{CUS} to form CO_2 and H_2O via formate reaction intermediate with hydrogen adsorption on the bridge site (OH_{BRI}) computed using the same unit cell in red and different unit cells in grey to model high and low coverage scenarios.
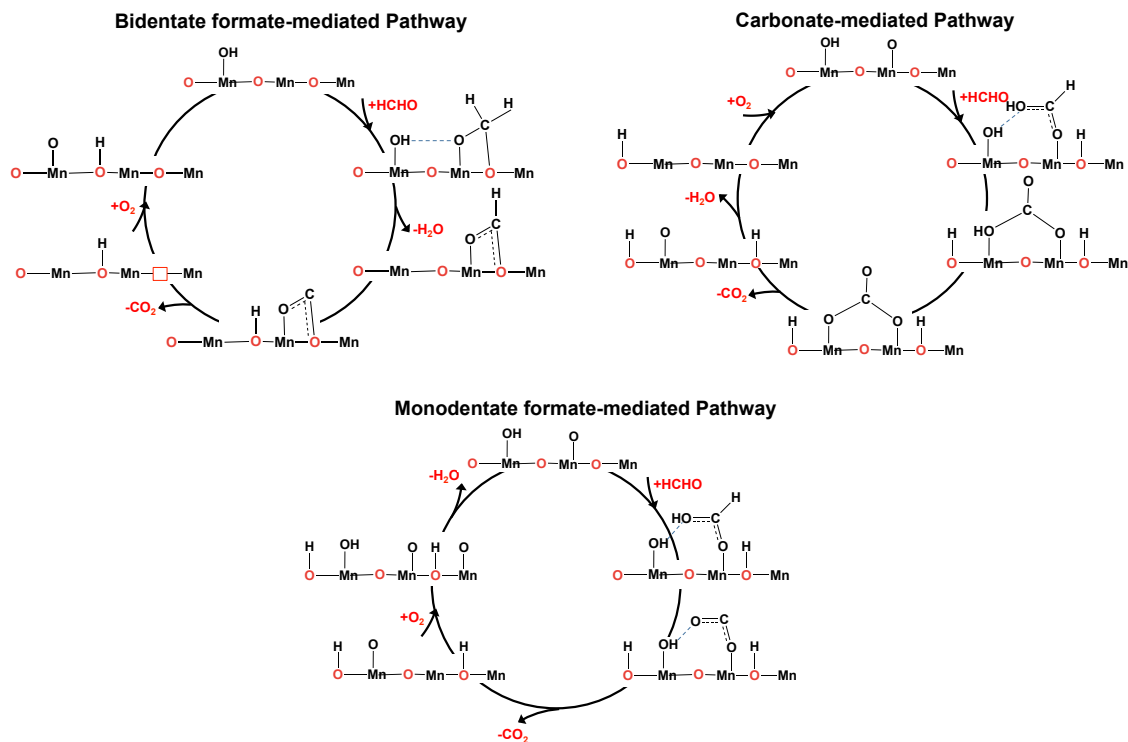
$$HCHO + O_{CUS1} + OH_{CUS2} + O_{BRI1} \rightarrow HCO_{CUS1}O - OH_{CUS2} + OH_{BRI1} (G_2 = -3.72 \text{ eV})$$

$$HCO_{CUS1}O - OH^{CUS2} + O^{BRI2} \rightarrow CO_2 + OH^{BRI2} + OH_{CUS2} (G_2 = -4.01 \text{ eV})$$

$$COO_{CUS1}OH_{CUS2} + O_{BRI3} \rightarrow \ CO_2 + O_{CUS1}^{vac} + OH_{CUS2} + O_{BRI3} \ (G_3 = -0.06 \text{ eV})$$

$$O_2 + O_{CUS1}^{vac} + O_{CUS3}^{vac} \rightarrow \ O_{CUS1} + O_{CUS3} \ (G_3 = +1.61 \text{ eV})$$

$$O_{CUS3} + OH_{BRI1} + OH_{BRI2} \rightarrow O_{BRI2} + OH_{BRI1} + O_{CUS3}^{vac} (G_5 = +0.68 \text{ eV})$$
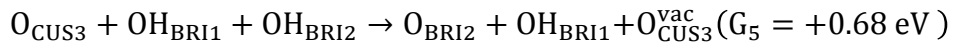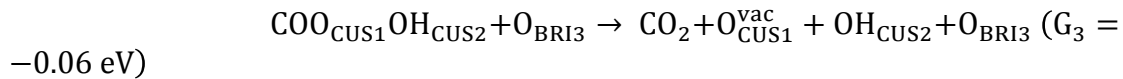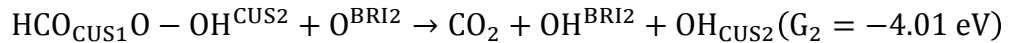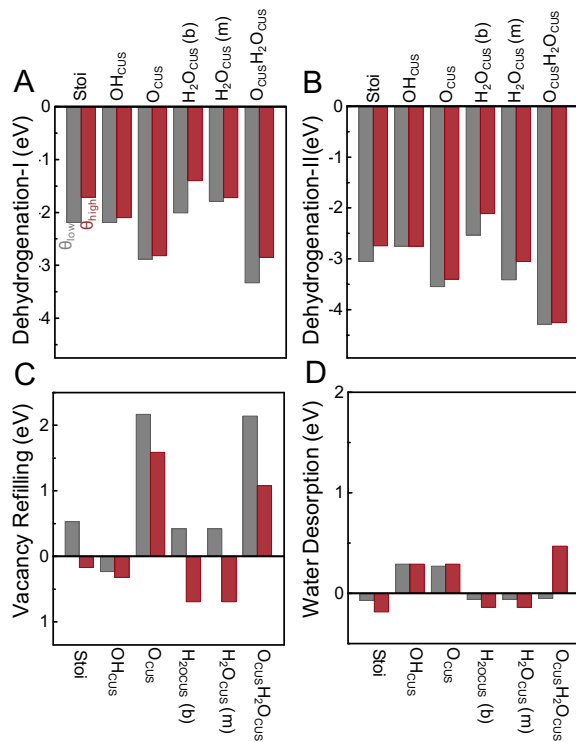
Figure A.1.24: Role of bridging hydroxyl coverage for surface energetics. Surface energetics for A) Dehydrogenation-I for conversion of DOM (H_2COO_{oxide}) to formate ($HCOO_{oxide}$), B) Dehydrogenation-II for formate ($HCOO_{oxide}$) conversion to CO_2, C) molecular oxygen re-adsorption and D) for water desorption at low and high bridging hydroxyl coverage for a surface with stoichiometric, OH_{CUS}, O_{CUS} OCUSH2OCUS, H_2O_{CUS}(b) for HCHO adsorption in a bidentate configuration, and H_2O_{CUS} (m) for HCHO adsorption in a monodentate configuration, $O_{CUS}H_2O_{CUS}$ reaction conditions. The grey data bars show the energy of bridging hydroxyl energy calculated in separate simulation cell to model low coverage reaction conditions (θ_{low}) and the red diagram showing the energetics in the co-adsorbed case to model high coverage reaction conditions (θ_{high}).
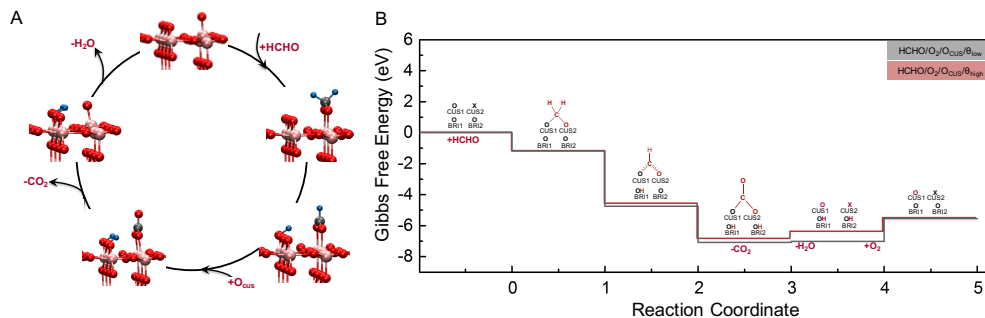
Figure A.1.25: DFT calculated reaction mechanism for MnO$_2$ with O$_{CUS}$. A) Schematic of reaction mechanism for HCHO oxidation aided by O$_{CUS}$ via carbonate reaction intermediate and B) DFT-calculated free energy diagram of formaldehyde oxidation on the (110) surface of MnO$_2$ surface with adsorbed oxygen (O$_{CUS1}$). The grey diagram showing the energy of bridging hydroxyl energy calculated in separate simulation cell to model low coverage reaction conditions (θ_{low}) and the red diagram showing the energetics in the co-adsorbed case to model high coverage reaction conditions (θ_{high}). Pink, manganese; blue, hydrogen; dark red, oxygen; grey, carbon. The equations and energetics for each step are reported in Reaction Scheme S8. The equations and energetics for each step are reported in Reaction Scheme S5.

Reaction Scheme A.15: Energetics of reaction of HCHO and O$_2$ assisted by O$_{CUS}$ to form CO$_2$ and H$_2$O via carbonate reaction intermediate with hydrogen adsorption on the bridge site (OH$_{BRI}$) computed using the same unit cell in red and different unit cells in grey to model high and low coverage scenarios.

$$HCHO + O_{CUS1} + O_{CUS2}^{vac} \rightarrow H_2CO_{CUS1}O_{CUS2} \ (G_1 = -1.19 \text{ eV})$$

$$H_2CO_{CUS1}O_{CUS2} + O_{BRI1} \rightarrow HCO_{CUS1}O_{CUS2} + OH_{BRI1} + H_2O \ (G_2 = -3.55 \text{ eV}, -3.40 \text{ eV})$$

$$HCO_{CUS1}O_{CUS2} + O_{CUS3} + O_{BRI2} \rightarrow$$
$$CO_{CUS1}O_{CUS2}O + OH_{BRI2} + H_2O \ (G_3 = -2.33 \text{ eV}, -2.28 \text{ eV})$$

$$CO_{CUS1}O_{CUS2}O \rightarrow O_{CUS1} + CO_2 \ (G_4 = +0.05 \text{ eV}, +0.46 \text{ eV})$$

$$O_{CUS1} + OH_{BRI1} + OH_{BRI2} + O_2$$
$$\rightarrow H_2O + O_{BRI1} + O_{BRI2} + O_{CUS1} (G_5 = +1.48 \text{ eV}, +0.88 \text{ eV})$$
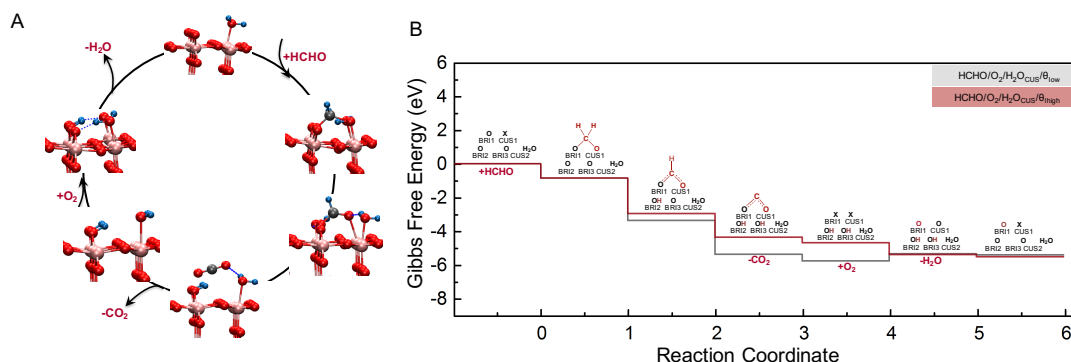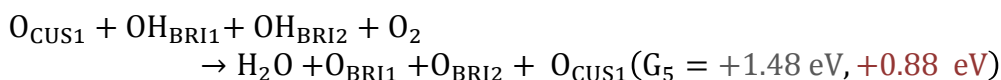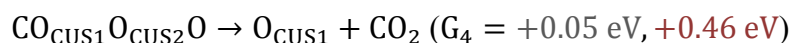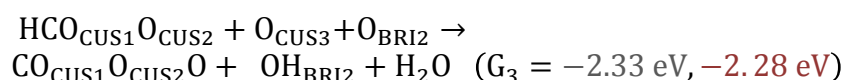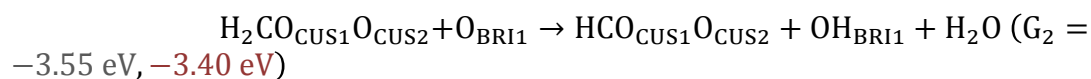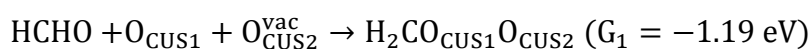
Figure A.1.26: DFT calculated reaction mechanism for MnO$_2$ with H$_2$O$_{CUS}$. A) Reaction mechanism for HCHO oxidation aided by H$_2$O$_{CUS}$ and B) Potential energy landscape of formaldehyde oxidation on the (110) surface of MnO$_2$ surface with adsorbed water (H$_2$O$_{CUS2}$) with the energy of bridging hydroxyl energy was calculated separately in grey and the co-adsorbed case in red. HCHO adsorbs preferably in a BRI-CUS bidentate configuration to form DOM (H$_2$CO$_{BRI1}$O$_{CUS2}$) with adsorption energy of -0.85 eV. Dehydrogenation of DOM to bidentate formate (HCO$_{BRI1}$O$_{CUS2}$) occurs via the formation of OH$_{BRI1}$ with energy of -2.53 eV for low coverage and -2.11 eV for the high hydroxyl coverage case. The second dehydrogenation leads to the formation of adsorbed CO$_2$ and OH$_{BRI2}$ (-2.00 eV, -1.40 eV for the low and high hydroxyl coverage cases) followed by desorption of CO$_2$ (-0.40 eV, -0.34 eV for the low and high hydroxyl coverage cases). The refilling of the resulting vacancies by molecular oxygen has energy of +0.42 and -0.69 eV respectively for the low coverage high hydroxyl coverage cases. Finally, the two hydrogen, OH$_{BRI1}$ and OH$_{BRI2}$ combine with adsorbed oxygen to desorb as H$_2$O to regenerate the surface (-0.06 eV and -0.14 eV respectively for low and high hydroxyl coverage cases. The grey diagram showing the energy of bridging hydroxyl energy calculated in separate simulation cell to model low coverage reaction conditions (θ_{low}) and the red diagram showing the energetics in the co-adsorbed case to model high coverage reaction conditions (θ_{high}). Pink, manganese; blue, hydrogen; dark red, oxygen; grey, carbon. The equations and energetics for each step are reported in Reaction Scheme S6A.

Reaction Scheme A.16A: Energetics of reaction of HCHO, HCHO, and O$_2$ on a stoichiometric surface via formate intermediate to form CO$_2$ and H$_2$O with hydrogen adsorption on the bridge site (OH$_{BRI}$) computed using the same unit cell in red and different unit cells in grey to model high and low coverage scenarios.

$$HCHO + O_{BRI1} + H_2O_{CUS2} + O^{vac}_{CUS1} \rightarrow H_2CO_{BRI1}O_{CUS1} - H_2O_{CUS2}(G_1 = -0.85 \text{ eV})$$

$$H_2CO_{BRI1}O_{CUS1} - H_2O_{CUS2} + O_{BRI2} \rightarrow HCO_{BRI1}O_{CUS1} - H_2O_{CUS2} + OH_{BRI2} (G_2 = -2.53 \text{ eV}, -2.11 \text{ eV})$$

$$HCO_{BRI1}O_{CUS1} - H_2O_{CUS2} + O_{BRI3} \rightarrow CO_{BRI1}O_{CUS1} + OH_{BRI3} + H_2O_{CUS2} (G_3 = -2.00 \text{ eV}, -1.40 \text{ eV})$$

$$CO_{BRI1}O_{CUS1} \rightarrow CO_2 + +O^{vac}_{BRI1} + +O^{vac}_{CUS1}(G_4 = -0.40 \text{ eV}, -0.34 \text{ eV})$$

$$H_2O_{CUS2} + O^{vac}_{BRI1} + OH_{BRI2} + OH_{BRI3} + O_2$$
$$\rightarrow O_{CUS1} + O_{BRI1} + H_2O_{CUS2} + OH_{BRI2}$$
$$+ OH_{BRI3} (G_4 = +0.42 \text{ eV}, -0.69 \text{ eV})$$

$$H_2O_{CUS2} + O_{CUS1} + OH_{BRI2} + OH_{BRI3}$$
$$\rightarrow H_2O_{CUS2} + H_2O + O_{BRI2} + O_{BRI3} (G_5 = -0.06 \text{ eV}, -0.14 \text{ eV})$$
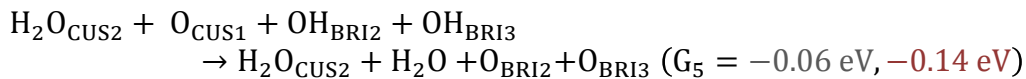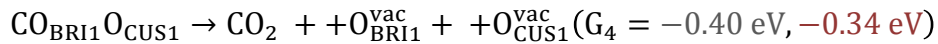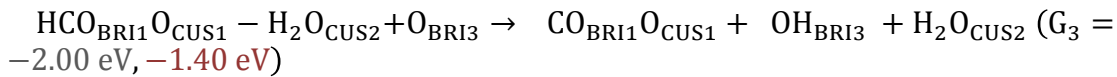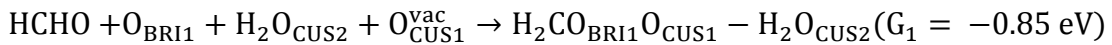
Figure A.1.27: DFT calculated reaction mechanism for MnO$_2$ with H$_2$O$_{CUS}$. A) Reaction mechanism for HCHO oxidation aided by H$_2$O$_{CUS}$ and B) Potential energy landscape of formaldehyde oxidation on the (110) surface of MnO$_2$ surface with adsorbed water (H$_2$O$_{CUS2}$) with the energy of bridging hydroxyl energy was calculated separately in grey and the co-adsorbed case in red. HCHO adsorbs in a BRI-CUS monodentate configuration to form DOM (H$_2$CO$_{BRI1}$O) with adsorption energy of +0.14 eV. Dehydrogenation of DOM to monodentate formate (HCO$_{BRI1}$O) occurs via the formation of OH$_{BRI1}$ with energy of -3.41 eV for low coverage and -3.05 eV for the high hydroxyl coverage case. The second dehydrogenation leads to the formation of adsorbed CO$_2$ and OH$_{BRI2}$ (-1.79 eV, -1.72 eV) followed by desorption of CO$_2$ (-0.83 eV, -0.10 eV). The refilling of the resulting vacancies by molecular oxygen has energy of +0.42 and -0.69 eV respectively for the for low coverage high hydroxyl coverage cases. Finally, the two hydrogen, OH$_{BRI1}$ and OH$_{BRI2}$, combine with adsorbed oxygen to desorb as H$_2$O to regenerate the surface (-0.06 eV and -0.14 eV respectively). The grey diagram showing the energy of bridging hydroxyl energy calculated in separate simulation cell to model low coverage reaction conditions (θ_{low}) and the red diagram showing the energetics in the co-adsorbed case to model high coverage reaction conditions (θ_{high}). Pink, manganese; blue, hydrogen; dark red, oxygen; grey, carbon. The equations and energetics for each step are reported in Reaction Scheme S6B.

Reaction Scheme A.16B: Energetics of reaction of HCHO, HCHO, and O$_2$ on a stoichiometric surface via formate intermediate to form CO$_2$ and H$_2$O with hydrogen adsorption on the bridge site (OH$_{BRI}$) computed using the same unit cell in red and different unit cells in grey to model high and low coverage scenarios.

$$\text{HCHO} + \text{O}_{BRI1} + \text{H}_2\text{O}_{CUS2} + \text{O}_{CUS1}^{vac} \rightarrow \text{H}_2\text{CO}_{BRI1}\text{O}_{CUS1} - \text{H}_2\text{O}_{CUS2}\,(G_1 = +0.14 \text{ eV})$$

$$\text{H}_2\text{CO}_{BRI1}\text{O}_{CUS1} - \text{H}_2\text{O}_{CUS2} + \text{O}_{BRI2}$$
$$\rightarrow \text{HCO}_{BRI1}\text{O}_{CUS1} - \text{H}_2\text{O}_{CUS2} + \text{OH}_{BRI2}\,(G_2 = -3.41 \text{ eV}, -3.05 \text{ eV})$$

$$\text{HCO}_{BRI1}\text{O}_{CUS1} - \text{H}_2\text{O}_{CUS2} + \text{O}_{BRI3} \rightarrow$$
$$\text{CO}_{BRI1}\text{O}_{CUS1} + \text{OH}_{BRI3} + \text{H}_2\text{O}_{CUS2}\,(G_3 = -1.79 \text{ eV}, -1.72 \text{ eV})$$

$$CO_{BRI1}O_{CUS1} \rightarrow CO_2 + O_{BRI1}^{vac} + O_{CUS1}^{vac} (G_4 = -0.83\ eV, -0.10\ eV)$$

$$H_2O_{CUS2} + O_{BRI1}^{vac} + OH_{BRI2} + OH_{BRI3} + O_2$$
$$\rightarrow O_{CUS1} + O_{BRI1} + H_2O_{CUS2} + OH_{BRI2}$$
$$+ OH_{BRI3}\ (G_4 = +0.42\ eV, -0.69\ eV)$$

$$H_2O_{CUS2} + O_{CUS1} + OH_{BRI2} + OH_{BRI3}$$

$$\rightarrow H_2O^{CUS2} + H_2O + O_{BRI2} + O_{BRI3}\ (G_5 = -0.06\ eV, -0.14\ eV)$$
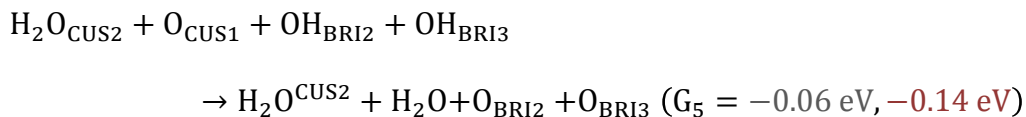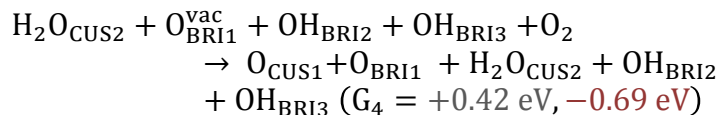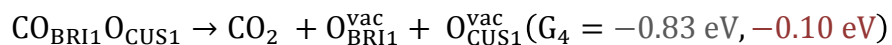
Reaction Scheme A.17: Energetics of reaction of HCHO, HCHO, and O_2 on surface with O_{CUS} via formate intermediate with hydrogen adsorption on the bridge site (OH_{BRI}) computed using the same unit cell in red and different unit cells in grey to model high and low coverage scenarios.

$$HCHO + O_{CUS1} + H_2O_{CUS2} \rightarrow H_2CO_{CUS1}O - H_2O_{CUS2}$$
$$H_2CO_{CUS1}O - H_2O_{CUS2} + O_{BRI2} \rightarrow HCO_{CUS1}O - H_2O_{CUS2} + OH_{BRI2} + H_2O\ (G_2 = -4.29\ eV, -4.25\ eV)$$

$$HCO_{CUS1}O - H_2O_{CUS2} + O_{BRI3} \rightarrow CO_2 + H_2O_{CUS2} + +OH_{BRI3} + H_2O + O_{CUS1}^{vac} (G_3 = -3.33\ eV, -2.85\ eV)$$

$$H_2O_{CUS2} + O_{CUS2}^{vac} + O_{CUS3}^{vac} + OH_{BRI2} + OH_{BRI3} + O_2 \rightarrow O_{CUS1} + O_{CUS2} + H_2O_{CUS2} + OH_{BRI2} + OH_{BRI3}$$

$$(G_5 = +2.15\ eV, +1.08\ eV)$$

$$O_{CUS1} + O_{CUS2} + H_2O_{CUS2} + OH_{BRI2} + OH_{BRI3}$$
$$\rightarrow H_2O + O_{CUS1} + O^{BRI2} + O^{BRI3}$$
$$+ O_{CUS2}^{vac} + H_2O_{CUS2} (G_6 = -0.05\ eV, +0.48\ eV)$$

214
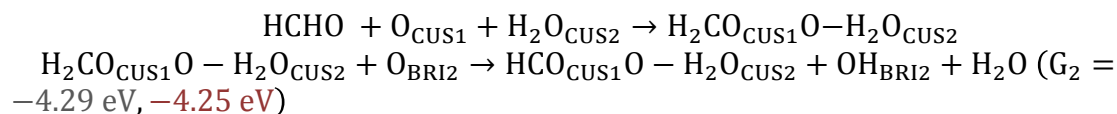
Figure A.1.28: DFT calculated reaction mechanism for MnO$_2$ with H$_2$O$_{CUS}$ and OH$_{CUS}$.
A) Reaction mechanism for HCHO oxidation aided by H$_2$O$_{CUS}$ and OH$_{CUS}$ via formate
reaction intermediate and B) Potential energy landscape of formaldehyde oxidation on the
(110) surface of MnO$_2$ surface with H$_2$O$_{CUS}$ and OH$_{CUS}$. The grey diagram showing the
energy of bridging hydroxyl energy calculated in separate simulation cell to model low
coverage reaction conditions (θ_{low}) and the red diagram showing the energetics in the co-
adsorbed case to model high coverage reaction conditions (θ_{high}). Pink, manganese; blue,
hydrogen; dark red, oxygen; grey, carbon. The equations and energetics for each step are
reported in Reaction Scheme S8.

Reaction Scheme A.18: Energetics of reaction of HCHO, HCHO, and O$_2$ on surface with
OH$_{CUS}$ via formate intermediate with hydrogen adsorption on the bridge site (OH$_{BRI}$)
computed using the same unit cell in red and different unit cells in grey to model high and
low coverage scenarios.

$$HCHO + O_{BRI1} + OH_{CUS2} + H_2O_{CUS1}$$
$$\rightarrow H_2CO_{BRI1}O - H_2O_{CUS1} + OH_{CUS2} (G_1 = -0.68 \text{ eV})$$

$$H_2CO_{BRI1}O - H_2O_{CUS1} + OH_{CUS2} \rightarrow HCO_{BRI1}O - H_2O_{CUS1} + H_2O_{CUS2} (G_2 = -2.33 \text{ eV})$$

$$HCO_{BRI1}O - H_2O_{CUS1} + O_{BRI2} \rightarrow CO_{BRI1}O + OH_{BRI2} \quad (G_3 = -2.38 \text{ eV}, -1.56 \text{ eV})$$

$$CO_{BRI1}O \rightarrow CO_2 + O_{BRI1}^{vac} (G_4 = -0.57 \text{ eV}, -0.51 \text{ eV})$$

$$O_2 + O_{BRI1}^{vac} + H_2O_{CUS1} + H_2O_{CUS2} \rightarrow 2H_2O + O_{CUS2} + O_{BRI1} + (G_5 = +1.01 \text{ eV}, +0.19 \text{ eV})$$

$$OH_{BRI2} + H_2O + O_{CUS2} \rightarrow +O_{BRI2} + OH_{CUS2} + H_2O_{CUS1} (G_2 = -0.56 \text{ eV}, -0.62 \text{ eV})$$
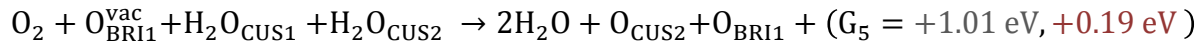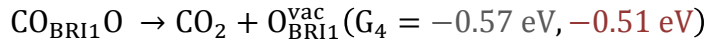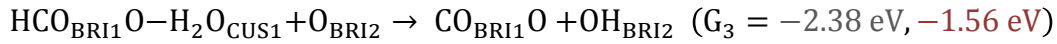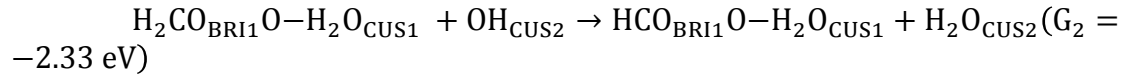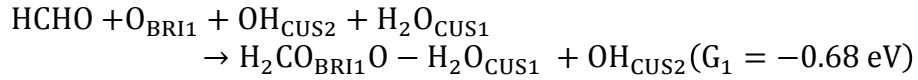
Figure A.1.29: Proposed reaction mechanism for HCHO oxidation via bidentate formate, carbonate, and monodentate formate-mediated pathways.

References

(1)   Wang, J.; Zhang, P.; Li, J.; Jiang, C.; Yunus, R.; Kim, J. Room-Temperature Oxidation of Formaldehyde by Layered Manganese Oxide: Effect of Water. *Environ. Sci. Technol.* **2015**, *49* (20), 12372–12379. https://doi.org/10.1021/acs.est.5b02085.

(2)   Wang, J.; Li, J.; Jiang, C.; Zhou, P.; Zhang, P.; Yu, J. The Effect of Manganese Vacancy in Birnessite-Type MnO2 on Room-Temperature Oxidation of Formaldehyde in Air. *Appl. Catal. B Environ.* **2017**, *204*, 147–155. https://doi.org/10.1016/J.APCATB.2016.11.036.

(3)   Bo, Z.; Guo, X.; Wei, X.; Yang, H.; Yan, J.; Cen, K. Mutualistic Decomposition Pathway of Formaldehyde on O-Predosed δ-MnO2. *Appl. Surf. Sci.* **2019**, *498*, 143784. https://doi.org/10.1016/j.apsusc.2019.143784.

(4)   Latimer, A. A.; Abild-Pedersen, F.; Nørskov, J. K. `. *ACS Catal.* **2017**, *7* (7), 4527–4534. https://doi.org/10.1021/acscatal.7b01417.

(5)   Nanayakkara, C. E.; Dillon, J. K.; Grassian, V. H. Surface Adsorption and Photochemistry of Gas-Phase Formic Acid on TiO2 Nanoparticles: The Role of Adsorbed Water in Surface Coordination, Adsorption Kinetics, and Rate of Photoproduct Formation. *J. Phys. Chem. C* **2014**, *118* (44), 25487–25495. https://doi.org/10.1021/jp507551y.

(6)   Li, X.; Paier, J. Vibrational Properties of CO2 Adsorbed on the Fe3O4 (111)

Surface: Insights Gained from DFT. *J. Chem. Phys.* **2020**, *152* (10), 104702. https://doi.org/10.1063/1.5136323.

(7) Ye, J.; Liu, C.; Ge, Q. DFT Study of CO 2 Adsorption and Hydrogenation on the in 2O 3 Surface. *J. Phys. Chem. C* **2012**, *116* (14), 7817–7825. https://doi.org/10.1021/jp3004773.

(8) Grinter, D. C.; R. Remesal, E.; Luo, S.; Evans, J.; Senanayake, S. D.; Stacchiola, D. J.; Graciani, J.; Fernández Sanz, J.; Rodriguez, J. A. Potassium and Water Coadsorption on TiO 2 (110): OH-Induced Anchoring of Potassium and the Generation of Single-Site Catalysts. *J. Phys. Chem. Lett.* **2016**, *7* (19), 3866–3872. https://doi.org/10.1021/acs.jpclett.6b01623.

(9) L. M. Liu, †,‡; B. McAllister, ‡; H. Q. Ye, † and; P. Hu*, ‡. Identifying an O2 Supply Pathway in CO Oxidation on Au/TiO2(110): A Density Functional Theory Study on the Intrinsic Role of Water. **2006**. https://doi.org/10.1021/JA056801P.

A.2: Supplementary Data for Chapter 3

A

B
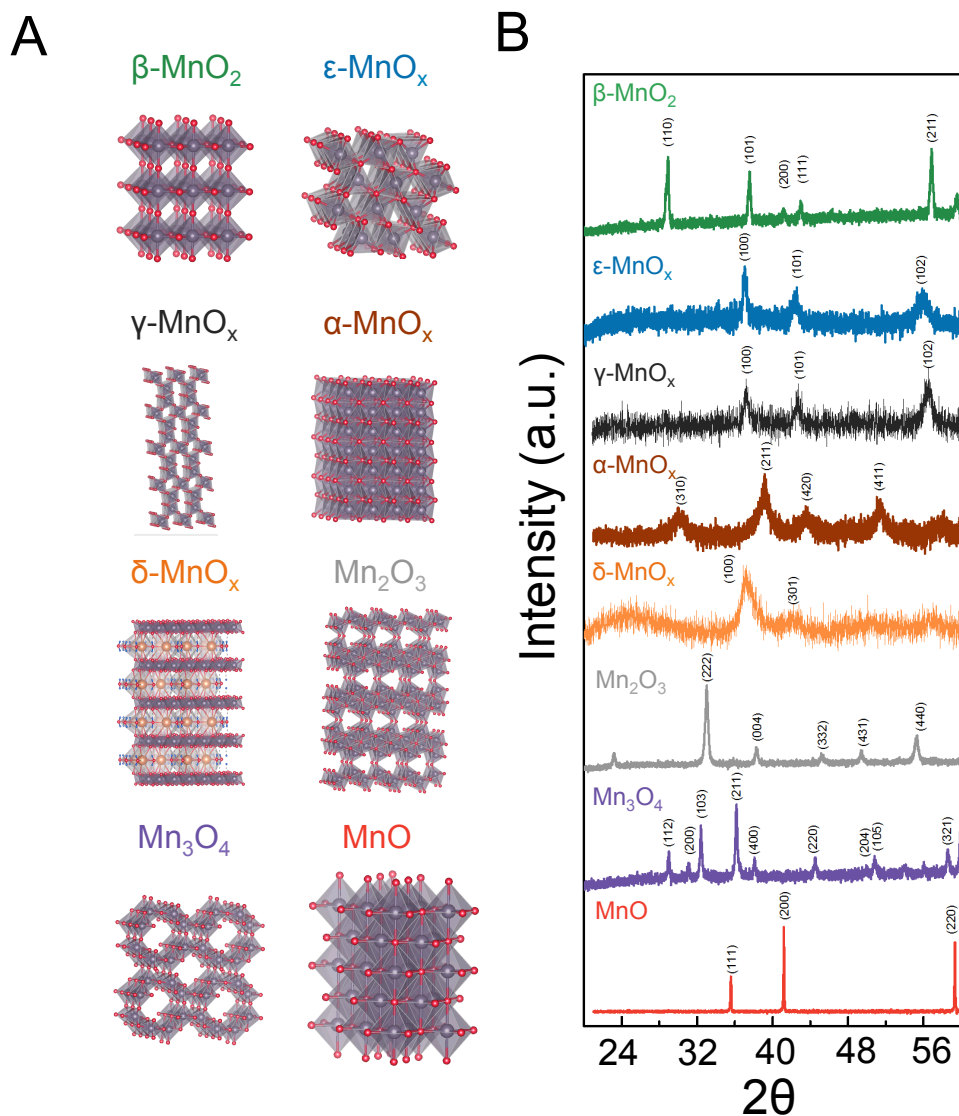
Figure A.2.1: Crystal structure of manganese oxides. A) Structures of the β-MnO₂, γ, ε, α, δ, Mn_2O_3, Mn_3O_4, and MnO manganese oxides used in this study. The γ, α, and δ-MnO_x manganese oxides contain water, alkali metals, and hydroxyl species while ε-manganese oxides contains water and hydroxyl species, B) XRD for all the oxides to confirm the crystal structures.
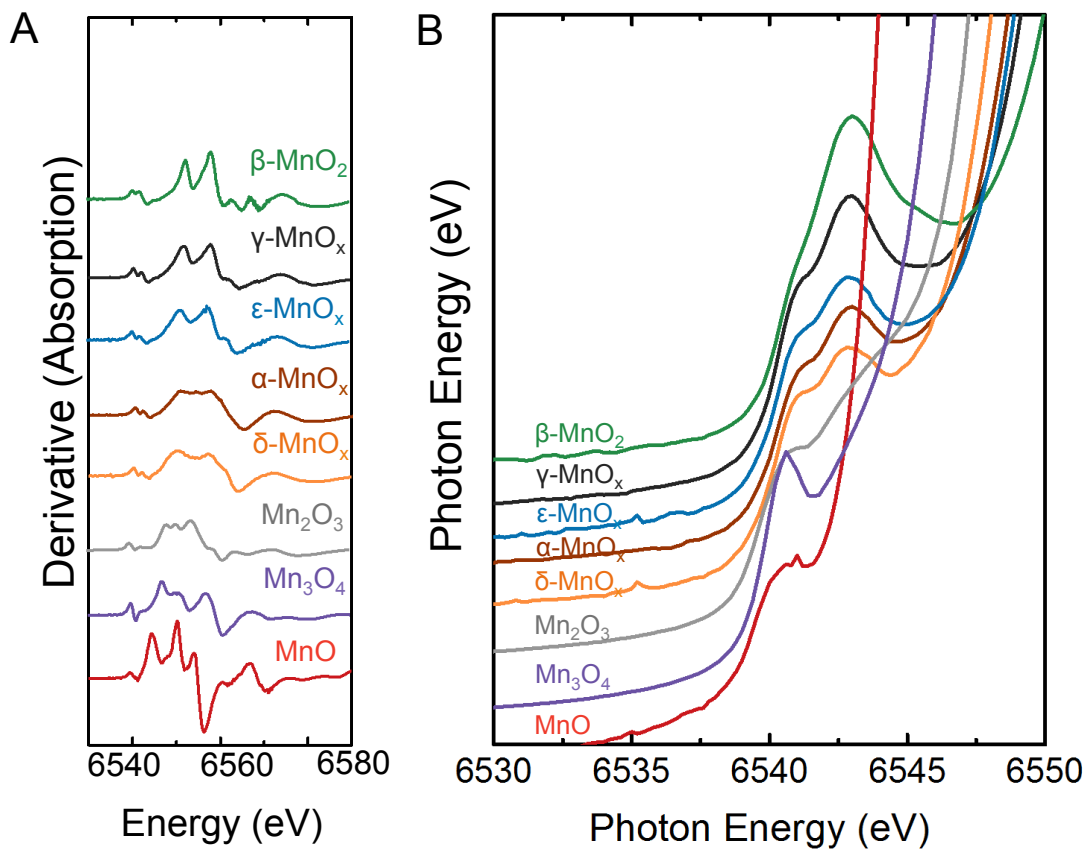
Figure A.2.2: XAS of manganese oxides. A) Derivative of the XAS spectrum from Figure 1A used to obtain the first inflection point for calibration of manganese valence for the different manganese oxide catalysts and B) Normalized pre-edge region X-ray absorption spectrum for the different manganese oxides. The pre-peak positions are reported in Table S1.

Table A.2.1: Pre-edges and inflection positions for the different manganese oxide catalysts obtained from the XAS spectrum in Figure 1A and Figure S2B. The formal valence was estimated by calibrating the formal valence of reference compounds (MnO, Mn_3O_4, Mn_2O_3, β-MnO_2) versus the inflection point from Figure S2A of the different oxides.

Oxide	Pre-Edge Peaks (eV)	Inflection Point (eV)	Formal Valence (eV)
MnO	6540.36	6544.47	2
Mn_3O_4	6540.55	6546.75	2.66
Mn_2O_3	6540.72	6548.31	3
δ-MnO_x	6540.96, 6542.75	6551.4	3.40
α-MnO_x	6541.14, 6542.81	6550.25	3.50
ε-MnO_x	6541.07, 6542.89	6550.99	3.65
γ-MnO_x	6541.26, 6542.81	6551.82	3.74
β-MnO_2	6540.96, 6542.93	6552.50	4
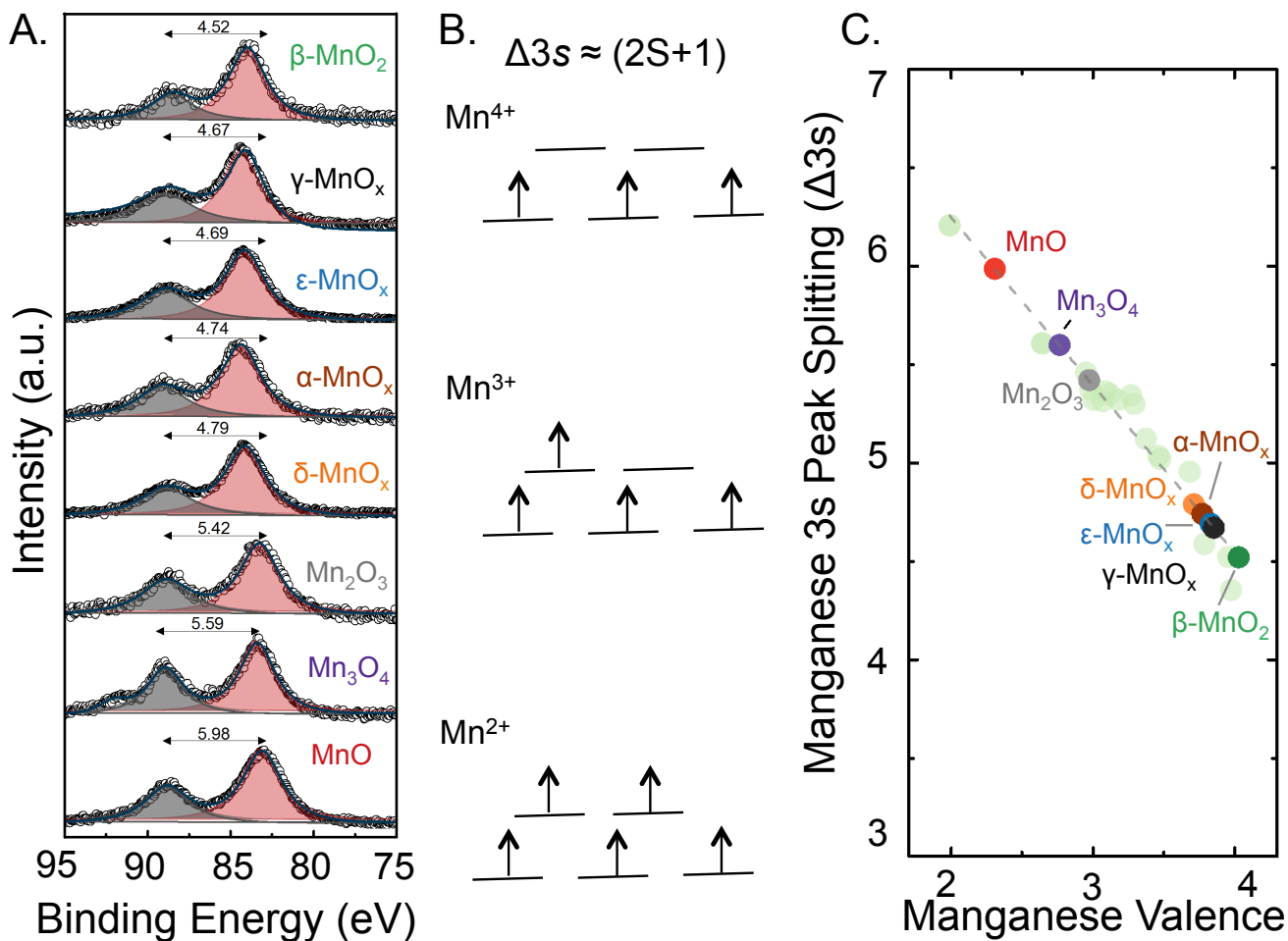
Figure A.2.3: XPS of manganese oxides. A) XPS Mn 3*s* spectrum of β-MnO₂, γ, ε, α, δ-MnOₓ, Mn₃O₄, Mn₂O₃, and MnO manganese oxides used in this study showing the increase in the Mn 3*s* peak splitting from β-MnO₂ to MnO, and B) Orbital configuration showing that the Mn 3*s* peak splitting is proportional to 2S+1 where S is the spin of the manganese 3d orbital. For ideal Mn^{4+}, Mn^{3+}, and Mn^{2+} with S = 3/2, 2, 5/2 the expected peak splitting is 4, 5, and 6 respectively, C) Linear trend of 3*s* peak splitting versus the formal valence previously developed was used to map the 3*s* peak splitting obtained from XPS (Mn Formal Valence = (7.95- Δ 3s)/ 0.85061).[1]

Table A.2.2: XPS Mn 3*s* peak splitting for all the oxides and the manganese formal valence estimated.

Oxide	$\Delta 3s$ (eV)	Formal Valence
MnO	5.98	2.30
Mn_3O_4	5.59	2.76
Mn_2O_3	5.42	2.97
δ-MnO$_x$	4.79	3.71
α-MnO$_x$	4.74	3.77
ϵ-MnO$_x$	4.69	3.83
γ-MnO$_x$	4.67	3.85
β-MnO$_2$	4.52	4.03
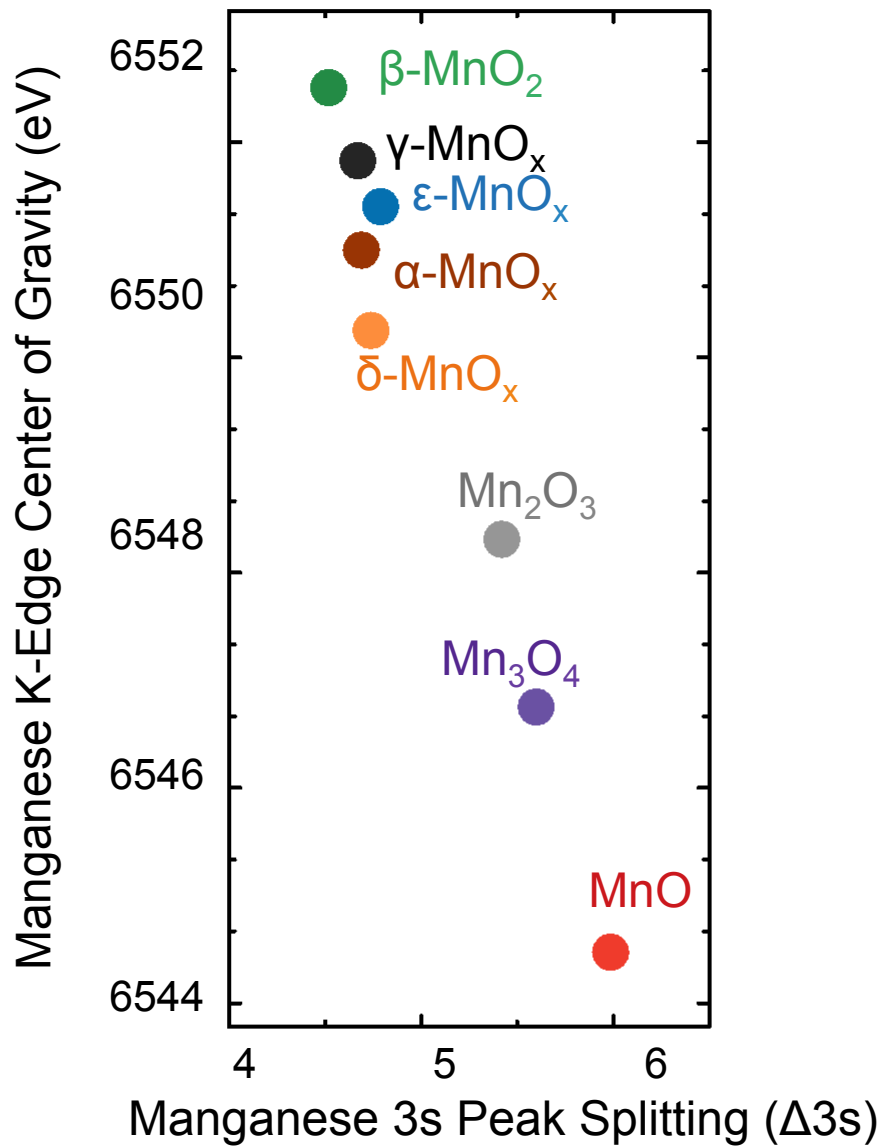
Figure A.2.4: Correlation between the manganese 3s peaks splitting ($\Delta 3s$) obtained from XPS (Figure A.2.3A) and the manganese K-edge center of gravity obtained from XAS (Figure 1B) suggesting that both techniques can be used to obtain manganese valence.
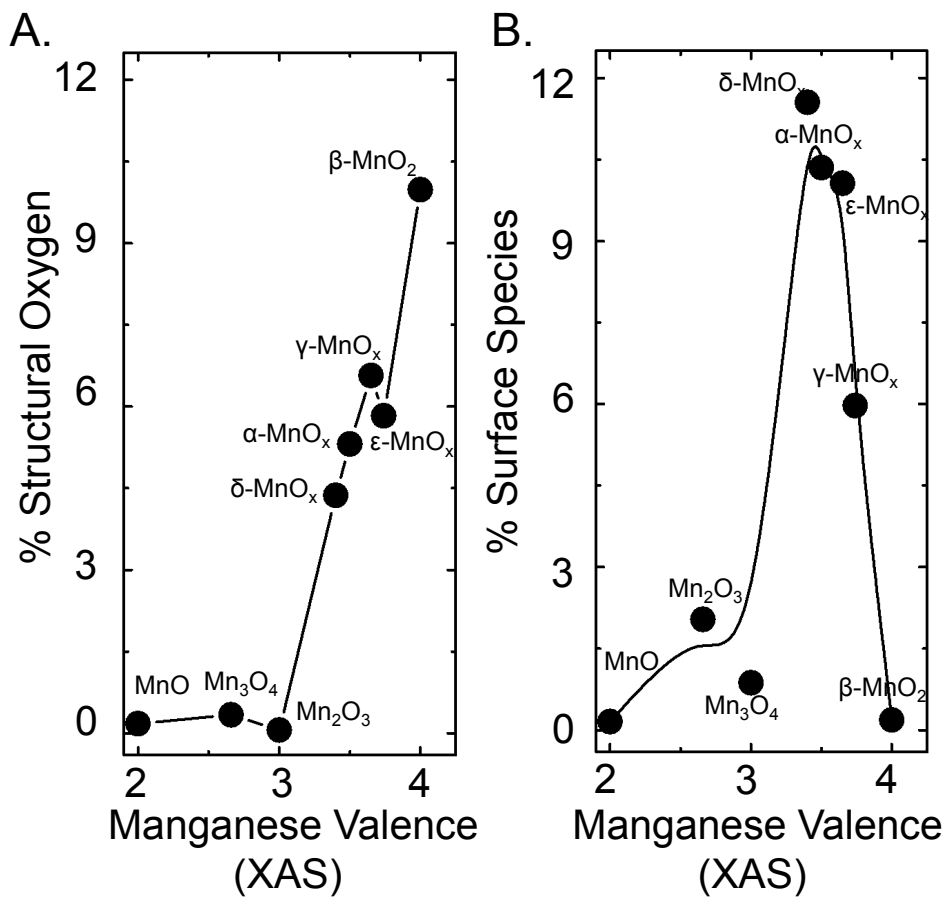
Figure A.2.5: Correlation between the A) surface species content (surface oxygen and hydroxyl) and the manganese formal valence estimated using XAS showing a volcano type trend and B) a linear trend for structural oxygen content measured using TGA versus the manganese formal valence obtained using XAS.
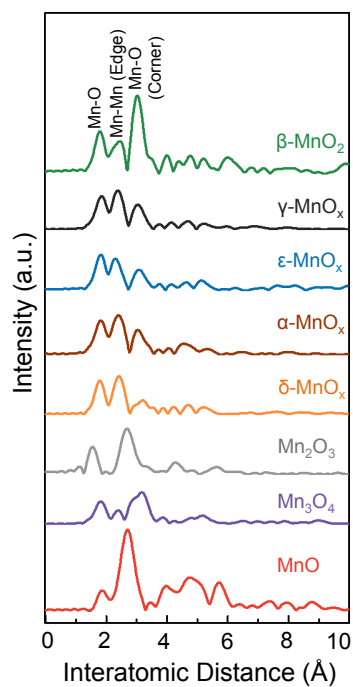
Figure A.2.6: EXAFS of the manganese oxides used in this study showing the peak positions and relative contributions of the Mn-O, Mn-Mn (edge), and Mn-O (corner) vectors.

Table A.2.3: EXAFS data of the catalysts showing the peak positions for the of Mn-O, Mn-Mn (corner), and Mn-Mn (edge) vectors.

Oxide	Mn-O(Å)	Mn-O (Edge)(Å)	Mn-Mn (corner)(Å)
MnO	1.82	2.68	3.49
Mn_3O_4	1.77	2.32	3.18
Mn_2O_3	1.55	2.62	-
$\delta\text{-}MnO_x$	1.76	2.41	3.22
$\alpha\text{-}MnO_x$	1.77	2.36	3.03
$\varepsilon\text{-}MnO_x$	1.73	2.32	3.09
$\gamma\text{-}MnO_x$	1.77	2.31	3.03
$\beta\text{-}MnO_2$	1.73	2.45	2.99
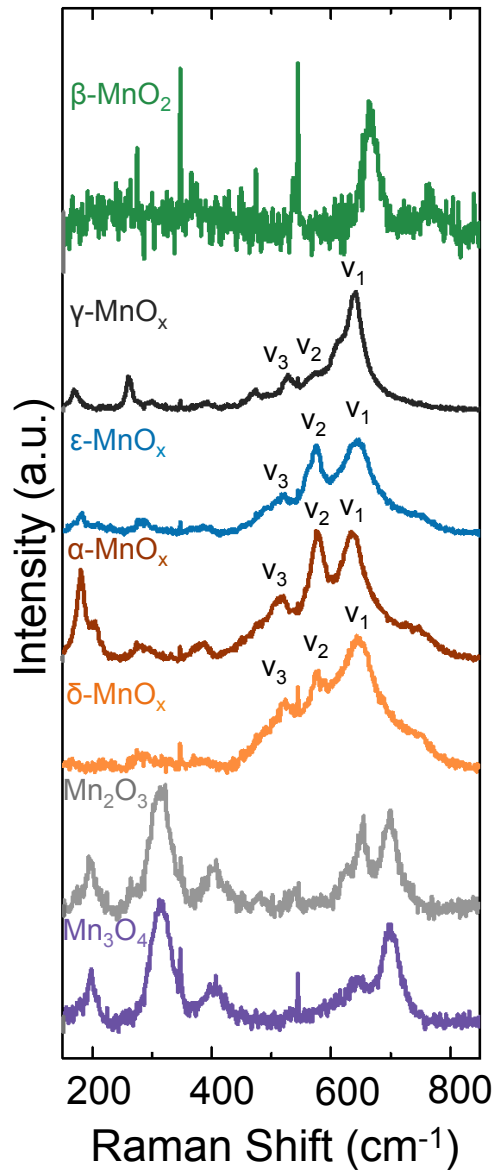
Figure A.2.7: Raman spectrum of the catalysts used in this study identifying the key γ_1, γ_2, and γ_3 lattice vibration for the defective γ, ε, α, δ-MnO$_x$ catalysts. The characteristics vibrations are reported in Table A.2.4.

Table A.2.4: Characteristic Raman peaks of the 4 water containing manganese oxide peaks

Catalyst	ν_1 (cm^{-1})	ν_2 (cm^{-1})	ν_3 (cm^{-1})
δ-MnO$_x$	646	576	520
α-MnO$_x$	635	576	513
ϵ-MnO$_x$	646	572	513
γ-MnO$_x$	638	572	524

Figure A.2.8: Trends of surface species content measured using TGA with surface area normalized A) HCHO adsorbed and B) CO_2 generated. CO_2 generated was calculated by normalizing the total amount of CO_2 converted as a function of time in Figure 3B by the BET surface area (Table S4). HCHO adsorbed was calculated subtracting the CO_2 converted from the HCHO adsorbed from Figure 3A,B.

Table A.2.5: Peak positions of reaction intermediates in DRIFTS for the different manganese oxide catalyst

Oxide	DOM HCHOO$_{oxide}$ (cm^{-1})	Carbonate COO$_{2oxide}$ (cm^{-1})	Formate HCOO$_{oxide}$ (cm^{-1})	Surface Hydroxyl OH$_{surface}$ (cm^{-1})	Lattice Hydroxyl OH$_{lattice}$ (cm^{-1})	Molecular Water (cm^{-1})
MnO	920-1180	-	-	-	3285	-
Mn$_3$O$_4$	920-1150	-	1575	-	3352	-
Mn$_2$O$_3$	920-1170	1497	1586	-	3452	-
δ-MnO$_x$	920-1130	1524	1575	3600	3287	-
α-MnO$_x$	920-1140	1521	1565	3520	3289	-
ε-MnO$_x$	920-1100	1508	1583	3490	3390	-
γ-MnO$_x$	920-1110	1517	1566	3490	3390	-
β-MnO$_2$	920-1110	-	1584	-	-	-
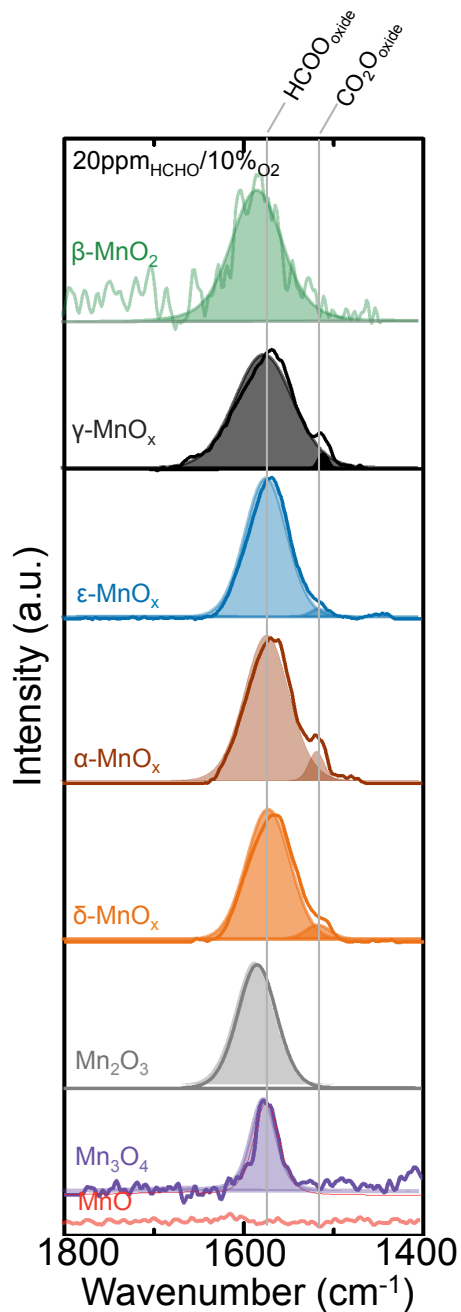
Figure A.2.9: De-convolution of the bidentate formate (HCOO$_{oxide}$) and carbonate peaks (COO$_{2oxide}$) of DRIFTS for the different manganese oxides collected at the breakthrough point. For all the measurements, inlet HCHO gas composition of 20 ppm HCHO and 10% O$_2$ with a flow rate of 200 ml min^{-1} was used at room temperature. Catalyst loading of 25 mg with 25 mg KBr was used. MnO$_2$ and MnO catalysts were ball milled in acetone for 12 hr prior to the DRIFTS measurements to improve the surface area.
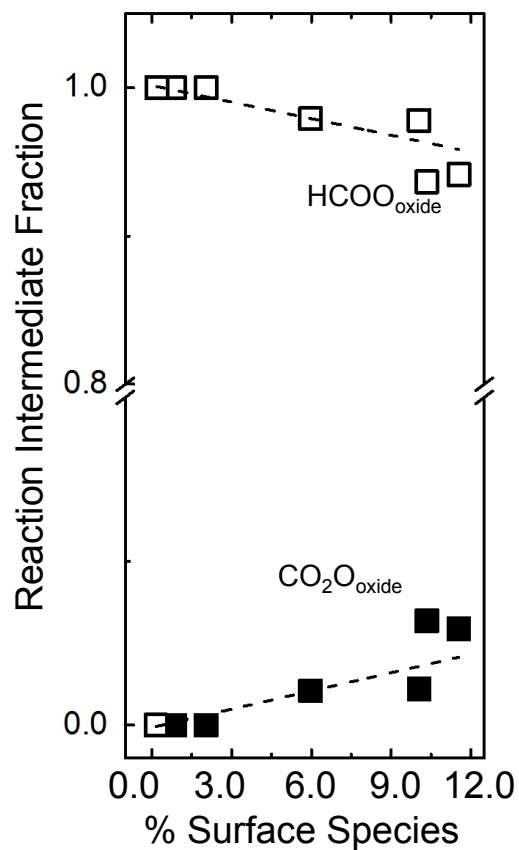
Figure A.2.10: Trends of surface species content measured using TGA with the fraction of bidentate formate ($HCOO_{oxide}$) and carbonate (COO_{2oxide}) reaction intermediates measured using DRIFTS and obtained from de-convolution of the DRFITS in Figure S9.
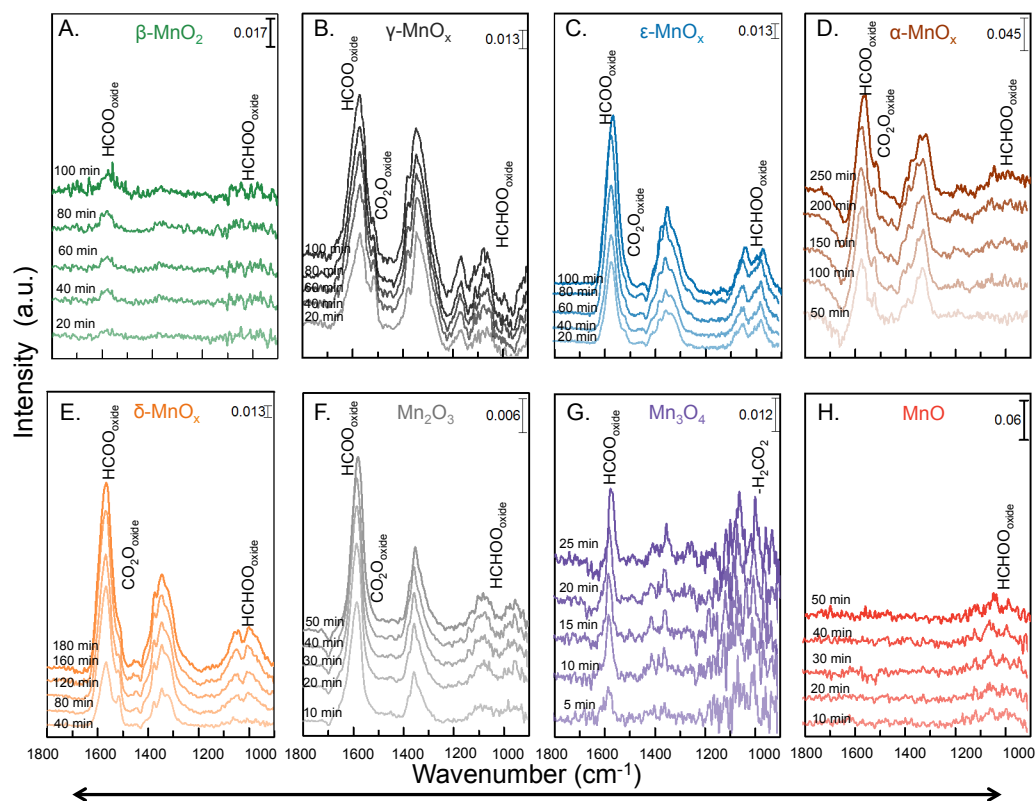
Figure A.2.11: DRIFTS of room temperature HCHO adsorption showing the formation and growth of dioxymethylene ($HCHOO_{oxide}$:1000-1200 cm^{-1}), carbonate (COO_{2oxide}:1500-1520 cm^{-1}), and bidentate formate reaction intermediates ($HCOO_{oxide}$:1565-1580 cm^{-1}) with time for all oxides after room temperature HCHO and O_2 adsorption. For all the measurements, inlet HCHO gas composition of 20 ppm HCHO and 10% O_2 with a flow rate of 200 ml min^{-1} was used at room temperature. Catalyst loading of 25 mg with 25 mg KBr was used. MnO_2 and MnO catalysts were ball milled in acetone for 12 hr prior to the DRIFTS measurements to improve the surface area.
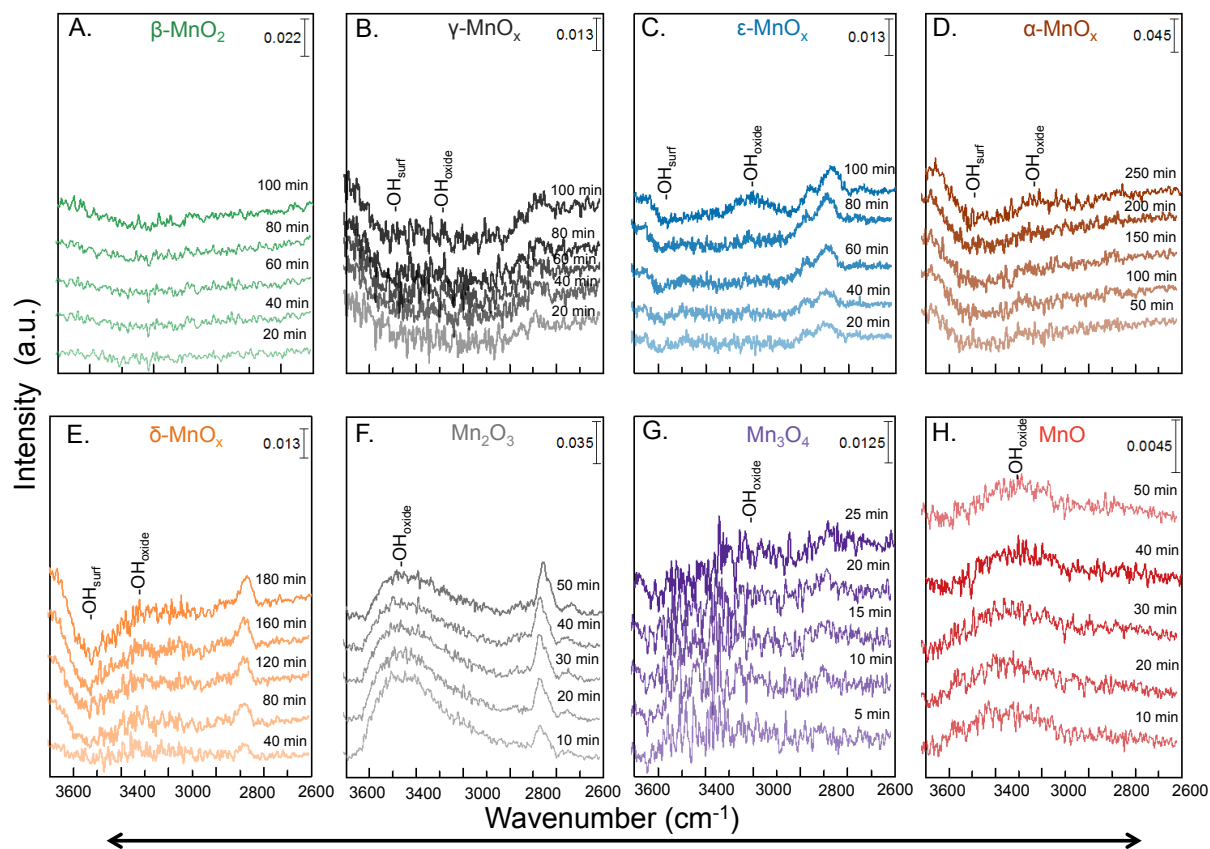
Figure A.2.12: DRIFTS of room temperature HCHO adsorption in the O-H region showing decrease in intensity of surface hydroxyl (OH_{surf}: 3595-3610 cm^{-1} region for γ, δ, ε, α MnO_x with increasing exposure time to the gas mixture. An increase in the lattice hydroxyl (OH_{oxide}: 3000-3500 cm^{-1}) was also observed for the Mn_2O_3. For all the measurements, inlet HCHO gas composition of 20 ppm HCHO and 10% O_2 with a flow rate of 200 ml min^{-1} was used at room temperature and catalyst loading of 25 mg with 25 mg KBr was used.
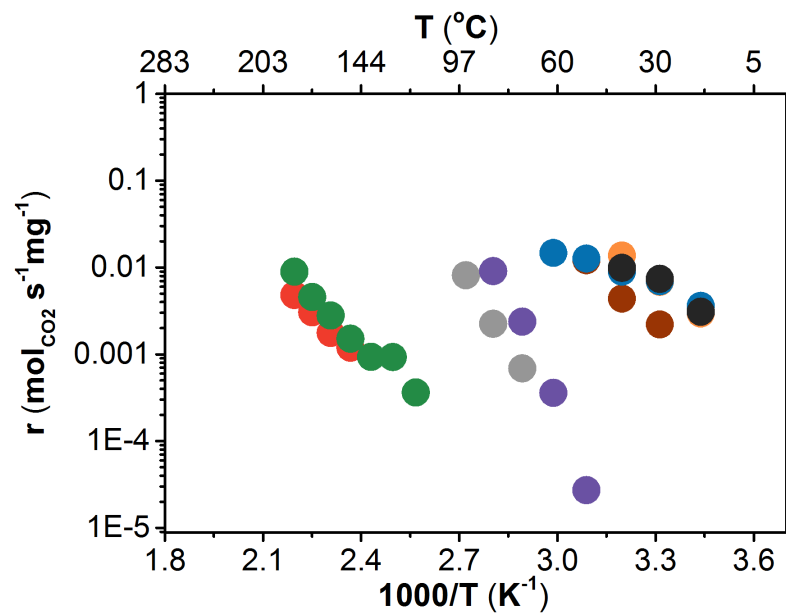
Figure A.2.13: Mass normalized reaction rates for the manganese oxides obtained from the light off curves in Figure 4A. For all the measurements, inlet HCHO gas composition of 20 ppm HCHO and 10% O_2 with a flow rate of 200 ml min^{-1} was used at room temperature and catalyst loading of 25 mg. The catalyst was first exposed to 20 ppm HCHO and 10 % O_2 at room temperature until breakthrough was achieved prior to heating up the sample.
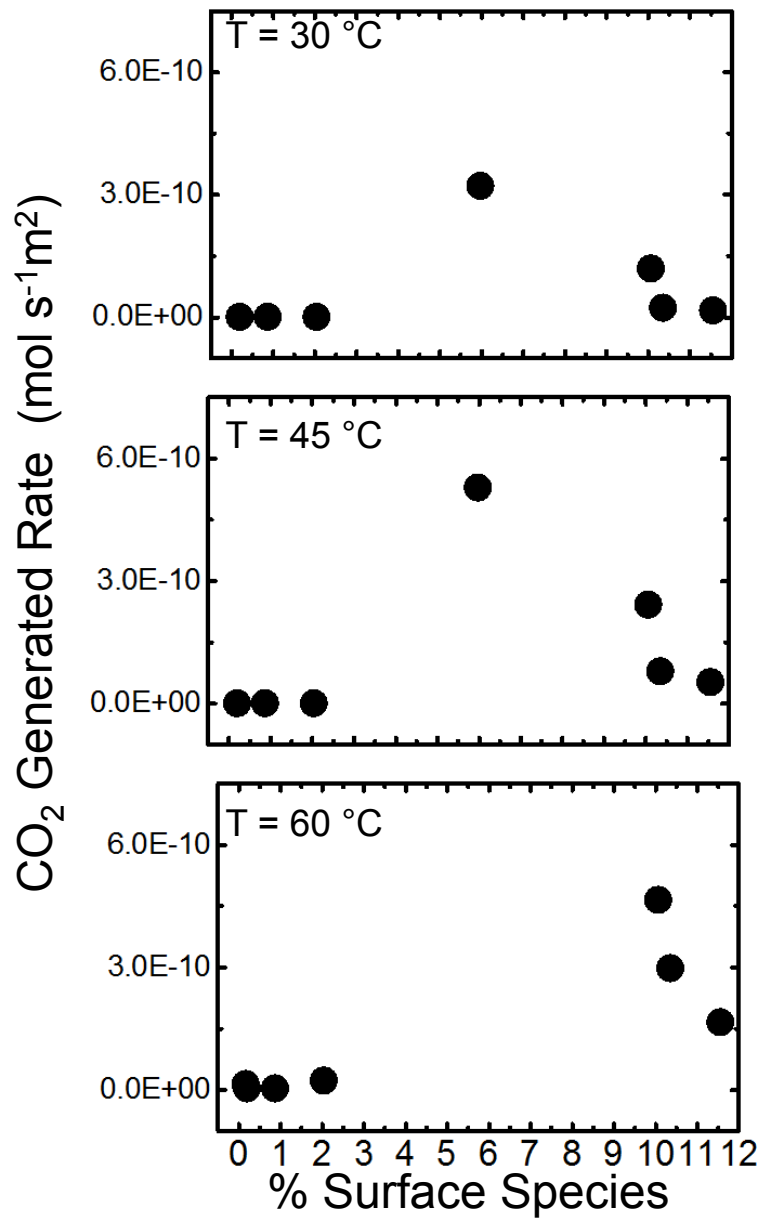
Figure A.2.14: Trends for surface area normalized CO_2 generation rate as a function of % surface species obtained from TGA for 30 °C, 45 °C, and 60 °C.

Table A.2.6: BET surface area of the catalysts

Catalyst	Surface Area (m^2/g)
MnO	0.78
Mn_3O_4	41
Mn_2O_3	15
$\delta\text{-MnO}_x$	101
$\alpha\text{-MnO}_x$	57
$\varepsilon\text{-MnO}_x$	180
$\gamma\text{-MnO}_x$	21
$\beta\text{-MnO}_2$	0.3

References

1.   Galakhov, V. R. *et al.* Mn 3 s exchange splitting in mixed-valence manganites. *Phys. Rev. B* **65**, 113102 (2002).

A.3: Supplementary Data for Chapter 4
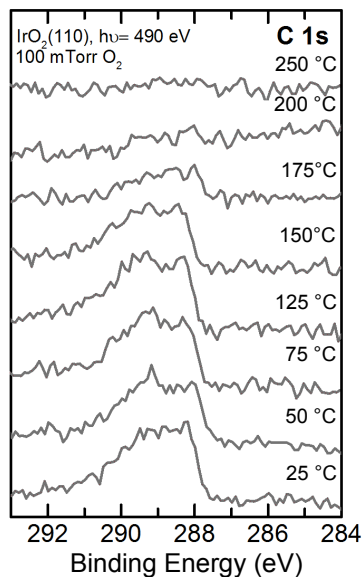
Figure A.3.1: AP-XPS of the C 1*s* region obtained during cleaning of IrO$_2$(110) surface under 100 mTorr O$_2$ to obtain a surface with minimum carbon contamination at 250 °C. C 1*s* spectra were collected at 735 eV.
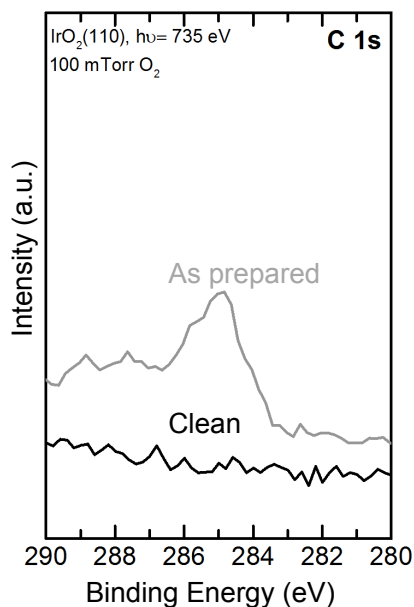
Figure A.3.2: AP-XPS of IrO$_2$(110) at room temperature comparing as-prepared and clean surface obtained by cleaning the sample in 100 mTorr O$_2$ at 250 °C and cooling down to 25 °C. C 1*s* spectra were collected at 735 eV.
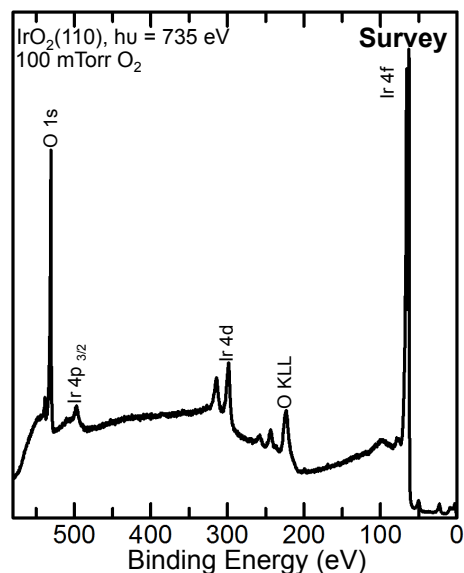
Figure A.3.3: Survey spectrum of $IrO_2(110)$ collected at room temperature at 100 mTorr O_2 after cleaning the surface at 250 °C under 100 mTorr O_2 and cooling back to room temperature. Survey spectrum was collected at 735 eV.
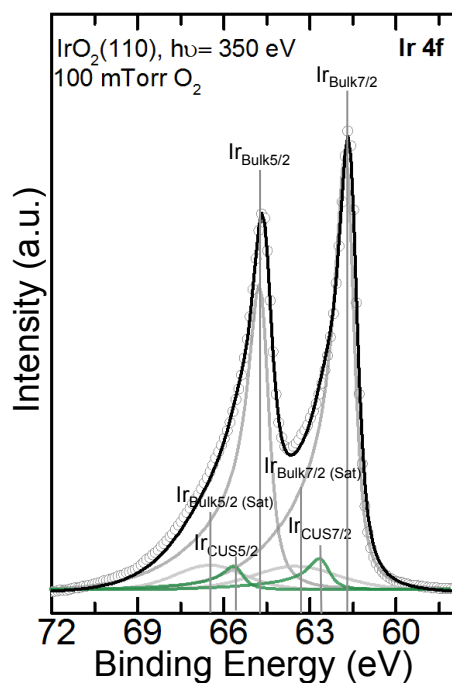
Figure A.3.4: Representative peak fitting Ir 4*f* region. Peak fitting for Ir 4*f* region with the higher binding energy features for Ir 4*f* spectrum identified as $Ir_{CUS7/2}$ at 62.4 eV and $Ir_{CUS5/2}$ at 65.4 eV while $Ir_{Bulk7/2}$ at 61.8 eV and the corresponding $Ir_{Bulk5/2}$ at 64.8 eV and the corresponding satellite features are assigned to the peaks at 63.3 eV ($Ir_{Bulk7/2\,(Sat)}$) and 66.1 eV ($Ir_{Bulk5/2\,(Sat)}$) respectively. Spectra were collected at room temperature under 100 mTorr O_2 and source energy 350 eV was used for Ir 4*f*. All intensities are fitted after background subtraction.

238

Table A.3.1: Fitting parameters of O 1s spectra with details of line shape, position, and fwhm constraints shown.

Species	Position (eV)	FWHM (eV)	Line Shape
O_{CUS}	528.8 – 529	0.9 – 1.1	GL(30)
O_{Bulk}	529.9 – 530.1	0.7 – 0.9	GL(30)
OH_{BRI}/OCH_3	531.1 – 531.3	1.2 – 1.4	GL(10)
$OH_{CUS}/HCOO$	532.1 – 532.3	1.6 –1.8	GL(40)
b-CO_2	533.8 – 534	1.1 –1.3	GL(30)

Table A.3.2: Fitting parameters and constraints for the Ir 4f spectra with details of line shape, position, and FWHM constraints shown. Fitting parameters have been adapted from refs. [1,2] with modifications.

Species	Position (eV)	FWHM (eV)	Line Shape	Constraints
$Ir_{Bulk}4f_{7/2}$	61.7 – 61.9	0.7 – 0.8	LF (0.375, 1.65, 100)	–
$Ir_{Bulk}4f_{5/2}$	64.7 – 64.9	0.7 – 0.8	LF (0.375, 1.65, 100)	Position: $Ir_{Bulk}4f_{7/2}$+ 3 eV, Area=0.75* $Ir_{Bulk}4f_{7/2}$;
$Ir_{Bulk}4f_{7/2\,(Sat)}$	63.2 – 63.4	3.5 – 3.7	GL(40)	Area=0.13* $Ir_{Bulk}4f_{7/2}$;
$Ir_{Bulk}4f_{5/2\,(Sat)}$	66.2 – 66.4	3.5 – 3.7	GL(40)	Position: $Ir_{Bulk}4f_{7/2\,(Sat)}$ + 3 eV; Area=0.11* $Ir_{Bulk}4f_{7/2\,(Sat)}$
$Ir_{CUS}4f_{7/2}$	62.2 – 62.4	0.7 – 0.8	LF (0.375, 1.65, 100)	–
$Ir_{CUS}4f_{5/2}$	65.2 – 65.4	0.7 – 0.8	LF (0.375, 1.65, 100)	Position: $Ir_{CUS}4f_{7/2}4f_{7/2}$+ 3 eV, Area=0.75* $Ir_{CUS}4f_{7/2}$
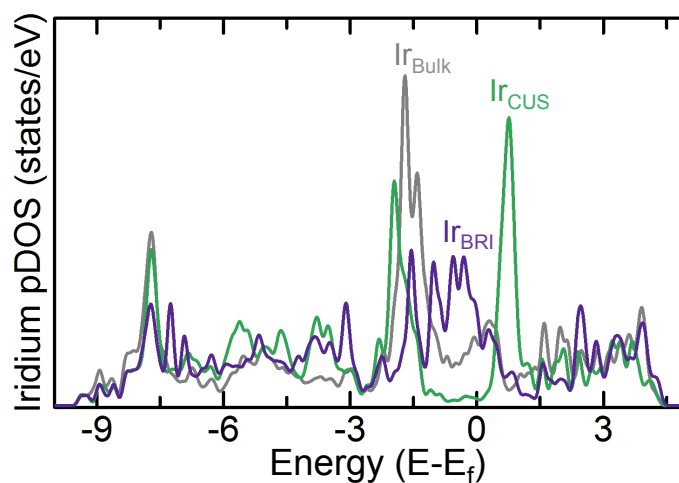
Figure A.3.5: Calculated pDOS of Iridium states for Ir_{BRI} (violet), Ir_{CUS} (green), and Ir_{Bulk} (grey) species showing increase in intensity closer to the Fermi edge for Ir_{CUS} species. Iridium DOS are calculated by summing up Ir d states for the respective species for $IrO_2(110)$ shown in Fig. 2A.

Table A.3.3: Normalized intensities of O_{CUS} and Ir_{CUS} species relative to the corresponding O_{Bulk} in Figs. 1 and 2.

Reaction Condition	O_{CUS} (Normalized)	Ir_{CUS} (Normalized)
As-prepared	0.03	0.00
Clean	0.11	1.46
100 mTorr $CH_3OH/200mTorrO_2$	0.00	0.00
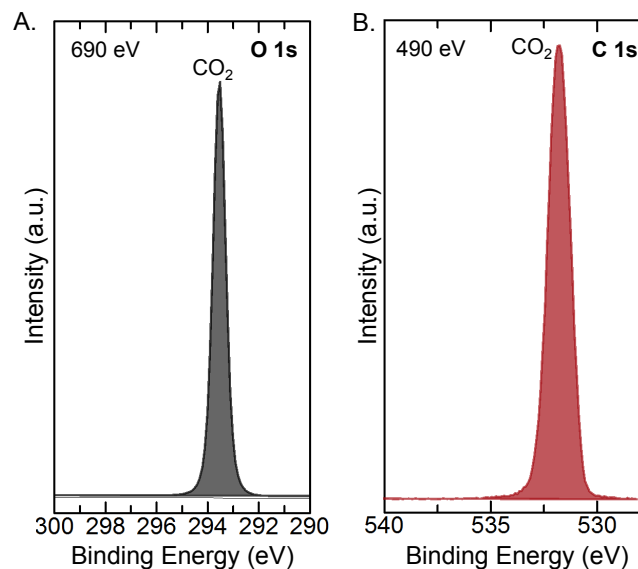
Figure A.3.6: Gas-phase CO_2 spectra collected after retracting the sample in the AP-XPS chamber using source energy of A) 690 eV and B) 490 eV. Relative sensitivity factor (RSF) obtained using intensity of gas phase CO_2 spectra measured at 490 eV and 690 eV as 2*(C $1s$ peakarea)/ (O $1s$ peakarea) = ~0.9.[3]

Table A.3.4: Summary of peak de-convolution parameters for the C $1s$ spectra.

Species	Position (eV)	FWHM (eV)	Line Shape
C-C/CH$_X$[4]	284.7 – 284.9	1.2 – 1.4	GL(30)
CH$_3$O[5]	286.1 – 286.3	0.9 – 1.1	GL(30)
HCOO[6]	287.1 – 287.4	1.1– 1.3	GL(30)
b-CO$_2$[6]	288.1 – 288.4	1.0–1.2	GL(30)
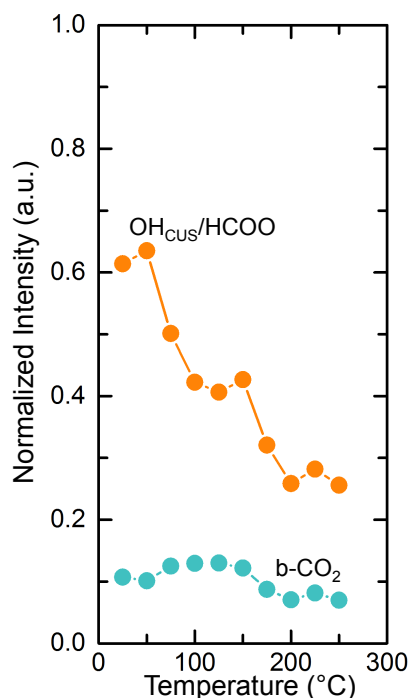
Figure A.3.7: Normalized AP-XPS intensities of O $1s$ surface species, OH_{CUS}/HCOO and b-CO_2 relative to O_{Bulk} as a function of temperature from 25 °C to 250 °C in the presence of 25 mTorr CH_3OH-100 mTorr O_2. Source energy of 690 eV was used for the O $1s$ spectrum.
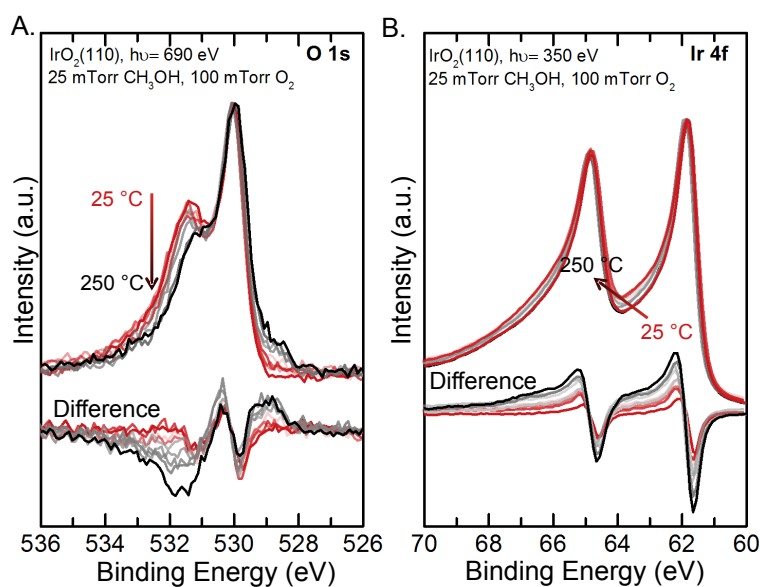
Figure A.3.8: AP-XPS difference spectrum under methanol-oxygen gas mixture upon heating. Low temperature methanol oxidation showing A) appearance and growth of O_{CUS} species from 25 °C to 250 °C as well as the loss of OH_{CUS}, HCOO, CH_3O species in the O $1s$ spectrum, B) appearance and growth of Ir_{CUS} species from 25°C to 250 °C in the Ir $4f$ spectrum. Source energy of 690 eV was used for the O $1s$ spectrum, while 350 eV was used for Ir $4f$ and valence band spectra. The total intensities of O $1s$ and Ir $4f$ have been normalized to the O_{Bulk} and Ir_{Bulk} prior to obtaining the difference spectrum.
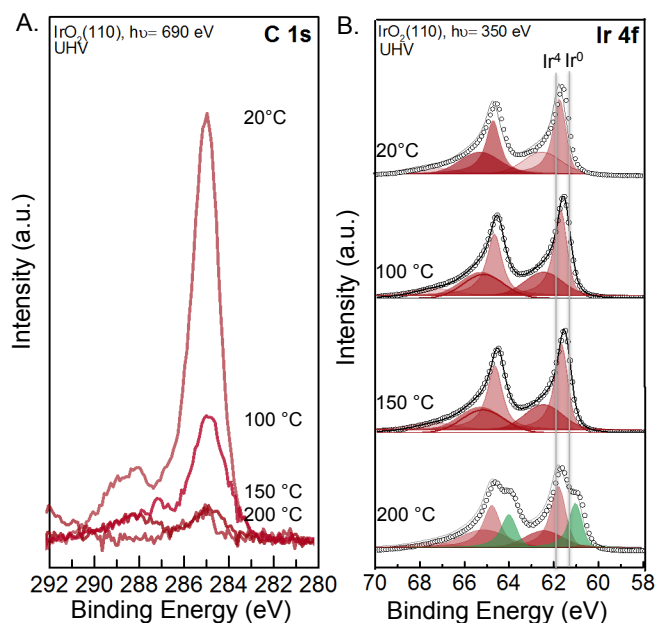
Figure A.3.9: Optimizing a cleaning procedure for IrO_2 (110) thin films to study CH_4 activation by A) minimizing the amount of carbonaceous reaction intermediates seen in the C 1s spectrum and B) avoiding surface reduction of IrO_2 (Ir^{4+}) leading to the formation of metallic Ir (Ir^0) as a function of final cooling temperature (20, 100, 150, and 200 °C) in the Ir 4f spectrum after cleaning at 250 °C. A relatively carbon-free surface was identified at 125 °C under UHV conditions after a tradeoff between carbon contamination and surface reduction at different temperatures. Source energy of 490 eV was used for the C 1s spectra, and 350 eV was used for Ir 4f spectra. All intensities are plotted after background subtraction without normalization.
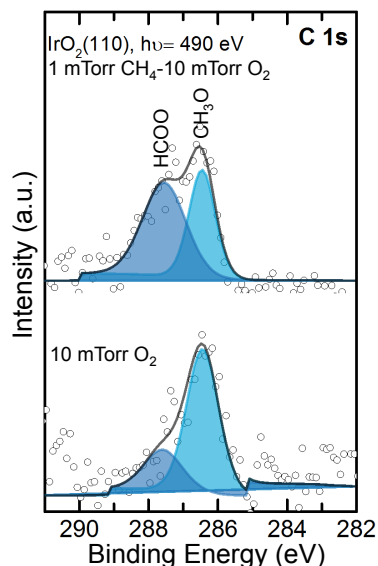
Figure A.3.10: C 1s spectrum for the reaction conditions of 10 mTorr O_2 obtained after cleaning at 250 °C and cooling back to 125 °C and after introduction of 1 mTorr CH_4-10 mTorr O_2. Source energy of 490 eV was used for the C 1s spectrum. All intensities are plotted after background subtraction without normalization.
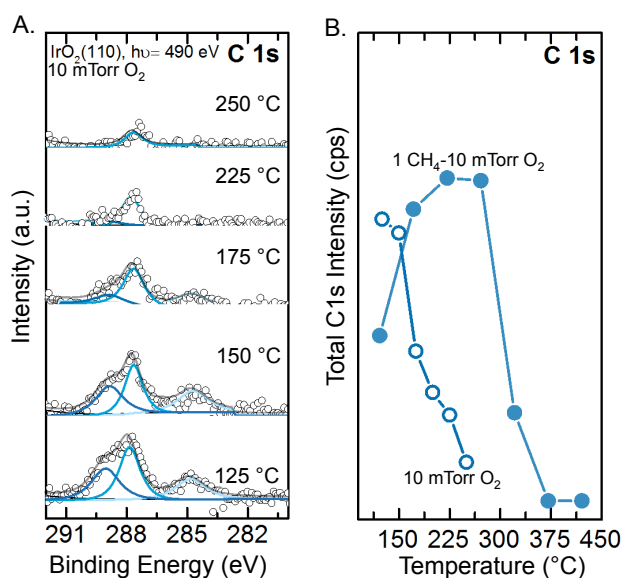
Figure A.3.11: A) AP-XPS spectrum of the C 1*s* region under 10 mTorr O_2 in the temperature range 125 °C and 250 °C after initial exposure to 1 mTorr CH_4-10 mTorr O_2 at 125 °C and B) Comparison of total C 1*s* intensities for the reaction conditions of 1 mTorr CH_4 -10 mTorr O_2 and 10 mTorr O_2 showing an increase in intensity for the reaction condition containing CH_4 while no such increase was seen for the oxygen only case. This result suggests that methane activation was achieved between 125 °C and 175 °C. Source energy of 490 eV was used for the C 1*s* spectrum. All intensities are plotted after background subtraction without normalization.
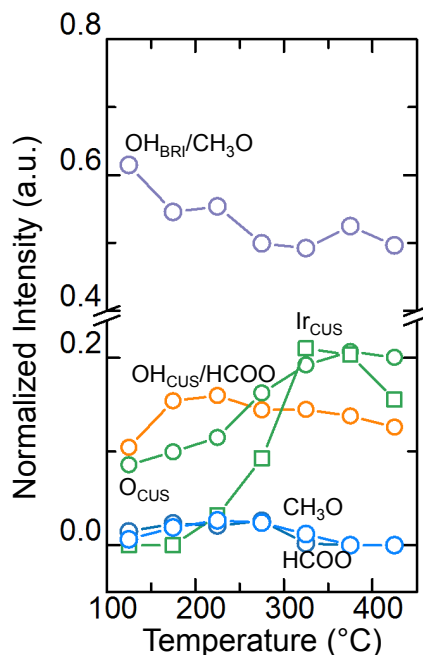
Figure A.3.12: Normalized AP-XPS intensities of C 1*s* surface species, CH_3O, HCOO and O 1*s* surface species, O_{CUS}, OH_{BRI}/CH_3O, $OH_{CUS}/HCOO$, and Ir 4*f* surface, $Ir_{CUS,}$ relative to the respective O_{Bulk} intensity as a function of temperature from 125 °C to 425 °C in the presence of 1mTorr CH_4-10 mTorr O_2.

244
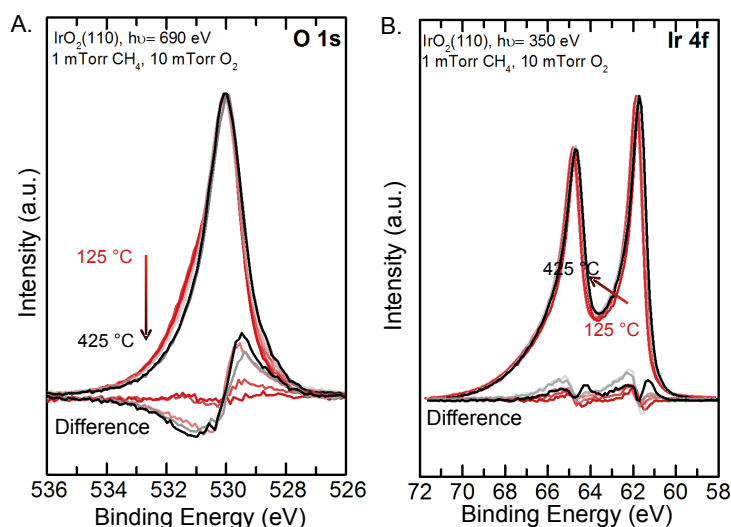
Figure A.3.13: Difference spectra for methane oxidation reaction conditions under 1 mTorr CH_4 -10 mTorr O_2 showing A) appearance and growth of O_{CUS} species from 125 °C to 425 °C as well as the loss of OH_{BRI}/CH_3O (531.1 eV) and $OH_{CUS}/HCOO$ (532.1 eV) in the O 1s spectrum, B) appearance and growth of Ir_{CUS} species (62.3 eV) from 225°C to 425°C in the Ir 4f spectrum. Source energy of 690 eV was used for the O 1s spectrum, while 350 eV was used for Ir 4f spectra. The intensities of O 1s and Ir 4f have been normalized to the O_{Bulk} and Ir_{Bulk} respectively prior to spectrum difference.
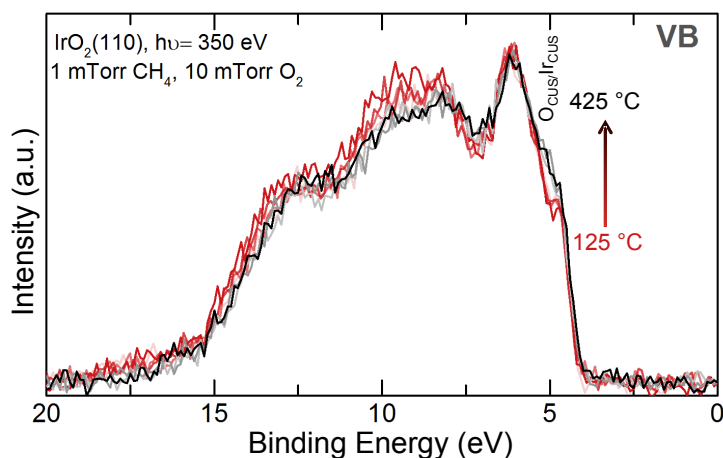
Figure A.3.14: Valence band spectrum under methane oxidation reaction conditions of 1 mTorr CH_4 -10 mTorr O_2 showing increase in intensity closer to the Fermi edge corresponding to O_{CUS}/Ir_{CUS} species and decrease of intensity away from the edge with increase in temperature from 125 °C to 425 °C. Source energy of 350 eV was used for valence band spectra collection.
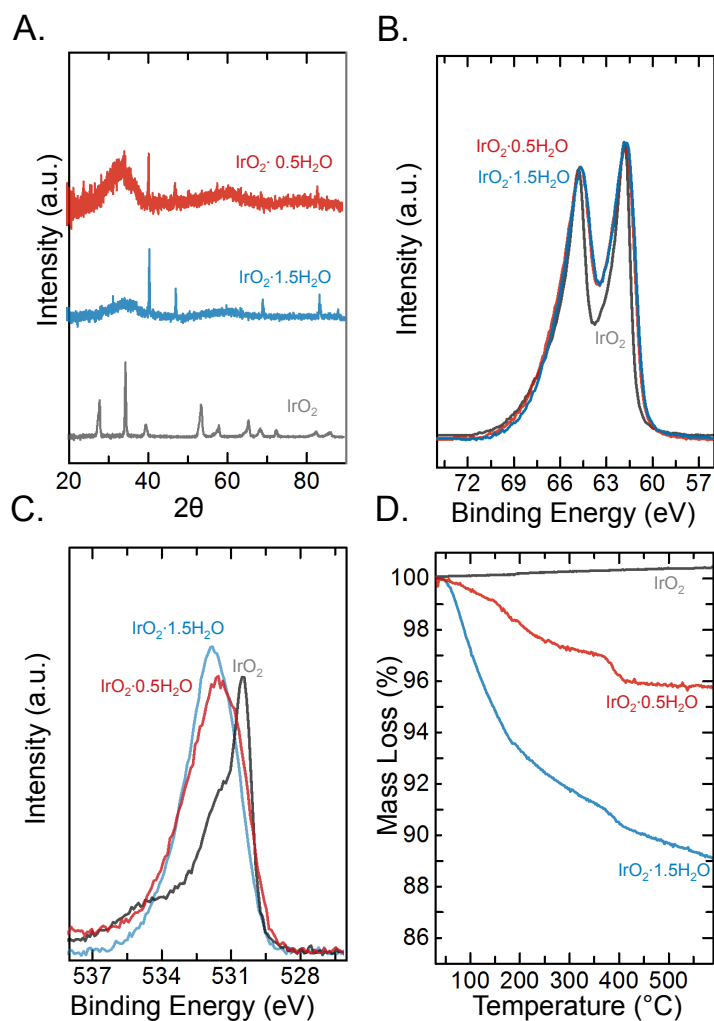
Figure A.3.15: A) XRD pattern of the rutile Iridium oxide and Iridium oxide with 2 different water contents, $IrO_2 \cdot 0.5H_2O$ and $IrO_2 \cdot 1.5H_2O$, B) Ir *4f* spectral region with higher Ir_{CUS} for the $IrO_2 \cdot 0.5H_2O$ and $IrO_2 \cdot 1.5H_2O$, C) O *1s* spectrum showing larger carbonaceous and hydroxyl related peaks (531-534 eV) for the $IrO_2 \cdot 0.5H_2O$ and $IrO_2 \cdot 1.5H_2O$ compared to rutile IrO_2, D) TG mass loss showing the highest mass loss for the $IrO_2 \cdot 1.5H_2O$ and negligible mass loss for rutile IrO_2. XPS spectra were collected using lab source XPS with source energy of 1100 eV.
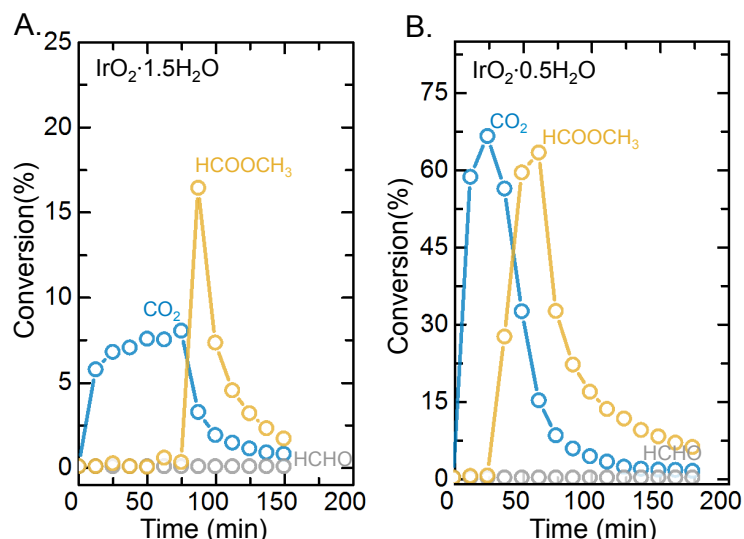
Figure A.3.16: Reactor data for CH_3OH conversion (%) to $HCOOCH_3$, HCHO, and CO_2 for A) $IrO_2 \cdot 0.5H_2O$, B) $IrO_2 \cdot 1.5H_2O$ as a function of time at room temperature. %Conversion to CO_2 is defined as $100*(CO_{2ppm,out}/CH_3OH_{ppm,in}$, to HCHO is defined as $100*(HCHO_{ppm,out}/CH_3OH_{ppm,in}$; and to $HCOOCH_3$ is defined as $100*(HCOOCH_{3ppm,out}/CH_3OH_{ppm,in}$; Catalyst loading of 50 mg, inlet flow rate of 150 ml min^{-1}, and gas concentration of 70 ppm CH_3OH/560 ppm O_2 was used for all the measurements.
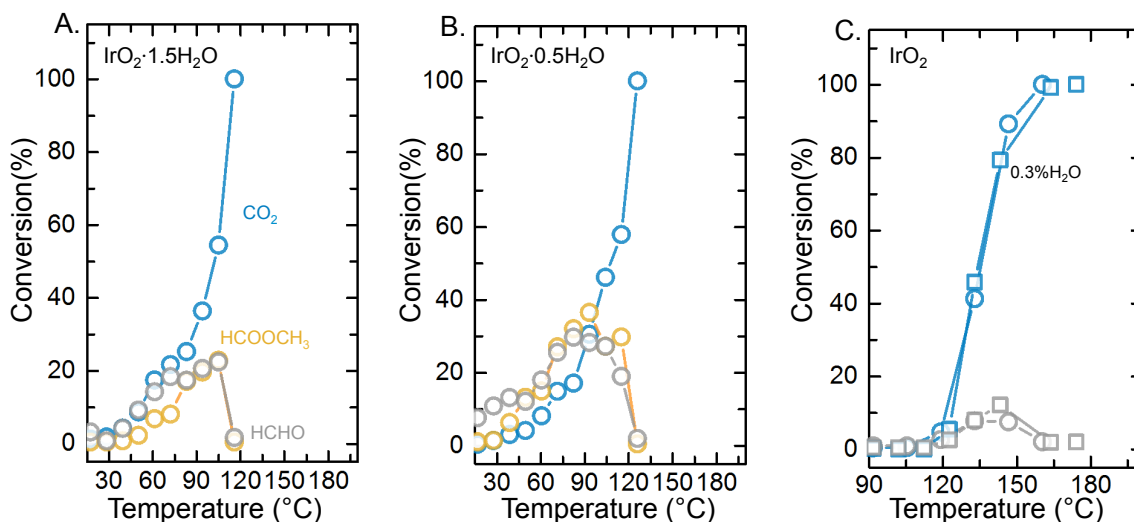
Figure A.3.17: Reactor data for CH_3OH conversion (%) to $HCOOCH_3$, HCHO, and CO_2 for A) $IrO_2 \cdot 0.5H_2O$, B) $IrO_2 \cdot 1.5H_2O$, and C) IrO_2 catalysts with and without 0.3% H_2O (square) in the gas stream as a function of temperature. %Conversion to CO_2 is defined as $100*(CO_{2ppm,out}/CH_3OH_{ppm,in}$; to HCHO is defined as $100*(HCHO_{ppm,out}/CH_3OH_{ppm,in}$; and to $HCOOCH_3$ is defined as $100*(HCOOCH_{3ppm,out}/CH_3OH_{ppm,in}$; Catalyst loading of 50 mg, inlet flow rate of 150 ml min^{-1} , and gas concentration of 70 ppm CH_3OH/560 ppm O_2 was used for all the measurements.
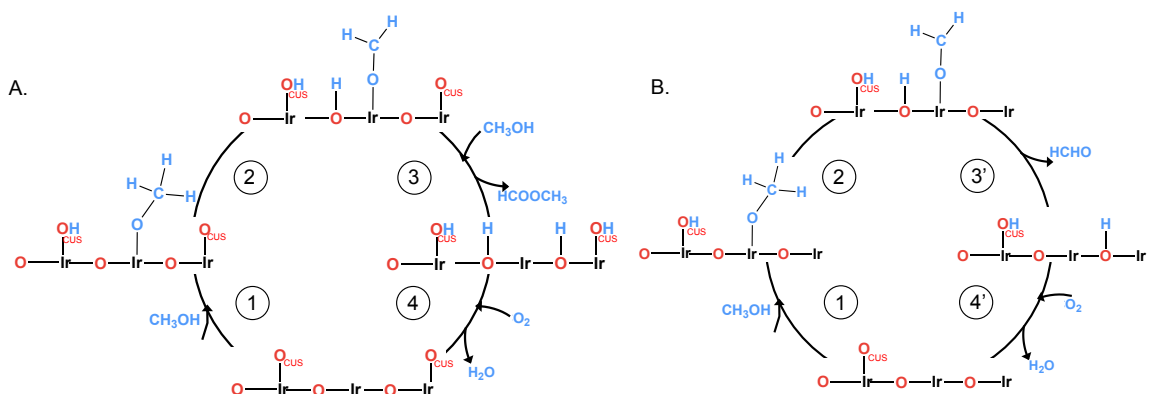
Figure A.3.18: A) Reaction mechanism for selective methanol (CH₃OH) oxidation to methyl formate (HCOOCH₃) with higher O_{CUS} coverage and B) reaction mechanism for selective methanol (CH₃OH) oxidation to formaldehyde (HCHO) formation with lower O_{CUS} coverage.
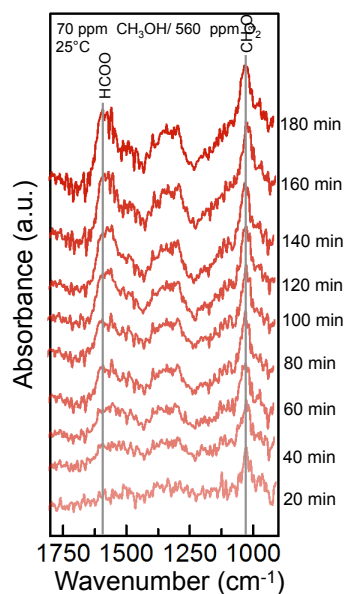
Figure A.3.19: DRIFTS of $IrO_2 \cdot 1.5H_2O$ upon exposure to 70 ppm CH₃OH and 560 ppm O₂ at room temperature in the 900-1900 cm⁻¹ region showing the formation of methoxy (CH₃O, 1100 cm⁻¹), and formate (HCOO, 1565 cm⁻¹) reaction intermediates.
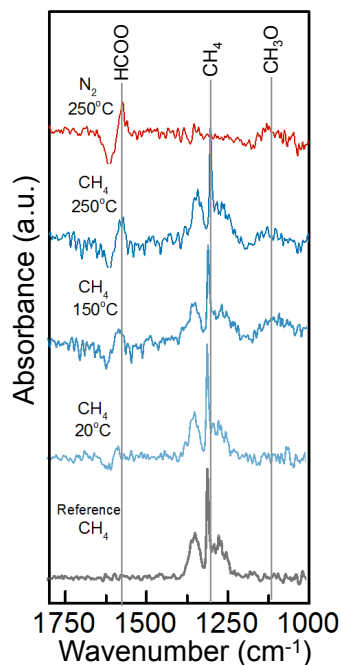
Figure A.3.20: A) DRIFTS of $IrO_2 \cdot 1.5H_2O$ upon exposure to CH_4 at 20, 150, and 250 ° in the 900-1900 cm^{-1} region showing the formation of formate (HCOO, 1565 cm^{-1}) and methoxy (CH_3O, 1110 cm^{-1}) reaction intermediate.
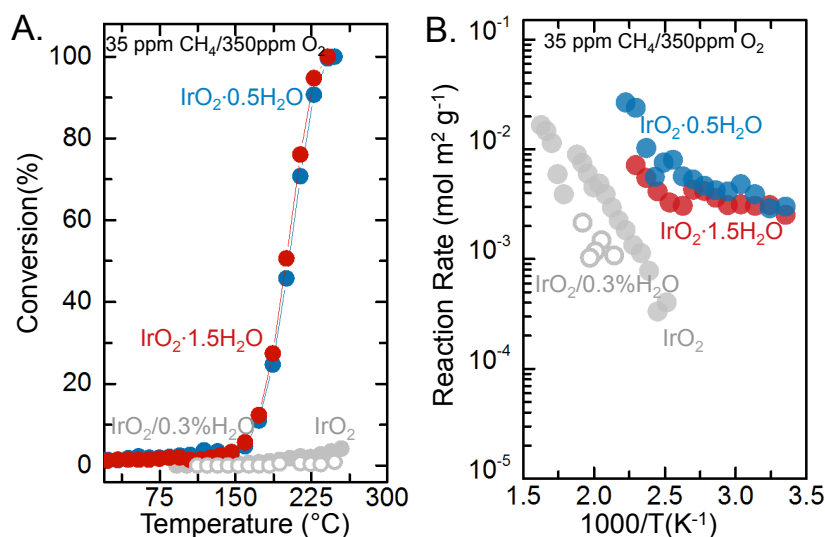
Figure A.3.21: A) Complete light off profile for CH_4 conversion to CO_2 for the three catalysts, $IrO_2 \cdot 0.5H_2O$, $IrO_2 \cdot 1.5H_2O$, and IrO_2 with and without 0.3% H_2O in the gas stream in the temperature range of 25-300 °C and B) Arrhenius-type mass normalized CH_4 oxidation reaction rates for the $IrO_2 \cdot 0.5H_2O$, IrO_2. $\cdot 1.5H_2O$, IrO_2 with and without 0.3% H_2O added to the gas stream. Catalyst loading of 50 mg, inlet flow rate of 150 ml min^{-1}, and gas concentration of 35 ppm CH_4/ 350 ppm O_2 was used for all the measurements

.

Table A.3.5: BET surface area of the IrO$_2$ powders

Material	Surface Area (m^2/g)
IrO$_2$	1.92
IrO$_2$·0.5H$_2$O	18.42
IrO$_2$·1.5H$_2$O	40.92
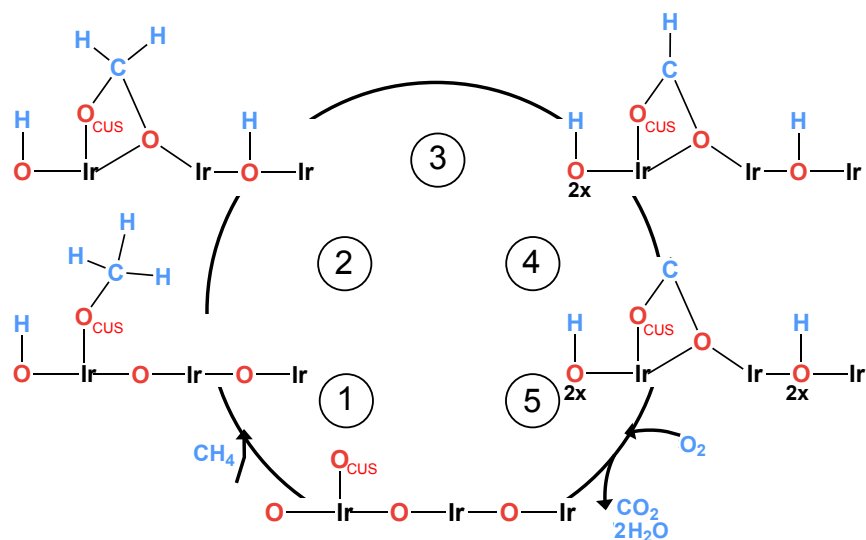
Figure A.3.22: Reaction mechanism for CH$_4$ oxidation to CO$_2$ centered on O$_{CUS}$ sites via the formation of CH$_3$O, HCOO-, and b-CO$_2$ reaction intermediates.
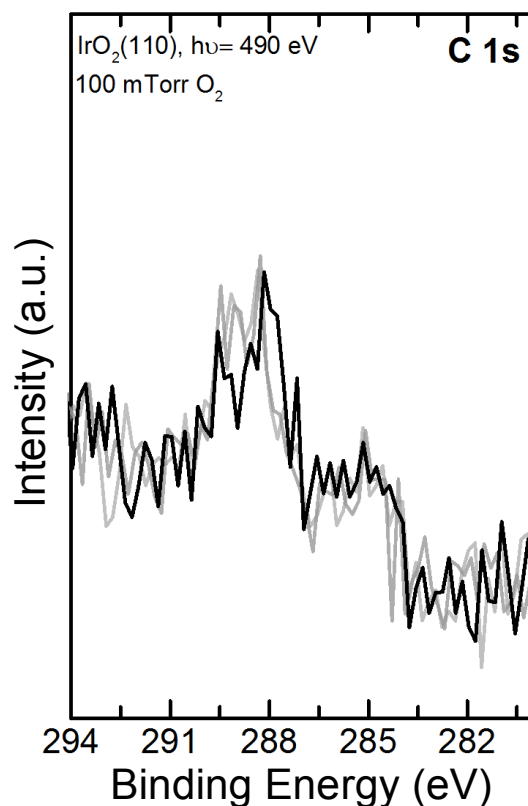
Figure A.3.23: C 1*s* collected at 490 eV at 5 min (light grey), 15 min (dark grey), and 20 min (black) intervals showing minimum change in speciation as a function of time suggesting no beam damage effects.

References:

1. Pfeifer, V. *et al.* The electronic structure of iridium and its oxides. *Surf. Interface Anal.* **48**, 261–273 (2016).
2. Martin, R. *et al.* Isothermal Reduction of IrO $_2$ (110) Films by Methane Investigated Using In Situ X-ray Photoelectron Spectroscopy. *ACS Catal.* **11**, 5004–5016 (2021).
3. Goodacre, D. *et al.* Methanol Adsorption on Vanadium Oxide Surfaces Observed by Ambient Pressure X-ray Photoelectron Spectroscopy. *J. Phys. Chem. C* **125**, 23192–23204 (2021).
4. Hwang, J. *et al.* CO $_2$ Reactivity on Cobalt-Based Perovskites. *J. Phys. Chem. C* acs.jpcc.8b06104 (2018). doi:10.1021/acs.jpcc.8b06104
5. Trotochaud, L. *et al.* Room temperature decomposition of dimethyl methylphosphonate on cuprous oxide yields atomic phosphorus. *Surf. Sci.* **680**, 75–87 (2019).
6. Favaro, M., Xiao, H., Cheng, T., Goddard, W. A. & Crumlin, E. J. Subsurface oxide plays a critical role in CO2 activation by Cu(111) surfaces to form chemisorbed CO2, the first step in reduction of CO2. *Proc. Natl. Acad. Sci. U. S. A.* **114**, 6706–6711 (2017).

A.4: Supplementary Data for Chapter 5
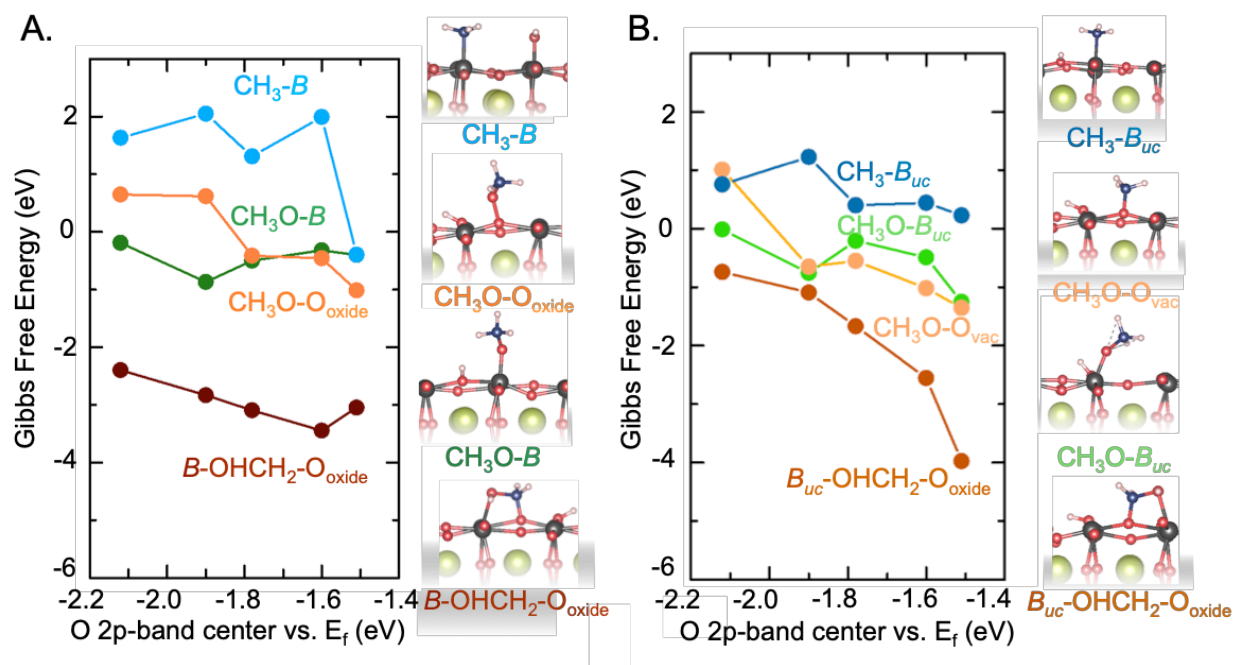
Figure A.5.1: Free energy of first hydrogen removal from CH_3OH. A) Free energy of dissociative adsorption energy of CH_3OH adsorption via O-H bond scission on the Co surface site (CH_3O-B, dark green, $BO_2 + CH_3OH \rightarrow CH_3O$-$B$ + H-O_{oxide}), on surface oxygen site (CH_3O-O_{oxide}, dark orange, $BO_2 + CH_3OH \rightarrow CH_3O$-$O_{oxide}$ + H-O_{oxide}), C-H bond dissociation with carbon bound to surface oxygen and oxygen bound to surface Co site, (B-$OHCH_2$-O_{oxide}, dark brown, $BO_2 + CH_3OH \rightarrow B$-$OHCH_2$-$O_{oxide}$ + H-O_{oxide}), C-O bond dissociation on Co surface site (CH_3-B, blue, $BO_2 + CH_3OH \rightarrow CH_3$-$B$ + HO-B), B) via O-H bond scission on under-coordinated surface Co site (CH_3O-B_{uc}, green, $BO_2 + CH_3OH \rightarrow CH_3O$-$B_{uc}$ + H-O_{oxide}+ ½O_2), via O-H bond scission on surface oxygen vacancy site (CH_3O-O_{vac}, orange, $BO_2 + CH_3OH \rightarrow CH_3O$-$O_{vac}$ + H-O_{oxide} + ½O_2), via C-O bond scission on under-coordinated cobalt surface site (CH_3-B_{uc}, dark blue, $BO_2 + CH_3OH \rightarrow CH_3$-$B_{uc}$ + H-O_{oxide}+ ½O_2), C-H bond dissociation with carbon bound to lattice oxygen and oxygen bound to adjacent under-coordinated Co site, (B_{uc}-$OHCH_2$-O_{oxide}, brown, $BO_2 + CH_3OH \rightarrow B_{uc}$-$OHCH_2$-$O_{oxide}$ + H-O_{oxide}+ ½O_2), as a function of the surface O $2p$-band center relative to the Fermi level. Data points were obtained from the BO_2-terminated (001) surface of $La_{1-x}Sr_xCoO_3$ with increasing Sr (x = 0.00, 0.25, 0.50, 0.75, and 1.00). Adsorption free energy is calculated with respect to the BO_2 surface CH_3OH and O_2 in the gas phase (T = 100 °C, pCH_3OH = 100 mTorr and pO_2 = 20 mTorr). Oxygen: red, cobalt: grey, lanthanum/strontium: green, carbon: dark blue, hydrogen: white are used for the atomic structures of the configurations.

Table A.5.1: Reactions used to compute reaction free energies reported in Figure 1 and Supplementary Figure S1.

Species	Equation
CH_3-B	$BO_2 + CH_3OH \rightarrow CH_3$-$B$ + HO-B
CH_3O-O_{oxide}	$BO_2 + CH_3OH \rightarrow CH_3O$-$O_{oxide}$ + H-O_{oxide}
B-$OHCH_2$-O_{oxide}	$BO_2 + CH_3OH \rightarrow B$-$OHCH_2$-$O_{oxide}$ + H-O_{oxide}
CH_3O-B	$BO_2 + CH_3OH \rightarrow CH_3O$-$B$ + H-O_{oxide}
CH_3O-O_{vac}	$BO_2 + CH_3OH \rightarrow CH_3O$-$O_{vac}$ + H-O_{oxide} + ½O_2
CH_3O-B_{uc}	$BO_2 + CH_3OH \rightarrow CH_3O$-$B_{uc}$ + H-O_{oxide} + ½O_2
B_{uc}-$OHCH_2$-O_{oxide}	$BO_2 + CH_3OH \rightarrow B_{uc}$-$OHCH_2$-$O_{oxide}$ + H-O_{oxide} + ½O_2
CH_3-B_{uc}	$BO_2 + CH_3OH \rightarrow CH_3$-$B_{uc}$ + H-O_{oxide} + ½O_2

Table A.5.2: Bader charges of the surface adsorbed CH_3OH species on $LaCoO_3$.

Species	Bader Charge
CH_3-B	-0.19
CH_3O-O_{oxide}	+0.65
B-$OHCH_2$-O_{oxide}	+1.22
CH_3O-B	+0.26
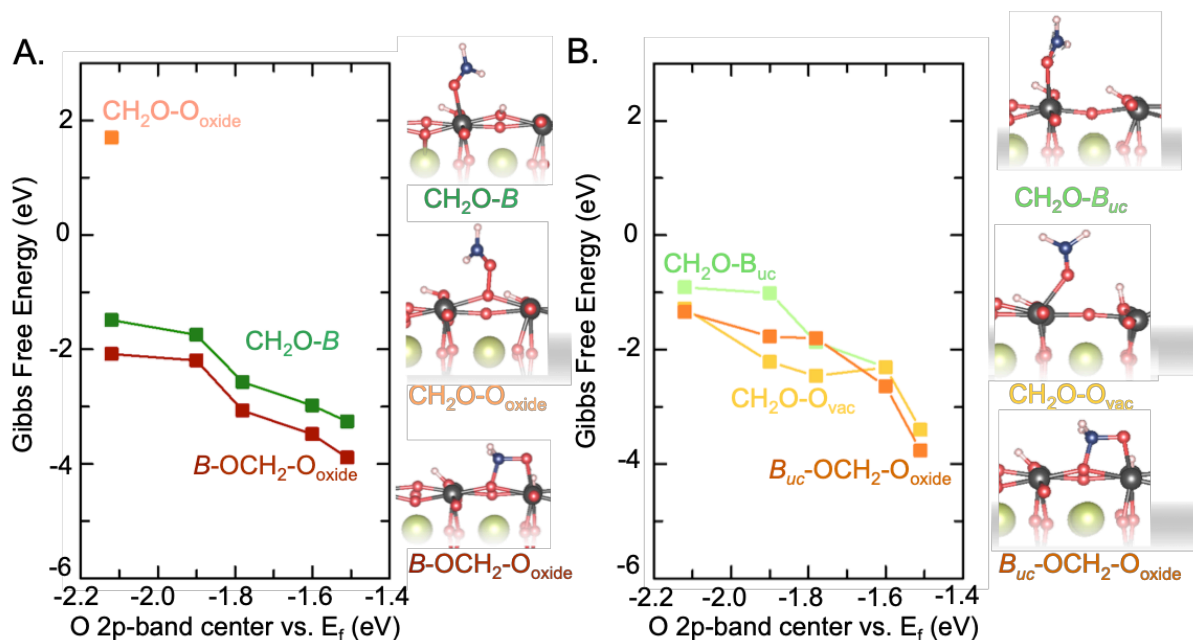
Figure A.5.2: Free energy of two hydrogens removal from CH_3OH. A) Free energy of dissociative adsorption of CH_3OH via O-H bond and C-H scission on the Co surface site (CH_2O-*B*, medium green, $BO_2 + CH_3OH \rightarrow CH_2O$-*B*+ 2H-$O_{oxide}$), on surface oxygen site via O-H bond and C-H scission (CH_2O-O_{oxide}, medium orange, $BO_2 + CH_3OH \rightarrow CH_2O$-$O_{oxide} + 2H$-$O_{oxide}$), C-H bond and O-H scission with a carbon bound to surface oxygen and oxygen bound to surface cobalt site, (*B*-OCH_2-O_{oxide}, medium brown, $BO_2 + CH_3OH \rightarrow B$-$OCH_2$-$O_{oxide} + 2H$-$O_{oxide}$), B) on under-coordinated cobalt site via C-H and O-H bond scission (CH_2O-B_{uc}, light green, $BO_2 + CH_3OH \rightarrow CH_2O$-$B_{uc}$+ 2H-$O_{oxide}$ + ½O_2), on the surface oxygen vacancy site via O-H and C-H bond scission (CH_2O-O_{vac}, light orange, $BO_2 + CH_3OH \rightarrow CH_2O$-$O_{vac}$+ 2H-$O_{oxide}$ + ½O_2), C-H and O-H bond dissociation with carbon bound to surface oxygen site and oxygen bound to under-coordinated site, (B_{uc}-OCH_2-O_{oxide}, light brown, $BO_2 + CH_3OH \rightarrow B_{uc}$-$OCH_2$-$O_{oxide} + 2H$-$O_{oxide}$ + ½O_2), as a function of the surface O 2*p*-band center relative to the Fermi level. Data points were obtained from the BO_2-terminated (001) surface of $La_{1-x}Sr_xCoO_3$ with increasing Sr (x = 0.00, 0.25, 0.50, 0.75, and 1.00). Adsorption free energy is calculated with respect to the BO_2 surface CH_3OH and O_2 in the gas phase (*T* = 100 °C, pCH_3OH = 100 mTorr and pO_2 = 20 mTorr). Oxygen: red, cobalt: grey, lanthanum/strontium: green, carbon: dark blue, hydrogen: white are used for the atomic structures of the configurations.

Table A.5.3: Reactions used to compute reaction free energy reported in Figure 1 and Supplementary Figure S2.

Species	Equation
CH_2O-*B*	$BO_2 + CH_3OH \rightarrow CH_2O$-*B*+ 2H-$O_{oxide}$
CH_2O-O_{oxide}	$BO_2 + CH_3OH \rightarrow CH_2O$-$O_{oxide} + 2H$-$O_{oxide}$

B-OCH$_2$-O$_{oxide}$,	BO$_2$ + CH$_3$OH→ B-OCH$_2$-O$_{oxide}$ + 2H-O$_{oxide}$
CH$_2$O-B_{uc}	BO$_2$ + CH$_3$OH→ CH$_2$O-B_{uc}+ 2H-O$_{oxide}$ + ½O$_2$
CH$_2$O-O$_{vac}$	BO$_2$ + CH$_3$OH→ CH$_2$O-O$_{vac}$+ 2H-O$_{oxide}$ + ½O$_2$
B_{uc}-OC$_2$-O$_{oxide}$,	BO$_2$ + CH$_3$OH→ B_{uc}-OCH$_2$-O$_{oxide}$ + 2H-O$_{oxide}$ + ½O$_2$
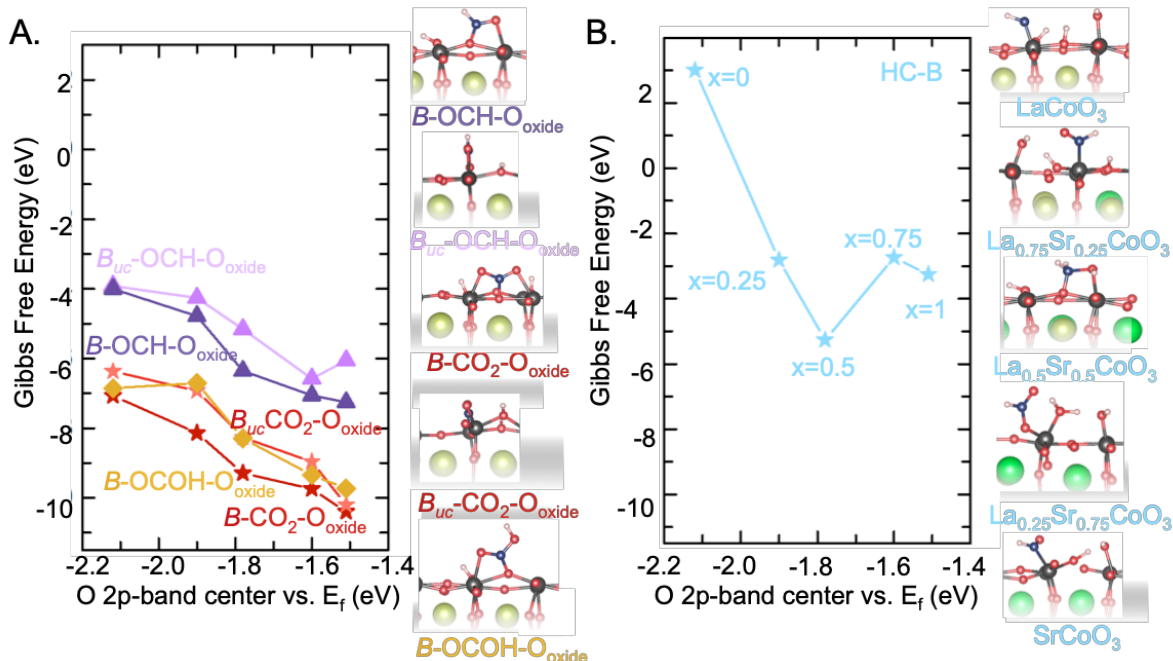
Figure A.5.3: Free energy of 3, 4 hydrogen removal from CH_3OH. A) Free energy of adsorption of CH_3OH via O-H and two C-H bond scission on surface oxygen and under-coordinated cobalt sites (B_{uc}-OCH-O_{oxide}, light purple, BO_2 + $CH_3OH \rightarrow B_{uc}$-OCH-$O_{oxide}$ + 2H-O_{oxide} + H-O_{oxide}* +½O_2), via O-H and two C-H bond scission on the surface oxygen and cobalt sites (B-OCH-O_{oxide}, dark purple, BO_2 + $CH_3OH \rightarrow B$-OCH-O_{oxide} + 2H-O_{oxide} + H-O_{oxide}*), complete dehydrogenation leading with carbon bound to the surface oxygen and oxygen bound to surface under-coordinated cobalt site (B_{uc}-CO_2-O_{oxide}, light red, BO_2 + $CH_3OH \rightarrow B_{uc}$-$CO_2$-$O_{oxide}$ +2H-O_{oxide} + 2H-O_{oxide}*), complete dehydrogenation with carbon bound to the surface oxygen and oxygen bound to cobalt surface site (B-CO_2-O_{oxide}, dark red, BO_2 + CH_3OH+0.5$O_2 \rightarrow B$-CO_2-O_{oxide} +2H-O_{oxide} + 2H-O_{oxide}*), complete dehydrogenation with carbon bound to the surface oxygen and oxygen bound to cobalt surface site (B-OCHO-O_{oxide}, dark yellow, 2BO_2 + CH_3OH+ ½$O_2 \rightarrow B$-OCHO-O_{oxide} + 2H-O_{oxide} + 2H-O_{oxide}*), B) Free energy of adsorption of CH_3OH via C-O and C-H bond scissions as a function of the surface O 2p-band center relative to the Fermi level. Only $LaCoO_3$ surface has a stable CH-B (light blue, BO_2 + CH_3OH+$\rightarrow$ CH-B + HO-B + 2H-O_{oxide}) type configuration as seen in the stable atomic configuration. Data points were obtained from the BO_2-terminated (001) surface of $La_{1-x}Sr_xCoO_3$ with increasing Sr (x = 0, 0.25, 0.50, 0.75, and 1.00). Adsorption free energy is calculated with respect to the BO_2 surface CH_3OH and O_2 in the gas phase (T = 100 °C, pCH$_3$OH = 100 mTorr and pO$_2$ = 20 mTorr). Oxygen: red, cobalt: grey, lanthanum: green, strontium: neon green: dark blue, hydrogen: white is used for the atomic structures of the configurations. * Indicates that free energy of H-O_{oxide} reaction intermediate was calculated on a separate unit cell.

Table A.5.4: Reactions used to compute reaction free energy reported in Figure 1 and Supplementary Figure S3.

Species	Equation
B-OCH-O$_{oxide,}$	$BO_2 + CH_3OH \rightarrow B\text{-}OCH\text{-}O_{oxide} + 2H\text{-}O_{oxide} + H\text{-}O_{oxide}{}^*$
B-CO$_2$-O$_{oxide}$	$BO_2 + CH_3OH + 0.5O_2 \rightarrow B\text{-}CO_2\text{-}O_{oxide} + 2H\text{-}O_{oxide} + 2H\text{-}O_{oxide}{}^*$
CH-B	$BO_2 + CH_3OH \rightarrow CH\text{-}B + HO\text{-}B + 2H\text{-}O_{oxide}$
B-OCHO-O$_{oxide}$	$BO_2 + CH_3OH + \frac{1}{2}O_2 \rightarrow B\text{-}OCHO\text{-}O_{oxide} + 2H\text{-}O_{oxide} + 2H\text{-}O_{oxide}{}^*$
B_{uc}-OCH-O$_{oxide,}$	$BO_2 + CH_3OH \rightarrow B_{uc}\text{-}OCH\text{-}O_{oxide} + 2H\text{-}O_{oxide} + H\text{-}O_{oxide}{}^* + \frac{1}{2}O_2$
B_{uc}-CO$_2$-O$_{oxide}$	$BO_2 + CH_3OH \rightarrow B_{uc}\text{-}CO_2\text{-}O_{oxide} + 2H\text{-}O_{oxide} + 2H\text{-}O_{oxide}{}^*$

Table A.5.5: Comparison of hydrogen adsorption on surface oxygen site with and on surface oxygen site with adjacent surface oxygen vacancy (B_{uc}) for $LaCoO_3$ and $SrCoO_3$.

Surface	E (H-O$_{oxide}$)	E(H-O$_{oxide}$-B$_{uc}$)
$LaCoO_3$	-0.84	-0.77
$SrCoO_3$	-1.76	-1.36
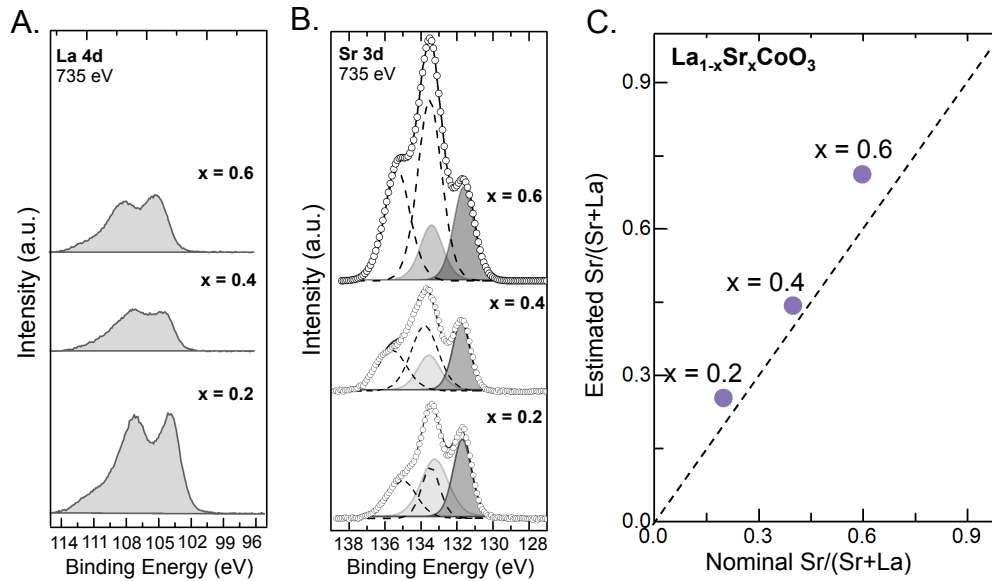
Figure A.5.4: A) La $4d$ and B) Sr $3d$ spectra of $La_{1-x}Sr_xCoO_3$ (x= 0.2, 0.4, and 0.6) thin films at room temperature under 100 mTorr CH_3OH and 25 mTorr O_2, and C) nominal versus expected Sr/La ratio content in the thin films. Sr/La ratio was estimated using the total integrated areas of

the Sr 3*d* and La 4*d* spectra in Figs. S4A, B after normalizing to photoionization cross-sections of 0.7 and 0.5 respectively.[1]
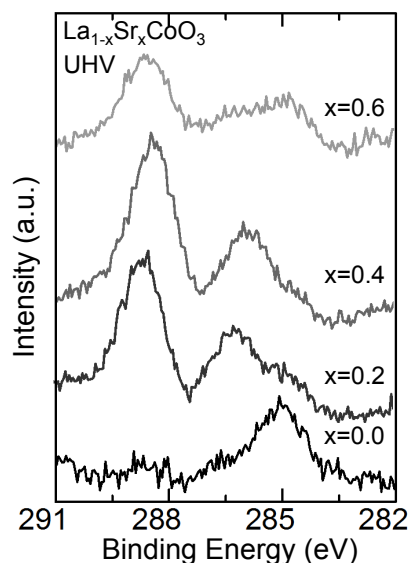
Figure A.5.5: C 1*s* 490 eV spectra of La$_{1-x}$Sr$_x$CoO$_3$ (x = 0.0, 0.2, 0.4, and 0.6) thin films at room temperature prior to dosing of CH$_3$OH and O$_2$. Carbonaceous species were observed on the thin Film surface in the C 1*s* spectra are likely originating from trace background species in the AP-XPS chamber.
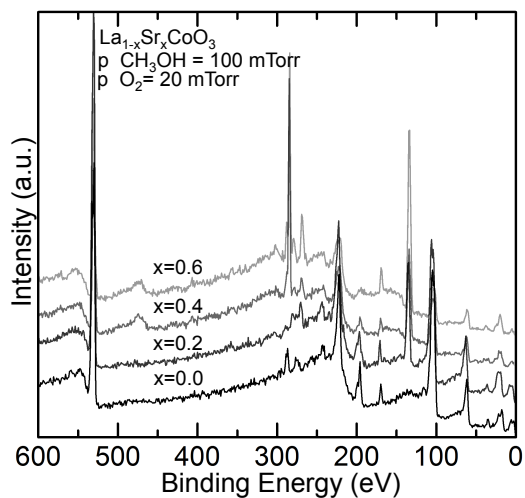
Figure A.5.6: Survey spectrum collected at 735 eV of La$_{1-x}$Sr$_x$CoO$_3$ (x = 0.0, 0.2, 0.4, and 0.6) thin films at room temperature under pCH$_3$OH = 100 mTorr and pO$_2$ = 20 mTorr.

Table A.5.6: Summary of peak deconvolution parameters used for the C 1s spectra.

Species	FWHM (eV)	Binding Energy (eV)	Gaussian-Lorentzian
CH$_3$-B_{uc}(C-C/CH$_x$-)	1.2-1.4	284.8-285.1	30
CH$_3$O-O$_{vac}$ (CH$_3$O-)	1.2-1.4	285.8-286.1	30
CH$_3$OH (g)	0.5-0.7	287.6-286.7	30
B-CO$_2$-O$_{oxide}$ (CO$_3$-)	1.2-1.4	288.1-288.4	30
B-OCOH-O$_{oxide}$ (HCO$_3$-)	1.2-1.4	290-290.3	30
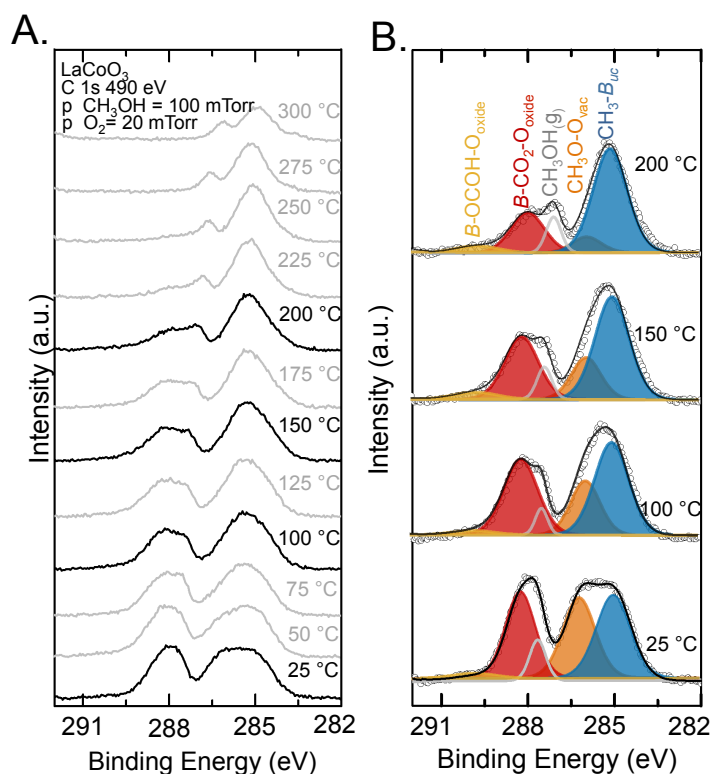
Figure A.5.7: AP-XPS of CH$_3$OH and O$_2$ on LaCoO$_3$ thin film. A) Raw isobar spectrum of C 1s collected at 490 eV incident photon energy under pCH$_3$OH = 100 mTorr and pO$_2$ = 20 mTorr from T = 25°C–300 °C. B) Representative deconvolution of the C 1s 490 eV spectrum. Deconvoluted peaks are CH$_3$-B_{uc} (adventious, dark blue), CH$_3$O-O$_{vac}$ (methoxy, orange), B-CO$_2$-O$_{oxide}$ (carbonate, dark red), B-OCOH-O$_{oxide}$ (bicarbonate, dark yellow), and CH$_3$OH (g) (unfilled).
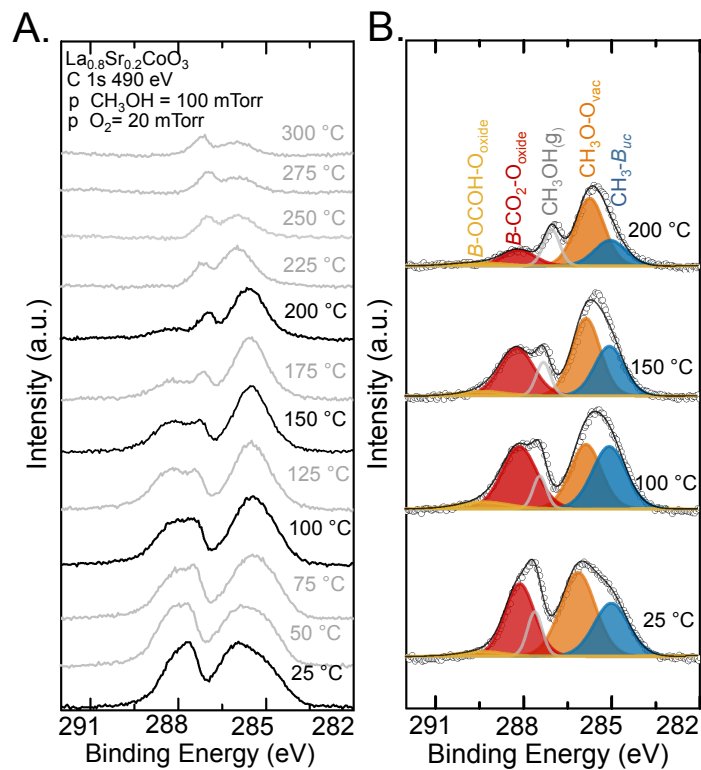
Figure A.5.8: AP-XPS of CH_3OH and O_2 on $La_{0.8}Sr_{0.2}CoO_3$ thin film. A) Raw isobar spectrum of C $1s$ collected at 490 eV incident photon energy under $pCH_3OH = 100$ mTorr and $pO_2 = 20$ mTorr from T = 25°C–300°C. B) Representative deconvolution of the C $1s$ 490 eV spectrum. Deconvoluted peaks are CH_3-B_{uc} (adventious, dark blue), CH_3O-O_{vac} (methoxy, orange), B-CO_2-O_{oxide} (carbonate, dark red), B-OCOH-O_{oxide} (bicarbonate, dark yellow), and CH_3OH (g)(unfilled).
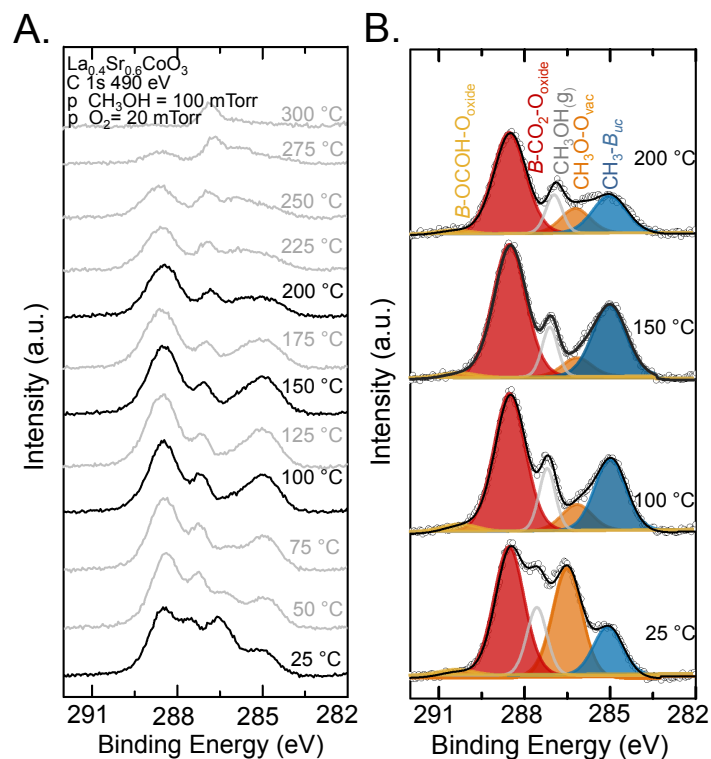
Figure A.5.9: AP-XPS of CH₃OH and O₂ on La₀.₄Sr₀.₆CoO₃ thin film. . A) Raw isobar spectrum of C 1*s* collected at 490 eV incident photon energy under pCH₃OH = 100 mTorr and pO₂ = 20 mTorr from T = 25°C–300°C. B) Representative deconvolution of the C 1*s* 490 eV spectrum. Deconvoluted peaks are CH₃-B_{uc} (adventious, dark blue), CH₃O-O_{vac} (methoxy, orange), B-CO₂-O_{oxide} (carbonate, dark red), B-OCOH-O_{oxide} (bicarbonate, dark yellow), and CH₃OH (g) (unfilled).
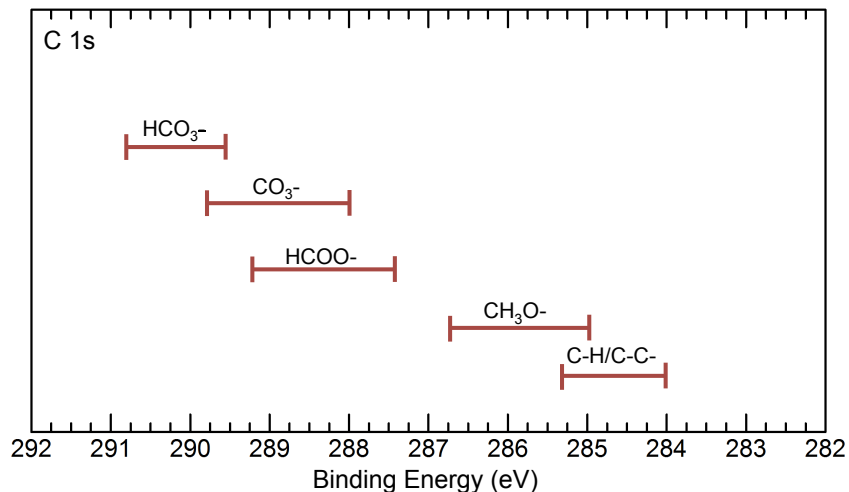
Figure A.5.10: Identification of the range of binding energy for carbonaceous species in the C 1*s* spectra as previously reported.[2–8] Figure has been adapted and modified from ref.[9].
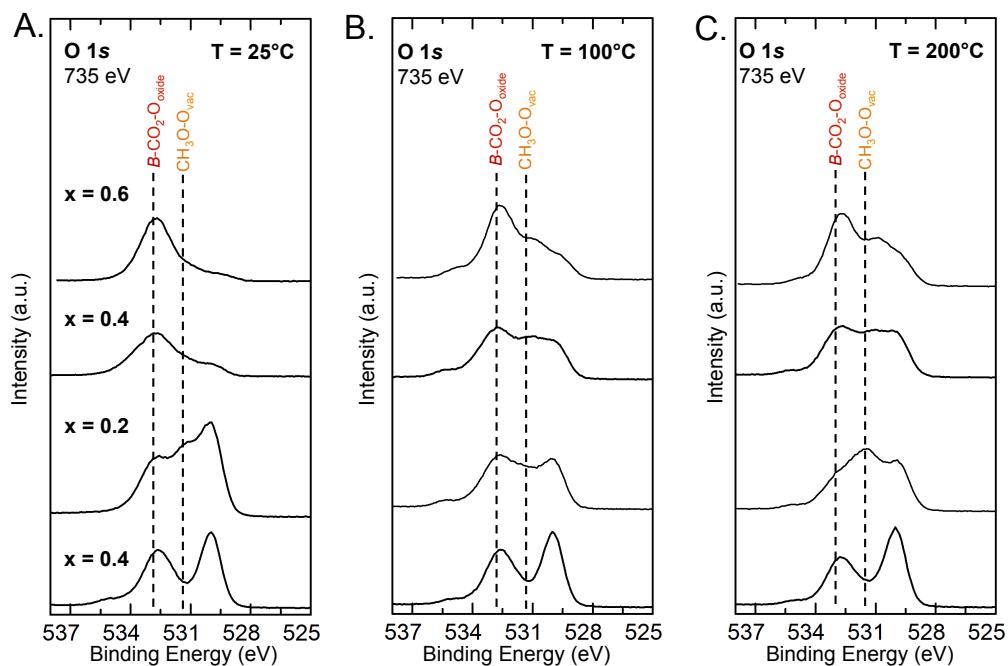
Figure A.5.11: O 1*s* spectra collected at 735 eV incident photon energy for $La_{0.6}Sr_{0.4}CoO3$ (x = 0, 0.2, 0.4,0.6) at A) 25 °C, B) 100 °C, and C) 200 °C under pCH_3OH = 100 and pO_2 = 20 mTorr showing B-CO_2-O_{oxide} (533 eV)[10,11]and CH_3O-O_{vac}[53.31] (531.5 eV) reaction intermediates. Surface Sr species (531.9 eV)[12] and other species such as SrO (529.7 eV)[13]and $Sr(OH)_2$ (533 eV) [13] have also been reported in the O 1*s* spectra but have not been explicitly identified here.

262
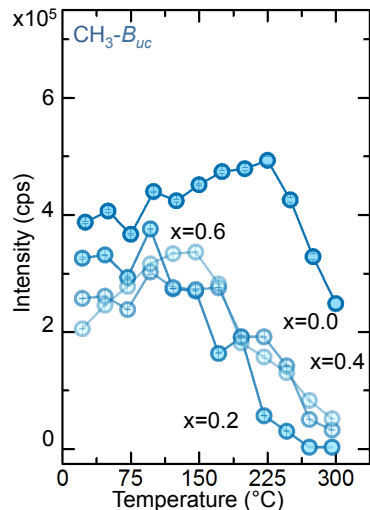
Figure A.5.12: Integrated peak intensity of adventious carbon, CH_3-B_{uc} (adventious, blue), species as a function of temperature from the C $1s$ 490 eV spectra from AP-XPS for the $La_{1-x}Sr_xCoO_3$ thin films. AP-XPS integrated intensities error bars (standard deviations) were calculated by Monte Carlo simulation of the peak fitting.
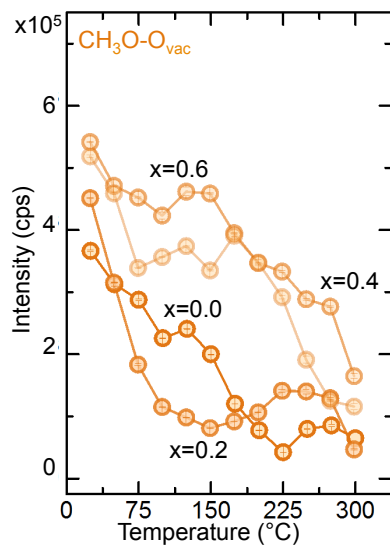
Figure A.5.13: Integrated peak intensity of CH_3O-O_{vac} (methoxy, orange) species as a function of temperature from the C $1s$ 490 eV spectra from AP-XPS for the $La_{1-x}Sr_xCoO_3$ thin films. AP-XPS integrated intensities error bars (standard deviations) were calculated by Monte Carlo simulation of the peak fitting.
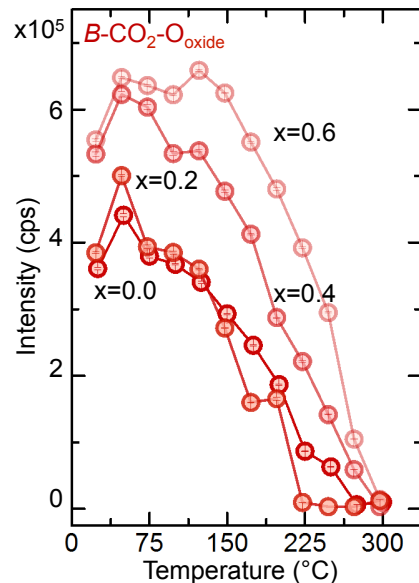
Figure A.5.14: Integrated peak intensity of carbonate, B-CO_2-O_{oxide}, (carbonate, dark red) species as a function of temperature from the C $1s$ 490 eV spectra from AP-XPS for the $La_{1-x}Sr_xCoO_3$ thin films. AP-XPS integrated intensities error bars (standard deviations) were calculated by Monte Carlo simulation of the peak fitting.
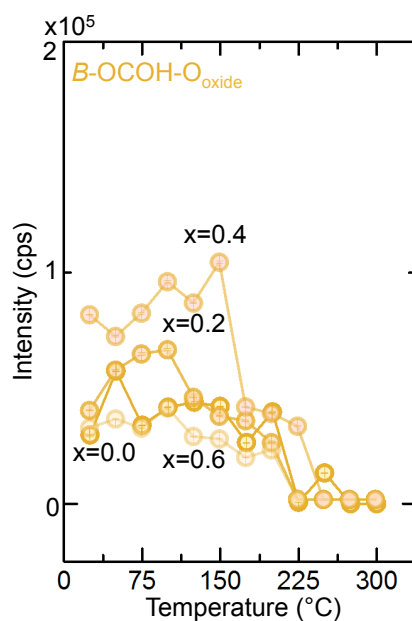
Figure A.5.15: Integrated peak intensity of bicarbonate, B-OCOH-O_{oxide} (bicarbonate, dark yellow) species as a function of temperature from the C $1s$ 490 eV spectra from AP-XPS for the $La_{1-x}Sr_xCoO_3$ thin films. AP-XPS integrated intensities error bars (standard deviations) were calculated by Monte Carlo simulation of the peak fitting.
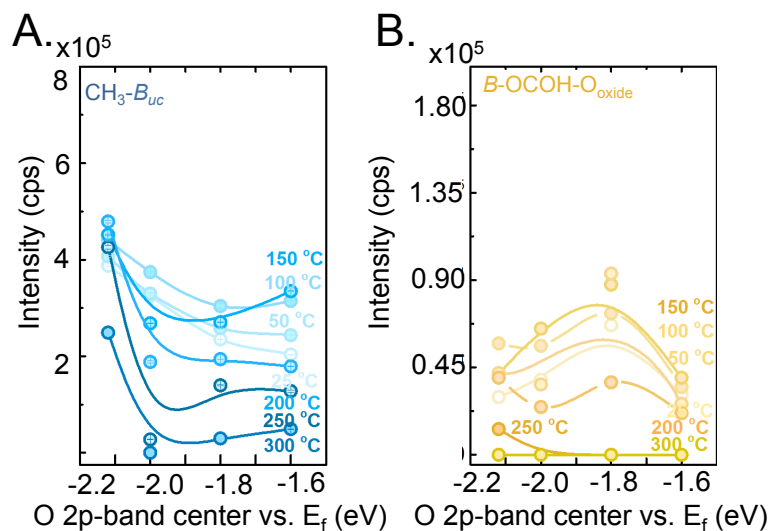
Figure A.5.16: Role of Sr-substitution on AP-XPS surface speciation. Surface quantity of A) CH_3-B_{uc} (adventious, dark blue), and B) B-OHCO-O_{oxide} (bicarbonate, dark yellow) reaction intermediates as a function of surface O $2p$-band center, where surface species quantity was determined by the counts per second (cps) after background subtraction for a range of temperatures. (T = 25, 50, 100, 150, 200, 250, and 300 °C) AP-XPS integrated intensities error bars (standard deviations) were calculated by Monte Carlo simulation of the peak fitting.
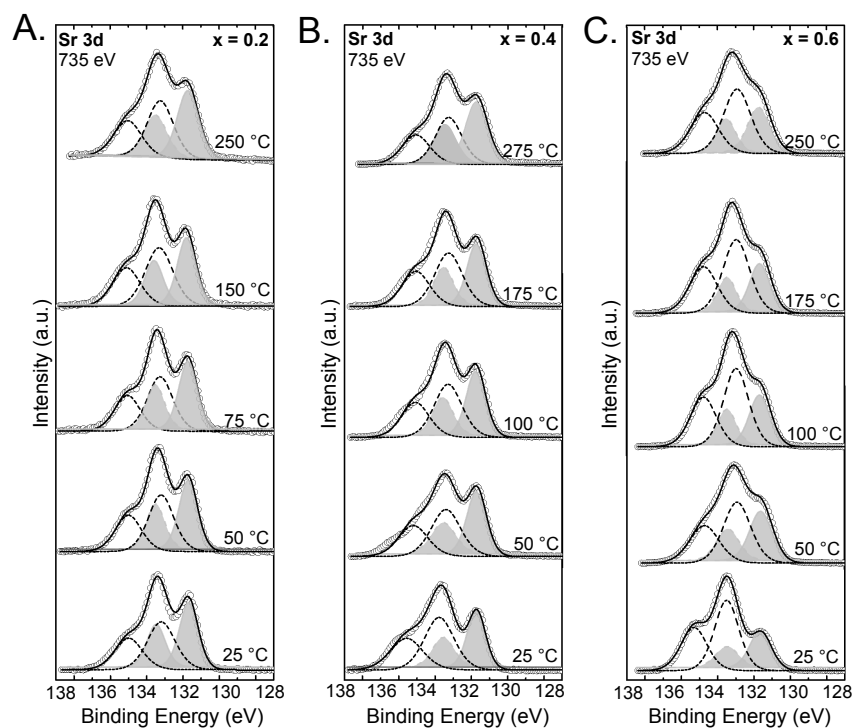
Figure S17: Sr $3d$ spectra collected at 735 eV incident photon energy for $La_{1-x}Sr_xCoO_3$ (left: x = 0.2, middle: x = 0.4, right: x = 0.6) in the temperature range of 25-275 °C. Minimal changes in the $Sr_{surface}$ (dotted) peaks for x = 0.2, and 0.4, while larger surface Sr enrichment was observed

for $x = 0.6$ are observed under $pCH_3OH = 100$ and $pO_2 = 20$ mTorr at the temperature ranges indicated is addressed via a Sr segregation model. $Sr_{Surface}$ and $Sr_{Lattice}$ components are fitted with a separation of 1.8 eV and an intensity ratio of 3:2.[1,14]

Details of Sr segregation model

Strontium segregation on the surface of perovskites is a well-known phenomenon affecting both catalyst stability and performance.[15] To model Sr segregation, we consider film thickness of 10 nm (Figure. S5). We next assume that the surface Sr concentration follows an exponential decay profile as observed previously for $La_{0.5}Sr_{0.5}CoO_3$[16] and $La_{0.6}Sr_{0.4}CoO_3$[17] measured using low-energy scattering spectroscopy (LEIS). We also assume that the surface Sr segregation levels off at ~5 nm[16,17] and the Sr composition becomes the same as the bulk composition ($Sr_{Bulk} = 0.6$). Next, to estimate the extent of Sr surface segregation, we first calculate the inelastic mean free path (IMFP) of the photoelectrons in AP-XPS (grey region in Fig. S5) as 1.5 nm for 735 eV using the NIST Standard Reference Database 71 "NIST Electron Inelastic-Mean Free Path Database" version 1.2".[14] Next, the average composition of the grey region was calculation using the intensity ratios of Sr 3d and La 4d peak regions and was estimated to be 0.72. (Fig. S4) Based on the penetration depth of AP-XPS (grey in Figure. S5) and the average Sr composition, we estimate the Sr concentration profile with a maximum of 0.81 at the surface which is in agreement with previously reported maximum Sr composition s for $La_xSr_{1-x}CoO_3$.[16,17] Finally, to estimate the relative compositions of $Sr_{Surface}$ and $Sr_{Lattice}$ species, we assume an average $Sr_{Surface}/Sr_{Lattice}$ ratio of 1.88 (obtained from Sr 3d) for $La_{0.6}Sr_{0.4}CoO_3$ in the 25 - 250 °C temperature range. We then calculate the $Sr_{surface}$ to be ~0.7 nm thick and the $Sr_{lattice}$ to be ~0.8 nm thick.
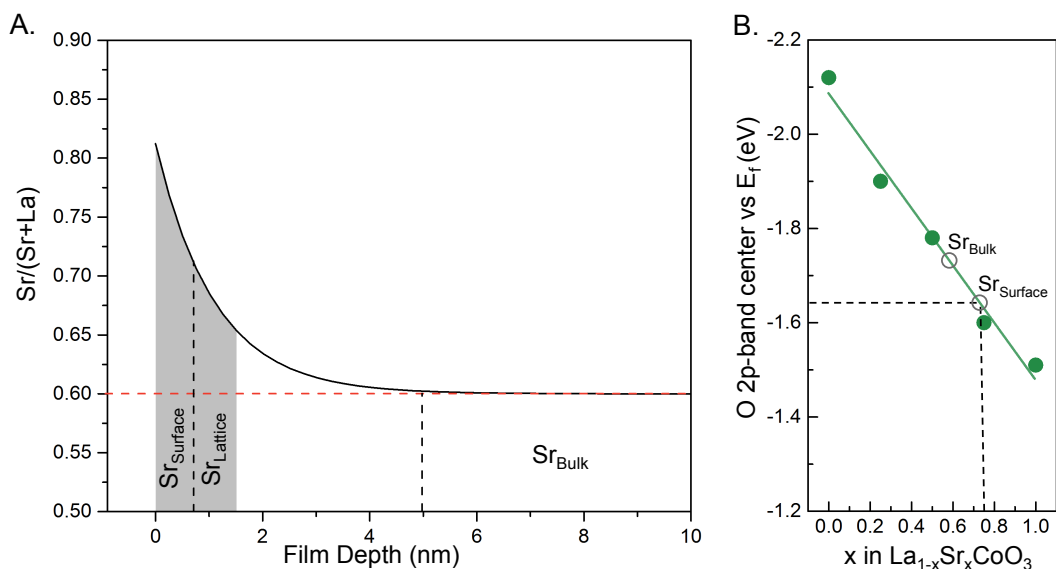
Figure A.5.18: A) Surface Sr segregation model for $La_{0.6}Sr_{0.4}CoO_3$ and **B)** estimated $Sr_{Surface}$ content using a linear correlation between the O 2p-band center and x in $La_{1-x}Sr_xCoO_3$.
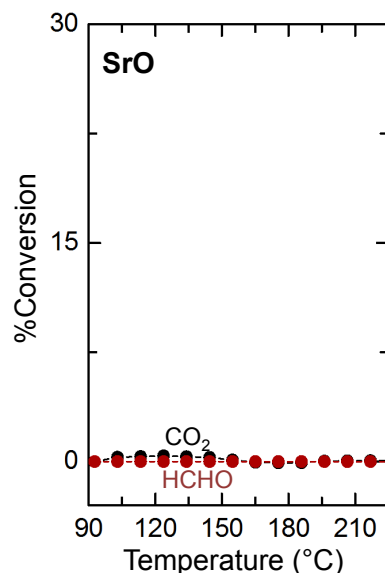
Figure A.5.19: CH_3OH oxidation activity shown as %conversion to HCHO and CO_2 as a function of temperature for SrO conducted in a flow reactor. The percentage conversion of CH_3OH oxidation was calculated by determining the percentage of inlet CH_3OH reacted during the course of the reaction, which can be calculated by the formula, % Conversion = $100*((CO_2/HCHO_{ppm,\ out})/CH_3OH_{ppm,\ in})$, where $CH_3OH_{ppm,\ in}$ was the total concentration of the initial CH_3OH reactant and $CO_2/HCHO_{ppm,\ out}$ was the concentration of CO_2/HCHO gases observed after reaction with the catalyst. Catalyst loading of 750 mg, inlet CH_3OH flow rate of 150 ml min^{-1}, and gas concentration of 30 ppm CH_3OH- 3% O_2 was used for all the measurements. SrO was prepared after calcining $SrCO_3$ (Sigma Aldrich, 99.99%) at 1200 °C for 24 hrs.
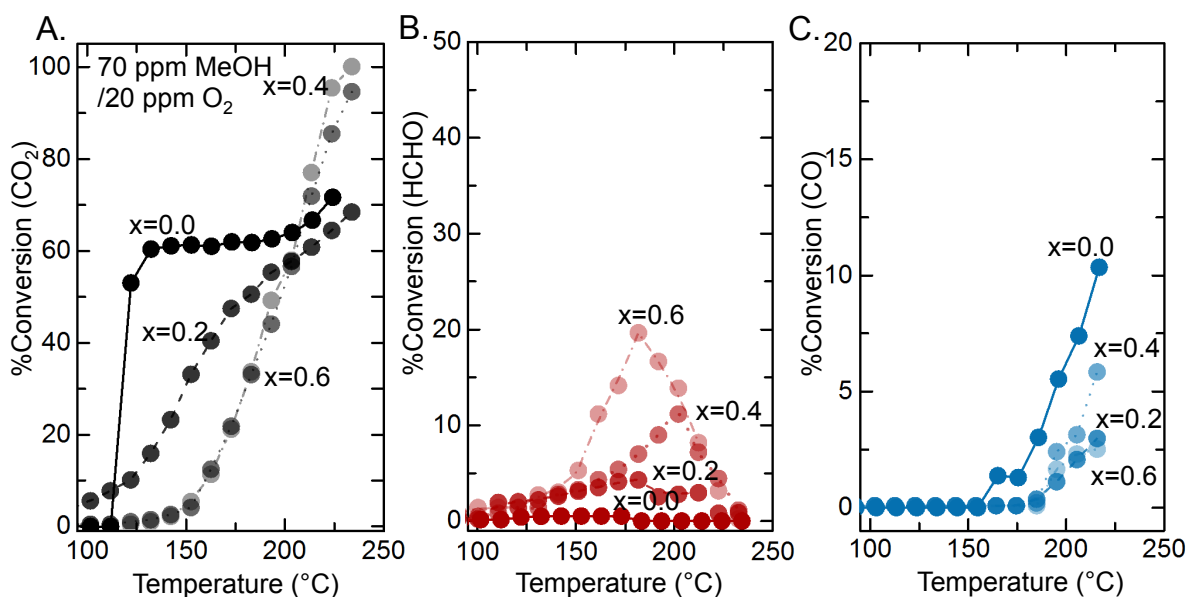
Figure A.5.20: CH_3OH oxidation activity shown as %conversion to A) CO_2, B) HCHO, and C) CO as a function of temperature for the $La_{1-x}Sr_xCoO_3$ (x = 0-0.6) series conducted in a flow

reactor. The percentage conversion of CH_3OH oxidation was calculated by determining the percentage of inlet CH_3OH reacted during the course of the reaction, which can be calculated by the formula, % Conversion $= 100*((CO_2/HCHO/CO_{ppm, out})/CH_3OH_{ppm, in})$, where $CH_3OH_{ppm, in}$ was the total concentration of the initial CH_3OH reactant and $CO_2/HCHO/CO_{ppm, out}$ was the concentration of $CO_2/HCHO/CO$ gases observed after reaction with the catalyst. Catalyst loading of 750 mg, inlet CH_3OH flow rate of 150 ml min^{-1}, and gas concentration of 70 ppm CH_3OH-20 ppm O_2 was used for all the measurements.
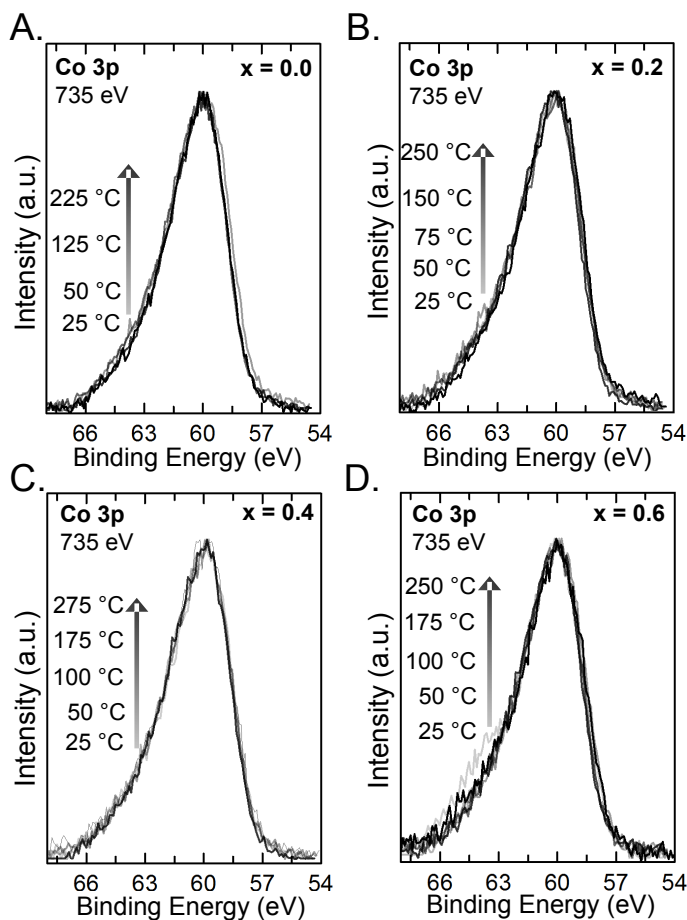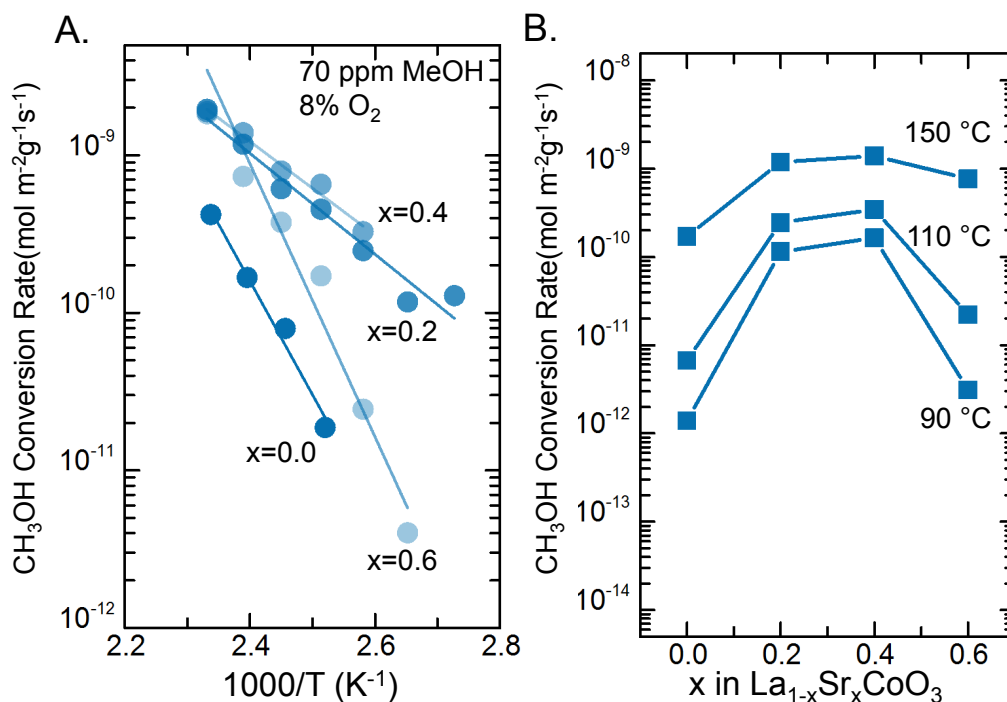

Figure A.5.21: Co $3p$ spectra collected at 735 eV incident energy A) $LaCoO_3$, B) $La_{0.8}Sr_{0.2}CoO_3$, C) $La_{0.6}Sr_{0.4}CoO_3$, and D) $La_{0.4}Sr_{0.6}CoO_3$ in the temperature range of 25-275 °C under pCH_3OH = 100 and pO_2 = 20 mTorr showing no appearance of Co $3p$ satellite peaks (Co $3p_{sat}$) which is indicative of reduced cobalt species.[18]
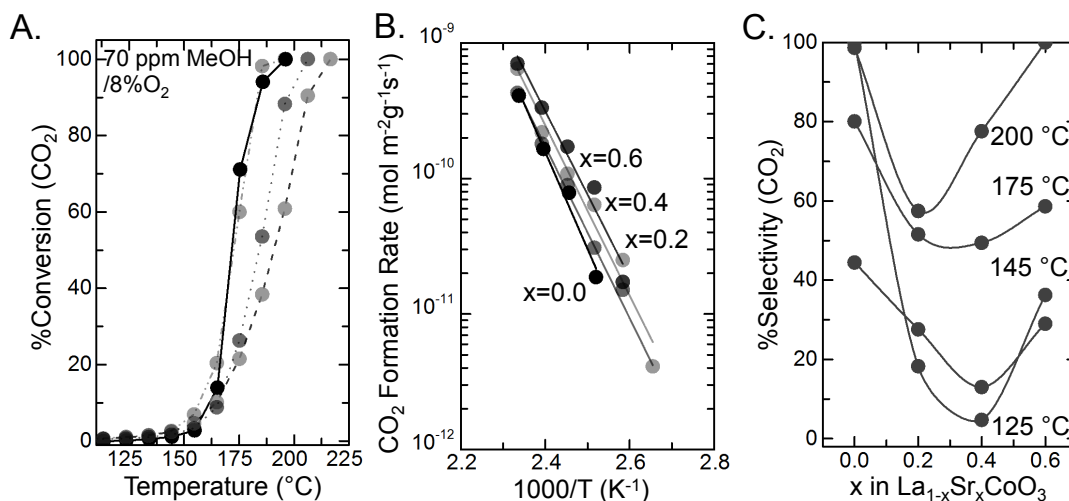
Figure A.5.22: A) CH_3OH oxidation activity shown as conversion to CO_2 as a function of temperature, B) Arrhenius type plots for CO_2 formation rate (mol s^{-1} g^{-1} m^{-2}) obtained by plotting for $La_{1-x}Sr_xCoO_3$, C) CH_3OH selectivity towards CO_2 at 125, 145, 175, and 200 °C, as a function of x in $La_{1-x}Sr_xCoO_3$. % Conversion = $100*(CO_{2ppm, out})/(CH_3OH_{ppm, in})$, where $CH_3OH_{ppm, in}$ was the concentration of the initial CH_3OH reactant and $CO_{2ppm, out}$ was the concentration of CO_2 gases observed after reaction with the catalyst. % Selectivity = $100*((CO_{2ppm, out})/(CO_{2ppm, out}$ $+HCHO_{ppm, out}))$, where $CH_3OH_{ppm, in}$ was the total concentration of the initial CH_3OH reactant and $CO_{2ppm, out}$, $HCHO_{ppm, out}$ was the concentration of HCHO and CO_2 gases observed after reaction with the catalyst. CO_2 formation rate was determined using the formula, $r_{Formation} = \frac{r_{mass} \cdot 10^{-6}}{A_S} \{\frac{ml. \ min^{-1}}{l. \ mol^{-1}. \ g. \ m^2. g^{-1}}\}$, Where mass activity was estimated using the formula, $r_{mass} = \frac{\% \ conversion. F_{CH3OH}}{6. \ V_m \ . \ m_{cat}} \{\frac{ml. \ min^{-1}}{l. \ mol^{-1}. \ g}\}$, For % conversion less than 12.5% obtained for the $La_{1-x}Sr_xCoO_3$ (x = 0-0.6) series conducted in a flow reactor. Catalyst loading of 750 mg, inlet CH_3OH flow rate of 150 ml min^{-1} and gas concentration of 70 ppm CH_3OH-8% O_2 was used for all the measurements.

Figure A.5.23: A) Arrhenius type plots for HCHO formation rate (mol s^{-1} g^{-1} m^{-2}) for La$_{1-x}$Sr$_x$CoO$_3$ (x = 0-0.6) and B) HCHO selectivity as function of temperature for La$_{1-x}$Sr$_x$CoO$_3$ (x=0-0.6). % Selectivity is defined as 100*(HCHO$_{ppm, out}$)/ (CO$_{2ppm, out}$ +HCHO $_{ppm, out}$), where CO$_{2ppm, out}$ and HCHO $_{ppm, out}$ are the concentrations of HCHO and CO$_2$ gases observed after reaction with the catalyst. HCHO formation rate activity was determined using the formula, $r_{Formation} = \frac{r_{mass} \cdot 10^{-6}}{A_S} \{\frac{ml.\ min^{-1}}{l.\ mol^{-1}.\ g.\ m^2.g^{-1}}\}$, Where mass activity was estimated using the formula, $r_{mass} = \frac{\%\ conversion. F_{CH3OH}}{6.\ V_m \cdot m_{cat}} \{\frac{ml.\ min^{-1}}{l.\ mol^{-1}.\ g}\}$, For % conversion less than 12.5% obtained for the La$_{1-x}$Sr$_x$CoO$_3$ (x = 0-0.6) series conducted in a flow reactor. Catalyst loading of 750 mg, inlet CH$_3$OH flow rate of 150 ml min^{-1} and gas concentration of 70 ppm CH$_3$OH-8% O$_2$ was used for all the measurements.

Figure A.5.24: A) Arrhenius type CH_3OH conversion rate (mol s^{-1} g^{-1} m^{-2}) plots for $La_{1-x}Sr_xCoO_3$ and B) CH_3OH conversion rates (mol s^{-1} g^{-1} m^{-2}) obtained at 90, 120, and 150 °C from A) as a function of x in $La_{1-x}Sr_xCoO_3$ (x=0-0.6). CH_3OH conversion rates were determined using the formula, $r_{Formation} = \frac{r_{mass} \cdot 10^{-6}}{A_S} \{\frac{ml.\ min^{-1}}{l.\ mol^{-1}.\ g.\ m^2.\ g^{-1}}\}$, Where mass activity was estimated using the formula, $r_{mass} = \frac{\%\ conversion.\ F_{CH3OH}}{6.\ V_m.\ m_{cat}} \{\frac{ml.\ min^{-1}}{l.\ mol^{-1}.\ g}\}$, For % conversion less than 12.5% for the $La_{1-x}Sr_xCoO_3$ (x = 0-0.6) series conducted in a flow reactor. The percentage conversion of CH_3OH oxidation was calculated by determining the percentage of inlet CH_3OH reacted during the course of the reaction, which can be calculated by the formula, % Conversion = 100*($CO_{2ppm,\ out}$ +HCHO $_{ppm,\ out}$)/$CH_3OH_{ppm,\ in}$), where CH_3OH $_{ppm,\ in}$ was the total concentration of the initial CH_3OH reactant and $CO_{2ppm,\ out}$, HCHO $_{ppm,\ out}$ was the concentration of CO_2 and HCHO gas observed after reaction with the catalyst. Catalyst loading of 750 mg, inlet CH_3OH flow rate of 150 ml min^{-1} and gas concentration of 70 ppm CH_3OH-8% O_2 was used for all the measurements.
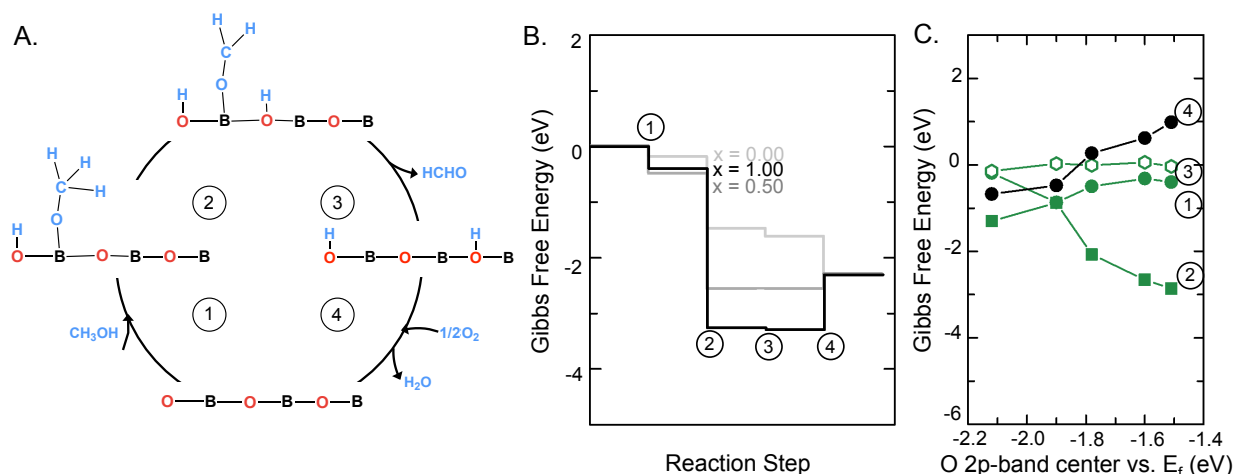
Figure A.5.25: A) Proposed reaction mechanism CH$_3$OH selective oxidation to HCHO occurring on the surface Co site via O-H bond scission of CH$_3$OH to form CH$_3$O-*B* (Step 1), followed by dehydrogenation of CH$_3$O-*B* to adsorbed CH$_2$O-*B* (Step 2), desorption of CH$_2$O-*B* to HCHO (Step 3). Following desorption of HCHO, H$_2$O desorption and oxygen adsorption occurs to complete the catalytic cycle (Step 4). B) Computed Gibbs free energy profile on LaCoO$_3$ (x=0.00), La$_{0.5}$Sr$_{0.5}$CoO$_3$ (x=0.50), and SrCoO$_3$ (x=1.00) for the proposed reaction mechanism on the metal site. C) Trends in Gibbs free energy for the reaction steps (Steps 1-4) as a function of the surface O 2p-band center relative to the Fermi level. Data points were obtained from the *B*O$_2$-terminated (001) surface of La$_{1-x}$Sr$_x$CoO$_3$ with increasing Sr (*x* = 0.00, 0.25, 0.50, 0.75, and 1.00). Adsorption and desorption free energy is calculated with respect to the *B*O$_2$ surface and CH3OH, HCHO, H$_2$O, and O$_2$ in the gas phase (*T* = 100 °C, *p*CH$_3$OH = 100 mTorr, *p*O$_2$ = 20 mTorr, *p*HCHO = 1 mTorr , and pH$_2$O= 1 mTorr)

Figure A.5.26: A) Proposed reaction mechanism CH$_3$OH selective oxidation to HCHO occurring on surface oxygen site via O-H bond scission of CH$_3$OH to form CH$_3$O-O$_{oxide}$ (Step 1), followed by dehydrogenation of CH$_3$O-O$_{oxide}$ to CH$_2$O-O$_{oxide}$ (Step 2), desorption of CH$_2$O-O$_{oxide}$ to HCHO (Step 3). Following desorption of HCHO, H$_2$O desorption and oxygen adsorption occurs to complete the catalytic cycle (Step 4). B) Computed Gibbs free energy profile on LaCoO$_3$ (x=0.00), La$_{0.5}$Sr$_{0.5}$CoO$_3$ (x=0.50), and SrCoO$_3$ (x=1.00) for the proposed reaction mechanism on the oxygen site. C) Trends in Gibbs free energy for the reaction steps (Steps 1-4) as a function of the surface O 2p-band center relative to the Fermi level. Data points were obtained from the *B*O$_2$-terminated (001) surface of La$_{1-x}$Sr$_x$CoO$_3$ with increasing Sr (x = 0.00, 0.25, 0.5, 0.75, and 1.00). Adsorption and desorption free energy is calculated with respect to the

BO_2 surface and CH_3OH, $HCHO$, H_2O, and O_2 in the gas phase (T = 100 °C, pCH_3OH = 100 mTorr, pO_2 = 20 mTorr, $pHCHO$ = 1 mTorr, and pH_2O= 1 mTorr)
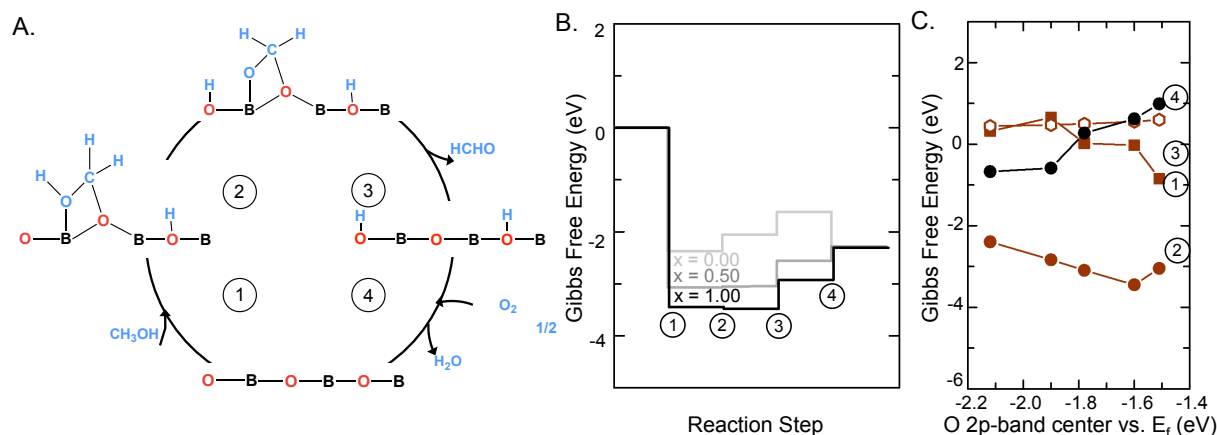
Figure A.5.27: A) Proposed reaction mechanism CH_3OH selective oxidation to HCHO occurring in a bidentate configuration on both the surface Co and oxygen sites via O-H bond scission of CH_3OH to form B-OHCH$_2$-O$_{oxide}$(Step 1), followed by dehydrogenation of B-OHCH$_2$-O$_{oxide}$ to B-OCH$_2$-O$_{oxide}$ (Step 2), desorption of B-OCH$_2$-O$_{oxide}$ to HCHO (Step 3). Following desorption of HCHO, H_2O desorption and oxygen adsorption occurs to complete the catalytic cycle (Step 4). B) Computed Gibbs free energy profile on $LaCoO_3$ (x=0.00), $La_{0.5}Sr_{0.5}CoO_3$ (x=0.50), and $SrCoO_3$ (x=1.00) for the proposed reaction mechanism. C) Trends in Gibbs free energy for the reaction steps (Steps 1-4) as a function of the surface O $2p$-band center relative to the Fermi level. Data points were obtained from the BO_2-terminated (001) surface of $La_{1-x}Sr_xCoO_3$ with increasing Sr (x = 0.00, 0.25, 0.5, 0.75, and 1.00). Adsorption and desorption free energy is calculated with respect to the BO_2 surface and CH_3OH, $HCHO$, H_2O, and O_2 in the gas phase (T = 100 °C, pCH_3OH = 100 mTorr, pO_2 = 20 mTorr, $pHCHO$ = 1 mTorr, and pH_2O= 1 mTorr)
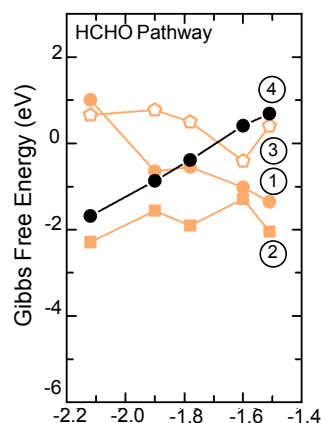
Figure A.5.28. Trends in Gibbs free energy for the reaction steps (Steps 1-4) for selective HCHO formation as a function of the surface O $2p$-band center relative to the Fermi level for the reaction mechanism described in Fig. 4. Data points were obtained from the BO_2-terminated (001) surface of $La_{1-x}Sr_xCoO_3$ with increasing Sr (x = 0.00, 0.25, 0.50, 0.75, and 1.00). Adsorption and desorption free energy is calculated with respect to the BO_2 surface and

CH$_3$OH, HCHO, H$_2$O, and O$_2$ in the gas phase (T = 100 °C, pCH$_3$OH = 100 mTorr, pO$_2$ = 20 mTorr, pHCHO = 1 mTorr, and pH$_2$O= 1 mTorr)
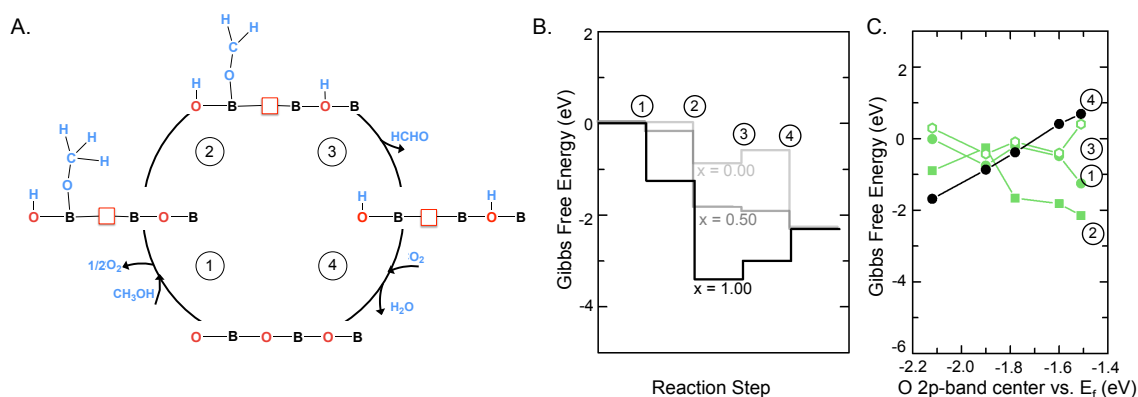
Figure A.5.29: A) Proposed reaction mechanism CH$_3$OH selective oxidation to HCHO occurring on the under coordinated cobalt site via O-H bond scission of CH$_3$OH to form CH$_3$O-B_{uc} after oxygen vacancy formation (Step 1), followed by dehydrogenation of CH$_3$O-B_{uc} to adsorbed CH$_2$O-B_{uc} (Step 2) and dehydrogenation of CH$_2$O-B_{uc} as HCHO (Step 3). Following desorption of HCHO, oxygen adsorption and H$_2$O desorption occur to complete the catalytic cycle (Step 4), B) Computed Gibbs free energy profile on LaCoO$_3$(x = 0.00), La$_{0.5}$Sr$_{0.5}$CoO$_3$ (x = 0.50), and SrCoO$_3$ (x = 1.00) for the proposed reaction mechanism on the under coordinated cobalt site, C) Trends in Gibbs free energy for the reaction steps (Step 1-4) as a function of the surface O 2p-band center relative to the Fermi level. Data points were obtained from the BO$_2$-terminated (001) surface of La$_{1-x}$Sr$_x$CoO$_3$ with increasing Sr (x = 0.00, 0.25, 0.50, 0.75, and 1.00). Adsorption and desorption free energy is calculated with respect to the BO$_2$ surface and CH$_3$OH, HCHO, H$_2$O, and O$_2$ in the gas phase (T = 100 °C, pCH$_3$OH = 100 mTorr, pO$_2$ = 20 mTorr, pHCHO = 1 mTorr, and pH$_2$O = 1 mTorr)
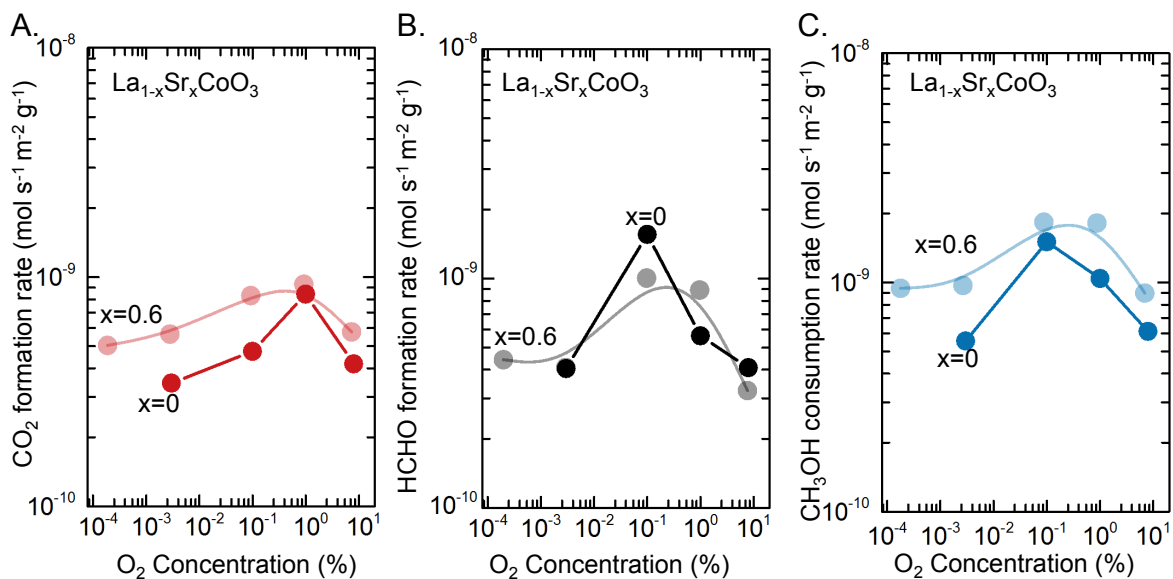
Figure A.5.30: Oxygen reaction order studies on $LaCoO_3$ and $La_{0.4}Sr_{0.6}CoO_3$. Effect of oxygen concentration on A) HCHO formation rate, B) CO_2 formation rate, and C) methanol consumption rate at 150 °C for the oxygen concentration range of 20 ppm-8%O_2 for the $LaCoO_3$ and $La_{0.4}Sr_{0.6}CoO_3$ catalysts. Formation rates for HCHO and CO_2 and conversion rate for CH_3OH were determined using the formula, $r_{Formation} = \frac{r_{mass} \cdot 10^{-6}}{A_S} \{\frac{ml.\ min^{-1}}{l.\ mol^{-1}.\ g.\ m^2.g^{-1}}\}$, where mass activity was estimated using the formula, $r_{mass} = \frac{\%\ conversion. F_{CH3OH}}{6.\ V_m \cdot m_{cat}} \{\frac{ml.\ min^{-1}}{l.\ mol^{-1}.\ g}\}$, for $CH_3OH\%$ conversion less than 12.5% obtained. Catalyst loading of 750 mg, inlet CH_3OH flow rate of 150 ml min^{-1}, and gas concentration of 70 ppm CH_3OH-(20 ppm- 8%) O_2 was used for the measurements.

Table A.5.7: Elementary reaction steps and rate/equilibrium constants for CH_3OH oxidation to HCHO and CO_2

Step	Elementary reaction step	Rate and equilibrium constant
1.1	$CH_3OH + O_{vac} + O_{oxide} \rightarrow CH_3O\text{-}O_{vac} + H\text{-}O_{oxide}$	$k_{1.1}$
1.2	$CH_3OH + B + O_{oxide} + O_{oxide} \rightarrow B\text{-}OHCH_2\text{-}O_{oxide} + H\text{-}O_{oxide}$	$k_{1.2}$
2.1	$CH_3O\text{-}O_{vac} + O_{oxide} \rightarrow CH_2O\text{-}O_{vac} + H\text{-}O_{oxide}$	$k_{2.1}$
2.2	$B\text{-}OHCH_2\text{-}O_{oxide} + O_{oxide} \rightarrow B\text{-}OCH_2\text{-}O_{oxide} + H\text{-}O_{oxide}$	$k_{2.2}$
3.1	$CH_2O\text{-}O_{vac} \rightarrow HCHO + O_{vac}$	$k_{3.1}$
4.1	$2H\text{-}O_{oxide} \rightarrow H_2O + O_{vac} + O_{oxide}$	k_6
3.2	$B\text{-}OCH_2\text{-}O_{oxide} + O_{oxide} \rightarrow B\text{-}OCH\text{-}O_{oxide} + H\text{-}O_{oxide}$	$k_{3.2}$
5.1	$B\text{-}OCH\text{-}O_{oxide} + O_{oxide} \rightarrow B + O_{vac} + CO_2 + H\text{-}O_{oxide}$	$k_{4.1}$
5.2	$B\text{-}OCH\text{-}O_{oxide} + O_{oxide} + 0.5O_2 \rightarrow B\text{-}CO_2\text{-}O_{oxide} + H\text{-}O_{oxide}$	$k_{4.2}$
6	$B\text{-}CO_2\text{-}O_{oxide} \rightarrow B + CO_2 + O_{oxide}$	k_5
7	$2H\text{-}O_{oxide} \rightarrow H_2O + O_{vac} + O_{oxide}$	k_6
8	$O_2 + 2O_{vac} \rightarrow 2O_{oxide}$	k_7

Micro kinetic model in low oxygen concentration regime

At low oxygen concentrations (20 ppm-1%), as we observed an increasing reaction rate with increasing oxygen concentration in Fig. S31, we considered the relevant oxygen dissociation step 7,[19]

$$r_7 = \frac{k_7[O_2][O_{vac}]^2}{[\theta_T]^2}$$

$$[\theta_T] = [O_{vac}] + [O_{oxide}] + [HO_{oxide}] + [B] + [CH_3O - O_{vac}] + [CH_2O - O_{vac}]$$
$$+ [B - OHCH_2 - O_{oxide}] + [B - OCH_2 - O_{oxide}] + [B - OCH - O_{oxide}]$$
$$+ [B - CO_2 - O_{oxide}]$$

Approximating $[\theta_T] \sim [O_{vac}]$, as oxygen vacancies are the dominant surface species under low oxygen concentrations,

$$r_7 \cong k_7[O_2]$$

Micro kinetic model in high oxygen concentration regime

At higher oxygen concentrations (1-8%), as we observed an increasing reaction rate with increasing oxygen concentration, and we considered the relevant oxygen dissociation step,[19]

$$r_{1.1} = \frac{k_{1.1}[CH_3OH][O_{vac}][O_{oxide}]}{[\theta_T]^2}$$

$$\frac{d[O_{oxide}]}{dt} = 0 = 2k_7 - k_{1.1} = 2k_7[O_2][O_{vac}]^2 - 2k_{1.1}[CH_3OH][O_{vac}][O_{oxide}]$$

Solving for $[O_{oxide}]$,

$$\frac{[O_{oxide}]}{[O_{vac}]} = \frac{k_7[O_2]}{k_{1.1}[CH_3OH]}$$

Using the derived expression for $[O_{oxide}]$ into $r_{1.1}$,

$$r_{1.1} = \frac{k_7[CH_3OH][O_{vac}]\frac{k_7[O_2][O_{vac}]}{k_{1.1}[CH_3OH]}}{[\theta_T]^2}$$

$$r_{1.1} = \frac{k_7[CH_3OH][O_{vac}]\frac{k_7[O_2][O_{vac}]}{k_{1.1}[CH_3OH]}}{[[O_{vac}] + [O_{oxide}] + [HO_{oxide}] + [B] + [CH_3O - O_{vac}] + [CH_2O - O_{vac}]^2 \atop +[B - OHCH_2 - O_{oxide}] \atop +[B - OCH_2 - O_{oxide}] + [B - OCH - O_{oxide}] + [B - CO_2 - O_{oxide}]]}$$

Approximating $[\theta_T] \sim [O_{oxide}]$, as oxygen vacancies are the dominant surface species under low oxygen concentrations,

$$r_{1.1} = \frac{k_{1.1}{}^2[CH_3OH]^2}{k_7[O_2]}$$
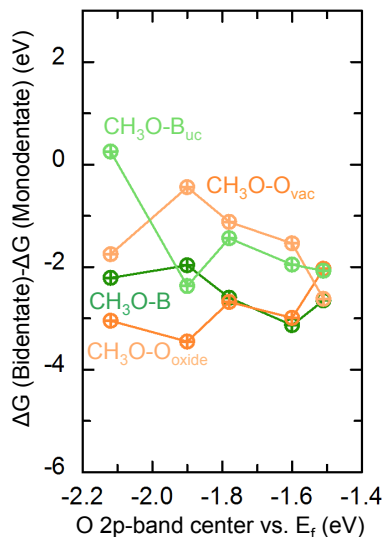
Figure A.5.31: Trends in Gibbs free for the conversion of monodentate reaction intermediates adsorbed only on the surface Co site (CH_3-*B*, CH_3-*B*$_{uc}$) or the surface oxygen site (CH_3O-O_{oxide}, CH_3O-O_{vac}) to form the corresponding bidentate configuration of *B*-OH_2C-O_{oxide} or *B*$_{uc}$-OH_2C-O_{oxide} for a stoichiometric and oxygen vacancy containing $La_{1-x}Sr_xCoO_3$ surfaces described for the reaction mechanisms in Figs. S21-S24 as a function of the surface O 2*p*-band center relative to the Fermi level. Data points were obtained from the BO_2-terminated (001) surface of $La_{1-x}Sr_xCoO_3$ with increasing Sr ($x = 0.00$, 0.25, 0.50, 0.75, and 1.00).
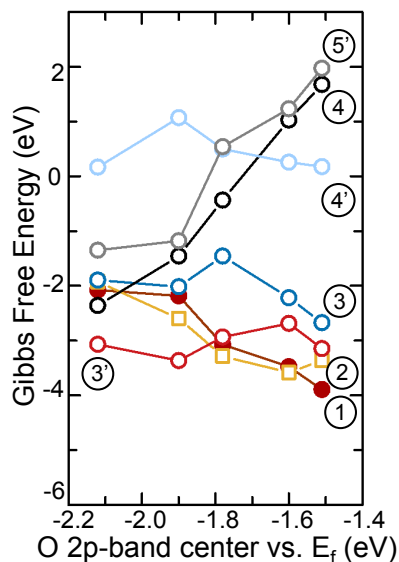
Figure A.5.32: Trends in Gibbs free energy for CO_2 formation via vacancy mediated pathway (Steps 1,2,3,4) and via carbonate mediated pathway (Steps 1,2,3',4',5') described in Fig. 5 as a function of the surface O 2*p*-band center relative to the Fermi level. Data points were obtained from the BO_2-terminated (001) surface of $La_{1-x}Sr_xCoO_3$ with increasing Sr ($x = 0.00$, 0.25, 0.50, 0.75, and 1.00). Adsorption and desorption free energy is calculated with respect to the BO_2 surface and CH_3OH, CO_2, H_2O, and O_2 in the gas phase ($T = 100$ °C, $p$$CH_3OH = 100$ mTorr, $p$$O_2 = 20$ mTorr, $p$$CO_2 = 1$ mTorr, and $p$$H_2O = 1$ mTorr)

References

(1)   Gao, R.; Fernandez, A.; Chakraborty, T.; Luo, A.; Pesquera, D.; Das, S.; Velarde, G.; Thoréton, V.; Kilner, J.; Ishihara, T.; Nemšák, S.; Crumlin, E. J.; Ertekin, E.; Martin, L. W. Correlating Surface Crystal Orientation and Gas Kinetics in Perovskite Oxide Electrodes. *Adv. Mater.* **2021**, *33* (20), 2100977. https://doi.org/10.1002/ADMA.202100977.

(2)   Setvin, M.; Shi, X.; Hulva, J.; Simschitz, T.; Parkinson, G. S.; Schmid, M.; Di Valentin, C.; Selloni, A.; Diebold, U. Methanol on Anatase TiO2 (101): Mechanistic Insights into Photocatalysis. *ACS Catal.* **2017**, *7* (10), 7081–7091. https://doi.org/10.1021/acscatal.7b02003.

(3)   Hwang, J.; Rao, R. R.; Katayama, Y.; Lee, D.; Wang, X. R.; Crumlin, E.; Venkatesan, T.; Lee, H. N.; Shao-Horn, Y. CO 2 Reactivity on Cobalt-Based Perovskites. *J. Phys. Chem. C* **2018**, acs.jpcc.8b06104. https://doi.org/10.1021/acs.jpcc.8b06104.

(4)   Trotochaud, L.; Head, A. R.; Büchner, C.; Yu, Y.; Karslıoğlu, O.; Tsyshevsky, R.; Holdren, S.; Eichhorn, B.; Kuklja, M. M.; Bluhm, H. Room Temperature Decomposition of Dimethyl Methylphosphonate on Cuprous Oxide Yields Atomic Phosphorus. *Surf. Sci.* **2019**, *680*, 75–87. https://doi.org/10.1016/j.susc.2018.10.003.

(5)   Montero, J. M.; Isaacs, M. A.; Lee, A. F.; Lynam, J. M.; Wilson, K. The Surface Chemistry of Nanocrystalline MgO Catalysts for FAME Production: An in Situ XPS Study of H2O, CH3OH and CH3OAc Adsorption. *Surf. Sci.* **2016**, *646*, 170–178. https://doi.org/10.1016/j.susc.2015.07.011.

(6)   Favaro, M.; Xiao, H.; Cheng, T.; Goddard, W. A.; Crumlin, E. J. Subsurface Oxide Plays a Critical Role in CO2 Activation by Cu(111) Surfaces to Form Chemisorbed CO2, the First Step in Reduction of CO2. *Proc. Natl. Acad. Sci. U. S. A.* **2017**, *114* (26), 6706–6711. https://doi.org/10.1073/pnas.1701405114.

(7)   Orozco, I.; Huang, E.; Mahapatra, M.; Kang, J.; Shi, R.; Nemšák, S.; Tong, X.; Senanayake, S. D.; Liu, P.; Rodríguez, J. A. Understanding Methanol Synthesis on Inverse ZnO/CuOx/Cu Catalysts: Stability of CH3O Species and Dynamic Nature of the Surface. *J. Phys. Chem. C* **2021**, *125* (12), 6673–6683. https://doi.org/10.1021/acs.jpcc.1c00392.

(8)   Mirabella, F.; Balajka, J.; Pavelec, J.; Göbel, M.; Kraushofer, F.; Schmid, M.; Parkinson, G. S.; Diebold, U. Atomic-Scale Studies of Fe3O4(001) and TiO2(110) Surfaces Following Immersion in CO2-Acidified Water. *ChemPhysChem* **2020**, *21* (16), 1788–1796. https://doi.org/10.1002/cphc.202000471.

(9)   Taifan, W.; Boily, J. F.; Baltrusaitis, J. Surface Chemistry of Carbon Dioxide Revisited. *Surface Science Reports*. Elsevier B.V. December 1, 2016, pp 595–671. https://doi.org/10.1016/j.surfrep.2016.09.001.

(10)   Stoerzinger, K. A.; Hong, W. T.; Azimi, G.; Giordano, L.; Lee, Y. L.; Crumlin, E. J.; Biegalski, M. D.; Bluhm, H.; Varanasi, K. K.; Shao-Horn, Y. Reactivity of Perovskites with Water: Role of Hydroxylation in Wetting and Implications for Oxygen Electrocatalysis. *J. Phys. Chem. C* **2015**, *119* (32), 18504–18512. https://doi.org/10.1021/acs.jpcc.5b06621.

(11)   Domingo, N.; Pach, E.; Cordero-Edwards, K.; Pérez-Dieste, V.; Escudero, C.; Verdaguer, A. Water Adsorption, Dissociation and Oxidation on SrTiO3 and Ferroelectric Surfaces

Revealed by Ambient Pressure X-Ray Photoelectron Spectroscopy. *Phys. Chem. Chem. Phys.* **2019**, *21* (9), 4920–4930. https://doi.org/10.1039/c8cp07632d.

(12)   Hong, W. T.; Stoerzinger, K. A.; Crumlin, E. J.; Mutoro, E.; Jeen, H.; Lee, H. N.; Shao-Horn, Y. Near-Ambient Pressure XPS of Higherature Surface Chemistry in Sr2Co2O5 Thin Films. *Top. Catal.* **2016**, *59* (5–7), 574–582. https://doi.org/10.1007/S11244-015-0532-4/FIGURES/6.

(13)   Opitz, A. K.; Rameshan, C.; Kubicek, M.; Rupp, G. M.; Nenning, A.; Götsch, T.; Blume, R.; Hävecker, M.; Knop-Gericke, A.; Rupprechter, G.; Klötzer, B.; Fleig, J. The Chemical Evolution of the La0.6Sr0.4CoO3−Δ Surface Under SOFC Operating Conditions and Its Implications for Electrochemical Oxygen Exchange Activity. *Top. Catal.* **2018**, *61* (20), 2129–2141. https://doi.org/10.1007/S11244-018-1068-1/FIGURES/10.

(14)   Crumlin, E. J.; Mutoro, E.; Liu, Z.; Grass, M. E.; Biegalski, M. D.; Lee, Y.-L.; Morgan, D.; Christen, H. M.; Bluhm, H.; Shao-Horn, Y. Surface Strontium Enrichment on Highly Active Perovskites for Oxygen Electrocatalysis in Solid Oxide Fuel Cells. *Energy Environ. Sci.* **2012**, *5* (3), 6081–6088. https://doi.org/10.1039/C2EE03397F.

(15)   Koo, B.; Kim, K.; Kim, J. K.; Kwon, H.; Han, J. W.; Jung, W. C. Sr Segregation in Perovskite Oxides: Why It Happens and How It Exists. *Joule* **2018**, *2* (8), 1476–1499. https://doi.org/10.1016/J.JOULE.2018.07.016.

(16)   Chen, Y.; Téllez, H.; Burriel, M.; Yang, F.; Tsvetkov, N.; Cai, Z.; McComb, D. W.; Kilner, J. A.; Yildiz, B. Segregated Chemistry and Structure on (001) and (100) Surfaces of (La1-XSrx)2CoO4 Override the Crystal Anisotropy in Oxygen Exchange Kinetics. *Chem. Mater.* **2015**, *27* (15), 5436–5450. https://doi.org/10.1021/ACS.CHEMMATER.5B02292/SUPPL_FILE/CM5B02292_SI_001.PDF.

(17)   Rupp, G. M.; Téllez, H.; Druce, J.; Limbeck, A.; Ishihara, T.; Kilner, J.; Fleig, J. Surface Chemistry of La 0.6 Sr 0.4 CoO 3−δ Thin Films and Its Impact on the Oxygen Surface Exchange Resistance. *J. Mater. Chem. A* **2015**, *3* (45), 22759–22769. https://doi.org/10.1039/C5TA05279C.

(18)   Xiao, J.; Chernova, N. A.; Whittingham, M. S. Layered Mixed Transition Metal Oxide Cathodes with Reduced Cobalt Content for Lithium Ion Batteries. *Chem. Mater.* **2008**, *20* (24), 7454–7464. https://doi.org/10.1021/cm802316d.

(19)   Tu, W.; Chin, Y. H. Catalytic Consequences of Chemisorbed Oxygen during Methanol Oxidative Dehydrogenation on Pd Clusters. *ACS Catal.* **2015**, *5* (6), 3375–3386. https://doi.org/10.1021/acscatal.5b00068.

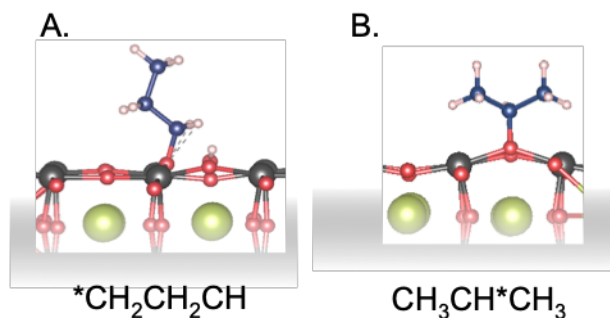# A.5: Supplementary Data for Chapter 6

Figure A.5.1: Dissociative adsorption of C_3H_8 via A) terminal C-H bond and B) allylic C-H bond dissociation on the surface oxygen sites of the BO_2-terminated (001) ABO_3 perovskites.
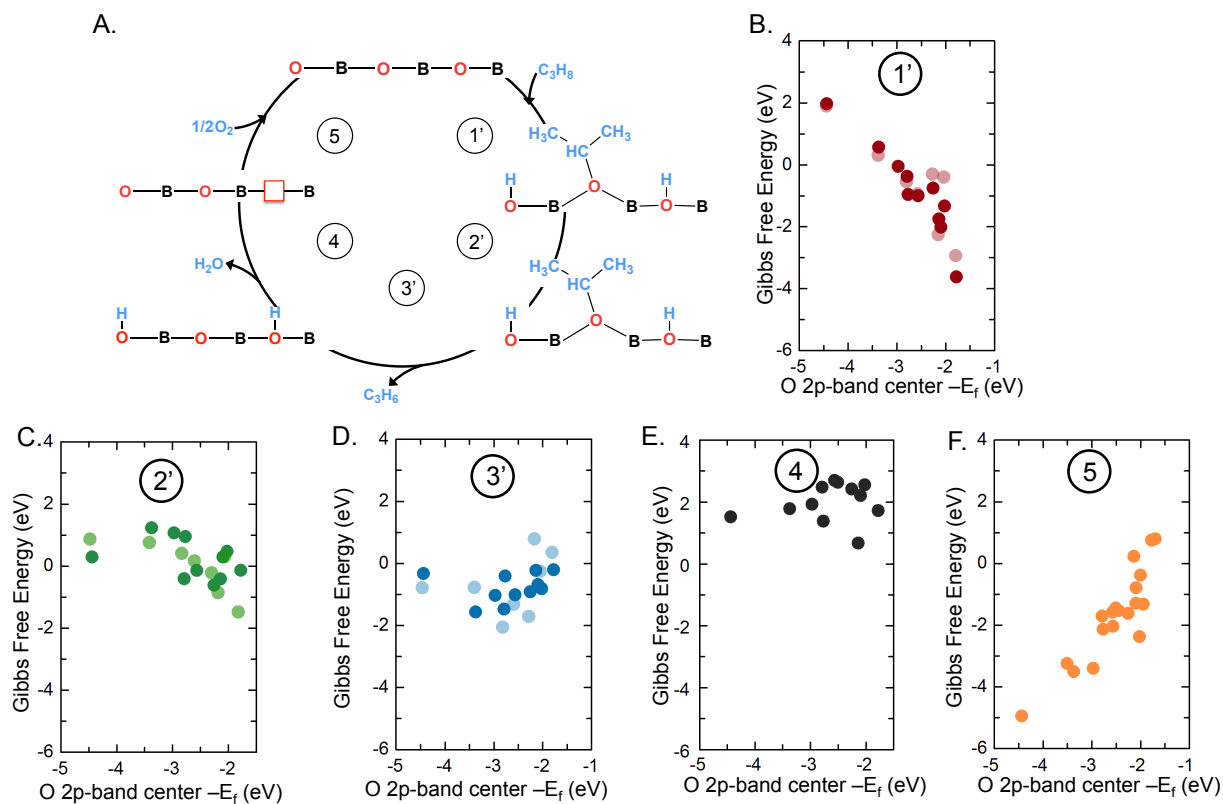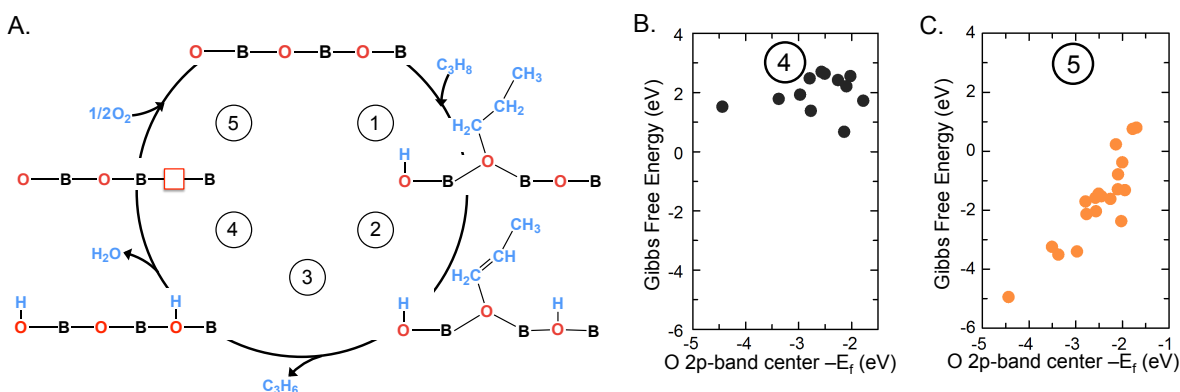
Figure A.5.2: Reaction mechanism for selective propene generation under dry conditions. A) Proposed reaction mechanism for C_3H_8 selective oxidation to C_3H_6 occurring on the surface oxygen site via terminal C-H bond scission of C_3H_8 to form C_3H_7-O_{oxide} and O_{oxide}-H (Step 1), followed by dehydrogenation of C_3H_7-O_{oxide} to C_3H_6-O_{oxide} and O_{oxide}-H (Step 2), and desorption of C_3H_6-O_{oxide} as C_3H_6 (Step 3). Following desorption of C_3H_6, H_2O desorption occurs leading to oxygen vacancy formation (Step 4), and finally molecular oxygen re-adsorption to r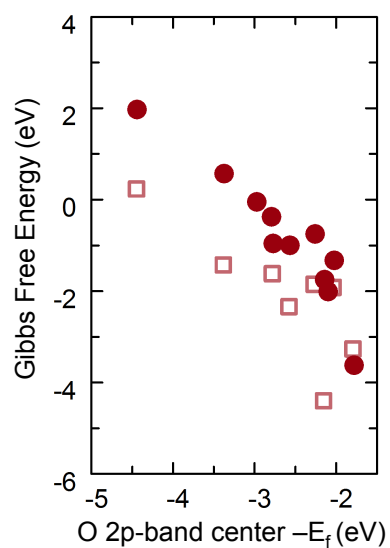e-fill the oxygen vacancies to complete the reaction cycle (Step 5), B) Correlation between first dehydrogenation adsorption energy of C_3H_8 on the surface oxygen surface site (C_3H_7-O_{oxide}, dark red), C) second dehydrogenation adsorption energy of C_3H_8 on the surface oxygen surface site (C_3H_7-O_{oxide}, dark green), D C_3H_6 desorption energy from the C_3H_6-O_{oxide} adsorbed on surface oxygen sites (dark blue), E) H_2O desorption energy from the $2O_{oxide}$-H adsorbed on surface oxygen sites (dark black), F) oxygen vacancies re-filling energy (dark orange), as a function of the surface O $2p$-band center relative to the Fermi level for ABO_3 perovskites. Data points were obtained from the BO_2-terminated-(100) surface of ABO_3 (A = La, Sm; B = Cr, Co, Mn, Fe, and Ni), calculated by DFT with the binding configurations C_3H_8 on the surface oxygen sites shown here with reference to C_3H_8 and O_2 in the gas phase (T = 300 °C, pC_3H_8 = 1 atm, pC_3H_6 = 1 atm, and pO_2 = 20 mTorr
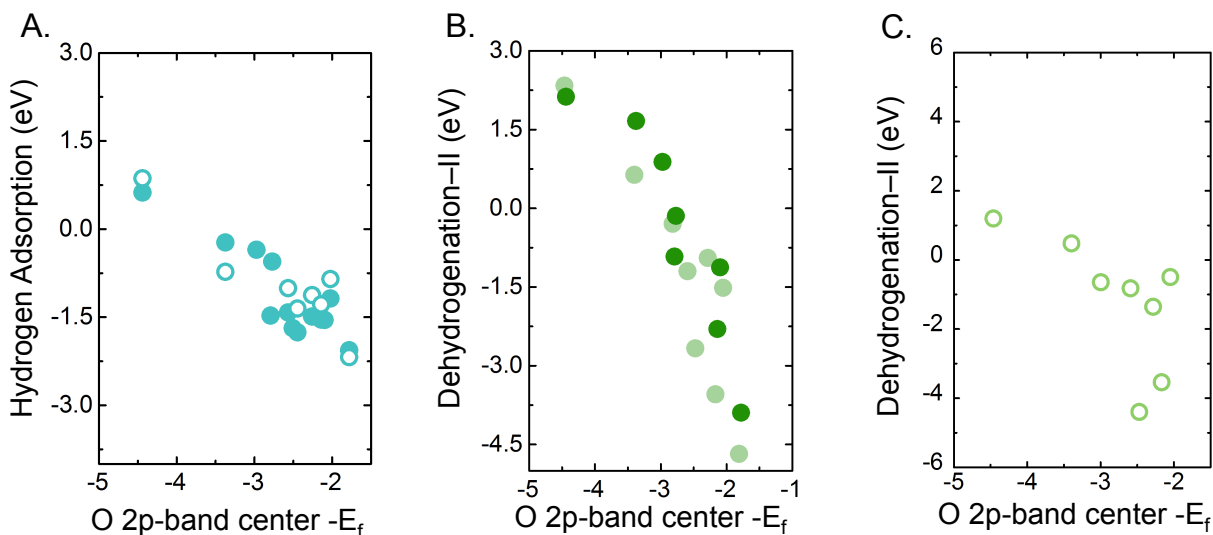
Figure A.5.3: Trends in gas phase adsorption energy. Trends in adsorption of A) hydrogen adsorption energy (blue, filled) and hydrogen adsorption in the presence of adsorbed water (blue, unfilled), B) direct dehydrogenation of C_3H_8 to from C_3H_6-O_{oxide} + 2H-O_{oxide} with reference to gas phase via 2 terminal C-H bond scissions (green) and allylic carbon (light green) C-H bond scission, C) direct dehydrogenation of C_3H_8 to from C_3H_6-O_{oxide} + 2H-O_{oxide} with reference to gas phase C_3H_8 and H_2O via 2 terminal C-H bond scissions (green), as a function of the surface O $2p$-band center relative to the Fermi level for ABO_3 perovskites. Data points were obtained from the AO and BO_2-terminated-(100) surface of ABO_3 (A = La, Sm; B = Cr, Co, Mn, Fe, and Ni), calculated by DFT with the binding configurations C_3H_8 on the surface oxygen sites.

Figure A.5.4: Reaction mechanism for selective propene generation under dry conditions.
A) Proposed reaction mechanism for C_3H_8 selective oxidation to C_3H_6 occurring on the surface oxygen site via terminal C-H bond scission of C_3H_8 to form C_3H_7-O_{oxide} and O_{oxide}-H (Step 1), followed by dehydrogenation of C_3H_7-O_{oxide} to C_3H_6-O_{oxide} and O_{oxide}-H (Step 2), and desorption of C_3H_6-O_{oxide} as C_3H_6 (Step 3). Following desorption of C_3H_6, H_2O desorption occurs leading to oxygen vacancy formation (Step 4), and finally molecular oxygen re-adsorption to re-fill the oxygen vacancies to complete the reaction cycle (Step 5), Correlation between B) H_2O desorption energy from the $2O_{oxide}$-H adsorbed on surface oxygen sites (black), and F) oxygen vacancies re-filling energy (dark orange), as a function of the surface O $2p$-band center relative to the Fermi level for ABO_3 perovskites. Data points were obtained from the AO and BO_2-terminated-(100) surface of ABO_3 (A = La, Sm; B = Cr, Co, Mn, Fe, and Ni), calculated by DFT with the binding configurations C_3H_8 on the surface oxygen sites shown here with reference to C_3H_8 and O_2 in the gas phase (T = 300 °C, pC_3H_8 = 1 atm, pC_3H_6 = 1 atm, and pO_2 = 20 mTorr).
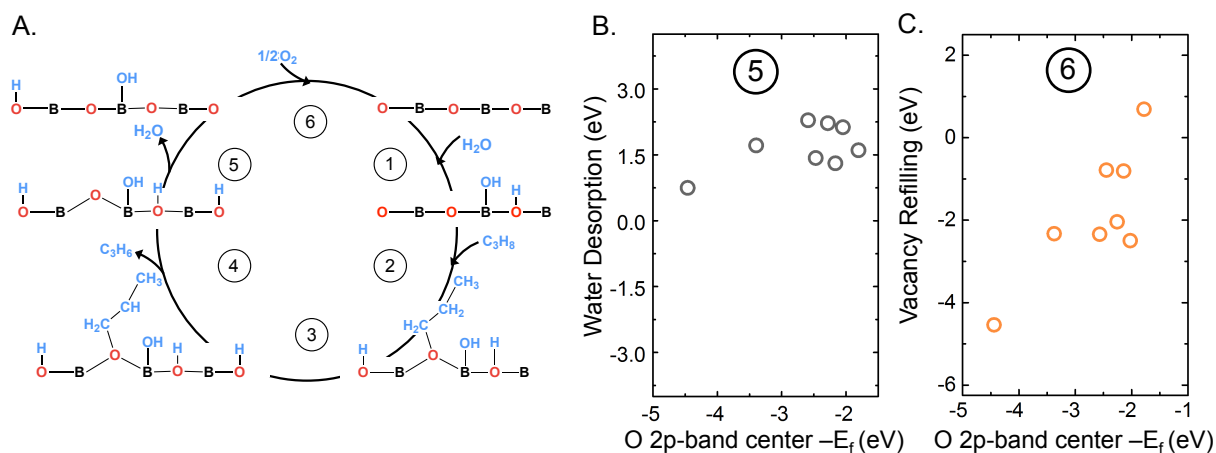
Figure A.5.6: Reaction mechanism for selective propene generation under wet conditions A) Proposed reaction mechanism for C_3H_8 selective oxidation to C_3H_6 occurring on the oxygen sites via terminal C-H bond scission with dissociative H_2O adsorption (Step 1), followed up C_3H_8 adsorption to form C_3H_7-O_{oxide} and O_{oxide}-H in the presence of dissociated water (Step 2), followed by dehydrogenation of C_3H_7-O_{oxide} to C_3H_6-O_{oxide} and O_{oxide}-H (Step 3) and desorption of C_3H_6-O_{oxide} as C_3H_6 (Step 4). Following desorption of C_3H_6, H_2O desorption occurs leading to oxygen vacancy formation (Step 5), and finally molecular oxygen re-adsorption to re-fill the oxygen vacancies to complete the reaction cycle (Step 6), Correlation between B) H_2O desorption energy from the O_{oxide}-H surface sites (black), C) oxygen vacancies re-filling energy (orange), as a function of the surface O $2p$-band center relative to the Fermi level. Data points were obtained from the AO and BO_2-terminated-(100) surface of ABO_3 (A = La, Sm; B = Cr, Co, Mn, Fe, Ni with respect to the AO and BO_2 surface, C_3H_8 and O_2 in the gas phase (T = 300 °C)
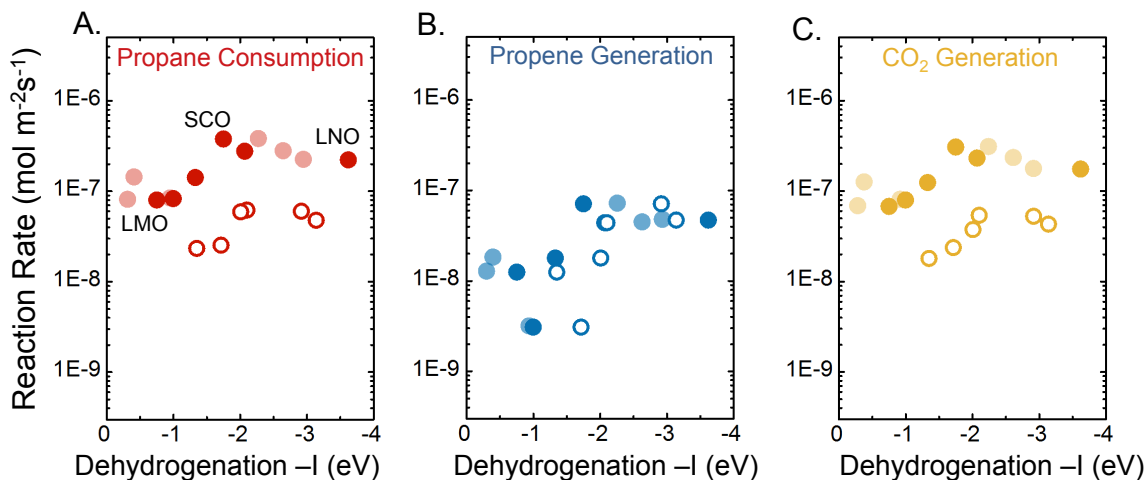
Figure A.5.7: Correlation between first dehydrogenation adsorption energy of C_3H_8 on the surface oxygen surface site and the reaction rate for A) propane consumption, B) propene formation, C) CO_2 formation under wet (un-filled) and dry conditions (filled). Data points were obtained from the BO_2-terminated-(100) surface of ABO_3 (A = La, Sm; B = Cr, Co, Mn, Fe, and Ni), calculated by DFT with the binding configurations C_3H_8 on the surface oxygen sites shown here with reference to C_3H_8 and O_2 in the gas phase (T = 300 °C)
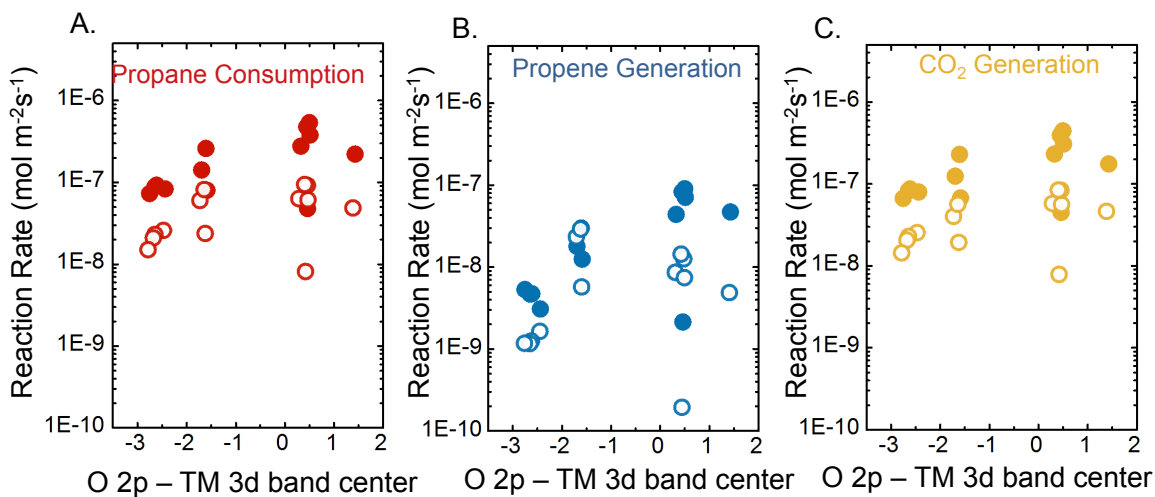

Figure A.5.8: Correlation between covalency, defined as the difference of the O $2p$ and TM $3d$ –band center, and the reaction rate for A) propane consumption, B) propene formation, C) CO_2 formation under wet (un-filled) and dry conditions (filled). Data points were obtained from the BO_2-terminated-(100) surface of ABO_3 (A = La, Sm; B = Cr, Co, Mn, Fe, and Ni), calculated by DFT with the binding configurations C_3H_8 on the surface oxygen sites shown here with reference to C_3H_8 and O_2 in the gas phase (T = 300 °C)
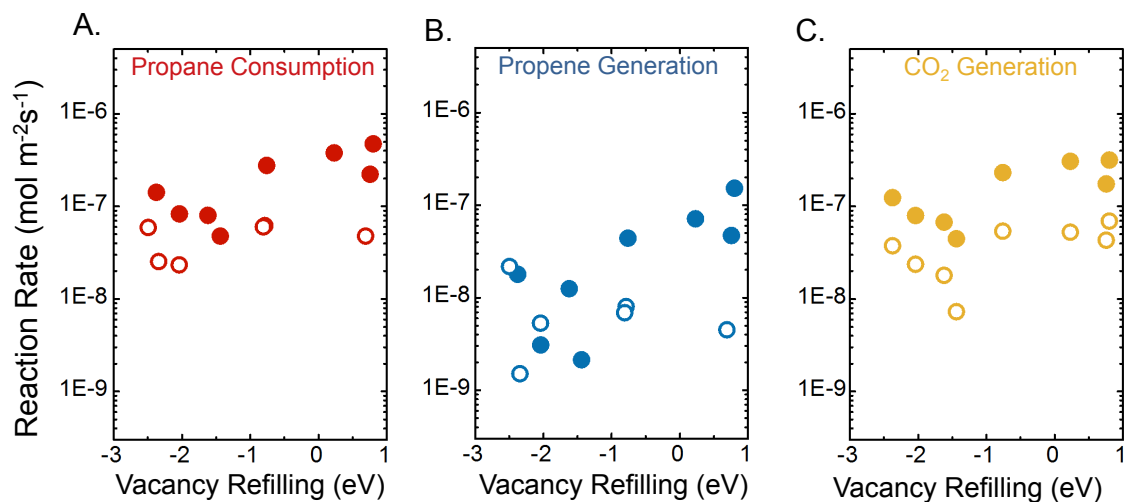
Figure A.5.9: Correlation between oxygen vacancy formation energy, and the reaction rate for A) propane consumption, B) propene formation, C) CO_2 formation under wet (un-filled) and dry conditions (filled). Data points were obtained from the BO_2-terminated (100) surface of ABO_3 (A = La, Sm; B = Cr, Co, Mn, Fe, and Ni), calculated by DFT with the binding configurations C_3H_8 on the surface oxygen sites shown here with reference to C_3H_8 and O_2 in the gas phase (T = 300 °C)
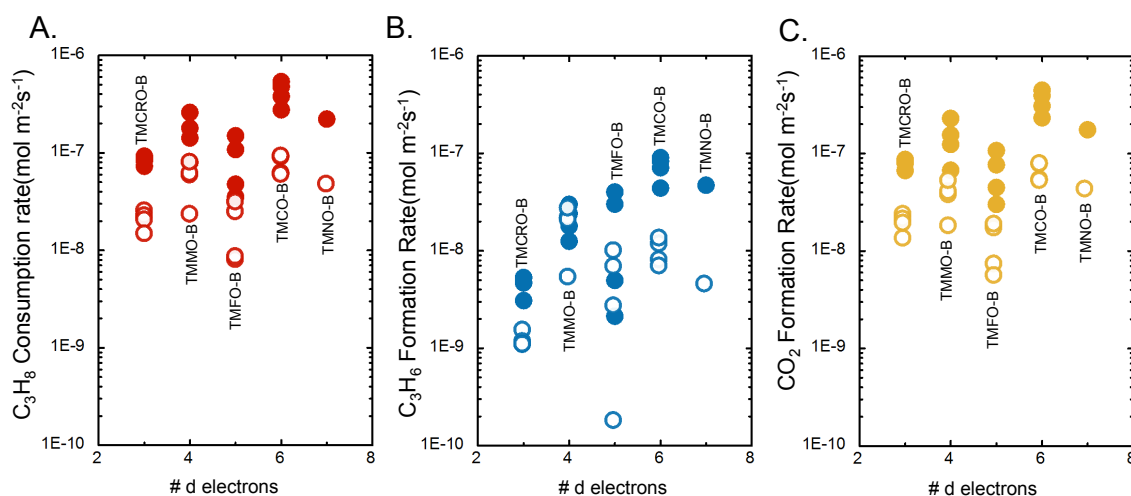

Figure A.5.10: Correlation between #d electrons of the TM, and the reaction rate for A) propane consumption, B) propene formation, C) CO_2 formation under wet (un-filled) and dry conditions (filled). Data points were obtained from the BO_2-terminated (100) surface of ABO_3 (A = La, Sm; B = Cr, Co, Mn, Fe, and Ni), calculated by DFT with the binding configurations C_3H_8 on the surface oxygen sites shown here with reference to C_3H_8 and O_2 in the gas phase (T = 300 °C)